



FACULDADE DE CIÊNCIAS UNIVERSIDADE DE LISBOA
DEPARTAMENTO DE FÍSICA

**From CP violation in
primordial baryogenesis to the role of
detector alignment in the
HERA-B spectrometer**

João Miguel Nobre Batista

Mestrado em Astronomia e Astrofísica

2005



FACULDADE DE CIÊNCIAS UNIVERSIDADE DE LISBOA
DEPARTAMENTO DE FÍSICA

From CP violation in primordial baryogenesis to the role of detector alignment in the HERA-B spectrometer

Dissertação submetida por

João Miguel Nobre Batista

como requisito parcial para a obtenção do grau de
Mestre de Astronomia e Astrofísica

Dissertação orientada por

Prof. Dr. António Joaquim Rosa Amorim Barbosa

Mestrado em Astronomia e Astrofísica

2005

From CP violation in primordial baryogenesis to the role of detector alignment in the HERA-B spectrometer

João Miguel Nobre Batista

Resumo

Um dos grandes desafios actuais para a Física de Partículas e para a Cosmologia é a explicação de uma constatação tão fundamental quanto importante: o Universo possui apenas matéria, ou pelo menos esta é bastante mais abundante que a anti-matéria. O objecto de estudo central das teorias de bariogénese é explicar a evolução de um Universo “vazio” e simétrico, para um estado “quase vazio” e ligeiramente assimétrico, com base no conhecimento daquelas duas áreas da Física.

Um requisito fundamental dos processos bariogénicos é a violação da conservação de simetria $\hat{C}\hat{P}$ em interacções de partículas fundamentais. A medição deste fenómeno em experiências de Física Experimental de Partículas, concebidas para o efeito, é difícil por duas importantes razões. Em primeiro lugar, as incertezas associadas à medição dos parâmetros que descrevem a violação de $\hat{C}\hat{P}$ são, geralmente elevadas, apesar da qualidade e rigor empregues na concepção, construção e operação dos detectores usados nessas experiências. Em segundo lugar, os eventos de interesse para o estudo do fenómeno são bastante raros. Para minimizar os erros de medição, é importante um bom conhecimento da resposta do detector. Nomeadamente, importa saber em que medida a deslocação de partes do detector influi na reconstrução dos eventos que servem de sinal.

A experiência HERA-*B* foi concebida para estudar a violação de $\hat{C}\hat{P}$ no decaimento de mesões B . O software de reconstrução de eventos em HERA-*B* foi usado para estimar a ordem de grandeza de deslocamentos do detector que influem na reconstrução de decaimentos $B^0/\bar{B}^0 \rightarrow J/\psi K_S^0$, os quais são um importante canal na medição de violação de $\hat{C}\hat{P}$. O foco deste trabalho é a reconstrução de trajectórias de partículas para diferentes disposições geométricas do detector de HERA-*B*, para eventos simulados daquele canal de decaimento. Foi também estudado um pequeno conjunto de eventos, simulados e medidos, para verificar os resultados da reconstrução.

PALAVRAS-CHAVE: Bariogénese primordial; violação de $\hat{C}\hat{P}$; experiência HERA-*B*; reconstrução de eventos.

From CP violation in primordial baryogenesis to the role of detector alignment in the HERA-B spectrometer

João Miguel Nobre Batista

Abstract

One of the current major challenges for Particle Physics and for Cosmology is explaining a realization as fundamental as it is important: the Universe has only matter, or at least it is much more abundant than anti-matter. The central subject of the theories of baryogenesis is explaining the evolution of a “empty” symmetric Universe, to an “nearly empty”, slightly asymmetric state, based on the knowledge of those two major bodies of Physics.

A fundamental requirement of baryogenic processes is the violation of conservation of $\hat{C}\hat{P}$ symmetry in the interactions of fundamental particles. Measuring this phenomenon in High Energy Physics experiments, created for this purpose, is difficult for two reasons. Firstly, the uncertainties associated to the $\hat{C}\hat{P}$ -violation parameters’ measurement are generally high, in spite of the quality and rigor employed in the conception, construction and operation of the detectors used in those experiments. Secondly, the events of interest for $\hat{C}\hat{P}$ -violation studies are quite rare. To minimize the measurement errors, it is important to have a sound knowledge of the detector response. Namely, it is important to know how the displacement of detector parts influences the reconstruction of signal events.

The HERA-*B* experiment was conceived to study $\hat{C}\hat{P}$ violation in *B* meson decays. The event reconstruction software of HERA-*B* was used to estimate the magnitude of detector displacements with influence on the reconstruction of $B^0/\bar{B}^0 \rightarrow J/\psi K_S^0$ decays, which are important channel of $\hat{C}\hat{P}$ violation measurements. The focus of the present work is the reconstruction of particle tracks for different alignment dispositions of the HERA-*B* detector, in simulated events of that decay channel. A small set of events, simulated and measured, was also studied, to check the reconstruction results.

KEYWORDS: Primordial baryogenesis; $\hat{C}\hat{P}$ violation; HERA-*B* experiment; event reconstruction.

Acknowledgements

The idea for this dissertation emerged after a report presented in a Nuclear Astrophysics course under the Master of Astronomy and Astrophysics at the Faculty of Sciences of the University of Lisbon. At the time I started to work on that report I was completely unaware of the extent and depth of the subject of primordial baryogenesis — and to this date I still feel I have a lot of catching-up to do. I was very surprised to see how it involves areas of Physics seemingly on diametrically opposite sides of the scale spectrum, namely Quantum Physics for the very small and Cosmology for the very large. After a slow start about 40 years ago, investigation in primordial baryogenesis has been steadily gaining momentum, which is apparent by the flowing number of work produced on this subject. The principal focus of it has been the investigation of different scenarios for baryogenesis, with each author using his/her favorite theories to try to reproduce the matter-to-radiation ratio measured from large-scale surveys of the Universe — at least within the order of magnitude. It is personally very exciting to see how it might be possible to explain how matter is created from a symmetric initial condition. There are many available scenarios for baryogenesis, each with their own Particle Physics and Cosmology models. To help decide which ones are best fit, it is imperative to obtain solid experimental data. This becomes more critical when attending that a significant portion of the baryogenesis scenarios involve energy scales many orders of magnitude above what is possible to get with present-day particle accelerators. If the significant baryogenic reactions did indeed occur far above the TeV energy scale, it is natural to expect that very-high precision Particle Physics and Cosmology measurements are required to discern between models manifesting small differences in a “cold” present-day Universe.

I take this opportunity to thank the many people that one way or the other contributed to ease the difficulties I stood through the work on this dissertation. The people left uncredited are so only because of the fleeting capacity of my memory, and not because of any lack of appreciation.

To Doctor Filipe Duarte Santos of the Faculty of Sciences of the University of Lisbon I owe the suggestion of the work which introduced me to primordial baryogenesis. From the same institution, I am indebted to Doctor António Amorim for the opportunity to initiate my work in Science and for the realization of how important it is to ask the right questions. I am always pleasantly surprised by how he finds the time to guide me amidst his many daily solicitations. It was also through Doctor Amorim that I met Doctor João Carvalho of the Department of Physics of the Faculty of Sciences of the University of Coimbra, to whom I owe the chance to work in HERA-*B* through its portuguese team. Doctor Carvalho offered precious

guidance on the occasions Doctor Amorim was unavailable. I thank Doctor João Bastos of LIP-Coimbra on the discussion of details of the HERA-*B* reconstruction software. I also thank Teresa, of the LIP facilities in Coimbra, for her patience in helping me keep up to date with my scholarship application duties.

At DESY, Patricia, “Dima” Goloubkov and Irina were very patient with my troubles in the first stages of fumbling with ARTE; I thank Dima for his humorous insights on that fine piece of software. To Patricia I also thank for not snapping out on my insisting questions, particularly during my last stays at Hamburg. I am indebted to Vasco Amaral for his generosity and guidance, particularly during my first stays. Alexander Lanyov and Boris Fominykh offered helpful discussion on Prism. I thank José Hernandez, Mauro Villa, Alan Schwartz and Sergej Vassiliev for their insight on various other subjects. I owe to Silvia Masciocchi and Maaijke Mevius for the physics events of 2002, that were invaluable to my work. During my stay for the 2001 DESY Summer Students program I also benefited from the guidance of Francesco Sciacca and Torsten Jagla, who taught me much about the VDS. I thank Iris Abt for the personalized tour of the VDS. To Daniel, Andrej, Samo, Steve, Dickson and Galia I thank for the good times at Hamburg.

To Sérgio, Tomé, Vasco Teixeira, Paula, Sofia, Carlos Marques and the rest of the FCUL’s M. Sc. in Astronomy and Astrophysics goes my thanks for their support and friendship. For the good times at lunch and coffee breaks I thank Jorge Lucas, Rui Barros, Rui Ferreira, Jorge Lima, Luis Pedro, “Carlitos”, Belmiro, Prof. António Melo, Luis Correia, Nuno, Lívia and Marta. To Luis Silva I thank the patience for always listening to my problems, for his precious suggestions and his friendship, and the privilege of venturing into HERA-*B* as first scientific endeavour. I look forward to work with him again if chance is so inclined.

To my sister, nephews and nieces for listening to my ramblings and wild ideas, even when they could not hide a look of deep puzzlement; fortunately, the youngests’ obliviousness to it all kept reminding me that there is also life away from Science. To my uncles and aunts, and to grandmother Alda, I thank the pleasant stories, family gatherings and encouragement.

Finding the right words to thank my parents is somewhat more difficult. Far from deserving it any less than others, the words I do know hardly seem adequate to express my deepest respect, gratitude and recognition. Too many times my faults have bitterly tested their love and care, which likely later in life I may come to fully understand how much it alleviates me. I earnestly hope the product of my work serves to strengthen their just expectations and faith in me.

João Batista
Setúbal, March 2005

Contents

List of Figures	IV
List of Tables	XVIII
1 Introduction	1
1.1 The discovery of anti-matter	1
1.2 Matter in our Universe	3
1.3 Purpose and overview of this dissertation	5
2 Primordial baryogenesis and $\hat{C}\hat{P}$ violation	7
2.1 Baryon asymmetry parameters	8
2.1.1 Baryon-to-photon ratio	8
2.1.2 The baryon-to-entropy ratio	11
2.2 The Sakharov conditions	12
2.2.1 The violation of the baryon number conservation	14
2.2.2 The violation of charge conjugation, parity and charge-parity symmetries	16
2.2.3 Departure from thermal equilibrium	19
2.3 An overview of $\hat{C}\hat{P}$ symmetry violation and of quark flavor mixing	21
2.3.1 The CKM quark-mixing matrix and $\hat{C}\hat{P}$ violating phase	21
2.3.2 The violation of the \hat{C} , \hat{P} and $\hat{C}\hat{P}$ symmetries	25
2.3.3 The <i>ansatz</i> : $\hat{C}\hat{P}$ violation in the neutral kaon system	27
2.3.4 $\hat{C}\hat{P}$ violation in the B^{neut} golden decay	28
2.4 Rounding-up: from the measurement of $\hat{C}\hat{P}$ asymmetry to baryogenesis	31
3 The HERA-<i>B</i> experiment	32
3.1 The HERA proton beam	32
3.2 The HERA- <i>B</i> detector	34
3.2.1 Internal target	38
3.2.2 Dipole magnet	41
3.2.3 Proton beam pipe at HERA- <i>B</i>	43
3.2.4 Silicon vertex detector	43
3.2.5 Inner tracker system	46
3.2.6 Outer tracker system	48
3.2.7 Ring imaging Čerenkov detector	50
3.2.8 Transition radiation detector	53

3.2.9	Electromagnetic calorimeter	54
3.2.10	Muon detection system	56
3.2.11	High- p_T trigger	58
3.3	Trigger system. Data acquisition system	60
3.3.1	Front-end drivers	62
3.3.2	Fast control system	63
3.3.3	Pretriggers	63
3.3.4	First level trigger	65
3.3.5	Second level trigger	69
3.3.6	Third level trigger	71
3.3.7	Fourth level trigger	72
3.3.8	Data acquisition system	73
3.4	The HERA- B databases	76
3.5	Event reconstruction chain	81
3.5.1	Monte Carlo simulation	82
3.5.2	Digitization of Monte Carlo events	84
3.5.3	Event reconstruction	84
3.6	ARTE table information	89
3.6.1	The PRISM event display	91
3.7	A summary of status and physics results at HERA- B	94
3.7.1	Run period of year 2000	95
3.7.2	Run period of 2002/2003	96
4	Single event analysis	99
4.1	Reconstruction and selection of Monte Carlo B^0 “golden decay” events	101
4.1.1	Description of the event sample	101
4.1.2	Selection of Monte Carlo golden decay events	104
4.2	Validation of selected Monte Carlo events	105
4.2.1	Event 235	108
4.2.2	Event 24	120
4.2.3	Remaining events	131
4.2.4	Conclusions	132
4.3	A sample of B decay candidates measured in HERA- B	136
4.3.1	The golden decay event candidate in run 20645	137
4.3.2	Two $B^+ \rightarrow J/\psi K^+$ candidate decays	142
4.3.3	Comparison with run selection from year 2000	143
4.4	Conclusions	143
5	Detector misalignment and single event reconstruction	147
5.1	VDS module displacements	148
5.1.1	Discussion	153
5.2	Displacements of the VDS, Main Tracker, RICH and Muon Detector systems	154
5.2.1	Discussion	154
5.3	Conclusions	155
6	Concluding remarks	160

A	Misalignment maps for one golden decay event	162
A.1	VDS module displacements	163
A.2	Displacements of VDS, Main Tracker, RICH and Muon detector . . .	180
B	Useful algebraic expressions	201
B.1	Minimum distance between two skewed lines	201
B.2	Distance of a point to a line	202
B.3	Momentum estimation in the HERA- <i>B</i> Main Tracker	202
B.4	Momentum determination of a charged track in a uniform magnetic field	204
B.5	Useful relations of relativistic kinematics	206
B.5.1	Lorentz transforms and center-of-mass energy	206
B.5.2	Rapidity and pseudo-rapidity	208
B.5.3	Feynman- x	209
B.5.4	Multiple scattering angle	209
B.6	Cross section and decay width	210
B.7	Dynamics of the B^0 - \bar{B}^0 meson system	211
C	Error propagation formulas	213
C.1	Error propagation of two-track invariant mass	214
C.2	Error propagation of minimum separation between two tracks	216
C.3	Error propagation of the track-to-vertex distance of closest approach	217
C.4	Error propagation of the coordinates of a two-track point of closest approach	218
D	ARTE KUIP macros	221
D.1	Monte Carlo kumac	221
D.2	Real data kumac	225
E	C source code	229
E.1	Impact parameters and invariant masses	229
E.2	Geometry misalignment	264
	Bibliography	267

List of Figures

1.1	One of the tree-level Feynman diagrams for the B_d^0 meson “golden” decay (1.2). The blobs represent the initial- and final-state particles. Their quarks (straight lines) are assumed unbound at decay, and hadronize at the final state.	6
2.1	Tree-level Feynman graphs for the decays of the X and Y heavy bosons.	19
2.2	One-loop corrections to X and Y decay.	19
2.3	Some interference terms between the diagrams 2.1 and 2.2 for the squared amplitudes of X decay. The vertical dotted line cutting through the fermion lines represents a unitary cut applied to them — it means the corresponding propagators are evaluated on mass shell.	19
2.4	Representation of the unitarity triangle (2.30) in the (ρ, η) plane of the CKM matrix’s Wolfenstein parameterization [108]. The vertices at $(0, 0)$ and $(1, 0)$ are fixed; the sides are normalized to $ V_{cd}V_{cb}^* \simeq \lambda V_{cb} $. The blob [131] depicts the 95% confidence level bound for the (ρ, η) triangle vertex, given present knowledge of $\sin 2\beta$ measurements.	24
3.1	The HERA (left) and PETRA (right) storage rings [131]. The proton beam circulates counter-clockwise. HERA- B is installed in the West Hall.	33
3.2	Periodic structure of the HERA proton beam [124]. Each PETRA fill contains six DESY III fills. The bunch crossing rate is 96ns, and each of them may (or not) be filled with protons; the latter correspond to empty bunches.	33
3.3	Top view of the HERA- B detector in the HERA west hall [108].	35
3.4	Isometric view of the HERA- B detector with the year 2001 configuration. The Magnet is cutout to show the High- p_T trigger chambers, described in section 3.2.11. The proton beam enter from the left side.	35
3.5	Schematic overview of the HERA- B detector in its 2002 configuration.	36
3.6	Overview of the HERA- B trigger levels, with design values for event rates, suppression and latency [154] [124].	38

- 3.7 Left: schematic view of the HERA-*B* target, consisting of eight wires mounted on independently movable forks, which group in two stations with a beam-wise separation $\Delta z \approx 5\text{cm}$ and move radially into the beam halo (transversing arrow). Adapted from [108]. Right: reconstructed vertices while all eight target wires are operated simultaneously at the beam [1]. 39
- 3.8 Left: Azimuthal angle distribution of charged particles emitted from fixed-target 920GeV proton-proton collisions, from 10^3 events generated with the PYTHIA Monte Carlo event generator [143]; the beam orientation corresponds to the angle 0 rad. Right: pseudo-rapidity coverage of the charged particles from the same events. The dash-filled histogram (red) corresponds to tracks within a conical trunk aperture equal to the VDS horizontal acceptance. The dash-filled (red) region is approximately 60% of the left histogram's area and corresponds to a conic aperture given by HERA-*B*'s Vertex Detector System (horizontal) geometric acceptance, $10\text{mrad} < \theta_h < 250\text{mrad}$. The unshaded regions $\theta < 10\text{mrad}$ and $\theta > 250\text{mrad}$ are occupied by, respectively, 25% and 15% of the particles. 41
- 3.9 The design of the HERA-*B* spectrometer magnet [83]. It consists of two iron poles, an iron flux return yoke and two cylindrical copper coils. In the topview, the proton beam entry window is to the right. 42
- 3.10 Schematization of a VDS module (far right) for superlayers SL5/6 (see fig. 3.13); the enveloping dotted line is the aluminium foil isolating the module from the beam vacuum [140]. The detector (middle views) sits on a support structure (far left). The module blocks are refrigerated to maintain a temperature around $+10^\circ\text{C}$ 44
- 3.11 Transversal cut of the VDS silicon wafer (courtesy of Klaus Ehret). A thin layer of p-type semiconductor ("p-comp") serves as insulator for the n-type strips, allowing its capacitative coupling to the readout aluminium strips. 44
- 3.12 Four VDS modules and their caps arranged in one superlayer [108]. The aluminium foils that cover the caps are not shown. 44
- 3.13 Left: The VDS vessel (left) [38] contains the target system and silicon strip detectors. The superlayers SL1 through SL7 are steered into the beam halo inside the roman pots. The eighth superlayer, SL8, is placed outside the vessel, right after the exit window (far left). Right: The eight silicon superlayers [99]. The detached plane (409) is a set of two back-to-back modules; their strip orientations form angles of $\pm 90^\circ \pm 2.5^\circ$ with the HERA-*B* *xy* plane orientation. The target system (not shown) is in front of SL1. 44
- 3.14 Left: illustration of the MSGC chamber with GEM technique [131]. Right: view of the sensitive areas of four MSGCs surrounding the proton beam [140]. The covered area is about $40 \times 40\text{cm}^2$; two layers (0° and $+5^\circ$) are shown. 47
- 3.15 Spacial view of the OTR modules, with upper right quadrant cutout for visibility [121]. The layers MC2-MC8 were removed for the 2002/2003 running period due to large production of bremsstrahlung [98]. 48

3.16	Left: the honeycomb structure of OTR drift chambers [131]. Right: downstream perspective of the sections in superlayer TC02 [83]. . . .	49
3.17	Left: schematic side view of the HERA- <i>B</i> RICH detector [129]. The HERA- <i>B</i> target is to its right. Right: example of the observed RICH hits in an inelastic event. The Čerenkov photons, caused by charged tracks with $v > c/n$, are focused into the planar mirrors by the RICH's spherical mirror array, and the detected photon hits are projected as a circle with apperture related to the particle's Čerenkov angle.	50
3.18	At left and at center: molecular dipole distribution in dielectric medium caused by the passage of a low- and a high-velocity charged particle, respectively [129]. On the right: the Čerenkov wave front construction by superposition of elementary spherical waves produced by a $v > c/n$ charged particle along its trajectory.	51
3.19	Left: isometric view of the Transition Radiation tracker (left). The darkened cylinder crossing the TRD layers represents the proton beam direction. Right: transversal section of a TRD block [108] [83].	54
3.20	Left: the "shashlik" structure of one ECAL module [108], showing the 5×5 photomultiplier tube (PMT) array of a outer ECAL module with their wavelength shifter (WLS) fibers. Right: schematic back (downstream) view of the ECAL regions [131]. The granularity grows towards the center. The central and lower right holes make room for the proton and electron beam pipes, respectively. The structure is enclosed by a support frame.	55
3.21	The four tracking stations of the Muon detector system and the concrete absorbers separating them [131]. Stations MU03 and MU04 are only separated by about 5cm of iron.	57
3.22	Cross section views of the Muon detector elements [131]. The tube chambers form double layers in MU01 and MU02. The pad chambers also form double layers in MU03 and MU04, with cathode planes between the two layers. The pixel chambers are the detector elements in the region closer to the proton beam. The proton beam direction (not shown) is transversal for the tube and pad schematics (left and center), and along the sensing and potencial wires in the pixel chamber representation (right).	57
3.23	The high- p_T straw tubes superlayer layout [83]; all dimensions are given in mm. The four pixel chambers modules at the center slightly overlap. There is room for the proton beam pipe crossing at the center.	59
3.24	Sketch of the pad coincidence combinations in the High- p_T superlayers PT1, PT2 and PT3 [83]. A trigger road which contains at least one of the dark-shaded cells, in each and all superlayers, elicits a positive trigger response. This logical AND coincidence scheme produces almost 100% efficiency for $B^0 \rightarrow \pi^+\pi^-$ decays [83].	59
3.25	The cross section dependence of b and c quark production in pN collisions at beam energy E_b [64]. The HERA- <i>B</i> $c\bar{c}$ production cross section is $\sigma(c\bar{c}) = 124 \pm 34_{-24}^{+21} \mu\text{b}$ per nucleon [76].	62

3.26	Illustration of the conditions that must be fulfilled in order to initiate a pretrigger in ECAL (a), in the two rearmost muon superlayers (b), or in the high- p_T chambers (c). For (a) the smallest unit shown is a calorimeter cell, for (b) and (c) is a pad [140].	64
3.27	Track finding procedure at the FLT for high- p_T triggers (top) and electron triggers (bottom) [83]. The figure is not to scale (even relatively).	66
3.28	Overview of the FLT network [124]. The data flow within the network is twofold: on one hand, hit data (represented by arrows pointing from the detector layers) are sent through optical fibers from the FEDs to the TFUs; on the other hand, the track candidate data are transported through each superlayer's TFUs to the TPUs and finally the TDU. The High- p_T pretrigger is not shown in the figure. The Regions of Interest (RoIs) are represented by the grey triangles envolving the tracks between consecutive detector layers.	68
3.29	Schematic representation of one FLT Track Finding Unit [1].	69
3.30	Overview of the SHARC cluster board, which carries six Analog Devices ADSP21060 SHARC TM processors that share a 160MB/s on-board memory global bus [1].	70
3.31	HERA- <i>B</i> Data Acquisition system scheme and correspondence to the HERA- <i>B</i> trigger levels [1].	74
3.32	Sketch of the online distribution of Calibration and Alignment (CnA) constants [1].	74
3.33	The distribution of Calibration and Alignment constants in the HERA- <i>B</i> trigger system [16]. The gatherer process — which belongs to the Data Quality system — subscribes the online databases. The new information on these servers is tagged and registered in the “key” table database server. The C&A Manager synchronizes the distribution of the updated constants. It requests the Event Controller (EVC) to pause the run and the involved formatters to build and distribute the updated constants to the trigger processes. Once the distribution is concluded successfully the EVC is contacted again to resume the run. The 4LT processes retrieve the new constants from fast memory database caches when events with the new key arrive to the farm.	78
3.34	Simplified sketch of the association of events to Calibration and Alignment constants [13]. The indexed events identify the set of calibration and alignment constants; when either of these change, a new index is generated and the new events are tagged with the new key.	78
3.35	The general architecture of the HERA- <i>B</i> Database system [16] runs under the DAQ server infrastructure. Each “folder” represents a tier, where machine-independent data blobs are transported, with an attached key describing the table name and version to be accessed within the Database.	80
3.36	Main processes in the software analysis chain [108]. The TRD was not used in the 2000 and 2002 runs, therefore its information is excluded from Real Data event reconstruction.	83

3.37	Comparison of the Real Data and the Monte Carlo event processing chains in HERA- <i>B</i> [90].	83
3.38	A simple illustration of the segment model: segments connect hits across one or two layers [8]. The filled dots are cells that represent hits defining a good track candidate; the void cells are excluded from the two tracks found in this example.	86
3.39	The operation diagram of the discrete Kalman filter [56].	87
3.40	Main ARTE tables, used for event reconstruction [103]. Table information is read/stored from top to bottom. In simulated events, tables HITB and HITC (not shown) are filled by hits generated by the HBGEAN package. Except for the geometry tables and table TOPP, the information stored in the remaining tables has the validity of one event.	90
3.41	The relations of particle properties data (left) and Monte Carlo particles data (right) to geometry configuration objects [103].	90
3.42	PRISM representation of the HERA- <i>B</i> detector. The axes' scale is in centimeters. Top: <i>zx</i> plane. The pink circle represents the Magnet boundaries. Bottom: <i>zy</i> plane.	92
3.43	Top: PRISM representation of a 3D view of one Monte Carlo event in HERA- <i>B</i> . MTRAs are drawn in red, RTRAs in blue, the black "blobs" are MIMPs, vertical green segments in the OTR and MUON represent HITBs. The insensitive materials ("walls" [111]) are not shown. The close-ups of the Target and first three superlayers of the VDS (bottom left) and of a superlayer of the Outer Tracker TC02 layer (bottom right) show the graphic elements detailed in the text.	93
3.44	The integrated number of reconstructed J/ψ as a function of time indicates the performance of the dilepton trigger [73] [139]. In the regions of small increments, either minimum bias data was taken (December 2002) or no beam was available for HERA- <i>B</i>	97
4.1	In gluon-fusion events (4.1), a gluon pair g', g'' from each parton in a proton-nucleon collision creates a $b\bar{b}$ pair, which may hadronize as a B^0-B^- pair (or the flavour-symmetric pair \bar{B}^0-B^+). At HERA- <i>B</i> CMS energy, one possible decay channel for the B^0 is the "golden decay" (see figure 1.1). The remaining partons produce hadron jets.	101
4.2	Contour histogram of Kalman χ^2 probability (vertical axis; see text) versus longitudinal coordinate of RVERs in DST 22 (horizontal axis). The good quality tracks (high probability) accumulate within the wire boundary (vertical lines) whereas low-quality tracks spread outside the boundaries.	102
4.3	The fraction of primary vertices (DST 22) falling within the target wire longitudinal boundaries is at the 60% level. Gaussian fits are shown for the primary vertex entries (thick continuous line) and the vertices within the target wire's Z boundaries (dashed line).	102
4.4	Effect of the rejection of low- p_T RTRAs on the invariant mass of RVERs built from two tracks (run 20838, with 6750 events, see text). The K^0 mass signal vanishes for $p_T > 0.4\text{GeV}/c$. The mass signal at the J/ψ mass ($3.1\text{GeV}/c^2$) was searched in MC $gg \rightarrow b\bar{b} \rightarrow J/\psi(ee)X$ events, but not found.	103

4.5	Kalman χ^2 probability for 2-track RVERs (obtained from ARTE) versus the distance of closest approach between the two RTRAs, for an invariant mass range of $3.1 \pm 0.4\text{GeV}/c^2$ of the RVER.	103
4.6	Momentum distribution of Monte Carlo charged tracks (MTRAs, red) and reconstructed tracks (RTRAs, blue). The MTRA and RTRA momentum histograms meet at $8\text{GeV}-9\text{GeV}$. No RTRAs are built for $p < 0.3\text{GeV}/c$, which excludes $\sim 68\%$ of MTRAs; $\sim 0.57\%$ of RTRAs have $p \geq 920\text{GeV}/c$	104
4.7	Number of long-lived charged MTRAs in a 500-event Monte Carlo sample, from DST file <code>run05_00055_0022.dst</code> for $gg \rightarrow b\bar{b} \rightarrow J/\psi(\mu^+\mu^-)+X$ events (see text).	106
4.8	PRISM representation of the event 235 in the zx plane. All of the 676 MTRAs from the $b\bar{b}$ hadron shower and spectator event are shown — charged particles (continuous lines), photons (dashed), and other neutral (dotted).	110
4.9	PRISM representation of the event 235 in the zx plane. Top: B^0 golden decay MTRAs. The dotted V track at the RICH is a backscattered $p \simeq 0.2\text{GeV}$ neutron. Bottom: superimposition of B^0 MTRAs and all event's RTRAs. Most RTRAs are not drawn beyond the ECAL plane, since most particles are scatter and decay at the iron absorber blocks in front of the Muon detector (not shown).	111
4.10	Same as figure 4.9, but on the zy plane.	112
4.11	Top: reconstructed ECAL clusters (RCCLs) for Monte Carlo event 235. The Monte Carlo Impact Points (MIMPs) are omitted for clarity. The MTRAs originate from the B^0 golden decay. Bottom: representation of RICH hits (green) and reconstructed rings (blue). The (φ, λ) coordinates represent the angle (in miliradians) relative to the target region, in the zx and zy planes respectively.	113
4.12	PRISM 3D views of the golden decay MTRAs and the four RVERs found by ARTE in this event. The RVERs have their RTRAs extended to them. Top: the target and first three VDS superlayers are shown. MIMPs are drawn as black dots, HITBs as green segments. Bottom: magnified view of the target region. The RVERs are drawn as ellipsoids. The dotted red line represent the B^0 MTRA.	114
4.13	The tagging B meson decay in event 235 — PRISM representation in the zx plane. Particle name tags and MTRAs of the remainder of the event were omitted for clarity. Bottom: all the event's RTRAs are superimposed with the B decay MTRAs (neutral MTRAs were omitted).	115
4.14	Views similar to those of figure 4.13 are shown for event 235, but this time in a projection on the zy plane.	116
4.15	The tagging B meson decay in event 235 — PRISM representation of the ECAL. Particle name tags and neutral MTRAs were omitted for clarity. Top: the reconstructed clusters (RCCLs) are presented for comparison with the decay's Monte Carlo. Bottom: detail of the inner ECAL region.	117

-
- 4.16 PRISM representation of the event 24 in the zx plane. All of the event's 878 MTRAs from the $b\bar{b}$ hadron shower and spectator event are shown — charged particles (continuous lines), photons (dashed), and other neutral (dotted). 121
- 4.17 PRISM representation of the event 24 in the zx plane. Top: B^0 golden decay MTRAs. The dotted V track at the RICH is a backscattered $p \simeq 0.2\text{GeV}$ neutron. Bottom: superimposition of B^0 MTRAs and all event's RTRAs. Most RTRAs are not drawn beyond the ECAL plane, since most particles are scatter and decay at the iron absorber blocks in front of the Muon detector (not shown). 122
- 4.18 Same as figure 4.17, but on the zy plane. 123
- 4.19 Top: reconstructed ECAL clusters (RCCLs) for Monte Carlo event 24. The Monte Carlo Impact Points (MIMPs) are omitted for clarity. The MTRAs originate from the B^0 golden decay. Bottom: representation of RICH hits (green) and reconstructed rings (blue). The (φ, λ) coordinates represent the angle (in miliradians) relative to the target region, in the zx and zy planes respectively. 124
- 4.20 PRISM 3D views of the golden decay MTRAs and the four RVERs found by ARTE in this event. The RVERs have their RTRAs extended to them. Top: the target and first three VDS superlayers are shown. MIMPs are drawn as black dots, HITBs as green segments. Bottom: magnified view of the target region. The RVERs are drawn as ellipsoids. The dotted red line represent the B^0 MTRA. 125
- 4.21 The tagging B meson decay in event 24 — PRISM representation in the zx plane. Particle name tags and MTRAs of the remainder of the event were omitted for clarity. Bottom: all the event's RTRAs are superimposed with the B decay MTRAs (neutral MTRAs were omitted). 126
- 4.22 Views similar to those of figure 4.21 are shown for event 24, but this time in a projection on the zy plane. 127
- 4.23 The tagging B meson decay in event 24 — PRISM representation of the ECAL. Particle name tags and neutral MTRAs were omitted for clarity. Top: the reconstructed clusters (RCCLs) are presented for comparison with the decay's Monte Carlo. Bottom: detail of the inner ECAL region. 128
- 4.24 Left: ratio of muon RTRA momentum to MTRA momentum, for muons from the J/ψ decay. Right: Ratio of transverse momenta p_T of RTRA muons (from the dimuons selected for the Monte Carlo event sample) to the p_T of the corresponding MTRAs. The p_T errors are negligible — below the percent level. 133
- 4.25 Left: Transverse momentum of the RTRAs selected for charge tag in each event. Right: Kalman χ^2 probability of RTRAs selected by the PI tool as relevant for the golden decay identification — muons (filled bars, blue and red), pions (shaded bars, cyan and orange) and tagging RTRA (vertical fill bars, green). 133

- 4.26 Reconstructed masses of the dimuon (blue circles), dipion (red squares) and $\mu\mu\pi\pi$ (black losangles). Notice that only event 235 has all three masses near the respective nominal values for the J/ψ (dashed blue line, center), K^{neutr} (dash-dot red line, bottom) and B^{neutr} (dotted line, near top). 134
- 4.27 Distance of closest approach for the dimuon, dipion and $\mu\mu\pi\pi$ sets. For event 235 all three distances are below $200\mu\text{m}$ (see figure 4.5). . . 134
- 4.28 Longitudinal separation of the J/ψ vertex to the center of the target wire (left) and to the primary RVER (right). Events 131, 174 and 235 are viable candidates for a “detached vertex” flag. 135
- 4.29 Contour histogram of the vertex coordinates in the zx plane, from primary vertices in DST 22, with 501 events (see text). Figure 4.3 is the contour’s projection in z . The seven Monte Carlo events here analysed have primary vertices reconstructed close or within the target wire; the black square markers represent their median positions in the zx plane. The thick dashed line represents the target wire boundary projected in the zx plane. Note axes’ scales are not equal. 135
- 4.30 Top: zx projection of event 1528001531 in run 20645, displayed by PRISM. The measure scale is in centimeters. The two muons RTRAs used to reconstruct the J/ψ decay are seen transversing the Muon detector. Bottom: 3D detail (almost a projection in the zx plane) of the target wire and of the two reconstructed vertices (RVERs) in the same run, see table 4.18. The y direction points to the top, the proton beam is directed from left to right. The 1σ variance ellipsoid of the primary vertex intersects the inner II target (large rectangle) used in this run. The RTRAs associated with the reconstructed vertices were drawn into them. The two extrapolated muon RTRAs meet at the J/ψ RVER (rightmost ellipsoid). 140
- 4.31 The hypotheses for $B^{\text{neutr}} \rightarrow J/\psi(\mu^+\mu^-)K^{\text{neutr}}(\pi^+\pi^-)$ and $B^\pm \rightarrow J/\psi(\mu^+\mu^-)K^\pm$ were tested with PI. The event from run 20545 has a good $\mu^+\mu^-K^\pm$ invariant mass combination near the B mass, whereas for the event in run 20639 the $\mu\mu K$ combination (filled square) is favoured when compared to the $\mu\mu\pi\pi$ (open losangle). The event from run 20645 is shown on the right for comparison. 143
- 4.32 Invariant mass of RTRA sets for the golden decay hypothesis, $B_d^{\text{neutr}} \rightarrow J/\psi(\mu^+\mu^-)K_S^0(\pi^+\pi^-)$ from the event sample in table 4.15. Values computed with PI. 144
- 4.33 Distance of closest approach (DCA) of RTRA sets for the golden decay hypothesis, $B_d^{\text{neutr}} \rightarrow J/\psi(\mu^+\mu^-)K_S^0(\pi^+\pi^-)$ from the event sample in table 4.15. Values computed with PI. 144
- 4.34 Invariant mass of RTRA sets for the $B^\pm \rightarrow J/\psi(\mu^+\mu^-)K^\pm$ decay hypothesis, from the event sample in table 4.15. Values computed with PI. 145
- 4.35 DCA of RTRA sets for the $B^\pm \rightarrow J/\psi(\mu^+\mu^-)K^\pm$ decay hypothesis, from the event sample in table 4.15. Values computed with PI. . . . 145

-
- 5.1 The dimuon RTRAs in event 235 (section 4.2.1), seen in 3D perspective from the outer radius of HERA. Only the VDS modules (rectangles) and Target (far left) are shown; the proton beam passes through from left to right. The remainder of the dimuon RTRAs includes segments from the Main Tracker and Muon detector (not shown), which are matched by ARTE. 149
- 5.2 PRISM XY projection of the VDS modules (rectangles) and target wires (vertical and horizontal blue segments, center). The reconstructed VDS hits are shown as black dots. The dimuon RTRAs are also painted, see figure 5.1. The axes' scales are in centimeters. . . . 149
- 5.3 The dimuon RTRAs (figure 5.1) were detected by VDS modules of superlayers 4–6. The “inner”, “outer” and “below” quadrant labels refer to the VDS modules' positions. Horizontal axis: VDS modules' longitudinal coordinate. The vertical bands are bounds for the respective modules' position. Vertical axis: module index number. . . 149
- 5.4 Invariant mass of RTRA pair identified with the dimuon from the J/ψ decay, for translations of VDS modules in the z direction (measured in the vertical axis); see figure A.5 for similar plots for translations in x and y . The mass was computed from RTRA parameters with PI (see section E.1). The horizontal axis refers to the modules' z position ($Z_{\text{VDS module}}$) according to table GEDE (i.e. in the absence of translation); see figure 5.3. Only the VDS modules with dimuon hits were analysed. The histogram bin size is $0.5\text{cm} \times 0.1\text{cm}$. The inset shows only displacements $|\Delta z| < 0.6\text{cm}$. See the discussion on main text (page 147) concerning the “dashed” plot structure for $1\text{cm} < |\Delta z| < 2\text{cm}$ 150
- 5.5 Dimuon invariant mass (in GeV/c^2) for displacements of the VDS modules with the J/ψ 's dimuon reconstructed hits, in the z (+), x (Δ) and y (\diamond) directions. The nominal value of the J/ψ mass is marked by a horizontal dashed line near $3.1\text{GeV}/c^2$. The marks for Δz displacements represent a projection of the histogram in figure 5.4 along its yy axis; the other two marks sets are for their respective displacements (see histograms in figure A.5). The error bars represent the root mean square of the values in each yy bin for the corresponding module translations Δz , Δx , Δy . The inset plot is a detail for $|\Delta z| < 0.6\text{cm}$ (boxed square in the main plot). 150
- 5.6 Histogram similar to the one shown in figure 5.4, but here for the minimum separation (measured in μm) between the μ^+ and μ^- RTRAs from the J/ψ dimuon. Notice the color scale is logarithmic. See figure A.7 for the results of VDS module displacements in x and y . The minimum separation was computed with PI from RTRA information. 151
- 5.7 Plot similar to figure 5.5, but representing the $\mu^+-\mu^-$ minimum separation (measured in μm), for Δ displacements of the VDS modules with J/ψ dimuon hits. The inset plot is for displacements $|\Delta_i| < 0.6\text{cm}$ (dashed rectangle in the main plot). 151

- 5.8 Histogram similar to the one shown in figure 5.4, but here for the $\mu\mu\pi\pi$ mass (measured in GeV/c^2) from RTRA information. The inset plot is for displacements $|\Delta z| < 0.6\text{cm}$. See figure A.19 for the results of VDS module displacements in x and y . The $\mu\mu\pi\pi$ mass was computed with the PI tool from the four RTRAs' information. 152
- 5.9 Plot similar to figure 5.5, but representing the $\mu\mu\pi\pi$ mass (in GeV/c^2) from RTRA table data, for *Delta* displacements of the VDS modules with J/ψ dimuon hits. The inset plot is for displacements $|\Delta_i| < 0.6\text{cm}$ (dashed rectangle in the main plot). 152
- 5.10 Histogram similar to the one shown in figure 5.4, but here for the $B^{\text{neutr.}}$ flavour from the reconstructed golden decay for z displacements of the VDS modules with J/ψ RTRA dimuon hits. The inset is for displacements $|\Delta z| < 0.6\text{cm}$. See figure A.32 for the results of VDS module displacements in x and y . The result was obtained from computation with the PI tool. 153
- 5.11 The whole VDS system is displaced in the z , x and y directions, by amounts given in the horizontal axis. The J/ψ 's dimuon mass remains mostly within the range of the nominal value (dashed horizontal line), except for a few displacements in the x direction. The inset is for displacements $|\Delta_i| < 0.6\text{cm}$. Computed from RTRA values with PI. See figure A.37 for the results of translations of the Main Tracker, RICH and Muon Detector systems. 156
- 5.12 Plot similar to figure 5.11, but representing the $\mu^+\mu^-\pi^+\pi^-$ invariant mass in GeV/c^2 . Contrary to figure 5.11, there is visible withdrawal from the nominal value (horizontal dashed line) for displacements from 0.2cm–0.3cm in the z and x directions; variations for detector displacements in the y direction are only sensible in the centimeter scale. The inset plot is for displacements $|\Delta_i| < 0.6\text{cm}$ (dashed rectangle in the main plot). The mass values were computed from RTRA values with PI. See figure A.51 for results on Main Tracker, RICH and Muon Detector systems. 156
- 5.13 Plot similar to figure 5.11, but representing the J/ψ 's dimuon minimum separation (in μm). The inset plot is for displacements $|\Delta_i| < 0.6\text{cm}$ (dashed rectangle in the main plot). See figure A.39 for results on Main Tracker, RICH and Muon Detector systems. 157
- 5.14 Plot similar to figure 5.11, but representing the J/ψ 's dimuon longitudinal coordinate $z_{\mu\mu}$ (in cm). The target wire's bounds are represented by the horizontal gray band. The inset plot is for displacements $|\Delta_i| < 0.6\text{cm}$ (dashed rectangle in the main plot). The $z_{\mu\mu}$ quantity was computed with PI. See figure A.40 for results on Main Tracker, RICH and Muon Detector systems. 157
- 5.15 Plot similar to figure 5.11, but representing the $\mu\mu\pi\pi$ longitudinal coordinate $z_{\mu\mu\pi\pi}$ (in μm), computed with PI. The target wire's bounds are represented by the horizontal gray band. The inset plot is for displacements $|\Delta_i| < 0.6\text{cm}$ (dashed rectangle in the main plot). See figure A.54 for results on Main Tracker, RICH and Muon Detector systems. 158

5.16	Plot similar to figure 5.11, but representing the golden decay B meson flavour under VDS displacements Δ , obtained from the charge tag of the highest- p_T RTRA. The rectangles on top are for \bar{B}^0 flavour tags, and the rectangles on bottom for B^0 ; the rectangles in the middle of the plot are for untagged reconstructions. The color scale is for the number of histogram counts in the 0.1cm-wide bins of the horizontal axis. See figures A.67, A.69 and A.71 for results on Main Tracker, RICH and Muon Detector systems, respectively. . . .	158
A.1	Number of reconstructed tracks in event (ARTE) for VDS module displacements in Z (topmost), X (next) and Y (next-to-last). The bottommost histogram is a vertical axis projections of the first three histograms. Insets are for displacements $ \Delta_i < 600\mu\text{m}$	164
A.2	Number of reconstructed vertices in event (ARTE) for VDS module displacements in Z (topmost), X and Y . The bottommost histogram is a projection of the first three histograms in the vertical axis (Δ_i). Insets are for displacements $ \Delta_i < 600\mu\text{m}$	164
A.3	Number of degrees of freedom for μ^+ RTRA (ARTE).	165
A.4	Number of degrees of freedom for μ^- RTRA (ARTE).	165
A.5	Dimuon mass for VDS module displacements (horizontal axes) in different directions (vertical axes) — Z (top), X (middle) and Y (bottom). The insets are for displacements below $600\mu\text{m}$. Masses were computed with PI.	166
A.6	RVER 2 mass for VDS module displacements (horizontal axes) in different directions (vertical axes) — Z (top), X (middle) and Y (bottom). The insets are for displacements below $600\mu\text{m}$. Masses obtained from ARTE table RVER.	166
A.7	Minimum separation (in micrometers) between the μ^\pm RTRAs. . . .	167
A.8	Vertex longitudinal coordinate (in centimeters) of the dimuon, $z_{\mu\mu}$. . .	167
A.9	Longitudinal separation (in centimeters) between the dimuon and the $\mu\mu\pi\pi$ (PI).	168
A.10	Longitudinal separation (in centimeters) between the dimuon (PI) and the RVER 2 (ARTE).	168
A.11	D.C.A. (in micrometers) of μ^+ to RVER 1. Computed with PI. . . .	169
A.12	D.C.A. (in micrometers) of μ^- to RVER 1. Computed with PI. . . .	169
A.13	Impact parameter (in micrometers) of μ^+ to target wire. Computed with PI.	170
A.14	Impact parameter (in micrometers) of μ^- to target wire. Computed with PI.	170
A.15	D.C.A. (in micrometers) of dimuon to RVER 1. Computed with PI. . .	171
A.16	Impact parameter (in micrometers) of dimuon to target wire. Computed with PI.	171
A.17	Number of degrees of freedom for RVER 1 (ARTE).	172
A.18	Number of degrees of freedom for RVER 2 (ARTE).	172
A.19	$\mu\mu\pi\pi$ mass (computed with PI) for VDS module displacements in Z (top), X (middle) and Y (bottom).	173
A.20	RVER 1 mass (from ARTE) for VDS module displacements in Z (top), X (middle) and Y (bottom).	173

A.21	Minimum separation (in micrometers) between the dimuon and the dipion. Computed with PI.	174
A.22	Vertex longitudinal coordinate (in centimeters) of the $\mu\mu\pi\pi$. Computed with PI.	174
A.23	Longitudinal separation (in centimeters) of the $\mu\mu\pi\pi$ (PI) and the RVER 1 (ARTE).	175
A.24	Longitudinal separation (in centimeters) of the RVER 2 to the RVER 1 (ARTE).	175
A.25	RVER 1 longitudinal coordinate (ARTE).	176
A.26	RVER 2 longitudinal coordinate (ARTE).	176
A.27	$q \times p_T$ (in GeV/c) of RTRA selected (PI) for B flavour tag. The charge $q = \pm 1$ is the sign of deflection (in the zx projection) of RTRA inside the Magnet. The gap in the color scale corresponds to the cut $p_T > 0.3\text{GeV}/c$ applied.	177
A.28	Impact parameter (in micrometers) of the tagging RTRA. Computed with PI.	177
A.29	D.C.A. of tagging RTRA to RVER 1. Computed with PI.	178
A.30	D.C.A. of tagging RTRA to RVER 2. Computed with PI.	178
A.31	Impact parameter (in micrometers) of $\mu\mu\pi\pi$ to RVER 1. Computed with PI.	179
A.32	Golden decay B meson flavour, obtained with charge tag from highest- p_T RTRA (ARTE).	179
A.33	Number of RTRAs in event for displacements of detectors along three orthogonal axes. From top to bottom: VDS, Main Tracker (ITR+OTR), RICH and Muon detector.	181
A.34	Number of RVERs in event for displacements of detectors along three orthogonal axes. From top to bottom: VDS, Main Tracker (ITR+OTR), RICH and Muon detector.	181
A.35	Number of degrees of freedom for μ^+ RTRA (ARTE).	182
A.36	Number of degrees of freedom for μ^- RTRA (ARTE).	182
A.37	Dimuon mass for Z, X, Y displacements (horizontal axes). From top to bottom: VDS; Main Tracker; RICH; and Muon detector displacements. The insets are for $ \Delta_i < 200\mu\text{m}$. The masses were computed with PI.	183
A.38	RVER 2 mass for Z, X, Y displacements (horizontal axes). From top to bottom: VDS, Main Tracker, RICH, and Muon detector displacements. The insets are for $ \Delta_i < 200\mu\text{m}$. The masses were obtained from ARTE table RVER.	183
A.39	Minimum separation (in micrometers) between the μ^\pm RTRAs.	184
A.40	Vertex longitudinal coordinate (in centimeters) of the dimuon, $z_{\mu\mu}$. The horizontal band represents the longitudinal bounds of the target wire.	184
A.41	Longitudinal separation (in centimeters) between the dimuon and the $\mu\mu\pi\pi$ (PI).	185
A.42	Longitudinal separation (in centimeters) between the dimuon (PI) and the RVER 2 (ARTE).	185
A.43	D.C.A. (in micrometers) of μ^+ to RVER 1. Computed with PI.	186
A.44	D.C.A. (in micrometers) of μ^- to RVER 1. Computed with PI.	186

A.45 Impact parameter (in micrometers) of μ^+ to target wire. Computed with PI.	187
A.46 Impact parameter (in micrometers) of μ^- to target wire. Computed with PI.	187
A.47 D.C.A. (in micrometers) of dimuon to RVER 1. Computed with PI.	188
A.48 Impact parameter (in micrometers) of dimuon to target wire. Computed with PI.	188
A.49 Number of degrees of freedom for RVER 1 (ARTE).	189
A.50 Number of degrees of freedom for RVER 2 (ARTE).	189
A.51 $\mu\mu\pi\pi$ mass (computed with PI) for VDS module displacements in Z (top), X (middle) and Y (bottom).	190
A.52 RVER 1 mass (from ARTE) for VDS module displacements in Z (top), X (middle) and Y (bottom).	190
A.53 Minimum separation (in micrometers) between the dimuon and the dipion. Computed with PI.	191
A.54 Vertex longitudinal coordinate (in centimeters) of the $\mu\mu\pi\pi$. Computed with PI.	191
A.55 Longitudinal separation (in centimeters) of the $\mu\mu\pi\pi$ (PI) and the RVER 1 (ARTE).	192
A.56 Longitudinal separation (in centimeters) of the RVER 2 to the RVER 1 (ARTE).	192
A.57 RVER 1 longitudinal coordinate (ARTE).	193
A.58 RVER 2 longitudinal coordinate (ARTE).	193
A.59 $q \times p_T$ (in GeV/ c) of RTRA selected (PI) for B flavour tag. The charge $q = \pm 1$ is the sign of deflection (in the zx projection) of RTRA inside the Magnet. The gap in the color scale corresponds to the cut $p_T > 0.3\text{GeV}/c$ applied.	194
A.60 Impact parameter (in micrometers) of the tagging RTRA. Computed with PI.	194
A.61 D.C.A. of tagging RTRA to RVER 1. Computed with PI.	195
A.62 D.C.A. of tagging RTRA to RVER 2. Computed with PI.	195
A.63 Impact parameter (in micrometers) of $\mu\mu\pi\pi$ to RVER 1. Computed with PI.	196
A.64 Flavour of highest- p_T RTRA (ARTE) used for B flavour tagging, for VDS displacements in Z (top), X (middle) and Y (bottom).	197
A.65 Golden decay B meson flavour, obtained with charge tag from highest- p_T RTRA (ARTE), for VDS displacements in Z (top), X (middle) and Y (bottom).	197
A.66 Flavour of highest- p_T RTRA (ARTE) used for B flavour tagging, for Main Tracker displacements.	198
A.67 Golden decay B meson flavour, obtained with charge tag from highest- p_T RTRA (ARTE), for Main Tracker displacements in Z (top), X (middle) and Y (bottom).	198
A.68 Flavour of highest- p_T RTRA (ARTE) used for B flavour tagging, for RICH displacements.	199
A.69 Golden decay B meson flavour, obtained with charge tag from highest- p_T RTRA (ARTE), for RICH displacements.	199
A.70 Flavour of highest- p_T RTRA (ARTE) used for B flavour tagging, for Muon detector displacements.	200

A.71	Golden decay B meson flavour, obtained with charge tag from highest- p_T RTRA (ARTE), for Muon detector displacements.	200
B.1	Geometrical estimate of the momentum of a charged track found in the TC chambers. This track candidate is defined by a segment $[CD]$ between the TC01 and TC02 chambers. The segment's extremities' coordinates are (z_1, x_1) and (z_2, x_2) , measured in the bending plane. The angles θ_1 and θ_2 are defined relative to the beam direction, $\vec{z}_{12} = (z_2 - z_1, 0)$	203
B.2	Feynman- x of particles from a sample of 10^5 Monte Carlo pN events generated with PYTHIA. The values of x_F were Lorentz-boosted from the fixed-target frame into the pN CM frame. The solid histogram represents the final state particles, and the dashed histogram is for particles falling in HERA- B geometric acceptance, $10\text{mrad} < \theta_{\text{lab}} < 250\text{mrad}$. Compare with figure 3.8.	209
E.1	Profile histogram of the dimuon invariant mass versus RVER 2 mass for Monte Carlo event 235 (see chapters 4 and 5). The function <code>InvMass_PID</code> in the PI tool (line 1096), to get the invariant mass of RTRA pairs, has a linear response in the range of the J/ψ mass for dimuon candidates.	230

List of Tables

3.1	Overview of different HERA- B subdetectors in the context of the readout system [83]. The bitwidth refers to the data size needed for each channel. The bandwidth is simply the product of the number of channels by the bitwidth, per event; the values are approximated to unity for readability.	60
3.2	Expected subdetector resolutions and efficiencies in simulated events [108].	83
4.1	Number of Monte Carlo $gg \rightarrow b\bar{b} \rightarrow J/\psi(\mu^+\mu^-) + \text{anything}$ events surviving different cuts; the K^{neutr} is either K^0 or \bar{K}^0 . For items 1.–14., the counted RTRAs are associated to a single MTRAs by ARTE.	106
4.2	Summary description of the Monte Carlo golden decay sample, with all particles from state $\mu^+\mu^-\pi^+\pi^-$ with good RTRAs (see item 11. of table 4.1). The numbers $nnnn$ in the “DST” column pertain to the DST files <code>run05_00052_nnnn.dst</code> . When available, the correct charge MC tagging particle is indicated (e.g. $B^\pm \rightarrow \ell^\pm X$), and whether it has a corresponding RTRA.	107
4.3	Summary of the Monte Carlo truth for the \bar{B}^0 decay (top) and tagging B^+ meson (bottom) of event 235; see also the figures 4.9 and 4.13. Units: GeV/ c (momentum p and transverse momentum p_T), cm (z coordinate of the MTRA’s start), cm (MTRA length). The J/ψ decays promptly. The decay stages of the B^+ meson (see figure 4.13) are separated by double vertical separators <code> </code> . All quantities are measured in the laboratory frame.	110
4.4	Relevant vertices in event 235; this information is presented in the ARTE tables for this reconstructed event.	118
4.5	Momenta and transverse momenta of RTRAs relevant for the reconstruction of the golden decay in event 235. The RTRA chosen through the highest- p_T criterium is included (last column). The p_T errors are all $\leq 5\text{MeV}/c$. All shown tracks have no ITR hits. $ndof = N_{\text{VDS hits}} + N_{\text{ITR hits}} + N_{\text{OTR hits}} - 5$	118
4.6	Momenta and transverse momenta of golden decay particles reconstructed in event 235. See also tables 4.3 and 4.5.	118

4.7	Vertex longitudinal coordinates, DCAs and impact parameter to wire of golden decay relevant RTRAs (top) and RTRA sets (bottom) for event 235. All quantities were calculated with the PI tool (section E.1). The RTRA used for flavour tag is shown (see table 4.5).	118
4.8	Longitudinal separation of the PI-reconstructed vertices, RVER and Monte Carlo truth for event 235.	119
4.9	Summary of the Monte Carlo truth for the \bar{B}^0 decay (top) and tagging Λ_b^0 meson (bottom) of event 24; see also the figures 4.17 and 4.21. Units: GeV/c (momentum p and transverse momentum p_T), cm (z coordinate of the MTRA's start), cm (MTRA length). The J/ψ decays promptly. The decay stages of the Λ_b^0 meson (figure 4.21) are separated by double vertical separators $\ $. The muon comes from the Λ_c^+ decay and the last two MTRAs come from Λ_0 (with a track length of 230.8cm); see (4.4b). All quantities are measured in the laboratory frame.	121
4.10	Summary information for the relevant reconstructed vertices in event 24.	129
4.11	Momenta and transverse momenta of RTRAs relevant for the reconstruction of the golden decay in event 24. The RTRA chosen through the highest- p_T criterium is included (last column). The p_T errors are all $\leq 5\text{MeV}/c$. All shown tracks have no ITR hits.	129
4.12	Momenta and transverse momenta of golden decay particles reconstructed in event 24. See also tables 4.9 and 4.11.	129
4.13	Vertex longitudinal coordinates, DCAs and impact parameter to wire of golden decay relevant RTRAs (top) and RTRA sets (bottom) for event 24, including the RTRA used for flavour tag (table 4.11). The shown quantities were calculated with the PI tool (section E.1) . . .	129
4.14	Longitudinal separation of the PI-reconstructed vertices, RVER and Monte Carlo truth for event 24.	130
4.15	Selection of events recorded with the HERA- B detector. The events with run number 16014 through 16798 were selected from reference [2]; the remaining are from reference [119]. The event classification, dimuon mass, decay length and significance are from those two references.	136
4.16	ARTE setup for analysis of the event selections presented in table 4.15. "Repro" refers to the official reprocessing cycle in the offline event reconstruction.	136

4.17	List of RTRAs from a golden decay candidate measured in HERA- <i>B</i> —run 20645, event 1528001531. The full event was reconstructed with 29 RTRAs with hits; only those RTRAs with hits up- and downstream of the Magnet, and with a formulated likelihood PID, are shown. The RTRAs' covariance matrices are omitted. The primary vertex, RVER 1, in this event lies practically inside the corresponding target wire, $ \vec{r}_{\text{wire}} - \vec{r}_{\text{RVER 1}} \simeq 0.5\text{mm}$. (z, x, y) are the RTRA's first point coordinates, (tx, ty) are its tangents $tx = p_x/p_z$ and $ty = p_y/p_z$ in the zx and zy planes. The signed p column indicates the measured momentum and the RTRA's charge (positive or negative). The <i>PID</i> indicates the particle identification information from RICH likelihood (for pions, kaons and protons), or the presence of hits in the MUON detector (for muons); the charge is obtained from tracking information (p column). Rightmost column gives the χ^2 probability, obtained from the Kalman filter technique, for this hits used to build the RTRA. On the second line are the RICH likelihoods for the pion, kaon and proton hypotheses (the likelihoods for the electron and muon hypotheses are omitted), the ECAL likelihood for electron and hadron hypotheses (the minimum-ionizing particle likelihood is the complement of these two), and the MUON likelihood for muon hypothesis; the likelihoods are evaluated only at the presence of associated hits for the corresponding detector(s). The next-to-last column give the resulting PID decision; this is useful to improve invariant mass calculations. The last column gives the extrapolated distance of closest approach to the reconstructed primary vertex (see appendix E.1). Entry "4+21" represents the add-up of RTRA directions from RTRA 4 and RTRA 21. The two RTRAs are estimated to meet at $z \simeq 45\text{cm}$, with a distance of closest approach of $0.5 \pm 17.7\mu\text{m}$	139
4.18	Summary information for the all the vertices reconstructed in the event selected from run 20645.	141
4.19	Momenta and transverse momenta of RTRAs relevant for the reconstruction of the selected event from run 20645. The RTRA chosen through the highest- p_T criterium is included (last column). The p_T errors are all $\leq 5\text{MeV}/c$. All shown tracks have no ITR hits.	141
4.20	Momenta and transverse momenta of golden decay particles reconstructed in the event from run 20645. See also table 4.19.	141
4.21	Vertex longitudinal coordinates, DCAs and impact parameter to wire of golden decay relevant RTRAs (top) and RTRA sets (bottom) for the selected event from run 20645, including the RTRA used for flavour tag (table 4.19). The shown quantities were computed with the PI tool (section E.1).	141
4.22	Longitudinal separation of the PI-reconstructed vertices and RVER for the selected event in run 20645.	142

Introduction

One of the Great Questions posed by Mankind refers to the origin of the Universe, namely *how* it was created. Apart from those cosmogonies where the Universe has “always” existed (which therefore immediately puts away any creationist investigations), many others admit that some knowledgeable entity was the driving force behind the creation of the raw materials of the Universe — and also much of the finished product. But the attempts to find out the manner by which *something* (or *everything*), regardless of its complexity, can be created out from — for all practical purposes — *nothing* was often put out on accounts of begin too complicated to solve and, on some occasions, avoided altogether.¹

Even until very late into modern science, the origin of matter in the Universe was not properly addressed due to the lack of proper theoretical tools. Only in the past 40 years or so has there been enough knowledge gathered to concretely define a scientifically meaningful paradigm for the creation of matter in the primordial Universe. In spite of this, the full and satisfactory answer is still veiled, if only partly. The modern theories for the creation of matter in the early Universe borrows from the both the very small (Particle Physics) and the very large (Cosmology). The first hint to the nature of matter came about in the first quarter of the XX century.

1.1 The discovery of anti-matter

The existence of anti-matter was proposed by Paul Dirac in 1927 [47], based on his relativistic wave equation of the electron, which describes the quantum state of a free, point-like (i.e., without internal structure) spin- $\frac{1}{2}$ particle that couples with the electromagnetic field. Dirac coped with the negative-energy solutions in his “hole theory”, where they describe a class of particles having quantities symmetric to those of the electron — such as electric charge, momentum, and also energy. In Dirac’s model of vacuum, the $E < 0$ energy levels are completely filled by an undetectable “sea” of electrons and

¹It is reported that, when asked what God did before creating Heaven, St. Augustine ominously replied that “He was creating Hell for those who ask that question.”

are therefore inaccessible due to the Pauli exclusion principle. A detectable $E > 0$ electron can be created by exciting one of the sea electrons. This leaves a “hole” in $E < 0$ levels, which is physically indistinct to creating a particle with charge opposite to the electron but with negative energy. The energy required to excite both the electron and the “hole” so that both have $E > 0$ is at least $2m_e c^2$. Dirac’s hypothesis for the existence of these “anti-electron” particles was successfully verified in 1932 by Carl Anderson [18], who found experimental evidence for the existence of the then-named “positrons”; however, Anderson’s suggestion of renaming the electron to “negatron” did not catch on [157].

It should be mentioned [82] that Dirac’s interpretation of the vacuum, as a completely-filled sea of $E < 0$ particles, was abandoned after 1934, at which time Pauli and Weisskopf [126] introduced a more sensible interpretation of the negative energy free particle solutions of Dirac’s equation, by reviving the probability density from Klein–Gordon equation through the definition of a electron charge-current density,²

$$J^\mu = -ie(\psi^* \partial^\mu \psi - \psi \partial^\mu \psi^*) , \quad (1.1)$$

with $\mu = 0, \dots, 3$, ∂^μ as the μ -th component of the four-vector differential operator $\left(\frac{\partial}{\partial t}, \frac{\partial}{\partial x}, \frac{\partial}{\partial y}, \frac{\partial}{\partial z} \right)$ (when written in cartesian coordinates), and the electron wave function in the form

$$\psi(\vec{x}, t) \propto e^{-i(Et - \vec{p} \cdot \vec{x})} .$$

In this form the current density J^μ is applicable to bosons (integer-spin particles) and fermions (half-integer spin particles). Later on, Stückelberg (1941) and Feynman (1948) separately [147] [60] prescribed a formalism based on the current density J^μ — which is ultimately at the crux of the introduction of Feynman diagrams, used on difficult calculations involving current densities. In the Stückelberg–Feynman interpretation, the positron current density solutions $J^\mu(e^+)$ with energy $-E$ and three-momentum $-\vec{p}$ are equal to electron current densities $J^\mu(e^-)$ with energy E and three-momentum \vec{p} . In this scheme, a system emitting a positron with energy $-E$ would behave as if absorbed an electron with energy E . This symmetrization in terms of time can be easily understood attending that $e^{-i(-E)(-t)} = e^{-iEt}$.

After the discovery of the positron, an increasing number of particles and anti-particles were both produced in laboratory and found in cosmic rays. There is now overwhelming evidence to the existence of anti-particles, and therefore they are now recognized as entities in their own right, as are also their particle counterparts. The anti-particles were found to have exactly the same (absolute) intrinsic values — mass, spin, charge, etc.— as their respective particles, as far as experimental accuracy allows it.

²Throughout the text, the natural units system $c = \hbar = k_B = 1$ system will be used unless stated otherwise.

1.2 Matter in our Universe

It is well known that the matter permeating the Universe is not solely composed of electrons; we must include the nucleons (protons and neutrons, each of them being composed of three quarks), that together with the electrons aggregate to build the atoms of which matter is made of. A full description of these particles require more than electromagnetism.³ Quantum Electrodynamics (QED) is a very good description of the dynamics involving electrons and positrons, and of the force's carrier particle, the photon; this theory is the simplest and earliest quantum field theory. The Glashow–Salam–Weinberg (GSW) model of electroweak (electromagnetic + nuclear weak) interactions may be written as an extension to QED — see, for example, reference [21, chapter 2]. The GSW model incorporates QED, but it also presents many other advances in the prediction of measurable quantities — cross sections, decay widths, lifetimes, particle masses, etc. — making it a more complete and very successful scenario for the interpretation of current High Energy Physics (HEP) results. One other theory is used to describe the quark–quark interactions, namely Quantum Chromodynamics (QCD). The GSW and QCD theories compound the current knowledge of particle interactions, called the Standard Model (SM). The two theories together are widely accepted within the scientific community on account of their proven success in the result-prediction efforts within HEP experiments. The measurements quoted in literature are often at the 0.1% error level.

The Standard Model lagrangian is the sum of the electroweak's and the QCD's own lagrangians — see for example in references [82, chapter 15] and [40, chapter 13]. In quantum field theories such as these, the laws of conservation of certain dynamic quantities (like momentum or energy) result from certain symmetries in those theories' lagrangian, as ensured by Noether's theorem. Additional symmetries in the theory's lagrangian may exist, denouncing the existence of more conserved quantities. In either case, the quantum operator of those quantities should commute with the theory's hamiltonian operator. An alternative way of expressing the conservation of those quantities comes in terms of conserved currents, whose field divergence would vanish; one example is the electric charge. experimentally verified by the absence of experimental evidence for the violation of such laws. If those conservation laws were disproved, it would not surprise much that it would emerge from the nuclear weak sector of the Standard Model Lagrangian, since past experience has revealed it to be at the origin of significant, albeit small, violation effects.

At its core, the Standard Model imposes that the theory's Lagrangian be invariant under local gauge transformations, in order to ensure renormal-

³Gravity is left out from this frame due to its feeble strength (at our energy scale) in relation to electromagnetism and nuclear interactions.

izability — i.e., that any measurable quantity be finite. The effort to obtain a renormalizable theory of those three interactions resulted in the present Standard Model of particle physics, which has revealed to be very fruitful in predicting several results. The gauge invariance principle, which started as a way to describe Quantum Electrodynamics as a model quantum field theory, has lend itself to such fruitfulness that it is nowadays at the basis of extensions to the Standard Model theory. These extensions are sought based on the belief that the Standard Model, in spite of its success in HEP, is not a complete and final theory; a few theoretical⁴ details (such as the need for a significant number of parameters, to be input by hand) hint that there should be a better theory, described by a single symmetry group that incorporates the SM's three fundamental interactions.

The motivation to extend the Standard Model comes also from scientific areas beyond the Particle Physics realm. One may qualify the observation of the Universe in two sentences [32]:

1. the Universe is not empty;
2. the Universe is *almost* empty.

Notwithstanding its success in the HEP community, it is not evident how one uses the Standard Model to depict the particle interactions that originated the matter content of the Universe, under the Big Bang cosmology. The Standard Model already incorporates some conditions necessary for generating matter — and anti-matter — at different rates (from annihilation and recombination reactions $X + \bar{X} \rightleftharpoons 2\gamma$ for example). These conditions come from the violation of the discrete symmetries of charge conjugation $\hat{C} : q \mapsto -q$, parity $\hat{P} : \vec{r} \mapsto -\vec{r}$, and the operation of both $\hat{C}\hat{P}$, which would ultimately lead to a given reaction having a different rate from its inverse; this will be further discussed in the following chapter. However, since in principle nothing prevents the particle interactions from being reversible at the microscopic level, one expects that, under thermal equilibrium, some given matter-creating interaction might cancel with its reverse, and consequently (given enough time) dissolve the generated asymmetry between the matter and anti-matter content. One other crippling fault to this scenario remains in the Standard Model. If we assume the Universe to start out perfectly symmetric (no matter and no anti-matter, therefore no dominance of one over the other), there is no *obvious* way under the Standard Model on how to violate that symmetry. In effect, the SM's Hamiltonian commutes with both the baryon number and lepton number operators — which give the number of baryons (three-quark particles like the nucleons) and leptons (like the electron), respectively — making the corresponding quantities conserved with time. Only quantum corrections might destroy those conservation laws, but the problem persists that it may not be strong enough

⁴Some might say “aesthetical”...

to recreate the extent of symmetry breaking. These arguments together are strong motivators to look for extensions of the Standard Model where the matter–anti-matter asymmetry might emerge naturally.

The set of those HEP scenarios, together with the standard or the inflation Cosmology models, constitute the *theories of baryogenesis*. The major objectives for the theories of baryogenesis are, on one hand, the prediction — or better yet, “*postdiction*” — of the observed asymmetry parameter η , which quantifies the extent of primordial matter generation, and on the other hand the explanation of the causes behind the asymmetry. The common thread joining these theories is the *Sakharov conditions* [136], which will be further discussed in chapter 2. One of these conditions is the violation of $\hat{C}\hat{P}$ -symmetry in particle interactions; the great interest on this phenomenon lies in the fact that, along with \hat{C} - and \hat{P} -symmetry violation, it is the only aspect of the Sakharov conditions that has been measured in controlled laboratory conditions so far and is possible of measurement in today’s HEP experiments. Nuclear weak interactions typically violate those three symmetries. Although the \hat{C} and \hat{P} symmetries’ violation is rather conspicuous — as demonstrated in the results from Wu *et al.* (1957) and from Goldhaber *et al.* (1958) — $\hat{C}\hat{P}$ violation is comparably much weaker. Besides the importance of \hat{C} and $\hat{C}\hat{P}$ violation for cosmology, in terms of contributing for a baryon-asymmetric Universe through baryogenesis, they are also significant for the HEP community as e.g. a means to measure the electric dipole moment of elementary particles: its detection would hint that these particles would, in fact, be composite [36].

It is currently believed that the decay modes of B^0 mesons exhibit larger $\hat{C}\hat{P}$ asymmetries than on the K^0 meson system, where $\hat{C}\hat{P}$ violation was originally measured [42]. The relative strength of $\hat{C}\hat{P}$ violation is related to the parameters of the Cabibbo–Kobayashi–Maskawa (CKM) matrix. The decay represented in figure 1.1,

$$B_d^0 \rightarrow J/\psi + K_S^0, \quad (1.2)$$

is a preferred channel since [108] it does not involve poorly known hadronic elements of the CKM matrix in the former’s transition amplitude. In this system, $\hat{C}\hat{P}$ violation manifests as a time-dependent difference between the B^0 and \bar{B}^0 (its anti-particle) transition rates.

1.3 Purpose and overview of this dissertation

The bulk of the work presented in this Dissertation concerns the analysis and validation of a limited set of HEP events that were detected, recorded and reconstructed within the HERA-*B* experiment. This experiment was designed to “study $\hat{C}\hat{P}$ violation in the *B* meson system”, as stated in its

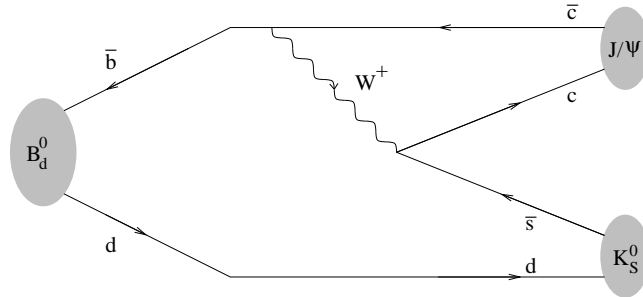


Figure 1.1. One of the tree-level Feynman diagrams for the B_d^0 meson “golden” decay (1.2). The blobs represent the initial- and final-state particles. Their quarks (straight lines) are assumed unbound at decay, and hadronize at the final state.

proposal [108], with the “golden decay” (1.2) as one of its prime $\hat{C}\hat{P}$ violation channels. Although measuring $\hat{C}\hat{P}$ violation-related parameters is beyond the scope of this Dissertation, I investigate the extent to which the alignment of the HERA- B detector influences the reconstruction of a given event. This becomes even more important in a situation where limited statistics is available. In such case, it is important, and feasible, to thoroughly investigate the individual software-reconstructed events constituting the signal. This Dissertation will present how a few candidate events to (1.2) are reconstructed with HERA- B ’s software.

The remainder of this Dissertation is structured as follows. Chapter 2 synthesizes some important elements of primordial baryogenesis scenarios. It will present concepts of Cosmology and equilibrium thermodynamics relevant to an adequate motivation of the subject in terms of the standard definition of the requirements of baryogenic interactions, called the Sakharov conditions. The same chapter will skim through one fundamental aspect of the Sakharov conditions in terms of the interactions between particles, namely the violation of $\hat{C}\hat{P}$ symmetry conservation in nuclear reactions. In chapter 3, HERA- B is presented as an experiment conceived to precisely measure $\hat{C}\hat{P}$ violation using specific and clear physics channels, such as the golden decay (1.2). Chapters 4 and 5 delve into the event reconstruction of B^0 meson decay candidates in HERA- B , first using Monte-Carlo events with simulated reconstruction for this experiment, and next from a sample of selected events recorded during the experiment’s physics data acquisition. Finally, Chapter 6 summarizes the main findings of this Dissertation.

Primordial baryogenesis and $\hat{C}\hat{P}$ violation

“As exceções têm sido o ludíbrio dos mais assisados pensadores, tanto no especulativo como no experimental.”¹

— *Camilo Castelo Branco (1825–1890) [35]*

The theories of baryogenesis, which were introduced in the previous chapter, describe the plausible mechanisms for creating matter and anti-matter at different rates to lead to an asymmetry, in the form of matter “residue” after those reactions cease. These theories seek then to explain the final quantity of matter of the Universe relative to the cosmic radiation background. The main focus of these theories is often on baryons (bound states of three quarks) instead of leptons (electron, muon, tau, and respective neutrinos) or mesons (quark-antiquark pair particles). The reasons for this are the following:

- The present-age Universe is matter dominated, as is described in the standard cosmology [101]. In other words, the main contribution to the Universe’s energy density comes from matter — whether from atoms or exotic particles.
- Disregarding the possible existence of exotic long-life particles, the main contribution to the matter content of the Universe should be from atomic matter.
- For atomic matter, the main mass contribution comes from nucleons — they are much heavier than electrons and typically more numerous.

As stated in the previous chapter, in face of the Sakharov conditions, the conservation of the baryon number in the Standard Model makes a strong case for the search of alternative quantum field theories. Nevertheless, some

¹“Exceptions have been the deceit of the most knowledgeable thinkers, both in the speculation and in the experimentation.”

theoreticians also look for clever mechanisms that lead to a baryon number violation within the SM, specifically under the context of *electroweak baryogenesis*. However, it is found that $\hat{C}\hat{P}$ violation in the SM might be too weak to generate enough baryon asymmetry if quantum field phase transitions are not sufficiently abrupt, see e.g. [59]. Therefore, alternative scenarios to the SM are investigated, such as supersymmetric models (also involving electroweak baryogenesis) and Grand Unification Theories, although they too have their own shortcomings. These theories describe new channels for $\hat{C}\hat{P}$ and baryon number violation occurring at energies higher than the electroweak scale $o(100\text{GeV})$.

2.1 Baryon asymmetry parameters

2.1.1 Baryon-to-photon ratio

To quantify the assertion “the Universe is almost empty”, we will center the discussion around the Universe’s baryon-to-photon ratio, also called the *asymmetry parameter*

$$\eta \equiv \frac{n_B - n_{\bar{B}}}{n_\gamma} . \quad (2.1)$$

In this expression, $n_B - n_{\bar{B}}$ is the difference of baryon and anti-baryon number densities and n_γ is the density of cosmic microwave background (CMB) photons; these densities are given as the species’ quantity per comoving volume unit. It is believed that at our era the typical energy density is too low for baryogenesis at the cosmological scale, therefore $n_B - n_{\bar{B}}$ should reasonably remain constant. Furthermore, since there is no definite proof of large concentrations of anti-matter in the large-scale Universe (following pages), it is customary to make $n_B - n_{\bar{B}} \simeq n_B$ for our era. Accordingly, we define $\eta_0 \equiv n_{B,0}/n_{\gamma,0}$ as the asymmetry parameter measured at our era.

The current estimate [62] for the baryon-to-photon ratio is

$$2.6 < \eta_0 \times 10^{10} < 6.2 \quad (2.2)$$

and has been inferred from primordial nucleosynthesis (the deuterium-to-hydrogen ratio, $[^2\text{H}/^1\text{H}]$), as opposed to direct observations of baryonic matter — which account for roughly one third [49] of the quoted value for η . The abundances of light elements produced in the first stages of the Universe are sensitive indicators of the baryonic number density at that epoch. In other words, for each $\approx 10^{10}$ baryon-antibaryon pair² that annihilated to create the presently observed CMB radiation, one baryon does (did) not annihilate! It is assumed that the asymmetry is not significantly modified at and after the nucleosynthesis era.

²In rigor, *all* flavors of fermions should be accounted. However, at the present cosmological age the asymmetry derives mainly from nucleons.

The baryon-to-photon ratio η_0 is related to the ratio of baryon-to-critical densities $\Omega_B \equiv \rho_B/\rho_c$ by [62]

$$\Omega_B = 3.66 \times 10^{11} \eta_0 H^{-2}, \quad (2.3)$$

with $H_0 = 71 \pm 7 \text{ km s}^{-1} \text{ Mpc}^{-1}$ as the present-era Hubble expansion rate and

$$\rho_c = \frac{3H_0^2}{8\pi G_N} = 2.76 \times 10^9 H^2 M_\odot \text{Mpc}^{-3} = 1.88 \times 10^{-31} H^2 \text{g cm}^{-3} \quad (2.4)$$

as the critical density of the Universe. The baryonic matter density of the Universe $\Omega_B = (0.023 \pm 0.001)/(H_0/100)^2$ amounts to roughly 17% of the matter density $\Omega_m = (0.134 \pm 0.006)/(H_0/100)^2$ [144].

The CMB photon density $n_\gamma(T)$ can be written as

$$n_\gamma = \frac{1}{\pi^2} \left(\frac{k_B T}{\hbar c} \right)^3 \int_0^\infty \frac{x^2}{e^x - 1} dx \simeq 20.3 T^3 [\text{K}^{-3} \cdot \text{cm}^{-3}] \quad (2.5)$$

(k_B is the Boltzmann constant, h is the Planck constant, and c is the speed of light in vacuum). The integral evaluates as $2\zeta(3) \simeq 2.404$, with $\zeta(n)$, $n \in \mathbb{N}$ as the Riemann zeta function. The expression for n_γ may also be written in the natural units system³

$$n_\gamma = \frac{2.404}{\pi^2} T^3. \quad (2.6)$$

Given the current average CMB temperature $T = 2.725 \pm 0.002 \text{ K}$ [120], we then get

$$n_\gamma(T = 2.725 \text{ K}) = 411 \text{ cm}^{-3}. \quad (2.7)$$

Calculating the baryonic number density is more tricky, though. Naively, one could attempt counting the galaxy density in the largest region observable, and from assumptions on the typical mass of those galaxies obtain a ballpark value for $n_B - n_{\bar{B}}$ from the number of nucleons. Making such estimate is, expectingly, very difficult: it would require deep field surveys of extensive portions of the sky, with exposition times long enough to reveal the faintest and farthest galaxies. This has been done, though for small sky areas, which naturally have different galaxy densities. At small cosmological scales, the Universe is very inhomogeneous, with high density regions like the Virgo cluster, with about 2000 galaxies within a 15 Megaparsec radius, interspersed with regions comparatively void of galaxies such as the Boötes

³In this units system, useful in High Energy Physics and Cosmology, $c = \hbar = k_B = 1$ are adimensional constants. Consequently, many expressions are considerable simplified and measurable quantities come in units of e.g. energy: cross sections are given in GeV^{-2} , coordinates and time in $\text{GeV}^{1/2}$, temperature in GeV ($1 \text{ GeV} = 1.0080 \times 10^{13} \text{ K}$), etc..

void, with a radius of 100 Megaparsec [39]. Using typical values for galaxy density (Virgo cluster), number of stars per galaxy (our own has 10^{11}) and star mass (2×10^{41} kg for our Sun), we get 2×10^{41} kg (intergalactic matter is disregarded). Assuming this mass is entirely composed of atomic matter, the average atomic number is around $\bar{A} = 76\% \times 1 + 24\% \times 4 = 1.72$ (the percentages are respective abundances of hydrogen and helium in the Sun). Correspondingly, the nucleon density of the Virgo cluster should be $7.0 \times 10^{67} / (4\pi/3 \times (10^{25} \text{cm})^3) \simeq 1.7 \times 10^{-8} \text{cm}^{-3}$, and the resulting asymmetry parameter ($n_B - n_{\bar{B}} \simeq n_B \simeq n_{\text{nucleons}}$) is just one order of magnitude below the quoted value:

$$\eta(\text{Virgo cluster}) \simeq \frac{1.7 \times 10^{-8}}{4 \times 10^2} \simeq 4 \times 10^{-11} . \quad (2.8)$$

It must be noted that however close this estimate is to the measured value of η_0 for the whole Universe (2.2), and even in face of the observed homogeneity of the Universe in terms of its cosmic background radiation distribution, this is still a fortunate coincidence — as it pertains only to the Virgo cluster. Nevertheless, to measure the effective baryonic number density $n_B - n_{\bar{B}}$ one must still somehow count the number of nucleons in the Universe. For atomic matter, it suffices to count only atoms of light elements, since heavier atoms from e.g. stellar synthesis have a diminute contribution to the cosmological abundances.

It so happens there is no evidence of significantly large domains of anti-matter in the Universe: it is assumed that some physical process produced this matter–antimatter asymmetry at early times, which produced a matter excess after the antimatter annihilation, finally leading to $n_{\bar{B}} \ll n_B$ and $\eta \simeq \eta_0 = n_B/n_\gamma$. The fraction of anti-protons to protons in cosmic rays is $n_{\bar{p}}/n_p \sim 3 \times 10^{-4}$ [101] and consistent with the hypothesis of cosmic rays collisions with the interstellar medium. The fraction of light anti-nuclei to nuclei in the nearest 10 Megaparsec is $n_{\overline{\text{He}}}/n_{\text{He}} < 10^{-5}$ [39]. There is also no strong evidence of regions dominated by anti-matter farther than the Mpc scale. If they existed, it is expected that the strongest sign of presence of such domains would be a flux of annihilation radiation from the interface with matter domains; assuming negligible interface dynamics, this would show as energy spectrum peaks around or at e.g. the proton rest mass and/or electron rest masses ($938 \text{MeV}/c^2$ and $0.511 \text{MeV}/c^2$ respectively), or at [49] twice the proton rest mass ($p + \bar{p} \rightarrow N\pi$, followed by $\pi^0 \rightarrow 2\gamma$). These facts point to a maximal baryonic asymmetry at the galactic scale.

For very large scales the evidence for whether the baryon asymmetry persists or not is more scarce. Suppose that the Universe is locally baryon symmetric. In this situation, the nucleons and antinucleons are in thermal equilibrium down to $\sim 22 \text{MeV}$ when they tend to aggregate as atomic nuclei. At that point, the baryon-to-entropy ratio (described in the next section)⁴ is

⁴For now we may use $s \simeq 7n_\gamma$, see (2.6) and (2.9).

$n_b/s = n_{\bar{b}}/s \simeq 7 \times 10^{-20}$ [101] [134], which is around 9 orders of magnitude lower than the observed value. To prevent the catastrophic annihilation, the separation of matter and antimatter should occur when $n_b/s = n_{\bar{b}}/s \simeq 8 \times 10^{-10}$, which corresponds to a temperature around 38MeV [101]. At this energy the Universe was $t \simeq (1\text{MeV}/T)^{-2} = 0.7\text{ms}$ old, with a corresponding causal comoving element of size $ct \sim 10^{-17}\text{Mpc}$ encompassing $\approx 10^{-7}M_{\odot}$ [134]. On the other hand, no significant domains of antimatter are found in patches containing $10^{12}M_{\odot}$ to $10^{14}M_{\odot}$, which contradicts the original supposition of local baryon symmetry.

Remarkably, the elemental abundances of primordial light elements depend almost solely on η_0 [34]. As will be described in the following sections, at the nucleosynthesis and lower energy scales at a time scale — corresponding to a time later than $t \sim (T/1\text{MeV} \cdot \text{s}^{1/2})^{-2} \sim 1\text{s}$ — the reactions generating baryon asymmetry have stopped and η remains reasonably constant. The constancy of the η parameter is not, however, maintained throughout the Universe's history. Indeed, the particle annihilation processes increases the number density n_{γ} for low enough temperatures $T \lesssim m$. For this effect, the baryon-to-entropy ratio $\eta_s \equiv n_B/s$ is the parameter of preferential use in the subject of baryogenesis.

2.1.2 The baryon-to-entropy ratio

In the expanding Universe [101], the second law of thermodynamics applied to a unit comoving volume with physical volume $V = R^3$ implies that

$$TdS = d(\rho V) + pdV = d[(\rho + p)V] - Vdp ,$$

where ρ and p are the equilibrium energy density and pressure, T is the equilibrium temperature and S is the entropy. Moreover, the integrability condition,

$$\frac{\partial^2 S}{\partial T \partial V} = \frac{\partial^2 S}{\partial V \partial T}$$

relates the energy density and pressure:

$$T \frac{dp}{dT} = \rho + p ,$$

or equivalently,

$$dp = \frac{\rho + p}{T} dT .$$

It follows that

$$dS = \frac{1}{T} d[(\rho + p)V] - (\rho + p)V \frac{dT}{T^2} = d \left[\frac{(\rho + p)V}{T} + \text{const.} \right] .$$

The entropy density s is [101]

$$s \equiv \frac{S}{V} = \frac{p + \rho}{T} \simeq \frac{2\pi^2}{45} g_{*S}(T) T^3 , \quad (2.9)$$

where

$$g_{*S}(T) = \sum_{i=\text{bosons}} g_i \left(\frac{T_i}{T}\right)^3 + \frac{7}{8} \sum_{j=\text{fermions}} g_j \left(\frac{T_j}{T}\right)^3 \quad (2.10)$$

is the number of degrees of freedom of “massless” ($m_i \ll T$) particles⁵ and T is the thermal bath temperature. The approximation in (2.9) results from the dominant contribution of relativistic particles such as photons and neutrinos [134]. Assuming 3 massless neutrino species, and considering that at $T \ll m_e$ only the photons are in equilibrium, we have⁶

$$g_{*S}(\text{today}) = 2 + \frac{7}{8} \times 2 \times 3 \times \frac{4}{11} = 3.91 .$$

During most of the Universe’s history, the entropy per unit comoving volume s has remained reasonably constant due to local thermal equilibrium. Then, since $s \propto R^{-3}$ (R is the time-dependent scale factor for distances in comoving coordinates), $g_s(T)T^3 R^3$ remains constant as the Universe expands. Therefore, the number of a species X in a comoving volume, $N_X = R^3 n_X$ varies with the inverse of s , i.e. $N_X \propto n_X/s$. The “good” parameter is instead the baryon number density per entropy density (again, measured in a given comoving volume),

$$\eta_s \equiv \frac{n_B - n_{\bar{B}}}{s} . \quad (2.11)$$

2.2 The Sakharov conditions

Prior to the publication of Sakharov’s paper in 1967 [136], the bulk of the scientific community believed that, at the beginning of the Universe, either:

1. all quantum numbers were cancelled — hence there was “nothing” before the Big Bang; or
2. some quantum numbers were not zero — therefore there was “something” before the beginning of the Universe.

The second scenario had the advantage that, having the adequate quantum numbers (e.g. the total baryonic number of the Universe) different from zero,

⁵The relative factor $7/8$ accounts for the different equilibrium densities for the Fermi–Dirac and the Bose–Einstein statistics [101]. The particle species’ temperatures are not all the same, although their assemble is at a local equilibrium temperature T . For neutrinos and photons [34] at $kT < m_e$, entropy conservation yields $T_\nu = g_\gamma/(g_\gamma + \frac{7}{8}g_e) = (4/11)^{1/3}T_\gamma$; at this temperature scale, neutrinos have decoupled from the remaining thermal bath consisting of γ, e^\pm . On the other hand, for higher temperatures $m_\mu \gtrsim kT \gtrsim m_e$, the additional relativistic degrees of freedom from electrons and positrons yield $T_\nu = T_\gamma$.

⁶The factor $4/11$ comes from the ratio of entropies for two states of the system $e^+ + e^- \rightleftharpoons 2\gamma$. See e.g. [101].

offered a way out of a catastrophic annihilation of matter into radiation after primordial stages of the Universe — some process would translate those quantum numbers into matter, albeit the number density of the radiation field would predominate as it is at present. This scenario uncomfortably suggests, however, the existence of a mechanism outside the Universe that would generate the presence of non-zero quantum numbers *before* the Big Bang; the “discomfort” comes from the generalized philosophical belief that the Universe contains everything (space, time, and matter/energy density with given quantum numbers) and therefore nothing else exists outside of it — the perspective that the “region outside” the Universe had *any* baryonic number (or other quantum number for what matters) seems at least strange under such point of view. The first scenario, however, passes over this disconcerting hypothesis: the single problem remains in finding the set of physical properties that leads from a perfectly symmetric Universe (a balance between matter and anti-matter through the radiation field, $X + \bar{X} \rightleftharpoons 2\gamma$) to one where either matter is predominant.⁷

In his ground-breaking publication, Sakharov describes the set of properties required by eligible matter-generating processes. Those properties are now known as the Sakharov conditions. Under these, the set of physical processes that enable baryogenesis must:

1. Violate the conservation of total baryonic number B .
2. Violate the conservation of both \hat{C} and $\hat{C}\hat{P}$ discrete symmetries.
3. Occur away from a state of thermal equilibrium.

In the first two conditions the term “violation” means that the physical system has different values for the enumerated quantum numbers before and after the responsible physical process. All these three conditions must be met concomitantly for baryogenesis to happen. Sakharov’s work remained mostly unnoticed for about seven years, until the hypothesis for baryon number violation found a suitable theoretical paradigm in the form of the Grand Unification models; for an in-depth description of the investigation in baryogenesis see [49]. The work volume on the subject of baryogenesis has grown steadily over time. Presently, the depth and complexity of the investigation is only matched by the scarcity of related publications from those early years.

Though evidence points out that the matter–antimatter asymmetry is maximal, at high temperatures the quarks and anti-quarks existed in large quantities coupled with the thermal bath, $n_q = n_{\bar{q}} \sim n_\gamma$. Therefore, given

⁷The choice for naming the baryogenesis-favored mass content of the Universe as “matter” is anthropomorphic. However, this convention does not affect the writing of the physical laws, as matter and anti-matter behave differently under \hat{C} and $\hat{C}\hat{P}$ symmetries.

the present asymmetry, this points out that a very small asymmetry must have existed at remote times ($t \lesssim 10^{-6}\text{s}$), with [101]

$$\frac{n_q - n_{\bar{q}}}{n_q} \simeq 3 \times 10^{-8} .$$

The rest of this section describes the so-called out-of-equilibrium decay scenario as an example of baryogenesis model [101]. In an expanding Universe, the abundance of massive baryogenic particles is thermal, $n_X = n_{\bar{X}} \sim n_\gamma$. However, for $T < m_X$ an overabundance of X and \bar{X} arises, and finally for $T \ll m_X$ these particles freely decay and their regeneration is thermally suppressed. The final baryon number-to-entropy ratio is given by (2.23). Still in [101], a more realistic model is worked out (but not developed here), which involves the Boltzmann equations to study the evolution of baryon asymmetry. What is most remarkable about those equations is how the Hubble constant H , typically showing up in Cosmology (the ‘‘Very Large’’) appears along with quantities related to Particle Physics (the ‘‘Very Small’’). For example, the equation for the evolution of the number density n_X of a heavy boson X (e.g. decaying as $X \rightarrow bb$) can be written as

$$\begin{aligned} \frac{dn_X}{dt} + 3Hn_X &= \int \sum_j |\mathcal{M}_j|^2 (2\pi)^4 \delta^4 \left(p_X - \sum_i p_{x_i} \right) \frac{d\vec{p}_X}{2E_X} \prod_i \frac{d\vec{p}_{x_i}}{2E_{x_i}} = \\ &= -\Gamma_X^{\text{dec.}} (n_X - n_X^{\text{eq.}}) , \end{aligned} \quad (2.12)$$

with p_X and p_{x_i} as the four-momenta of X and its decay products x_i , $f_r(E) = \exp(-(E - \mu_r)/T)$ as the phase space densities of the particle species $r = X, x_i$, $\Gamma_X^{\text{dec.}}$ as the thermally-averaged decay width of X , $n_X^{\text{eq.}}$ as X ’s equilibrium number density, and the integration symbol running through the three-momenta elements $d\vec{p}_X$ and $d\vec{p}_{x_i}$.

2.2.1 The violation of the baryon number conservation

The first Sakharov condition might seem a tautology — after all, we are looking to describe the means by which the Universe evolves into a state of differing baryonic number. However, to this day no definite interaction has been measured in laboratory that registers a different net value of B before and after its occurrence, i.e. $\Delta B \neq 0$. In fact, the Standard Model expects that B is globally conserved (at least at first order), which can be written as the vanishing of the commutator of this operator with the SM classic hamiltonian, $\hat{B}\hat{H} - \hat{H}\hat{B} = 0$. Surprisingly, it is still possible for B conservation to be violated within the SM [49] [148] through anomalous quantum mechanical effects of higher order — namely, chiral anomalies [10] [28]. However, these electroweak-scale effects seem too faint to ultimately

account for the observed baryon asymmetry of the Universe.⁸ Nevertheless, and according to the Sakharov conditions, “ B violation” is *essential* for baryogenesis. This shortfall of the Minimal Standard Model constitutes a strong argument in favor of the search for New Physics.

Several alternatives have been proposed which naturally include B -violating reactions. One such set of theories are the Grand Unified Theories (GUTs), which describe the strong, weak and electromagnetic interactions under a single symmetry group, in a similar way to what the Electroweak theory does to unify the electromagnetic and the nuclear weak interactions. GUTs accept heavy bosons with decay into quarks and leptons and for which B violation is naturally unsurpressed. Due to the great stability of the proton, with a decay rate lower bound estimated at $\tau_p^{\text{exp.}} \gtrsim 5 \times 10^{32}$ years, the GUT energy scale should be much higher than what is possible to attain with our technology,

$$\tau_p \sim (G_{\text{GUT}}^2 m_p^5)^{-1} \sim \frac{M_X^4}{\alpha_{\text{GUT}}^2 m_p^5} \sim 10^{32} \text{ years} \quad \implies \quad M_X \sim 10^{15} \text{ GeV} ,$$

with G_{GUT} as the GUT-scale coupling constant and $\alpha_{\text{strong}} \simeq \alpha_{\text{GUT}} \simeq 0.1$ as the nuclear strong interaction’s coupling constant at GUT scale.⁹ Furthermore, considering couplings with the Higgs boson, the energy scale estimation can be brought down to 10^{10} GeV [101], which makes for a strong suppression of these processes at the electroweak scale. In spite of the initial enthusiasm build around GUTs as a possible mechanism for large baryogenesis, its adequacy has been questioned. Riotto [134] remarks that X -mediated interactions are adequate, but insufficient, for B violation. Other GUT theories, such as the simplest theory described by the SU(5) gauge group, has been ruled out by its prediction of the proton lifetime $\tau_p^{\text{SU}(5)} \sim 10^{30}$ years. Experimental results obtained at LEP suggest that the supersymmetric extension of SU(5) gives a viable candidate; see [134] and references therein.

Though GUTs, beyond their simplest versions, seem the most obvious candidates (due to naturally incorporating B -violating reactions), the supersymmetric (SUSY) extensions to the Standard Model present another chance for massive B -violating bosons. Currently, the most fashionable scenarios use the electroweak baryogenesis theories [49]. These enjoy the advantage of allowing experimental tests at the currently-accessible accelerator energies $o(100)$ GeV, which is much lower than the energy scale of competing

⁸It is estimated that the proton decay $p \rightarrow e^+ \pi^0$, which violates B conservation, has a very large lifetime, $\tau_p \gtrsim 10^{33}$ years. Would the baryon number be absolutely conserved [128] as a result of a local gauge symmetry, and one would expect to find a long-range field couple to it, for which no evidence has been found (the upper limit for such coupling is less than 10^{-9} of gravitational coupling).

⁹The actual energy scale estimation depends on the chosen GUT theory, and can range from 10^{14} GeV– 10^{15} GeV for non-supersymmetric GUTs to 10^{16} GeV– 10^{18} GeV for supersymmetric GUTs. See e.g. the chapter on Grand Unified Theories on [52].

theories — for SUSY GUTs it lies in the 10^{16}GeV – 10^{18}GeV range. In all these theories, the B -violating processes might also stem from lepton number violating processes, which is generically named as *leptogenesis*; in those scenarios, $B+L$ is violated but $B-L$ is conserved throughout. Other generators of baryogenesis were also investigated, such as black hole evaporation and topological defects [48] [49].

2.2.2 The violation of charge conjugation, parity and charge-parity symmetries

It is known for roughly four decades that the charge conjugation \hat{C} and the parity \hat{P} symmetries are maximally violated in weak interactions [159] [75]. As stated in section 2.3.2, in roughly eight years it was found that, beyond parity violation, also the $\hat{C}\hat{P}$ symmetry was not perfectly conserved in nuclear reactions. The extent of $\hat{C}\hat{P}$ violation is less impressive than that of \hat{C} or \hat{P} , but is still enough to produce very significant effects. $\hat{C}\hat{P}$ violation has been parameterized in the Standard Model of Particle Physics through the *CKM mechanism*. However it is not yet completely understood what causes $\hat{C}\hat{P}$ violation and why, which leads to assume that it may also occur at energies above the electroweak scale $o(100\text{GeV})$ attainable with particle accelerators. A knowledge of $\hat{C}\hat{P}$ violation at different energy scales is very important for baryogenesis because it was assumedly very significant at energies far above the electroweak scale, where processes other than quark decays may become more significant. As stated at the end of section 2.2.3, $\hat{C}\hat{P}$ violation does not have to be too large to produce viable B -violating effects; the main interest lies in finding the theory that correctly predicts the observed asymmetry.

It is known in principle that antiparticles are not mere mirror reflections of particles — they have essentially distinct interactions and are produced with different probabilities in \hat{C} -conjugated processes. The “ $\hat{C}\hat{P}\hat{T}$ theorem” was formulated by Schwinger and Zumino, and later on was demonstrated by Lüders [109] and Pauli; refer to e.g. [80] and [36] for details. In reference [163], Zumino and Lüders investigate some consequences of Nature’s invariance under $\hat{C}\hat{P}\hat{T}$ symmetry. Due to this theorem — which implies that all interactions remain symmetric under the operation of \hat{C} , \hat{P} and time-reversal \hat{T} — the different behavior introduced by a $\hat{C}\hat{P}$ -transformed system corresponds to a difference under the time reversal operation. As a result of $\hat{C}\hat{P}\hat{T}$ symmetry, the masses and *total* decay widths¹⁰ must be equal for particles and anti-particles. However, the probabilities of specific channels should be different for charge-conjugated processes if both the \hat{C} and $\hat{C}\hat{P}$ symmetries are broken. As noted in reference [49], this effect involves at least next-to-leading order (NLO) terms in a perturbation theory, in the

¹⁰The decay width of a particle is related to the inverse of its lifetime, $\Gamma = \hbar/\tau$.

form of corrections of the inelastic rescattering of the decay products. This contributes to suppress \hat{C} and $\hat{C}\hat{P}$ violation.

Next is reproduced a toy model described in reference [101]; see a similar analysis in [134]. Consider two massive bosons X and Y which have B -violating decays. For simplicity, we may consider the bosons to have only two decay channels each, with quark and lepton final states — e.g. $X \rightarrow qq$ and $X \rightarrow \bar{q}\bar{l}$, which respectively have final state baryon numbers $B_{qq} = 2/3$ and $B_{\bar{q}\bar{l}} = -1/3$ and branching ratios $r \equiv \Gamma(X \rightarrow qq)$ and $1 - r \equiv \Gamma(X \rightarrow \bar{q}\bar{l})$. For a general definition of the decay width Γ refer to section B.6 in appendix.

The antiboson \bar{X} decays as $\bar{X} \rightarrow \bar{q}\bar{q}$ ($B_{\bar{q}\bar{q}} = -2/3$ and branching ratio \bar{r}) and $\bar{X} \rightarrow ql$ ($B_{ql} = 1/3$ and branching ratio $1 - \bar{r}$). Though the decay widths of X and \bar{X} must be equal because of the $\hat{C}\hat{P}\hat{T}$ theorem, no assumptions are made for r and \bar{r} *a priori*. In fact, it happens that \hat{C} and $\hat{C}\hat{P}$ are violated if the asymmetry parameter $\varepsilon_{\hat{C}\hat{P}} \equiv r - \bar{r} \neq 0$, defined from the average baryonic number of the $X\bar{X}$ system,

$$B_X = \frac{2}{3}r + \left(-\frac{1}{3}\right)(1-r) = r - \frac{1}{3},$$

$$B_{\bar{X}} = \left(-\frac{2}{3}\right)\bar{r} + \frac{1}{3}(1-\bar{r}) = -\bar{r} + \frac{1}{3}.$$

A similar reasoning can be applied to the $Y\bar{Y}$ system. Generalizing for an arbitrary number of final states f , the asymmetry parameters would be

$$\varepsilon_X = \sum_f B_f \frac{\Gamma(X \rightarrow f) - \Gamma(\bar{X} \rightarrow \bar{f})}{\Gamma_X}, \quad (2.14)$$

$$\varepsilon_Y = \sum_f B_f \frac{\Gamma(Y \rightarrow f) - \Gamma(\bar{Y} \rightarrow \bar{f})}{\Gamma_Y}, \quad (2.15)$$

with Γ_X and Γ_Y as the respective total decay widths of X and Y . In this simple model the total asymmetry is $\varepsilon = \varepsilon_X + \varepsilon_Y$.

Given the bosons' decay modes¹¹ $X \rightarrow \bar{f}_1 f_2$, $X \rightarrow \bar{f}_3 f_4$, $Y \rightarrow f_1 \bar{f}_3$ and $Y \rightarrow f_2 \bar{f}_4$ for fermion states f_1, f_2, f_3, f_4 , the lagrangian can be written as¹²

$$\mathcal{L} = g_1 X f_2^\dagger f_1 + g_2 X f_4^\dagger f_3 + g_3 Y f_1^\dagger f_3 + g_4 Y f_2^\dagger f_4 + \text{h.c.}, \quad (2.16)$$

with (possibly complex) coupling constants g_1, g_2, g_3, g_4 at each decay vertex and X, Y , and the f_i and f_i^\dagger representing the particles' currents in the respective decay modes. The tree-level processes do not contribute to ε since

$$\Gamma(X \rightarrow \bar{f}_1 f_2) = |g_1|^2 I_X = \Gamma(\bar{X} \rightarrow f_1 \bar{f}_2) = |g_1^*|^2 I_{\bar{X}}$$

¹¹The final state particles are hereon, and to the end of this section, indexed to allow easier evaluation of the subsequent expressions.

¹²The abbreviation "h.c." stands for "hermitian conjugate" of the preceding summation.

with $I_X = I_{\bar{X}}$ as kinematic factors obtained from the phase space integrals (see e.g. the discussion on equation (B.39) in appendix B). The lowest-order non-vanishing contribution to ε comes from terms corresponding to tree-level graph interferences with one-loop correction terms (see figures 2.2 and 2.3). The interference terms are given by

$$\Gamma(X \rightarrow \bar{f}_1 f_2) = g_1 g_2^* g_3 g_4^* I_{XY} + (g_1 g_2^* g_3 g_4^* I_{XY})^* , \quad (2.17a)$$

$$\Gamma(\bar{X} \rightarrow f_1 \bar{f}_2) = g_1^* g_2 g_3^* g_4 I_{XY} + (g_1^* g_2 g_3^* g_4 I_{XY})^* , \quad (2.17b)$$

with I_{XY} as the kinematic factors for these diagrams. For example, for diagram (a) in figure 2.3, I_{XY} accounts for the integration over the final state phase space of f_2 and \bar{f}_1 and over the momenta of the internal states f_4 and \bar{f}_3 . As explained in [134], $\Im I_{XY} \neq 0$ if any internal line propagates on mass shell,¹³ thereby picking the pole of the propagator,

$$\frac{1}{p^2 - m^2 + i\epsilon} = \text{P.V.} \left(\frac{1}{p^2 - m^2} \right) + i\pi\delta(p^2 - m^2) , \quad (2.18)$$

with $\epsilon \rightarrow 0$ and P.V. standing for the Cauchy principal value (equation (2.18) is derived elsewhere, see e.g. [78]). This happens if $M_X > m_1 + m_2$ and $M_X > m_3 + m_4$ — as is the case for light fermions.

The difference between (2.17a) and (2.17b) gives

$$\begin{aligned} \Gamma(X \rightarrow \bar{f}_1 f_2) - \Gamma(\bar{X} \rightarrow f_1 \bar{f}_2) &= 2i I_{XY} \Im (g_1 g_2^* g_3 g_4^*) + 2i I_{XY} \Im (g_1^* g_2 g_3^* g_4) = \\ &= 4\Im I_{XY} \Im (g_1^* g_2 g_3^* g_4) . \end{aligned} \quad (2.19)$$

For the remaining decays of X and Y the expressions are similar. The baryon asymmetry is then

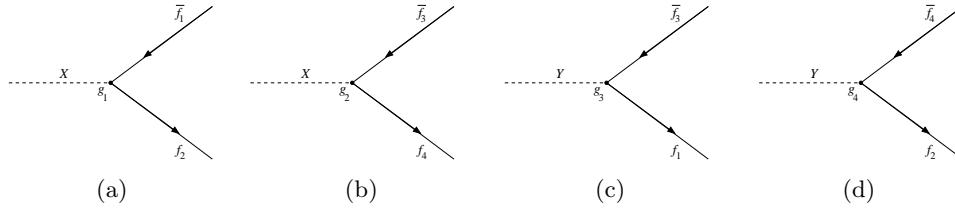
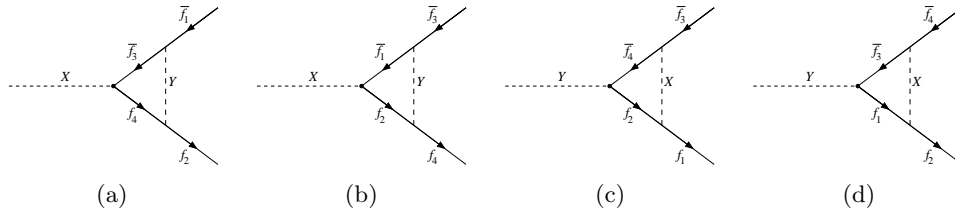
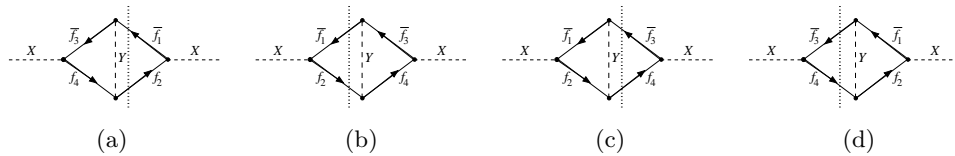
$$\varepsilon_X = \frac{4}{\Gamma_X} \Im I_{XY} \Im (g_1^* g_2 g_3^* g_4) [(B_{f_4} - B_{f_3}) - (B_{f_2} - B_{f_1})] . \quad (2.20a)$$

Repeating the calculations for Y , we have

$$\varepsilon_Y = -\frac{4}{\Gamma_Y} \Im I_{YX} \Im (g_1^* g_2 g_3^* g_4) [(B_{f_4} - B_{f_3}) - (B_{f_2} - B_{f_1})] . \quad (2.20b)$$

Three conclusions may be extracted from this simple model. In the first place, it requires that a X, Y pair of B -violating bosons exist, each with mass greater than the sum of masses of final state fermions, to give $\Im I_{XY} \neq 0$. Secondly, we see that \hat{C} and $\hat{C}\hat{P}$ violation manifests at second and upward orders, which results in that the processes are suppressed by factors of α^N for a coupling constant α and N loops. Thirdly, X and Y must not be degenerate mass states, $\Gamma_X \neq \Gamma_Y$, otherwise the baryonic number of the products of X would cancel with the baryonic number of the products of Y .

¹³A particle is said to propagate “on mass shell” if its four-momentum satisfies $p^\mu p_\mu \equiv E^2 - \vec{p}^2 = m^2$; otherwise, it is said to propagate “off mass shell”.

Figure 2.1. Tree-level Feynman graphs for the decays of the X and Y heavy bosons.Figure 2.2. One-loop corrections to X and Y decay.Figure 2.3. Some interference terms between the diagrams 2.1 and 2.2 for the squared amplitudes of X decay. The vertical dotted line cutting through the fermion lines represents a unitary cut applied to them — it means the corresponding propagators are evaluated on mass shell.

2.2.3 Departure from thermal equilibrium

The third condition — namely, the system’s departure from thermal equilibrium,¹⁴ — is required so that matter–anti-matter asymmetries (generated by \hat{B} -, \hat{C} - and $\hat{C}\hat{P}$ -violating processes) are not dissipated. Under thermal equilibrium, any asymmetry caused by a given reversible reaction $i \rightleftharpoons f$ is inevitably diluted by its inverse reaction, even if the direct reaction’s rate is higher than the inverse’s, $\tau_{i \rightarrow f} \neq \tau_{f \rightarrow i}$. To prevent the thermalization of the reaction products f of an arbitrary asymmetry-generating reaction, those products should be drawn apart faster than the time required to restore local equilibrium through recombination $f \rightarrow i$. This condition is satisfied by the expansion of the Universe. For the departure from thermodynamic equilibrium to occur, the space-time expansion rate H should be greater than the direct reaction’s rate $\tau_{i \rightarrow f} = \Gamma_{i \rightarrow f}^{-1}$, i.e. we have $\tau_{i \rightarrow f} < H$, leading to an overabundance of particles from the initial state i .

¹⁴Kolb and Turner point out [101] that, in the scenario of the “hot Big Bang” Standard Cosmology, the Universe cannot achieve a rigorous state of thermal equilibrium; however, in most of its history it is in a state close enough to equilibrium.

Taking again the toy model from the previous section [101], in local thermal equilibrium the number densities of bosons X and \bar{X} follows separate regimes according to the thermal bath temperature,

$$n_X = n_{\bar{X}} \simeq \begin{cases} n_\gamma & T \gtrsim m_X \\ (m_X/T)^{3/2} e^{-m_X/T} & T \lesssim m_X \end{cases}. \quad (2.21)$$

The equilibrium holds as long as the creating and annihilation rates of X and \bar{X} are greater than the rate of expansion of the Universe. The $X + \bar{X} \rightarrow 2\gamma$ annihilation process is “self-quenched”, since its rate $\tau_{\text{ann.}} = \Gamma_{\text{ann.}}^{-1} \propto n_X$; therefore, only the decays of X and \bar{X} are considered. For high temperatures $T \gtrsim m_X$ the rates $\tau_{X \rightarrow f} \simeq \tau_{f \rightarrow X} \simeq \alpha m_X^2/T$, and for low temperatures $T \lesssim m_X$ we have $\tau_{X \rightarrow f} \propto \alpha m_X$ and $\tau_{f \rightarrow X} \simeq \alpha m_X (m_X/T)^{3/2} e^{-m_X/T}$; $\alpha \sim g^2/4\pi$ is the coupling strength of the X boson. For $2 \rightleftharpoons 2$ B -violating scattering processes mediated by X and \bar{X} , the scattering rate is $\tau_\sigma \simeq n\sigma \simeq \alpha^2 T^5/(T^2 + m_X^2)^2$. The rate of expansion is given by $H \simeq g_*^{1/2} T^2/m_{\text{Pl}}$ for a Planck mass m_{Pl} . At high temperatures the decay rates are further inhibited by the usual time dilation factor. For low temperatures the inverse decays $f \rightarrow X$ are suppressed by the Boltzmann factor $e^{-m_X/T}$. The scattering cross section σ for the $2 \rightleftharpoons 2$ processes is $\propto T^{-2}$ for $T \gtrsim m_X$ and $\propto T^2$ for $T \lesssim m_X$. It should also be noted that the reaction rates τ depend on m_X , but not H .

The most significant reaction rate for baryogenesis comes from the decay width $\tau_{X \rightarrow f}$ due to its influence on the regulation of the bosons’ number density. The parameter

$$K \equiv \left. \frac{\tau_{X \rightarrow f}}{2H} \right|_{T=m_X} = \frac{\alpha m_{\text{Pl}}}{3.3 g_*^{1/2} m_X} \quad (2.22)$$

measures the decay effectiveness for the temperature scale $T \sim m_X$ at which the gauge bosons X, \bar{X} must decrease in number if they are to stay in equilibrium. If $K \ll 1$, for $T \sim m_X$ we have $\tau_{X \rightarrow f} \lesssim H$ (equivalently: $\tau_X \gtrsim t$) and the bosons do not reach thermal equilibrium. Below the threshold $T \sim m_X$ the bosons are overabundant until they decay, $n_X = n_{\bar{X}} \sim n_\gamma$ and there is no exponential suppression. For an average baryonic number ε , the resulting baryonic density is $\varepsilon n_X \sim \varepsilon n_\gamma$. The entropy density is $s \sim g_* n_\gamma$ and consequently we have

$$\eta_s \simeq \frac{n_B}{s} \sim \frac{\varepsilon n_\gamma}{g_* n_\gamma} \sim \frac{\varepsilon}{g_*}. \quad (2.23)$$

The inverse decay of X (i.e. creation of X, \bar{X}) and $2 \rightleftharpoons 2$ B -violating scattering processes are suppressed for $T \lesssim m_X$ and can therefore be ignored.

Using $10^2 \lesssim g_* \lesssim 10^3$, we see that for $K \lesssim 1$ only a small $\hat{C}\hat{P}$ violation amplitude is necessary: $10^{-8} \lesssim \varepsilon \lesssim 10^{-7}$ is enough to give $n_b/s \sim 10^{-10}$.

The massive bosons' mass is very high in this scenario, $m_X \gg \alpha/10^2 \times 10^{16}\text{GeV}$ and results from the condition $K \ll 1$. The coupling constant $\alpha = \alpha_{\text{GUT}} \simeq 1/45$ is lowered if we consider the coupling to the Higgs boson, and m_X may be as low as 10^{10}GeV . For $K \gg 1$, we get $\tau_{X \rightarrow f} \gg H$ for $T \sim m_X$ and the departure from thermal equilibrium is suppressed. The intermediate regime $K \simeq 1$ is more interesting but is not abridged here — see e.g. [101].

2.3 An overview of $\hat{C}\hat{P}$ symmetry violation and of quark flavor mixing

This section summarizes a few important concepts related with $\hat{C}\hat{P}$ violation in the Standard Model and its measurement. Historically, the discovery of this phenomenon (1964) precedes the invention of the Cabibbo–Kobayashi–Maskawa (CKM) matrix as a means to write the probabilities of transitions between quark families. Nevertheless, because the CKM matrix incorporates well the $\hat{C}\hat{P}$ violation in quark decays, its formalism is presented foremost. Next, a resumé of the discovery of $\hat{C}\hat{P}$ violation is presented and it is described in one of the first systems where it was found, the neutral K meson. At last, a transition to the B meson system is done from the former, finalizing with the general concept used to measure $\hat{C}\hat{P}$ violation in neutral B decays in an experiment designed for the effect, HERA- B (chapter 3).

2.3.1 The CKM quark-mixing matrix and $\hat{C}\hat{P}$ violating phase

In the electroweak sector of the Standard Model, both the quarks and leptons are assigned as three families of left-handed doublets and right-handed singlets;¹⁵ for quarks, they are respectively $\begin{pmatrix} u_L \\ d_L \end{pmatrix}$, $\begin{pmatrix} c_L \\ s_L \end{pmatrix}$, $\begin{pmatrix} t_L \\ b_L \end{pmatrix}$ and d_R, s_R, b_R . Quark and lepton family transitions are suppressed, whereas transitions between doublet partners e.g. $u_L \rightleftharpoons d_L$ are allowed and can be described in terms of Feynman diagram vertices with a charged weak boson W^\pm ; see e.g. the two vertices with the W^+ boson in figure 1.1. The quark mass eigenstates are not equal to the weak eigenstates, and the matrix relating these eigenbases is defined in the Standard Model lore for six quarks in the three families, as given in an explicit parameterization by Kobayashi and Maskawa in 1973 [100]. The Kobayashi–Maskawa (KM) *ansatz* generalizes the four-quark (two quark families) case, where the matrix is described by a single parameter, the Cabibbo angle [41], which was introduced in 1963 as a means to accommodate the particle doublet picture for the different particle families.

¹⁵In the lepton sector, this translates as the inexistence of right-handed (massless) neutrinos. The extension to the quark sector can be gathered from the hypothesis of universality of weak interactions.

The Cabibbo angle θ_C appears in a rotation matrix applied to the d and s quarks' mass eigenstates [82],

$$\begin{pmatrix} d' \\ s' \end{pmatrix} = \begin{pmatrix} \cos \theta_C & \sin \theta_C \\ -\sin \theta_C & \cos \theta_C \end{pmatrix} \begin{pmatrix} d \\ s \end{pmatrix}, \quad (2.24)$$

and the weak interactions involving charged currents (W^\pm weak bosons) are then described using doublets of “rotated” quark states

$$\begin{pmatrix} u \\ d' \end{pmatrix}, \quad \begin{pmatrix} c \\ s' \end{pmatrix}, \quad \text{etc..}$$

The weak transition amplitudes are then written as¹⁶ $\mathcal{M} = \frac{4G}{\sqrt{2}} J^\mu J_\mu^\dagger$, with $G = \sqrt{2}e^2/(8M_W^2 \sin^2 \theta_C) \simeq 1.17 \times 10^{-5} \text{GeV}^{-5}$ as the Fermi constant,

$$J^\mu = \begin{pmatrix} \bar{u} & \bar{c} \end{pmatrix} \frac{\gamma^\mu(1 - \gamma_5)}{2} U_C \begin{pmatrix} d \\ s \end{pmatrix}, \quad (2.25)$$

as weak currents and U_C as the quark rotation matrix from (2.24). Favored (intra-family) transitions such as $u \rightleftharpoons d$ and $c \rightleftharpoons s$ contribute to \mathcal{M} with factors proportional to $\cos \theta_C$, whereas suppressed (inter-family) transitions give contributions proportional to $\sin \theta_C$.

In a generalized complex matrix U of dimension $n \times n$, the number of real parameters is $2n^2$. However, given the requirements of orthogonality and quark phase arbitrariness, the matrix should have a lesser amount of independent parameters. Because a rotation matrix should be orthogonal, it has only $\frac{1}{2}n(n-1)$ real parameters, and the quark phase arbitrariness further restricts the number of independent parameters — $\frac{1}{2}n(n-1)$ Euler angles and $\frac{1}{2}(n-1)(n-2)$ complex phases [82] [32]. In the Cabibbo *ansatz* $n = 2$, therefore we have one single real parameter — the Cabibbo angle — and no complex phases. However, for the $n = 3$ quark generations in the Standard Model we have three angles, and a complex phase which is responsible for $\hat{C}\hat{P}$ violation in the quark sector.

By convention, the quark mixing is often expressed in terms of a 3×3 unitary matrix V , called the Cabibbo–Kobayashi–Maskawa (CKM) matrix. This matrix operates on the charge $-e/3$ quark mass eigenstates d , s and b :

$$\begin{pmatrix} d' \\ s' \\ b' \end{pmatrix} = \begin{pmatrix} V_{ud} & V_{us} & \boxed{V_{ub}} \\ \boxed{V_{cd}} & \boxed{V_{cs}} & V_{cb} \\ \boxed{V_{td}} & \boxed{V_{ts}} & V_{tb} \end{pmatrix} \begin{pmatrix} d \\ s \\ b \end{pmatrix}. \quad (2.26)$$

¹⁶ *N.B.*: Hereon we use the natural units system $c = \hbar = k = 1$ unless otherwise explicitated.

The matrix elements in the diagonal are related to the favored (interfamily) quark transitions and therefore are close to 1. The values of individual matrix elements can, in principle, all be determined from weak decays of the relevant quarks. $\hat{C}\hat{P}$ violation arises from a single (complex) phase factor $e^{i\delta}$ that appears in the boxed matrix elements in (2.26), see e.g. [21]; the remaining (unboxed) elements of the CKM quark-mixing matrix are real. Defining $c_{ij} \equiv \cos \theta_{ij}$ and $s_{ij} \equiv \sin \theta_{ij}$ for the three family mixing angles θ_{ij} ($i, j = 1, 2, 3$, $i > j$), the standard parameterization of the CKM matrix V_{CKM} appears as [81] [79]

$$\begin{aligned}
 V_{\text{CKM}} &= \begin{pmatrix} 1 & 0 & 0 \\ 0 & c_{23} & s_{23} \\ 0 & -s_{23} & c_{23} \end{pmatrix} \begin{pmatrix} 1 & 0 & 0 \\ 0 & 1 & 0 \\ 0 & 0 & e^{i\delta} \end{pmatrix} \begin{pmatrix} c_{13} & 0 & s_{13} \\ 0 & 1 & 0 \\ -s_{13} & 0 & c_{13} \end{pmatrix} \begin{pmatrix} c_{12} & s_{12} & 0 \\ -s_{12} & c_{12} & 0 \\ 0 & 0 & 1 \end{pmatrix} \begin{pmatrix} 1 & 0 & 0 \\ 0 & 1 & 0 \\ 0 & 0 & e^{-i\delta} \end{pmatrix} = \\
 &= \begin{pmatrix} c_{12}c_{13} & s_{12}c_{13} & s_{13}e^{-i\delta} \\ -s_{12}c_{13} - c_{12}s_{23}s_{13}e^{i\delta} & c_{12}c_{23} - s_{12}s_{23}s_{13}e^{i\delta} & s_{23}c_{13} \\ s_{12}s_{23} - c_{12}c_{23}s_{13}e^{i\delta} & -c_{12}s_{23} - s_{12}c_{23}s_{13}e^{i\delta} & c_{23}c_{13} \end{pmatrix}. \quad (2.27)
 \end{aligned}$$

The matrices involving the parameters c_{ij} and s_{ij} in the first line each represent the quark mixing between the families of order i and j . The mixing angles satisfy the hierarchy $\theta_{13} \ll \theta_{23} \ll \theta_{12} \ll 1$ [54]. As part of the CKM scheme, the $\hat{C}\hat{P}$ -violating phase $e^{i\delta}$ becomes possible only with the introduction of the third doublet family. For energies scales below the mass threshold of the quarks from the third family, the CKM matrix can be approximated by the Cabibbo mixing matrix, which has no $\hat{C}\hat{P}$ -violating phase angle δ . Above the b mass threshold the kinematic suppression vanishes, and so does the suppression on $\hat{C}\hat{P}$ violation. This makes the B meson physics a very attractive testground for $\hat{C}\hat{P}$ physics.

In the context of B meson physics, it is useful to write the CKM matrix in a form suggested by Wolfenstein [158], with real-valued parameters $\lambda \equiv \sin \theta$, A , ρ and η :

$$\mathbf{V} = \begin{pmatrix} 1 - \frac{\lambda^2}{2} & \lambda & A\lambda^3(\rho - i\eta) \\ -\lambda & 1 - \frac{\lambda^2}{2} & A\lambda^2 \\ A\lambda^3(1 - \rho - i\eta) & -A\lambda^2 & 1 \end{pmatrix} + o(\lambda^4). \quad (2.28)$$

Whereas the parameters $\lambda = 0.2205 \pm 0.0018$ and $A = 0.824 \pm 0.075$ [36] are relatively well known, the parameters ρ and η are much more uncertain. The main goal of $\hat{C}\hat{P}$ -violation experiments [36] is to over-constrain these parameters and, possibly, to find inconsistencies suggesting the existence of new physics beyond the Standard Model.

The unitarity conditions for the CKM matrix elements describe triangles in the complex plane, called *unitarity triangles* [32] [36]. In figure 2.4 one

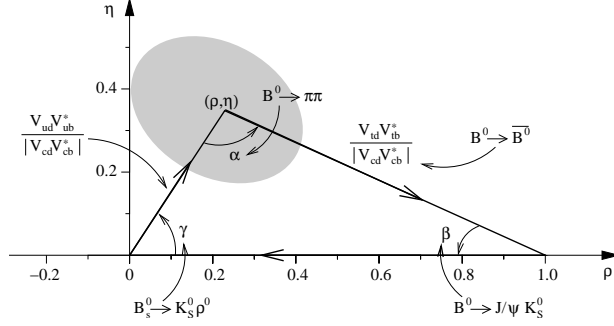


Figure 2.4. Representation of the unitarity triangle (2.30) in the (ρ, η) plane of the CKM matrix's Wolfenstein parameterization [108]. The vertices at $(0, 0)$ and $(1, 0)$ are fixed; the sides are normalized to $|V_{cd}V_{cb}^*| \simeq |\lambda V_{cb}|$. The blob [131] depicts the 95% confidence level bound for the (ρ, η) triangle vertex, given present knowledge of $\sin 2\beta$ measurements.

such triangle is represented. $\hat{C}\hat{P}$ violation is possible when the area of the triangle is different from zero (i.e. conventioning $V_{cd}V_{cb}^*$ as real and negative, $\eta \neq 0$) and its effect grows with the area. The unitarity condition applied to the first and second columns of the CKM matrix yields

$$V_{ud}^*V_{us} + V_{cd}^*V_{cs} + V_{td}^*V_{ts} = 0. \quad (2.29)$$

The parcels in the equation are related to the lengths of the triangle's sides. The first two parcels are $o(\lambda)$ and the third one is $o(\lambda^5)$. Because the last parcel is very small, the triangle is strongly flattened and the $\hat{C}\hat{P}$ violation effect on the K meson system is small. The unitarity condition associated to B meson decays is

$$V_{ud}V_{ub}^* + V_{cd}V_{cb}^* + V_{td}V_{tb}^* = 0. \quad (2.30)$$

The three parcels of the left member of equation (2.30) are $o(\lambda^3)$, so the triangle's sides should have comparable lengths and the $\hat{C}\hat{P}$ violation effects on this system should be relatively high. This is one of the main motivations to study $\hat{C}\hat{P}$ violation in the B meson system. After dividing (2.30) by $V_{cd}V_{cb}^*$, the triangle takes a particularly simple form in the (ρ, η) plane of the Wolfenstein parameterization, see figure 2.4. The triangle's tip is at

$$\frac{V_{ud}V_{ub}^*}{|V_{cd}V_{cb}^*|} = \bar{\rho} + i\bar{\eta}, \quad (2.31)$$

with $\bar{\rho} \equiv \rho \left(1 - \frac{\lambda^2}{2}\right)$ and $\bar{\eta} \equiv \eta \left(1 - \frac{\lambda^2}{2}\right)$. The triangle's angles *by definition* verify $\alpha + \beta + \gamma = \pi \pmod{2\pi}$,¹⁷ and are given by e.g. [36]

$$\alpha = \arg\left(-\frac{V_{td}V_{tb}^*}{V_{ud}V_{ub}^*}\right), \quad \beta = \arg\left(-\frac{V_{cd}V_{cb}^*}{V_{td}V_{tb}^*}\right), \quad \gamma = \arg\left(-\frac{V_{ud}V_{ub}^*}{V_{cd}V_{cb}^*}\right). \quad (2.32)$$

¹⁷This may not be true for theories beyond the Standard Model, and therefore its violation is a sign for New Physics.

It is possible to relate $\bar{\rho}$ and $\bar{\eta}$ to the angles β and γ by using (see e.g. [22])

$$\tan \beta = \frac{\bar{\eta}}{1 - \bar{\rho}} \quad \text{and} \quad \tan \gamma = \frac{\bar{\eta}}{\bar{\rho}}. \quad (2.33)$$

Experimentally, the coordinates (ρ, η) — or, in alternative, $(\bar{\rho}, \bar{\eta})$ — of the unitarity triangle’s tip is constrained by e.g. measurements of $\hat{C}\hat{P}$ violation in K^0 decays, or by the rate of $B^0-\bar{B}^0$ mixing (related to V_{td}). Unfortunately, the relations between observational quantities and the basic CKM parameters involve large uncertainties due to poorly known hadronic elements.

In B meson physics the angles of the unitarity triangle are often presented in the form of a sine or cosine of *twice* the angle, e.g. $\sin 2\beta$; this is seen in the expressions (2.40).¹⁸ Although the unitarity angles can be used to draw the shape of the unitarity triangle in $(\bar{\rho}, \bar{\eta})$ coordinates, it is instead the quantities $\sin 2\alpha$ and $\sin 2\beta$ that have physical significance; the third angle can be calculated from $\tan \gamma = \tan(\pi - (\alpha + \beta))$ in the Standard Model. The angle γ represents the $\hat{C}\hat{P}$ -violating phase angle δ in the CKM matrix appearing in the boxed elements of (2.26).

2.3.2 The violation of the \hat{C} , \hat{P} and $\hat{C}\hat{P}$ symmetries

The concept of parity was first introduced in the context of atomic physics by Wigner in 1927 [156]. For almost 30 years it was tacitly assumed that the microscopic laws of nature, and in particular nuclear reactions, were invariant for the inversion of a quantum state’s electric charge $\hat{C} : q \mapsto -q$, spatial reflection (or *parity*) $\hat{P} : \vec{r} \mapsto -\vec{r}$ and time reversal $\hat{T} : t \mapsto -t$. In Classical Mechanics, as well as in early formulations of Quantum Mechanics, measurements done on a unperturbed system yield the same results as a “mirrored” copy of that system, even though their states evolve differently. In particular, it is said that the system’s hamiltonian operator commutes with each of those (global) symmetry operations; in turn, Noether’s theorem ensures that such symmetries of the system’s lagrangian signals the presence of one (or more) conserved quantities.

However, in 1956 Lee and Yang argued [104] that there were no experimental confirmation of the conservation of \hat{C} and \hat{P} symmetries in nuclear reactions. Their work was primed by the observation of the violation of \hat{P} symmetry violation in meson decays $K^+ \rightarrow \pi^+\pi^0$ and $K^+ \rightarrow \pi^+\pi^+\pi^-$. This was known as the “ τ - θ ” puzzle,¹⁹ see e.g. [32] [31]. The evidence from

¹⁸One might interpret this choice based on the fact that the measurable quantities are *real* numbers, with transition amplitudes calculated from the matrix elements in the CKM matrix. This is hopefully evident in equations (2.39) and (2.40).

¹⁹The τ and θ were the names attributed to the (charged) particles seeding the two decays. The “puzzle” had to do with the fact that the invariant mass of the two decay products were experimentally indistinguishable.

their experiments suggested a *strong* violation of these symmetries — as seen, for example, in the Wu experiments in 1957 [159] — as a complete symmetrization of nuclear reactions in terms of *helicity*. They found that, concerning nuclear weak interactions, there are no “right” helicity particles (specifically, neutrinos and electrons) and no “left” helicity anti-particles (specifically, anti-neutrinos and positrons). The fact that no (anti-)particles of “forbidden” helicity were found made this a “strong” symmetry break, both for \hat{C} in the case of the Wu experiments and also for the \hat{P} case in the Goldhaber experiments in 1958 [75]. However, it should be noted that the verification of \hat{T} symmetry conservation is more tricky; it has been attempted in many ways, such as measuring the presence of a permanent atomic electric dipole moment [118].

To illustrate the neutrinos’ helicity asymmetry, it is now often said that “there are no right-handed neutrinos” and “there are no left-handed neutrinos”. Because neutrinos are spin- $\frac{1}{2}$ particles, *a priori* their helicity may take only two values $h = \pm 1$ — usually denoted in the literature by an indices “L” (left, $h = -1$) and “R” (right, $h = +1$). However, it is now known that neutrinos are emitted with left-handed helicity, and their right-handed counterparts are suppressed; similarly, Nature prefers right-handed anti-neutrinos to left-handed ones. Concretizing, given that $\hat{C}|\nu_{\pm}\rangle = |\bar{\nu}_{\pm}\rangle$ and $\hat{P}|\nu_{\pm}\rangle = |\nu_{\mp}\rangle$, the $|\nu_{+}\rangle$ and $|\bar{\nu}_{-}\rangle$ states were strongly suppressed. This is a very strong effect — these symmetries are said to be “maximally violated” because there are no left-over “wrong”-handedness neutrinos. However, since $|\nu_{-}\rangle$ and $|\bar{\nu}_{+}\rangle$ were the only “allowed” states, it was believed that the weak nuclear force intervening in these reactions was symmetric under the operation of \hat{C} and \hat{P} *in tandem*, $\hat{C}\hat{P}|\nu_{-}\rangle = \hat{C}|\nu_{+}\rangle = |\bar{\nu}_{+}\rangle$, even though it was not symmetric for each of those two operations individually. Therefore, at the time $\hat{C}\hat{P}$ seemed to be a “good” symmetry. It was later discovered that even this symmetry is not conserved although, as described in section 2.3.3 and following, this effect is rather weak. Incidentally, as stated in [31], the discovery of $\hat{C}\hat{P}$ violation in “strange particles” (e.g. K mesons) led to postulating the existence of a third quark family.

The $\hat{C}\hat{P}\hat{T}$ “theorem” [36] is believed to be always valid, since it is solely founded on two general assumptions, namely Lorentz invariance and the spin-statistics theorem — so that evidence of $\hat{C}\hat{P}\hat{T}$ violation would cause suspicion on the validity of those two general laws! This theorem states that all quantum system’s hamiltonian are invariant under the simultaneous operation of those symmetries, \hat{C} , \hat{P} and \hat{T} , even if the invariance does not hold under one or two of those symmetries. Under $\hat{C}\hat{P}\hat{T}$ invariance, $\hat{C}\hat{P}$ -violation implies a violation of time-reversal invariance \hat{T} . This intrinsic distinction between past and future on the *microscopic* level is beyond mere statistical considerations — it is a fundamental and remarkable aspect of Nature.

2.3.3 The *ansatz*: $\hat{C}\hat{P}$ violation in the neutral kaon system

The neutral K meson, or kaon, was labeled a “strange” particle, shortly after its discovery, for several reasons. Firstly, because of the unusually long lifetime (as high as $o(10^{-8}\text{s})$);²⁰ secondly, because the produced kaon beams show two distinct nonleptonic decay modes, $\pi\pi$ and $\pi\pi\pi$, at separate distances from the source and therefore with different lifetimes (by a factor of ≈ 600); and thirdly, because of the proximity of the invariant mass of the products of the two decays²¹, which caused some suspicions that a single particle could have those two decay modes. To distinguish between the short- and long-lived K^0 s, they are indexed respectively with a “S” and a “L”. The corresponding decay modes are $K_S^0 \rightarrow \pi\pi$ and $K_L^0 \rightarrow \pi\pi\pi$, respectively with odd and even final state parity: because pions are parity-odd systems, $\hat{P}|\pi\rangle = -|\pi\rangle$, we have $\hat{P}|\pi\pi\rangle = |\pi\pi\rangle$ and $\hat{P}|\pi\pi\pi\rangle = -|\pi\pi\pi\rangle$. The longer lifetime of the K_L^0 is foreseeable given its more restricted phase space: $3m_\pi \simeq 420\text{MeV}/c^2$ compared to $m_K \simeq 500\text{MeV}/c^2$, which barely gives enough mass to allow this decay mode.

The conservation of *both* charge conjugation \hat{C} and parity \hat{P} in a particle’s decay, i.e. $\hat{C}\hat{P}$ conservation, would *in principle* ensure that each superposition state would always decay in the same fashion, since the 2π and 3π states are $\hat{C}\hat{P}$ -distinct. However, the first evidence of $\hat{C}\hat{P}$ violation was found on $K_L^0 \rightarrow \pi^+\pi^-$ decays and reported by Cronin, Fitch and collaborators in 1964 [42]. They observed that one out of every ≈ 500 K_L^0 decays would have the “wrong” $\pi\pi$ final state. This anomaly is the sign of a violation, albeit small, of $\hat{C}\hat{P}$ -symmetry conservation in neutral kaon decays.

The neutral kaon system can be described by a quantum superposition of $\hat{C}\hat{P}$ eigenstates $|K_L^0\rangle$ and $|K_S^0\rangle$; this is useful also in explaining e.g. the regeneration of the K_S^0 component of the kaon beam when it transverses nuclear matter. An alternative base for the neutral kaon is the mass eigenstates $|K^0\rangle$ and $|\bar{K}^0\rangle$, which behave differently under the strong interaction (they have symmetric isospin and strangeness) but can mix, under the weak interaction, through $K^0 \rightleftharpoons \pi\pi \rightleftharpoons \bar{K}^0$.

The general relation between the mass and $\hat{C}\hat{P}$ eigenbases is given by

$$|K_L^0\rangle = p_K |K^0\rangle + q_K |\bar{K}^0\rangle, \quad (2.34a)$$

$$|K_S^0\rangle = p_K |K^0\rangle - q_K |\bar{K}^0\rangle, \quad (2.34b)$$

with $|p_K|^2 + |q_K|^2 = 1$. The two states $|K_L^0\rangle$ and $|K_S^0\rangle$ may be projected

²⁰This has to do with the suppression of decays that violate the conservation of the *strangeness* quantum number — associated to the quark strange content.

²¹The mass asymmetry $|m_{\pi\pi\pi} - m_{\pi\pi}|/(m_{\pi\pi\pi} + m_{\pi\pi})$ is below 10^{-18} [34]. The mass difference $\Delta m_K = o(\text{ns}^{-1})$ of the kaon system’s mass eigenstates K^0 and \bar{K}^0 makes for a oscillation between the two states which is slower than on heavier systems like the B^0 .

into $\hat{C}\hat{P}$ -odd states using the operator $\frac{1}{2}(1 + \hat{C}\hat{P})$ [79], to obtain

$$(1 + \hat{C}\hat{P}) |K_L^0\rangle = (p_K - q_K) (|K^0\rangle - |\bar{K}^0\rangle) , \quad (2.35a)$$

$$(1 + \hat{C}\hat{P}) |K_S^0\rangle = (p_K + q_K) (|K^0\rangle - |\bar{K}^0\rangle) . \quad (2.35b)$$

The ratio R of transition amplitudes of the decays $K_L^0 \rightarrow \pi\pi$ and $K_S^0 \rightarrow \pi\pi$ is then

$$R = \frac{A(K_L^0 \rightarrow \pi\pi)}{A(K_S^0 \rightarrow \pi\pi)} = \frac{\langle \pi\pi | (1 + \hat{C}\hat{P}) |K_L^0\rangle}{\langle \pi\pi | (1 + \hat{C}\hat{P}) |K_S^0\rangle} = \frac{p_K - q_K}{p_K + q_K} \approx \frac{1 - q_K/p_K}{2} . \quad (2.36)$$

Would the $\hat{C}\hat{P}$ symmetry be invariant, and we would have $q_K = p_K$ and $R = 0$. However, $\hat{C}\hat{P}$ asymmetry does exist, although it is quite small, $R = (3.01 \pm 0.05) \times 10^{-3}$ [81].

2.3.4 $\hat{C}\hat{P}$ violation in the B^{neut} golden decay

The quantum superposition similar to (2.34) can be applied to the $B^0\text{--}\bar{B}^0$ system. In this case, the heavy and light mass eigenstates are, respectively,

$$|B_H^0\rangle = p |B^0\rangle + q |\bar{B}^0\rangle , \quad (2.37a)$$

$$|B_L^0\rangle = p |B^0\rangle - q |\bar{B}^0\rangle \quad (2.37b)$$

(in the p and q parameters, the B index was dropped for simplification). It can be shown [36] [32] [124] that, in the case of B_d^{neut} mesons present in golden decays (1.2), the p and q parameters are related to the CKM matrix elements and unitarity angle β by

$$\frac{q}{p} \approx -\frac{V_{tb}^* V_{td}}{V_{tb} V_{td}^*} \simeq \frac{(1 - \rho)^2 - 2i\eta(1 - \rho) - \eta^2}{(1 - \rho)^2 + \eta^2}; \quad (2.38)$$

the minus sign comes from the system's $\hat{C}\hat{P}$ parity. This quantity is very sensitive, since $|V_{tb}| \simeq 1$ and $|V_{td}| \simeq 0$. The rigorous equality includes additional phase factors, which denounce further phenomena; see [36].

A special class of B^{neut} meson (B_d^0 , or its antiparticle \bar{B}_d^0) decays, where the final state is a $\hat{C}\hat{P}$ eigenstate, are predicted to show strong $\hat{C}\hat{P}$ asymmetries directly related to the shape of the unitarity triangle, without involving poorly known hadronic amplitudes. The two amplitudes, which interfere to generate a particle–antiparticle asymmetry, come from the direct decay $B^0 \rightarrow X$ and the decay through mixing $B^0 \rightarrow \bar{B}^0 \rightarrow X$. Examples of the direct decay modes are the golden decay (1.2) and, to a lesser extent (due to spoiling “penguin”²² contributions), $B^0 \rightarrow \pi^+\pi^-$ and $B_s^0 \rightarrow \rho^0 K_S^0$.

²²For an amusing illustration of the naming origin of these Feynman diagrams, see page 134 of reference [32].

The amplitude of $\hat{C}\hat{P}$ asymmetry is given by the angles of the unitarity triangle, which in turn are best measured in a few key decays — α (the decay $B^0 \rightarrow \pi^+\pi^-$), β ($B^0 \rightarrow J/\psi K_S^0$) and γ ($B_s^0 \rightarrow \rho^0 K_S^0$). For example, the golden decays of B^0 (and \bar{B}^0) to $J/\psi K_S^0$ yield [32]

$$\frac{q}{p} \frac{A(\bar{B}^0 \rightarrow J/\psi K_S^0)}{A(B^0 \rightarrow J/\psi K_S^0)} \simeq -\frac{V_{tb}^* V_{td} V_{cb} V_{cs}^*}{V_{tb} V_{td}^* V_{cb}^* V_{cs}} = -e^{-2i\beta} ; \quad (2.39)$$

the quotient of the decay amplitudes, $|A(\bar{B}^0 \rightarrow \dots)/A(B^0 \rightarrow \dots)| = 1$ (i.e., it only contributes with a complex phase factor). The rates of golden decays from B^0 and \bar{B}^0 mesons are given by [108] [36]

$$n(t) \propto e^{-\Gamma_B t} (1 + \sin(2\beta) \sin(xt)) , \quad (2.40a)$$

$$\bar{n}(t) \propto e^{-\Gamma_B t} (1 - \sin(2\beta) \sin(xt)) \quad (2.40b)$$

respectively, with Γ_B as the B 's decay width (see section B.7 in appendix), which experimentally is found to be very close to the \bar{B} 's [81]. The mixing parameter $x \equiv \Delta M/\Gamma = 0.71 \pm 0.06$ [32] [81], where ΔM is the mass difference of the mass eigenstates and $\Gamma = 1/\tau$ and τ the particle's lifetime. The time t is measured in units of B lifetime. The factor $\sin(2\beta)$ accounts for the $\hat{C}\hat{P}$ asymmetry, and $\sin(xt)$ is related to $B^0 \rightleftharpoons \bar{B}^0$ mixing (with a rate $x\Gamma \simeq 5.3\text{ps}^{-1}$ [81]). Because x is relatively large, the mixing of B^0 and \bar{B}^0 is an significant effect.

To detect $\hat{C}\hat{P}$ violation in the golden decay mode, one needs samples of pure B^0 and \bar{B}^0 mesons, and measures of their decay widths. A reconstructed $J/\psi K_S^0$ decay could result from either a B^0 or a \bar{B}^0 , therefore the initial flavor of a reconstructed B needs to be determined from the second B in the event (the “tagging B ”). If B and \bar{B} are produced equally and detected with equal efficiency, the observable asymmetry A_{int} of time-integrated rates is then

$$A_{\text{int}} = \frac{N - \bar{N}}{N + \bar{N}} = \frac{x}{1 + x^2} A_{\hat{C}\hat{P}} \quad (2.41)$$

(the last equality holds for $t = 0$), with $N = \int n(t)dt$, $\bar{N} = \int \bar{n}(t)dt$ and $A_{\hat{C}\hat{P}} = \sin(2\beta)$ in the case of perfect tagging. Direct $\hat{C}\hat{P}$ violation (i.e., not involving B - \bar{B}^0 oscillation) has been recently measured in $B^0 \rightarrow K^+\pi^-$ and $\bar{B}^0 \rightarrow K^-\pi^+$ decays in the BABAR experiment, obtaining a decay asymmetry of $(N_{K^-\pi^+} - N_{K^+\pi^-})/(N_{K^-\pi^+} + N_{K^+\pi^-}) = -0.13 \pm 0.01$ [20].

Experimentally, one requires a minimum separation between the primary vertex and the B decay vertex, in order to suppress background. This requirement, normally called a “*detached vertex*”, may be approximated by a cut in the proper decay time, $t > t_0$. The asymmetry for $t > t_0$ is then

$$A_{\text{int}}(t_0) = \frac{N(t_0) - \bar{N}(t_0)}{N(t_0) + \bar{N}(t_0)} = M(t_0) A_{\hat{C}\hat{P}} , \quad \text{with } M(t_0) = \frac{\sin(xt_0) + x \cos(xt_0)}{1 + x^2} . \quad (2.42)$$

Mixing in the B meson system, and therefore $\hat{C}\hat{P}$ asymmetries, are governed by time scales $t \approx \pi/(2x) \approx 2$; the contribution of early decays to A_{int} is small. This property can be used to improve statistical accuracy, by fitting the time-dependent asymmetry

$$a(t) = \frac{n(t) - \bar{n}(t)}{n(t) + \bar{n}(t)} = A_{\hat{C}\hat{P}} \sin(xt) .$$

Since the $\hat{C}\hat{P}$ asymmetry builds up slowly, the cut in the B decay time at t_0 costs little in terms of statistical significance. By cutting away all events below $t_0 = 0.7$, the statistical errors are almost unaffected [108]. This property simplifies $\hat{C}\hat{P}$ experiments considerably, and allows to select clean B samples by a cut on vertex separation.

Nevertheless, the tagging of the initial B meson flavor is unfortunately never perfect, and the observable asymmetry $A_{\text{obs}} < A_{\text{int}}$. Two effects dilute the tagging:

- Mixing of the tagging B .
- Wrong tags due to particle misidentification, ambiguous tagging signatures, etc.

The effects of mixing in the tag are only relevant if B^0 or B_s^0 tags are used. If no lifetime cuts are applied for the tagging B , the probability that it has changed its flavor when it decays is $f_M = \frac{x^2}{2(1+x^2)}$. For B^0 one finds $f_M \approx 0.16$, compared to $f_M \approx 0.5$ for B_s^0 . The detectable (integrated) $\hat{C}\hat{P}$ asymmetry is reduced by a dilution factor $D_M = 1 - 2f_M = 1/(1+x^2)$, yielding

$$A_{\text{obs}} = D_M M(t_0) A_{\hat{C}\hat{P}} .$$

For the typical case of lepton tagging, the net dilution factor $D_M = \langle \frac{1}{1+x^2} \rangle \approx 0.67$. Mistagging with a probability f_T due to other reasons will reduce the observable asymmetry by another dilution factor $D_T = (1 - 2f_T)$. For example, a lepton from the decay chain $b \rightarrow c \rightarrow l + X$ will carry the wrong sign compared to a direct lepton and will cause mistagging. The final observable asymmetry is therefore

$$A_{\text{obs}} \approx D_M D_T M(t_0) A_{\hat{C}\hat{P}} , \quad (2.43)$$

and the error on $A_{\hat{C}\hat{P}}$ is

$$\Delta A_{\hat{C}\hat{P}} \approx \frac{1}{M(t_0) P} \frac{1}{\sqrt{N_{B^0}}} , \quad (2.44)$$

where N_{B^0} is the total number of reconstructed B^0 mesons after all cuts, the ‘‘tagging power’’ factor is

$$P = D_M D_T \sqrt{\epsilon_{\text{tag}}} \quad (2.45)$$

and ϵ_{tag} is the probability to finding a tag. All studies yield similar results of $P \simeq 0.3$ for HERA- B [1].

2.4 Rounding-up: from the measurement of $\hat{C}\hat{P}$ asymmetry to baryogenesis

As stated in the previous section, the strength of $\hat{C}\hat{P}$ violation in the hadronic sector of the Standard Model can be described by a pair of parameters — either (ρ, η) , or two of the three angles from the unitarity triangle (with $\alpha + \beta + \gamma = \pi$). In particular, the golden decay (1.2) is favorable for measuring the angle β . Knowledge of the quark mixing matrix (2.28) requires two additional parameters A and λ ; however, the fundamental $\hat{C}\hat{P}$ -violating effects originate from a complex phase factor, expressible in terms of those angles. The prediction of e.g. decay widths makes use of transition amplitudes, which themselves incorporate complex factors with symmetric phases for particles and anti-particles, and ultimately leads to different rates, i.e. $\Gamma(X \rightarrow f) \neq \Gamma(\bar{X} \rightarrow \bar{f})$.

For the past two decades or so some attempts were made to clarify whether the Standard Model is a sufficient source for the observed baryon asymmetry of the Universe $10^{-11} < n_B/s < 10^{-10}$. The findings are, however, contradictory: on one hand, positive results were obtained [57] [58], where asymmetries as high as 10^{-11} are assumed to appear under optimal conditions; on the other hand, the negative results obtained in [67] [69] [68] [88] tell how several factors conspire to bring down the expected asymmetry to values not higher than 10^{-20} [141]. The outlook on the Standard Model of particle physics is that it is likely not the best framework for scenarios of baryogenesis, and this motivates the search of alternatives. In either case, it is obvious that those estimates require actual experimental results.

The HERA-*B* experiment

*“A modern detector like HERA-*B* is about as complicated as a fighter jet.”*
— in *HERA-*B* Technical Design Report [83]*, pg. 428

The HERA-*B* detector was proposed in 1994 as an “Experiment to study CP violation in the *B* meson system” [108]. This chapter is devoted to describing the detector apparatus and the data reconstruction chain. Most of the information compiled here was extracted from the experiment’s Proposal [108] and Technical Design Report [83]. The last section of this chapter briefly overviews some important results obtained at HERA-*B*.

3.1 The HERA proton beam

The HERA accelerator is installed in the 6.3km-long toroidal HERA (Hadron Electron Ring Anlage) ring accelerator, at the DESY (Deutsches Elektron Synchrotron) facility in Hamburg, Germany; see figure 3.1. Inside the HERA tunnel, 27.5GeV/*c* electrons and 920GeV/*c* protons circulate in separate vessels, guided by distinct sets of dipole (bending) and quadrupole (focusing) magnets for each beamline. Beam steering is achieved with conventional 0.165T-electromagnets in the electron beamline (HERA-e), and superconducting 4.65T-magnets in the proton beamline (HERA-p). The two beams cross the four distinct experiment sites installed in the HERA halls — H1 (North hall), ZEUS (South hall), HERMES (East hall) and HERA-*B* (West hall). The proton beam is of use to the two later experiments; HERA-*B* does not use of the electron beam. The particle beams are injected into the HERA storage ring in stages, each providing more beam kinetic energy than the last. This chapter will focus on the description of the HERA-*B* detector.

The generating and controlling of the HERA proton beam is independent of the experiments that are served by it. The proton beam is sourced from H^- ions. The ions are created from molecular hydrogen with a magnetron and are then directed into a “stripping foil” that removes the ions’ electrons [102]. The resulting proton stream is then accelerated in radiofrequency

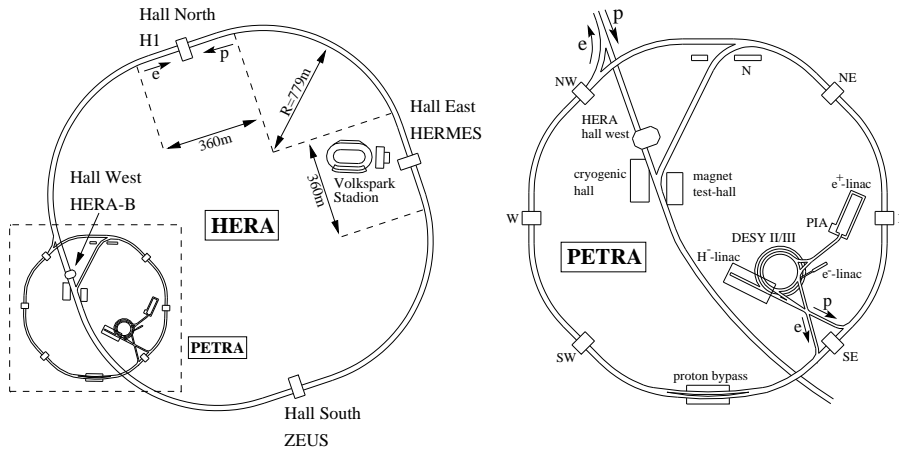


Figure 3.1. The HERA (left) and PETRA (right) storage rings [131]. The proton beam circulates counter-clockwise. HERA-B is installed in the West Hall.

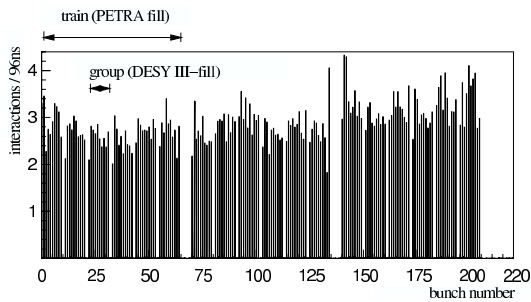


Figure 3.2. Periodic structure of the HERA proton beam [124]. Each PETRA fill contains six DESY III fills. The bunch crossing rate is 96ns, and each of them may (or not) be filled with protons; the latter correspond to empty bunches.

resonator cavities and injected into the DESY storage ring by a linear accelerator (LINAC III), at the end of which the particles have a nominal kinetic energy $E_k = 50\text{MeV}$. The RF cavities give the beam a bunch-like structure, with $\mathcal{O}(10^{11})$ protons per bunch. In the DESY III storage ring, ten protons bunches are stored and accelerated up to an energy $E_k = 7.5\text{GeV}$. Upon obtaining a stable circulating beam, it is injected into the next stage, a larger storage ring called PETRA (Positron Electron Tandem Ring Accelerator), where the beam energy is increased to $E_k = 40\text{GeV}$. PETRA collects six DESY III fills, in a total of 60 bunches. Once again, after obtaining a stable beam, it is then injected into the next stage, the HERA ring. HERA stores three PETRA beam trains, and accelerates them to the final beam energy $E_k = 920\text{GeV} \pm 0.2\text{MeV}$ [81]. The proton bunch structure is depicted in figure 3.2.

The rate at which the bunches transverse the HERA-B target region is called bunch crossing (or “bx”), and has a nominal value of $1/96\text{ns} = 10.4\text{MHz}$; the bunch length is about 8.5cm [81]. The stable HERA proton beam holds $6.3\text{km}/(c \times 96\text{ns}) \simeq 220$ “buckets”, out of which 180 are filled with proton bunches. Therefore, the bx rate of *filled* proton bunches is

$\approx 8.5\text{MHz}$. Two sets of scintillators (VETO counters) placed upstream of the target, at $z = -34\text{cm}$ and $z = -100\text{cm}$, detect background events originated by beam protons lost upstream — therefore giving means to validate events from beam–target collisions. The typical proton beam current is of a few 10mA , wherefore each (filled) bunch has typically $o(10^{10})$ protons.¹ It has also been observed that the bunches' size increases with time so that, after a typical maximum of 10 to 20 hours running, the proton beam develops an enveloping continuous current called *coasting beam* [51]; electron–proton collisions in other experiments in HERA also create a slow growth of the proton beam's transverse emission [108]. The coasting beam grows in time to form a population of beam particles whose orbits are unstable; those particles, which have energy deviations $|\Delta E/E| \gtrsim 10^{-4}$ [1], eventually abandon the designed beam orbit and are lost. The transverse density distribution of beam particles is gaussian relative to the design trajectory; the typical transverse r.m.s. size scale of the beam is $\sigma = o(1)\text{mm}$ [83], with an ellipsoid shape wider in the horizontal axis. Additional information about HERA (both particle beams) is summarized in reference [81].

Two important reasons for using protons as beam particles in HERA-B are: higher beam energies can be achieved with a storage ring of a given radius; and also, energy losses due to synchrotron radiation $\Delta E \propto m_{\text{beam}}^{-4}$ [117] are lower when compared to electrons, for example. From the first aspect one gains a higher center-of-mass energy (than using electrons, for example), see equation (B.27):

$$E_{\text{CM}} = \sqrt{m_1^2 + m_2^2 + 2E_1m_2} \approx \sqrt{2E_1m_2} \quad \text{if } E_1 \gg m_1, m_2 \quad (3.1)$$

(indexes 1 and 2 are for a beam and a target particle, respectively); one may also conclude that higher E_{CM} values are achieved when using massive particles, such as nucleons, for target — i.e. the CM energy contribution from a proton–electron collision is negligible when compared to proton–nucleon collisions. From the second aspect one gets a stable beam environment, with shorter delays between data-taking periods for beam refills.

3.2 The HERA-B detector

The HERA-B detector occupies a volume of $20 \times 9 \times 9\text{m}^3$ in the HERA West Hall, see figures 3.3 and 3.4; this relates merely to the room for the detector's sensitive and support surfaces and radiation shielding, and excludes the volume required for data processing electronics, manual controls and gauges, computer farm and hardware and personnel access. The hardware is remotely managed from a control room detached from the detector hall.

¹Actually, the proton current is set to somewhat lower, in order to reduced undesired radiation backgrounds in HERA-B.

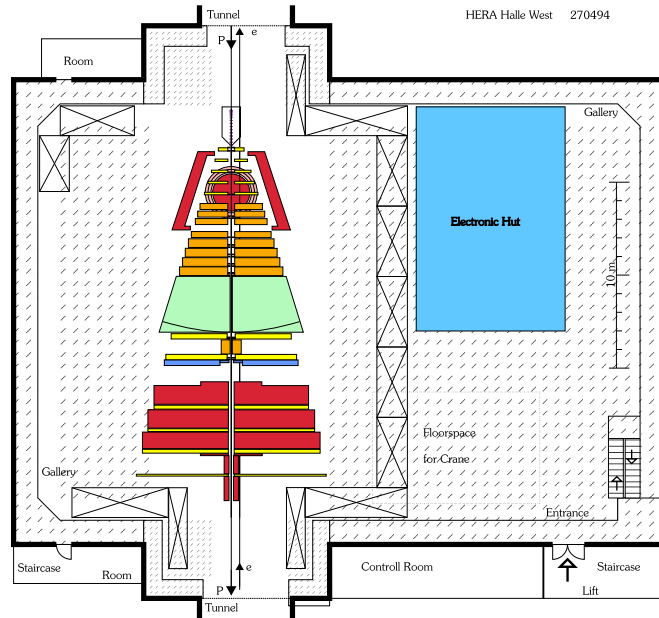


Figure 3.3. Top view of the HERA-B detector in the HERA west hall [108].

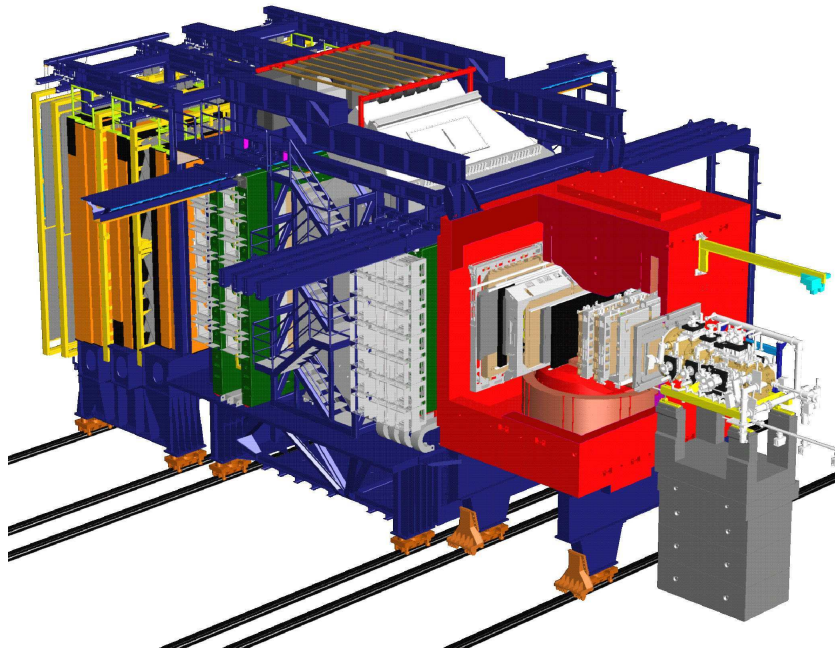


Figure 3.4. Isometric view of the HERA-B detector with the year 2001 configuration. The Magnet is cutout to show the High- p_T trigger chambers, described in section 3.2.11. The proton beam enter from the left side.

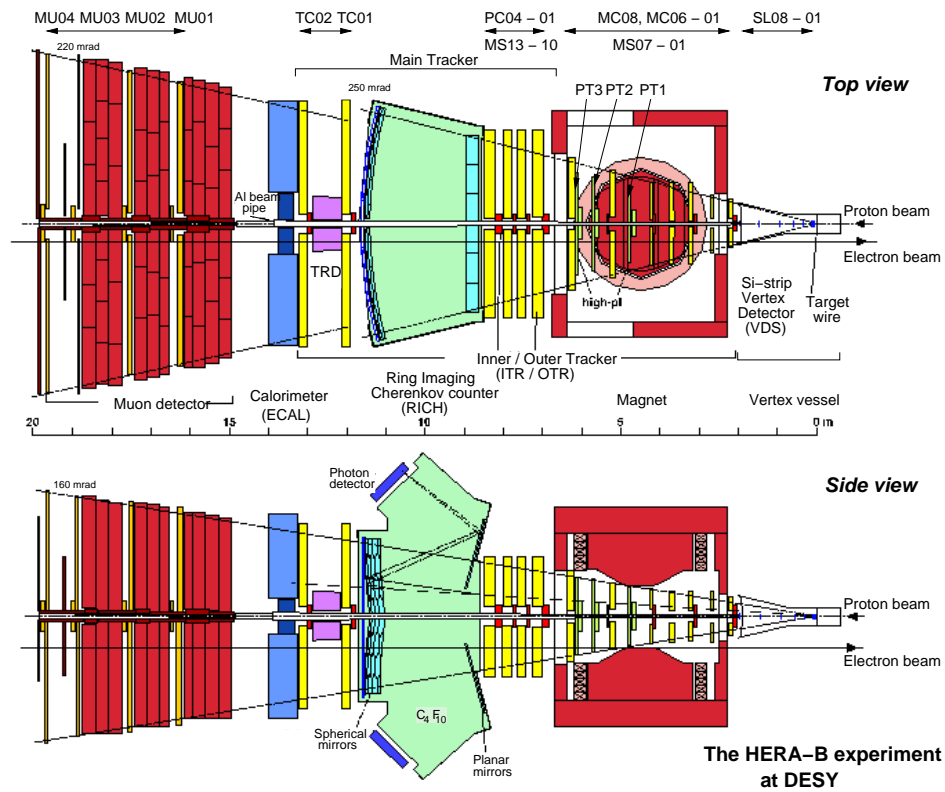


Figure 3.5. Schematic overview of the HERA-B detector in its 2002 configuration.

The composition of the detector is similar to other fixed target particle detectors, with instruments specialized in measuring specific particles' properties, see figure 3.5. For example, the use of a Silicon Vertex Detector close to the interaction region is an idea adapted from the P238 collaboration — an experiment in the CERN $S\bar{p}\bar{p}S$ hadron collider that demonstrated the feasibility of operating such device inside the accelerator's storage ring vacuum proposal. HERA-B's instruments are basically classified as either:

Tracking devices: ² Silicon Vertex detector (VDS); Microstrip Gas Chambers (MSGC) detector (Inner Tracker, or ITR); straw/honeycomb drift chambers (Outer Tracker, or OTR). The ITR+OTR combination is also known as the *main tracker* in HERA-B.

Particle identification devices: Ring Imaging Čerenkov detector (RICH); Transition Radiation detector (TRD); Electromagnetic Calorimeter (ECAL); and Muon detector chambers.

Each of these instruments will be discussed in detail in subsequent sections. The tracking devices' sensitive surfaces are responsible for detecting the

²Also called *hodoscopes*— which literally translates from greek as “pathviewer” [34].

particle flux and convert it into recordable electronic signals. These surfaces must have the highest possible interaction length, in order to detect the particles' passage while disturbing them minimally. On the other hand, some of the particle identification (PID) devices, namely the ECAL and Muon detector, intentionally convert most (or all) of the particle's kinetic energy, so it is measured (ECAL) or its passage detected (Muon). The electronic signals from the tracking and PID instrumentation are digitized and used in an online event reconstruction chain to ascertain that individual events are eligible for detailed physics analysis. The rejected events are discarded, and the events flagged for analysis are stored in magnetic tape at the end of the event reconstruction chain.

The electronic readout from the different subdetectors is used in the full event reconstruction, but since the number of channels times the event rate is too high ($\mathcal{O}(0.5 \times 10^6) \times \mathcal{O}(\text{MHz}) = \mathcal{O}(\text{TB/s})$) to be handled by any communications and magnetic storage hardware, many events must be discarded. The candidate physics events go through a series of four selection stages, or *trigger levels*, where gradual refinements in the online event reconstruction find out which events are suitable for detailed (offline) analysis and physics studies. These trigger levels are discussed in more detail in sections 3.3.4 through 3.3.7. The first two levels are called First Level Trigger (FLT) and Second Level Trigger (SLT), respectively. The FLT is implemented with fast hardware electronics, and the SLT in a hybrid of electronics for data buffering and software. These trigger levels look for suitable decay candidates — such as two muon candidates whose invariant mass make them a possible decay $J/\psi \rightarrow \mu^+ \mu^-$. Such triggering events, selected by the FLT and the SLT, are fully reconstructed and classified in a PC-based networked computer farm, which implement the Third and Fourth Level Trigger (TLT and 4LT). Each event passing all selection criteria implemented in the triggering scheme is finally stored in magnetic tape from the 4LT for offline physics analysis. Figure 3.6 presents an overview of the HERA-B trigger system. The sequential event filtering reduces the data flow at each stage to a suitable rate and improves the signal-to-background ratio by eliminating obviously unfit events: the ratio of $b\bar{b}$ -quark to inelastic events is $\sigma_{b\bar{b}}/\sigma_{\text{inelastic}} \approx 10^{-6}$, and the “golden decay” (1.2) branching ratio is $\mathcal{O}(10^{-4})$ [108]. The 4LT output rate is around 1Mb/s, which corresponds to roughly 10 HERA-B events per second. The total number of b -quark events with opposite-charged dileptons (e^+e^- or $\mu^+\mu^-$) in the J/ψ mass range ($m_{J/\psi} \simeq 3.1\text{GeV}$) found in the year 2000 data-taking was 40 [5]; the reduced statistics is largely due to the fact that during that year some relevant detector parts were still being commissioned.

All tracking detectors consist of layers which form planes perpendicular to the proton beam axis. Many layers appear in pairs called “double layers” where the two single layers have the same (TRD) or different (VDS, MSGC) projections, or “stereo angles”. Several neighbouring layers of var-

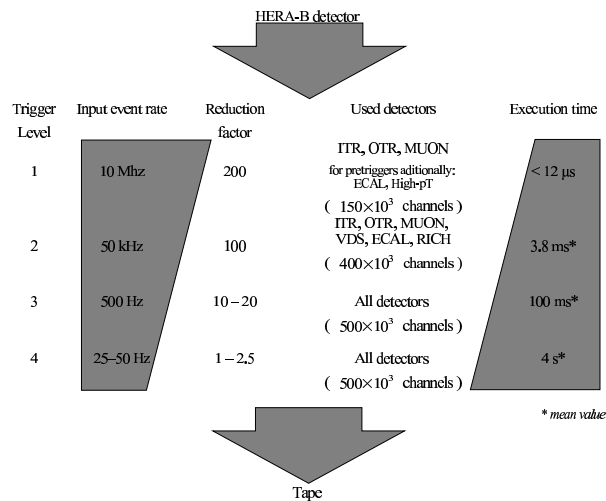


Figure 3.6. Overview of the HERA-B trigger levels, with design values for event rates, suppression and latency [154] [124].

ious detector types and of various stereo angles form a detector unit called “superlayer” — a unit in mechanical sense, concerning the construction, as well as in logical sense, concerning the trigger and offline reconstruction strategy. Layers and superlayers cannot be built as one mechanical rigid piece because the enclosed beam pipe would not allow removal of detector parts. Consequently, one layer has to consist of several layer “segments” which can be moved apart from each other. Due to frames and in order to avoid dead angular regions, the segments must overlap slightly. Such overlap can be achieved only if the segments are set up in two or even three consecutive planes along the beam axis.

The HERA-B coordinate system is defined by a direct orthogonal triadron (z, x, y); see representation in figure 3.7. By convention, the z coordinate has the orientation of the proton beam; the x axis and y axis have the horizontal (towards the HERA inner radius) and vertical directions, respectively. The choice of the frame’s origin is arbitrary and not too important. However, it is not possible to define it as the point where beam–target collisions occur, since it is a finite volume (assumed to be inside the target material) rather than a point.

3.2.1 Internal target

HERA-B is described as a “fixed target” detector, in the sense that the beam particles collide with a target that is stationary in the detector frame. Rigorously, the target is not “fixed”; rather, its position in the beam halo environment is controlled by stepping motors, which respond to instructions from HERA-B’s Slow Control system. The target position is changed at a rate of 10Hz; the stepping motors precision is of the order of $1\mu\text{m}$ [86]. During data-taking, the Slow Control system adjusts the target position to maintain a constant beam–target interaction rate o (MHz). Nevertheless, the

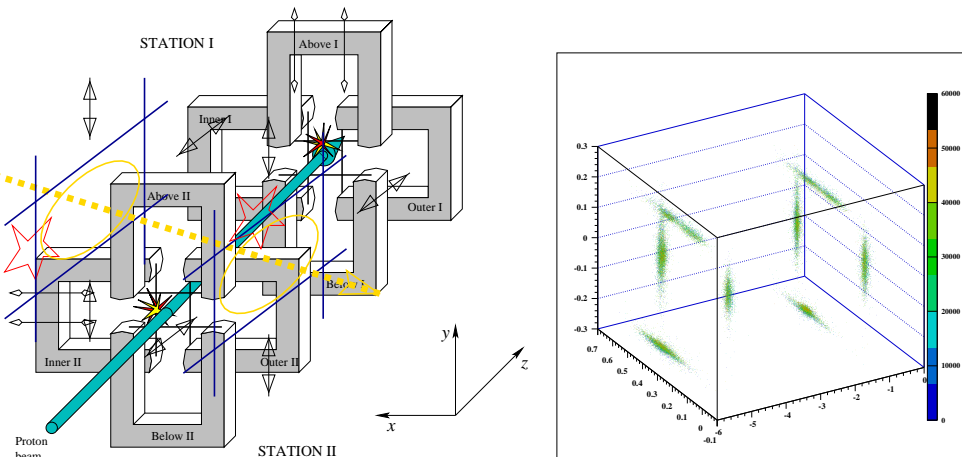


Figure 3.7. Left: schematic view of the HERA-B target, consisting of eight wires mounted on independently movable forks, which group in two stations with a beam-wise separation $\Delta z \approx 5\text{cm}$ and move radially into the beam halo (transversing arrow). Adapted from [108]. Right: reconstructed vertices while all eight target wires are operated simultaneously at the beam [1].

frequency of target placement corrections (and the target's speed in motion) is negligible when compared to the beam, so it is perfectly acceptable to consider the target as stationary.

The HERA-B embedded internal target consists of a set of eight wires made of different materials: three wires made of carbon, two of titanium, and the remaining are each of tungsten, aluminium and palladium. The wires are very thin (with a diameter $\approx 500\mu\text{m}$ for carbon and $\approx 50\mu\text{m}$ for the remaining materials) and mounted on fork-like supports that move perpendicularly to and from the beam. The different materials are used to study the dependence of b quark production cross section on the target's atomic number, $\sigma_{b\bar{b}} \propto A^\alpha$, with α close to 1; see e.g. [153]. Using several target wires at once results in higher interaction rates. The choice of massive target wires instead of a gas stream target also reduces the interference with HERA operation. The target wires are placed in the beam halo, where they “clean up” the beam from protons in unstable orbits, on the verge of being lost and no longer necessary for beam luminosity; a gas stream target would intersect the whole beam instead. The target wires not used in a data-taking run are retracted. The scheme in figure 3.7 depicts the target concept of HERA-B.

The important reason for choosing a fixed target detector configuration has to do with its improvement on the separation of production and decay vertexes of heavy, short-lived particles [36]. If one such particle moves slowly in the center-of-mass frame ($\beta \ll 1$), the distance covered in one particle lifetime is often much less than the detector's spacial resolution, and this

results in not being possible to separate the particle's production and decay space points. However, the Lorentz boost from the center-of-mass to the detector frame stretches the separation of these vertexes and eases the reconstruction of the decaying particle track. HERA-B was conceived for adequate primary vertex separation and its association with individual target wires. Simulations show that an average of one interaction per bunch crossing occurs for each wire [23]. The main disadvantage of the fixed target configuration is the lower available center-of-mass energy for a given ring accelerator, see equation (B.27). The ZEUS experiment, for example, measures proton-electron collisions of the two HERA beams, at a center-of-mass energy of 332GeV. Higher CM energies in such scattering experiments becomes important when the creation of new particles ($E = mc^2$) and/or resolution ($E = hc/\lambda$) in finding the nucleons' parton distribution are being studied.

The fixed target proton-proton collisions in HERA-B occur at a total center-of-mass energy $E_{\text{CM}} \simeq 41.57\text{GeV}$ (see equation (3.1)). The lower E_{CM} (than ZEUS for example) is of lesser importance in HERA-B: the interest is focused on properties of intermediate-mass particles such as the B^0 (with a mass $m_B \simeq 5.2\text{GeV}/c^2$), and it outperforms most other experiments in its high interaction rate (up to 10MHz) for obtaining a significant number of those rare particles.

The Lorentz boost from the center-of-mass frame to the laboratory frame has boost parameter $\gamma = E_{\text{CM}}/(2m_p) = 22.16$ (see equation (B.28)). This corresponds to a pseudo-rapidity (equation (B.34)) $\eta_{\text{HERA-B}} = 3.79$; therefore, a $\beta \lesssim 1$ particle right-angle-deflected in the CM frame has a deflection angle of $\theta = 45.2\text{mrad}$ (equation (B.32)) in the laboratory frame. HERA-B has an angular acceptance from 10 up to 220 milliradians in the horizontal plane, and 10 to 160 milliradians in the vertical plane, yielding CM pseudorapidity coverages $-1.59 < \eta_{\text{horz}} < 1.51$ and $-1.26 < \eta_{\text{vert}} < 1.51$ in the horizontal and vertical planes, respectively. This translates as a center-of-mass angular coverage with horizontal and vertical plane angles (relative to the beam direction), respectively, from roughly 25° up to 157° (or 435mrad up to 2740mrad), and from 25° to 148° (435mrad to 2590mrad). The CM solid angle coverage is then, approximately,

$$\frac{(2.740 - 0.435) \times (2.590 - 0.435)}{\pi^2} \simeq 50\% . \quad (3.2)$$

Figure 3.8 presents the laboratory angular distribution of 1000 Monte Carlo minimum bias events; the HERA-B geometric acceptance under these conditions is similar to (3.2). The Vertex Detector's (section 3.2.4) geometric acceptance was found to be 59.8%; the fraction of particles with azimuthal angles $\theta < 10\text{mrad}$ and $\theta > 250\text{mrad}$ are 25.4% and 14.8% respectively.

The HERA-B internal target is placed inside the VDS vessel under vacuum. It consists of two stations with four target wires each, positioned at

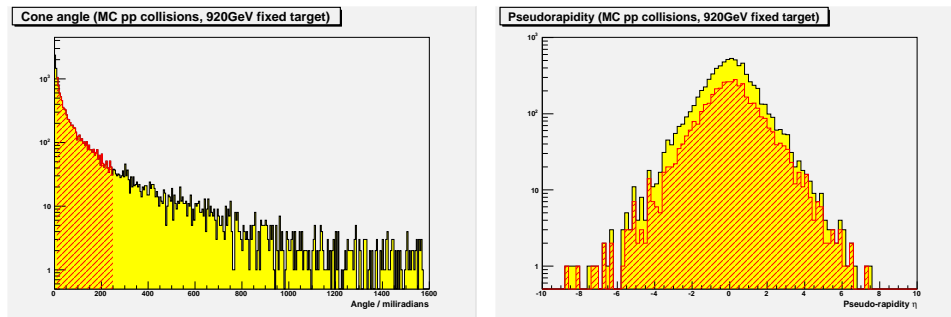


Figure 3.8. Left: Azimuthal angle distribution of charged particles emitted from fixed-target 920GeV proton–proton collisions, from 10^3 events generated with the PYTHIA Monte Carlo event generator [143]; the beam orientation corresponds to the angle 0 rad. Right: pseudo-rapidity coverage of the charged particles from the same events. The dash-filled histogram (red) corresponds to tracks within a conical trunk aperture equal to the VDS horizontal acceptance.

The dash-filled (red) region is approximately 60% of the left histogram’s area and corresponds to a conic aperture given by HERA-B’s Vertex Detector System (horizontal) geometric acceptance, $10\text{mrad} < \theta_h < 250\text{mrad}$. The unshaded regions $\theta < 10\text{mrad}$ and $\theta > 250\text{mrad}$ are occupied by, respectively, 25% and 15% of the particles.

$z \simeq -5\text{cm}$ (station II) and $z \simeq 0\text{cm}$ (station I). Each wire is positioned at the top, bottom, inner (i.e., towards the HERA curvature radius) and outer positions.

3.2.2 Dipole magnet

The HERA-B dipole magnet design is depicted in figure 3.9. Its purpose is the generation of a static magnetic field that bends the trajectory of transversing charged particles. In association with the tracking system, this makes it possible to measure each charged particle track’s momentum from their curvature radius inside the magnetic field. The momentum p (in GeV/c) of a beam particle of charge q (in units of electron charge) is related to the curvature radius ρ (in meters) of the particle’s trajectory in a (static, uniform) magnetic field of intensity B (in Tesla) by [117]

$$p = 0.3qB\rho . \quad (3.3)$$

The HERA-B dipolar magnetic field is generated by 10 piled-up electromagnet coils, with 32 turns each, with a current of 4.5kA per turn and per coil. The magnetic field is a cylindrical region, of approximately $z_{\text{max}} - z_{\text{min}} = 2.7\text{m}$ base diameter and 2.4m height, centered at $z = 4.5\text{m}$ downstream from the target, with the field lines flowing vertically, from top to bottom. A $5.8 \times 10^5\text{kg}$ iron yoke shields the region outside the magnet

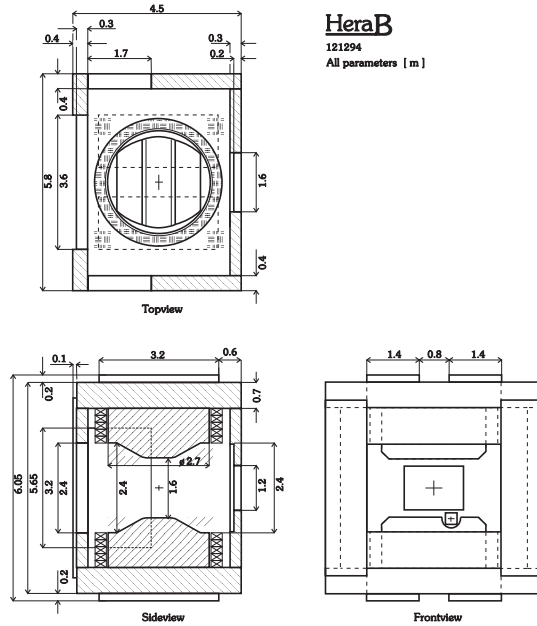


Figure 3.9. The design of the HERA-B spectrometer magnet [83]. It consists of two iron poles, an iron flux return yoke and two cylindrical copper coils. In the topview, the proton beam entry window is to the right.

against the magnetic flux inside. The field intensity is usually expressed in terms of a quantity called *field integral*, which for HERA-B is

$$e \int_{z_{\min}}^{z_{\max}} B dz = 0.635 \text{ GeV}/c = 2.12 \text{ T m} . \quad (3.4)$$

Because the magnetic field is static, $\partial B/\partial t = 0$ and the track's momentum is conserved. Therefore, a track of length $z_{\max} - z_{\min}$ inside the magnetic field gets a transversal (relative to the original trajectory in the bending plane) component of momentum equal to $0.635 \text{ GeV}/c$.

The HERA-e beam transverses the detector, parallel to the proton beam pipe and approximately 90cm away from it. All components, except the Vertex detector, have acceptance “blind spots” where the beam pipe cuts through them for passage. But, the presence of the HERA-B magnet makes it also necessary to shield the electron beam from the magnet's influence. For this effect, the HERA-e beam is surrounded by an array of superconductors running parallel to the beam at the magnet location. These superconductors' currents will adjust themselves during the ramping of the magnet to the proper values required to shield the field [108]. The presence of the magnet also requires the compensation of the HERA-p beam. For this purpose, two additional beam magnets are used, one just before the target (with a field integral of about 2.5 T m) and a second one behind the spectrometer (field integral of about 0.8 T m). The peak beam deflection from its nominal orbit occurs in the center of the spectrometer magnet and amounts to $\approx 5 \text{ mm}$.

3.2.3 Proton beam pipe at HERA-*B*

The HERA-*B* proton beam pipe is divided in three major sections, connected by all metal sealed flanges: the vacuum chamber housing the Vertex Detector System (3.2.4); a 0.5mm-thick, 12m-long aluminium pipe extending downstream to the Electromagnetic Calorimeter (section 3.2.9); and a 11–15cm diameter stainless steel beam pipe transversing the Muon Detector System (section 3.2.10). The sectioned pipe has greater diameter downstream from the target, widening with an half-angle of 7mrad [1]. The interaction length of these materials are typically a few decimeters. The HERA-*B* beam pipe is designed to satisfy these major requirements: minimal secondary-particle production in the beam pipe; sectioned pipe to allow step-by-step installation of the different detector parts; and a good 10^{-8} mbar vacuum, which is required by the HERA machine group to prevent any impact on the proton beam lifetime and emittance. Two vacuum pumps are installed upstream and downstream of the HERA-*B* detector; one additional pump is installed 15m downstream of the target.

3.2.4 Silicon vertex detector

The Silicon Vertex Detector, or VDS in HERA-*B* jargon, is arguably the most important detector component of this experiment, since its main task is to allow the reconstruction of the production and decay vertexes of the short-lived particles that are the experiment's object of study. The VDS vessel is shaped as a conical trunk, approximately 2.6m long and 1.4m wide at its greater radius, and it covers the first 2m downstream of the target. Its internal diameter starts at an inner radius of 10mm upstream that extends to about 70mm downstream. Since the vessel acts as a resonant field cavity for the beam, four $5\mu\text{m}$ -thin, 13mm-wide steel bands are positioned at 7mm from the beam to reduce the wake fields and shield the beam from this negative effect. The vessel also incorporates the HERA-*B* internal target, which remains in the beampipe vacuum environment.

The detecting surfaces of the Silicon Vertex Detector are $50\text{mm} \times 70\text{mm}$ areas centered on the face sides of $52\text{mm} \times 72\text{mm} \times 280\mu\text{m}$ silicon wafers. Those surfaces are etched with $25\mu\text{m}$ -pitch strips of doped p-type semiconductor on one side and n-type on the opposite side. Every second diode strip is capacitively couple to one aluminium strip, laying on top of it; the resulting readout pitch is $50\mu\text{m}$. The aluminium strip corresponds to one readout channel. A thin SiO_2 layer insulates the aluminium and semiconductor strip layers. Lastly, the polarization is achieved with bias voltage of over 300V applied between the two sides of the wafer with regularly spaced "guard ring" structures. Figure 3.11 depicts the transversal cut of a VDS silicon wafer. The p- and n-type sides hold 1024 and 1280 readout channels respectively. The strip orientation on the wafer surfaces' planes are almost

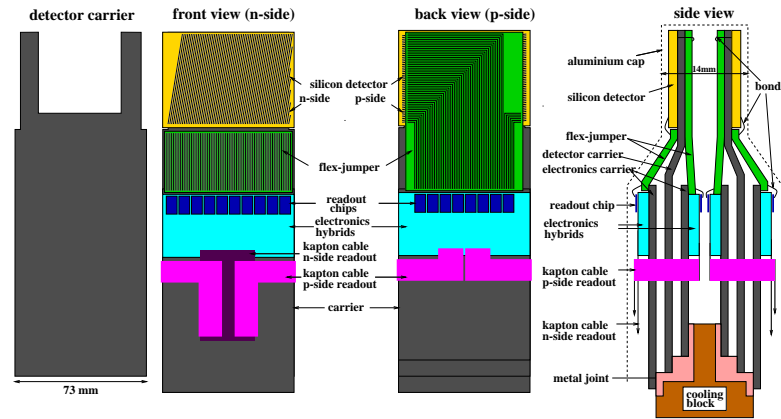


Figure 3.10. Schematization of a VDS module (far right) for superlayers SL5/6 (see fig. 3.13); the involving dotted line is the aluminium foil isolating the module from the beam vacuum [140]. The detector (middle views) sits on a support structure (far left). The module blocks are refrigerated to maintain a temperature around $+10^{\circ}\text{C}$.

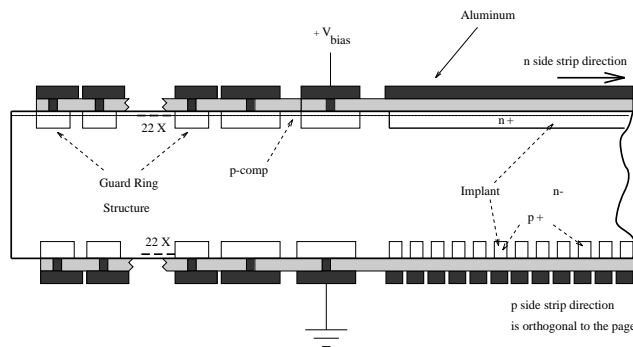


Figure 3.11. Transversal cut of the VDS silicon wafer (courtesy of Klaus Ehret). A thin layer of *p*-type semiconductor (“*p*-comp”) serves as insulator for the *n*-type strips, allowing its capacitive coupling to the readout aluminium strips.

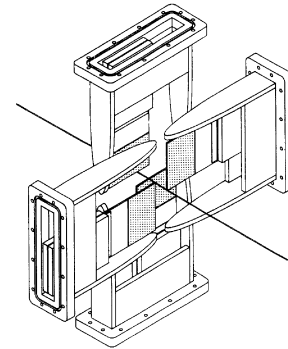


Figure 3.12. Four VDS modules and their caps arranged in one superlayer [108]. The aluminium foils that cover the caps are not shown.

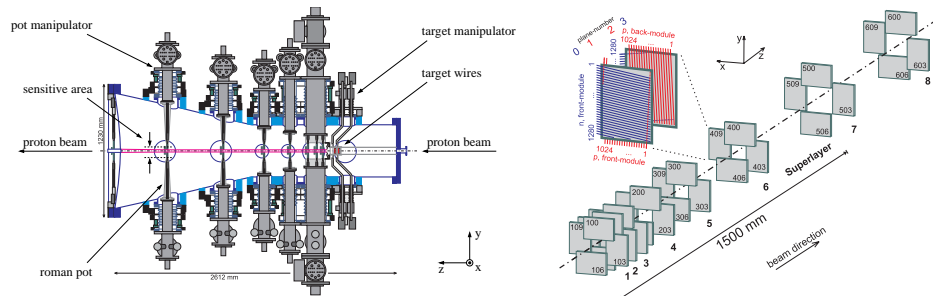


Figure 3.13. Left: The VDS vessel (left) [38] contains the target system and silicon strip detectors. The superlayers SL1 through SL7 are steered into the beam halo inside the roman pots. The eight superlayer, SL8, is placed outside the vessel, right after the exit window (far left). Right: The eight silicon superlayers [99]. The detached plane (409) is a set of two back-to-back modules; their strip orientations form angles of $\pm 90^{\circ} \pm 2.5^{\circ}$ with the HERA-B *xy* plane orientation. The target system (not shown) is in front of SL1.

perpendicular; on one side, it is 2.5° (relative to one edge), on the opposite side it is 92.5° .

The passage of ionizing particles through the silicon wafer produces roughly 2×10^4 electron-hole pairs, and each charge drifts to the doped strips of adequate polarization. The charge accumulation then produces a pulse signal on the aluminum strip lying on top of the corresponding semi-conducting strip. Depending on the incidence angle with the module's silicon surface, the ionising particles can elicit a measurable signal within one or more neighbouring strips (called clusters in this context) of each side. More than half the clusters have a width of two strips, and one quarter of clusters are one strip wide; only 5% of hits are signaled with cluster of more than 4 strips [155]. The measured signals from the strips laid on both sides of the active area of a module allows the determination of the coordinates of the transversing particle. In a worst case scenario, only around 6×10^3 electrons are collected as signal; the conservative expectancy of the signal-to-noise ratio was $S/N \gtrsim 9$ [108], but values of around 20 were obtained, dropping to 14 for the most radiation-damaged strips [155] — those closer to the beam. For each (x, y) coordinate set of the passing particle on one plane, the signal of each strip from a cluster of activated strips is weighted for higher location precision. The resulting error in hit position measurement is estimated to be within $15\mu\text{m}$ [108] [155]. The geometric efficiency determined in simulation is quite high [83] — around 96% for electrons and leptons, and 89% for K mesons.

Each wafer defines a (single- or double-sided) layer, and with its readout electronics it constitutes one $138\text{mm} \times 72\text{mm}$ module. Figure 3.10 shows the front and back views of a detector surface, as well as the side view of an assembled double-side module. The readout electronics is a set of 8 and 10 specialized radiation-resistant chips (HELIX), respectively for each 1024 or 1280 strips on opposing sides of a silicon layer. Each readout chip amplifies the analogic signal of one batch of 128 neighboring strips, and temporarily stores it in a read-write pipeline buffer with a depth of 128 samples/channel.³ The strip readout and buffer sampling is synchronized with the proton bunch crossing. The analogic output of these readout chips is piped with Kapton cables, one for each side. A module may hold either one or two layers, with their respective electronics and thermal drains mounted in a module support. Double-layered modules have one 1mm-thick berillium slice between them for additional structural strength and cooling. The back-to-back disposition of a pair of layers in a module gives strip orientations of -2.5° , 87.5° , 2.5° and 92.5° ; the resulting redundancy of hit's plane coordinates is sufficient for adequate reconstruction demands. Each module is placed inside one shield-

³The buffer depth of the HELIX chips, used in the VDS and ITR, is slightly higher: 141samples/channel. These subdetectors have are subject to the highest track densities, therefore have the highest channel numbers. The extra buffer depth is present to satisfy the requirements for a sufficient readout time after the $128\text{samples} \times 96\text{ns} = 12.3\mu\text{s}$ period.

ing cap in partial vacuum (10^{-6} mbar), separated from the beampipe's own 10^{-8} mbar vacuum; the cap is made of a thin (around $150\mu\text{m}$) aluminium foil that isolates its contents from the electromagnetic medium of the beam. The caps intrude the vessel in a "roman pot" system, which allows the detectors to come closer to the beam (with positive influence on impact parameter resolution [108]) and minimize the matter to be crossed by particles from the interaction point with the beampipe that would otherwise be in place. The roman pots move into place for data-taking and are retracted $\approx 30\text{cm}$ for beam fills to minimize radiation damage on the modules. Four modules, placed perpendicularly to the beam direction (above, below, and inside and outside beam radiuses) group as a superlayer — see figure 3.12.

The VDS has a total of 8 superlayers (one more than originally proposed [108] [83]) holding 28 modules, with 112 single-sided layers; see figure 3.13. The superlayers are positioned to allow uniform coverage in rapidity. A particle from the target region typically crosses 6 to 7 (super)layers [108]. It has a high spatial granularity, at a total of about 176×10^3 electronic readout channels.

3.2.5 Inner tracker system

In face of the large forward boost, it is important to track the particles that travel close to the beam and correspond to a significant fraction of the forward hemisphere in the beam-target center of mass. The detector units of the ITR are Microstrip Gaseous Chambers (MSGCs), each coupled with a foil of Gas Electron Multiplier (GEM). They were designed to withstand particle fluxes of up to $10^6\text{mm}^{-2}\text{s}^{-1}$. The ITR has 135×10^3 channels.

The inner tracker system, or ITR for short, covers the range of distances between 7cm and 20cm from the proton beam — corresponding to an angular range between $\approx 10\text{mrad}$ and $\approx 100\text{mrad}$ — with the forward superlayers placed right after the VDS at $z \simeq 2.0\text{m}$ and the most downstream layers in front of the ECAL, at $z = 12.9\text{m}$. Each layer consists of four L-shaped independent detectors which overlap in their sensitive regions by $\sim 4\text{mm}$ to cover the full area. The overlapping also guarantees full efficiency and commonly-measured tracks for relative alignment. The geometric placement of the detectors is done to reduce the radiation length seen by particles (around 0.03% per module [129]) and detectors' occupancies (below 10%); for example, the vertical subdivision of the layers at the beam height reduces the occupancy per strip by a factor of two [83], and the horizontal subdivision allows the extraction of layers without removal of the beam pipe.

Each detector module is a $23\text{cm} \times 25\text{cm}$ unit, with a sensitive area enclosing a $\sim 19.4\text{cm} \times 13.0\text{cm}$ region, cut out at one corner to allow placing it by the beam pipe; the remaining module area is occupied by electronics. The MSGC volume is a glass box made of $400\mu\text{m}$ -thick glass substrate, with a gaseous mixture of 70% argon and 30% CO_2 at $10\text{N}/\text{m}^2$ (i.e., $\sim 10^{-2}\%$ of the

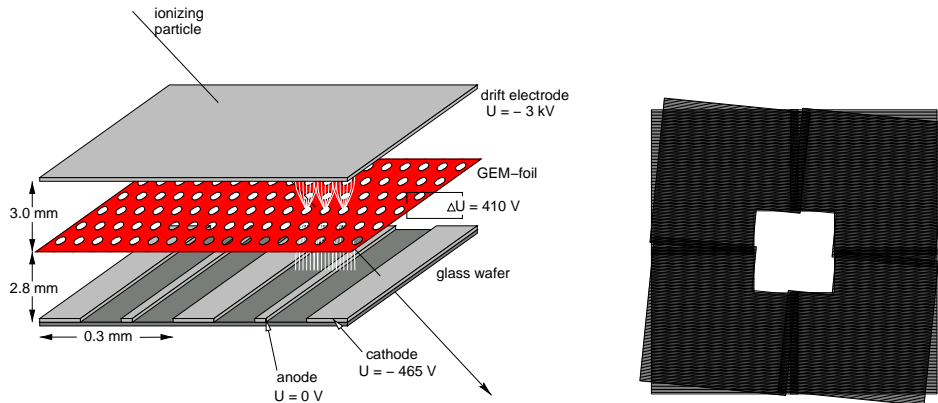


Figure 3.14. Left: illustration of the MSGC chamber with GEM technique [131]. Right: view of the sensitive areas of four MSGCs surrounding the proton beam [140]. The covered area is about $40 \times 40 \text{ cm}^2$; two layers (0° and $+5^\circ$) are shown.

atmospheric pressure). Inside the MSGC, the detector's readout structure lays on the opposite surface of the common drift electrode, made of copper and placed $\sim 6 \text{ mm}$ away from it. The readout structure of the MSGC consists of a microelectrode structure of 500 nm -thick gold cathodes and anodes, which are lithographically laid on the glass wafer. The anodes and cathode widths are $10 \mu\text{m}$ and $170 \mu\text{m}$ respectively, with a $60 \mu\text{m}$ gap between them; therefore, the pitch is $300 \mu\text{m}$. The anode and cathode voltages are respectively 0 V and -465 V ; the drift cathode voltage is -3 kV . Finally, the MSGCs are complemented with Gas Electron Multipliers (GEMs), which allows lower electrode voltages while keeping the total multiplication factor. The GEM is a $50 \mu\text{m}$ -thick kapton foil, clad with $7 \mu\text{m}$ -thick layers of copper on both sides. The GEM has a regular grid of $55 \mu\text{m}$ -diameter holes, staggered with a pitch of $140 \mu\text{m}$.

During the design phase it was found that if the field strength is adjusted to provide sufficient signals for minimum ionizing particles, then heavy ionizing particles (such as α particles) will often produce sparks that destroy the delicate structure of the MSGC. The intermediate gas amplification is introduced by the GEM layer, which allows for a reduction of the cathodes' voltages. A minimum ionizing particle transversing the MSGC-GEM ionizes the gas mixture and produces about 30 electrons in the 3 mm gap between the drift electrode and the GEM, where primary ionization typically occurs [53]. The electrons drift through the holes in the GEM layer, which multiplies the electron avalanche. The gas amplification works in two stages, with gains significantly depending on the gas mixture conditions and electrode voltages: the MSGC yields a gain factor between 100 and 1000, and the GEM step contributes with another factor of 15 to 50.

The MSGCs are positioned perpendicularly to the proton beam, except

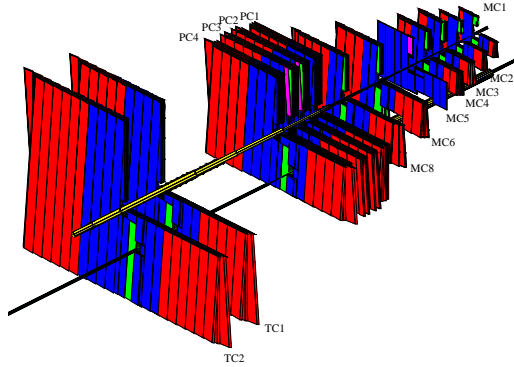


Figure 3.15. Spatial view of the OTR modules, with upper right quadrant cutout for visibility [121]. The layers MC2–MC8 were removed for the 2002/2003 running period due to large production of bremsstrahlung [98].

inside the magnet where they're tilted by a small angle (up to 8°) to compensate for the magnetic dipolar field. In the plane perpendicular to the beam, the MSGCs are aligned so that the electrode strips lie in angles of 0° and $\pm 5^\circ$ relative to the vertical. The resulting spacial resolution is better than $100\mu\text{m}$ horizontally and 1mm vertically. This design is used because the magnetic field bends charged particles in the horizontal plane and precision is needed for the momentum measurement. The spacial resolution, granularity, and track separation capabilities are fully sufficient for the track density in the region occupied by the ITR.

3.2.6 Outer tracker system

The outer tracker system, or OTR for short, complements the ITR acceptance coverage for the track reconstruction downstream of the magnet. It has the same number of superlayers than the ITR, except for the magnet where it has three additional superlayers. The chambers inside the magnet are commonly called *magnet chambers*, or “MC”. Downstream from the magnet there are six superlayers — four in front of the RICH, labeled PC01–PC04 (the *pattern chambers*), and two behind it labeled TC01 and TC02 (*trigger chambers*). The OTR chamber layers are situated in the region $210\text{cm} < z < 1320\text{cm}$; see figure 3.15. The magnet and pattern chambers are used for track finding, momentum measurement and reconstruction of K_S^0 decays; the trigger chambers are primarily dedicated to hardware event triggering, and are also used for track matching with the calorimeter and muon detector. The OTR stations are placed at the roughly the same downstream position as the ITRs'. Each OTR plane encompasses an angle greater than the ITR coverage. The use of the same technology as the ITR's for the wide area covered by the OTR would make it expensive — the costs per unit area are about 60 times as much for the ITR as it is for the OTR [108]. Nevertheless, the performance requirements for the OTR-covered region of the detector makes it acceptable the use of its less costly technology.

The OTR detector units consist of planar layers of drift tubes arranged

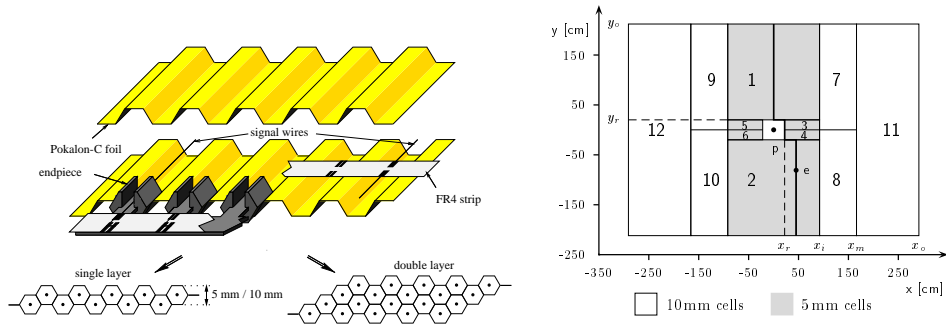


Figure 3.16. Left: the honeycomb structure of OTR drift chambers [131]. Right: downstream perspective of the sections in superlayer TC02 [83].

perpendicularly to the proton beam; those tubes form collections of Honeycomb Drift Chambers (or HDCs), so called because of the tubes' hexagonal-shaped section. The tubes are grouped in 32cm-wide modules, and within each superlayer they are arranged in twelve sections characterized by different tube lengths. The innermost sections are placed slightly in front of the surrounding outer sections and overlap them to avoid dead space and to satisfy the space requirements of HDCs of different orientations — 0° , $+5^\circ$ and -5° relative to the vertical. The choice of tube widths takes into consideration a balance between acceptable channel occupancies (below the 20% level at 40MHz interaction rate) and number of channels (one tube per channel, in a total of 96×10^3 channels for the OTR system [83]); the sections closer to the beam pipe have HDCs of smaller diameter (5mm) than those further away (10mm). The orientation of the HDCs are relevant for track reconstruction in the bending plane (perpendicular to the dipolar magnetic field), and are ideal for track momentum measurement. The TC chambers are double-layered (with wires paired as logical OR), whereas the remaining are single-layered. The double-layered chambers used for triggering purposes consist of double layer 0° wires sandwiched by double layers of $\pm 5^\circ$ wires. The thinnest superlayers (MC2–MC9) have transverse thicknesses of $\Delta z = 11.5\text{cm}$ whereas the thickest superlayers (used for triggering) are up to $\sim 26\text{cm}$ thick.

Each hexagonal tube is assembled from folded foils of $50\mu\text{m}$ -thick polycarbonate (Pokalon-C), with an thin gold coating on the inner surface which serves as cathode. The anode wire is a $25\mu\text{m}$ -thick gold-plated tungsten wire mounted at the tube length before the cells are closed by two merged Pokalon foils. The result is a single layer of HDCs. The voltage applied between tube electrodes is $o(2)$ kV [83]. The drift gas is a mixture of $\text{Ar}/\text{CF}_4/\text{CO}_2$ at normal pressure. The passage of charge particles through the HDCs ionizes the gas mixture, and the resulting electrons drift to the anode at fast enough speeds $o(100)$ $\mu\text{m}/\text{ns}$ [83]. This allows higher precision of position deter-

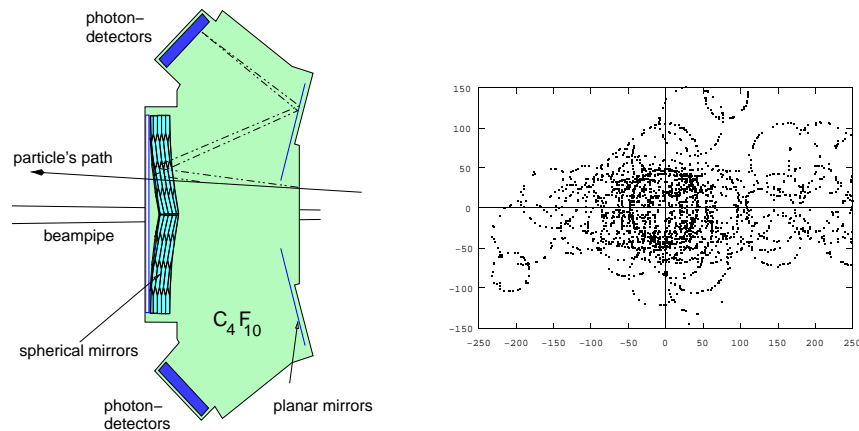


Figure 3.17. Left: schematic side view of the HERA-B RICH detector [129]. The HERA-B target is to its right. Right: example of the observed RICH hits in an inelastic event. The Čerenkov photons, caused by charged tracks with $v > c/n$, are focused into the planar mirrors by the RICH's spherical mirror array, and the detected photon hits are projected as a circle with aperture related to the particle's Čerenkov angle.

mination by measuring the drift time (between bunch crossing and a tube signal); the left/right ambiguity in the drift charges' origin within a tube is obviously unavoidable, but e.g. double-layered OTR planes have enough redundancy to allow accurate track reconstruction by relating hits in consecutive layers. Up to year 2000 the hit resolution was at $\sim 0.2\text{mm}$ [161]. The cell hit efficiencies were between 90% and 95%, which has significant impact on the hardware triggering efficiency — the reduction from the expected 98% to 94% produces a drop in the First Level Trigger efficiency by approximately a factor of three [89].

3.2.7 Ring imaging Čerenkov detector

The Ring Imaging Čerenkov detector, or RICH for short, is the forwardest component of the HERA-B detector used in charged hadron identification, namely for distinguishing protons and kaons. It consists of a stainless steel vessel with a volume of 108m^3 [162], placed downstream of the OTR's PC chambers and in front of the two OTR Tracker Chambers layers. The vessel houses a gas volume serving as the detector's active medium, two sets of mirrors, and photodetectors. The particle entry and exit windows are made of 1mm-thick aluminium instead of the steel used in the remainder of the vessel. The vessel is transversed by the proton and electron beam pipes, with necessary cutouts.

The RICH's function is based on the phenomenon of Čerenkov radiation, the coherent electromagnetic radiation emission of a charged particle that

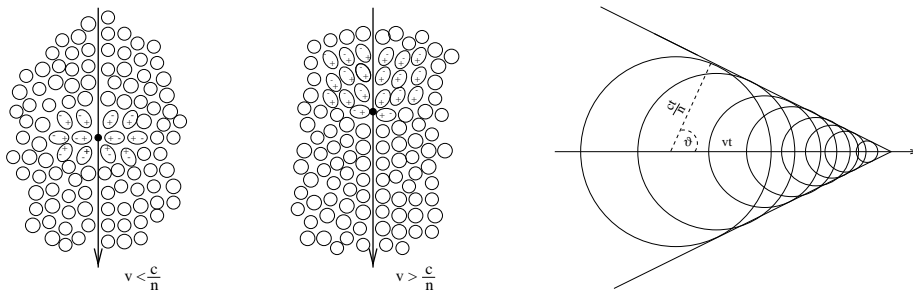


Figure 3.18. At left and at center: molecular dipole distribution in dielectric medium caused by the passage of a low- and a high-velocity charged particle, respectively [129]. On the right: the Čerenkov wave front construction by superposition of elementary spherical waves produced by a $v > c/n$ charged particle along its trajectory.

transverses a dielectric medium at a speed greater than the speed of light in it. The fast transversing particle produces non-isotropic polarization in the dielectric's atoms along its path, and causes those atoms to emit light when they de-excite. If the particle's speed is less than the light's speed in the medium, the light is destroyed by destructive interference; if, however, the particle's speed is greater than the light's in the medium, then light is emitted by constructive interference in the medium. The Čerenkov photons are emitted at an angle θ_C relative to the particle track, given by

$$\cos \theta_C = \frac{1}{\beta n}, \quad (3.5)$$

with $\beta \equiv v/c$ as the particle's speed in units of c and n as the medium's refraction index for Čerenkov photons of a given energy. Therefore, for each particle type there exists a certain *threshold* momentum below which $1/(\beta n) > 1$ and for which there is no Čerenkov radiation emission. For pions, kaons and protons, the threshold momenta are, respectively, $2.5\text{GeV}/c \sim 9.5\text{GeV}/c$ and $\sim 18\text{GeV}/c$; see e.g. [76]. The number of Čerenkov photons of wavelength λ , emitted per unit path length, is [117]

$$N(\lambda)d\lambda = 2\pi\alpha \left(1 - \frac{1}{\beta n}\right)^2 \frac{d\lambda}{\lambda^2}. \quad (3.6)$$

After measuring the Čerenkov angle of photons produced by a charged track, the corresponding particle's velocity is determined. From this the particle may be identified, in the form of a constraint on its mass obtained from the velocity β and the linear momentum p found by tracking techniques (using the vertex detector and the main tracker). At high momenta ($pc \gg mc^2$) the velocity difference between two different particles decreases with

the squared momentum and the separation is more difficult [129]:

$$\Delta\beta = \frac{(m_K^2 - m_\pi^2)c^4}{2p^2}. \quad (3.7)$$

The choice of this technology is more adequate than e.g. time-of-flight measurement solutions because of the tiny time difference (below $o(10)$ ps in a flight path of a few meters) between kaons and protons of typical momentum (a few $o(10)$ GeV) in HERA-B [129].

The adequate choice of radiator gas (the dielectric medium) is determinant [129] for good resolution on θ_C measurements: on one hand the refractive index must be close enough to unity ($n - 1 \leq 10^{-3}$) to allow sufficient ring aperture resolution at high momenta (0.2mrad around 50GeV/c [108]); and on the other hand, the hadron's (specifically, protons and kaons) threshold momenta should be as low as possible, which dictates $n - 1 \geq 10^{-3}$. The chosen radiator is perfluorbutane C_4F_{10} at standard temperature and pressure conditions: it combines a refractive index in the adequate range $n|_{3.3\text{eV}} - 1 = 1.3 \times 10^{-3}$ and low dispersion $(\Delta n / \Delta E)|_{3.3\text{eV}} = 3 \times 10^{-5} \text{eV}^{-1}$. The STP C_4F_{10} radiator produces around 10 photons per meter of radiator path for a $\beta \simeq 1$ particle,⁴ of which around 30 are detected [1]. The approximate threshold momenta for different particles are the following: electrons 10MeV/c, muons 2GeV/c, pions 3GeV/c, kaons 10GeV/c, and protons 18GeV/c. The error contribution of single photon to the Čerenkov angle of a 50GeV/c track is below 2mrad [129].

The Čerenkov photons are reflected and focused, by four sets of mirrors, onto the photodetector array inside the RICH vessel: two sets, placed above and below the horizontal beamline plane, consist of a tiling of hexagonal-shaped spherical mirrors with 11.4m curvature radius covering a total area of $6\text{m} \times 4\text{m}$; the two other sets are planar mirrors made of rectangular tiling, facing the spherical mirrors. The tile separation is kept in the 1mm range [83]. The spherical mirror tile collection is made of 104 units of 70cm diagonal. The spherical mirror set focuses the incoming photons, which distribute as concentric rings, into a single ring of aperture θ_C , and the planar set of mirrors directs the light to an array of photodetectors. The photodetectors have a high quantum efficiency of 20% in the visible range of spectrum, and are coupled with 2240 high-gain (current amplification $o(10^7)$) multi-anode photomultiplier tubes [19] operating at gain voltage below 1kV. One field perspex lens and one condenser perspex lens per photodetector produces the required demagnification to fit the later's photocathode window surface. The central (i.e. closer to beam) regions are occupied by photocathodes of smaller area than those outside, therefore the inner regions have a position

⁴The average yield of Čerenkov photons is given by $N_\gamma = N_0 L \sin^2 \theta_C$, where L is the path length in radiator and the "figure of merit" N_0 incorporates efficiencies and reflection/transmission factors, see [108]. For HERA-B, $N_0 = (43 \pm 4) \text{cm}^{-1}$ [1].

resolution of $9\text{mm} \times 9\text{mm}$ and the outer regions have $18\text{mm} \times 18\text{mm}$ [129]. The total number of channels is about 160×10^3 [83], and the typical channel occupancy is at the 10% level.

The Čerenkov photons are emitted at the same polar angle relative to the particle's track. The mirror array in the RICH vessel focuses the photons from one track into a ring pattern with angular aperture θ_C . Ring reconstruction is performed by sophisticated pattern-recognition and optical correction algorithms. For a given ring pattern, the orientation of a candidate track responsible by the ring is given by a coordinate pair (λ, ϕ) , defined in the plane of the photomultipliers' surface at $z \simeq 1180\text{cm}$, which represent the horizontal (azimuth) and vertical (declination) angles of the track direction relative to the beam orientation.

3.2.8 Transition radiation detector

The transition radiation detector, or TRD for short, is used to distinguish electrons from hadrons in the region of highest occupancy in front of the electromagnetic calorimeter, covering the pseudo-rapidity interval $3 < \eta < 4.7$. The transition radiation is produced by relativistic charged particles when they cross the interface of two media with different dielectric constants. The total energy loss of a charge particle depends on its Lorentz factor $\gamma = E/mc^2$ and mostly directed forward, peaking at $o(1/\gamma)$. The TR photons produced by electrons is in the X-ray range of 5–15keV. However, the number of produced photons per interface crossing is very small: for particles with $\gamma = 2 \times 10^3$ about 0.8 X-ray photons are detected [108]. Therefore, several layers of interleaving materials are necessary to produce an adequately measurable signal. The particle identification proceeds from counting the number of TR clusters produced by a given track — electrons typically produce up to four times more TRD counts than pions of the same momentum [138]. Although the hardware was fully installed, the TRD was not used during the data-taking runs of year 2000.

The TRD is placed between the OTR's TC01 and TC02 superlayers and surrounds the proton beam pipe, leaving an area of $22\text{cm} \times 22\text{cm}$ free for its passage. Its transversal area is $134\text{cm} \times 89\text{cm}$ and extends in the interval $1200\text{cm} < z < 1280\text{cm}$. The TRD has close to 16×10^3 channels [83]. It is made of eight blocks placed in two parts, one in front of the other as seen from the target, aligned at angles of $+30^\circ$ and -30° relative to the horizontal plane. Each block is composed of alternating layers of radiator material and straw tubes. The radiator is made of $20\mu\text{m}$ -thick polypropylene fibers bunched in a 1.6cm-thick layer. The straw tube layers are the detecting element of the TRD. They are made of rows of 5mm-diameter cylindrical tubes, all glued together, with groups of five straws separated by a 0.2mm-thick 10mm-wide carbon fibre strip placed lengthwise to give rigidity to the layer structure. A transversal 3mm-deep into the radiator material allows the cir-

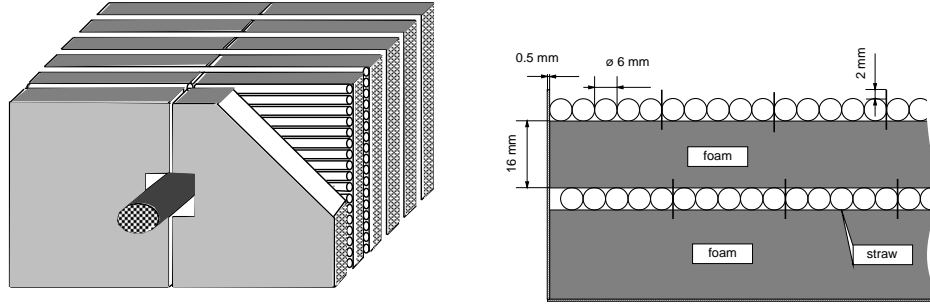


Figure 3.19. Left: isometric view of the Transition Radiation tracker (left). The darkened cylinder crossing the TRD layers represents the proton beam direction. Right: transversal section of a TRD block [108] [83].

culcation of cool, dry air to keep the radiator and the straws from overheating. The straw tubes are 6mm-diameter cylinders with a $50\mu\text{m}$ four-layered wall, with a centrally-placed lengthwise anode wire with $50\mu\text{m}$ diameter. They have different lengths, ranging from 65cm to 135cm, according to the block's size and straw tube orientation. The tube cathode is embedded in the wall in the form of two concentric 2000\AA -thick aluminium layers. The gas mixture inside the straw tubes is 70% Xe + 20% CF_4 + 10% CO_2 ; the xenon is used for the X-ray detection and the other gases adjust the electron drift time so it is below the bunch crossing rate [124]. The gas mixture proportions are kept within the percent level. Since the xenon gas is expensive and difficult to produce, it circulates in a closed circuit. The HERA-B TRD has 32 straw tube layers.

3.2.9 Electromagnetic calorimeter

The electromagnetic calorimeter, or ECAL for short, is used to identify electrons and photons based on their energy deposition and the cluster shape. Photons do not create a reconstructible track, so the ECAL provides the only possibility to detect them. The event's primary electrons and positrons should have $E/p \approx 1$ due to their high momenta (in the GeV/c range). The ECAL is also responsible for the electron trigger signals that initiate the First Level Trigger (FLT) algorithm. The ECAL has 5800 electronic channels.

The ECAL occupies the region $1325\text{cm} < z < 1411\text{cm}$ and its transversal dimensions are $|x| < 312\text{cm}$ and $|y| < 234\text{cm}$, with a central $22.3\text{cm} \times 22.3\text{cm}$ hole for the proton beam and a second hole at $(x, y) \simeq (44.6\text{cm}, -78.0\text{cm})$ of the same area for the electron beam pipe. It is composed of 2344 calorimeter modules with a transverse area of $11.15\text{cm} \times 11.15\text{cm}$. Each module holds a set of a sampling scintillator/absorber sandwich structures ("shashlik"), coupled to photomultiplier tubes for scintillation readout. Each module has 25, 4 and 1 photomultiplier tubes for the corresponding inner ($156\text{cm} \times 89\text{cm}$),

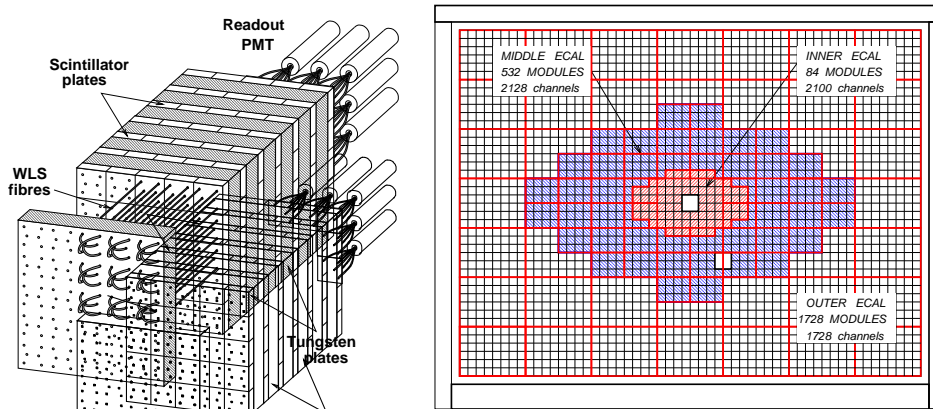


Figure 3.20. Left: the “shashlik” structure of one ECAL module [108], showing the 5×5 photomultiplier tube (PMT) array of a outer ECAL module with their wavelength shifter (WLS) fibers. Right: schematic back (downstream) view of the ECAL regions [131]. The granularity grows towards the center. The central and lower right holes make room for the proton and electron beam pipes, respectively. The structure is enclosed by a support frame.

middle ($446\text{cm} \times 245\text{cm}$) and outer ($624\text{cm} \times 468\text{cm}$) sections of the ECAL, with corresponding cell sizes of $2.23\text{cm} \times 2.23\text{cm}$, $5.575\text{cm} \times 5.575\text{cm}$ and $11.15\text{cm} \times 11.15\text{cm}$ respectively. The differing number of PM tubes per module is related to granularity requirements, which are highest closer to the beampipe regions, where particle flux is also highest. The PM high voltage supplies are 1.5kV Cockcroft-Walton bases. Each module’s shashlik is enveloped in an aluminium layer to improve light collection. The shashlik structure is different for the inner section and for the middle and outer sections of the calorimeter. In the inner section, there are alternating layers of 40 2.2mm-thick W-Ni-Fe metal alloy plates, 0.1mm-thick white reflecting paper sheets and 41 1mm-thick polystyrene-based scintillator tiles. The middle and outer sections have alternating layers of 37 3mm-thick lead absorber plates, white reflecting paper and 38 6mm-thick scintillator plates. The scintillator/absorber tiles are orthogonally oriented relative to the beam direction. The shashliks’ radiation lengths are $20X_0$ and $22X_0$ for the inner and for the middle/outer modules, respectively. The scintillation light is conducted to the PM tubes by 1.2mm-thick wavelength shifter (WLS) fibers that penetrate the entire length of shashlik, through holes arranged on a square lattice with center-to-center spacing of 11.1mm. Each inner ECAL tower (corresponding to one readout channel) has 4 WLS fibers connecting to the corresponding PM tube. The middle/outer ECAL modules have 72 u-shaped WLS fibers inserted in the holes of its scintillator/absorber stack. The bending radius of the loop is $\simeq 14\text{mm}$, so each fiber penetrates through the holes separated vertically by two holes. The middle and outer

modules yield, per 1GeV of deposited energy, $\approx 10^4$ photons [105] in the scintillator stack, yielding ≈ 1600 photoelectrons in the PM; the inner modules have a light yield smaller by a factor of 4 due to the thinner scintillator plates [108].

The ECAL identifies particles based on their energy loss within this detector and the shape of the energy cluster they produce. The showering particles (photons, electrons and positrons) produce electromagnetic showers (through bremsstrahlung and pair production) in the absorber plates; these EM showers typically deposit energy in several neighboring ECAL cells, which are grouped together by the ECAL pretrigger (see section 3.3.3) as clusters upon event reconstruction and used as candidates for electrons/positrons and photons. The shower particles have less energy than the seeding particles, and they yield light in the scintillator by exciting that material's atoms. The de-excitation photons are conducted by internal reflections in the WLS fibers into the PM tube.

The ECAL energy resolution is parametrised as $\sigma(E)/E = A/\sqrt{E} + B$ [108]; the sampling term A reflects fluctuations in the fraction of energy measured in the active medium and also photoelectron statistics, whereas the constant term B is due to non-uniformity, calibration errors, energy leakage and instability of response. The design values for the inner ECAL are $A = 17\%$, $B = 1.6\%$, and for the middle and outer are $A = 9.5\%$, $B = 1\%$ [83]. Prior to the first data-taking runs of year 2000, it was found [1] [152] that these parameters for the inner ECAL were $A = (22.5 \pm 0.5)\%$ and $B = (1.7 \pm 0.3)\%$ in the region $12\text{GeV} < E < 60\text{GeV}$. Spacial resolution was estimated to be $\sigma_{x,y} = 0.2\text{cm}$ and linearity better than 0.5% in the $12\text{GeV} < E < 80\text{GeV}$ range. Newer measurements [72], done after the 2002/2003 run period, put only slight improvements in energy resolution. The spatial resolution has an average of 0.5cm [73].

3.2.10 Muon detection system

The muon detection system, or MUD for short, is used to discriminate between muon and hadron tracks. This system plays a key role in the detection and tagging of golden decays (1.2) — in particular through the reconstruction of muon pairs with an invariant mass in the J/ψ meson mass range — as well as selecting semileptonic decays for B meson flavor tagging. The MUD's information is also used in event triggering, and in offline analysis for background rejection due to hadron misidentification, with rejection factors above 100 [108]. As with most other subdetectors in HERA-B preceding it, room is needed for the crossing proton and electron beam pipes. The number of channels for the MUD is about 31×10^3 [83].

The MUD detector components are in four superlayers, labeled MU1 through MU4, perpendicular to the beam direction. In front of the first three superlayers are three $o(1\text{m})$ beampipe-wise thick steel blocks, labeled

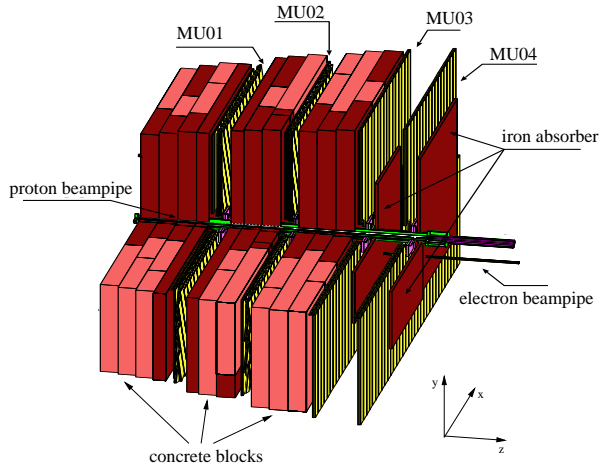


Figure 3.21. The four tracking stations of the Muon detector system and the concrete absorbers separating them [131]. Stations MU03 and MU04 are only separated by about 5cm of iron.

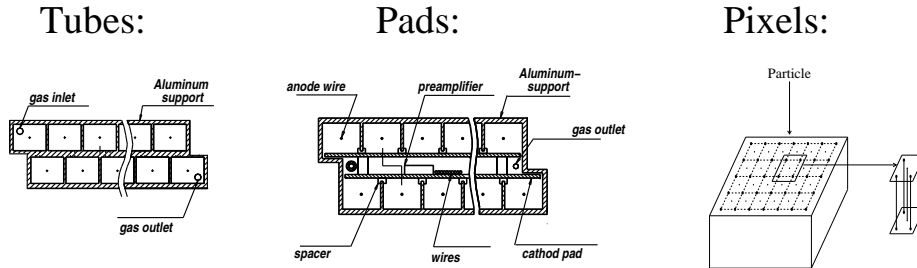


Figure 3.22. Cross section views of the Muon detector elements [131]. The tube chambers form double layers in MU01 and MU02. The pad chambers also form double layers in MU03 and MU04, with cathode planes between the two layers. The pixel chambers are the detector elements in the region closer to the proton beam. The proton beam direction (not shown) is transversal for the tube and pad schematics (left and center), and along the sensing and potencial wires in the pixel chamber representation (right).

MF1 through MF3, which function as absorbers; since the muons rank as the highest penetrating (long-lived) charged particles, it is tacitly assumed that the signals present in the downstream superlayers should belong to muons crossing them — all other particles suffer multiple scattering in the absorber and do not emerge from it. There is no absorber between MU3 and MU4 as in between the other superlayers — only a modest amount surrounding the beampipe to shield the detector from the beam background. The MU4 is used to measure track directions unimpeded by multiple scattering, and is mainly used in the hardware triggering. To limit the amount of readout channels, the signals from 2×2 cells in MU1 and MU2 and 1×4 cells in MU3 and MU4 are combined together in the readout [124]. Essentially, only muons with momentum greater than 5.0GeV are able to penetrate the thick absorbers in front of MU3 and MU4.

There are three different types of detector element used in the MUD,

called *tube chambers*, *pad chambers* and *gas pixel chambers*. Their location depends on whether they're close to the beampipe (pixel chambers) or, for the outermost elements, on the superlayer they're installed (MU1, MU2 for tube chambers; MU3, MU4 for pad chambers).

The *gas pixel chambers* are planar arrays of $9\text{mm} \times 9\text{mm}$ cells; those on MU4 are $9.4\text{mm} \times 9.4\text{mm}$. They are placed behind the tube/pad chambers. Each cell is 30mm deep beamline-wise, and contains a $30\mu\text{m}$ -thick gold-coated tungsten anode wire at its center and running at its length, and four 0.5mm-thick cathode wires along the cell's beamline-wise edges. The applied voltage is around 2kV. The drift gas mixture of 80%Ar + 20%CH₄ ensures a response rate below the bunch crossing rate [83]; this gas mixture is also used in the remaining detector elements of the MUD. The gas pixel chamber arrays on each superlayer are grouped as four 45cells \times 32cells units, disposed around the beampipe (with an inner radius of 138mm) and slightly overlapping by 2 cells with its neighbours to minimize dead spaces [108]. A charged particle transversing a cell ionizes the gas mixture, and the resulting electrons drift to the anode and produce a measurable signal. The gas pixel chambers' spatial resolution is adequate to measure the particles' coordinates [83].

The *tube chambers* are two-layered planar arrays of 16 3.5m-long, $15\text{mm} \times 12\text{mm}$ closed aluminium drift cells, placed vertically and in $\pm 20^\circ$ angles relative to the vertical. The cell wall thickness is 1mm. One layer is shifted by half a cell relative to the other, to minimize losses due to dead space. Inside each cell, a $40\mu\text{m}$ -thick gold-plated tungsten wire is stretched along the cell length and serves as anode. The voltage difference and drift gas mixture is the same as in the gas pixel chamber.

The *pad chambers* are assembled using two-sided, $15\text{mm} \times 11\text{mm}$ u-shaped aluminum profiles; the wall separating the two opposing sides is 3mm thick. The pad chambers are oriented in the vertical direction. One anode wire is stretched inside each cell, similar to what is done in the tube chambers. Placed on each side, 1mm away from the cell structure and parallel to it, a copper-covered G10 board is etched with a pad structure and is used for readout. Finally, the 16 + 15-cell pad chamber is enclosed in aluminium casing to isolate the gas mixture.

3.2.11 High- p_T trigger

The high- p_T trigger system was proposed in the detector's Technical Design Report [83], after the original Proposal [108]. It was designed to complement $\hat{C}\hat{P}$ physics in the B system with hadronic channels — such as $B^0 \rightarrow \pi^+\pi^-$ (whose pions have much higher transverse momentum than those coming from proton–nucleon inelastic collisions), which measures the angle α of the $\hat{C}\hat{P}$ unitarity triangle — while triggering at a rate low enough to not overload the trigger processor and steal data bandwidth from the J/ψ dilepton

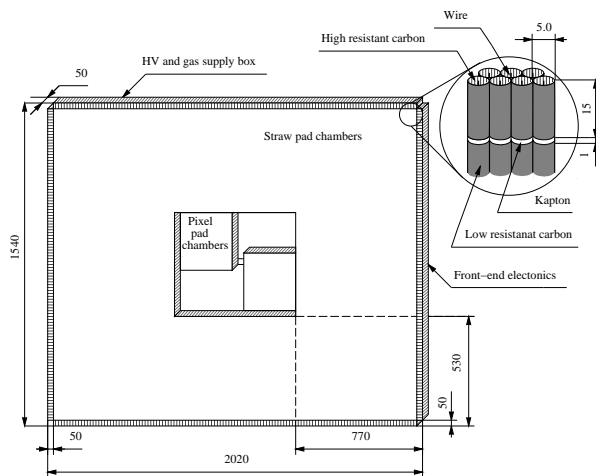


Figure 3.23. The high- p_T straw tubes superlayer layout [83]; all dimensions are given in mm. The four pixel chambers modules at the center slightly overlap. There is room for the proton beam pipe crossing at the center.

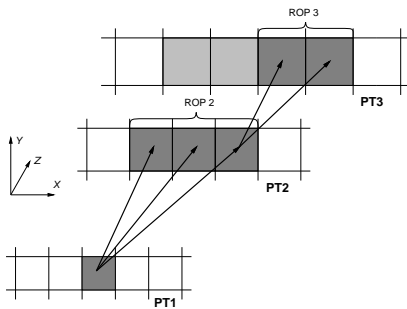


Figure 3.24. Sketch of the pad coincidence combinations in the High- p_T superlayers PT1, PT2 and PT3 [83]. A trigger road which contains at least one of the dark-shaded cells, in each and all superlayers, elicits a positive trigger response. This logical AND coincidence scheme produces almost 100% efficiency for $B^0 \rightarrow \pi^+\pi^-$ decays [83].

trigger. At pretrigger level, the filter imposes a transverse momentum p_T cut at $1.5\text{GeV}/c$ by selecting “stiff tracks at relatively large angles” [83]. The same source claims that this is likely to select few-body B meson decays, while exponentially rejecting track combinations from other sources: for example, the requirement that both charged tracks from that decay have $p_T > 1.5\text{GeV}/c$ suppresses the minimum bias background by a factor of 50 from its 6 orders of magnitude higher rate than $b\bar{b}$ events. The number of channels for the high- p_T trigger is about 26×10^3 , divided roughly equally in the inner (5cm to 50cm) and outer (50cm to 200cm) sections.

For this trigger, three new pad chamber sets, labelled PT1–PT3, were introduced during detector assembly, two of them positioned in the magnet region (at $z_1 \simeq 4.7\text{m}$ and at $z_2 \simeq 5.7\text{m}$) and downstream of the magnet (at $z_3 \simeq 6.1\text{m}$). The three superlayers enable the implementation of a coincidence trigger logic for track selection (figure 3.24), particularly at the pretrigger level — see section 3.3.3. Each layer (see figure 3.23) uses different technologies, depending on the radial beam distance; the inner regions use gas pixel chambers like in the muon system, the outer regions use straw chambers with resistive-cathode readout. In the pad area of each PT chamber, the inner pad cells are smaller than the outer pad cells to control channel

<i>Subdetector</i>	<i>Channels</i>		
	<i>Number</i> ($\times 10^3$)	<i>Bitwidth</i> (<i>per channel</i>)	<i>Bandwidth</i> (<i>per event</i>)
VDS	176.0	8	172kbytes
ITR	135.0	8	132kbytes
OTR	95.7	8	94kbytes
High- p_T	26.2	1	1kbytes
RICH	130.0	1	20kbytes
TRD	15.7	2	4kbytes
ECAL	5.8	14	10kbytes
MUON	31.3	1	4kbytes

Table 3.1. Overview of different HERA-B subdetectors in the context of the readout system [83]. The bitwidth refers to the data size needed for each channel. The bandwidth is simply the product of the number of channels by the bitwidth, per event; the values are approximated to unity for readability.

occupancies and numbers [83]. The pads in PT3 are shifted by half a pad in the horizontal direction. The sizes of pads and regions for PT2 and PT3 are projectively increased by z_2/z_1 and z_3/z_1 , respectively. In the non-bending plane (y direction), the pretrigger roads are chosen to be projective; the corresponding pads in PT1, PT2 and PT3 are combined in a logic AND.

3.3 Trigger system. Data acquisition system

The trigger system is a complex and essential part of the detector. Its primary purpose is the online selection (i.e. during data-taking) of events with clear signs of the presence of relevant decays — in the case of HERA-B, “beauty decays” ($b\bar{b}$ quarks). Such event selection is necessary because, on one hand the data output rate from all the detector’s channels is too high to be handled by storage hardware, and on the other hand because the vast majority of the beam–target interactions are irrelevant for analysis. The precise implementation of the trigger scheme was left for the final stages of the detector construction, and suffered significant changes since the original proposal [108]; this is especially so for the topmost trigger levels. The trigger and data acquisition hardware is installed in the West Hall, at the electronics hut next to the detector, except for the Front-End Drivers (section 3.3.1). The event analysis chain is detailed in section 3.5.

Assuming an event rate similar to the bunch crossing rate 10.4MHz and that the detector’s 6×10^5 channels yield around 450kbytes per event (see table 3.1), the raw data rate would then be as high as 5Tb/s. Fortunately,

the rate of interesting decays (and the corresponding data flow rate) is much lower than this: the fraction of events containing b and \bar{b} quarks at the HERA- B energy is $\sigma_{b\bar{b}}/\sigma_{\text{inelastic}} = o(10^{-6})$ [108]. Furthermore, one of the key decays channels used in HERA- B for $\hat{C}\hat{P}$ violation studies follows from the “golden decay” (1.2), whose branching ratio is

$$\begin{aligned} \text{BR}(B^0 \rightarrow J/\psi K_S^0) \times \text{BR}(J/\psi \rightarrow \ell^+\ell^-) \times \text{BR}(K_S^0 \rightarrow \pi^+\pi^-) &\simeq \\ &\simeq \left(\frac{1}{2} \times 8.9 \times 10^{-4}\right) \times 12.0\% \times 68.6\% = 3.7 \times 10^{-5}. \end{aligned} \quad (3.8)$$

The $\frac{1}{2}$ factor comes from the $\approx 50\%/50\%$ mixture of K_S^0 and K_L^0 in the neutral K mesons in $B^0 \rightarrow J/\psi K^0$ decays; the $\ell^+\ell^-$ include the e^+e^- and $\mu^+\mu^-$ final states [34]. The final state particles $\ell^+\ell^-$ and $\pi^+\pi^-$ in these decay modes do not allow to completely identify the initial state — it could be either a B^0 or a \bar{B}^0 , with a resulting doubling in the golden decay rate from the $b\bar{b}$ quark states. Assuming that in average one inelastic collision occurs at each crossing rate, the $b\bar{b}$ rate events is of the order of 1Hz and the golden decay rate is $2 \times 3.7 \times 10^{-5} \times o(1\text{Hz}) = o(10^{-4}\text{Hz})$ i.e. in the one-per-four-hours ballpark. Since the golden decay rate (which is still on of the best $\hat{C}\hat{P}$ violation channels in the B meson system) is so low, HERA- B depends on the high interaction rate to collect a reasonable amount of events.

The K^0 mesons are very common in hadronic collisions and therefore not well-suited for trigger purposes such as in the golden decay. But the lepton pairs from J/ψ decays are suitable this task, since they have high momentum, transverse momentum and pair invariant mass, which makes it possible to distinguish its presence from the background of the more common mesons. The requirement for the J/ψ decay vertex to be detached from the collision vertex can be used to further enhance background rejection: given the long lifetime τ_B of B mesons, their mean path is $\beta\gamma c\tau_B = o(1\text{cm})$ before decay, and since the J/ψ decays promptly ($\tau_{J/\psi} = \hbar/\Gamma_{J/\psi} = o(10^{-20})\text{s}$ [34]) it can be used to signal the possible presence of golden decays. Because $\sigma_{b\bar{b}}/\sigma_{\text{inel}} = o(10^{-6})$, one J/ψ is produced for every $\sigma_{\text{inel}}/\sigma_{c\bar{c}} = o(10^3)$ proton–nucleon collisions at the HERA- B beam energy — see figure 3.25.

To reduce the data stream to a suitable rate, the HERA- B trigger system has four levels of increasing analysis detail and latency time. The First Level Trigger is essentially based on fast hardware logic that performs a coarse reconstruction of charged tracks through pattern recognition, identification of candidates tracks from two-body decays like $J/\psi \rightarrow \ell^+\ell^-$, and calculation of the invariant mass of particle pair combinations. If the trigger hardware finds particle candidate pairs which pass these tests, the data is forwarded to the Second Level Trigger for a new and refined decision. This trigger’s output rate is even lower than the output from the preceding trigger level; the input data is digital/analog signals from the detector hardware, and the output data is the momenta of leptons (from J/ψ decays) and/or hadrons

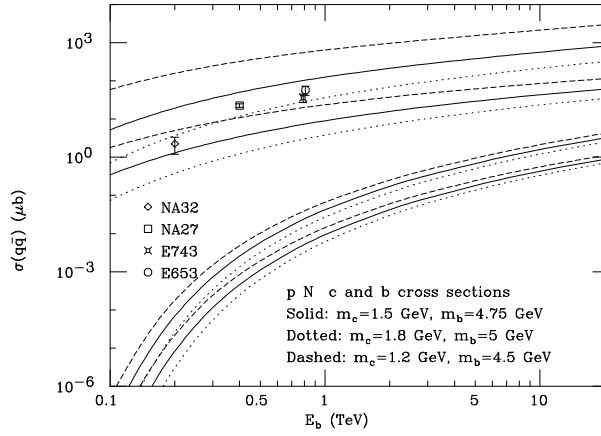


Figure 3.25. The cross section dependence of b and c quark production in pN collisions at beam energy E_b [64]. The HERA-B $c\bar{c}$ production cross section is $\sigma(c\bar{c}) = 124 \pm 34^{+21}_{-24} \mu\text{b}$ per nucleon [76].

(from e.g. $B^0 \rightarrow \pi^+\pi^-$ decays) track candidates, invariant masses, and raw detector hits (i.e., channels activated by the passage of particles). This new stream is fed to the topmost trigger layers, which process the entire event data and not just those trigger particles. The Third and Fourth Trigger Levels fully reconstruct the event, and are the final decision stages before an event can be deemed suitable for permanent storage in magnetic tape. Each Trigger Level has to decide whether the event is to be discarded or to be forwarded to the next Level for a new decision. The events kept on tape can be further selected with algorithms designed by the physicist for his/her own analysis purposes.

Parallel to this event selection trigger scheme, the hardware trigger system may also be set to, on occasion, select random events at a specified rate, without a decision from the First or Second Trigger Levels. These randomly selected events are reconstructed by the Fourth Level Trigger, classified and stored in tape. This minimum bias event population is of use for e.g. studies of the rate of triggered events to background events.

3.3.1 Front-end drivers

The detector's Front-End Drivers (FEDs) read the detector's signal wires with low-mass twisted pair cables, and transmit the readout to the Data Acquisition (DAQ) system (section 3.3.8) and the pretrigger logic, using optic fibers to reduce signal distortion related with distance. Because of the FEDs' purpose, they are placed next to the detector, just outside its acceptance. The FED electronics also perform signal amplification, shaping and digitization where necessary; the hardware is mounted on frames outside detector acceptance. The FED's ASD-8⁵ readout chips have a buffer pipeline with a depth of 128 samples, except for the VDS and ITR custom-made chips HELIX-128 3.1 [83], which read 128 channels and have a buffer

⁵Eight-channel Amplifier, Shaper and Discriminator analog chips [83].

depth of 141 samples to compensate for e.g. signal propagation delays to other detectors, or chip readout of the VDS's and ITR's greater number of channels. Therefore, the First Level Trigger's decision period must not exceed $128 \times 96\text{ns} = 12.3\mu\text{s}$, otherwise further detector readout is disabled.

There are four kinds of Front-End Drivers for the different types of readout: the analog type FED, used in the VDS and ITR; the hit type FED, for the High- p_T system, the RICH, the TRD and the Muon detector; the timing type FED, for the OTR; and the pulse height type FED, for the ECAL.

3.3.2 Fast control system

The Fast Control System (FCS) is used to synchronize the data flow from the FEDs to the First Level Trigger, to assign detector signals to events and to identify those events. Among the signals transmitted to the FEDs are the HERA bunch clock, the FED-specific delay between the bunch clock and the detector signals, the current event number tag, and event numbers of events accepted by the FLT. The FCS also inhibits detector readouts if the FED buffer is full. The FCS consists of one central unit, a signal distribution system and a collection of 210 receiving boards for each FED crate.

3.3.3 Pretriggers

The track recognition algorithm requires start regions, or *seeds*, for pattern search. Such procedure consumes less time than combining hits from the tracking devices.

In HERA-*B*, the lepton pretrigger scheme works by searching plausible hits on the Electromagnetic Calorimeter or the Muon System, which are candidates from respectively $J/\psi \rightarrow e^+e^-$ and $J/\psi \rightarrow \mu^+\mu^-$ decays. The lepton pretriggers reduce the number of lepton (or hadron, in the case of the High- p_T system, see section 3.2.11) candidates that serve as seeds for the First Level Trigger, without by itself making a trigger decision (i.e., acceptance or rejection of events). Depending on the pretrigger type, its latency is between $1\mu\text{s}$ and $4\mu\text{s}$.

The pretrigger level is hardware-based and is local to each detector subsystem, both physical and logically. Since the First Level Trigger requires a fast decision from the pretrigger, its operation has to be very fast. Each sub-detector's pretrigger is composed of several identical units, whose number is related to the number of channels to measure and the unit's processing time for a given number of channels. Figure 3.26 presents a schematic overview of the HERA-*B* pretrigger conditions.

The purpose [83] of the ECAL pretrigger electronics is to:

- Find the calorimeter clusters. The clusters are collections of neighbouring calorimeter cells, in nonets,⁶ that measure energy deposits

⁶In the year 2000 run, a 3×3 “+” cross-shaped cluster search was used instead of the

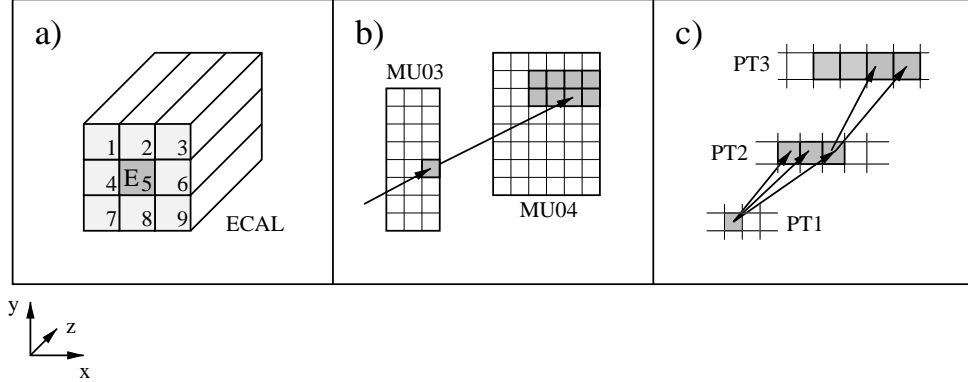


Figure 3.26. Illustration of the conditions that must be fulfilled in order to initiate a pretrigger in ECAL (a), in the two rearmost muon superlayers (b), or in the high- p_T chambers (c). For (a) the smallest unit shown is a calorimeter cell, for (b) and (c) is a pad [140].

above a certain threshold — e.g. 0.1GeV. The threshold reflects the transverse momentum of the electron that generates the cluster.

- Compute the cluster energy $E_{\text{cluster}} = \sum_i E_i$.
- Compute the cluster coordinates X_{cluster} and Y_{cluster} .
- Apply the appropriate selection cuts. One example of selection cut on a cluster is: its energy E_{cluster} must be above a given threshold value, and the central cell must be greater than half that value. The threshold cut reflects the transverse momentum of the electron that generated the cluster. The track bending due to the Magnet is ignored for simplicity and the transverse energy

$$E_T = E_{\text{cluster}} \frac{\sqrt{X^2 + Y^2}}{\sqrt{X^2 + Y^2 + Z^2}}$$

is used instead ($Z \simeq 1350\text{cm}$ is the downstream position of the ECAL). A cut E_T^{cut} in the transverse momentum is achievable by setting the threshold to [124]

$$E_{\text{thres}}^{\text{cluster}} = E_T^{\text{cut}} \frac{\sqrt{X^2 + Y^2 + Z^2}}{\sqrt{X^2 + Y^2}}.$$

The central cell energy cut avoids the generation of several seeds for the same physical cluster.

designed 3×3 square-shaped (“nonet”) clusters [131]. This was done to avoid various problems with the pretrigger electronics, which was generating fake seeds.

- Pass to the First Level Trigger the energy of bremsstrahlung photons to reconstruct the correct electron energy. The photons' trajectories are not affected by the Magnet field, and they are visible as a cluster in the same y position as the electron cluster, but separated in the x direction [124]. The separation depends on the momentum of the electron as it passes through the magnetic field and, therefore, on the measured electron cluster energy. However, bremsstrahlung recovery was not used during the data-taking of year 2000.

In the proposed scheme [83], a 100MHz digitized data transmission rate within the ECAL pretrigger is enough for its decisory task.

In the Muon detector system, the pretrigger logic hardware defines track seeds through coincidences of logic signals with the required topology, and transforms the result to a data stream of initial track parameters. Each pad of superlayer MU3 is put into coincidence with several pads in superlayer MU4, which are larger by a factor equal to the ratio z_4/z_3 of the z -coordinates of those two layers. To ensure efficiency, in superlayer MU4 four neighbouring pads in x and two neighbouring pads in y are connected in a logical OR. A pretrigger road is therefore defined as a logical AND between a pad from MU3 with the OR of eight pads in MU4. In the region closer to the beam pipe, the muons' momenta are harder than in the farther region, and it suffices to put each pad from superlayer MU3 in coincidence with only four pads in superlayer MU4 [83].

The RICH system may also be used to produce a veto signal for the pretrigger level. The RICH veto inhibits further processing of the event if the RICH occupancy is above a chosen threshold. The RICH veto is used to protect the Trigger and DAQ chains from data overflows.

3.3.4 First level trigger

HERA- B 's First Level Trigger (FLT) was designed as an array of fast electronics hardware to find dilepton pair candidates from J/ψ decays in the "Main Tracker" (ITR and OTR) section of the detector. It uses the Calorimeter and Muon detector to find candidate leptons and then match them with hits on the Tracker chambers. The sought ECAL clusters are selected amongst those above a certain energy threshold, and the muon candidates are selected amongst those whose Muon detector hits project into the Tracker Chambers. The FLT receives hit information from a subset of the tracking superlayers, namely PC01, PC04, TC01 and TC02 of the Outer Tracker, and from the muon tube chambers in layers MU01, MU03 and MU04. Since all these layers are placed after the Magnet in the field-free region, the tracks are straight lines. The electron candidates are selected from tracks with TC02 hits on top of calorimeter clusters; the muon candidates are selected from Main Tracker segments which project into paths in

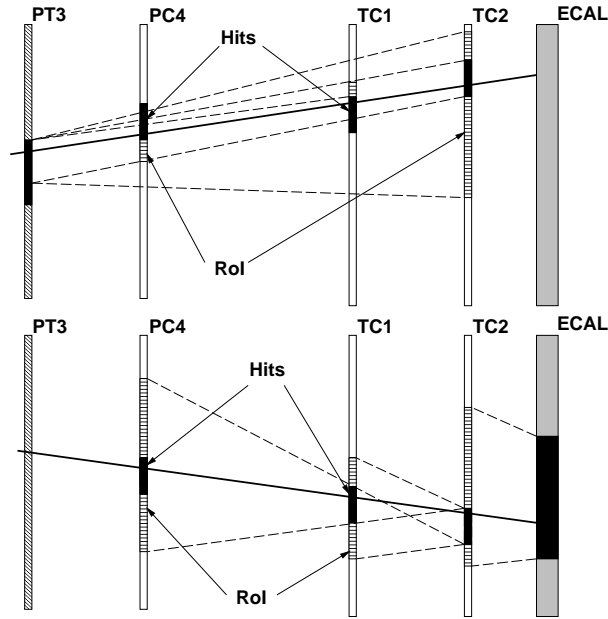


Figure 3.27. Track finding procedure at the FLT for high- p_T triggers (top) and electron triggers (bottom) [83]. The figure is not to scale (even relatively).

the Muon chambers. These are the seeds for the Kalman filter algorithm, described below. The FLT reduction factor is $o(200)$, whereby its trigger output rate is 50kHz for a 10MHz data input rate. A description of greater detail on the HERA-B First Level Trigger can be found in reference [124].

The track candidates are reconstructed using a Kalman filter algorithm optimized for fast processing in the trigger electronics. This algorithm provides an efficient iterative method to perform a least-squares fit on systems described by time-discrete state vectors. To estimate the system's evolution, two iterative steps are applied on each detector layer: based on the measurements in the preceding layer, the state and error estimates are predicted for the next measurement (prediction step); then the next measurement is incorporated for an improved estimation of the system's state (correction or filtering step). To start the iterative method, a first estimation of the system state is needed (seeding). Each fit step defines a new Region of Interest (RoI) region for each track in the next detector layer where detector hits are to be sought, based on the assumption that the particles move in a straight line in the field-free region behind (i.e. downstream) the Magnet. A track candidate "survives" the reconstruction if at least one hit is found at each step of the search in the RoI bounds, otherwise the track candidate is removed from processing and is not considered in the next steps. The processing ends when all tracks have been reconstructed through all trigger layers.

The geometrical parameters are found in these reconstruction steps, however the FLT also implements a coarse reconstruction of the track momentum. This is necessary to perform cuts on those lepton candidates that have

very low momentum — a typical cut of 5GeV is applied. The FLT produces a positive decision on the event if *any* dilepton pair is found which satisfies the momentum cuts and the dilepton invariant mass, $M = \sqrt{2p_1p_2(1 - \cos\theta)}$ (p_1 and p_2 are the norms of the tracks' momenta, θ is the angle between the tracks), with a cut specific of the dilepton pair — $2.0\text{GeV} < M < 3.5\text{GeV}$ for dielectron and $2.5\text{GeV} < M < 3.5\text{GeV}$ for dimuon. The track momentum is initially estimated by hardware units named Track Parameter Units (TPUs), which are further described below. Assuming that the track originates from the target region — the point $(z, x) = (0, 0)$ defined in the Magnet bending plane — the resulting momentum kick is used to obtain the track's momentum. See appendix B.3 for further details.

The floating point arithmetic calculations of the real parameters (track slopes, momentum, dilepton invariant masses) are too time-consuming and would quickly overload the FLT buffer. Instead, Look-up Tables (LUTs) are used; these are hardware implementations of programmable logic devices which store the possible values of a real function (within a preset range) and output them according to the ranges of the input values.

The trigger hardware is implemented by a series of trigger units; an overview of the FLT network is presented in figure 3.28. The Track Finding Units, or TFUs (figure 3.29), implement a Kalman filter algorithm in hardware. They combine the hit data from 2048 channels with the messages which represent the track candidates and perform track reconstruction. The TFUs are incorporated in electronics board, which include messaging units to receive and transmit messages to other units and parameter calculation using hit coincidence logic circuitry and LUTs. If a TFU finds a hit in the RoI of a track candidate it receives, it creates a new, refined track candidate and messages the information to the TFU of the next superlayer. These 80-bit messages are forwarded through the TFU network, starting at the pretriggers and ending at the TFUs in PC01. Each TFU handles a specifically assigned region of the tracking system.

The Track Parameter Units (TPUs) calculate the momenta of the found tracks and are able to reject tracks based on kinematical cuts and on comparison of tracks of one event (for clone removal). Track candidates accepted by the TPU are forwarded to the last step of the FLT trigger chain, the Trigger Decision Unit (TDU). This unit can base the trigger decision on simple counting of tracks or on the calculation of the invariant masses of all possible track pairs of each event. In case of a positive trigger decision, the TDU notifies the FCS, which then initiates the readout of the entire system to the Second Level Buffer, after which the event is processed by the Second Level Trigger. The whole system comprises 60 TFUs, 4 TPUs and 4 TDUs, all installed in five electronics racks called VME crates [83].

The latency timeslice for signal propagation between TFU layers is around 850ns (TFU processing + signal propagation) [83]. For the TPUs, this amounts to 700ns. The processing time in the TDU is the same as in a TPU

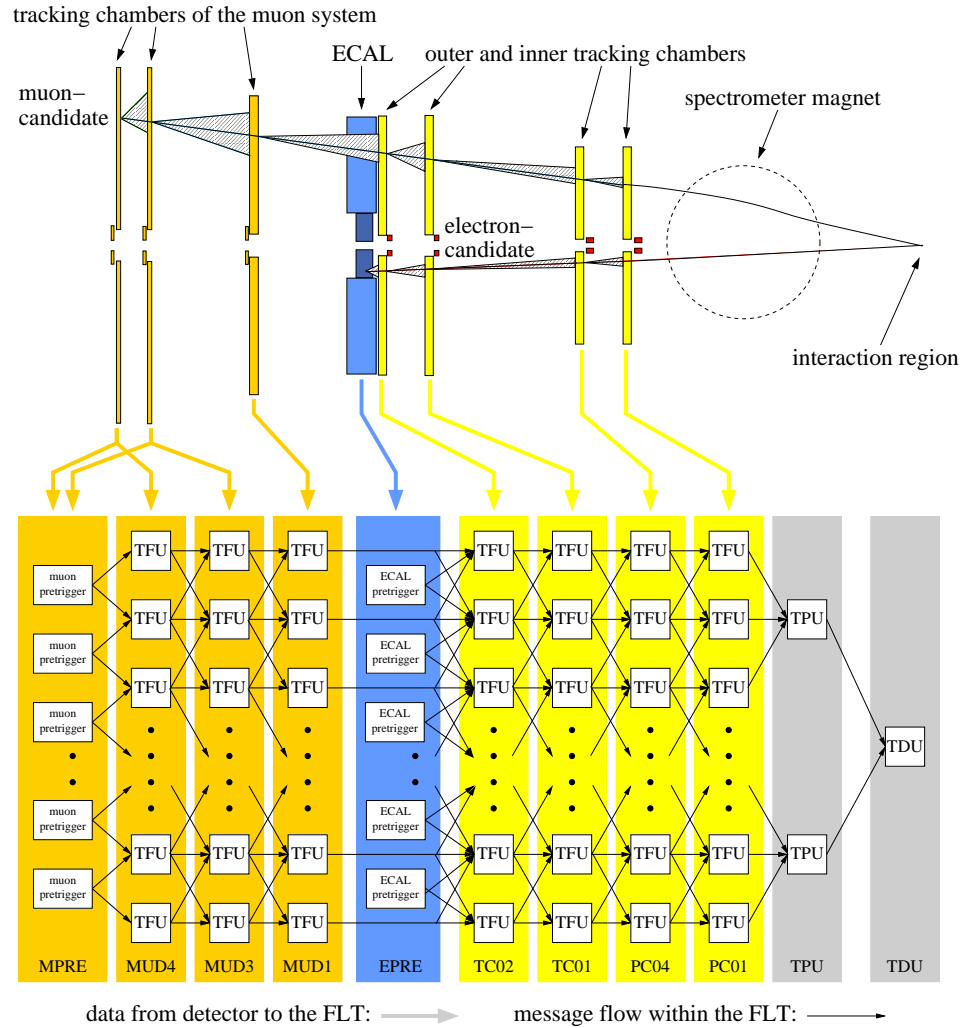


Figure 3.28. Overview of the FLT network [124]. The data flow within the network is twofold: on one hand, hit data (represented by arrows pointing from the detector layers) are sent through optical fibers from the FEDs to the TFUs; on the other hand, the track candidate data are transported through each superlayer's TFUs to the TPUs and finally the TDU. The High- p_T pretrigger is not shown in the figure. The Regions of Interest (RoIs) are represented by the grey triangles involving the tracks between consecutive detector layers.

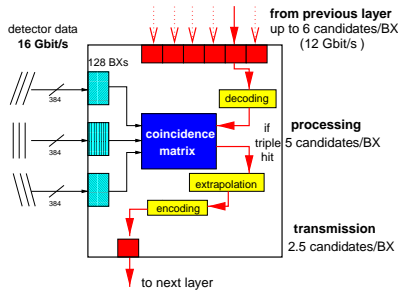


Figure 3.29. Schematic representation of one FLT Track Finding Unit [1].

400ns. Therefore, the FLT tracking for the electron trigger has a latency of $0.3\mu\text{s} + 4 \times 0.85\mu\text{s} + 0.7\mu\text{s} + 0.4\mu\text{s} = 4.8\mu\text{s}$ (the initial $0.3\mu\text{s}$ corresponds to the signal propagation from the Pretrigger).

3.3.5 Second level trigger

The Second Level Trigger (or SLT for short) works similarly to the FLT, i.e. using a Kalman filter algorithm. The SLT, however, performs a more refined track search; because such refinement requires more processing time, the SLT depends on the FLT to reject those events that have clear signs of a background event (no J/ψ dilepton decays and/or no high- p_T particles). The SLT algorithm has the following steps [131]:

- take the track candidates data from the FLT and all detector hits;
- remove ghost tracks, by requiring a minimum number of TC and PC hits lined up on an approximate straight line;
- refit the tracks behind the magnet, applying a Kalman filter in the xz and yz planes, and rejecting tracks with too few hits or poor χ^2 ; track parameters are improved by using the OTR chambers' drift times, instead of merely using OTR hits as done in the FLT;
- estimate the track orientation in front of the magnet with the new information; follows tracks through the VDS using a Kalman filter approach, again fitting separately in the xz and yz planes; and finally,
- reject the track from J/ψ dileptons candidates that do not have a common vertex, within a certain error tolerance. The vertex should be detached from all target wires, or with a large impact parameter relative to the target wires for semileptonic b decays, $B \rightarrow l\nu_l X$.

The SLT has a rejection factor of $o(100)$, therefore its output rate is 500Hz for a 50kHz input rate from the First Level Trigger.

The raw data of a single event encompasses about 440kB. The readout of FLT-accepted events from the FED pipeline at 50kHz involves thus the

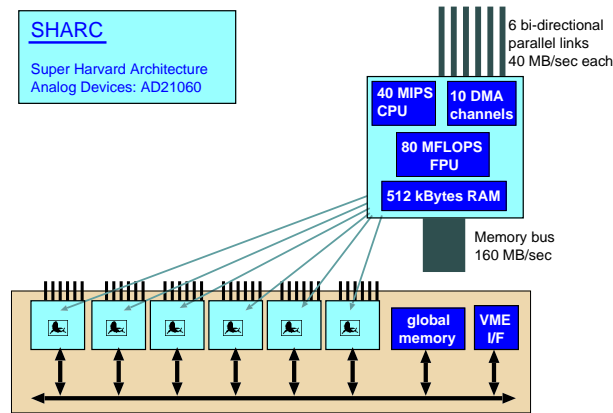


Figure 3.30. Overview of the SHARC cluster board, which carries six Analog Devices ADSP21060 SHARCTM processors that share a 160MB/s on-board memory global bus [1].

transmission of a 21GB/s data stream. The destination of the data packets sent by the FEDs is another buffer, the Second Level Buffer (SLB) [140], which holds the data during the SLT step and serves trigger requests for parts of the event data. The SLB is implemented by SHARC Digital Signal Processors (DSPs) connected to the FEDs by fast data links. The entire SLB consists of 140 SHARC cluster boards in VME standard, each carrying six DSPs — see figure 3.30. The SHARC cluster boards are grouped into 10 buffer blocks of 14 boards, and answers to data requests from the SLT processing component implemented by a farm of PC nodes, described below. On a single SHARC cluster board, a fast global bus (160MB/s) and Direct Memory Access (DMA) capabilities allow for communication of those six CPUs and rapid access to 512kB memory per processor. Each DSP has six 80MHz data links (SHARC-links) at its disposal, transmitting 4bit-messages at 40MB/s. The DSPs are interconnected to the FEDs, to other DSP boards, and finally to the SLT by appropriate cabling. In this way, the relation between a particular FED and a SHARC cluster board is fixed, i.e. one board stores the data from a defined detector region, but for several hundred events. In contrast to the pipelined event storage in the FEDs, a managed buffer system is used in the SLB. An event buffer is released and overwritten only after the SLT rejects an event or all data were read out from the SLB.

The SLT runs as a process on each node and all processing of an event is done inside this process, called the Second Level Process (SLP). The event data are stored in the Second Level Buffer (SLB), which is filled with all the detector's hits and FLT reconstructed tracks and invariant mass of track pairs when a positive FLT decision is performed. The SLP requests that information from the SLB for processing on an available SLT node. The SLT algorithm is split into several steps of increasing complexity and required data volume. At each step, only the data from the detector inside the RoIs investigated at that step are pulled from the SLB and processed in the SLT node. This is the opposite of the FLT strategy, where all event

data are transferred to the processor units; the SLT treats the complete event inside a single processor.

The SLT processing is implemented by a computer farm of 240 PCs [85], organized in 12 processor blocks each with its own Ethernet switch. In the PC farm, 30 nodes equipped with Intel Pentium III 300MHz processors and 64MB RAM memory, and the remaining nodes with Intel Celeron 1.3GHz and 256MB RAM. The PCs also have each a 100Mbit Ethernet network card and no hard disk drive. Each PC node is also equipped with one custom-made SHARC-to-PCI I/O board for data readout from the SLB. Communication with the SLB is done through one SHARC board for input and another for output [1]. The GNU/Linux operating system is used in the PC nodes because of its widespread use and the benefits of Open Source policy. It is loaded at boot time from a server machine in the computer network into each node's memory; this facilitates eventual software upgrade in all nodes by modifying the system image on the central server, and therefore no hard disk is required. The Linux system is prepared to run a minimal amount of processes, to reduce time consumption from otherwise frequent memory context changes.

3.3.6 Third level trigger

The Third Level Trigger (TLT) was designed to run on the same PC nodes as the SLT, working with data from complete detector instead of limiting itself to RoIs. It starts by reading out the complete event from the Second Level Buffer, therefore freeing the memory in the SLB for storing a new event accepted by the FLT. The full event data readout by the TLT constitutes the "event building", as it is the first time in the trigger chain that the complete event is stored in the same place. The TLT then does full track reconstruction in the VDS and proceeds to reconstruct primary vertices from the reconstructed tracks and searches for secondary vertices.

The primary and secondary vertices correspond to the best estimates for the production and decay⁷ of massive resonances such as B mesons in the case of HERA- B . The primary vertex is found by fitting the best vertex fit for a series of tracks which maximize the fit probability (i.e. "bad" tracks are not used). This vertex must also respect target location restrictions. Since the J/ψ has a decay rate around 12 orders of magnitude higher than the B mesons', it is therefore considered to decay promptly. In the presence of a

⁷The considered decays usually involve the weak nuclear force, and have characteristic times greater than the decays involving electromagnetic or nuclear strong interactions. The B mesons have lifetimes $\tau_B \simeq 1.6 \times 10^{-12}$ s and, correspondingly, they travel distances of up to $c\tau_B \sim 0.5$ cm. These decay lengths are possible of being measured, provided the production and decay vertices are properly reconstructed. Shorter-lived particles are considered to decay promptly after their creation, e.g. the J/ψ is a narrow resonance with a measured lifetime of $\hbar/\Gamma_{J/\psi} \simeq 8 \times 10^{-21}$ s [81].

J/ψ decay vertex separated $o(1)$ mm from the primary vertex, it is defined as a secondary vertex and defines the event as a B meson decay candidate.

The TLT is now considered [1] as a system to supply additional suppression for event classes where the information available at the SLT might not suffice to bring down the event rate without impairing the efficiency for signal events. In particular for the J/ψ trigger, the TLT step should be necessary. The good quality vertex formed by the two trigger leptons is a strong handle to reject background events. In addition, one can check at the SLT whether the measured momenta of the trigger particles sum up to a vector pointing from the vertex to the nearby target wire. The main focus of the TLT is on event classes with fewer kinematical constraints, notably without a vertex formed by two trigger particles. Such events occur when the trigger particles come from different B hadrons or from different stages of the decay chain of one B . In the VDS, the TLT tracking algorithm has been surpassed in precision and speed by the full event reconstruction cellular automaton algorithm CATS [8].

In the design [1], around 50 out of the 240 nodes in the SLT/TLT farm should be busy with the TLT algorithm, which, with an estimated input rate of 500Hz, would leave 100ms to read out the complete event and run the TLT algorithm. The typical reduction factor for the TLT is between 10 and 20, therefore output trigger rates between 25Hz and 50Hz are obtained.

3.3.7 Fourth level trigger

The main purpose of the Fourth Level Trigger (or 4LT for short) is to provide complete event reconstruction, classification and selection for the events accepted by the TLT. The online reconstruction of events, prior to their tape archiving, allows for some immediate data analysis and avoids time-consuming data reprocessing. The archiving rate is 20Hz [1], which for an average event size of 100kbytes and integrated run periods of 10^7 s/year, leads to a data volume of 20Tbytes/year. The 4LT also serves the tasks of Data Quality monitorization, of distribution of detector Calibration and Alignment constants updates and of event logging to high-capacity magnetic tape. Additionally, the 4LT computer farm is also used for event data reprocessing during shutdown periods.

Event reconstruction is performed inside the software framework ARTE, which mainly provides structured access in C++ and Fortran to event banks. These contain information such as raw data, hits and reconstructed tracks. The reconstruction itself is done by a long list of different packages. It starts by reconstructing partial tracks (called segments) independently in the different tracking detectors and electromagnetic clusters in the calorimeter. The segments from different detectors are then matched together into long tracks and a global refit of the tracks is done to estimate the optimal track parameters.

The 4LT is implemented on a farm of 100 PCs, organized in eight mini-farms with their own Ethernet switches. The processor nodes house dual Intel Pentium III 500MHz CPUs, with 256MB RAM, 13.6GB hard disk drive, Ethernet network card and GNU/Linux operating system.

3.3.8 Data acquisition system

A run [83] is a period of time where specific hardware and software are used to produce certain information. Beside the normal data-taking runs are the calibration runs and the test runs — some involving electronics, some exclusively software-related. The essential facts about each run are registered in a run database that is accessible by the online user for event monitoring, any authorized person on the computer network and the offline software.

The HERA-*B* Data Acquisition system (DAQ) is an integral part of the trigger system, see figure 3.31: the detector readout is forwarded through the different buffers and processors on a positive trigger decision, and the triggering decisions are formed based on the collected information. The 1400 FED boards used for detector readout, as well as the First Level Trigger, are synchronized with the beam bunch crossing through the HERA clock signal, which is received by the HERA-*B* Fast Control System. The raw data of a single event has a volume of about 450kbytes. Thus, the readout of events accepted by FLT from the pipeline, at an average rate of 50kHz, involves the transmission of a 22Gbytes/s data stream.

The events accepted by the FLT are communicated to the FCS, which then commands the transfer of the triggered event's data from the pipeline to the Second Level Buffer, by sending synchronized signals to all FEDs. The SLB is implemented by 140 SHARC cluster boards, which hold the data during the SLT decision step and answer requests for chunks of event data. The requests for tracking through RoIs ("range requests") originate from the 240 PC nodes at the SLT processor farm, grouped as 12 processor blocks. Due to the restriction to RoIs, the fraction of data requested per event is smaller than 0.5% [140]. A network switch made of SHARC boards is used for communication between the SLB cluster and the SLT processor farm. It uses a multicast messaging protocol called RPS [131], and one message has a maximum of around 1200bytes, including a header containing the origin and destination of the message. The average answer period for a SLT PC node request is about $70\mu\text{s}$ [140]. In contrast to the pipelined event storage in the FEDs, the SLB is managed by an Event Controller (EVC) implemented by one SHARC cluster board, which keeps track of the free buffer and node indices. This unit receives trigger signals from the FCS, and designates available SLT nodes for event processing. An event buffer is released and overwritten only after the SLT/TLT rejects an event, or when all data is transferred from the SLB to the 4LT trigger nodes. If the number

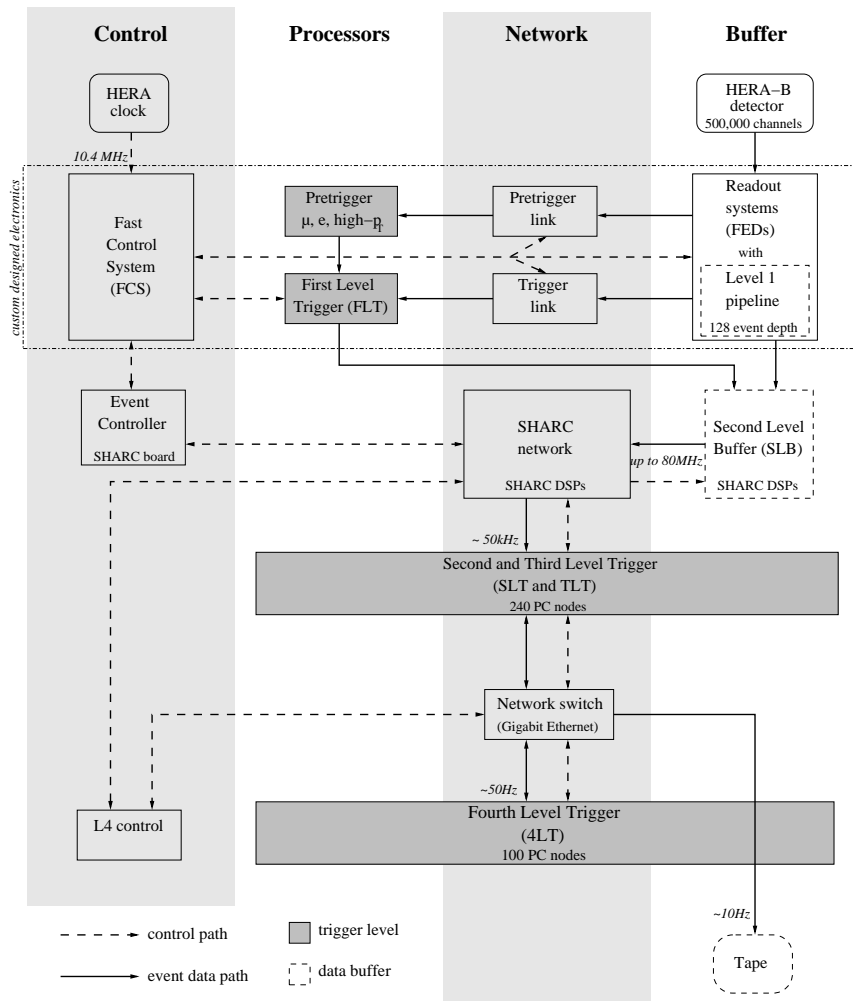


Figure 3.31. HERA-B Data Acquisition system scheme and correspondence to the HERA-B trigger levels [1].

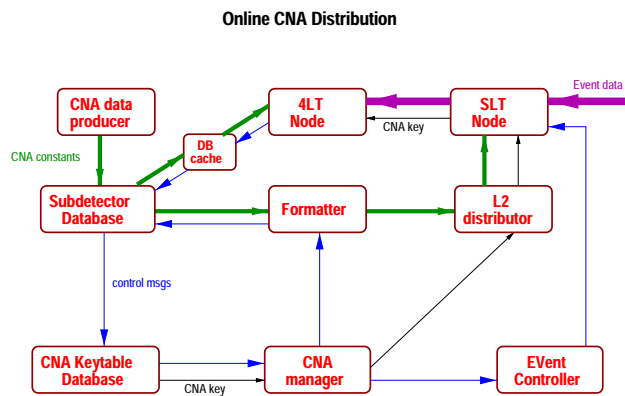


Figure 3.32. Sketch of the online distribution of Calibration and Alignment (CnA) constants [1].

of free SLB buffers drops below around 50 [131], the Event Controller can block the FCS from accepting triggers for a few milliseconds. The current implementation of the EVC is able to handle trigger rates up to 70kHz. The typical event processing time of a SLT node is around 3ms [1].

Each processing mini-farm switch in the SLT/TLT and 4LT is connected to the trigger level's own Fast Ethernet switch. The communication between trigger farms goes through a central Gigabit Ethernet switch. Each 4LT processing node buffers $o(10)$ events in its local memory [1]. Three PC nodes in the 4LT farm are reserved for farm services: a Network File System server for executables, a collector of Slow Control information which broadcasts through an HTTP server, and local event data logger. The online Database system is discussed in more detail in section 3.4.

The Slow Control system monitors the detector's state — such as the gas temperature, pressure and flow in the RICH vessel, the tube chambers in the OTR and Muon detector system, the CPU temperature and network response of SLT processor nodes, etc.. These quantities vary slowly in time, which allows a convenient response if an alarm is set off by quantity exceeding a preset threshold. Slow Control parameters are read and updated on time scales $o(10)$ s. Since the Slow Control data is not critical for detector readout, it uses UDP network protocol, while other services require TCP/IP communication protocol.

The logging node houses large SCSI disks which keep event data for several hours of standard running at 2MB/s. Mass storage of events is realized through the Gigabit Ethernet switch with the DESY Computer Center. The event data is stored in Data Summary Tape (DST) format, which contains $o(100)$ kbytes/event raw detector hits as well as $o(25)$ kbytes/event reconstructed elements like tracks and vertices; the typical DST file is 380MB. With offline reprocessing of event data stored in DST files, event information can be stored in Mini data format which contains 1% to 10% of the DST full information by forfeiting raw data. Event data logging from 4LT to the central logging facility could be performed at rates up to 12MB/s [1].

Since trigger efficiency and background suppression depend heavily on the quality of calibration and alignment of the detector components, online monitoring and updating of the constants database is implemented. During event reconstruction, quantities which are needed for calibration and alignment are derived and stored in a proper database. By making use of the data coming from the reconstruction, constants are updated. New constants are distributed to the reconstruction processes and to the trigger system.

3.4 The HERA-B databases

The purpose of the HERA-B Database system is to provide storage, management and read access to the detector's hardware and software status and configuration, as well as their validity periods in data taking. This information is necessary during full event reconstruction, so it is used both in the offline and online contexts.

The HERA-B databases are stored in a tabular fashion, and use indexing to provide table version identification, fast access and table relationing. The older table versions are not discarded, since they are required for the earlier configurations. The online and offline databases system has been successfully commissioned and is presently running stably. One PC node in the DAQ farm is reserved to run the necessary online Database servers. Four other PC machines, detached from the DAQ farm, run offline replicas of these servers to isolate the online servers from load fluctuations induced by offline processing. The server software runs on the GNU/Linux operating system and is based on a number of Open Source packages, optimized for specific tasks. The use of GNU C/C++ compilers, available on several different platforms, removes the limitation to specific hardware and/or operating system and facilitates the transition to other systems with little or no modifications on the source code.

The following type of information is stored and managed [13] in the HERA-B Database system:

- *Basic HEP constants*, including particle masses and lifetimes, which are useful e.g. in Monte Carlo simulations.
- *Setup*: cabling connections and farm software configuration.
- *Alignment*. The parameters that describe the geometric disposition of the target and the various subdetectors are stored as tables. The starting point is the nominal geometry, which describes the idealized positions and shapes of the subdetectors. The “real” geometry can differ from the nominal values by millimeters, due to e.g. detector reassembly after maintenance stops. The “real” geometry parameters are computed from the analysis of large numbers of events and are kept in a table separate from the nominal parameters'. The time scope information of each (real) geometry tag is stored as a table; see the “keytables” discussion below.
- *Calibration, status, luminosity*. This includes: any significant status alarms; high and low voltages; gas temperature, pressure, flux and mixture proportions, in tube chambers in the High- p_T , OTR and Muon systems, or the RICH gas vessel; HERA background status (from e.g. VETO counter coincidences) and proton beam bunch structure; detector “dead” (unresponsive) and “noisy” (with occupancy exceeding

a chosen threshold) channels and their pedestals (quiescent voltage value); calibration between deposited energy in calorimeter cells and their output signal amplitude; and status of the reconstruction farm (number of processes in PC nodes, their network occupancy and CPU temperature).

These quantities change significantly only over extended periods of time, therefore they can be safely monitored at low sampling rates (of the order of one minute) so to not overload network and processing activities. This Slow Control information is stored in a parallel database system, and can be used to guide detector functioning either automatically or through human intervention.

The physics constants and detector Setup and Alignment constitute setup information, and are not updated during runs: a new Setup implies stopping a run to make the necessary changes. The Slow Control quantities describe validity period information. The event data is kept outside of the Database Management System (DBMS), and is accessed during offline analysis by specifying the required run number tag (and, optionally, specific event numbers).

The most demanding parameter of the HERA-B database systems is the rate of inter-process data flow, generated by update requests from the SLT/TLT and 4LT trigger farms [16] [17]. Due to the large number ($o(10^3)$) of client processes, the access to clusters of objects with sizes of $o(\text{Mbytes})$ generates requests of Gigabyte magnitude on the database system. Such is the case of requests for Calibration and Alignment (CnA) constants, distributed through the SLT/TLT/4LT system. The replies are broadcast simultaneously to all SLT processor nodes, through a formatter and distributor process, and are also sent to a tree of cache databases which serves the 4LT processor farm. Instead of having the Database servers reply directly to these requests, a distribution system pauses the data taking and commands the distribution of the new CnA constants. When data taking is resumed, the events are tagged with a key that identifies the new set of CnA constants. See figures 3.33 and 3.34 for an overview.

The key used to tag CnA constants for each event, is an integer⁸ that identifies one record from a “keytable” [27]. The keytable contains identification keys for each table used to store the different CnA configuration (for example, VDS alignment, RICH voltage, etc.). The run number information and time stamp for the CnA constants’ scope is also stored in a keytable record as a table entry. Significant revisions of CnA constants, called “keyreleases”, are submitted by each detector group through a web interface [46], and the Database Administrator (DBA) commits the keyrelease to the configuration database. The keyreleases are indexed by a numeric key

⁸Rather, *two* integers, called “major” and “minor”. These two numbers are used e.g. within the MIZZI API.

Online Calibration & Alignment scheme

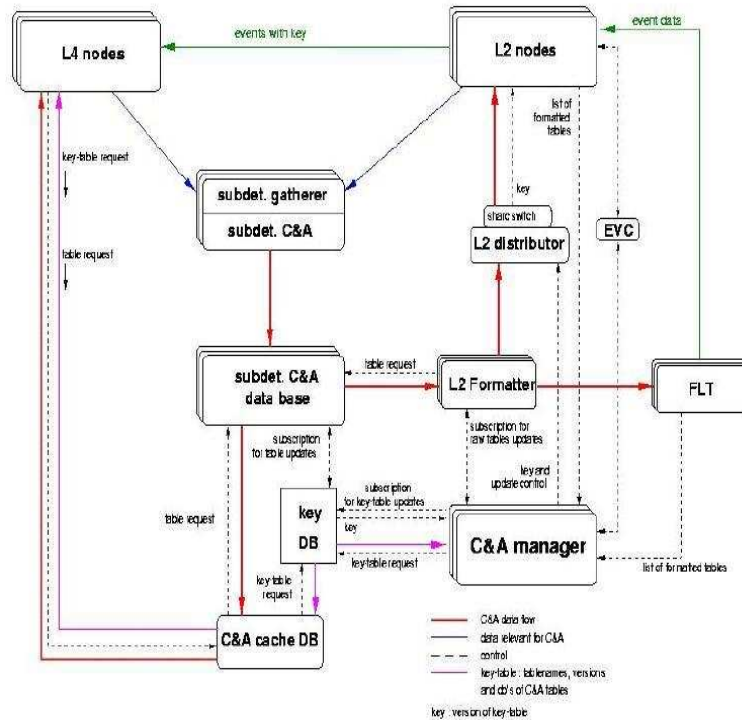


Figure 3.33. The distribution of Calibration and Alignment constants in the HERA-B trigger system [16]. The gatherer process — which belongs to the Data Quality system — subscribes the online databases. The new information on these servers is tagged and registered in the “key” table database server.

The C&A Manager synchronizes the distribution of the updated constants. It requests the Event Controller (EVC) to pause the run and the involved formatters to build and distribute the updated constants to the trigger processes. Once the distribution is concluded successfully the EVC is contacted again to resume the run. The 4LT processes retrieve the new constants from fast memory database caches when events with the new key arrive to the farm.

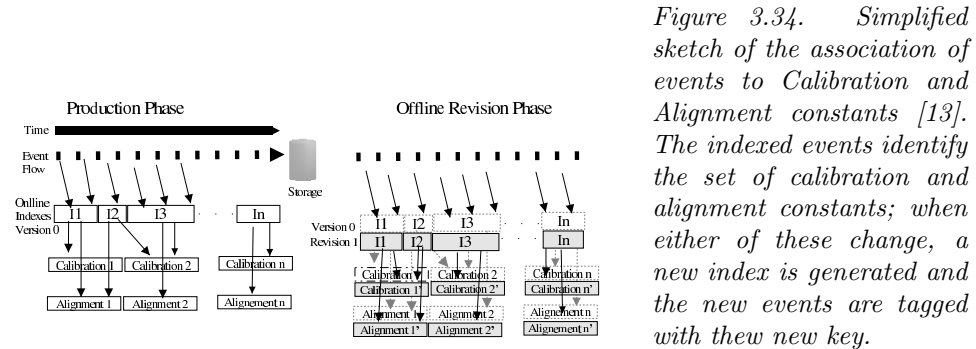


Figure 3.34. Simplified sketch of the association of events to Calibration and Alignment constants [13]. The indexed events identify the set of calibration and alignment constants; when either of these change, a new index is generated and the new events are tagged with the new key.

and identify the set of CnA constants, through the keytable mechanism, for a specific run scope.

The efficient monitorization of the detector state also poses a great challenge. In spite of the frequent monitorization, only a small parcel of the status information changes with each update. Storing all values at each update produces a huge amount of data. On the other hand, storing only the changing values reduces the data volume but creates many small objects. To avoid the presence of too many of these, the system can update individual channels that are part of a large collection of objects [16]. The main part of the work is done at server level, thus allowing a good performance. Upon request, the history of values is re-clustered on the database server before being sent to the clients.

The online replica is updated by the Calibration and Alignment system from reconstructed events. It is decoupled from offline replicas, which are used in offline analysis. The replication mechanism also provides incremental backup of the data. PC hardware today allows to run one database process per offline server replica, although not necessarily on the same machine. Cache servers may also be deployed for offline analysis. The cache is used to store limited amounts of the database information that is requested more frequently by client software. When the requested information is not found in cache, the request is sent to the database server, which responds to the client and forwards the information for the cache server. Prior to 2002, the Database servers and cache servers ran on single-threaded mode, which kept them from attending to more than one access request at a time. This required the introduction of a “gateway” server to manage requests from machines with lower network bandwidth or from institutes outside of DESY. The “gateway” server collected requests and forwards them to the database server cluster, and then returns the result through a port negotiated with the client. The multithread-aware network communication protocols now used [84] [135] in the servers allow the spawning of multiple threads, each dealing with a client request. This significant improvement improved the server performance [26] and now places potential performance bottlenecks at the hardware level (solved by e.g. distributing the database servers across more than one machine), and also possibly at the operating system level. A 2.1GB server file size limitation, found to originate from the filesystems of elder Linux kernels (2.2 and earlier), caused the database servers to crash when that limit was exceeded [24]. This problem, which especially critical in the functioning of the online servers, was solved by migrating to more recent kernel versions in 2002, and consequently eliminated the DBA task burden of constant monitorization of the database file size [15].

The transactions with the tables stored in the Database use an indexing key tag which uniquely identifies the table name and its version. The key scheme is preferable to a timestamp-based one because it avoids server accesses for each and every event. Figure 3.35 presents an overview of

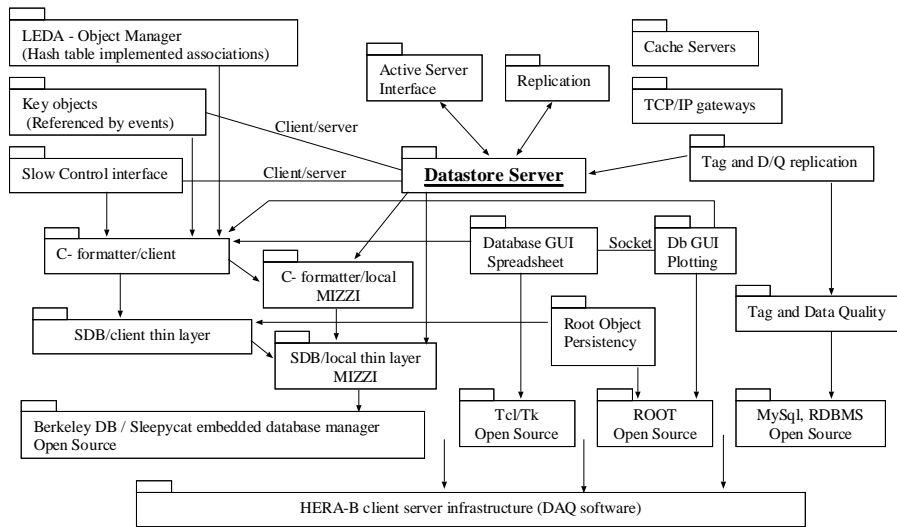


Figure 3.35. The general architecture of the HERA-B Database system [16] runs under the DAQ server infrastructure. Each “folder” represents a tier, where machine-independent data blobs are transported, with an attached key describing the table name and version to be accessed within the Database.

the multi-tier Database architecture. All client/server methods are built on top of the DAQ communication packages, with the exception of the database gateway for slower TCP/IP access. The software layers used in the database server application are the following [16]. The server software interface is implemented on top of the key-based embedded transactional database Berkeley DB [30] (also used e.g. in the Netscape WWW browser and the Apache web server), which provides a C Application Programming Interface (API) for the upper layers. The thin Sorted Database (SDB) layer encapsulates the Berkeley DB API and provides the infrastructure for client/server requests of indexed unformatted objects. The MIZZI [96] C interface, used since long in the collaboration, provides simple and efficient persistence to sets of formatted, variable-length arrays. The schema is managed together with the data, allowing the database servers to optimize the queries internally. The LEDA [150] tier is a simplified object manager developed to provide object persistence and manage associations between objects in related containers. The implemented many-to-many table associations are navigated, with the help of iterators, using hash tables. Keys are used as object identifiers that have the scope of classes. The LEDA package does not, however, allow the database server processes to optimize queries by following object associations.

The high event rate at HERA-B makes the efficient use of event tag databases difficult. Furthermore, runs are extended for periods in which conditions change several times. Therefore, tagged data sets have been introduced and are the basis for the Data Quality classification. They are

managed by the MySQL [123] Open Source relational database management system, which is periodically updated by a process that uses available information stored in the Berkeley DB databases. The data set properties used as selection criteria are the run conditions for each subdetector and the data quality assessments generated online for periods where the conditions did not change. The classification of the data in these periods can also be performed in relation to specific physics channels.

The database server application simultaneously provides persistence to data and locally performs operations that require access to a large number of objects. It notifies clients upon storage of subscribed data and provides information on the databases and file systems.

The management of the database servers is done through special tools that use configuration databases for the distributed system. The database browsing/editing tools are implemented on a reused spreadsheet tool named `dbedit`, written on a Tcl/Tk [125] interface, and which achieves good performance by hiding the data from the scripting language.

Additional solutions were successfully deployed [14] to facilitate the Database management by the DBAs, by making use of several Open Source software applications. On one case study, the database server's status is published as a Web page. To this effect, a Perl script parses the information at regular time intervals and submits it to a relational database (MySQL). After this, a ROOT [37] script queries the MySQL database, using a special ODBC⁹ interface, to obtain the latest values and from them produce histograms and a web page, which are submitted to an Apache web server. In a second case study, it was necessary to provide a solution for complex run queries, since the MIZZI DBMS provides only the simplest querying capabilities ("fetch the table registry with key X from table Y "). This was solved as follows. The DB2 DBMS server used by the DAQ system forwards the run log summary to the Perl `DBI::DBD` module for parsing and storage into the MySQL runlog database. The users' queries are submitted via Perl CGI¹⁰, which interfaces with the MySQL driver for data extraction. The MySQL database sends the results back to the Perl CGI, which dynamically generates the Web page with the formatted data to be read by the user's web browser.

3.5 Event reconstruction chain

The Analysis and Reconstruction Tool (ARTE) [12] is the common software tool for full event reconstruction and analysis in HERA- B . It is a collection

⁹The Open DataBase Connectivity is a standard database access method that allows the access to any database from any application, regardless of the nature of the DBMS handler.

¹⁰The Common Gateway Interface is a standard for running external programs from a WWW server [87].

of packages written by the HERA-B collaboration in Fortran, C and C⁺⁺. Packages already in existence were used whenever possible; such is the case of Monte Carlo event generators. The combined collaboration and external source code totalizes around 5×10^5 lines of code.¹¹

Event simulation is mainly done by the HERA-B Monte Carlo package HBGEAN [108], which is based on the GEANT [70] toolkit used for simulation of particle passage through matter. HBGEAN uses the output of the PYTHIA [143] [133] and FRITIOF [132] Monte Carlo event generator packages, which simulate heavy quark production and propagation within nuclear matter. The high-level 2D-graphics interface HIGZ [33] is used e.g. in the event display tool PRISM [111]. Interactive input is achieved with the KUIP [160] user interface. The Physics Analysis Workstation [127] has many histogramming facilities and is one of the tools used for analysis. Analysis with the ROOT [37] Object Oriented Framework, with its ROOTCINT C⁺⁺ interpreter and many other features like 1D, 2D and 3D histogramming facilities, is also used. ROOT can be used with analysis packages developed in the collaboration and loaded as shared libraries — such as GROVER [55] (Generic Reconstruction Of VERTices) for vertex finding, or the CLUE API which is based on HERA-B’s BEE [77] data analysis framework. A schematic overview of the software analysis chain is presented in figure 3.36. A comparison between the processing of events measured with the detector and the simulation of events is shown in figure 3.37.

3.5.1 Monte Carlo simulation

The input for the HBGEAN package comes from the results of the PYTHIA and the FRITIOF Monte Carlo event generator packages. PYTHIA simulates heavy quark production and decays. The initial state (proton–proton collision at $p_{\text{beam}} = 920\text{GeV}/c$ beam momentum in the target frame) is the PYTHIA input. Since PYTHIA can only generate events with target nucleons — but not whole nuclei — the propagation of the emerging light quarks inside the nuclear environment is instead simulated with FRITIOF. The heavy quark pair momentum is subtracted from the beam momentum, and the interaction of the resulting reduced momentum projectile with the target nucleus is simulated in FRITIOF as a “spectator event” which superposes with the heavy quark pair.

Minimum bias background events were completely generated with FRITIOF [108]. A variable number of events, chosen to follow a Poisson distribution, are merged together to form one “super-event”, corresponding to one bunch crossing. These “super-events” are then subjected to full GEANT simulation.

¹¹Line count of files under the ARTE source code tree with Unix command `wc -l`.

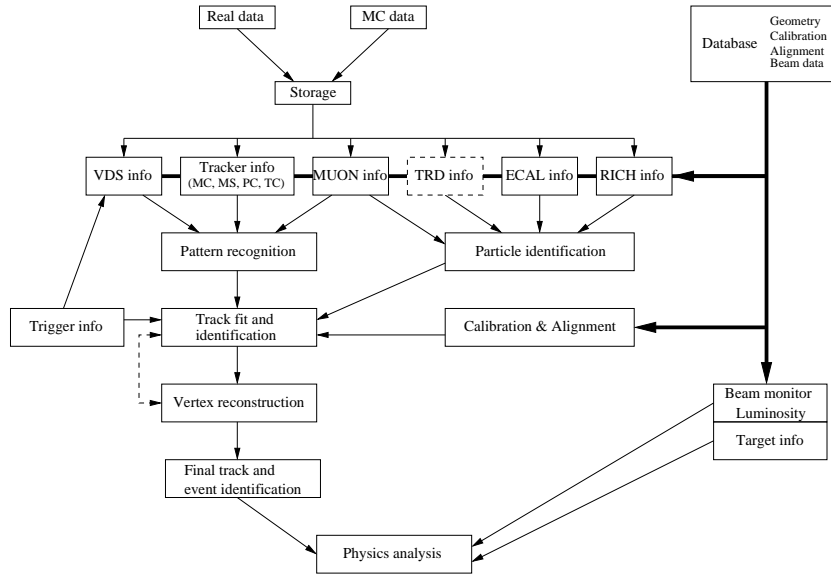


Figure 3.36. Main processes in the software analysis chain [108]. The TRD was not used in the 2000 and 2002 runs, therefore its information is excluded from Real Data event reconstruction.

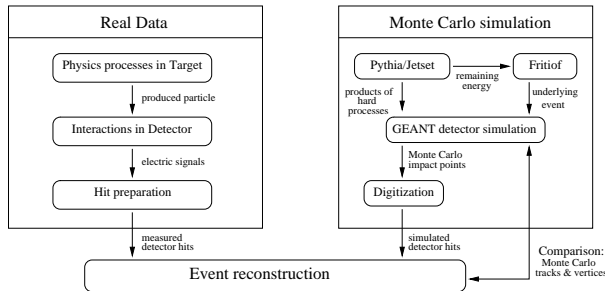


Figure 3.37. Comparison of the Real Data and the Monte Carlo event processing chains in HERA-B [90].

Subdetector	Resolution [μm]	Hit efficiency
VDS	12	95%
ITR	60	95%
OTR (MC)	200	98%
TRD	200	95%
MUON (pixel)	2200	99%
MUON (tube/pad)	4400	99%

Table 3.2. Expected subdetector resolutions and efficiencies in simulated events [108].

3.5.2 Digitization of Monte Carlo events

The event reconstruction of simulated events requires a *digitization* step, which uses the output of the simulation routines (PYTHIA, FRITIOF and GEANT) as input, and simulates the detectors' response to the passage of particles. The result of the digitization step is a set of simulated detector "hits". The digitized hits are also smeared and merged with background hits. This digitization step's output is fed to the reconstruction routines. The simulation of the detector response attempts to account for effects such as e.g. channel response efficiency (whether it produces a signal due to a crossing particle), noise and crosstalk (which leads to an increase in the hits' coordinates variances). A dead (i.e. unresponsive) channel mask is applied when available. The resolutions quoted in HERA-B's Proposal [108] are presented in table 3.2.

3.5.3 Event reconstruction

An ARTE executable can be compiled by an analysis person with the code of choice, in either of the supported procedural programming languages mentioned above. Typically, one writes the routines designed for the required analysis and makes extensive use of the libraries already provided by the ARTE framework. The editable source code templates can be copied to a local directory, and the customized routines are typed in those copies. The templates already include function calls for the required startup routines, which in turn incorporate function calls to the required initialization procedures for the different subdetector software. At startup, a Kumac¹² file is read, see one example at [71]; it contains the necessary startup parameters — DST file directories and event range, the location of the configuration Database, and several reconstruction-related parameters.

The event reconstruction algorithms are designed to process input from either simulated or real events with minimal changes. That input feed comes in the form of detector hits; see scheme in figure 3.37 for comparison. The detector hits are reconstructed from the set of detector channels producing an output signal. Each detector component's reconstruction software interprets the channel output to generate the hits. One example of such software package is MARVIN, which processes VDS raw output. MARVIN gathers VDS strip current signals in clusters to identify hit coordinates on opposite sides of a silicon wafer, while also following channel pedestals (quiescent voltage levels) and electronic noise. The mapping of pedestal and noise levels is useful in the context of Data Quality monitoring [25].¹³

Full event reconstruction proceeds from the measured or simulated hits

¹²KUIP macro.

¹³A different package, VDSRHP, is used for online monitoring. MARVIN is used for offline run processing.

to obtain reconstructed tracks and vertices for the event to be studied. The general strategy for the track finding is as follows [108]:

- find track segments (RSEGs) by pattern recognition in the ITR+OTR chambers outside of the Magnet field, and in the VDS. The tracking chambers downstream of the RICH are not used since in that region the number of particles is drastically increased due to radiation processes;
- extend the track segments (found in the ITR+OTR field-free region) through the magnet, to determine track momentum and charge. The sign of the track charge can be obtained from the location of the curvature radius relative to the track, as seen in the Magnet bending plane, zx . The momentum is related to the curvature radius of the track in the Magnet field — see section B.3;
- match track segments from the Main Tracker and the VDS at the SL8 plane, in front of the Magnet;
- refit the tracks using momentum information, for a more accurate treatment of multiple scattering effects;
- extrapolate the track segments from the Main Tracker to the RICH, the TC chambers and ITR chambers at the same z , the TRD, the ECAL and the MUON system, and associate the signals from these devices to the tracks;
- fit complete tracks and perform vertex fits;
- remove hits from well-defined tracks and repeat the whole process with the remaining hits;
- extrapolate unmatched track segments and try to find complete tracks.

For pattern recognition, HERA-*B* presently employs the cellular automaton CATS [8] [97] for track searching. CATS also incorporates the Kalman filter technique to fit the sets of raw detector hits (space points) from surviving cellular automaton cell combinations for track reconstruction. The OTR-CATS algorithm is similar to the CATS used in the VDS, and is applied for pattern recognition in the four PC chambers upstream of the RICH. The RANGER [112] [114] [115] [113] [116] algorithm is used to validate the OTR-CATS reconstruction and for extrapolating the OTR segments to the TC chambers, located downstream of the RICH.

Cellular automata [66] [149] are dynamical systems that evolve in discrete, usually two-dimensional spaces, consisting of cells. Each cell can take several states. In the simplest case, the cell state can be described by a single bit, 0 or 1. The evolution laws are local, i.e. the dynamics of the system is determined by an unchanged set of rules (for example, a table)

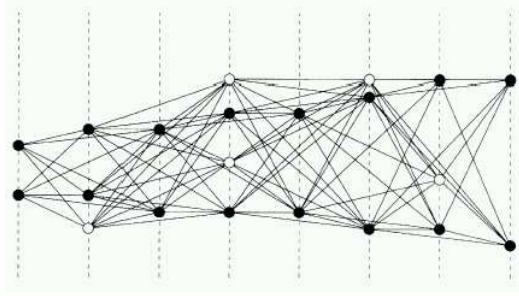


Figure 3.38. A simple illustration of the segment model: segments connect hits across one or two layers [8]. The filled dots are cells that represent hits defining a good track candidate; the void cells are excluded from the two tracks found in this example.

that relates the new state of a cell to the states of its nearest neighbors in contact with the cell. The update of the states of the cells is done simultaneously at discrete time instants. The CATS cellular automaton defines segments joining two space points with fixed z coordinates; each space point represents a detector hit, which is associated with a cell — see figure 3.38. The automaton then cycles through the segments joining all the activated neighbouring cells, and eliminates the segment combinations that are less likely to constitute straight lines.

The CATS and RANGER algorithms integrate the discrete Kalman filter technique to compute track parameters and associated covariance matrices. The Kalman filter [95] [110] [65] is a set of mathematical equations that provides an efficient recursive solution of the least squares method. Its implementation in CATS uses an optimized numerical algorithm to reduce the computational load [56]. Figure 3.39 presents a diagrammatic representation of the overall Kalman filter technique. The Kalman filter uses as input a seed state, e.g. a collection of hits in a detector layer and estimated directions, and propagates the expected tracks into the neighbouring layer. In the filtering step, the track parameters are updated by minimizing the sum of diagonal elements of an estimation error covariance $\hat{\Gamma}_k$ at step k . In the prediction step, the track's parameters and covariance matrix are extrapolated onto the next layer. The search region is limited by the knowledge of the multiple scattering angle [81] for particles transversing a thin layer of detector material. If a detector hit is not found in the search region for a given iteration, the hit search ends for that track; to improve track quality, it may be discarded if it does not have enough associated hits. At the end of the iteration procedure, we obtain a set of tracks. Each track is defined by a set of parameters, e.g. (z, x, y, tx, ty) , where (z, x, y) is the starting (or ending) point of the track and tx and ty define the tangent of the track in the zx and zy planes respectively. The Kalman filter also yields the tracks parameters' covariance matrices. The goodness-of-fit can be estimated from the probability associated to the χ^2 value obtained from the Kalman filter procedure. The number of degrees of freedom for the Kalman fit is

$$N_{\text{d.o.f.}} = N_{\text{VDS}} + N_{\text{ITR}} + N_{\text{OTR}} - 5 - N_{\text{constraints}} , \quad (3.9)$$

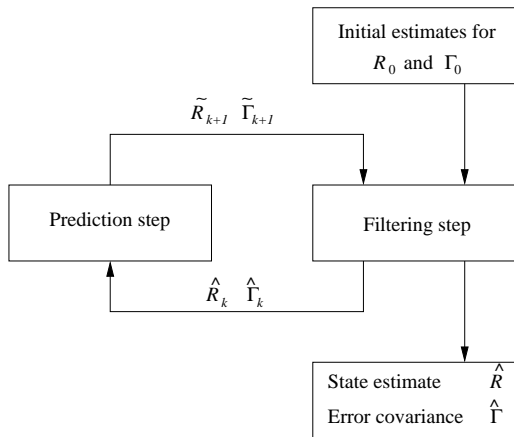


Figure 3.39. The operation diagram of the discrete Kalman filter [56].

with the N_i as the number of hits associated to the track in the detector i and 5 degrees of freedom corresponding to the spatial coordinates of a track's point plus two direction angles. The term $N_{\text{constraints}}$ is the number of additional constraints eventually used in the fitting procedure. For fitting N_{tr} tracks for reconstructing of one vertex, the corresponding number of degrees of freedom is $2N_{\text{tr}} - (3 + N_{\text{const}})$ for N_{const} constraints (e.g. mass constraints, bounding of coordinates to a target position, etc.) [106].¹⁴

The RICH hits are combined to form ring patterns through algorithms such as RISE (*R*Ing *S*Earch)¹⁵ and RITER (*R*Ich *i*TERative *R*econstruction software) [130], which implement differing techniques to reconstruct ring patterns from Čerenkov photon hits. The main difference between the two packages is [50] in the background treatment — RITER makes a global fit for all given seeds (RICH photon hits, along with tracking information such as momenta and slopes) such that photons are weighted differently if they can belong to different rings, while the RISE package uses solely the hit information and can run as a stand-alone package. The RITER package uses the seeded information to produce as output the likelihoods for electron, muon, pion, kaon and proton particle identification (PID) hypotheses [129] of the seeded tracks. The PID hypotheses are tested by [122] fitting the hit pattern of a ring to concentric circular crowns, each with an angular aperture range corresponding to the track's momentum under a given PID test. The ECAL information is processed by the CARE (*C*Alorimeter *R*Econstruction) package [151] [152], which estimates calorimeter clusters' properties (baricentric coordinates, cluster energy and shape, etc.). The MUREC (*M*Uon *R*Econstruction) package [63] is used for the reconstruction of Muon Detector hits [146].

At this point, the reconstruction information that is available is in the form of detector hits, track segments (RSEGs) in the VDS, Main Tracker

¹⁴See also the C++ source code in file `GroverVertex.C` of the GROVER package.

¹⁵Also named RIRE, for RIng REconstruction [50].

and Muon Detector,¹⁶ Čerenkov rings in the RICH and calorimeter clusters in the ECAL. Full track reconstruction requires matching these elements to identify the formers' parameters — momentum, particle identification (PID), etc.. The MARPLE package [91] [92] performs a recursive match of segments from the VDS and the Main Tracker, ECAL clusters, etc., with tighter requirements at each recursion step. The first iteration reduces combinatory background by requiring that all candidate Main Tracker segments matches to VDS segments differ by [142] $\Delta y \equiv |y_{\text{VDS}} - y_{\text{Main Tr.}}| < 35.7\text{cm}$ for the vertical coordinate, and by $\Delta x \equiv |x_{\text{VDS}} - x_{\text{Main Tr.}}| < 18.6\text{cm}$ for the horizontal coordinate, at the center magnet coordinate $z \simeq 450\text{cm}$. The resulting momentum estimation is then used on the next iteration along with more stringent coordinate differences between the matching candidates, e.g. $\Delta x < 2.6\text{cm}$ and $\Delta y < 5.6\text{cm}$.

The track candidates are obtained from the each segment pair match from the VDS and Main Tracker. The tracks' parameters are obtained by applying a Kalman filter [110] [145] on the hits associated to the matched segments, which adjusts and improves the tracks' parameters. The track candidates are picked foremost the from the one-to-one associations of VDS and Main Tracker segments, and only then the one-to-many associations; many-to-many and many-to-one associations of VDS and Main Tracker segments are rejected, since they do not follow a coherent multiple scattering model. The surviving candidates are matched with calorimeter clusters with CARE and with Čerenkov rings with MARPLE. Finally, the table of reconstructed tracks (RTRAs) is filled from the surviving candidates.

The track reconstruction procedure excludes the lowest-momentum tracks (below $0.2\text{GeV}/c$), which constitute a substantial part of the Monte-Carlo generated tracks (see figure 4.6). On one hand, the low-momentum tracks decay faster and therefore are likely not to be reconstructed at all. On the other hand, they are more sensible to multiple scattering. Since the Kalman filter method is set to search for straight tracks up- and downstream of the Magnet, it naturally rejects tracks with large deflection angles. The low-momentum cut on reconstructed tracks therefore improves RTRA quality. In the Electromagnetic Calorimeter, low-energy clusters are too not reconstructed, since they would fall below the photomultipliers' response region. The thresholds are set at¹⁷ 0.05GeV , 0.10GeV and 0.15GeV , respectively for the Inner, Middle and Outer ECAL cells. The muon track reconstruction cuts out tracks with momentum below $5\text{GeV}/c$, since those would not have enough energy to punch through the iron absorbers in the Muon Detector system.

The last step in the event reconstruction chain is the identification of vertices. Vertex fitting packages can run either in an ARTE executable, or

¹⁶The TRD was never used in event reconstruction in HERA-B.

¹⁷Values obtained from ARTE output, provided by the CARE package initialization.

also as a shared library inside ROOT, such as GROVER [55]. Those packages use track parameters and covariance matrices as input, along with geometric and kinematic constraints to augment the output quality. The vertex fit further improves the parameters of tracks associated with vertices, by using the common vertex hypothesis as constraint. GROVER proceeds iteratively: it begins by looking for position-averaged track clusters in the target region and selects the clusters that intersect the target wire to within 3 standard deviations of the tracks' coordinates at that location. This is used to reject the contributions from tracks that reduce vertex position resolution. Then, a new Kalman fit is performed to improve the vertex fit's χ^2 , and the tracks which contribute with $\chi_{\text{RTRA}}^2 > 20$ are rejected from the vertex association. This procedure is iterated to minimize the vertex fit's χ^2 , and it has a 10% rejection rate for legitimately-associated tracks [142].

3.6 ARTE table information

The input for the ARTE event reconstruction routines comes from detector configuration and from simulated/measured hits in the detector. The detector configuration is stored in tables and its scope spans over compact sets of events, whereas hits have the scope of one event and are streamed from tape. This section describes the relevant ARTE table information that was used in event reconstruction.

The input for full event reconstruction in ARTE is the set of detector hits measured for each event. The hits' coordinates are computed from the index numbers of the activated detector channels. Naturally, this results in the necessity of knowing the detector geometry, specifically in terms of the position and orientation of the detector layers relative to a chosen reference (in this case, close to the second target station, see section 3.2.1). The validity of the detector configuration tables is specified by time scope, or an index related to the time interval; the production and release of version of the configuration tables is based on the analysis of a multitude of events. The hit information is streamed from an input file and has the scope of one event. For simulated events, the Monte Carlo particles computed in ARTE's GEANT-like package, HBGEAN, is also streamed from an input file stored on tape.

The geometry configuration is kept in two sets of tables; one set contains the nominal values of the detector components involved in particle detection (i.e., cabling and support structures are not used in event reconstruction and/or simulation if they do not contribute to effects such as multiple scattering), and the other set contains the same values, updated from the nominal tables, by the reconstruction of several events. In other words, to obtain the geometry description of the "real" detector and to reconstruct the individual events, an iterative processing is required: pro-

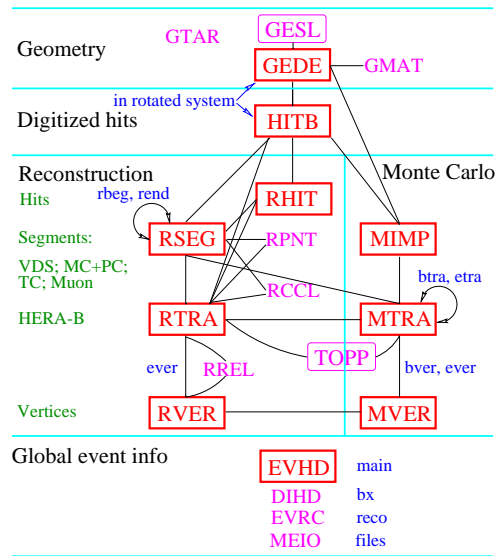


Figure 3.40. Main ARTE tables, used for event reconstruction [103]. Table information is read/stored from top to bottom. In simulated events, tables HITB and HITS (not shown) are filled by hits generated by the HBGEAN package. Except for the geometry tables and table TOPP, the information stored in the remaining tables has the validity of one event.

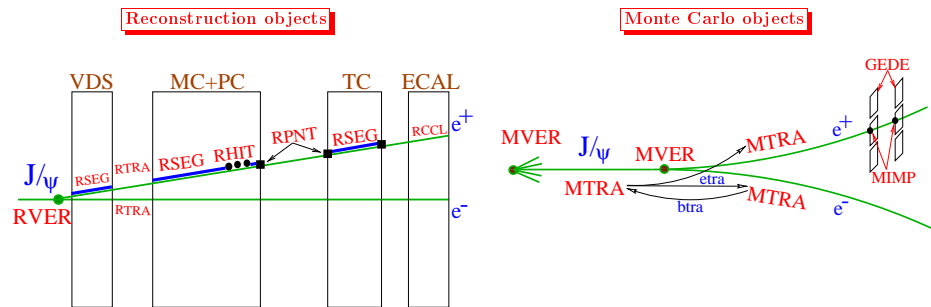


Figure 3.41. The relations of particle properties data (left) and Monte Carlo particles data (right) to geometry configuration objects [103].

cessing several events allows to improve knowledge on the real location of the detector elements, and this in turn improves the quality of reconstruction. The name format of tables containing the nominal values is “Nxxx”, where the “xxx” has to do with the nature of the information stored in the table; the “real” values are stored in tables named like “Gxxx”. The nominal positioning of the detector elements (their encompassing volumes) is stored in table NEDE (Nominal DEscription); the nominal positioning of superlayers is stored in table NESL; the nominal beam geometry is described in table NBEA; the nominal positioning and orientation of the target wires is kept in table NTAR; etc.

The measurement quantities for each simulated/reconstructed event is also kept in tables, and has the scope of that event; see figure 3.40 and reference [103]. The streamed input fills specific table structures in the computer process’ memory. Digitized hits are kept in a table called “HITB”, with the exception of calorimeter hits which fill up another table called

“HITC”. The Monte Carlo particles’ ARTE tables are named as “Mxxx”, where the “xxx” pertains to the nature of the elements stored in the table — points in the particle track, the tracks themselves, or vertices where on Monte Carlo particle branches (decays) into two or more other particles. The most used tables are named MTRA (Monte Carlo particle tracks) and MVER (Monte Carlo vertices). Table MIMP pertains to the particle impact points on the detector, as simulated with HBGEAN. The reconstruction-side tables store the data elements from the event reconstruction (tables with name format “Rxxx”). These tables contain information such as a track’s point coordinates, its direction and momentum, quality of reconstruction (number of hits used for the track reconstruction and a χ^2 from the Kalman filter algorithm) and relation with other table elements (segments, vertices, etc.). The relations between the reconstruction objects and the geometry configuration is represented in figure 3.41.

The tabular information can be listed through the interactive prompt implemented in the KUIP user interface. Data processing is achievable through routines written in C/C++ and/or Fortran using ARTE’s library routine set. In either case, the binary program is compiled and executed within the HERA-B computer framework. The output from the user’s routines can be directed as ASCII output, to ROOT file or to HIGZ ntuple.

3.6.1 The PRISM event display

ARTE’s PRISM package was used as “visual aid” in the events’ interpretation; see figures 3.42 and 3.43. Some of PRISM event display’s elements are [111]:

- the *relevant* detector elements (i.e., their sensitive surfaces), such as VDS planes and Outer Tracker cells, the target wires (thick blue lines), the Magnet dipole region (pink circle in zx projection) and the RICH vessel (yellow trapezoid);
- the MTRA Monte Carlo tracks (red-painted lines), and their intersections with the calorimeter (xy projection), with markers used for PID — electrons (+), muons (▼), pions (○), kaons (△), protons (□), photons (★) and anything else (◇);
- detector hits as green-painted wires (for the OTR cells, the drift time information is represented by one wire-centered isochrone circle in the zx projection);
- RHIT reconstructed detector hits from HITB digitized detector hits;
- RSEG reconstructed segments (green);
- RTRA reconstructed tracks (blue);

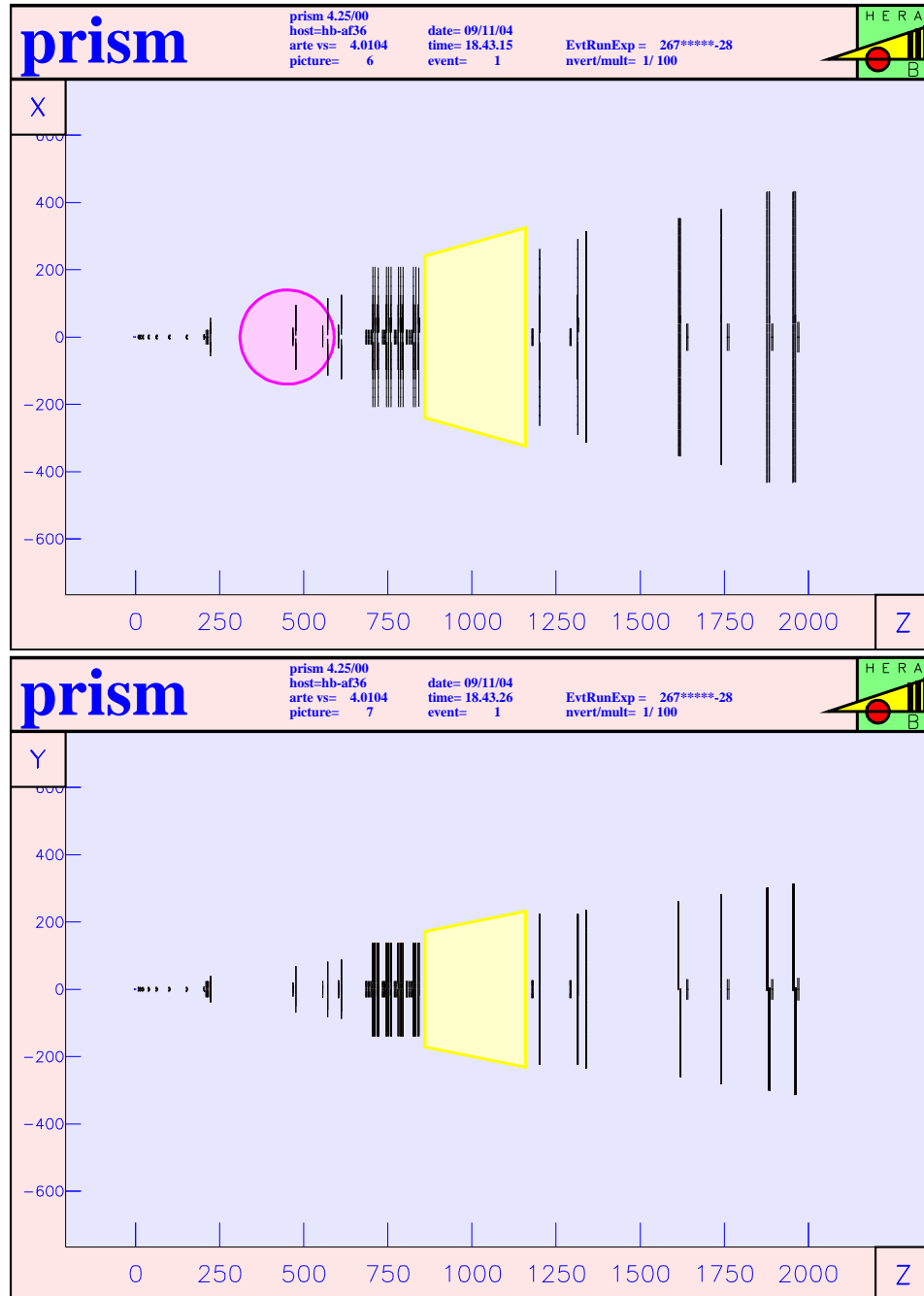


Figure 3.42. PRISM representation of the HERA-B detector. The axes' scale is in centimeters. Top: xz plane. The pink circle represents the Magnet boundaries. Bottom: zy plane.

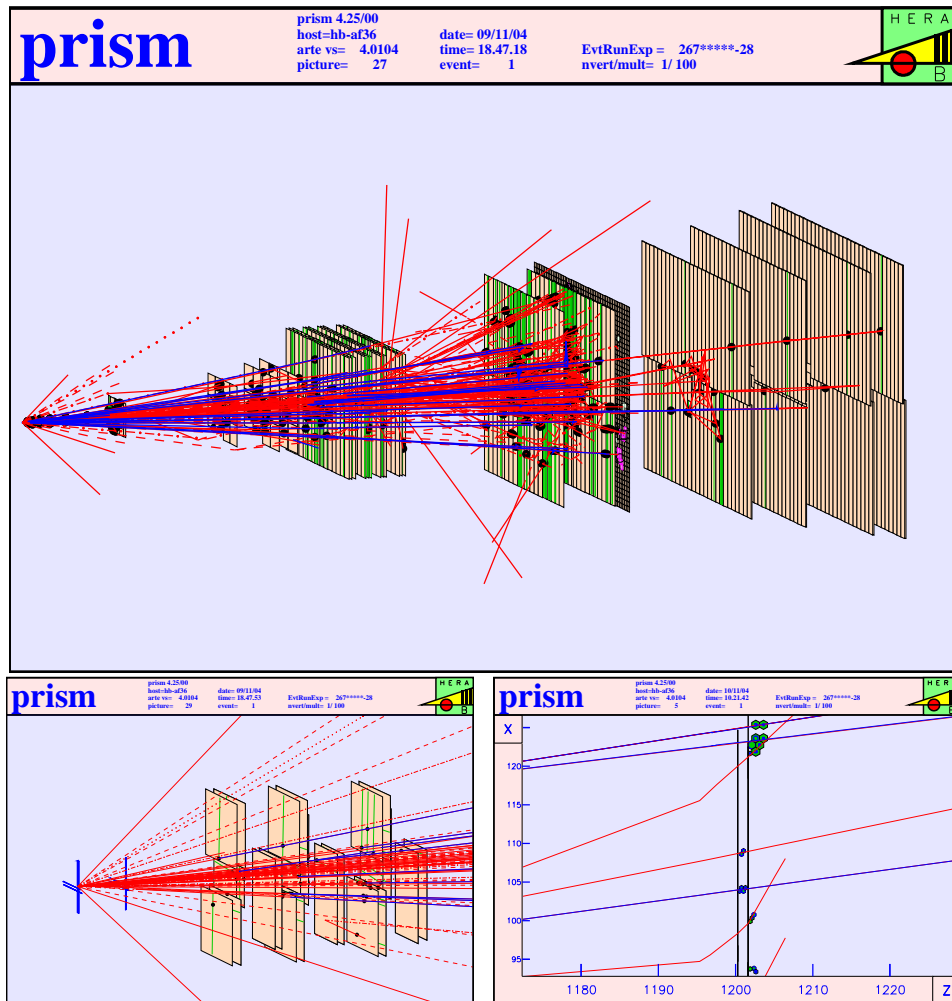


Figure 3.43. Top: PRISM representation of a 3D view of one Monte Carlo event in HERA-B. MTRAs are drawn in red, RTRAs in blue, the black “blobs” are MIMPs, vertical green segments in the OTR and MUON represent HITBs. The insensitive materials (“walls” [111]) are not shown. The close-ups of the Target and first three superlayers of the VDS (bottom left) and of a superlayer of the Outer Tracker TC02 layer (bottom right) show the graphic elements detailed in the text.

- RVER reconstructed vertices (black ovals represent 1σ bound of the vertices' positions);
- color-coded calorimeter cell energy measurements — red ($E > 3.33\text{GeV}$), yellow ($1 < E < 3.33\text{GeV}$), green ($0.33 < E < 1\text{GeV}$), medium green ($0.11 < E < 0.33\text{GeV}$) and light green ($E < 0.11\text{GeV}$) — and RCCL reconstructed calorimeter cluster bounds from HITC calorimeter hits;
- if the event passes the SLT algorithm cut (e.g. a dilepton with invariant mass close to the J/ψ), the respective Main Tracker segments are enclosed by cyan-colored wire rectangles to represent the approximate direction of the SLT-reconstructed track.

3.7 A summary of status and physics results at HERA-B

The construction of the HERA-B detector was finished in February 2000, roughly five years after its approval, with a two year delay. Physics data was collected from mid-April 2000 to late-August that year, and was followed by a prolonged shutdown for HERA upgrade which allowed detector access for improvements and repairs. HERA-B resumed data taking in November 2002 and shut down in March 2003. Overall, the 2002–2003 epoch's data have much higher quality than the year 2000's.

The physics program goals were changed after the 2000 run epoch, in face of both the over-optimistic expectancy on the detector performance and on the preliminary measurements of $\hat{C}\hat{P}$ violation in the golden decay mode obtained by competing experiments BELLE and BABAR (e^+e^- machines installed in the KEK and SLAC accelerators). The renewed physics program of HERA-B seeks to make the best use of this detector's phase space range (see section B.5.3 in appendix) and good PID capabilities.

The targeted physics program after the year 2000 run epoch includes e.g. the decay $B^0 \rightarrow \mu^+\mu^-K^{*0}$ [1], $B_s-\bar{B}_s$ mixture and the dependence of b quark production cross section with atomic number A of the target nuclei, σ_{bb}^A . The original program to study $\hat{C}\hat{P}$ violation in golden decays was abandoned in face of the loss of competitiveness with other experiments' results. The status on repairs and results prior to the 2002 run period are described in reference [44]. After the 2003 shutdown the physics program and prospects of HERA-B were evaluated [45]; however, it was decided that data taking would not be resumed and at the moment the collaboration is focused on producing results from the collected data [153].

3.7.1 Run period of year 2000

The technologies proposed for the Main Tracker in HERA-B [108] were proven to fail quickly when confronted with the high radiation environment required for the detector's operation [1]. This caused a two-year delay for detector completion and commissioning, during which a research and development program was implemented to design more robust technologies for the ITR and OTR. The First Level Trigger did not operate to full design specifications either, and it was required that the Target system operated at rates lower than the original specification, and the Second Level Trigger operate as a makeshift FLT. Because the SLT is not designed to operate at the rejection rates of the FLT, the Target had to operate at rates much lower than the design values of 20MHz–40MHz. The VDS, RICH, ECAL, DAQ, SLT and 4LT systems were installed and operated close or at the design specifications during that period; the remaining systems faced problems that were, for the most part, solved or at least improved by the year 2002. See reference [1] for a detailed evaluation of the HERA-B detector performance during this period.

The Target system was in operation during 94% of HERA luminosity periods, usually at rates of 5–10MHz, though with some background contribution from e.g. the unbunched beam. The VDS achieved overall efficiencies above 97%, but with secondary vertex resolutions a factor of two worse than expected ($630\mu\text{m}$ vs. $300\mu\text{m}$). The ITR endured low voltage power supply problems and significant GEM gain variations. To prevent ITR failure rate, the bias voltages had to be lowered which caused a drop of output rate. The OTR suffered many problems, found during regular operation. These problems included gas leaks, 2% of dead readout boards and 6.9% of high voltage group fails due to e.g. “shorts” from residue solder. Part of the failure rate was due to deficient mechanical stability, which after corrected decreased the failure rate by a factor of 10. The thresholds of all FLT OTR layers had to be raised due to noise induced by trigger electronics. A $240\text{--}300\mu\text{m}$ hit resolution was obtained, compared with $500\text{--}700\mu\text{m}$ from tracking methods; the discrepancy was attributed to the preliminary alignment knowledge available at the time. The high- p_T system experienced efficiency losses of up to 30% of the design value in its inner chambers. The RICH ran stably. The TRD was installed but not used, since only a few channels were connected due to budgetary limitations. The ECAL was fully installed and the energy and spacial resolutions are close to design values. The Muon Detector system suffered from low pad chamber efficiency, which were of 75% and 68% in the MU3 and MU4 pad layers respectively. This yields a dimuon track pretrigger efficiency of just 26%. The FLT did not operate satisfactorily, which was attributed to varying optical link stability caused by different attenuations, temperature drifts and other effects. Hardware adjustments require ‘in situ’ corrections, which are not possible during beam operation. Therefore, the SLT had to be used in place of the FLT, with a random trig-

ger to sufficiently reduce input rates to levels supported by the SLT. The DAQ/SLT endured stable operation for periods of many hours at input rates of up to 22kHz. The TLT was not used since it was found that the 4LT had sufficient performance to cope with the SLT output rate.

In 116 days of operation in the year 2000 run period, 18.1×10^6 $B \rightarrow J/\psi X \rightarrow \ell^+ \ell^- X$ events were accumulated. The trigger efficiency for these channels was much lower than expected: at an average 5MHz trigger rate, the trigger rate was of $1.0_{-0.3}^{+0.2}$ /hour and 0.2 ± 0.2 /hour respectively for the dielectron and dimuon channels, compared with the design rates of 10/hour and 15/hour [1]. The reconstruction efficiencies of golden decay events are a factor of two lower than the design values: 7.1% and 3.3% for the dimuon and dielectron channels, compared to 16% and 8.3% respectively. The tagging power (see equation 2.45) is [1]

$$P = D\sqrt{\epsilon} \simeq 0.3,$$

with ϵ as the b quark tagging efficiency, $D = 2\text{Pr}_b^{\text{correct}} - 1$ is the dilution factor and $\text{Pr}_b^{\text{correct}}$ is the probability of correctly measuring the b quark charge.

The main physics results were published under references [5], [3] and [4]; complementary papers dwelve into detector performance and operational experience. The b quark production cross section was measured in $B \rightarrow J/\psi(\ell^+ \ell^-)X$ decays, which made use of a sample of 1.35×10^6 dilepton trigger events, yielding $\sigma_{b\bar{b}} = 32_{-12}^{+14}(\text{stat})_{-7}^{+6}(\text{sys})\text{nb/nucleon}$, which is compatible with results from other sources ([5] and references therein). The inclusive differential cross sections $d\sigma_{pA}/dx_F$ and $d\sigma_{pA}/dp_T^2$, for V^0 production of the hadrons K_S^0 , Λ and $\bar{\Lambda}$ in proton-nucleus collisions at HERA-B's CM energy, were also measured [3], being this the first experiment to accumulate this information in the backscattering phase space region $-0.12 < x_F < 0$. The $\chi_c \rightarrow J/\psi\gamma$ decay mode — of interest for understanding the production of quarkonia states in hadronic collisions, for which different QCD models exist — mode was also investigated [4].

3.7.2 Run period of 2002/2003

The size of the event sample from this period has improved by a tenfold factor relative to the previous run period. After the 2000/2001 HERA shutdown, most of the detector components were used in 2002/2003 [73]. However, the available beam time was only around 10% of what was expected, with consequent limitations of accumulated statistics.

After the 2000/2001 shutdown, most¹⁸ of the detector components were commissioned and used in the 2002/2003 epoch [73], which lasted from early November 2002 to early March 2003. The available beam time was only a fraction of what was expected, which severely limited the available statistics. During this data taking schedule 158×10^6 dilepton trigger events

¹⁸The Transision Radiation Detector (TRD) was installed but not used.

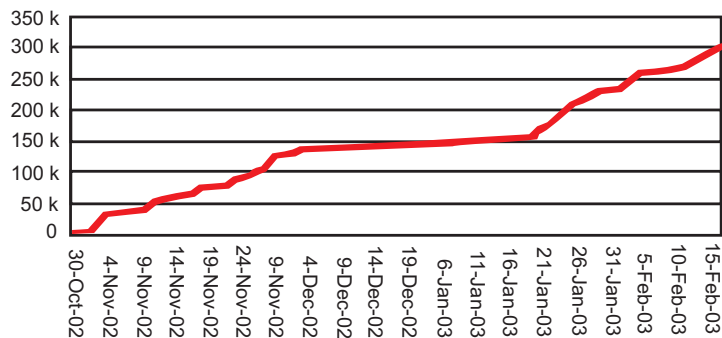


Figure 3.44. The integrated number of reconstructed J/ψ as a function of time indicates the performance of the dilepton trigger [73] [139]. In the regions of small increments, either minimum bias data was taken (December 2002) or no beam was available for HERA-B.

were recorded, with 150×10^6 events fully reprocessed [142]. The remaining data sample consists of 210×10^6 and 90×10^6 events, respectively for minimum bias and for hard photon and glueball events [153]. Most runs were reconstructed in the reprocessing number 4 (“repro 4”), and the latest reconstruction was started in June 2004 (“repro 5”). Until September 2004 around 38×10^6 events were reprocessed under the new repro [142], and more are under study.

Given the accumulated $N_{J/\psi} = 3 \times 10^5$ J/ψ events in (figure 3.44), the estimated number of golden decay events recorded is still very small: at best, it should mean that there are some $10^5 \times \sigma_{b\bar{b}}/\sigma_{c\bar{c}} \simeq 10^2$ B events, with an expectantly small fraction of these possible of producing viable golden decay candidates. Around 90% of events accounted in b production cross section $\sigma_{b\bar{b}}$ lie in the J/ψ acceptance range $-0.35 < x_F < 0.15$ [153]. The $b\bar{b}$ production cross section has also improved relative to the data set from the previous run period and is now at $\sigma_{b\bar{b}} = 9.9 \pm 2.9(\text{stat+sys})\text{nb}/N$ [73]. The production cross section for double semileptonic decays ($B \rightarrow \ell^+ X$, $B' \rightarrow \ell^- X$) was also measured, $\sigma_{b\bar{b}}^{\text{semilept}} = 27.0 \pm 29.5(\text{stat})\text{nb}/\text{nucleon}$ [142].

In the interest of persuing the physics program alternate to the original focus, a few results were published by the HERA-B collaboration. One subject that was investigated was the search for pentaquark (bound states of five quarks, such as $dds\bar{s}u$ for the $\Xi^{--}(1862)$) candidates in a minimum bias data sample, with the first evidence for the detection of $\Xi^{--} \rightarrow \Xi^- \pi^-$ events as a broad resonance [6]. The upper limit levels for the $\Xi^{\pm\pm}(1862)/\Xi^0(1530)$ fraction are at 0.6%–0.8% with 95% C.L.. No evidence was found for resonance decays in the $\Theta^+(1530)$ mass region; the upper limit on the particle yield ratio was measured $\Theta^+/\Lambda_{1520} < 0.02$ with 95% C.L.. Another significant result published by the collaboration was on the search for flavour changing neutral currents (FCNCs) in $D^0 \rightarrow \mu^+ \mu^-$ decays, for which no evidence was found within a sample of 50×10^6 dilepton trigger events [7].

In the $D^0 \rightarrow \mu^+ \mu^-$ analysis, only three events yield a dimuon mass in the D^0 mass window [153]; the branching ratio for the decay is below 2.0×10^{-6} at 90% C.L., which improved relative to the result from the CDF collaboration [9]. The relevance of the second work reflects upon the GIM mechanism [74], which describes the strong suppression of decays in the Standard Model, due to the presence of Cabibbo factors $\sin \theta_C$ in the decay amplitudes. Other physics subjects are under investigation and the results will be published [153].

Single event analysis

“Não compreendo como se consegue medir a violação de CP a partir de um único evento.”¹

— José Mariano Gago, *Jornadas do LIP (Lisbon, December 2002)*

In this chapter, a sample of simulated events for B_d^{neutr} (B_d^0 or \bar{B}_d^0) golden decays is studied with some detail (table 4.2) to find whether the reconstructed event is consistent with the presence of a golden decay. The same analysis techniques are also applied to a selection of events recorded with the detector in the run periods of years 2000 and 2002; see table 4.15. Other important subjects such as B_d^0 – \bar{B}_d^0 flavour oscillation and flavour-tagging efficiencies are left essentially unabridged.

The flavour of the golden decay B meson is measured by the charge of the remaining bottom quark hadron in the event. How the charge is measured depends on the particular *flavour-tagging* method applied. The kaon- and lepton-tagging method [108] [107] uses the charge of one of those particles originating from the second B meson. Its charge gives the charge of that meson, and in turn the flavour of the B_d^{neutr} . The particle is selected by requiring it to have a minimum transverse momentum, impact parameter to primary vertex, or some other combination of conditions. The kaon and lepton tags are preferable to e.g. a pion tag, since these have higher multiplicities than the previous (see figure 4.7) and are therefore harder to separate from the spectator event. Another tagging method [107] [137] uses the total charge of a set of reconstructed tracks observing minimum requirements such as transverse momentum and impact parameter. In this technique, the q_i -charged tracks contribute with a weight proportional to their squared transverse momentum, $w_i \propto p_{T,i}^2$, to the total charge $Q = \sum_i w_i q_i / \sum_j w_j$. The sign of the charge is used as a charge tag if $|\sum_i w_i q_i| > 0.8$. The tagging methods are typically rather inefficient ($\sim 50\%$ or even lower is common); to this adds the fact that those efficiencies are further limited by the beauty hadron production ratios of $\bar{b}(b) \rightarrow B_d^{\text{neutr}}$ and $b(\bar{b}) \rightarrow B^{\mp}$, which

¹“I don’t understand how you can measure CP violation from a single event.”

are around 40%. Therefore, these tagging techniques fail for flavour identification on individual events. At most, one could calculate the likelihoods that the flavour tag obtained with one of those methods is correct; but this is not done in this work. Rather, a very simple tagging method was used, based on reference [108], where the charge tag is attributed by the charge of the reconstructed track with the highest transverse momentum; the candidate tracks are also required that they do not belong to the golden decay, and that they have detector hits in the VDS and Main Tracker so that the charge and momentum are correctly measured.

Some quantities described in this chapter are not stored in ARTE tables, but can be calculated from this information. The ARTE tables filled after event reconstruction do not contain information which is usually presented as final results, such as impact parameters or cross sections (this last aspect is not characteristic of single events, although one may argue that it stems from the laws driving the events' unfolding). The invariant masses of RTRA sets were measured to identify the presence of V^0 decays such as the J/ψ and K_S^0 in golden decays. The distances of closest approach between pairs of RTRAs and between RTRAs and RVERs, and impact parameters to target wires, were also measured. Some of these quantities might still be inferred from ARTE tables data — such as invariant mass of reconstructed vertices.

In-house vertexing packages are commonly used in other analysis work at HERA-B; one such package is GROVER, a C++ API for reconstruction of vertices from known/selected RTRAs and for event display. However, I chose² to calculate some of those quantities (invariant masses, distances) directly from the output of ARTE tables, instead of using that API. The quantities mostly studied in this chapter, such as invariant masses of RTRA sets, RTRA distances to other RTRAs and RVERs, and impact parameters to target wires, along with their standard deviation errors, were calculated using the formulas in appendices B and C. The “number crunching” was done in C language (appendix E), to produce ASCII output parsable either by common spreadsheet software or with a ROOT parsing application; the source code used to parse and process the ASCII output from ARTE is presented in section E.1.

Concerning the argument quoted at the start of this chapter, I refute it as follows. The work presented here is not about actual measurement of $\hat{C}\hat{P}$ violation, but rather how individual events might be flagged as suitable for $\hat{C}\hat{P}$ violation studies. The nature of the $\hat{C}\hat{P}$ violation measurement technique briefly described in section 2.3.4 precludes any definite measurement from individual golden decay (or other) $\hat{C}\hat{P}$ -relevant events, since each of those events would individually give maximal asymmetry, i.e. for one event $A_{\text{int}} = \frac{N-\bar{N}}{N+\bar{N}} = \pm 1$ (see equation (2.41)).

²One of the main reasons for this choice was that, at the time of that decision, the tradeoff between doing the algebra (appendices B and C) and learning to use the GROVER API seemed to favour the former. Also, I felt that actually looking at the ARTE tables and doing the calculations would be important.

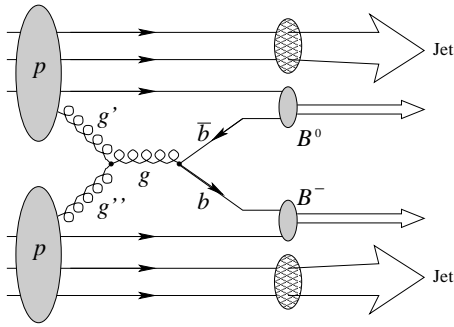


Figure 4.1. In gluon-fusion events (4.1), a gluon pair g', g'' from each parton in a proton–nucleon collision creates a $b\bar{b}$ pair, which may hadronize as a B^0-B^- pair (or the flavour-symmetric pair \bar{B}^0-B^+). At HERA-B CMS energy, one possible decay channel for the B^0 is the “golden decay” (see figure 1.1). The remaining partons produce hadron jets.

4.1 Reconstruction and selection of Monte Carlo B^0 “golden decay” events

4.1.1 Description of the event sample

The directory `/acs/mc4/p30520/d02.1205/w00001000/gen/run05_00052/` of the HERA-B directory tree at DESY contains 1000 DST files with Monte Carlo events

$$gg \rightarrow b\bar{b} \rightarrow J/\psi(\mu^+\mu^-) + \text{anything} , \quad (4.1)$$

from simulated proton–carbon (inner II wire) collisions. The geometry version used for HBGEAN is the standard version of December 5th, 2002. Since no information about event hierarchy was kept in the DST files, the work sample consist on DST files numbered 0001 through 0100 in that directory, corresponding to $\approx 51 \times 10^3$ Monte Carlo events of type (4.1). The event reconstruction was done under the ARTE-04-01-r4 version, with the settings of the KUIP macro listed in appendix D.1.

The histogram in figure 4.6 illustrates the fraction of charged tracks (electrons, muons, pions, kaons and protons) reconstructed by ARTE. Low-momentum tracks ($p < 0.3\text{GeV}$) are not reconstructed because it would increase the fraction of ghost (fake) tracks. For muons the cutoff momentum is at 5GeV, since they are strongly stopped by the Muon detector’s iron absorbers below that energy due to the reduced punch-through probability at low momentum [108]. The histograms in figures 4.2 and 4.3 show the distribution of primary vertex longitudinal coordinates around the target region and the relation of the longitudinal coordinates to the vertices’ Kalman χ^2 probabilities. Roughly half of the RVERs fall inside the target wire (longitudinal) boundary. The figure shows that good-quality vertices accumulate near the target wire boundary.

Three significant quantities discussed in the next sections are the transverse momentum $p_T \equiv \vec{z} \cdot \vec{e}_z$ of reconstructed tracks, how close one the pass to another track or vertex (distance of closest approach) and the longitudinal coordinate for the point of closest approach. These quantities can be used to reject the tracks that are manifestly unfit to reconstruct e.g. a $J/\psi \rightarrow \mu\mu$

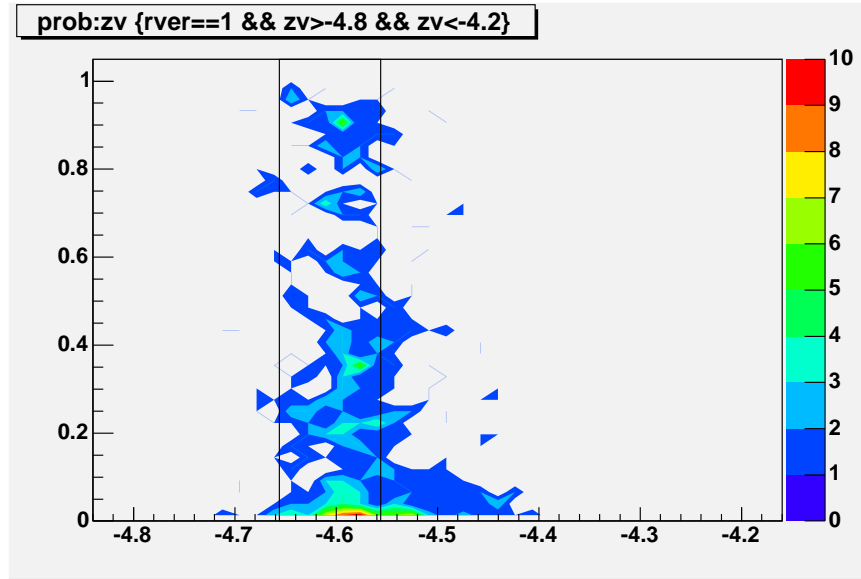


Figure 4.2. Contour histogram of Kalman χ^2 probability (vertical axis; see text) versus longitudinal coordinate of RVERs in DST 22 (horizontal axis). The good quality tracks (high probability) accumulate within the wire boundary (vertical lines) whereas low-quality tracks spread outside the boundaries.

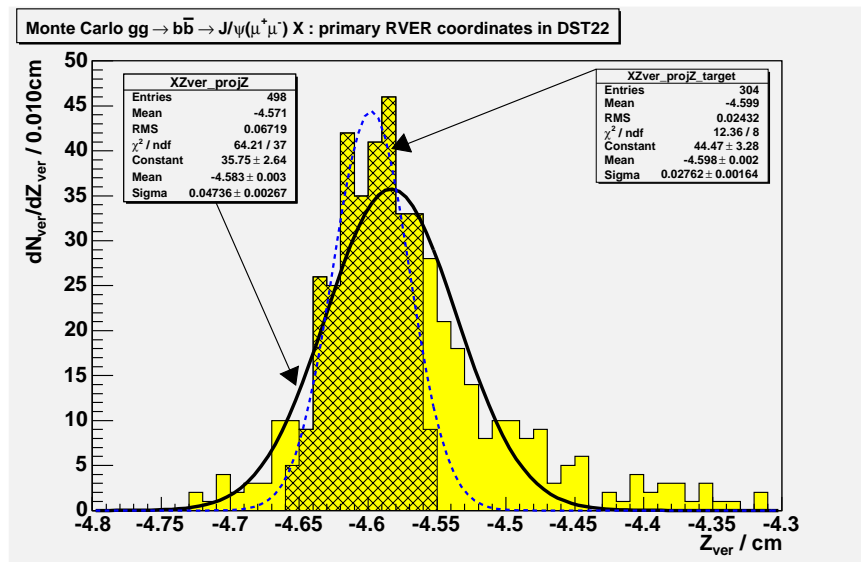


Figure 4.3. The fraction of primary vertices (DST 22) falling within the target wire longitudinal boundaries is at the 60% level. Gaussian fits are shown for the primary vertex entries (thick continuous line) and the vertices within the target wire's Z boundaries (dashed line).

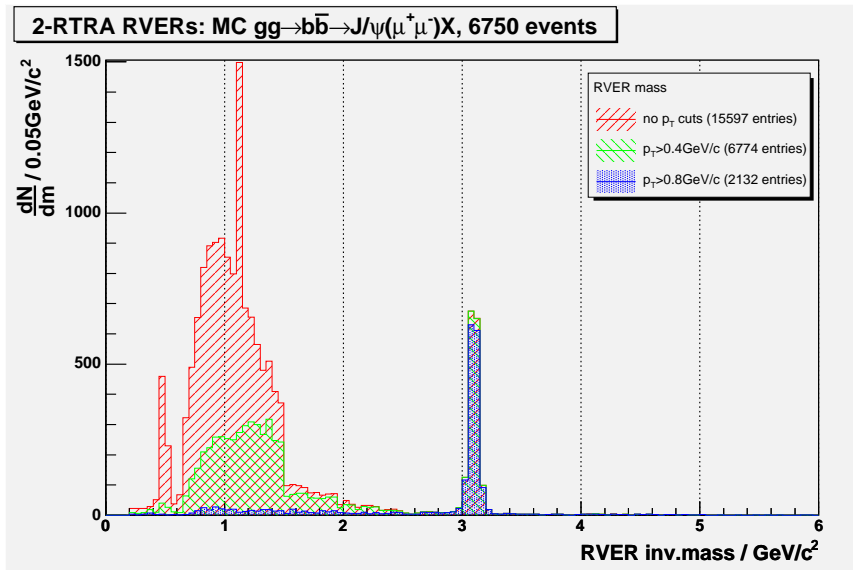


Figure 4.4. Effect of the rejection of low- p_T RTRAs on the invariant mass of RVERs built from two tracks (run 20838, with 6750 events, see text). The K^0 mass signal vanishes for $p_T > 0.4 \text{ GeV}/c$. The mass signal at the J/ψ mass ($3.1 \text{ GeV}/c^2$) was searched in MC $gg \rightarrow b\bar{b} \rightarrow J/\psi(ee)X$ events, but not found.

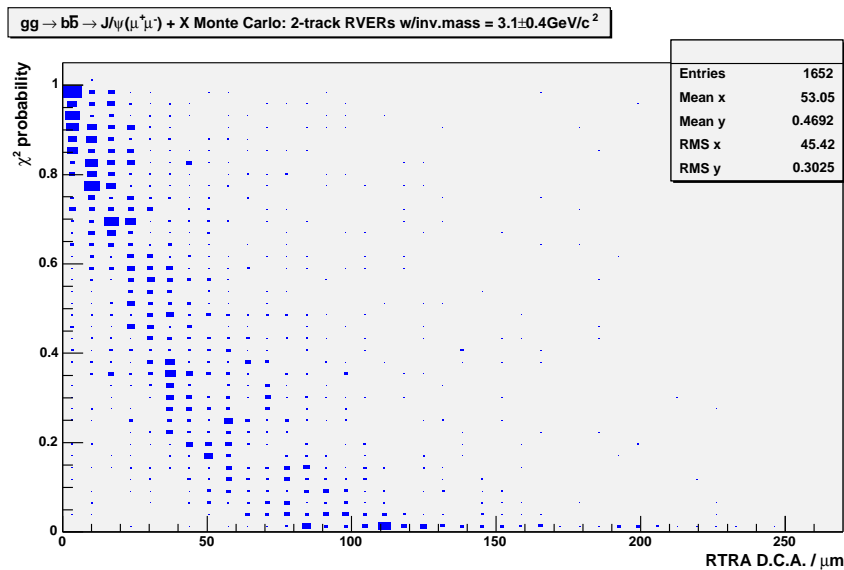


Figure 4.5. Kalman χ^2 probability for 2-track RVERs (obtained from ARTE) versus the distance of closest approach between the two RTRAs, for an invariant mass range of $3.1 \pm 0.4 \text{ GeV}/c^2$ of the RVER.

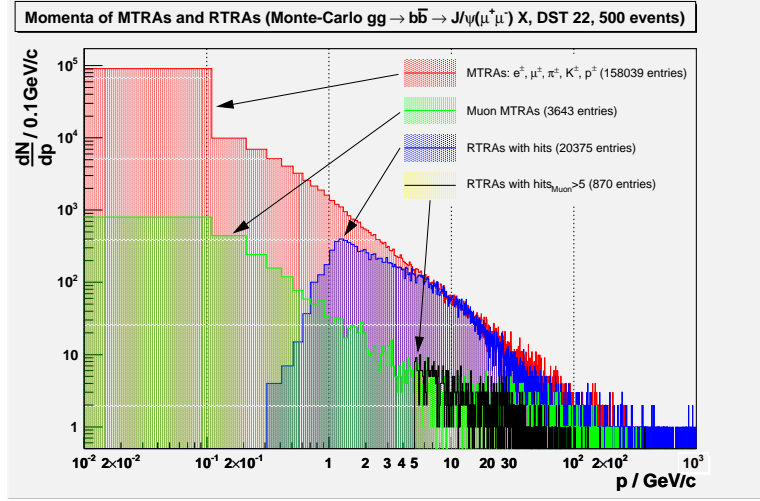


Figure 4.6. Momentum distribution of Monte Carlo charged tracks (MTRAs, red) and reconstructed tracks (RTRAs, blue). The MTRA and RTRA momentum histograms meet at $8\text{GeV} - 9\text{GeV}$. No RTRAs are built for $p < 0.3\text{GeV}/c$, which excludes $\sim 68\%$ of MTRAs; $\sim 0.57\%$ of RTRAs have $p \geq 920\text{GeV}/c$.

decay. It is quite visible in figure 4.4 that rejecting tracks with transverse momenta below $0.7\text{GeV}/c$ strongly clears out the background of track pairs outside of the J/ψ mass region without significant impact on the signal amplitude. Other selection cuts may be applied with the transverse momentum cut to further improve the J/ψ signal. On the other hand, figure 4.5 shows that two-track RVERs with invariant mass $3.1 \pm 0.4\text{GeV}/c^2$ with low Kalman χ^2 probability tend to be separated by distances over $100\mu\text{m} - 150\mu\text{m}$.

4.1.2 Selection of Monte Carlo golden decay events

The fractions of events that pass selection criteria (“cuts”) of differing stringency are listed in table 4.1. Out of the 586 Monte Carlo golden decays contained in the sample, 415 events were found to be suitable for the reconstruction of the K_S^0 vertex due to its $\pi^+\pi^-$ final state.

The Monte Carlo population of B^{neutr} (either B^0 or \bar{B}^0) golden decays with final state $\mu^+\mu^-\pi^+\pi^-$ was chosen due to the fact that neutral particles — such as those from the $K_S^0 \rightarrow \pi^0\pi^0$ decay mode — do not usually³ generate RTRAs; therefore, the $\mu^+\mu^-\pi^+\pi^-$ final state allows the reconstruction and search of the J/ψ and K_S^0 vertices. The choice of the exclusive $J/\psi \rightarrow \mu^+\mu^-$ di-muon decay mode — therefore rejecting the di-electron mode $J/\psi \rightarrow e^+e^-$ — was due to the fact that the muons are less subject to bremsstrahlung radiation losses. Therefore, the μ^+ and μ^- track recon-

³The exceptions are secondary particles produced in collisions of the neutral particles with detector material.

struction is “cleaner”, i.e. finding bremsstrahlung photons becomes of little concern in face of the di-electron decay mode. The vast majority of decay modes of the K_S^0 produce the pairs $\pi^+\pi^-$ and $\pi^0\pi^0$; other decay modes are not as significant, the sum of their branching ratios is $\approx 2.5 \times 10^{-3}$ [81].

Table 4.1 also shows the number of events surviving progressively stringent cuts applied to charged RTRAs. The association between Monte Carlo and reconstructed tracks (MTRAs and RTRAs) is done by ARTE. For the event sample used in this analysis it was further required that each golden decay MTRA is associated to a single RTRA. Though these cuts eliminated most events, they assure that a sample of superior quality is obtained: for example, requiring that a RTRA have hits in the VDS and Main Tracker allows a good quality measurement of its momentum.

In the Monte Carlo $B_d^{\text{neutr}} \rightarrow J/\psi(\mu^+\mu^-)K_S^0(\pi^+\pi^-)$ sample, 7 events survived the cuts described by items 12. and 13. of table 4.1, namely: the final state $\mu^+\mu^-\pi^+\pi^-$ from the B^{neutr} decay must have hits on the VDS, ITR/OTR and (for both μ^\pm) MUON detectors, without requirements as to the existence of a RTRA matched with a tagging particle from the second beauty hadron. Because the tagging charged leptons/kaons are less common than pions (see figure 4.7), they make for a better discriminator than pions for identifying the B^{neutr} flavour in the golden decay [108]. The tagging particle’s charge indicates the charge of the accompanying B meson — it is a B^\pm for a ℓ^\pm or K^\pm (or a π^\pm) from its decays.⁴ Identifying the charge of the second B meson directly gives the flavour of the B in the golden decay; see figure 4.1. An adequate choice of cuts of impact parameter and transverse momentum cuts for the tagging particle must also be used to discriminate the tagging particles from the background reactions that originate from outside the interaction (primary) vertex; the “good” tagging tracks should preferentially be those with small impact parameter and large transverse momentum.

In the 02.1205 geometry version used to reconstruct these events, the target wire is the inner II wire (carbon) situated at station II, which is aligned parallel to the yy axis. The target wire’s corners are at coordinates $(z, x, y) = (-4.606 \pm 0.050, 0.366 \pm 0.010, -0.057 \pm 4.200)\text{cm}$.

4.2 Validation of selected Monte Carlo events

The events listed in table 4.2 constitute the sample of Monte Carlo events which satisfy enough conditions to allow a good reconstruction of the J/ψ and K_S^0 vertices. Only RTRAs associated by ARTE with the golden decay MTRAs were selected; therefore, fortuitous combinations of RTRAs which

⁴It is assumed that the second beauty quark hadronizes as a charged B meson. The fraction of B mesons produced in a b quark hadronization further limits the charge tagging efficiency.

MC processes / cuts on RTRAs	Events
MC events, $gg \rightarrow b\bar{b} \rightarrow J/\psi(\mu^+\mu^-) + \text{anything}$	51089
$B^{\text{neutr}} \rightarrow J/\psi(\mu^+\mu^-) + K^{\text{neutr}}(\text{anything})$	1301
i. $B^{\text{neutr}} \rightarrow J/\psi(\mu^+\mu^-) + K^{\text{neutr}}(\pi^0\pi^0)$	171
ii. $B^{\text{neutr}} \rightarrow J/\psi(\mu^+\mu^-) + K^{\text{neutr}}(\pi^+\pi^-)$	415
$\mu^+\mu^-\pi^+\pi^-$ RTRAs from MC golden decay	
with > 1 hits on VDS	
1. either μ^\pm	329
2. either π^\pm	112
3. both μ^\pm	171
4. both π^\pm	80
with > 1 hits on ITR/OTR	
5. either μ^\pm	286
6. either π^\pm	229
7. both μ^\pm	119
8. both π^\pm	124
with > 1 hits on MUON detector (for μ^\pm)	
9. either μ^\pm	264
10. both μ^\pm	94
with > 1 hits on VDS, ITR/OTR, and (for μ^\pm) MUON	
11. with or without flavour tag RTRA	7
12. with ℓ^\pm lepton RTRA from tagging B	0
13. with K^\pm kaon RTRA from tagging B	0
14. with π^\pm pion RTRA from tagging B	2

Table 4.1. Number of Monte Carlo $gg \rightarrow b\bar{b} \rightarrow J/\psi(\mu^+\mu^-) + \text{anything}$ events surviving different cuts; the K^{neutr} is either K^0 or \bar{K}^0 . For items 1.-14., the counted RTRAs are associated to a single MTRAs by ARTE.

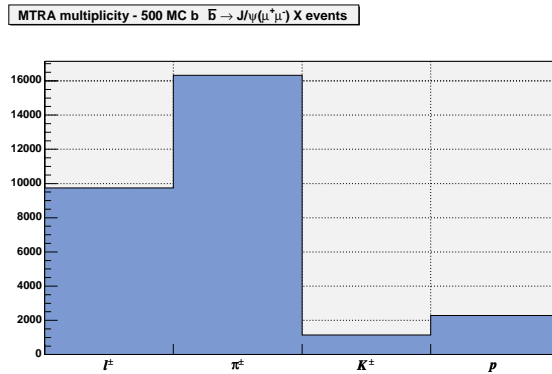


Figure 4.7. Number of long-lived charged MTRAs in a 500-event Monte Carlo sample, from DST file `run05_00055_0022.dst` for $gg \rightarrow b\bar{b} \rightarrow J/\psi(\mu^+\mu^-) + X$ events (see text).

<i>DST</i>	<i>Event</i>	<i>B^{neutr} flavour</i>	<i>Second b hadron</i>	<i>Charged tag MTRA</i>	<i>Has tagging RTRA ?</i>
0013	131	B^0	B^-	No tag	—
0022	267	B^0	\bar{B}^0	π^-	No
0028	233	\bar{B}^0	B^+	No tag	—
0044	174	B^0	\bar{B}^0	τ^-	No
0053	235	\bar{B}^0	B^+	π^+	Yes
0076	24	B^0	Λ_b^0	π^-	Yes
0081	124	\bar{B}^0	B^0	No tag	—

Table 4.2. Summary description of the Monte Carlo golden decay sample, with all particles from state $\mu^+\mu^-\pi^+\pi^-$ with good RTRAs (see item 11. of table 4.1). The numbers *nnnn* in the “DST” column pertain to the DST files *run05_00052_nnnn.dst*. When available, the correct charge MC tagging particle is indicated (e.g. $B^\pm \rightarrow \ell^\pm X$), and whether it has a corresponding RTRA.

would yield the J/ψ and K^{neutr} masses were not considered in this analysis. The events are hereon labeled by their event number, indicated in table 4.2. To identify the neutral B flavour it is necessary to recognize the presence of a tagging particle, originating from the tagging beauty hadron decay. The two sample events that have a RTRA identified with a Monte Carlo charged tag particle were studied in detail: event 235 has a golden decay of a \bar{B}^0 , and event 24 has a golden decay of a B^0 .

The calculations of invariant mass of pairs of RTRAs, minimum separation between pairs of RTRAs and impact parameter of RTRAs to the RVERs, as well as of their standard deviations, were done with routines written in C (see equations in appendix C). The ASCII output of these routines allows their importation into a spreadsheet program for detailed inspection, as well as calculation of the invariant mass of selected sets RTRAs. The plots of these quantities were done in ROOT [37] by reading and parsing the ASCII output.

ARTE identified the $\mu^+\mu^-\pi^+\pi^-$ state from the golden decays in table 4.2 with one (or more) RTRA for each MTRA in that state. The “correct” RTRA was chosen by requiring, consecutively: the highest number of hits in the Muon detector (for muons), in the VDS and in the Main Tracker; and (if those numbers are equal for the candidates) the highest probability calculated by ARTE through Kalman filter RTRA reconstruction. The events 235 and 24 of the Monte Carlo sample were studied in detail, as they have one RTRA associated with a charged tagging track, which allows *a priori* to identify the neutral B flavour. The remainder of the selection in table 4.2 was also studied; in their case, the choice of tagging particles was investigated and compared with the events’ Monte Carlo truth.

The selected events' validation was conducted by searching indicators of golden decays through in the reconstructed tracks and vertices. Checks were done on the following quantities:

1. The invariant mass of RTRA sets: the $\mu^+\mu^-$ and $\pi^+\pi^-$ RTRA pairs; the $\mu^+\mu^-\pi^+\pi^-$; and the RTRAs used by ARTE for the primary vertex reconstruction. The invariant masses of the RTRA sets, other than those from the $\mu^+\mu^-\pi^+\pi^-$ set, were also calculated.
2. The distance of closest approach of RTRA pairs $\mu^+\mu^-$ and $\pi^+\pi^-$, and the impact parameter of those pairs to the primary, J/ψ and K_S^0 vertices.
3. RVER longitudinal (z coordinate) separations, as well as of for the separation between the vertices defined by $\mu^+\mu^-$ and $\mu^+\mu^-\pi^+\pi^-$.

The calculation of the errors quoted for the invariant masses and impact parameters were done using the RTRAs' and RVERs' covariance matrices; see appendix C. For sets of two or more RTRA pairs with invariant masses m_i , the error on the set's invariant mass M (see equation B.25) was calculated with

$$\sigma_M^2 = \frac{1}{M^2} \sum_i m_i^2 \sigma_i^2 \quad (4.2)$$

(this expression assumes the masses m_i of RTRA pairs are uncorrelated). This gives better results for calculating e.g. the mass of the B^{neutr} meson compared to calculating it from the reconstructed J/ψ and K_S , which would introduce systematic errors.

The following subsections describe a detailed analysis of two of the seven reconstructed events in table 4.2, to illustrate how the events can be interpreted and validated as golden decays. The remainder of the Monte Carlo selection is next presented for comparison. Subsection 4.2.3 presents histograms of all of the 7 events in the Monte-Carlo sample.

The Ring Search algorithm for RICH Particle Identification (PID) calculates the likelihoods for five hypotheses — electrons, muons, pions, kaons and protons. However, the low mass of the first two make their discrimination very difficult, see (3.7). Therefore, in HERA- B the RICH system is used to distinguish kaons from protons. The PID hypotheses were obtained from the RICH likelihood information for each RTRA and was used to identify pions, kaons and protons. This information was used to correct and improve the invariant masses for the J/ψ , K^{neutr} and B^{neutr} searches.

4.2.1 Event 235

The event 235 of the DST file `run05_00052_0053.dst` was studied. The Monte Carlo truth of the event reveals that the B^+ meson decays as

$$B^+ \rightarrow \pi^+ f_2^0(\pi^0\pi^0) \gamma \bar{D}^0(\pi^0\pi^+\pi^- K_L^0); \quad (4.3)$$

see table 4.3 for a summary of the Monte Carlo truth on the B mesons' decays. The γ and the \bar{D}^0 resulted from the decay $\bar{D}^{*0} \rightarrow \gamma\bar{D}^0$. The K_L^0 produced an elaborate hadronic shower. Each π^0 meson decays produced electromagnetic showers, $\pi^0 \rightarrow \gamma\gamma \rightarrow \text{shower}$. Intermediate states and further decays are omitted for simplicity. Figures 4.8 through 4.15 show some PRISM displays for this event. The Monte Carlo tracks (red) and Reconstructed Tracks (blue) are shown for comparison between the simulation and event reconstruction by ARTE.

ARTE-reconstructed vertices. 19 vertices were reconstructed by ARTE for this event. 9 RVERs were reconstructed with a mass in the K^0 region, all with the same coordinates and mass value; however the error evaluation was unsuccessful. The longitudinal coordinate z , masses, number of tracks, χ^2 and probability are shown in table 4.4 for the relevant vertices.

Momenta, transverse momenta and number of hits for RTRAs. The event was reconstructed by ARTE, which produced 61 RTRAs of which 43 were reconstructed as charged tracks and the remaining as reconstructed resonances. The momenta and transverse momenta p_T of the RTRAs associated to the golden decay were measured with errors, respectively, at the percent level (these RTRAs were required to have hits on the VDS and ITR/OTR) and below $0.005\text{GeV}/c$. Table 4.5 shows those quantities for those RTRAs along with the number of detector hits and Kalman χ^2 probability, and table 4.6 shows the momenta and p_T for relevant combinations of those RTRAs (dimuon, dipion and $\mu\mu\pi\pi$).

Invariant masses. The dimuon, dipion and $\mu\mu\pi\pi$ masses were computed with RTRA table information from the ARTE tables for this event. The masses of the dimuon and dipion are essentially equal to those from the RVER table for the event; however, the $\mu\mu\pi\pi$ mass is different from the RVER 1 mass.

The invariant masses of the $\mu^+\mu^-$, $\pi^+\pi^-$ and $\mu^+\mu^-\pi^+\pi^-$ were compared to the masses of the J/ψ , neutral K and neutral B mesons — which are $3.097\text{GeV}/c^2$, $0.498\text{GeV}/c^2$ and $5.279\text{GeV}/c^2$ respectively [81]. The invariant mass of the RTRAs associated with MTRAs from the tagging b -hadron was also calculated; two cases were studied, one where a PID was used for the RTRAs' masses, and the other where no RTRA PID was used.

The invariant masses of the pairs (assuming the massless particles approximation (C.4)) were calculated with (B.25), and (C.5) for the error. The obtained values were $M_0(\mu^+\mu^-) = 3.171 \pm 0.029\text{GeV}/c^2$ for the dimuon pair and $M_0(\pi^+\pi^-) = 0.409 \pm 0.004\text{GeV}/c^2$ for the dipion pair. This yields a dimuon invariant mass equal to the J/ψ 's within less than 3 standard deviations, and the dipion within 24 standard deviations of the K^0 mass. The invariant mass of the (massless) 4-set is $M_0(\mu^+\mu^-\pi^+\pi^-) = 5.325 \pm 0.025\text{GeV}/c^2$, which is equal to the B^0 mass within less than two standard

MTRA	\bar{B}^0	J/ψ	μ^+	μ^-	K_S^0	π^+	π^-
p	79.359	65.263	24.297	41.040	14.189	6.247	7.948
p_T	1.231	1.147	1.356	1.927	1.619	0.847	0.806
z	-4.5970	-4.4352	-4.4352	-4.4352	-4.4352	6.1381	6.1381
Length	0.1618	(prompt)	2186	2186	10.64	1351	1512

MTRA	B^+	π^+	γ	\bar{D}^0	π^0	π^+	π^-	K_L^0
p	245.23	27.669	18.479	127.15	12.516	22.811	30.154	61.683
p_T	2.251	0.670	0.336	1.887	0.324	0.713	0.482	0.784
z	-4.5970	210.4	1183	0.09548	0.0	1342	1508	1324
Length	5.235	0.63773	0.63773	0.63773	0.7332	0.7332	0.7332	0.7332

Table 4.3. Summary of the Monte Carlo truth for the \bar{B}^0 decay (top) and tagging B^+ meson (bottom) of event 235; see also the figures 4.9 and 4.13. Units: GeV/c (momentum p and transverse momentum p_T), cm (z coordinate of the MTRA's start), cm (MTRA length). The J/ψ decays promptly. The decay stages of the B^+ meson (see figure 4.13) are separated by double vertical separators $\|$. All quantities are measured in the laboratory frame.

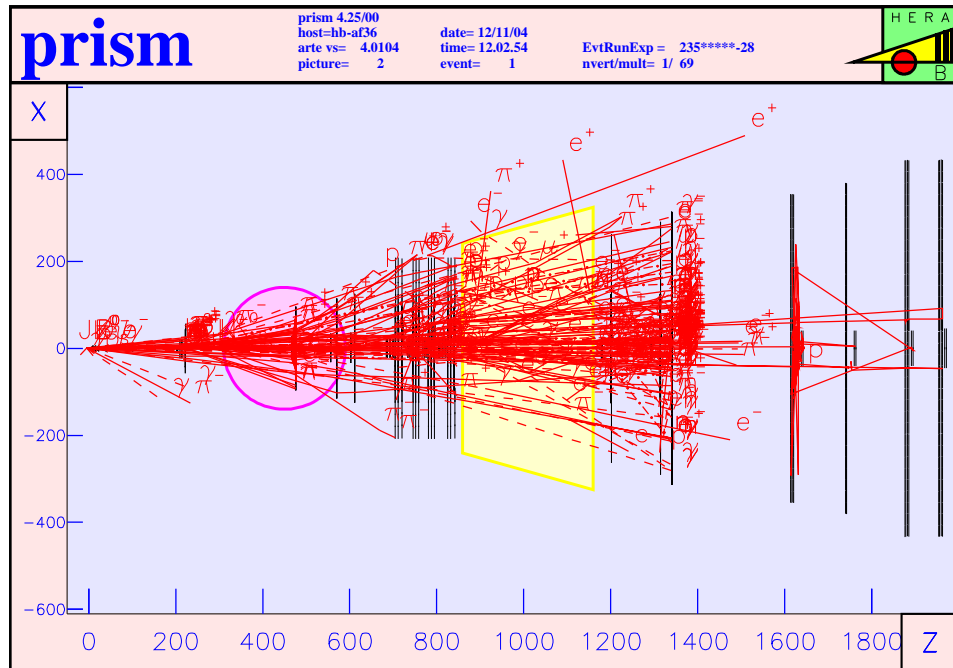


Figure 4.8. PRISM representation of the event 235 in the zx plane. All of the 676 MTRAs from the $b\bar{b}$ hadron shower and spectator event are shown — charged particles (continuous lines), photons (dashed), and other neutral (dotted).

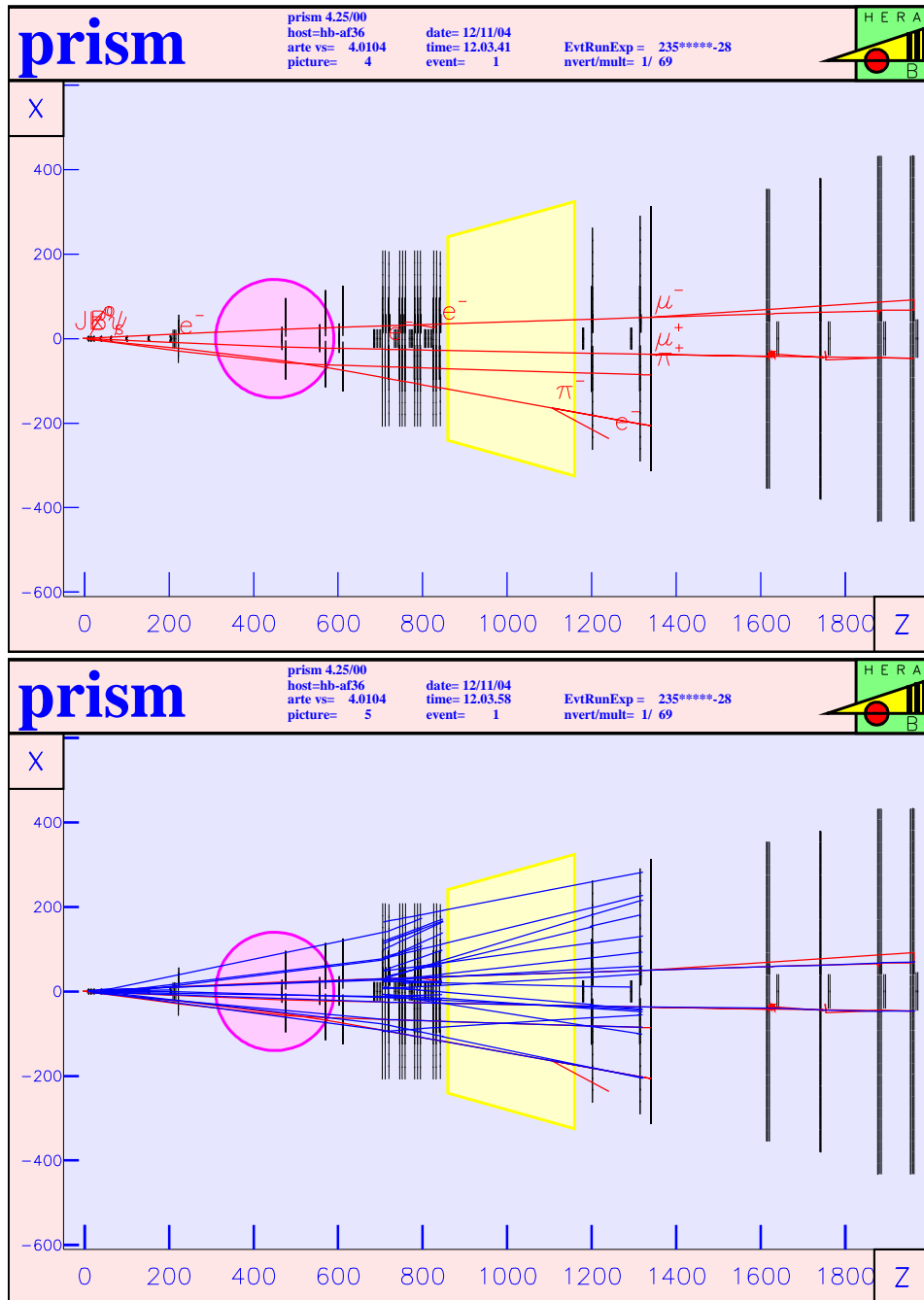


Figure 4.9. PRISM representation of the event 235 in the xz plane. Top: B^0 golden decay MTRAs. The dotted V track at the RICH is a backscattered $p \simeq 0.2\text{GeV}$ neutron. Bottom: superimposition of B^0 MTRAs and all event's RTRAs. Most RTRAs are not drawn beyond the ECAL plane, since most particles are scatter and decay at the iron absorber blocks in front of the Muon detector (not shown).

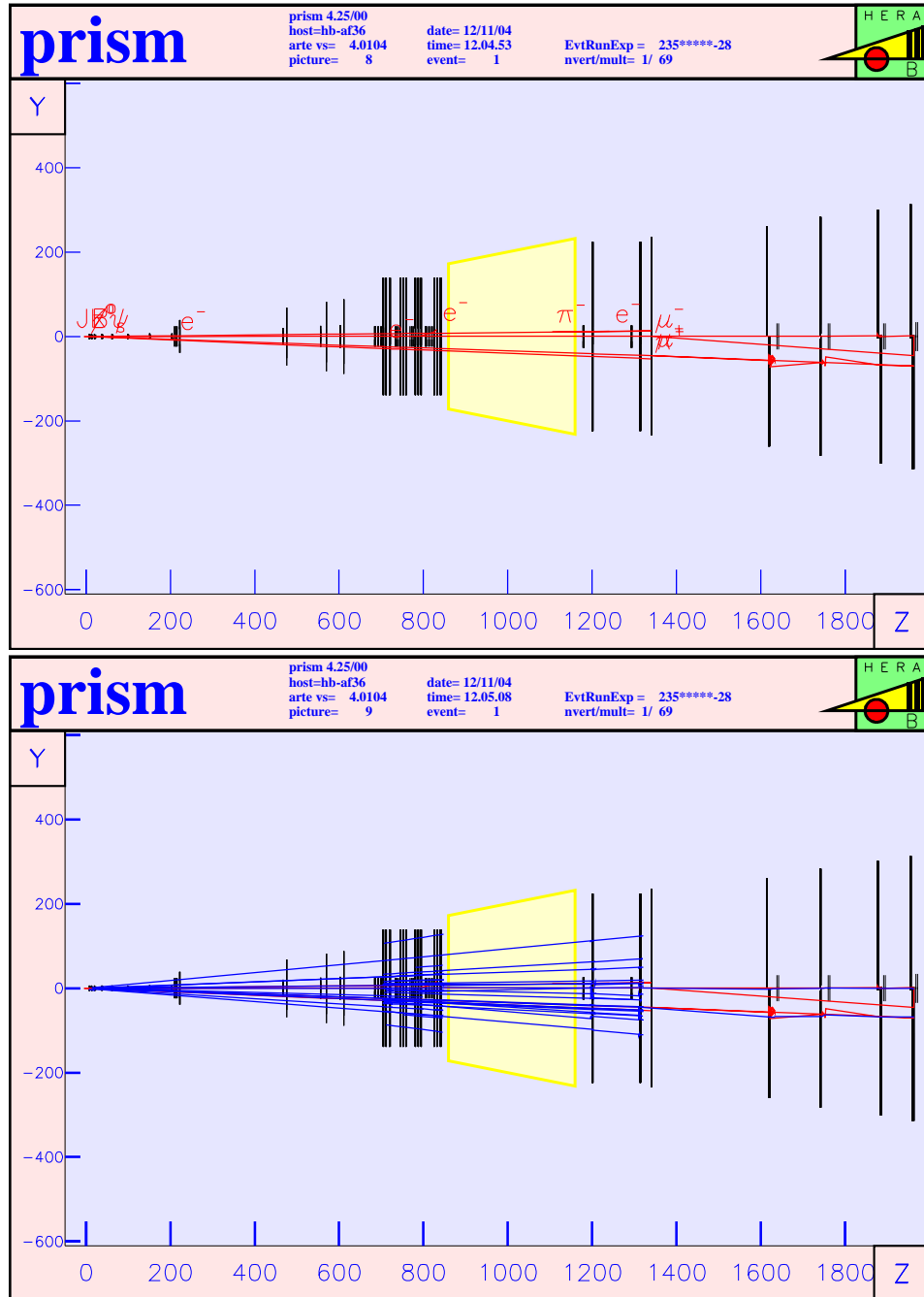


Figure 4.10. Same as figure 4.9, but on the zy plane.

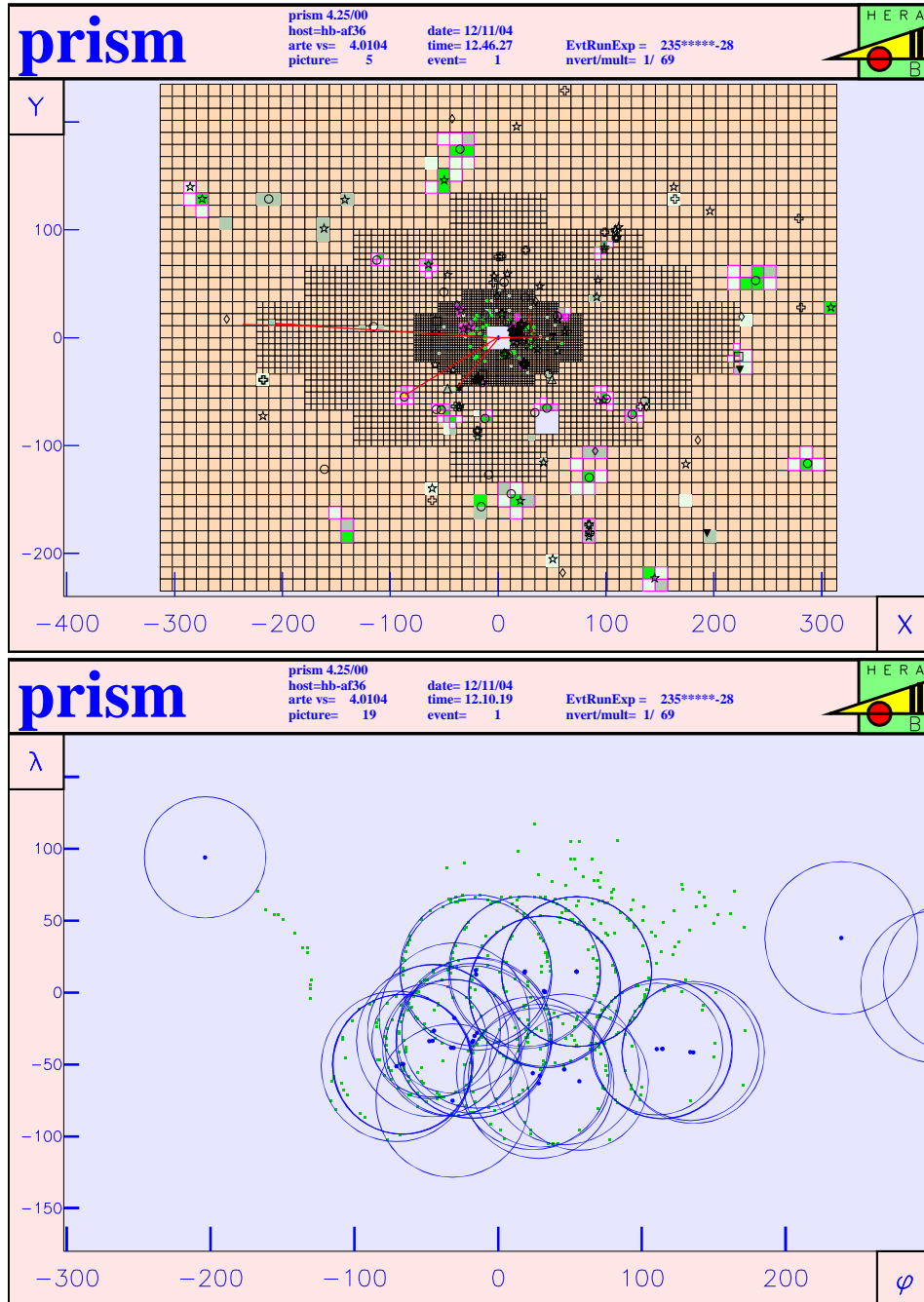


Figure 4.11. Top: reconstructed ECAL clusters (RCCLs) for Monte Carlo event 235. The Monte Carlo Impact Points (MIMPs) are omitted for clarity. The MTRAs originate from the B^0 golden decay. Bottom: representation of RICH hits (green) and reconstructed rings (blue). The (φ, λ) coordinates represent the angle (in milliradians) relative to the target region, in the zx and zy planes respectively.

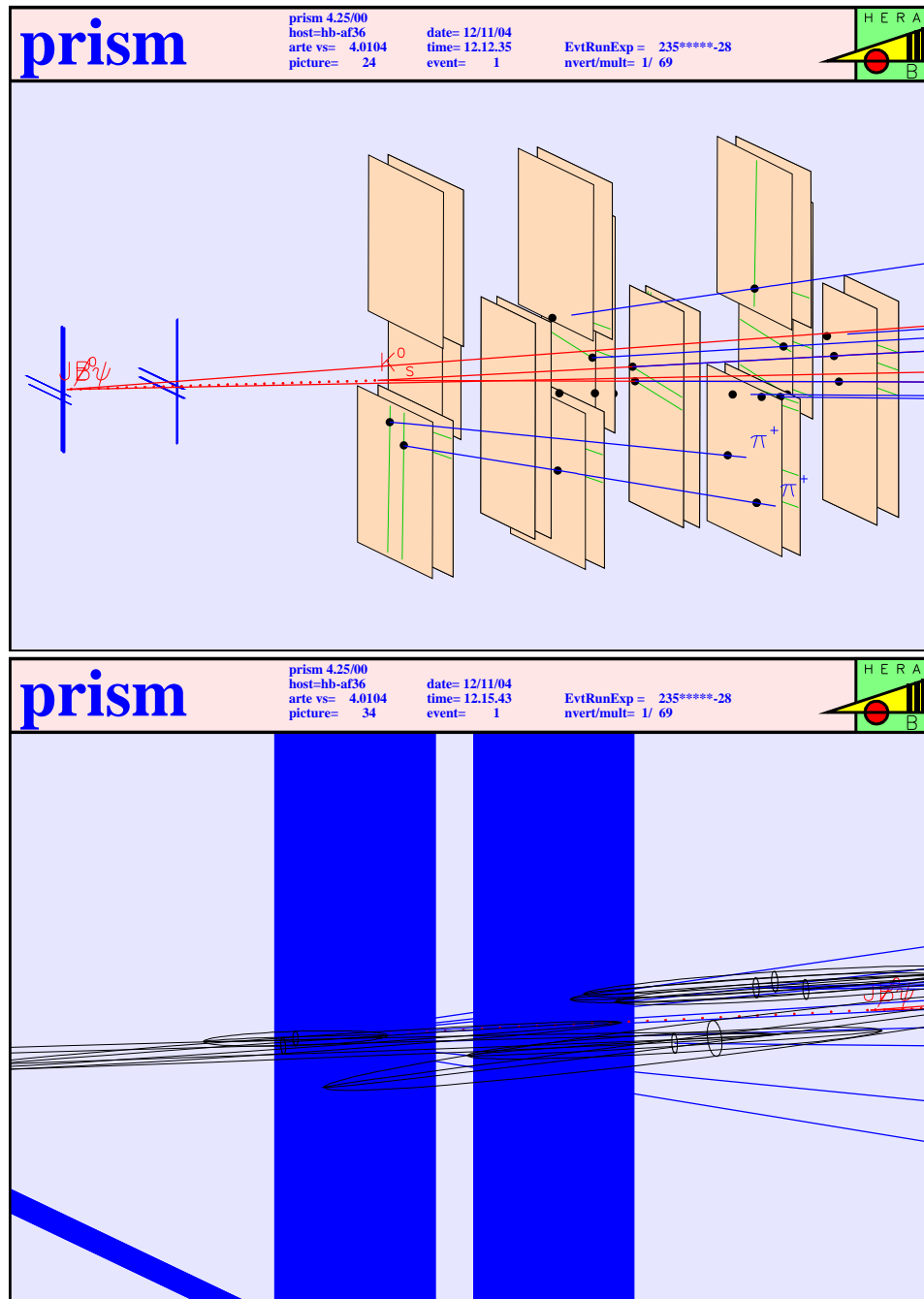


Figure 4.12. PRISM 3D views of the golden decay MTRAs and the four RVERs found by ARTE in this event. The RVERs have their RTRAs extended to them. Top: the target and first three VDS superlayers are shown. MIMPs are drawn as black dots, HITBs as green segments. Bottom: magnified view of the target region. The RVERs are drawn as ellipsoids. The dotted red line represent the B^0 MTRA.

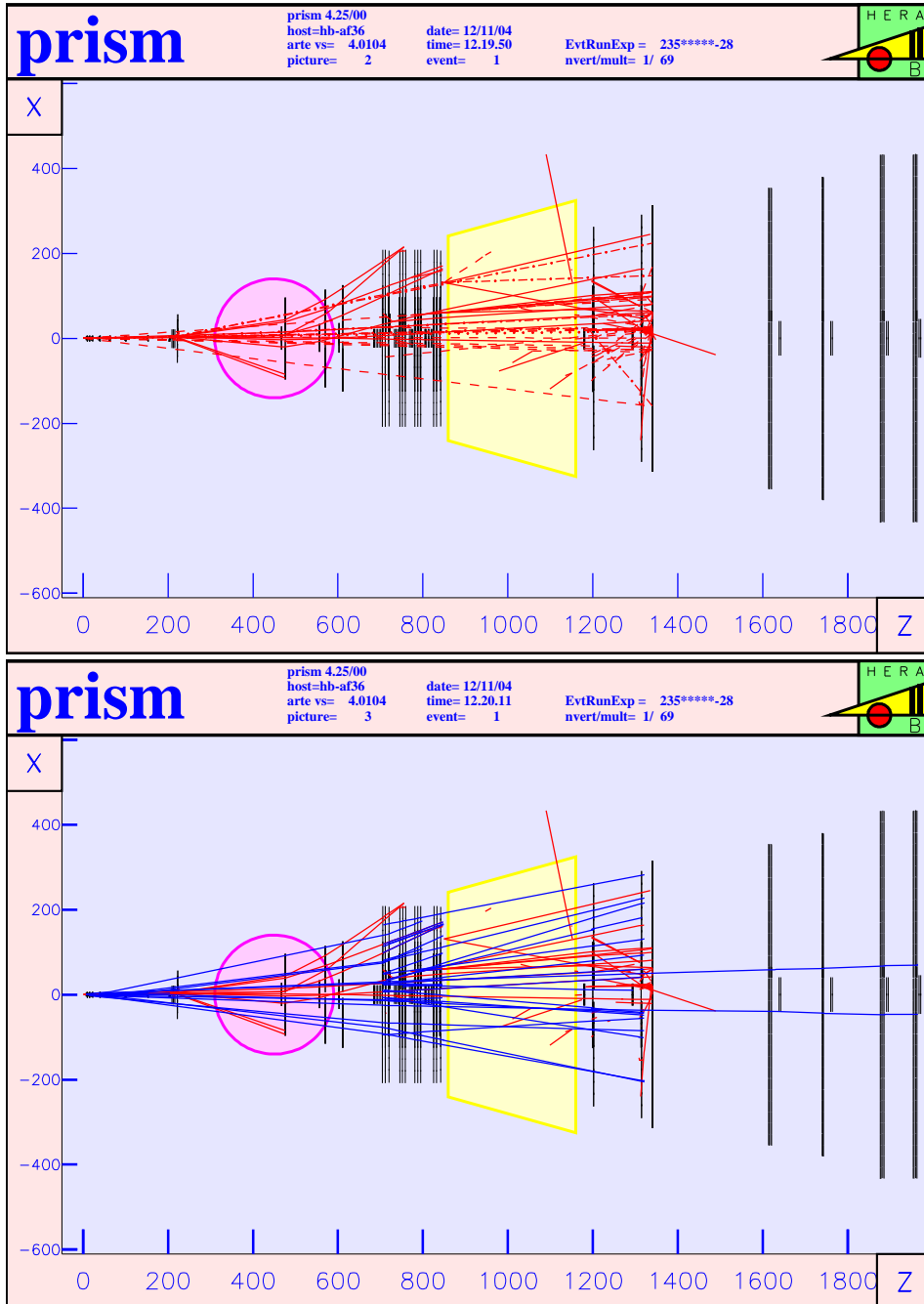


Figure 4.13. The tagging B meson decay in event 235 — PRISM representation in the xz plane. Particle name tags and MTRAs of the remainder of the event were omitted for clarity. Bottom: all the event's RTRAs are superimposed with the B decay MTRAs (neutral MTRAs were omitted).

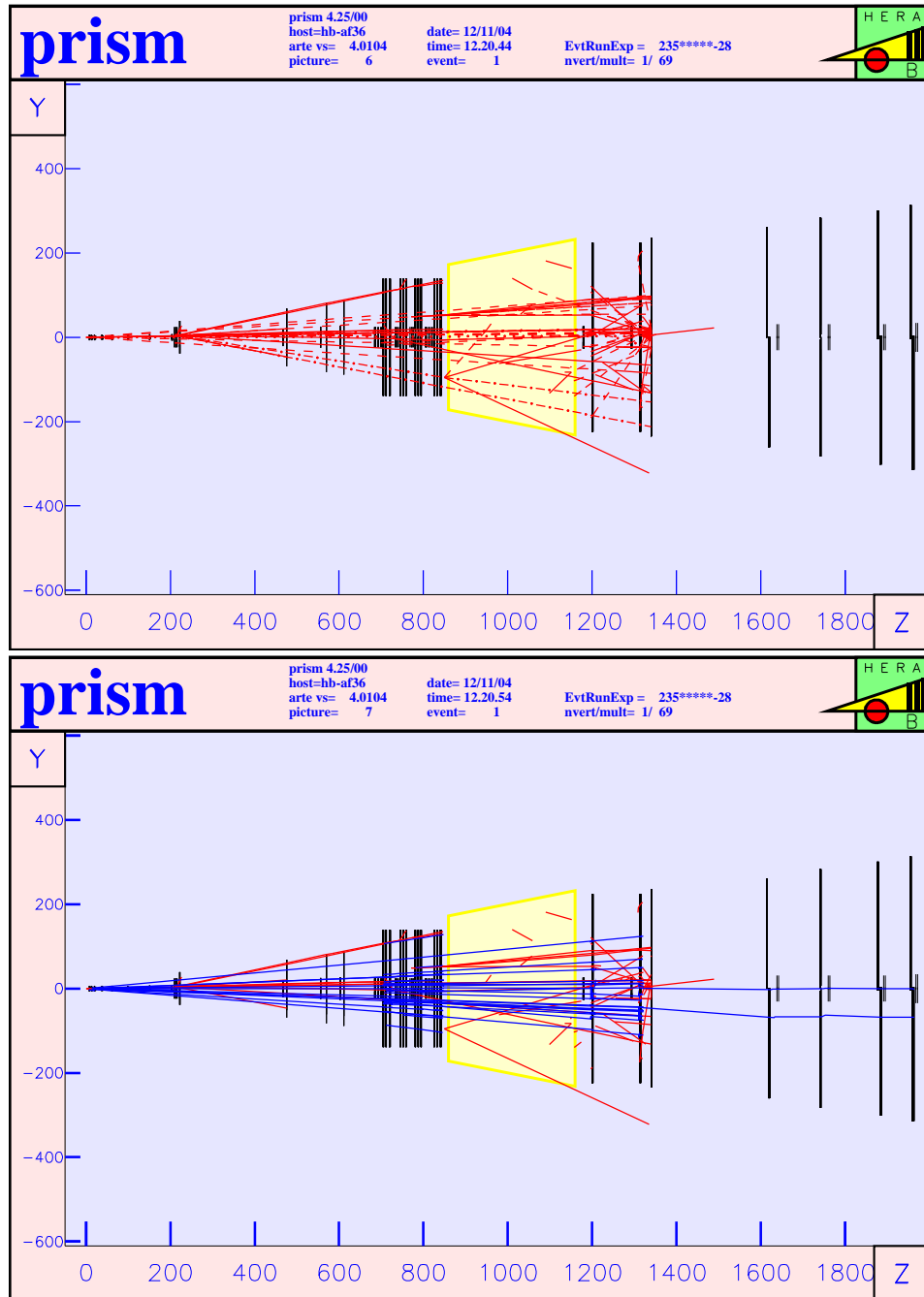


Figure 4.14. Views similar to those of figure 4.13 are shown for event 235, but this time in a projection on the zy plane.

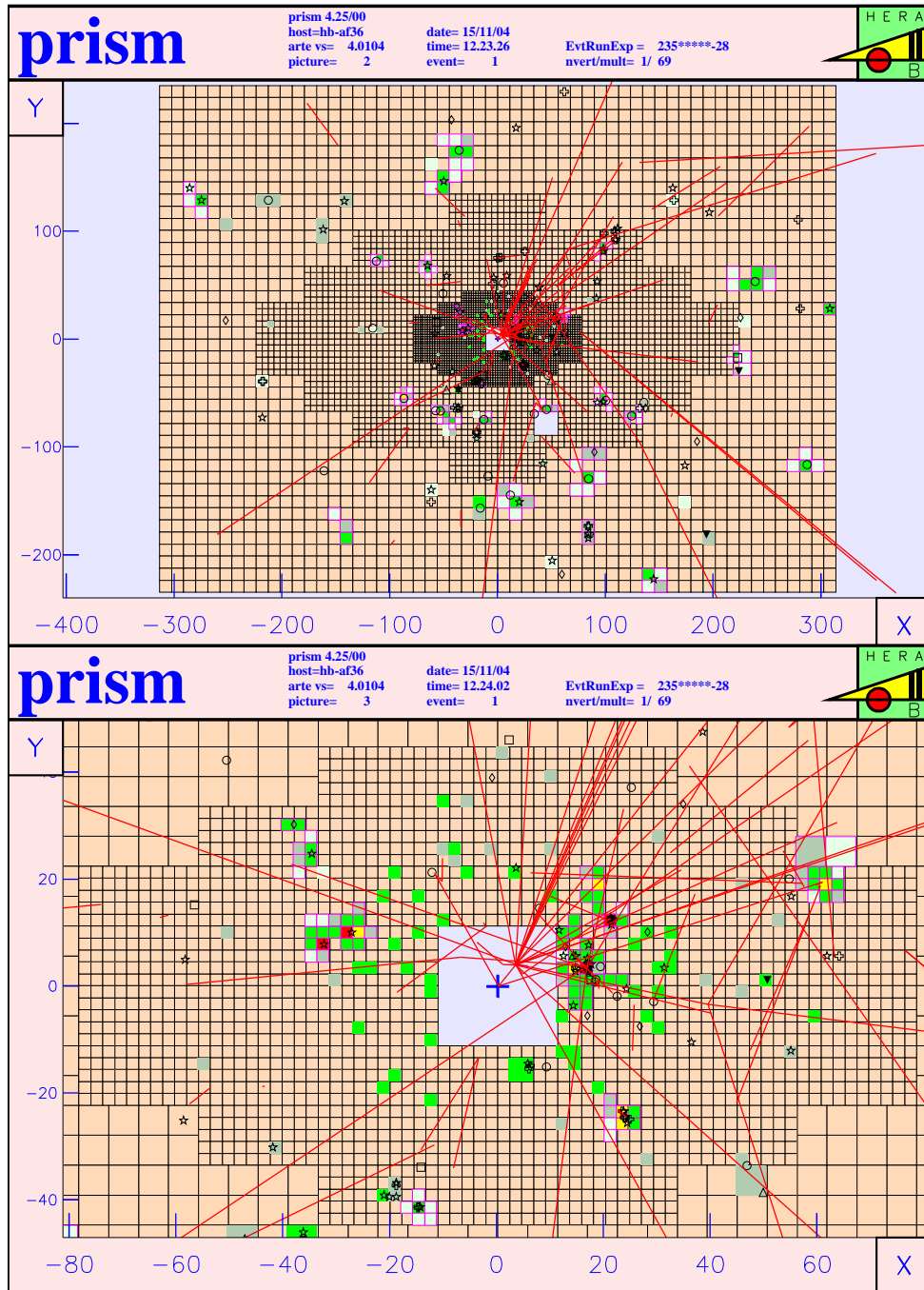


Figure 4.15. The tagging B meson decay in event 235 — PRISM representation of the ECAL. Particle name tags and neutral MTRAs were omitted for clarity. Top: the reconstructed clusters (RCCLs) are presented for comparison with the decay's Monte Carlo. Bottom: detail of the inner ECAL region.

RVER	z/cm	$M/\text{GeV}/c^2$	Num. tracks	χ^2	$\text{Pr}(\chi^2, \text{ndof})$
1	-4.625 ± 0.031	5.020 ± 0.486	12	29.292	10.7%
2	-4.241 ± 0.050	3.178 ± 0.029	2	1.803	17.9%
3	6.167 ± 0.056	0.496	2	n/a	n/a

Table 4.4. Relevant vertices in event 235; this information is presented in the ARTE tables for this reconstructed event.

PID	μ^+	μ^-	π^+	π^-	Tag
$p / \text{GeV}/c$	24.65 ± 0.29	42.26 ± 0.58	7.25 ± 0.06	7.89 ± 0.08	9.10 ± 0.08
$p_T / \text{GeV}/c$	1.39	1.99	0.86	0.81	0.69
VDS hits	12	12	11	13	13
OTR hits	37	34	38	34	27
Kalman χ^2	28.49	53.61	35.98	64.00	24.51
$\text{Pr}(\chi^2, \text{ndof})$	96.6%	9.0%	80.0%	1.6%	90.7%

Table 4.5. Momenta and transverse momenta of RTRAs relevant for the reconstruction of the golden decay in event 235. The RTRA chosen through the highest- p_T criterium is included (last column). The p_T errors are all $\leq 5\text{MeV}/c$. All shown tracks have no ITR hits. $\text{ndof} = N_{\text{VDS hits}} + N_{\text{ITR hits}} + N_{\text{OTR hits}} - 5$.

PID	$\mu^+\mu^-$	$\pi^+\pi^-$	$\mu^+\mu^-\pi^+\pi^-$
$p / \text{GeV}/c$	66.83	14.13	80.87
$p_T / \text{GeV}/c$	0.88	1.62	0.72

Table 4.6. Momenta and transverse momenta of golden decay particles reconstructed in event 235. See also tables 4.3 and 4.5.

PID	μ^+	μ^-	π^+	π^-	Tag
D.C.A.(RVER 1) / μm	213 ± 39	198 ± 34	3632 ± 54	2697 ± 43	24 ± 34
D.C.A.(RVER 2) / μm	39 ± 39	27 ± 28	3268 ± 65	2841 ± 47	291 ± 47
D.C.A.(RVER 3) / μm	7717 ± 49	17083 ± 92	17 ± 25	13 ± 22	9342 ± 53
$b_{\text{wire}}/\mu\text{m}$	48	63	1797	1054	-70

RTRA set	$\mu^+\mu^-$	$\pi^+\pi^-$	$\mu^+\mu^-\pi^+\pi^-$
z/cm	-4.241 ± 0.048	6.168 ± 0.058	-4.417 ± 0.049
$M/\text{GeV}/c^2$	3.178 ± 0.029	0.496 ± 0.003	5.373 ± 0.135
$DCA/\mu\text{m}$	66 ± 54	31 ± 25	11 ± 63
$b_{\text{wire}}/\mu\text{m}$	-48	89	3148
$b_{\text{RVER 1}}/\mu\text{m}$	94 ± 25	186 ± 38	761 ± 39

Table 4.7. Vertex longitudinal coordinates, DCAs and impact parameter to wire of golden decay relevant RTRAs (top) and RTRA sets (bottom) for event 235. All quantities were calculated with the PI tool (section E.1). The RTRA used for flavour tag is shown (see table 4.5).

Δz	Distance / cm
$\mu\mu$ to $\mu\mu\pi\pi$	$(-4.241 \pm 0.048) - (-4.417 \pm 0.049) = 0.176 \pm 0.097$
RVER 2 to RVER 1	$(-4.241 \pm 0.050) - (-4.625 \pm 0.031) = 0.384 \pm 0.081$
J/ψ to B^{neutr}	$-4.4352 - (-4.5970) = 0.1618$

Table 4.8. Longitudinal separation of the PI-reconstructed vertices, RVER and Monte Carlo truth for event 235.

deviations. By including the mass hypotheses ($m_{\mu^\pm} = 0.1057\text{GeV}/c^2$) and ($m_{\pi^\pm} = 0.1396\text{GeV}/c^2$) for the RTRAs in the dimuon and dipion sets, equations (C.8), (C.5) and (C.9) yield the corresponding values of $M_{\text{PID}}(\mu^+\mu^-) = 3.178 \pm 0.029\text{GeV}/c^2$ and $M_{\text{PID}}(\pi^+\pi^-) = 0.496 \pm 0.003\text{GeV}/c^2$ respectively. The invariant mass of the 4-set is $M_{\text{PID}}(\mu^+\mu^-\pi^+\pi^-) = 5.373 \pm 0.135\text{GeV}/c^2$. These values are, then, within $\delta_{\mu\mu} \equiv |m_{\mu\mu} - m_{J/\psi}|/\Delta m_{\mu\mu} = 2.8$, $\delta_{\pi\pi} = 0.7$ and $\delta_{\mu\mu\pi\pi} = 0.7$ standard deviations of the sought mass values, respectively.

For the second B meson in the event, the invariant mass was also measured using the knowledge of the RTRA–MTRA table associations filled by ARTE, yielding $M_{B^\pm} = 5.070 \pm 3.231\text{GeV}/c^2$ (particle masses hypotheses were disregarded). The main contribution to the very high invariant mass error associated to these tracks originates from poor momentum estimations: only one of the six tracks used for the calculation had hits before *and* after the magnet.

The primary vertex position was reconstructed by ARTE using 12 RTRAs (of the 61 listed in the event), of which 9 have hits on the VDS and Main Tracker and the remaining with hits solely on the VDS; none of those RTRAs included the ones from the $\mu^+\mu^-\pi^+\pi^-$ 4-set. The vertex's mass was found by ARTE to be $5.020 \pm 0.486\text{GeV}/c^2$. It was also calculated with (B.25) and found to be $4.440 \pm 12.824\text{GeV}/c^2$ when using the 12 RTRAs, and $3.286 \pm 0.019\text{GeV}/c^2$ when using only the primary vertex RTRAs with hits on both VDS and Main Tracker. Using these nine RTRAs plus the RTRAs from the $\mu^+\mu^-\pi^+\pi^-$ set, the invariant mass is $8.073 \pm 0.122\text{GeV}/c^2$.

Distances of closest approach. Impact parameters. Longitudinal coordinates of vertices. The minimum separations between RTRAs, impact parameter to wire and longitudinal coordinates of vertices, as reconstructed with the PI tool, are shown in table 4.7. The longitudinal coordinate of the point of closest approximation was also computed and are shown in table 4.8, where they are compared with RVER table information and Monte Carlo truth.

B^{neutr} flavour. Following the ideas presented in the HERA- B Proposal [108], the B^{neutr} flavour was identified through the charged of the RTRA with the highest transverse momentum emanated from the vertex region,

excluding the RTRAs associated to the $\mu\mu\pi\pi$. In this analysis it was also required that the RTRA tag candidates have VDS and Main Tracker hits, to allow good track parameter reconstruction — namely, the charge of the RTRA. The RTRA passing these criteria has positive charge and a RICH likelihood identifying it with a pion. This RTRA’s charge identifies the tagging B meson as a B^+ , and consequently the B^{neutr} as a \bar{B}^0 . Inspection of the ARTE Monte Carlo truth reveals that this RTRA is indeed a π^+ , however it emanates from the hadronic jet of the spectator event.

Conclusions. This event has characteristics suitable of a golden decay candidate: for example, it has a reasonably well detached J/ψ vertex and the checked invariant masses are within the nominal values of the respective resonances. However, it is critical for $\hat{C}\hat{P}$ violation measurements that the correct B flavour is tagged; by chance, the “best” tagging RTRA has the same charge as the accompanying B meson.⁵ The RTRA used for charge tag passes very close to the primary vertex. The presence of a candidate second B meson — the accompanying decay — can also be ascertained from the invariant mass of the remaining RTRAs with VDS hits; however, the high associated error would preclude a definitive identification of this decay. The RTRAs’ momenta and transverse momenta are consistent with the Monte Carlo truth for the corresponding particles, and only diverges for the J/ψ and \bar{B}^0 transverse momentum. The longitudinal separation between RVER 1 and RVER 2 is greater than the \bar{B}^0 - J/ψ Monte Carlo result; however the $z_{\mu\mu} - z_{\mu\mu\pi\pi}$ is consistent with the Monte Carlo truth.

4.2.2 Event 24

The event 24 of the DST file `run05_00052_0076.dst` was studied because it satisfies the selection cut 11., described in table 4.1, and because the tagging particle has hits on the VDS and Main Tracker, which allows for a good charge sign measurement. In this Monte Carlo event, the tagging \bar{b} quark hadronizes as a Λ_b^0 baryon, which decays as

$$\Lambda_b^0 \rightarrow \rho^-(\pi^0\pi^-) \pi^+\pi^0 \omega^0(\pi^0\pi^+\pi^-) \pi^0\pi^0\pi^- \Lambda_c^+, \quad (4.4a)$$

$$\Lambda_c^+ \rightarrow \Sigma^{0*}(\pi^0\Lambda^0(\pi^-p)) \nu_\mu \mu^+. \quad (4.4b)$$

In this notation, the particles in parenthesis represent the final state of the decay of the particle to its left.

ARTE-reconstructed vertices. This event has 21 reconstructed vertices, with 17 RVER reconstructed with the same mass (close to the K^{neutr} ’s) and coordinates but different combinations of RTRA pairs. A summary of the RVER information is shown in table 4.10.

⁵The correlation between the charge of the highest- p_T RTRAs and the charge of the accompanying B was not investigated.

MTRA	B^0	J/ψ	μ^+	μ^-	K_S^0	π^+	π^-
p	128.868	113.789	82.132	31.699	15.135	4.495	10.644
p_T	3.528	3.971	2.846	1.980	1.055	0.420	0.687
z	-4.6027	-4.5979	-4.5979	-4.5979	-4.5979	23.151	23.151
Length	0.00483	(prompt)	2186	2191	27.82	877.4	1324

MTRA	Λ_b^0	π^+	π^-	Λ_c^+	μ^+	p	π^-
p	238.12	5.228	14.753	138.32	25.655	80.585	23.885
p_T	3.210	0.052	0.239	2.595	0.918	1.284	0.444
z	-4.6027	-3.1420	-3.1420	-3.1420	-2.4517	228.31	228.31
Length	1.461	1508	1503	0.6905	2185	579.5	509.6

Table 4.9. Summary of the Monte Carlo truth for the \bar{B}^0 decay (top) and tagging Λ_b^0 meson (bottom) of event 24; see also the figures 4.17 and 4.21. Units: GeV/c (momentum p and transverse momentum p_T), cm (z coordinate of the MTRA's start), cm (MTRA length). The J/ψ decays promptly. The decay stages of the Λ_b^0 meson (figure 4.21) are separated by double vertical separators \parallel . The muon comes from the Λ_c^+ decay and the last two MTRAs come from Λ_0 (with a track length of 230.8cm); see (4.4b). All quantities are measured in the laboratory frame.

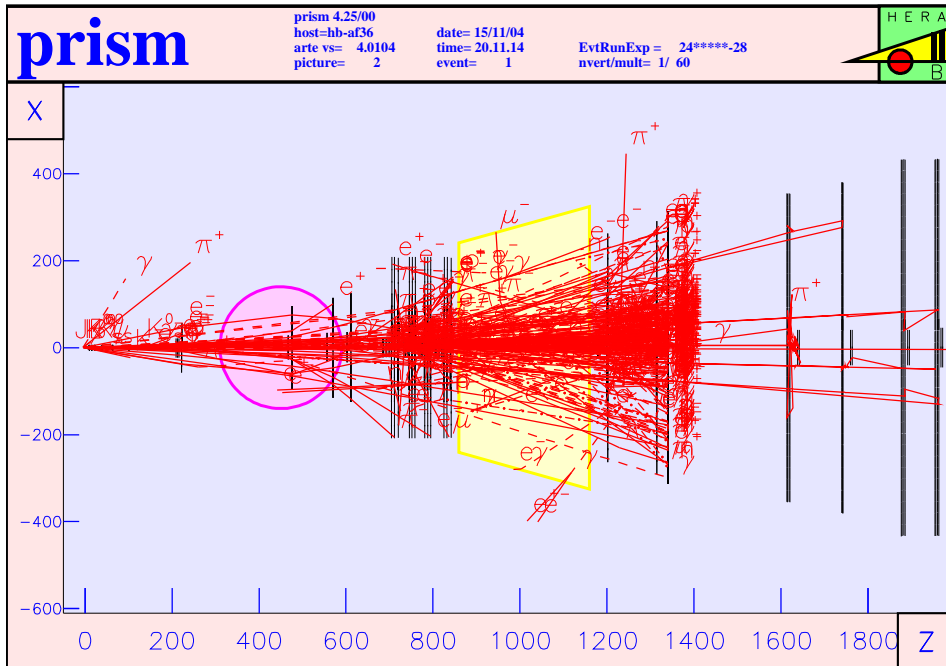


Figure 4.16. PRISM representation of the event 24 in the zx plane. All of the event's 878 MTRAs from the $b\bar{b}$ hadron shower and spectator event are shown — charged particles (continuous lines), photons (dashed), and other neutrals (dotted).

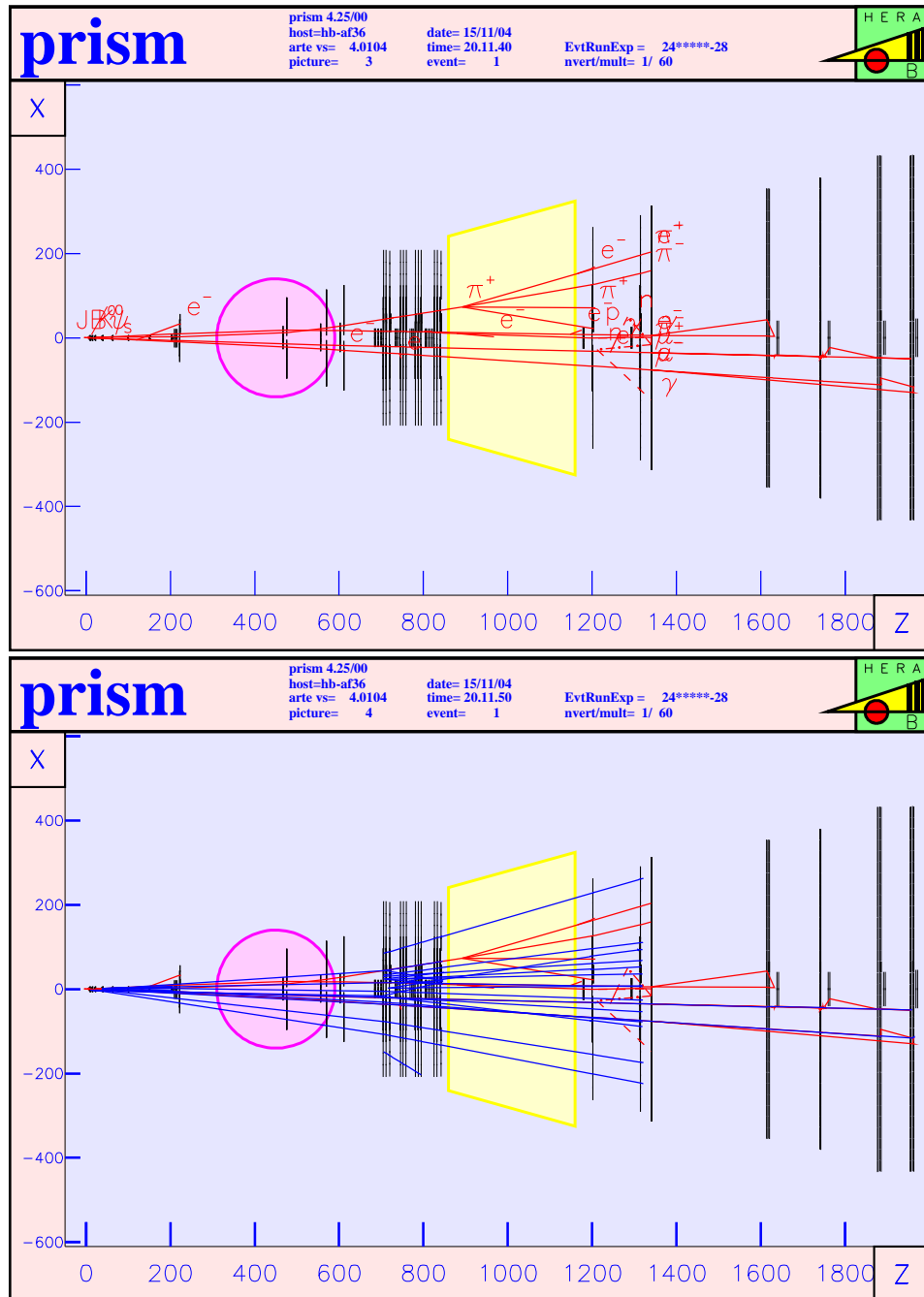


Figure 4.17. PRISM representation of the event 24 in the zx plane. Top: B^0 golden decay MTRAs. The dotted V track at the RICH is a backscattered $p \simeq 0.2\text{GeV}$ neutron. Bottom: superimposition of B^0 MTRAs and all event's RTRAs. Most RTRAs are not drawn beyond the ECAL plane, since most particles are scatter and decay at the iron absorber blocks in front of the Muon detector (not shown).

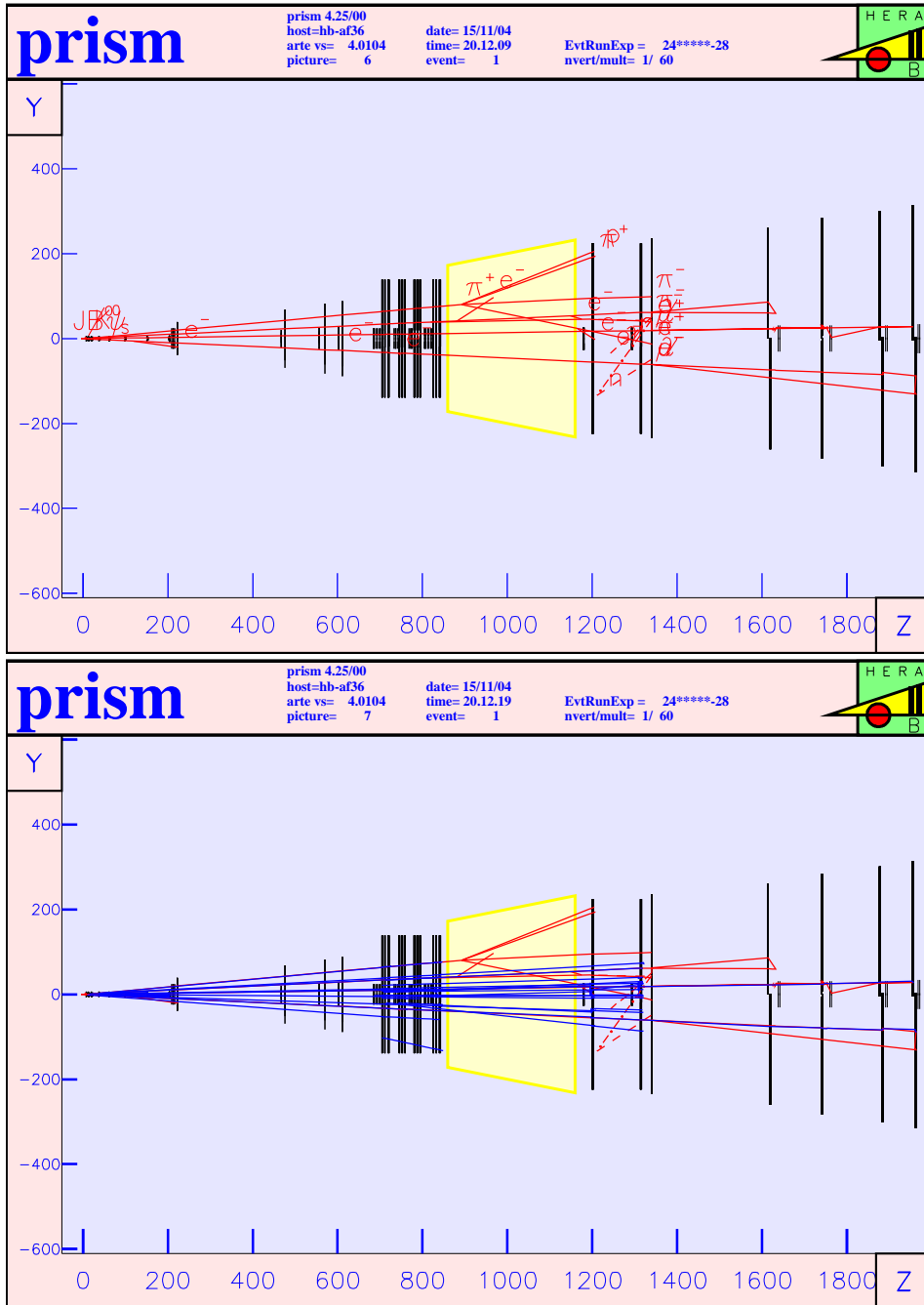


Figure 4.18. Same as figure 4.17, but on the zy plane.

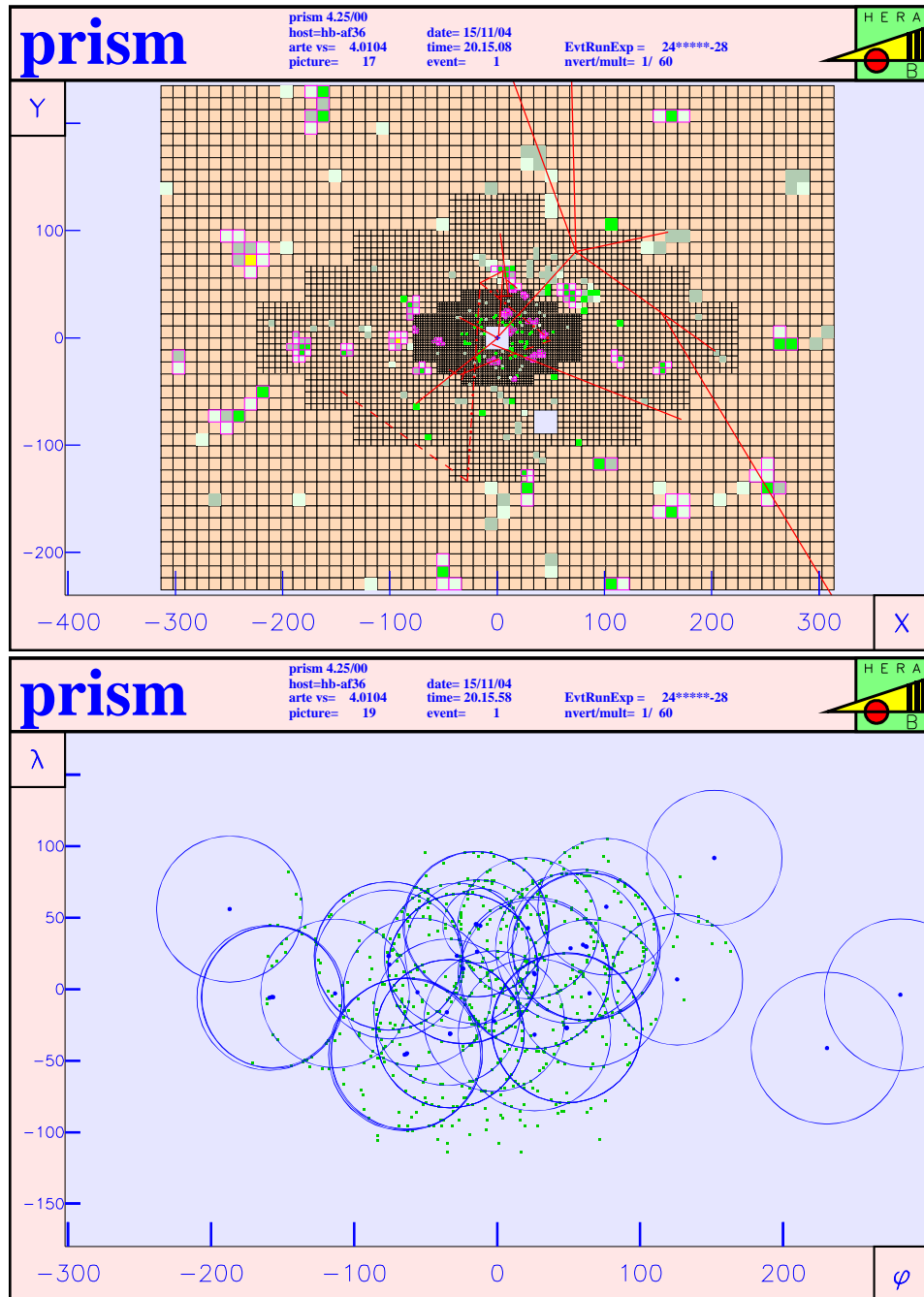


Figure 4.19. Top: reconstructed ECAL clusters (RCCLs) for Monte Carlo event 24. The Monte Carlo Impact Points (MIMPs) are omitted for clarity. The MTRAs originate from the B^0 golden decay. Bottom: representation of RICH hits (green) and reconstructed rings (blue). The (ϕ, λ) coordinates represent the angle (in milliradians) relative to the target region, in the zx and zy planes respectively.

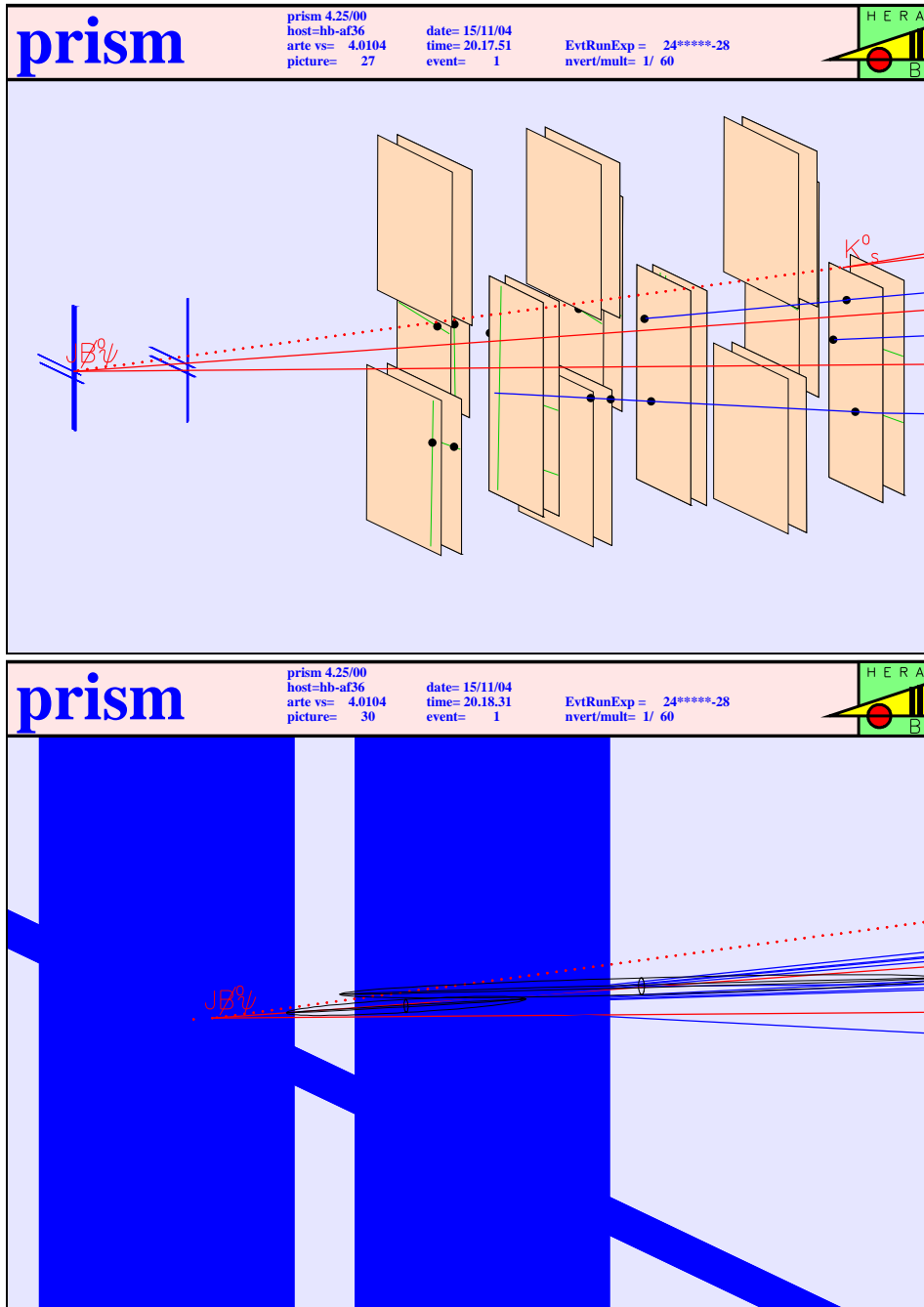


Figure 4.20. PRISM 3D views of the golden decay MTRAs and the four RVERs found by ARTE in this event. The RVERs have their RTRAs extended to them. Top: the target and first three VDS superlayers are shown. MIMPs are drawn as black dots, HITBs as green segments. Bottom: magnified view of the target region. The RVERs are drawn as ellipsoids. The dotted red line represent the B^0 MTRA.

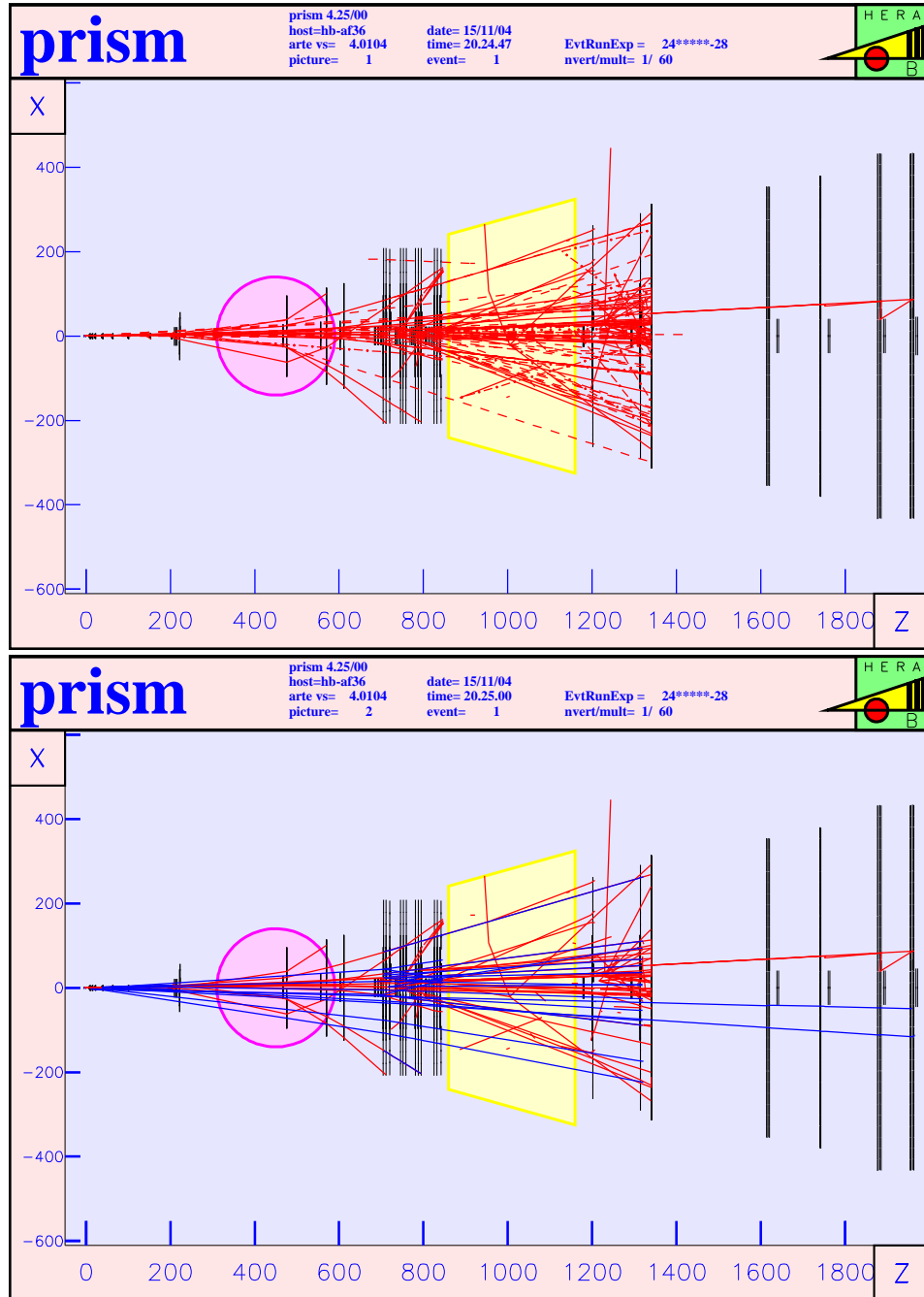


Figure 4.21. The tagging B meson decay in event 24 — PRISM representation in the xz plane. Particle name tags and MTRAs of the remainder of the event were omitted for clarity. Bottom: all the event's RTRAs are superimposed with the B decay MTRAs (neutral MTRAs were omitted).

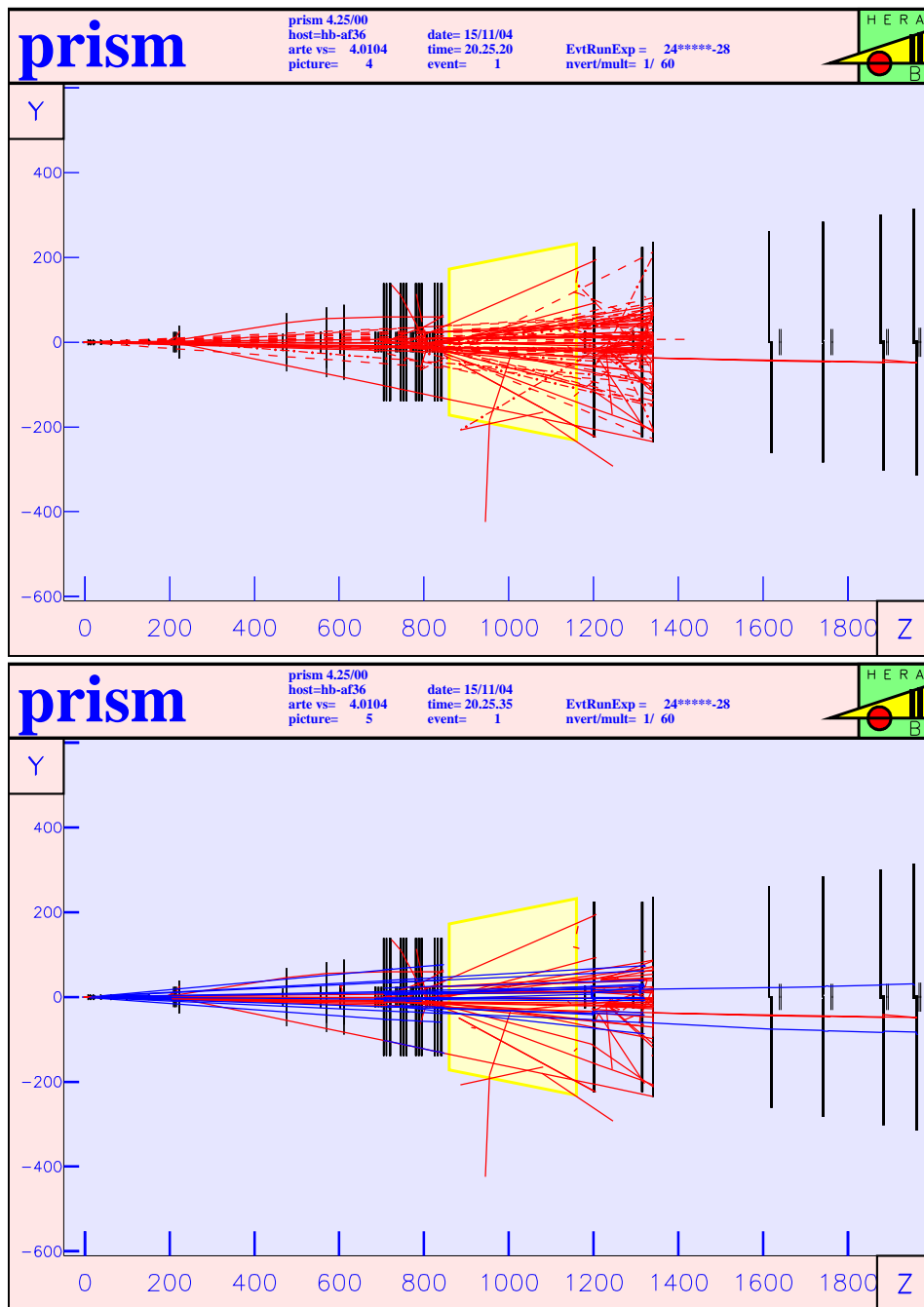


Figure 4.22. Views similar to those of figure 4.21 are shown for event 24, but this time in a projection on the zy plane.

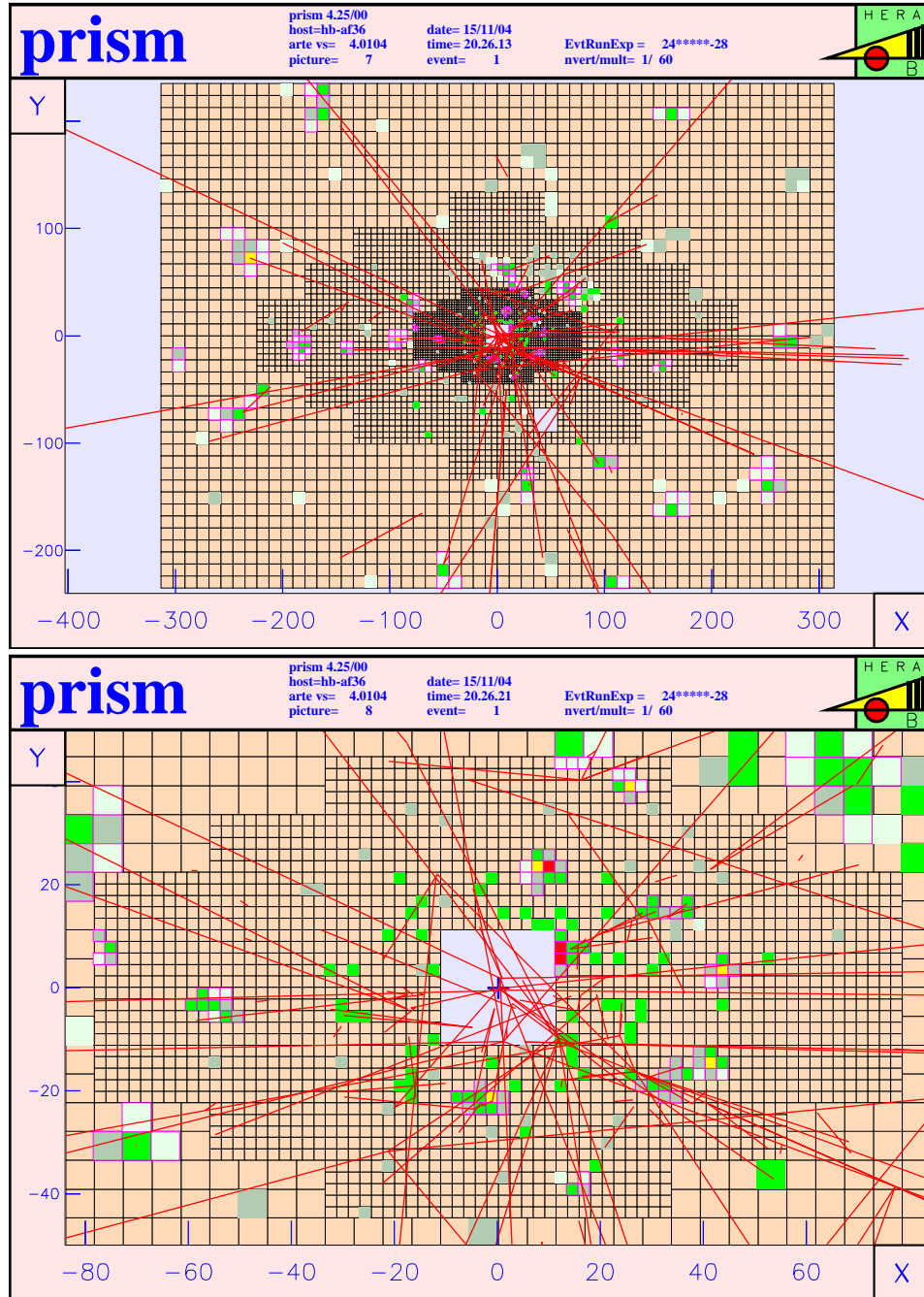


Figure 4.23. The tagging B meson decay in event 24 — PRISM representation of the ECAL. Particle name tags and neutral MTRAs were omitted for clarity. Top: the reconstructed clusters (RCCLs) are presented for comparison with the decay's Monte Carlo. Bottom: detail of the inner ECAL region.

RVER	z/cm	$M/\text{GeV}/c^2$	Num. tracks	χ^2	$\text{Pr}(\chi^2, ndof)$
1	-4.558 ± 0.025	11.158 ± 0.715	13	26.595	27.4%
2	-4.508 ± 0.063	3.086 ± 0.027	2	0.1439	70.4%
4	23.141 ± 0.112	0.496 ± 0.005	2	0.49947	48.0%

Table 4.10. Summary information for the relevant reconstructed vertices in event 24.

PID	μ^+	μ^-	π^+	π^-	Tag
$p / \text{GeV}/c$	81.99 ± 1.13	31.40 ± 0.35	4.47 ± 0.04	10.60 ± 0.11	10.33 ± 0.09
$p_T / \text{GeV}/c$	2.84	1.97	0.42	0.68	1.45
VDS hits	16	11	8	12	8
OTR hits	34	38	28	38	38
Kalman χ^2	39.87	54.40	39.77	40.90	37.80
$\text{Pr}(\chi^2, ndof)$	68.9%	13.5%	13.4%	64.6%	61.4%

Table 4.11. Momenta and transverse momenta of RTRAs relevant for the reconstruction of the golden decay in event 24. The RTRA chosen through the highest- p_T criterium is included (last column). The p_T errors are all $\leq 5\text{MeV}/c$. All shown tracks have no ITR hits.

PID	$\mu^+\mu^-$	$\pi^+\pi^-$	$\mu^+\mu^-\pi^+\pi^-$
$p / \text{GeV}/c$	113.35	15.06	128.38
$p_T / \text{GeV}/c$	4.03	0.51	0.72

Table 4.12. Momenta and transverse momenta of golden decay particles reconstructed in event 24. See also tables 4.9 and 4.11.

PID	μ^+	μ^-	π^+	π^-	Tag
D.C.A.(RVER 1) / μm	18 ± 18	35 ± 29	11084 ± 137	4694 ± 76	33 ± 33
D.C.A.(RVER 2) / μm	3 ± 21	10 ± 29	11058 ± 140	4693 ± 77	92 ± 67
D.C.A.(RVER 4) / μm	22229 ± 94	36333 ± 147	35 ± 53	11 ± 36	44767 ± 185
$b_{\text{wire}}/\mu\text{m}$	-68	-66	6583	2715	-68

RTRA set	$\mu^+\mu^-$	$\pi^+\pi^-$	$\mu^+\mu^-\pi^+\pi^-$
z/cm	-4.508 ± 0.092	23.141 ± 0.115	-4.641 ± 0.242
$M/\text{GeV}/c^2$	3.087 ± 0.028	0.496 ± 0.003	5.265 ± 0.114
$DCA/\mu\text{m}$	13 ± 14	45 ± 44	1406 ± 153
$b_{\text{wire}}/\mu\text{m}$	-64	-88	2322
$b_{\text{RVER 1}}/\mu\text{m}$	17 ± 16	100 ± 31	1227 ± 39

Table 4.13. Vertex longitudinal coordinates, DCAs and impact parameter to wire of golden decay relevant RTRAs (top) and RTRA sets (bottom) for event 24, including the RTRA used for flavour tag (table 4.11). The shown quantities were calculated with the PI tool (section E.1)

Δz	Distance / cm
$\mu\mu$ to $\mu\mu\pi\pi$	$(-4.508 \pm 0.092) - (-4.641 \pm 0.242) = 0.133 \pm 0.334$
RVER 2 to RVER 1	$(-4.508 \pm 0.063) - (-4.558 \pm 0.025) = 0.050 \pm 0.088$
J/ψ to B^{neutr}	$-4.5979 - (-4.6027) = 0.0048$

Table 4.14. Longitudinal separation of the PI-reconstructed vertices, RVER and Monte Carlo truth for event 24.

Momenta, transverse momenta and number of hits for RTRAs.

The momenta and transverse momenta p_T of the RTRAs associated to the golden decay in this event were required to have hits on the VDS and Main Tracker. They were measured with errors of $o(1\%)$ and $\leq 5\text{MeV}/c$, respectively. Table 4.11 shows those quantities and the number of detector hits in the VDS and Main Tracker and the Kalman χ^2 probabilities. Table 4.12 shows the momenta and p_T for the dimuon, dipion and $\mu\mu\pi\pi$ sets.

Invariant masses. The masses computed for the dimuon and dipion candidates are virtually identical to the masses in the RVER table (see tables 4.10 and 4.13); however, once again the $\mu\mu\pi\pi$ and RVER 1 masses differ.

ARTE identified four RTRAs with the MTRAs from the $\mu^+\mu^-\pi^+\pi^-$ final state of the golden decay. The invariant masses of the dimuon, dipion and 4-set were calculated and found to be, respectively, $3.078 \pm 0.028\text{GeV}/c^2$, $0.391 \pm 0.004\text{GeV}/c^2$ and $5.171 \pm 0.022\text{GeV}/c^2$. Including the PID hypotheses for the respective tracks improves these figures: $M_{\mu\mu} = 3.087 \pm 0.028\text{GeV}/c^2$, $M_{\pi\pi} = 0.496 \pm 0.003\text{GeV}/c^2$ and $M_{\mu\mu\pi\pi} = 5.265 \pm 0.114\text{GeV}/c^2$.

Based on the RTRAs identified with MTRAs from the tagging Λ_b^0 hadronic shower, the invariant mass of the RTRA set was calculated and found to be $5.220 \pm 4.566\text{GeV}/c^2$. The nominal value for the Λ_b^0 mass is $5.624 \pm 0.009\text{GeV}/c^2$ [81]. Of the 8 RTRAs used in the calculation, 2 have hits both before and after the Magnet and good (i.e. the error is below or at 1%) momentum resolution.

Distances of closest approach. Impact parameters. Longitudinal coordinates of vertices. These quantities were computed with the tool PI and are shown in table 4.13. The longitudinal coordinates of the point of closest approximation for the dimuon, dipion and $\mu\mu\pi\pi$ are shown in table 4.14, where they are compared with RVER table information and Monte Carlo truth.

B^{neutr} flavour. In this event, the RTRA with highest- p_T , not belonging to the dimuon or dipion candidates, and with hits before and after the Magnet (VDS and Main Tracker) is a π^- , which is revealed by ARTE Monte Carlo truth to be a pion from the spectator event. The track's charge was correctly

identified, and the tagging method hypothesis denounces the presence of a B^- meson. Consequently, the flavour of the golden decay B meson is B^0 .

Conclusions. This event was reconstructed as a suitable golden decay candidate. However, the detached vertex measurement $z_{\mu\mu\pi\pi} - z_{\mu\mu}$ has poor quality, in spite of having a positive value. The charge tag RTRA is consistent with the hypothesis of origin from the primary vertex, and gave the correct flavour tag. Comparing these figures with the Monte Carlo truth partially listed in table 4.9, and contrary to what was measured for event 235, the RTRAs' momenta are substantially different from the expected values. However, the momenta of the reconstructed resonances is very close to the corresponding MTRAs in the Monte Carlo. As seen in table 4.14, the longitudinal distance travelled by the B^0 meson is very small in this event, and it is better reproduced with RVER table data than with the PI tool.

4.2.3 Remaining events

The dimuon and dipion invariant masses were calculated for the remaining 5 of the 7-event MC selection. The dimuon and dipion candidates were selected automatically by the analysis tool PI (section appendix E.1 in appendix) according to the following criteria:

1. More than one hit on the VDS and Main Tracker, to allow good momentum measurement.
2. A track with Muon detector hits is classified as a muon. The hypotheses for pion, kaon and proton track are evaluated by selecting the highest RICH likelihood for each of them. The electron hypothesis is tested if no Muon or RICH hypothesis is available by requiring the RTRA to have ECAL hits and consistent with the highest ECAL likelihood for the electron hypothesis. These tags are used to improve the invariant mass of the pairs to be searched.
3. The dimuon is searched amongst the pairs of RTRAs identified as muons with an invariant mass closest to the J/ψ 's and with the lowest mass standard deviation error, see equation (C.5). A similar selection is done to search for $K_S \rightarrow \pi^+\pi^-$ among dipion candidates.
4. Additionally, the distance of closest approach between the muon (pion) pairs is required to be below $500\mu\text{m}$ for J/ψ (K_S) candidates.

The B^{neutr} mass is reconstructed from the dimuon–dipion invariant mass. The errors for momentum, p_T , mass, distance and impact parameter quantities are computed from the covariance matrices for the RTRAs generated by ARTE.

The B meson flavour was determined by selecting the RTRA that satisfies the following criteria:

1. The RTRAs must not belong to the dipion and dimuon sets attributed to the golden decay.
2. The RTRA candidates have “good momentum” (i.e., they have segments in the VDS and Main Tracker, thus allowing a good determination of momentum);
3. Reference [108] gives median p_T values of the lepton and kaon tags for the other B meson, respectively at $1.2\text{GeV}/c$ and $0.6\text{GeV}/c$. However, given the limited event sample it was chosen to instead select the RTRA with highest p_T ;
4. The RTRA must have a “good” distance of closest approach to the primary vertex, e.g. $b < 500\mu\text{m}$.

The charge tag of the second B in the event is taken as the charge of the selected RTRA. This promptly tags the flavour of the $B^{\text{neutr}} - B^0$ for a negative-charge tagging RTRA, or \bar{B}^0 in case of a positive-charge RTRA.

Using the conditions described above and comparing with the Monte Carlo truth, it was found that the identified B flavour was incorrect for events 131 and 233. In the remaining events, though the flavour was correctly identified, the highest- p_T RTRA was not associated to an MTRA from the second B decay. In events 233 and 267 the $K^{\text{neutr}} \rightarrow \pi^+\pi^-$ was wrongly reconstructed — the RTRAs chosen by the analysis tool PI using the previous criteria are attributed to MTRAs that do not belong to the golden decay’s K_S . In event 233, one of the pions of the “correct” dipion combination has no PID hypothesis formulated by PI, therefore it was not considered a good candidate for a dipion. The RTRAs in the “correct” dipion give an invariant mass $M_{\pi\pi} = 0.408 \pm 0.003\text{GeV}/c^2$, and combined with the correctly identified dimuon gives a $\mu\mu\pi\pi$ mass of $M_{\mu\mu\pi\pi} = 5.228 \pm 0.116$. The correct dipion has a better distance of closest approach (DCA) between the two RTRAs, but a worse wire impact parameter (WIP) than the dipion proposed by PI. In the event 267, the reconstructed dipion mass is again too far from the K^{neutr} mass — $1.190 \pm 0.008\text{GeV}/c^2$ given by PI, and $0.152 \pm 0.003\text{GeV}/c^2$ for the “correct” dipion. In the last pair, one of the RTRAs has no mass hypothesis; forcing the pion mass hypothesis on the “bad” RTRA gives a dipion invariant mass $0.494 \pm 0.002\text{GeV}/c^2$. However, the $\mu\mu\pi\pi$ mass would still be too low, $4.244 \pm 0.129\text{GeV}/c^2$.

4.2.4 Conclusions

It was seen that, though the selection cuts on the four RTRAs candidate for reconstructing J/ψ and K_S decays significantly restricts the number

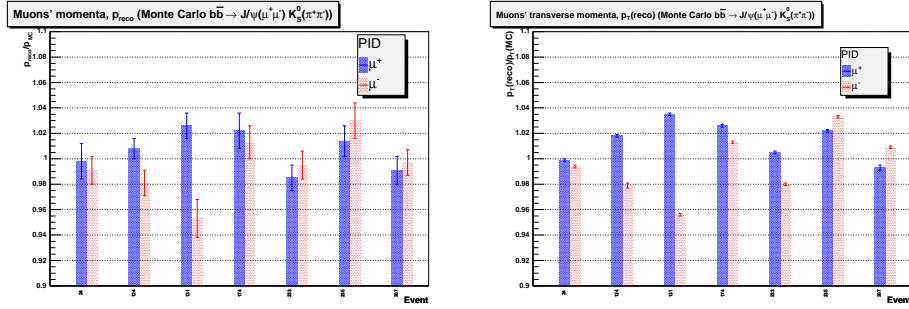


Figure 4.24. Left: ratio of muon RTRA momentum to MTRA momentum, for muons from the J/ψ decay. Right: Ratio of transverse momenta p_T of RTRA muons (from the dimuons selected for the Monte Carlo event sample) to the p_T of the corresponding MTRAs. The p_T errors are negligible — below the percent level.

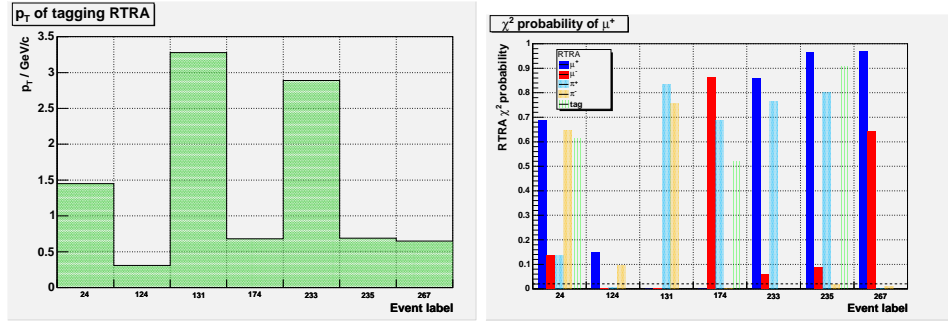


Figure 4.25. Left: Transverse momentum of the RTRAs selected for charge tag in each event. Right: Kalman χ^2 probability of RTRAs selected by the PI tool as relevant for the golden decay identification — muons (filled bars, blue and red), pions (shaded bars, cyan and orange) and tagging RTRA (vertical fill bars, green).

of eligible events, the resulting sample has very high quality and can be correctly identified as golden decays.

In the limited Monte Carlo sample, the event with tag 235 has the best quality. For the second event studied in detail, though according to the Monte Carlo truth the dipion and dimuon RTRAs in event 24 are associated with the golden decay MTRAs, the reconstructed B^0 has worse quality. Event 235 has the best distance of closest approach for the dimuon, dipion and $\mu\mu\pi\pi$ RTRA sets — all below $200\mu\text{m}$ — and invariant masses reasonably close to the nominal values of the J/ψ , K^0 and B^0 respectively.

With the used flavour-tagging method, none of the highest- p_T RTRAs selected by the PI tool is associated to an MTRA from the second beauty meson or baryon. The correct identification of the B^{neutr} flavour is critical for measuring $\hat{C}\hat{P}$ violation asymmetry (2.41). It should also be recalled that additional effects, such as $B^0-\bar{B}^0$ flavour oscillations, contribute to dilute the measured asymmetry. The flavour oscillation does not show up in the Monte Carlo truth and was also disregarded.

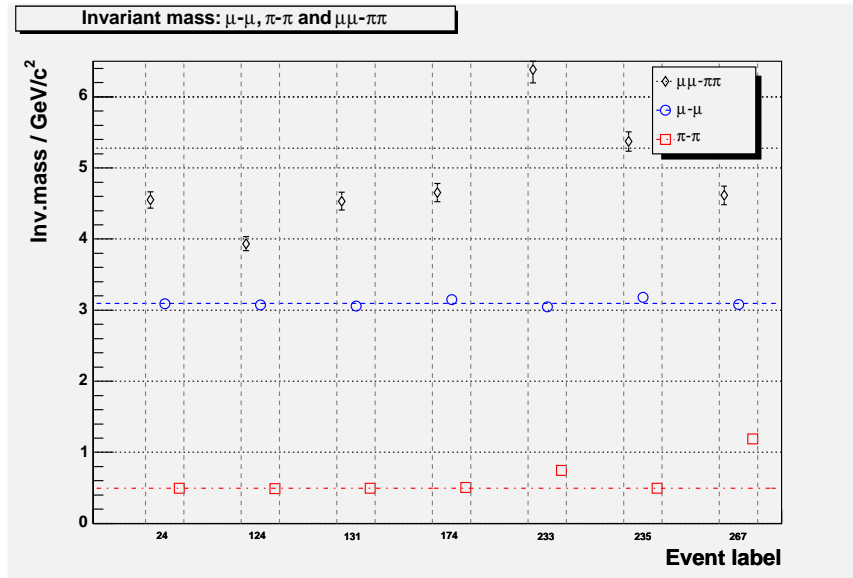


Figure 4.26. Reconstructed masses of the dimuon (blue circles), dipion (red squares) and $\mu\mu\pi$ (black losangles). Notice that only event 235 has all three masses near the respective nominal values for the J/ψ (dashed blue line, center), K^{neutr} (dash-dot red line, bottom) and B^{neutr} (dotted line, near top).

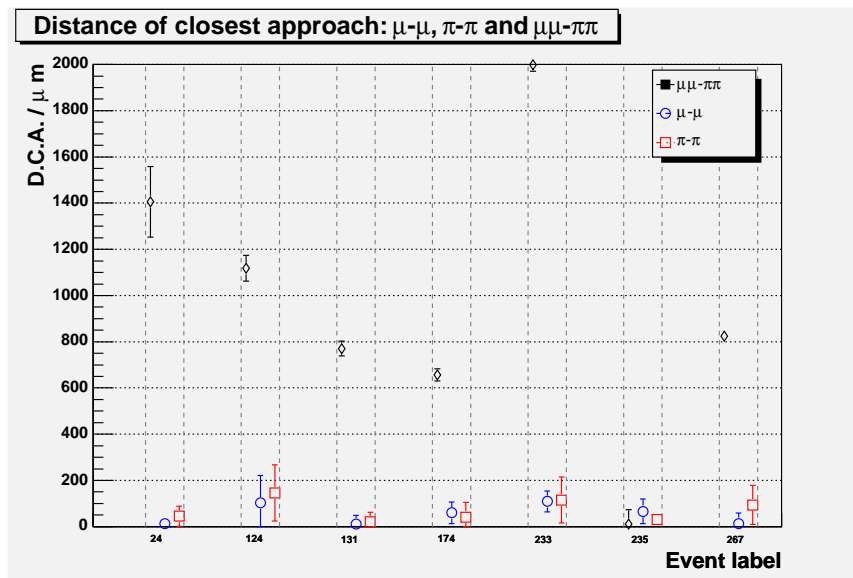


Figure 4.27. Distance of closest approach for the dimuon, dipion and $\mu\mu\pi$ sets. For event 235 all three distances are below $200\mu\text{m}$ (see figure 4.5).

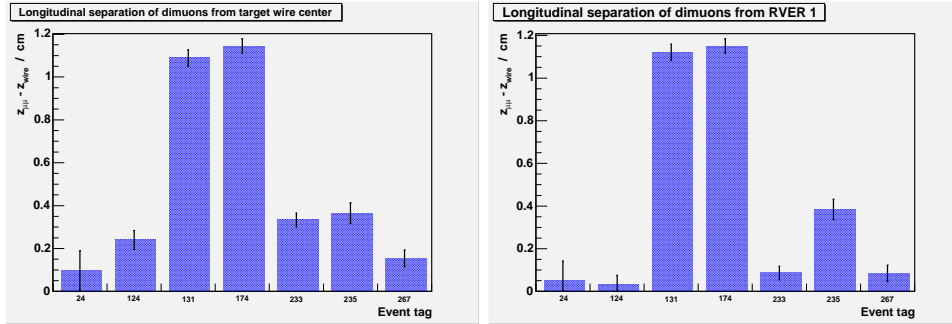


Figure 4.28. Longitudinal separation of the J/ψ vertex to the center of the target wire (left) and to the primary RVER (right). Events 131, 174 and 235 are viable candidates for a “detached vertex” flag.

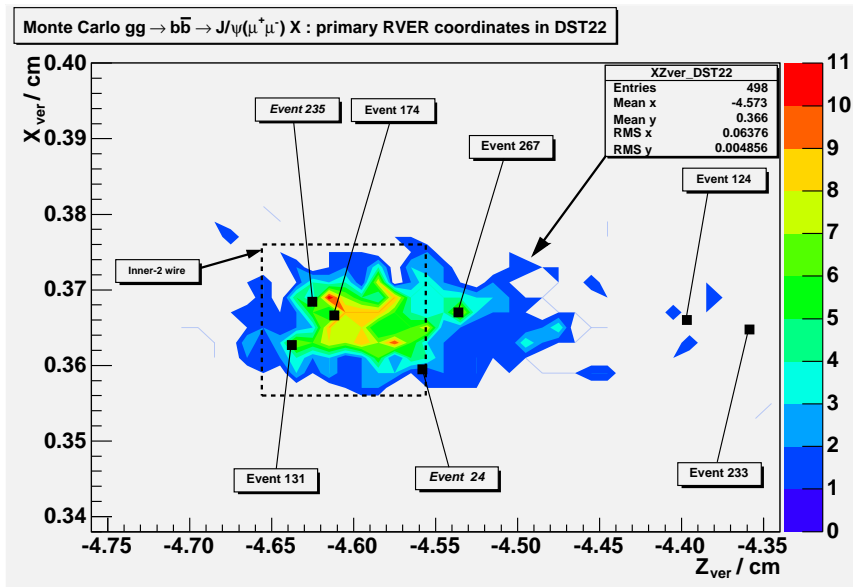


Figure 4.29. Contour histogram of the vertex coordinates in the zx plane, from primary vertices in DST 22, with 501 events (see text). Figure 4.3 is the contour’s projection in z . The seven Monte Carlo events here analysed have primary vertices reconstructed close or within the target wire; the black square markers represent their median positions in the zx plane. The thick dashed line represents the target wire boundary projected in the zx plane. Note axes’ scales are not equal.

Run number	Event number	Candidate event	$\mu^+\mu^-$ invariant mass (GeV/ c^2)	Decay length Δz (cm)	$\Delta z/\sigma_z$
16014	15568	$b\bar{b} \rightarrow \mu^+\mu^+X$	3.005	1.111	24.233
16069	172	$b\bar{b} \rightarrow \mu^+\mu^+X$	2.240	0.729	14.108
16078	31451	$b\bar{b} \rightarrow \mu^+\mu^+X$	3.122	0.696	31.104
16529	13848	$b\bar{b} \rightarrow \mu^+\mu^+X$	2.175	0.637	9.270
16602	13060	$b\bar{b} \rightarrow \mu^+\mu^+X$	2.390	0.672	13.009
16605	17638	$b\bar{b} \rightarrow \mu^+\mu^+X$	2.875	0.866	14.176
16681	52937	$b\bar{b} \rightarrow \mu^+\mu^+X$	3.241	0.500	11.299
16715	25940	$b\bar{b} \rightarrow \mu^+\mu^+X$	3.200	2.202	29.108
16784	22303	$b\bar{b} \rightarrow \mu^+\mu^+X$	2.229	0.346	8.183
16784	86655	$b\bar{b} \rightarrow \mu^+\mu^+X$	2.565	1.598	14.843
16798	2275	$b\bar{b} \rightarrow \mu^+\mu^+X$	2.730	2.266	33.051
20545	1216003542	$B^+ \rightarrow J/\psi K^+$	3.121	0.285	3.22
20639	373074	$B^+ \rightarrow J/\psi K^+$	3.042	0.355	10.3
20645	1528001531	$B^0 \rightarrow J/\psi K_S^0$	3.142	0.128	2.14

Table 4.15. Selection of events recorded with the HERA-B detector. The events with run number 16014 through 16798 were selected from reference [2]; the remaining are from reference [119]. The event classification, dimuon mass, decay length and significance are from those two references.

Selection	Run numbers	ARTE version	Geometry version	“Repro” number
Year 2000	16xxx	ARTE4-01-r3	01.0701	0002
Year 2002	20xxx	ARTE4-01-r5	02.1205	0005

Table 4.16. ARTE setup for analysis of the event selections presented in table 4.15. “Repro” refers to the official reprocessing cycle in the offline event reconstruction.

4.3 A sample of B decay candidates measured in HERA-B

Two selections of events recorded with the HERA-B detector were used, one from the year 2000 epoch [2] and the other from the year 2002 [119]. The events were recorded in DST format, and reconstructed for this analysis using different kumac setups (see one example in section D.2) for the year 2000 and the year 2002 selections; see table 4.16. Those setups were chosen to ensure enough compatibility with the software and geometry versions used at the time of data-taking and are presented for reference.

Analysis on the year 2000 selection is presented for comparison; greater attention is given to the three events selected from the year 2002 run epoch.

In this text, the events will be identified by the respective run number.⁶

Of the three events from the year 2002 selection, only the event from run 20645 is a candidate for a golden decay; the other two events are candidate charged B decay candidates. Nevertheless, the other two events from the selection were studied — on one hand, it makes an interesting scope extension beyond the exclusive “golden decay” cases; on the other hand, because the B^0 flavour-tagging depends on the reconstruction of the second beauty decay, this tests for its validation. Furthermore, the self-tagging decays of charged B mesons are of interest for the measuring of complementary parameters in $\hat{C}\hat{P}$ violation, even though the branching ratios of the alternative decay modes may be substantially lower than that of the golden decay. Because of the conception of the HERA- B Trigger scheme, the ideal B decays’ search includes those with a decaying $J/\psi \rightarrow \ell^+\ell^-$.

4.3.1 The golden decay event candidate in run 20645

The event 1528001531 in run 20645 was identified as a candidate for a golden decay event. The results presented here are consistent with those in reference [119], with differences amounting to $o(10^{-2})$.

The runlog information for run number 20645 states that the inner II (carbon) and inner I (tungsten) target wires were in use. The two wires’ respective positions, at $z_{i2} = -4.61\text{cm}$ and $z_{i1} = -0.58\text{cm}$ (ARTE table GTAR), allows good vertex longitudinal separation. The reconstruction of this event produced 2 vertices and 29 charged tracks (plus one “hitless” RTRA, reconstructed by ARTE as a short decay resonance at the J/ψ mass range). The reconstructed vertices have longitudinal coordinates $z_1 = -4.56\text{cm}$ and $z_2 = -4.46\text{cm}$ and were reconstructed with, respectively 7 RTRAs (corresponding to $ndof = 11$ degrees of freedom) and 2 RTRAs ($ndof = 1$). The χ^2 residual was calculated by ARTE, and the two vertices’ χ^2 probabilities are 2.2% and 32.6% respectively; these values pass the probability cut used in reference [73], $\text{Pr}(\chi^2, ndof) > 0.3\%$, with $ndof$ as the number of degrees of freedom for the hits-to-track fit.

Some parameters involving combinations of two RTRAs were investigated, namely: the invariant mass of the RTRA pair; the minimum separation between RTRAs; the RTRAs’ and the reconstructed resonance’s impact parameters (minimum distance) to the wire associated with the primary vertex. Since this event was a suspected golden decay event, the neutral B was reconstructed from the information on the dimuon and dipion corresponding to the reconstructed J/ψ and K^0 found in the event, and their invariant mass was calculated. The values were obtained from the C program `PI.c` listed in section E.1 in appendix. The following cuts were applied on the RTRA pairs:

⁶For run 16784, a letter is appended to distinguish between the two events in the selection: 16784a for event 22303 and 16784b for event 86655, in run 16784.

1. Both RTRAs must have hits on the VDS, Main Tracker (ITR and/or OTR), and also on the MUON detector for muon pairs.
2. The resonance's mass (J/ψ for dimuon, K^0 for dipion) must lie within less than 5 standard deviations of the measured value for the dimuon invariant mass.
3. The minimum separation between the dimuon RTRAs must not exceed $500\mu\text{m}$, and this point should be at a longitudinal coordinate z greater than the primary vertex's.
4. For pions and kaons, an unequivocal PID should be established through the likelihood hypotheses ($L_{\pi^\pm} > L_{\ell^\pm} + L_{K^\pm} + L_p$ for pion Particle Identification, and $L_{K^\pm} > L_{\ell^\pm} + L_{\pi^\pm} + L_p$ for kaon).

The first criterion ensures good momenta measurement, with errors below 1%. The MUON hits requirement for muons is the only criterion applied for muon PID. The second criterion allows to select the sought RTRA pairs. The third criterion allows to reject the RTRA pairs which are manifestly undesired, eliminating some spurious invariant mass combinations. The fourth criterion seeks to use the good PID separation granted by the RICH detector to further improve the selection quality. Although no p_T cut is specified, this is taken in consideration when searching for the relevant RTRAs.

The RTRAs from this event which have “good” momentum and a PID tag are listed in table 4.17. The RTRAs which best satisfy the hypothesis for a golden decay are presented in tables 4.19 and 4.21, with their respective invariant masses, vertex longitudinal coordinate, DCA, minimum distance to the primary vertex, and impact parameter at the target. Figure 4.30 shows two PRISM views for this event.

ARTE-reconstructed vertices. This event has only 2 reconstructed vertices, and only the second RVER was reconstructed with non-zero mass;⁷ see table 4.18.

Momenta, transverse momenta and number of hits for RTRAs.

This event was reconstructed in ARTE and yielded 30 RTRAs, one of which is flagged as a short decay resonance. The momenta of RTRAs with hits up- and downstream of the Magnet were measured with errors $o(1\%)$ and the transverse momenta were computed to be lower than $5\text{MeV}/c$. Table 4.19 shows those quantities, the number of detector hits and the Kalman χ^2 probability of the RTRAs.

⁷The GROVER package, used for vertex reconstruction in ARTE, uses geometric and kinematic constraints to add and fit tracks to a given vertex. If the resulting vertex is not consistent with the constraints, a “less constrained” vertex (e.g. no mass) is sought.

RTRA	z/cm	x/cm	y/cm	tx	ty	$p/\text{GeV} \cdot c^{-1}$	χ^2	$\text{Pr}(\chi^2, ndof)$
	$\mathcal{L}_{\text{RICH},\pi}$	$\mathcal{L}_{\text{RICH},K}$	$\mathcal{L}_{\text{RICH},p}$	$\mathcal{L}_{\text{ECAL},e}$	$\mathcal{L}_{\text{ECAL},h}$	$\mathcal{L}_{\text{MUON},\mu}$	PID	$b_{\text{RVER } 1}/\mu\text{m}$
1	37.221	+2.5968	-1.80170	+0.054863	-0.041790	+19.370	41.75	61.1%
	21.7%	10^{-25}	10^{-27}	10^{-5}	87.3%	93.8%	μ^+	114 ± 52
2	62.788	-1.8365	-0.56336	-0.031889	-0.0074088	-57.244	28.41	99.9%
	17.9%	10^{-9}	10^{-25}	10^{-4}	57.0%	100.0%	μ^-	19 ± 27
4	39.394	+2.4375	+0.38276	+0.048372	+0.010105	+7.0557	49.41	49.7%
	49.4%	16.7%	16.7%	10^{-4}	85.4%	—	π^+	46 ± 84
5	12.422	+0.74801	+1.65780	+0.0044742	+0.106900	-6.7921	52.12	1.8%
	78.1%	10^{-4}	10^{-4}	0.3%	99.6%	—	π^-	3736 ± 38
6	12.422	+1.0226	+1.5865	+0.066304	+0.090906	+6.2473	37.36	84.2%
	99.4%	10^{-8}	10^{-8}	10^{-5}	92.7%	—	π^+	4269 ± 45
7	20.466	+0.2867	-1.5944	-0.009243	-0.060774	-4.5620	36.81	73.5%
	100.0%	10^{-5}	10^{-5}	10^{-5}	59.6%	—	π^-	89 ± 52
8	22.480	+2.9369	+0.0491	+0.095695	-0.003866	-4.1046	39.54	9.2%
	3.8%	0.7%	0.7%	—	—	—	π^-	2229 ± 53
9	14.798	+2.1878	-0.0414	+0.096250	+0.001488	-4.0896	25.78	77.3%
	0.3%	10^{-3}	10^{-3}	—	—	—	π^-	153 ± 81
14	37.199	+0.2187	+1.7023	-0.002248	+0.042587	-5.8510	44.58	69.0%
	99.8%	10^{-5}	10^{-5}	10^{-6}	52.2%	—	π^-	107 ± 95
21	39.394	+2.4371	+0.3827	+0.048440	+0.010124	-17.5380	15.794	26.0%
	6.6%	10^{-8}	8.9%	—	—	—	\bar{p}	39 ± 39
4+21	39.394	+2.4371	+0.3827	+0.048475	+0.010130	-24.5562	—	—
	—	—	—	—	—	—	\bar{p}	47 ± 88

Table 4.17. List of RTRAs from a golden decay candidate measured in HERA-B— run 20645, event 1528001531. The full event was reconstructed with 29 RTRAs with hits; only those RTRAs with hits up- and downstream of the Magnet, and with a formulated likelihood PID, are shown. The RTRAs' covariance matrices are ommitted. The primary vertex, $RVER$ 1, in this event lies pratically inside the corresponding target wire, $|\vec{r}_{\text{wire}} - \vec{r}_{\text{RVER } 1}| \simeq 0.5\text{mm}$.

(z, x, y) are the RTRA's first point coordinates, (tx, ty) are its tangents $tx = p_x/p_z$ and $ty = p_y/p_z$ in the zx and zy planes. The signed p column indicates the measured momentum and the RTRA's charge (positive or negative). The PID indicates the particle identification information from RICH likelihood (for pions, kaons and protons), or the presence of hits in the MUON detector (for muons); the charge is obtained from tracking information (p column). Rightmost column gives the χ^2 probability, obtained from the Kalman filter technique, for this hits used to build the RTRA. On the second line are the RICH likelihoods for the pion, kaon and proton hipoheses (the likelihoods for the electron and muon hipoheses are omitted), the ECAL likelihood for electron and hadron hipoheses (the minimum-ionizing particle likelihood is the complement of these two), and the MUON likelihood for muon hipohesis; the likelihoods are evaluated only at the presence of associated hits for the corresponding detector(s). The next-to-last column give the resulting PID decision; this is useful to improve invariant mass calculations. The last column gives the extrapolated distance of closest approach to the reconstructed primary vertex (see appendix E.1).

Entry "4+21" represents the add-up of RTRA directions from RTRA 4 and RTRA 21. The two RTRAs are estimated to meet at $z \simeq 45\text{cm}$, with a distance of closest approach of $0.5 \pm 17.7\mu\text{m}$.

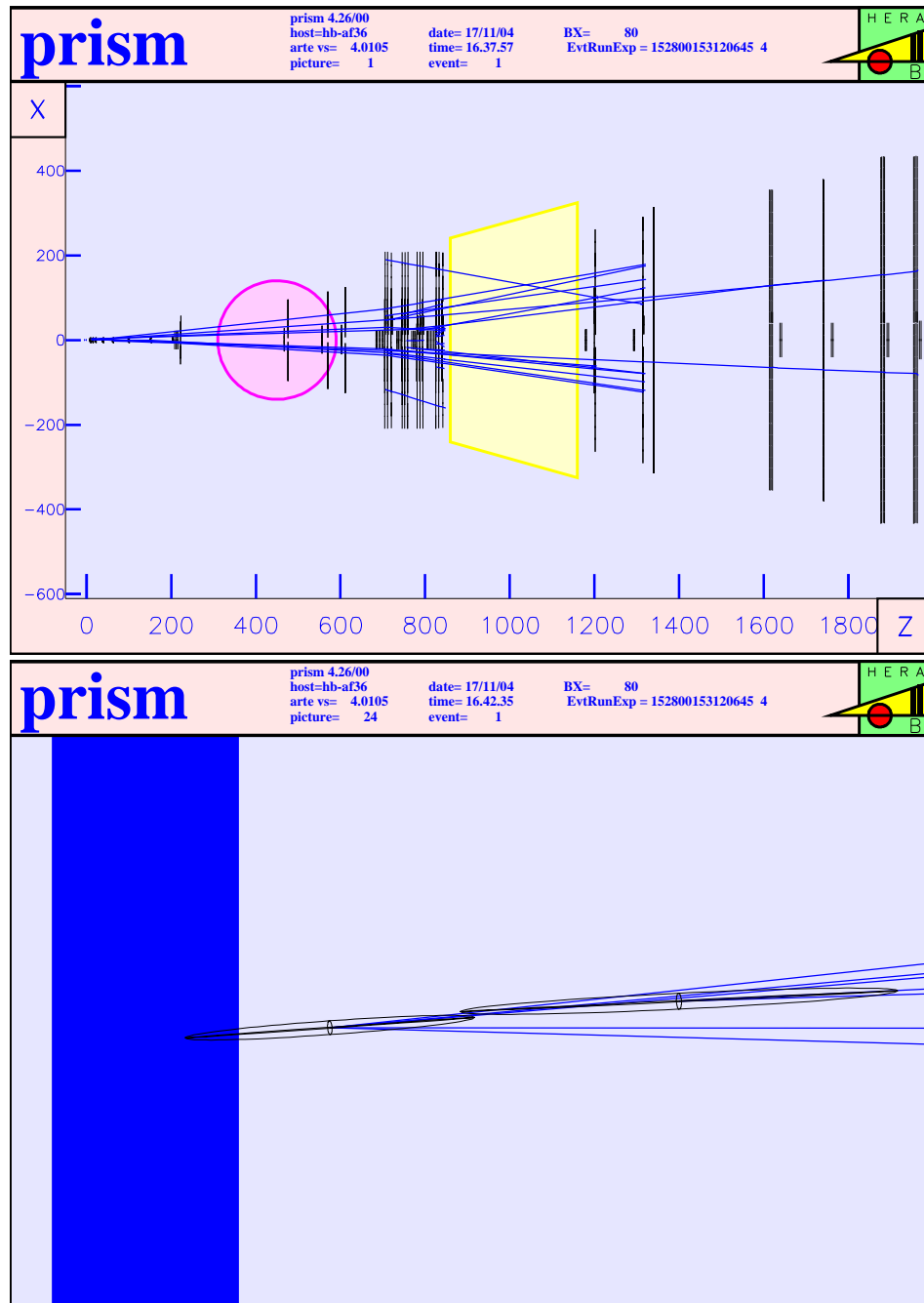


Figure 4.30. Top: zx projection of event 1528001531 in run 20645, displayed by PRISM. The measure scale is in centimeters. The two muons RTRAs used to reconstruct the J/ψ decay are seen transversing the Muon detector. Bottom: 3D detail (almost a projection in the zx plane) of the target wire and of the two reconstructed vertices (RVERs) in the same run, see table 4.18. The y direction points to the top, the proton beam is directed from left to right. The 1σ variance ellipsoid of the primary vertex intersects the inner H target (large rectangle) used in this run. The RTRAs associated with the reconstructed vertices were drawn into them. The two extrapolated muon RTRAs meet at the J/ψ RVER (rightmost ellipsoid).

RVER	z/cm	$M/\text{GeV}/c^2$	Num. tracks	χ^2	$\text{Pr}(\chi^2, \text{ndof})$
1	-4.560 ± 0.042	n/a	7	22.374	2.2%
2	-4.460 ± 0.063	3.112 ± 0.027	2	0.9663	32.3%

Table 4.18. Summary information for the all the vertices reconstructed in the event selected from run 20645.

PID	μ^+	μ^-	π^+	π^-	Tag
$p / \text{GeV}/c$	19.37 ± 0.24	57.24 ± 0.65	6.25 ± 0.06	6.79 ± 0.07	17.54 ± 0.26
$p_T / \text{GeV}/c$	1.34	1.87	0.70	0.73	0.87
VDS hits	12	15	10	9	12
OTR hits	38	47	43	38	10
Kalman χ^2	41.74	28.41	37.36	52.12	15.79
$\text{Pr}(\chi^2, \text{ndof})$	61.1%	99.9%	86.6%	13.6%	53.8%

Table 4.19. Momenta and transverse momenta of RTRAs relevant for the reconstruction of the selected event from run 20645. The RTRA chosen through the highest- p_T criterium is included (last column). The p_T errors are all $\leq 5\text{MeV}/c$. All shown tracks have no ITR hits.

PID	$\mu^+\mu^-$	$\pi^+\pi^-$	$\mu^+\mu^-\pi^+\pi^-$
$p / \text{GeV}/c$	76.55	13.03	89.57
$p_T / \text{GeV}/c$	1.23	0.44	0.32

Table 4.20. Momenta and transverse momenta of golden decay particles reconstructed in the event from run 20645. See also table 4.19.

PID	μ^+	μ^-	π^+	π^-	Tag
D.C.A.(RVER 1) / μm	113 ± 52	19 ± 26	4268 ± 45	3735 ± 38	39 ± 39
D.C.A.(RVER 2) / μm	47 ± 48	9 ± 28	4210 ± 53	3733 ± 39	54 ± 58
$b_{\text{wire}}/\mu\text{m}$	27	-83	4112	3473	-9

RTRA set	$\mu^+\mu^-$	$\pi^+\pi^-$	$\mu^+\mu^-\pi^+\pi^-$
z/cm	-4.460 ± 0.063	7.980 ± 0.039	-4.347 ± 0.140
$M/\text{GeV}/c^2$	3.112 ± 0.027	0.499 ± 0.003	5.316 ± 0.112
$DCA/\mu\text{m}$	56 ± 61	2 ± 34	1153 ± 82
$b_{\text{wire}}/\mu\text{m}$	-60	55	2878
$b_{\text{RVER 1}}/\mu\text{m}$	48 ± 21	100 ± 56	1073 ± 45

Table 4.21. Vertex longitudinal coordinates, DCAs and impact parameter to wire of golden decay relevant RTRAs (top) and RTRA sets (bottom) for the selected event from run 20645, including the RTRA used for flavour tag (table 4.19). The shown quantities were computed with the PI tool (section E.1).

Δz	Distance / cm
$\mu\mu$ to $\mu\mu\pi\pi$	$(-4.460 \pm 0.063) - (-4.347 \pm 0.140) = -0.113 \pm 0.203$
RVER 2 to RVER 1	$(-4.460 \pm 0.063) - (-4.561 \pm 0.042) = 0.101 \pm 0.105$

Table 4.22. Longitudinal separation of the PI-reconstructed vertices and RVER for the selected event in run 20645.

Invariant masses. The invariant masses measured for the dimuon, dipion and $\mu\mu\pi\pi$ with PID hypotheses are: $M_{\mu\mu} = 3.112 \pm 0.027\text{GeV}/c^2$, $M_{\pi\pi} = 0.499 \pm 0.003\text{GeV}/c^2$ and $M_{\mu\mu\pi\pi} = 5.316 \pm 0.112\text{GeV}/c^2$, which place them within 0.6σ , 0.6σ and 0.4σ of the nominal values for the invariant masses of the J/ψ , K^0 and B^0 respectively.

Distances of closest approach. Impact parameters. Longitudinal coordinates of vertices. These quantities are shown in table 4.21. The distances of closest approach (DCAs) for the dimuon and dipion RTRAs are consistent with the hypothesis that the pairs originate from a common vertex each. However, the DCA between the dipion and dimuon was evaluated with the PI tool to be $b_{\mu\mu}^{\pi\pi} = 1153 \pm 82\mu\text{m}$.

B^{neutr} flavour. The RTRA with highest p_T , not belonging to the dimuon or dipion, and with detector hits up- and downstream of the Magnet, has negative charge and a RICH PID of a proton. The corresponding flavour of the golden decay B^{neutr} is B^0 .

Conclusions. This is an event with very good indicators for the presence of a B^{neutr} golden decay, with flavour B^0 ; the charged RTRA used for flavour tag has a PID of an anti-proton. Though the longitudinal separation of the $\mu\mu$ and $\mu\mu\pi\pi$ vertices, found by the PI tool, are negative, the associated error is sufficient to intersect the result interval for the RVERs and ensure a consistent value. The production and decay vertices in this event are separated by roughly 1mm, which is about twice the quoted value for HERA- B 's longitudinal vertex resolution.

4.3.2 Two $B^+ \rightarrow J/\psi K^+$ candidate decays

Two events from the year 2002 selection were identified [119] as candidates for $B^+ \rightarrow J/\psi K^+$ decays (table 4.15) and are next studied briefly.

As was seen so far, the invariant mass and separation of RTRAs are good signs for the presence a given decay. In events 20545 and 20639, the PI tool selected an RTRA with K^+ PID as the flavour-tagging RTRA (highest p_T and “good” momentum). The DCAs of these RTRAs to the reconstructed RVER 2 (which have mass in the J/ψ region) for these two RTRAs are

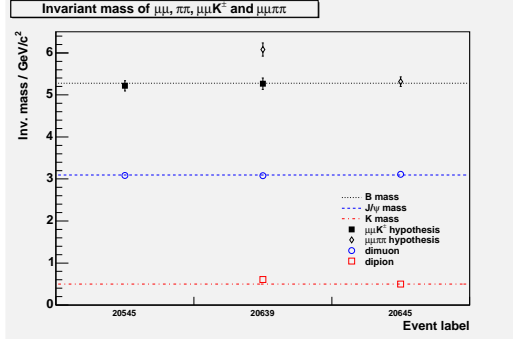


Figure 4.31. The hypotheses for $B^{\text{neutr}} \rightarrow J/\psi(\mu^+\mu^-)K^{\text{neutr}}(\pi^+\pi^-)$ and $B^\pm \rightarrow J/\psi(\mu^+\mu^-)K^\pm$ were tested with PI. The event from run 20545 has a good $\mu^+\mu^-K^\pm$ invariant mass combination near the B mass, whereas for the event in run 20639 the $\mu\mu K$ combination (filled square) is favoured when compared to the $\mu\mu\pi\pi$ (open losangle). The event from run 20645 is shown on the right for comparison.

$b_{K^+}^{\text{RVER } 2} = 150 \pm 104 \mu\text{m}$ and $b_{K^+}^{\text{RVER } 3} = 88 \pm 43 \mu\text{m}$, respectively for run 20545 and run 20639. These distances are close enough to be consistent with the hypothesis of a $B^+ \rightarrow J/\psi(\mu^+\mu^-)K^+$ decay. The hypotheses for this and a golden decay $B^{\text{neutr}} \rightarrow J/\psi K_S$ were tested, and it was found that the former is favoured relative to the later for the two events in runs 20545 and 20639, see figure 4.31. The coordinates for the point of closest approximation between the dimuon and the K^+ for the two events is at $z \simeq 7.5\text{cm}$, but with an undetermined error; this idiosyncrasy is likely due to limitations of the present tool code.

In event 20545, no good $\pi^+\pi^-$ hypothesis, in the K^{neutr} mass region, was found by the PI tool. In event 20369, a candidate dipion candidate for a K^{neutr} decay was found by PI, however its invariant mass ($0.606 \pm 0.004\text{GeV}/c^2$) falls outside the sought mass value and the tracks are borderline detached — $550 \pm 66 \mu\text{m}$. The distances of closest approach are included in the next subsection.

4.3.3 Comparison with run selection from year 2000

The selected events from the year 2000 sample are compared with the three events from year 2002. In terms of the invariant masses of reconstructed B candidates, the events from the last run period have better quality than those from the year 2000 — at least for this limited sample. Two hypotheses were tested when searching for B candidates — golden decays $B^{\text{neutr}} \rightarrow J/\psi(\mu^+\mu^-)K_S(\pi^+\pi^-)$ (figures 4.32 and 4.33); and decays $B^\pm \rightarrow J/\psi(\mu^+\mu^-)K^\pm$ (figures 4.34 and 4.35).

4.4 Conclusions

As is seen in figures 4.6 and 4.4, by selecting pairs of reconstructed tracks with sufficient transverse momentum (e.g. $p_T \gtrsim 0.8\text{GeV}/c$) and minimum separation (e.g. $b_{\mu\mu} \lesssim 200\mu\text{m}$), it is possible to improve the significance of

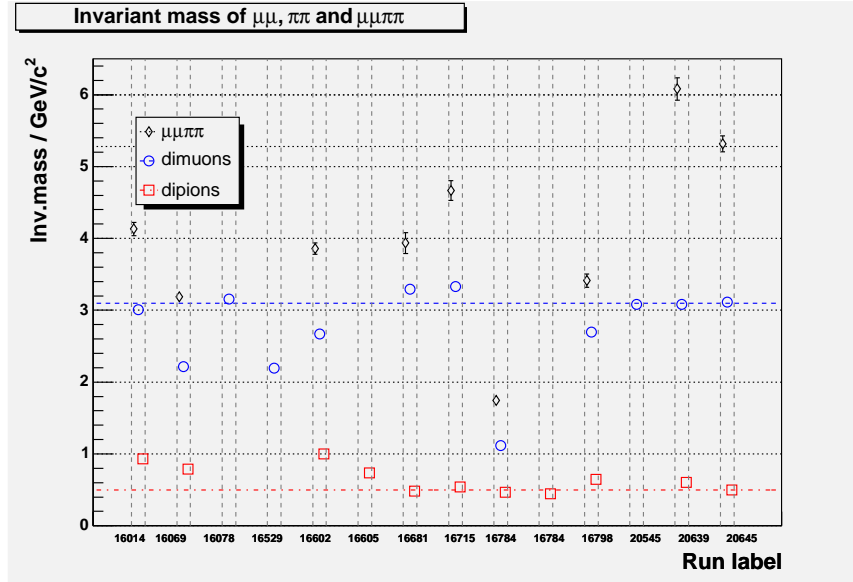


Figure 4.32. Invariant mass of RTRA sets for the golden decay hypothesis, $B_d^{neutr} \rightarrow J/\psi(\mu^+\mu^-)K_S^0(\pi^+\pi^-)$ from the event sample in table 4.15. Values computed with PI.

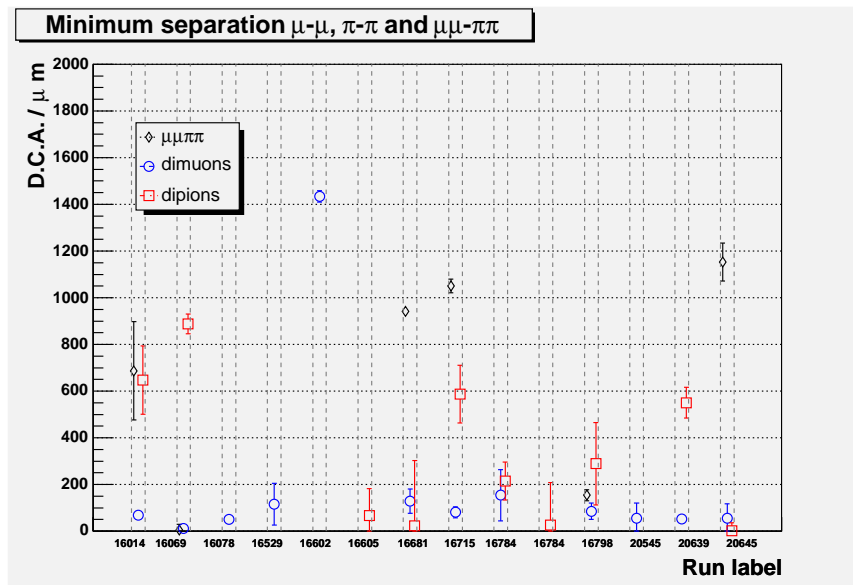


Figure 4.33. Distance of closest approach (DCA) of RTRA sets for the golden decay hypothesis, $B_d^{neutr} \rightarrow J/\psi(\mu^+\mu^-)K_S^0(\pi^+\pi^-)$ from the event sample in table 4.15. Values computed with PI.

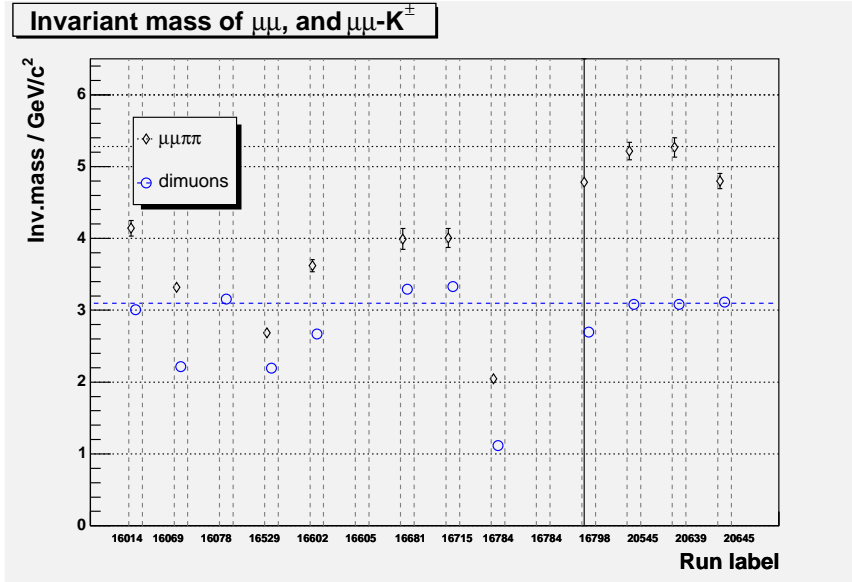


Figure 4.34. Invariant mass of RTRA sets for the $B^\pm \rightarrow J/\psi(\mu^+\mu^-)K^\pm$ decay hypothesis, from the event sample in table 4.15. Values computed with PI.

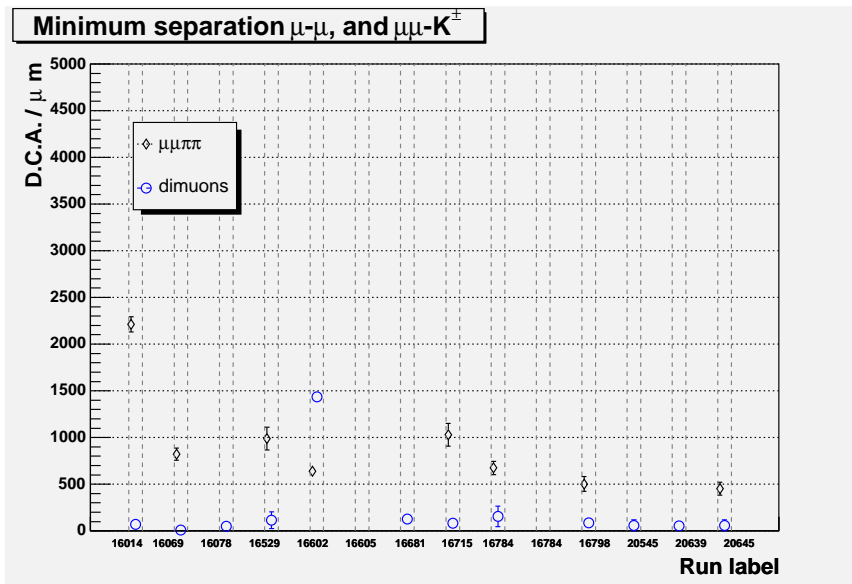


Figure 4.35. DCA of RTRA sets for the $B^\pm \rightarrow J/\psi(\mu^+\mu^-)K^\pm$ decay hypothesis, from the event sample in table 4.15. Values computed with PI.

the $J/\psi \rightarrow \mu\mu$ signal by a factor of ~ 2.5 without important changes on the signal amplitude. The Monte-Carlo truth of the simulated events shows the number of RTRA pairs with mass $3.1 \pm 0.4 \text{ GeV}/c^2$ selected with the $p_T > 0.8 \text{ GeV}/c$ cut is $\sim 23\%$ of the expected number of J/ψ s in a sample of 6750 events (1 J/ψ per event).

A high-quality sample of Monte Carlo golden decay events was reconstructed with ARTE and studied to verify the presence of indicators for that decay. The requirement that the four reconstructed tracks $\mu^+\mu^-\pi^+\pi^-$ have detector hits up- and downstream of the Magnet — to ensure good momentum resolution — limited the fraction of ~ 450 Monte Carlo events down to only 7. Of these, 5 events were reconstructed with dimuon and dipion masses up to 3σ of the nominal masses of the J/ψ and K^{neutr} ; in the other two events, the dipion mass was too far from the expected values because the RTRAs selected by the analysis tool PI did not correspond to the Monte Carlo $K_S^0 \rightarrow \pi^+\pi^-$ tracks. The B^{neutr} masses were poorly reconstructed and spread out in a $\sim 1.5 \text{ GeV}/c^2$ -wide band centered on the B nominal mass. Only the event labeled “235” has all three reconstructed masses within 3σ of the expected values. Concomitantly, the minimum separations between the muons, pions and $\mu\mu-\pi\pi$ pairs were below $200\mu\text{m}$ for that same event. In the remainder of the sample, the $\mu\mu-\pi\pi$ separation was above $500\mu\text{m}$ although the dimuons and dipions were separated by less than $200\mu\text{m}$.

Three $B \rightarrow J/\psi(\mu\mu)K$ events from the year 2002 run epoch were studied and the results from reference [119] were confirmed. One event is an excellent candidate for a golden decay, whereas the other two are classified as $B^+ \rightarrow J/\psi(\mu^+\mu^-)K^+$ candidates. The two hypotheses were tested on those events, and the track combination yielding the mass closest to the B 's was chosen; it was also found that the K^+ in the two events passes at less than $100\mu\text{m}$ of the dimuon vertex. The B flavour of the golden decay is B^0 , given that in the remaining RTRA sample the highest- p_T track has negative charge.

Detector misalignment and single event reconstruction

This chapter shows the results obtained with HERA-*B*'s event reconstruction software (ARTE), used on the Monte Carlo golden decay event labeled “235” (section 4.2.1), under the influence of translations of VDS modules and of whole subsystems (VDS, Main Tracker, RICH and Muon Detector system). Many plots presented here are color-coded profile histograms representing the variation of selected quantities in terms of displacements in the direction of the z , x and y axes. These studies sought to obtain the scale at which visible modifications due to detector translations produce different results at event reconstruction. Those quantities are listed in appendix A, where the respective results are also shown; some of those plots are reproduced in this chapter in larger print.

The translations of modules and detector systems were done along the coordinate directions individually, and follow a logarithmic sequence from $10\mu\text{m}$ up to 5cm, with three values per decade — e.g. $10\mu\text{m}$, $20\mu\text{m}$, $50\mu\text{m}$, $100\mu\text{m}$ and so on. For VDS module displacements Δz , Δx and Δy , additional samples at different step sizes were taken to improve granularity at the millimeter and centimeter scale: 1mm-steps for displacements $|\Delta i| < 1\text{cm}$; 2mm-steps for $1\text{cm} < |\Delta i| < 2\text{cm}$; and 1cm-steps for $2\text{cm} < |\Delta i| < 5\text{cm}$ ($i = z, x, y$). The sign of the Δi displacements is the same as the axes' notation denoted in figure 3.7 (left) on page 39. This choice of complementary displacement measurements causes the dashed vertical band patterns visible in the profile histograms in this chapter and in section A.1 in appendix, and therefore are not related to any detector- or reconstruction-related artifacts.

Only those VDS modules with hits belonging to the dimuon RTRAs from the J/ψ decay, which were measured for the undistorted detector, were used; see figures 5.1–5.3. The effect of moving other modules to, e.g., cause more hits to be included in those RTRAs' reconstruction, was not investigated.

The translations of detector modules were performed by the routine `remaskGEDE` (section E.2 in the appendices). This C language routine ran inside ARTE to shift modules, as well as the digitized hits' positions (relative

to the unchanged reference frame) before the event reconstruction step. The events were then reconstructed from the shifted hits. The $\mu\mu$ and $\mu\mu\pi\pi$ symbols refer to the sets of RTRAs used with the PI tool from RTRA data; the RVERs (labeled “RVER1” and “RVER2”) were extracted from ARTE.

The effect of rotations, shear or torsions on the event’s reconstruction was not studied. In reference [76] these effects are discussed (necessarily spanning over a sizeable event sample and not just one event) in the context of HERA-*B* Global Alignment (the geometric disposition of detectors relative to each other, i.e. between VDS, Main Tracker, and so on).

5.1 VDS module displacements

For the dimuon reconstructed in the vertex, the μ^+ (μ^-) is directed to the first (third) quadrant in the xy plane as seen from the target: the slopes in the zx and zy planes are $tx \equiv p_x/p_z \simeq 0.0471$ (-0.0450) and $ty \equiv p_y/p_z \simeq 0.0009$ (-0.0338) respectively — see figure 5.2.

Figure 5.1 shows the VDS segments of the dimuon RTRAs for this event, seen in a 3D view with PRISM. To measure the RTRAs’ momenta, their bending in the Magnet is computed by ARTE by fitting the VDS segments with Main Tracker segments (not shown in figure) and assuming they cross at mid-Magnet $z_{\text{Magnet}} \simeq 450\text{cm}$ (see section B.3). The RTRAs’ VDS hits are measured from superlayers 4 through 6, $z_{\text{SL4}} \simeq 40\text{cm}$, $z_{\text{SL5}} \simeq 65\text{cm}$ and $z_{\text{SL6}} \simeq 100\text{cm}$; see figure 5.3. The contributions from the different VDS modules are best visible for superlayer 4 ($z_{\text{SL4}} \simeq 40\text{cm}$). These superlayer’s modules are closer to the beamline than the modules downstream, therefore they are longitudinally shifted so they do not collide during normal operation position; see figure 5.3. For superlayer 4, the leftmost colored slits (joined) correspond to the μ^+ and the other two (which are seen with a small interval between them) correspond to the μ^- ; see also figure 5.3.

The color-coded 2D profile histograms representations of quantities was chosen to find out both the magnitude of displacements resulting in different values, and also whether it occurs for displacements closer or farther from the Target. The number of possible combinations for displacements that one can formulate is, obviously, huge. Therefore only a small set of VDS modules were chosen for measuring the effects displacements, namely those modules used to reconstruct the dimuon RTRAs’ segments in the Vertex Detector. The histograms in figures 5.4, 5.6, 5.8 and 5.10 represent some of the quantities plotted in appendix A for displacements in the beamwise direction (z axis).

In the histograms in figures 5.5, 5.7 and 5.9, each point is the average of the represented quantities over the VDS modules for the given displacement; in effect, e.g. the plots for displacements Δz represented therein are projections of the histograms in figures 5.4, 5.6 and 5.8 over their respective

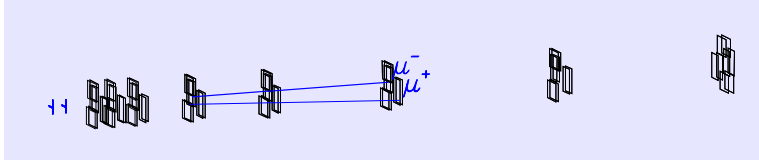


Figure 5.1. The dimuon RTRAs in event 235 (section 4.2.1), seen in 3D perspective from the outer radius of HERA. Only the VDS modules (rectangles) and Target (far left) are shown; the proton beam passes through from left to right. The remainder of the dimuon RTRAs includes segments from the Main Tracker and Muon detector (not shown), which are matched by ARTE.

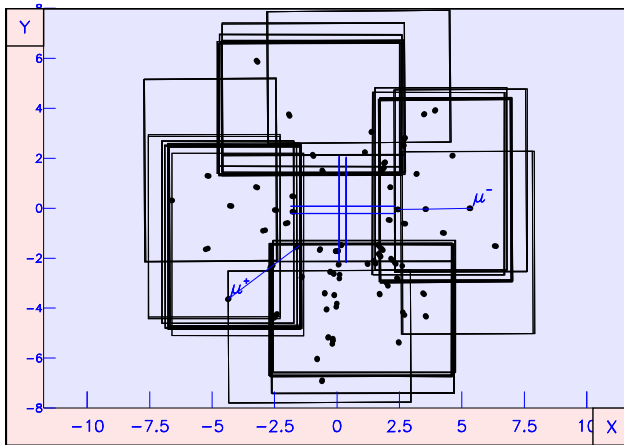


Figure 5.2. PRISM XY projection of the VDS modules (rectangles) and target wires (vertical and horizontal blue segments, center). The reconstructed VDS hits are shown as black dots. The dimuon RTRAs are also painted, see figure 5.1. The axes' scales are in centimeters.

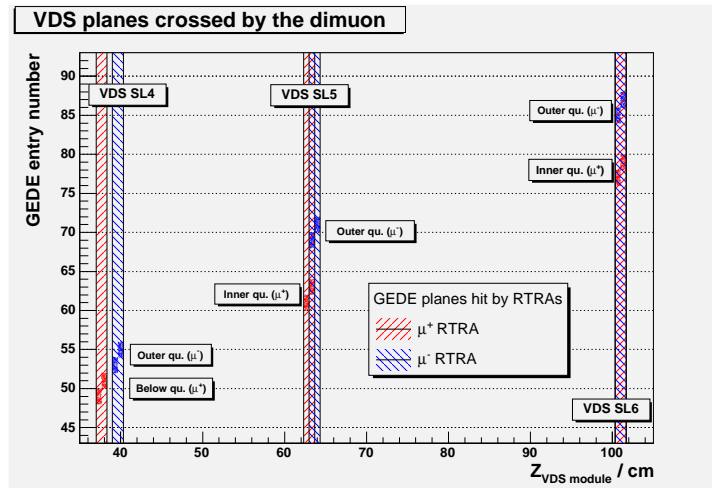


Figure 5.3. The dimuon RTRAs (figure 5.1) were detected by VDS modules of superlayers 4–6. The “inner”, “outer” and “below” quadrant labels refer to the VDS modules' positions. Horizontal axis: VDS modules' longitudinal coordinate. The vertical bands are bounds for the respective modules' position. Vertical axis: module index number.

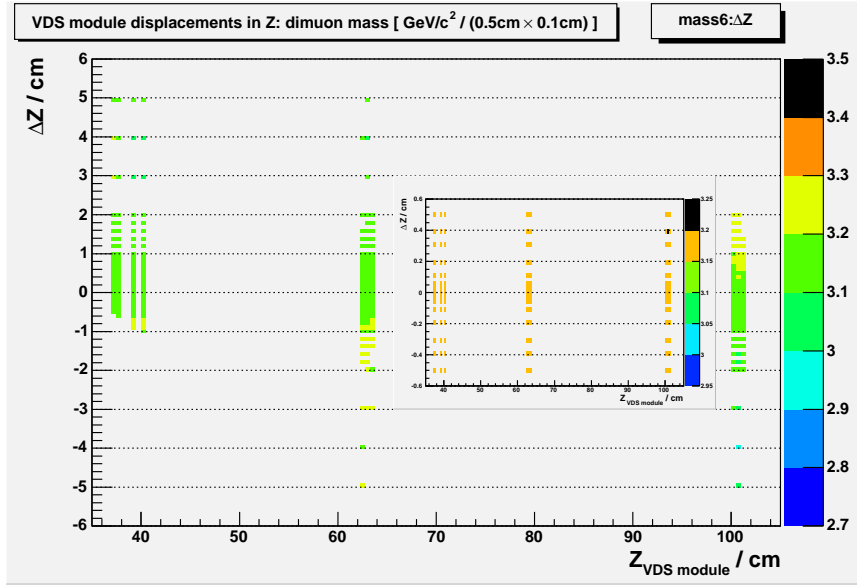


Figure 5.4. Invariant mass of RTRA pair identified with the dimuon from the J/ψ decay, for translations of VDS modules in the z direction (measured in the vertical axis); see figure A.5 for similar plots for translations in x and y . The mass was computed from RTRA parameters with PI (see section E.1). The horizontal axis refers to the modules' z position ($Z_{VDS\ module}$) according to table GEDE (i.e. in the absence of translation); see figure 5.3. Only the VDS modules with dimuon hits were analysed. The histogram bin size is $0.5\text{cm} \times 0.1\text{cm}$. The inset shows only displacements $|\Delta z| < 0.6\text{cm}$. See the discussion on main text (page 147) concerning the “dashed” plot structure for $1\text{cm} < |\Delta z| < 2\text{cm}$.

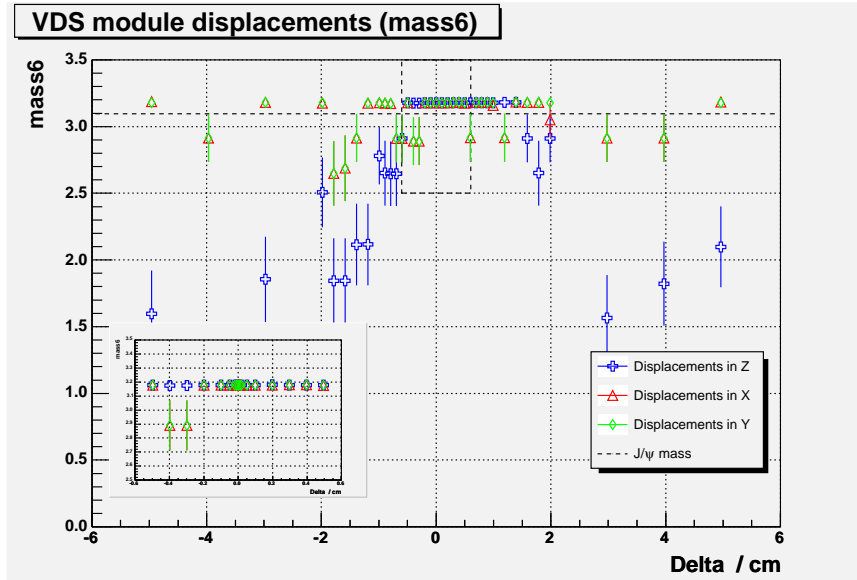


Figure 5.5. Dimuon invariant mass (in GeV/c^2) for displacements of the VDS modules with the J/ψ 's dimuon reconstructed hits, in the z (+), x (Δ) and y (\diamond) directions. The nominal value of the J/ψ mass is marked by a horizontal dashed line near $3.1\text{GeV}/c^2$. The marks for Δz displacements represent a projection of the histogram in figure 5.4 along its yy axis; the other two marks sets are for their respective displacements (see histograms in figure A.5). The error bars represent the root mean square of the values in each yy bin for the corresponding module translations Δz , Δx , Δy . The inset plot is a detail for $|\Delta z| < 0.6\text{cm}$ (boxed square in the main plot).

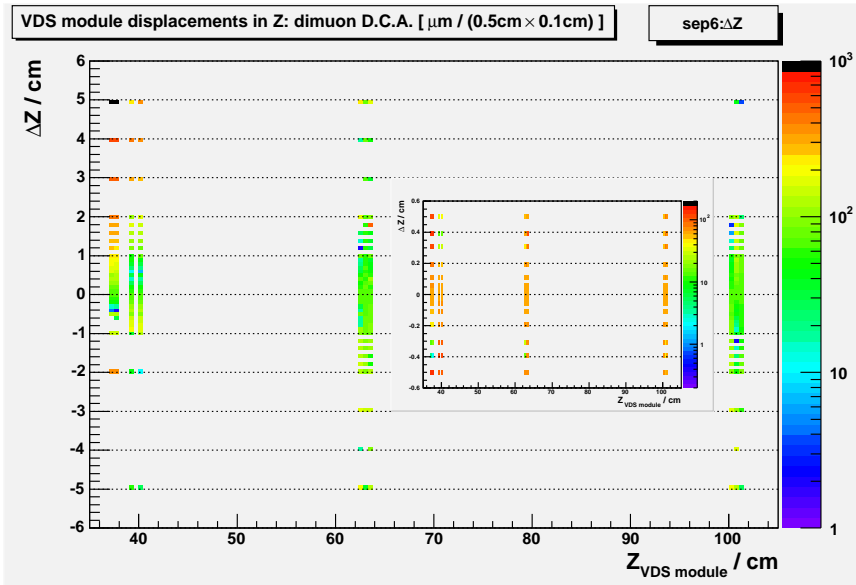


Figure 5.6. Histogram similar to the one shown in figure 5.4, but here for the minimum separation (measured in μm) between the μ^+ and μ^- RTRAs from the J/ψ dimuon. Notice the color scale is logarithmic. See figure A.7 for the results of VDS module displacements in x and y . The minimum separation was computed with PI from RTRA information.

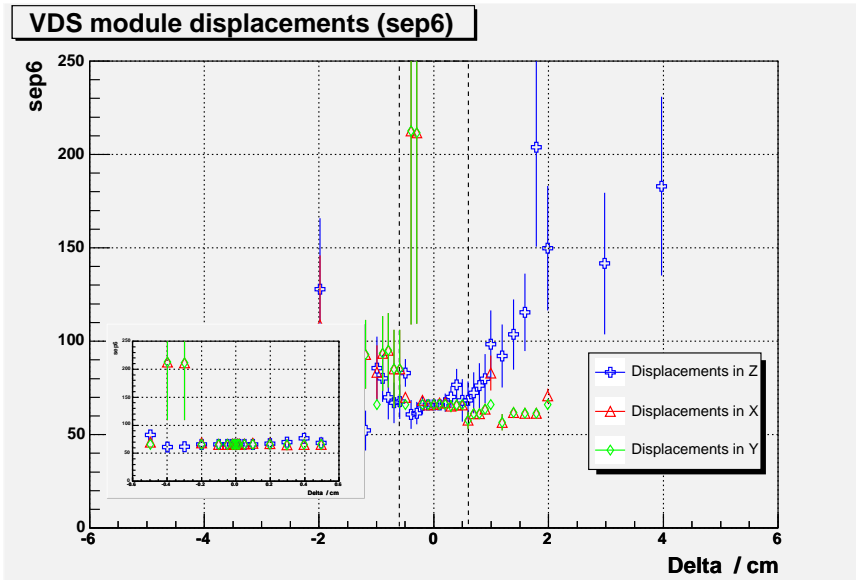


Figure 5.7. Plot similar to figure 5.5, but representing the $\mu^+ - \mu^-$ minimum separation (measured in μm), for Delta displacements of the VDS modules with J/ψ dimuon hits. The inset plot is for displacements $|\Delta_i| < 0.6\text{cm}$ (dashed rectangle in the main plot).

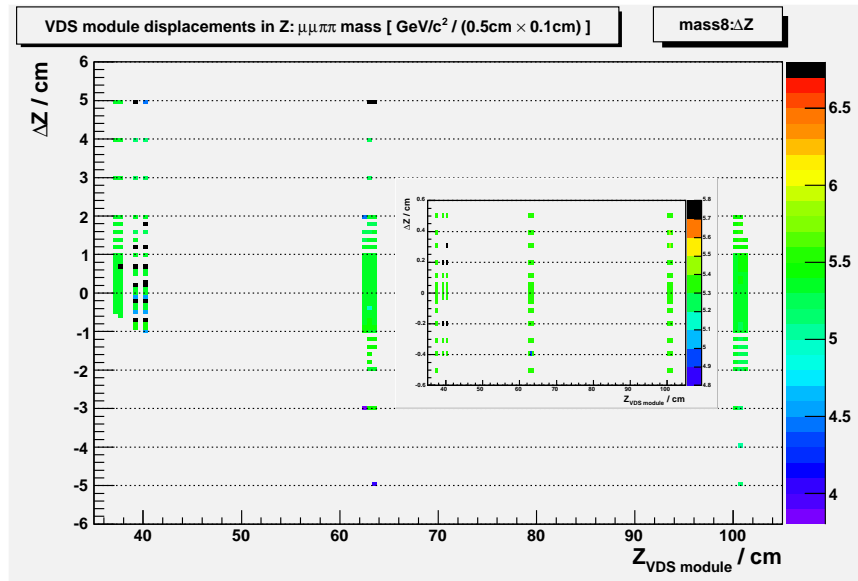


Figure 5.8. Histogram similar to the one shown in figure 5.4, but here for the $\mu\mu\pi\pi$ mass (measured in GeV/c^2) from RTRA information. The inset plot is for displacements $|\Delta z| < 0.6\text{cm}$. See figure A.19 for the results of VDS module displacements in x and y . The $\mu\mu\pi\pi$ mass was computed with the PI tool from the four RTRAs' information.

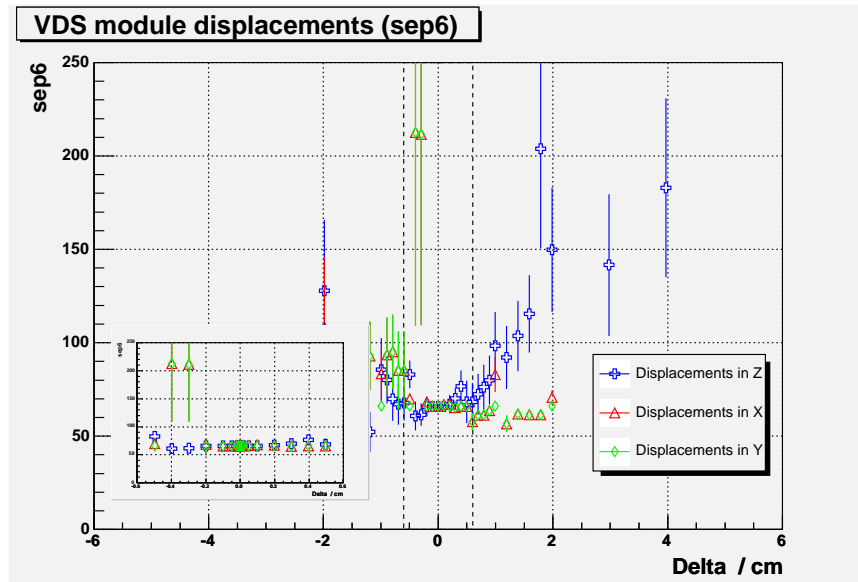


Figure 5.9. Plot similar to figure 5.5, but representing the $\mu\mu\pi\pi$ mass (in GeV/c^2) from RTRA table data, for Delta displacements of the VDS modules with J/ψ dimuon hits. The inset plot is for displacements $|\Delta_i| < 0.6\text{cm}$ (dashed rectangle in the main plot).

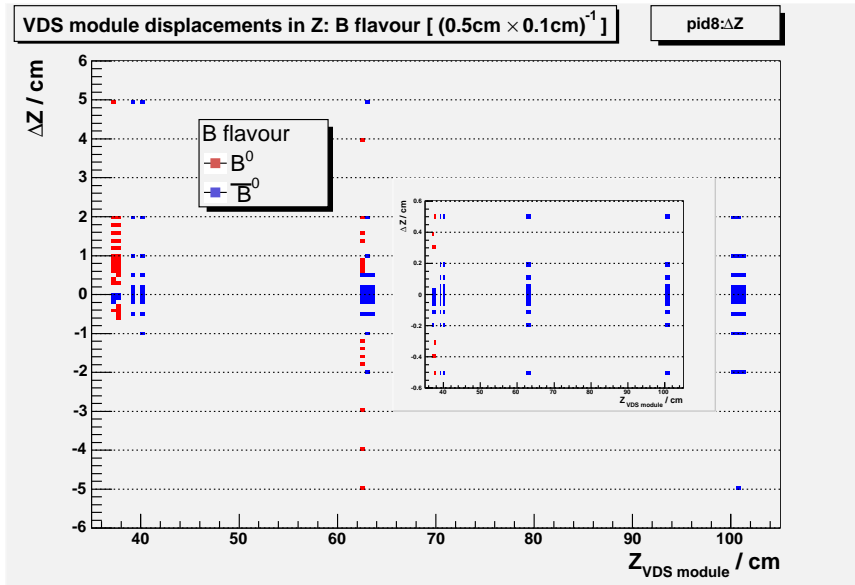


Figure 5.10. Histogram similar to the one shown in figure 5.4, but here for the $B^{\text{neutr.}}$ flavour from the reconstructed golden decay for z displacements of the VDS modules with J/ψ RTRA dimuon hits. The inset is for displacements $|\Delta z| < 0.6\text{cm}$. See figure A.32 for the results of VDS module displacements in x and y . The result was obtained from computation with the PI tool.

yy axes. For each quantity, the error bars' amplitudes are $\sqrt{X/N}$ for N entries of quantity X (see the ROOT manual [37]). In those histograms, a dashed rectangle depicts the bounds of the inset plot.

5.1.1 Discussion

Variations of the explored quantities (figures 5.4–5.10 and figures A.1–A.32 in section A.1 in appendix) become noticeable for displacements at a scale of $|\Delta| \gtrsim 0.2\text{cm}$. These quantities do not show visible variations when the VDS module displacements are below this value; see insets ($-0.6\text{cm} < \Delta < 0.6\text{cm}$) in the profile histograms.

The same profile histograms also show that the variations for x and y displacements are steeper than those for z displacements. This can be interpreted attending to the strong Lorentz boost of the proton–nucleus center of mass in the beam direction (z axis). The number of degrees of freedom (dof) of the RTRAs are related to the number of hits associated with the track, see equation 3.9 in page 86. Therefore, its variation (figure A.1) can be used as a signature for the possible disassociation of a VDS module hit from the reconstructed track.

The quantities related to the dimuon, see e.g. figure 5.4 or figure 5.10 (in appendix, figures A.3, A.4, A.5, A.7, A.8, A.11, A.12, A.13, A.14) have missing points for $\Delta z_{\text{SL } 4} \lesssim -0.5\text{cm}$ and lower. For those displacements of

superlayer 4 modules, the dimuons lose the VDS segment and are therefore not properly reconstructed. Attending that proper reconstruction of VDS segments requires a minimum number of hits in different superlayers (e.g. 3 or more consecutive layers for “good” reconstruction), this can be interpreted by the fact that the dimuons’ VDS segments vanish for such displacements.

The variation of the B flavour tagging for VDS module displacements was also evaluated (figure 5.10 for Δz displacements, see also figure A.32). The tagging may be lost for displacements as low as $|\Delta z|, |\Delta x| \simeq (0.05 - (-0.2))/2 \simeq 0.2\text{cm}$, and it was also found on some instances that wrong tagging appears for displacements above 0.2cm. The most influential modules for this event’s flavour tag are those closest to the target; one of the dimuon’s RTRAs shares a VDS module with the RTRA used for flavour tag, and consequently those module’s displacements reflect on the flavour reconstruction (painted as red marks in the figures). More points are missing on figures 5.10 and A.32 than on other figures from section 5.1 due to the stringent requirements of good dimuon and dipion masses (for the $\mu\mu\pi\pi$) and good tagging RTRA momentum.

5.2 Displacements of the VDS, Main Tracker, RICH and Muon Detector systems

In this section, the histograms shown are for displacements of entire sub-detectors in the direction of coordinate axes z , x and y . The VDS and Main Tracker were chosen due to their importance in track recognition and momentum determination. The influence of RICH and Muon detector displacements below 5cm was also investigated.

In the RICH and MUON detector histograms, there are less available points; for these, it was felt that the histogram granularity requirements could be relaxed. The sequence of sampled displacements follow a logarithmic scale with three values per decade n (i.e. 1×10^n , 2×10^n , 5×10^n).

5.2.1 Discussion

The detectors with most influence on the reconstruction of the Monte Carlo event are the VDS and, to a lesser extent, the Main Tracker modules.

The histograms in figures A.33–A.71 show that Main Tracker displacements have influence on the number of RTRAs, RVERs and hits associated to the RTRAs (figures A.33–A.36) for displacements $|\Delta z_{\text{M.Tr.}}|, |\Delta y_{\text{M.Tr.}}| \gtrsim 0.2\text{cm}$ and $|\Delta x_{\text{tracker}}| \lesssim 0.02\text{cm}$. However, they produce no visible effect on other quantities such as resonance masses, D.C.A.s and impact parameter to target wire.

The same figures show that Δz_{VDS} displacements of the VDS vessel

produce shallower variations of the measured quantities, whereas Δx_{VDS} shifts yield steeper variations. The event's reconstruction shows sensitivity for VDS displacements similar to those found for the Main Tracker displacements — $|\Delta z_{\text{VDS}}|, |\Delta y_{\text{VDS}}| \gtrsim 0.2\text{cm}$ and $|\Delta x_{\text{VDS}}| \gtrsim 0.02\text{cm}$. However, as expected, the VDS displacements' influence on more quantities (vertex coordinates, impact parameters, etc.) is visible. The $\mu\mu\pi\pi$ mass (figure A.51) was modified by VDS displacements above $\approx 0.2\text{cm}$, whereas the primary vertex's mass (see e.g. figure 5.12 for Δz and figure A.52 in appendix for this and other axis orientations) is altered by VDS displacements $|\Delta z|, |\Delta x| \gtrsim 0.01\text{cm}$ and $|\Delta y| \gtrsim 0.2\text{cm}$.

Displacements of the RICH vessel and Muon detector produced no visible effects on the reconstructed quantities, except for $1\text{cm} \simeq |\Delta Z| \simeq 2\text{cm}$ displacements of the Muon detector in the Particle ID of the tagging RTRA (π^+ to π^- , resulting in differing B flavour reconstruction), see figure A.70. This result is coherent with the $o(1\text{cm})$ size scale of the Muon Detector system cells (see section 3.2.10).

5.3 Conclusions

The principal focus of this chapter was on quantities related to the dimuon and the $\mu\mu\pi\pi$. The former is relatively easy to separate from the hadron background — the FLT/SLT are designed to make best use of the narrow width of the J/ψ resonance — and the later is important for tagging of golden decay events. These and other quantities are referenced in appendix A.

In section 5.1, the twelve VDS modules used to reconstruct the dimuon in the analysed event (section 4.2.1) were displaced individually in orthogonal directions (z , x and y) to obtain the variation of quantities, such as dimuon invariant mass and separation, under module displacement. In section 5.2, four detectors (VDS, ITR+OTR, RICH and Muon detector) were each displaced as a whole unit to again obtain the variation of those same quantities.

The histograms shown in this chapter and appendix A have visible variations of the plotted quantities for displacements at the scale of 1mm–2mm. Such variations are more noticeable for VDS displacements. Except for a small number of Main Tracker displacements, attributable to fortuitous combinations of hits that ARTE used to reconstruct tracks,¹ there is no visible influence of Main Tracker displacements on the RVER, dimuon and $\mu\mu\pi\pi$ masses. The transverse momentum of the highest- p_T RTRA, used to tag the B^{neutr} flavour, did not suffer significant modifications for Main Tracker displacements.

¹The nature of these reconstructions was not explored.

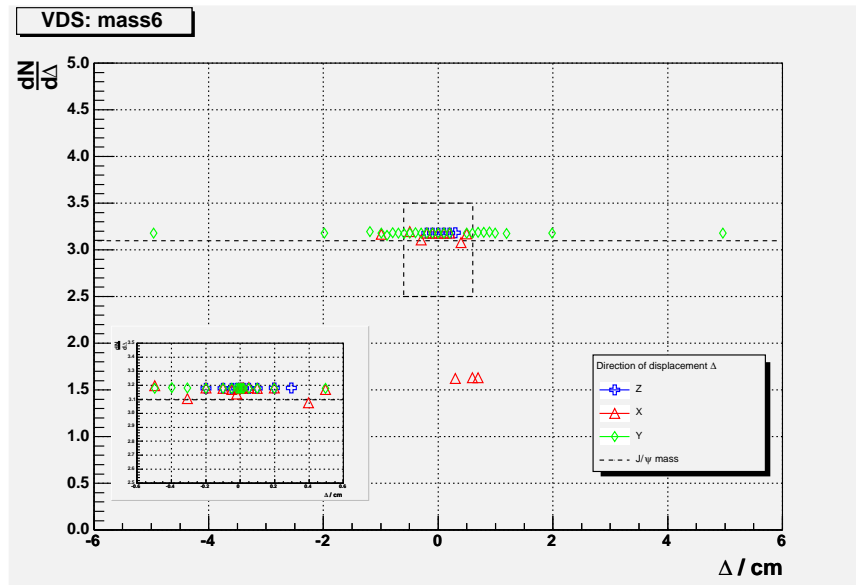


Figure 5.11. The whole VDS system is displaced in the z , x and y directions, by amounts given in the horizontal axis. The J/ψ 's dimuon mass remains mostly within the range of the nominal value (dashed horizontal line), except for a few displacements in the x direction. The inset is for displacements $|\Delta_i| < 0.6\text{cm}$. Computed from RTRA values with PI. See figure A.37 for the results of translations of the Main Tracker, RICH and Muon Detector systems.

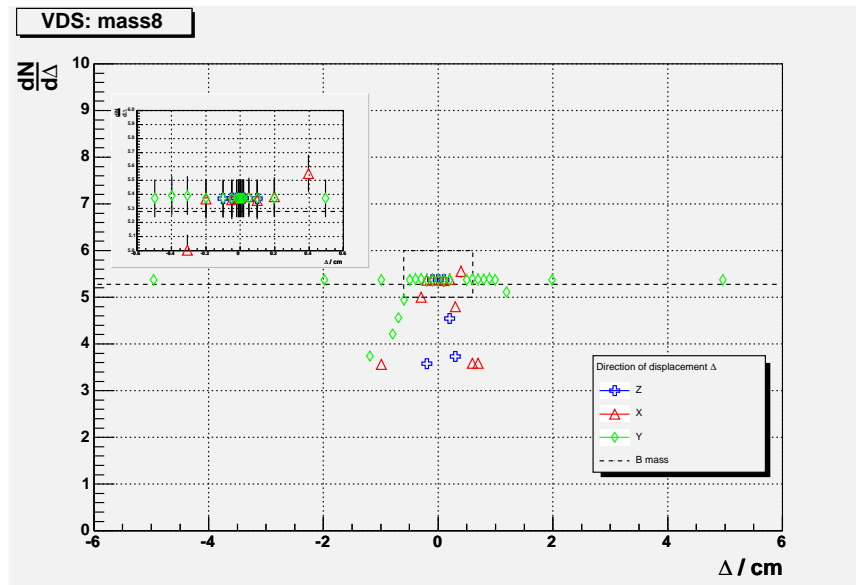


Figure 5.12. Plot similar to figure 5.11, but representing the $\mu^+\mu^-\pi^+\pi^-$ invariant mass in GeV/c^2 . Contrary to figure 5.11, there is visible withdrawal from the nominal value (horizontal dashed line) for displacements from 0.2cm – 0.3cm in the z and x directions; variations for detector displacements in the y direction are only sensible in the centimeter scale. The inset plot is for displacements $|\Delta_i| < 0.6\text{cm}$ (dashed rectangle in the main plot). The mass values were computed from RTRA values with PI. See figure A.51 for results on Main Tracker, RICH and Muon Detector systems.

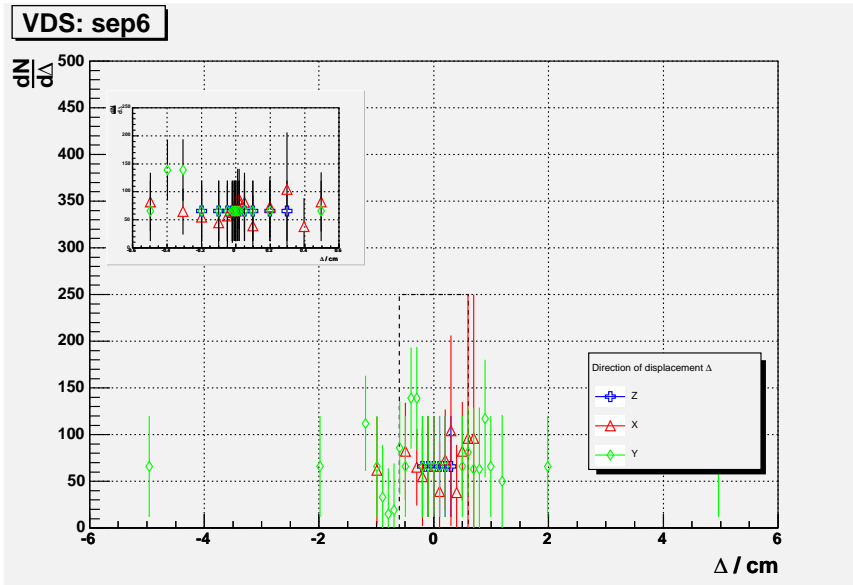


Figure 5.13. Plot similar to figure 5.11, but representing the J/ψ 's dimuon minimum separation (in μm). The inset plot is for displacements $|\Delta_i| < 0.6\text{cm}$ (dashed rectangle in the main plot). See figure A.39 for results on Main Tracker, RICH and Muon Detector systems.

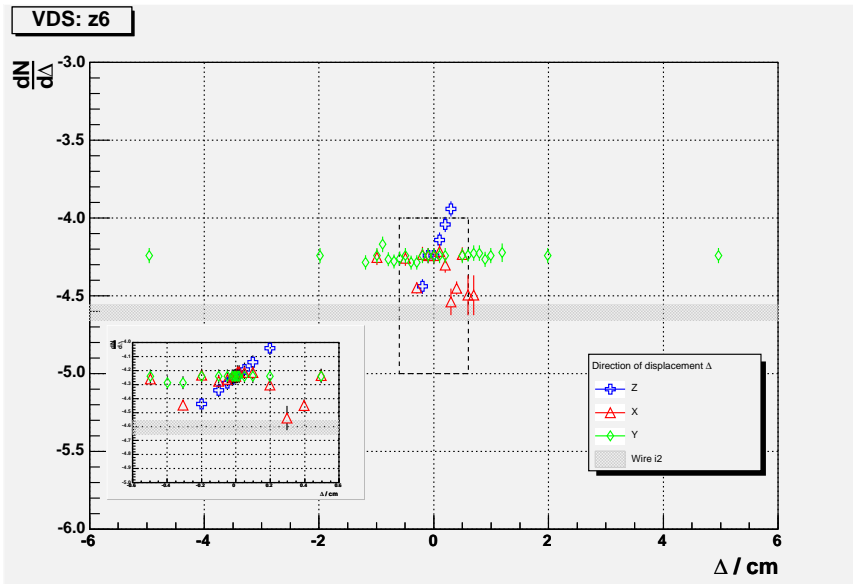


Figure 5.14. Plot similar to figure 5.11, but representing the J/ψ 's dimuon longitudinal coordinate $z_{\mu\mu}$ (in cm). The target wire's bounds are represented by the horizontal gray band. The inset plot is for displacements $|\Delta_i| < 0.6\text{cm}$ (dashed rectangle in the main plot). The $z_{\mu\mu}$ quantity was computed with PI. See figure A.40 for results on Main Tracker, RICH and Muon Detector systems.

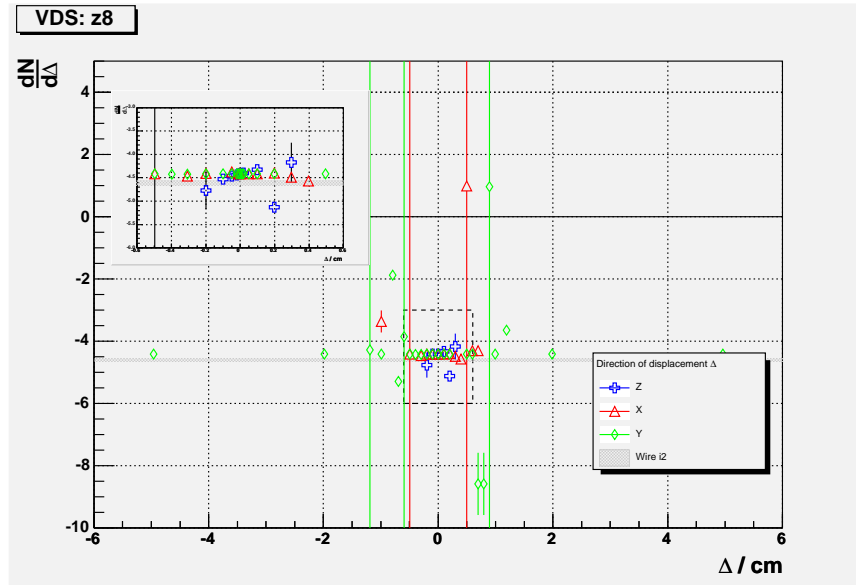


Figure 5.15. Plot similar to figure 5.11, but representing the $\mu\mu\pi\pi$ longitudinal coordinate $z_{\mu\mu\pi\pi}$ (in μm), computed with PI. The target wire's bounds are represented by the horizontal gray band. The inset plot is for displacements $|\Delta_i| < 0.6\text{cm}$ (dashed rectangle in the main plot). See figure A.54 for results on Main Tracker, RICH and Muon Detector systems.

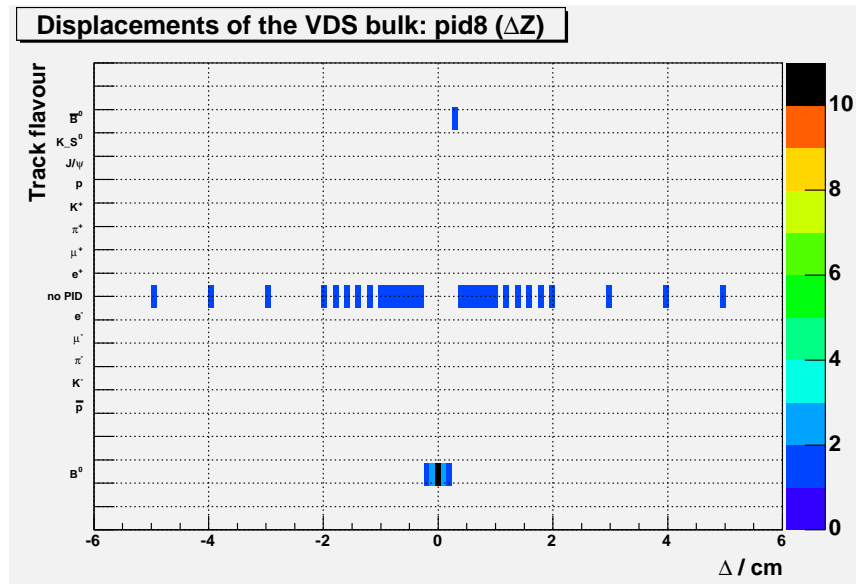


Figure 5.16. Plot similar to figure 5.11, but representing the golden decay B meson flavour under VDS displacements Δ , obtained from the charge tag of the highest- p_T RTRA. The rectangles on top are for \bar{B}^0 flavour tags, and the rectangles on bottom for B^0 ; the rectangles in the middle of the plot are for untagged reconstructions. The color scale is for the number of histogram counts in the 0.1cm -wide bins of the horizontal axis. See figures A.67, A.69 and A.71 for results on Main Tracker, RICH and Muon Detector systems, respectively.

We therefore see how the geometric placement of the Silicon Vertex Detector system is of large importance for the adequate reconstruction of vertices. The reconstruction of this single Monte Carlo event for a golden decay $B \rightarrow J/\psi(\mu\mu)K_S(\pi^+\pi^-)$ suggests the VDS geometric location should be well known. The figures 5.4–5.10 in section 5.1 and the figures A.1–A.32 in appendix A.1 indicate that it is necessary to correctly place the VDS modules to (at least) within $\approx 0.2\text{cm}$ of their nominal positions. Those histograms also suggest that the reconstruction of the dimuon is dependent on the location of the upstreammost module used to reconstruct the track. In the analysed event, this effect is evident for displacements $\Delta z \lesssim -0.5\text{cm}$. The results of sections 5.2 and A.2 suggest that the global alignment of the VDS relatively to its expected position should be known to within the millimeter in the z and y coordinates, and to the tenth of millimeter in the x direction.

Concluding remarks

Measuring $\hat{C}\hat{P}$ violation requires, on one side, a substantial set of relevant events measured with the detector, and on the other side, a good choice of selection criteria to reject events based on their topology (e.g. high- p_T tracks with invariant mass in a chosen range). The “best” $\hat{C}\hat{P}$ violation channels in the B meson system incorporate a series of traits such as relatively high branching ratios and sufficient amplitude of the intervening $\hat{C}\hat{P}$ -violating phases; one of the most favorable cases is the so-called “golden decay”, $B^0 \rightarrow J/\psi K_S^0$. This decay is far from being the perfect tool for measuring $\hat{C}\hat{P}$ violation: on one hand, it is rare (although by comparison with other $\hat{C}\hat{P}$ -violation B decays it has a reasonably high probability of occurrence); on the other hand, it still requires somewhat stringent selection criteria to isolate these decays from background. As is expected, these criteria also wrongly reject eligible events — and wrongly accept false positives — by a fraction that might be estimated through Monte-Carlo studies of detector and selection efficiencies [93].

In face of the selection criteria, a high-quality “clean” event sample might be scantily populated. For example, in reference [142], a single event measured in the HERA- B detector passed the analysis’ selection criteria tests, although the Monte Carlo population used in analysis was slightly more substantial (47 events). In spite of the small samples, some physics results may be obtained in the form of production cross sections and/or upper limits, although with relatively high associated uncertainties; however, the scarcely populated samples make $\hat{C}\hat{P}$ violation-related analyses that much difficult in face of the projected $o(10^3)$ -size sample [108]. Due to this reason and to the loss of competitiveness of HERA- B to other $\hat{C}\hat{P}$ -violation measuring experiments, the interest of HERA- B was diverted to other physics subjects (see section 3.7).

Stringent criteria were applied to select a set of Monte Carlo B^{neutr} golden decays. In a sample of 415 events, only 7 events were reconstructed with $\mu^+\mu^-\pi^+\pi^-$ tracks with enough hits to provide adequate track momentum measurement. The dimuon vertices in these events were reconstructed with mass within 5σ of the J/ψ mass, and in 5 events a dipion was also recon-

structed within 5σ of the K_S mass. Only 2 of the 7 events were reconstructed by ARTE with an RTRA from the second b hadron decay in the events. A single event has passed all these criteria (section 4.2.1) and has the three resonances' masses within 1σ of the nominal masses of the J/ψ , K^{neutr} and B^{neutr} . This Monte Carlo event was used in chapter 5 to study the influence of detector displacements in the event's reconstruction of tracks and vertices.

The same analysis was done on a sample of three events from HERA- B 's year 2002 run period (section 4.3). Two events were identified as candidate events for $B^+ \rightarrow J/\psi K^+$ decays, and one other as a golden decay candidate; the reconstructed masses and transverse momenta agree with reference [119], from where they were selected.

The single Monte Carlo golden decay identified in chapter 4 was reconstructed under several detector displacements in chapter 5. It was found that the VDS produces the largest variability of quantities for the analysed event. VDS module displacements greater than 0.2cm produce different results relatively to the original geometry.¹ The influence of the Global Alignment positioning of the VDS, ITR+OTR (Main Tracker), RICH and Muon detector were also studied, for displacements in the coordinate axes' directions. The VDS again has shown to have greater sensitivity, producing different values for the measured quantities (resonance masses, distances of closest approach, etc.) for displacements $|\Delta z_{\text{VDS}}|, |\Delta y_{\text{VDS}}| \gtrsim 0.2\text{cm}$ and $|\Delta x_{\text{VDS}}| \gtrsim 0.02\text{cm}$. These values are within the magnitude of those used for the nominal positioning of the detector, see e.g. [29].

The PI tool was developed informally during the work on this Dissertation as a means to calculate certain quantities and some of their associated errors. It developed reasonably to give results reasonably coherent with RTRA table information; see section E.1. As it is, the tool parses ASCII output from an ARTE session; however it could be easily modified to be incorporated in ARTE code and run as user routines. This was not done in this work since it was felt that it was important to have the ASCII tables as means to carefully debug the utility.

¹This value is well within the positioning capacity of the VDS modules' step motors', which have precisions around $50\mu\text{m}$.

Misalignment maps for one golden decay event

This appendix contains the variation of several event-specific and RTRA-specific quantities under detector module translations for the event labeled “235” (section 4.2.1); they are placed here to unclutter the main discussion in chapter 5.

The quantities studied are:¹

- Dimuons: mass $m_{\mu\mu}$; minimum separation between μ^+ and μ^- ; longitudinal vertex coordinate $z_{\mu\mu}$ and longitudinal separation from RVER 2 $z_{\mu\mu} - z_{\text{RVER}2}$; distance of closest approach (D.C.A.) of the μ^\pm and the dimuon to RVER 1; impact parameter, of the μ^\pm and the dimuon, to the target wire; and number of degrees of freedom of the μ^\pm RTRAs.
- $\mu^+\mu^-\pi^+\pi^-$: mass $m_{\mu\mu\pi\pi}$; minimum separation $\mu\mu-\pi\pi$; longitudinal vertex coordinate $z_{\mu\mu\pi\pi}$ and longitudinal separations from the dimuon $z_{\mu\mu} - z_{\mu\mu\pi\pi}$, and from RVER 1 $z_{\mu\mu\pi\pi} - z_{\text{RVER}1}$; and D.C.A. to RVER 1.
- RVERs 1 and 2: masses $m_{\text{RVER}i}$; longitudinal coordinate of the vertices $z_{\text{RVER}i}$, and longitudinal separation of the two vertices $z_{\text{RVER}2} - z_{\text{RVER}1}$; and number of degrees of freedom of the RVER*i*'s.
- Tagging RTRA: golden decay B flavour (according to the criterium of highest- p_T RTRA charge); transverse momentum p_T and charge q (presented in the form qp_T); D.C.A. to RVER 1, RVER 2; and impact parameter to target wire $b_{\text{tag}}^{\text{wire}}$.

The minimum separations/distances of closest approach (DCAs) are measured in 3D, whereas the impact parameter to wire is measured in the xy plane crossing the wire central coordinate $z_{\text{wire}} = -4.6061\text{cm}$ (ARTE table GTAR). The impact parameters are signed; negative values indicate

¹I use the definitions suggested in reference [73] for impact parameter to wire and for distance of closest approach (D.C.A.) from vertex.

the track crosses the wire. The number of unconstrained degrees of freedom of RTRAs and RVERs are related to the number of hits and tracks associated to each of them, respectively; see e.g. equation (3.9) in page 86 for RTRAs. The longitudinal separation of RVER 1 and RVER 2 (or of the $\mu\mu\pi\pi$ and $\mu\mu$ RTRA sets found with PI) can be used to measure the B lifetime, given that due to the large Lorentz boost it travels essentially parallel to the beam. The decay vertex of $B \rightarrow J/\psi X$ can be identified with the J/ψ decay vertex, given that this particle's lifetime is seven orders of magnitude below the B 's. The reference value for the decay length of the B is around $c\tau_B \sim 0.5\text{mm}$ [81], which is of the same order as the VDS longitudinal resolution (see e.g. [29]).

A.1 VDS module displacements

Figures A.1–A.32 illustrate the variation of the quantities, described at the beginning of this chapter, for displacements of VDS modules (indexed by their longitudinal position, horizontal axes) in three coordinate directions (vertical axes for Z , X and Y — see figure 3.7, on the left). For example, for displacements in Z the lower half of the histograms correspond to moving *towards* the Target, and the upper half correspond to detector shifts *away* from the Target. The quantities are color-coded (see detached scale to the right of each histogram). The bins' widths are $Z_{\text{module}} \times \Delta i = 0.5\text{cm} \times 0.1\text{cm}$. Each plot has an inset for displacements below 6mm; the bin size for this inset is $0.5\text{cm} \times 0.1\text{mm}$. Although the quantities are categorized separately for the dimuon, $\mu\mu\pi\pi$, RVERs and tag, they are placed side-by-side on occasion for easier comparison (e.g. $m_{\mu\mu}$ and $m_{\text{RVER } 2}$).

Finally, in the representation of the transverse momentum of the RTRA used for B flavour tag, p_T was multiplied by the RTRA's charge; see figure A.27. This way we may obtain the transverse momentum of the highest- p_T RTRA and also its charge.

The bottommost histogram in each column is a projection (of the other three histograms) along the vertical axis (displacements); the error bars amplitudes are $\sqrt{X/N}$ for N entries for quantity X [37]. In these profile histograms, a dashed rectangle represents the magnification bounds for use in the inset.

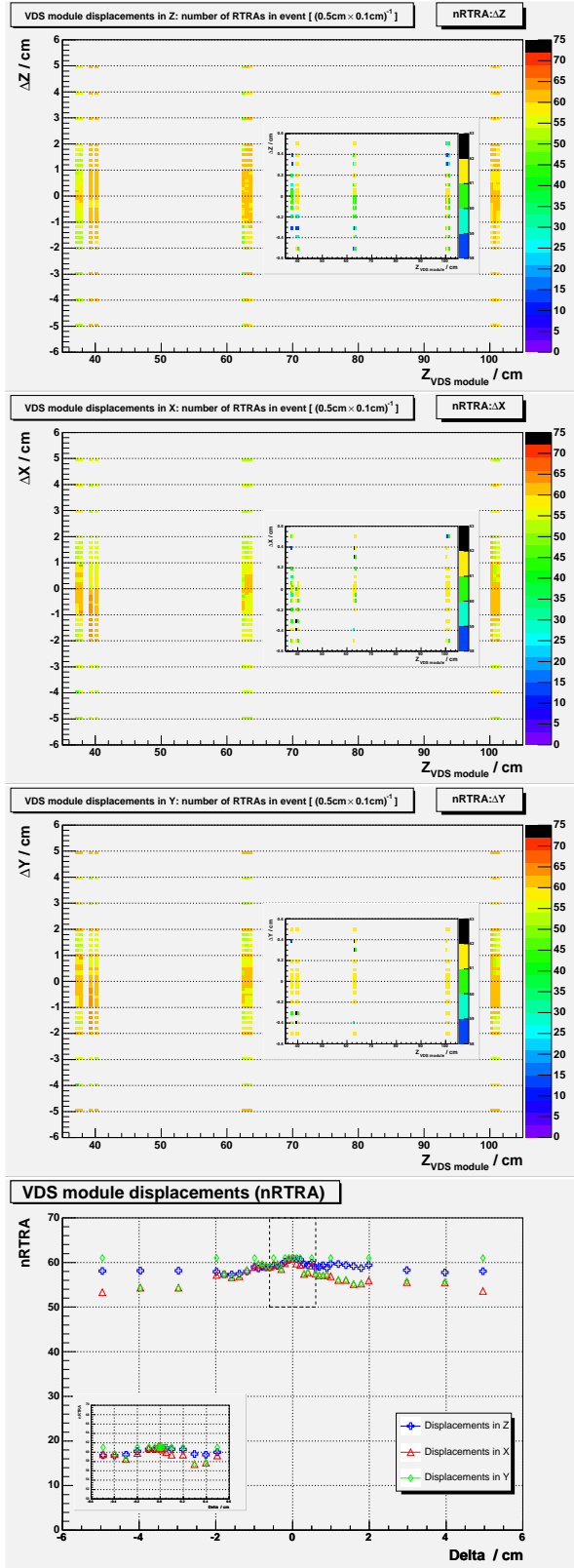


Figure A.1. Number of reconstructed tracks in event (ARTE) for VDS module displacements in Z (topmost), X (next) and Y (next-to-last). The bottommost histogram is a vertical axis projections of the first three histograms in the vertical axis (Δ_i). Insets are for displacements $|\Delta_i| < 600\mu\text{m}$.

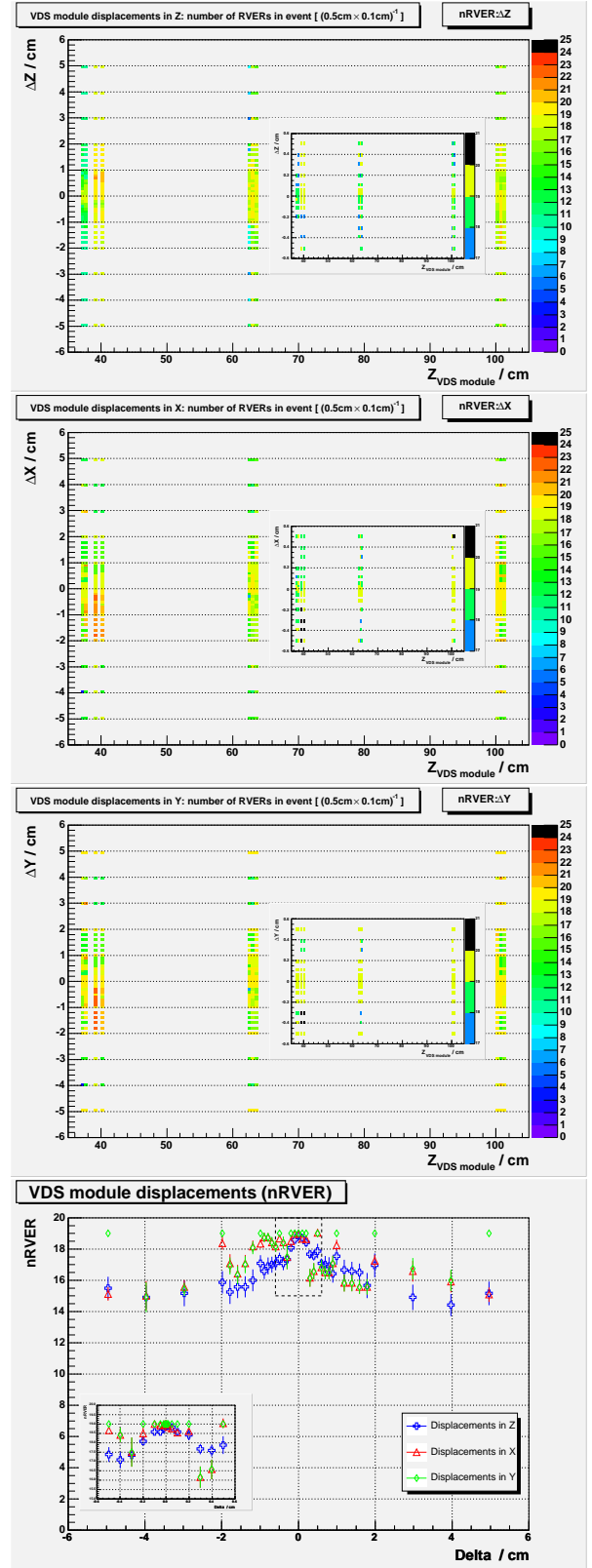


Figure A.2. Number of reconstructed vertices in event (ARTE) for VDS module displacements in Z (topmost), X and Y. The bottommost histogram is a projection of the first three histograms in the vertical axis (Δ_i). Insets are for displacements $|\Delta_i| < 600\mu\text{m}$.

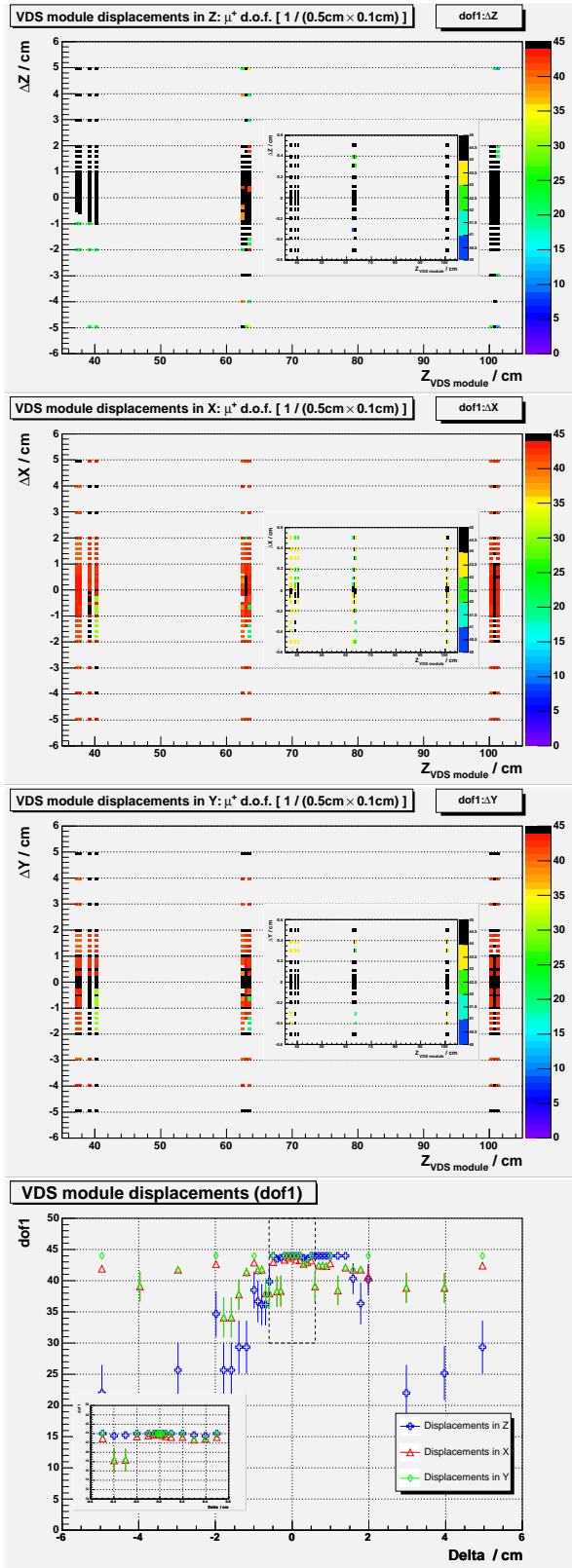


Figure A.3. Number of degrees of freedom for μ^+ RTRA (ARTE).

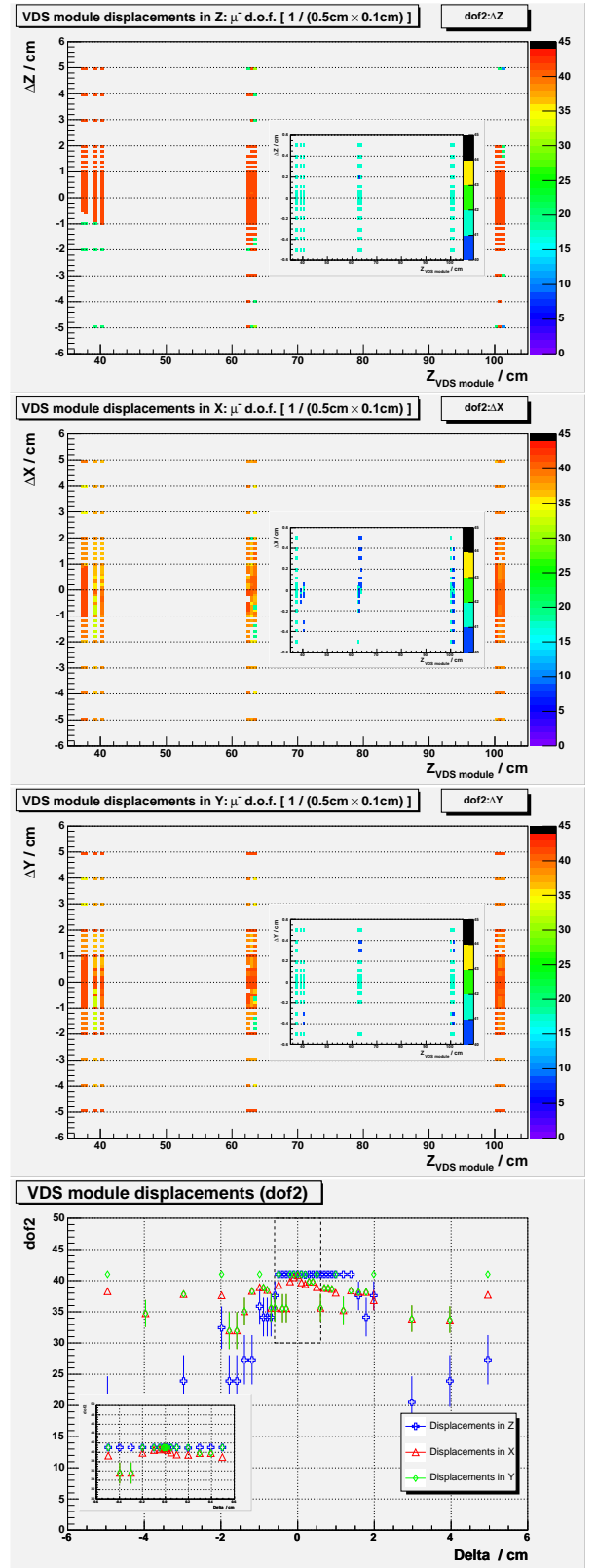


Figure A.4. Number of degrees of freedom for μ^- RTRA (ARTE).

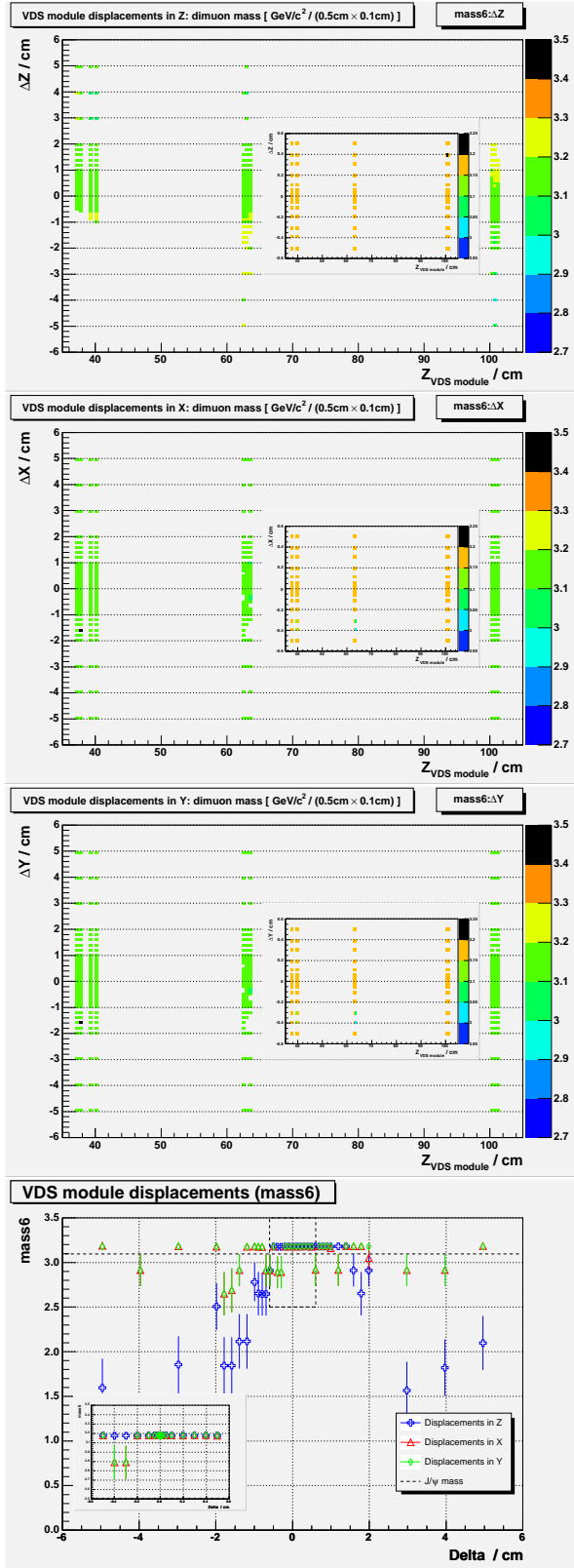


Figure A.5. Dimuon mass for VDS module displacements (horizontal axes) in different directions (vertical axes) — Z (top), X (middle) and Y (bottom). The insets are for displacements below $600 \mu\text{m}$. Masses were computed with PI.

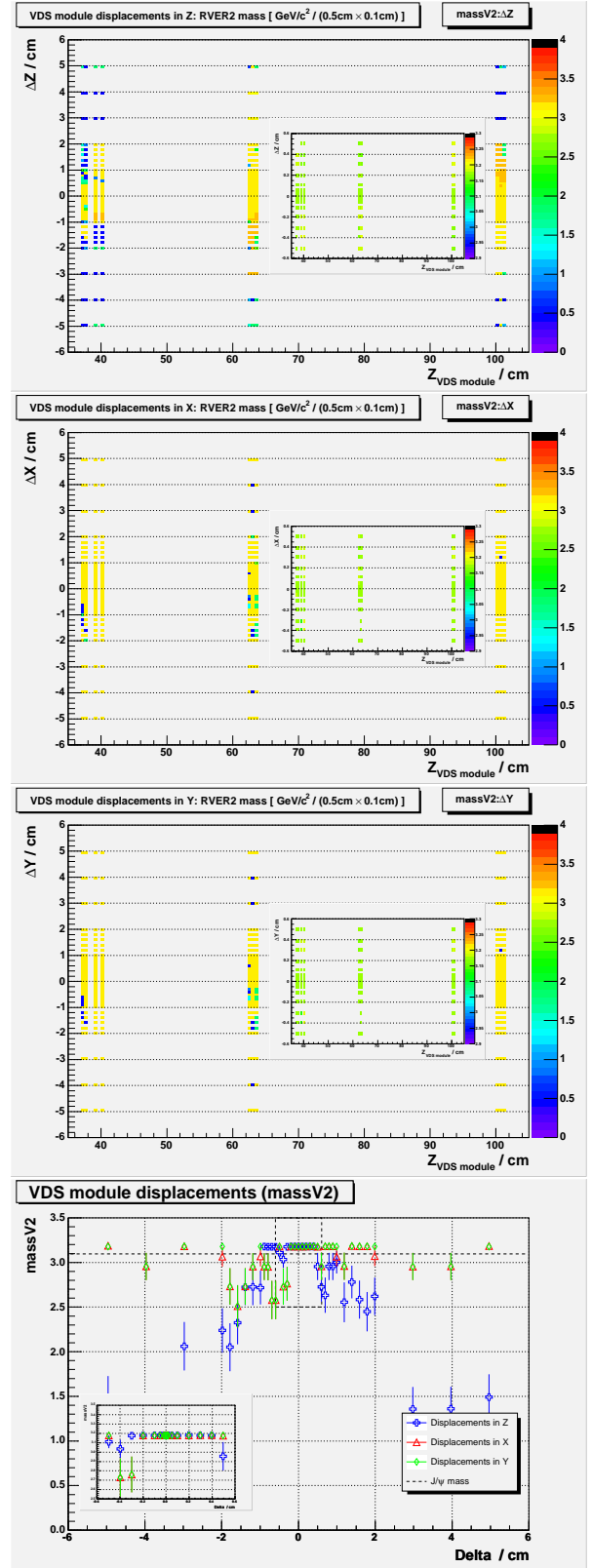


Figure A.6. RVER 2 mass for VDS module displacements (horizontal axes) in different directions (vertical axes) — Z (top), X (middle) and Y (bottom). The insets are for displacements below $600 \mu\text{m}$. Masses obtained from ARTE table RVER.

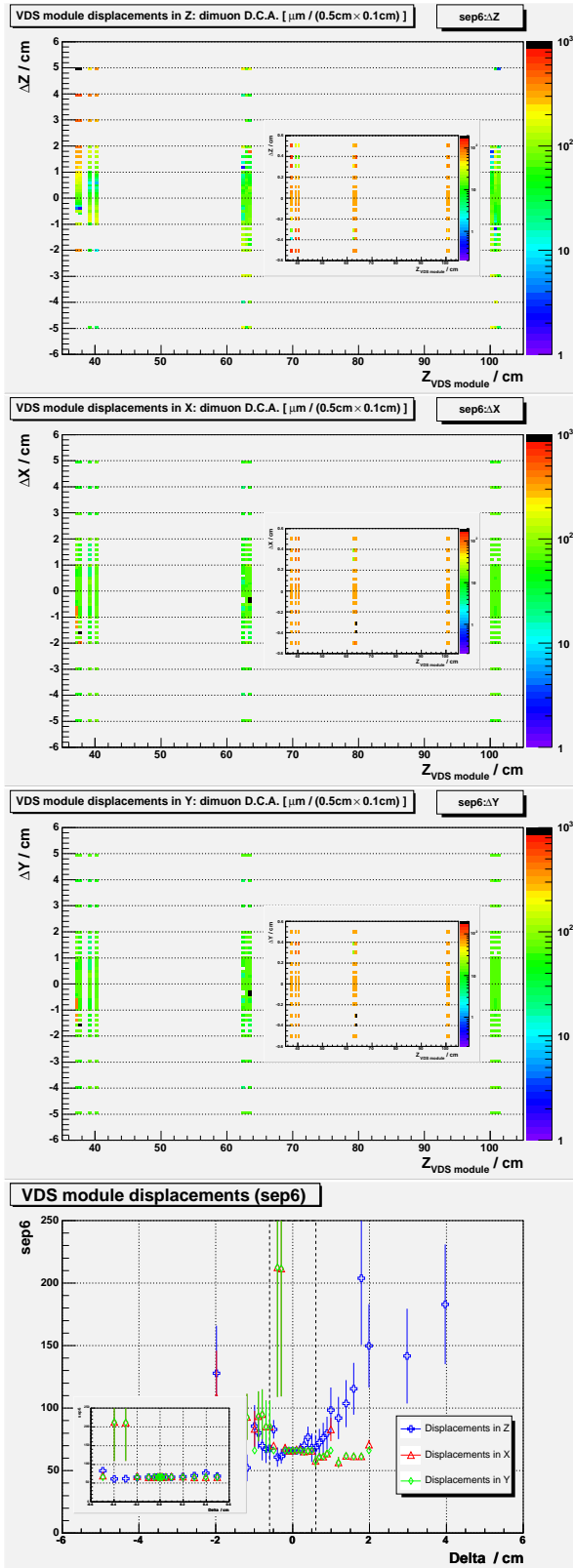


Figure A.7. Minimum separation (in micrometers) between the μ^\pm RTRAs.

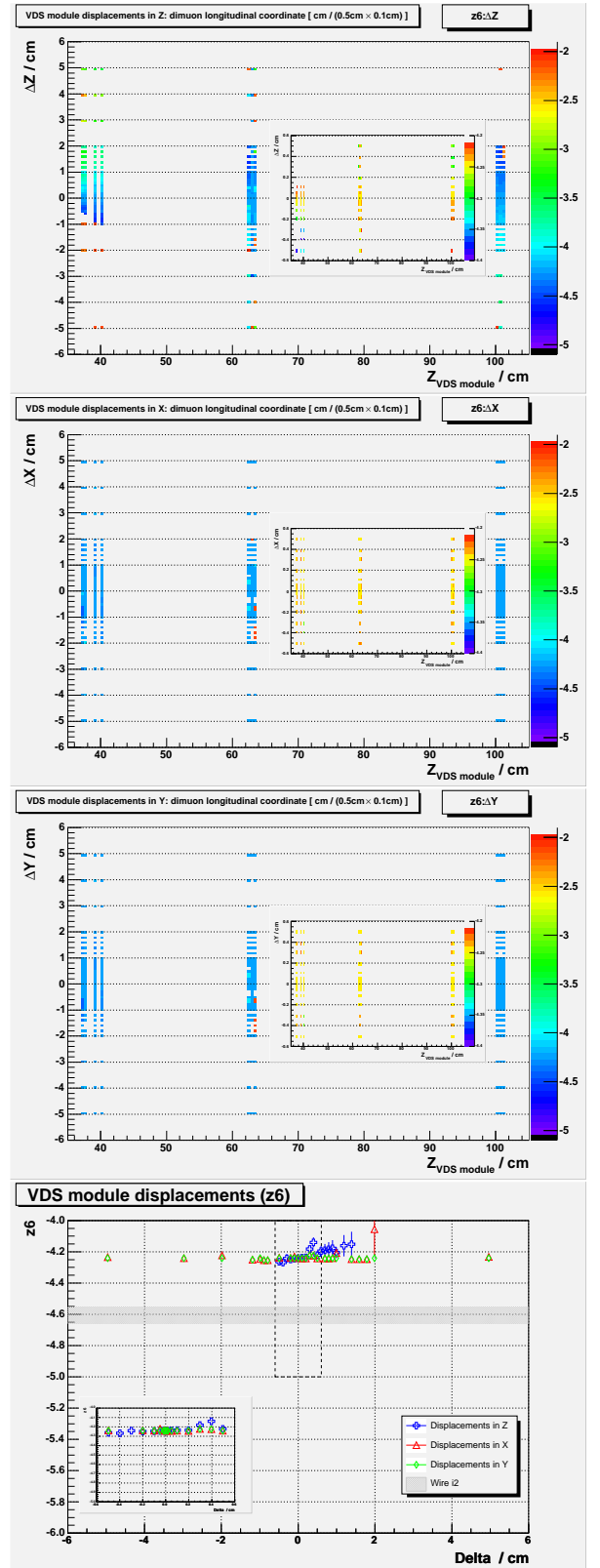


Figure A.8. Vertex longitudinal coordinate (in centimeters) of the dimuon, $z_{\mu\mu}$.

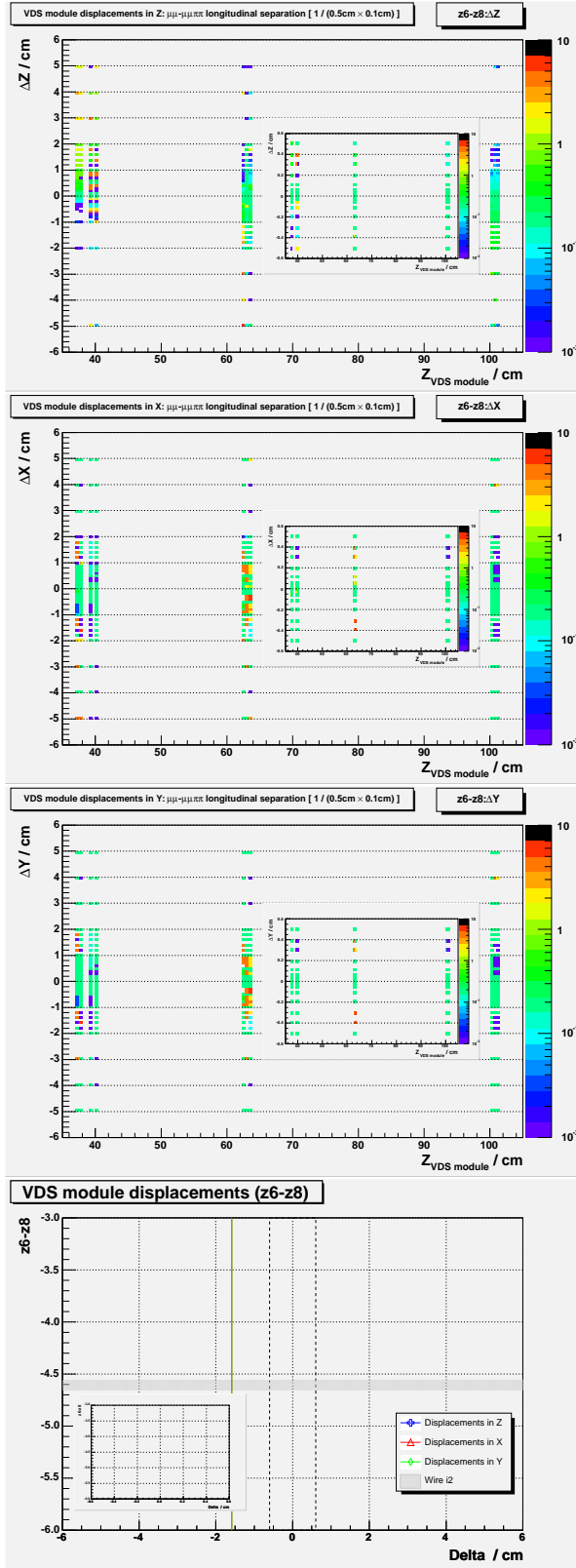


Figure A.9. Longitudinal separation (in centimeters) between the dimuon and the $\mu\pi\pi$ (PI).

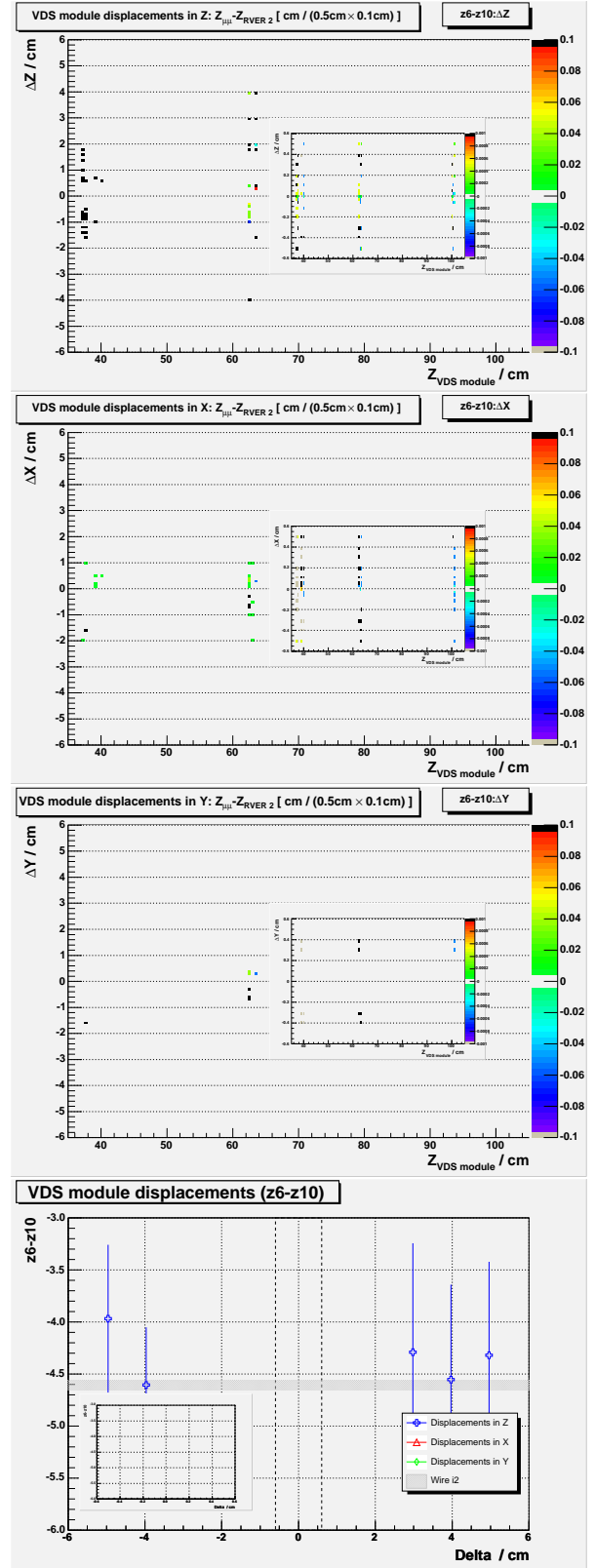


Figure A.10. Longitudinal separation (in centimeters) between the dimuon (PI) and the RVER 2 (ARTE).

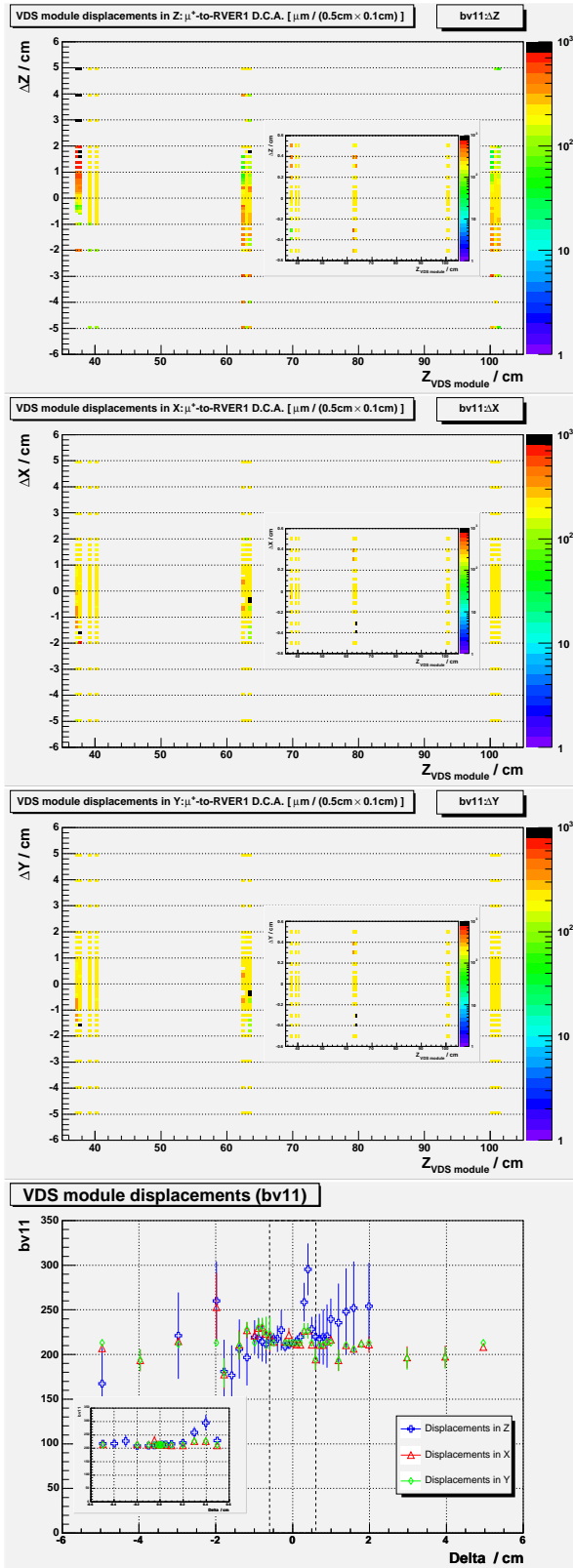


Figure A.11. D.C.A. (in micrometers) of μ^+ to RVER 1. Computed with PI.

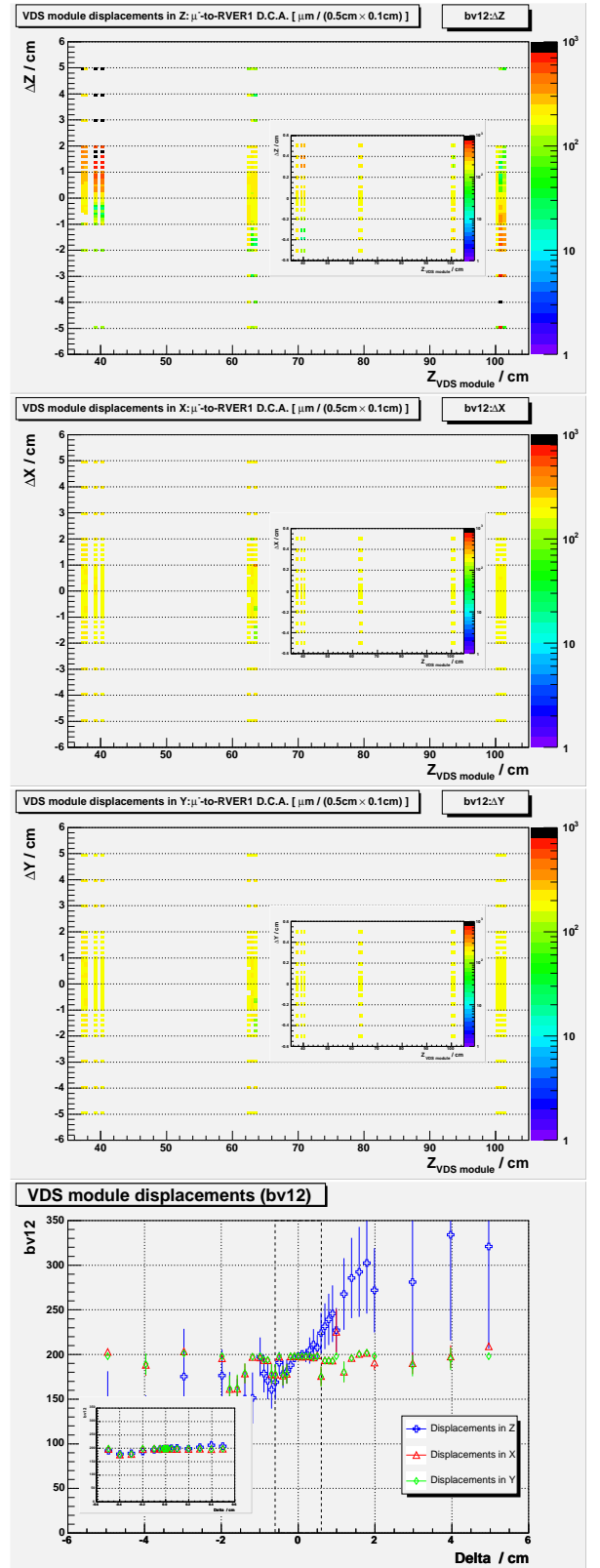


Figure A.12. D.C.A. (in micrometers) of μ^- to RVER 1. Computed with PI.

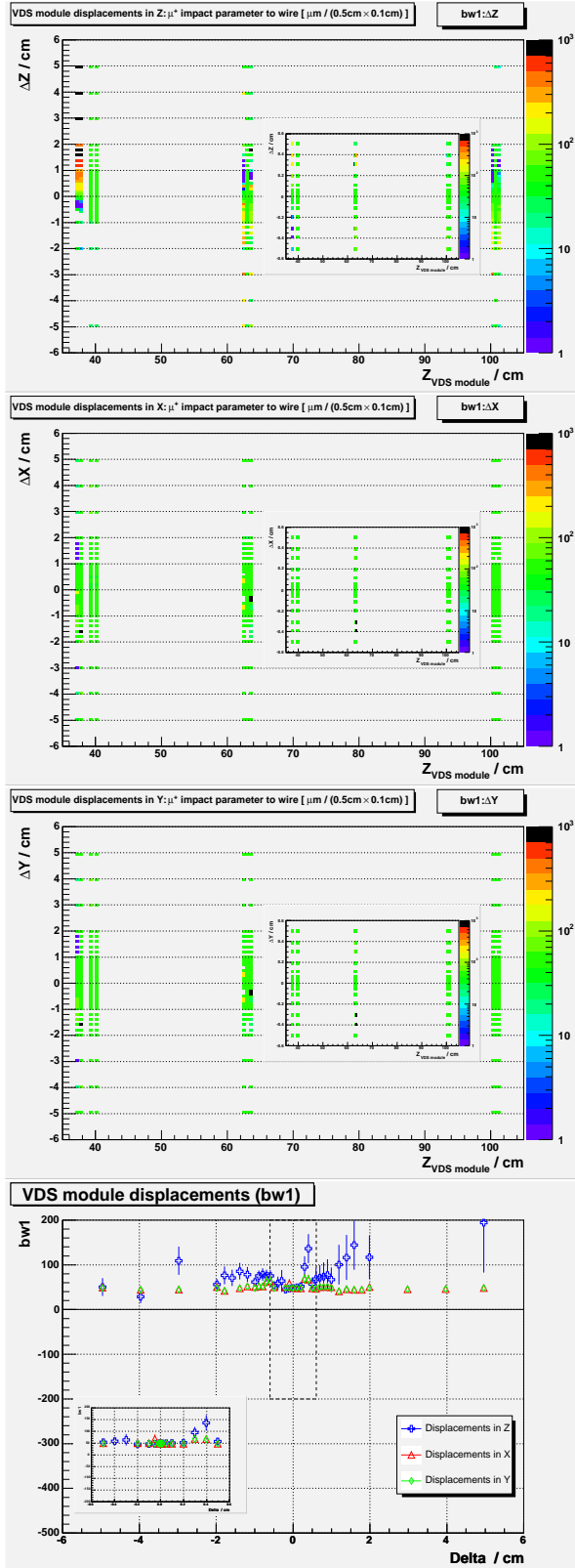


Figure A.13. Impact parameter (in micrometers) of μ^+ to target wire. Computed with PI.

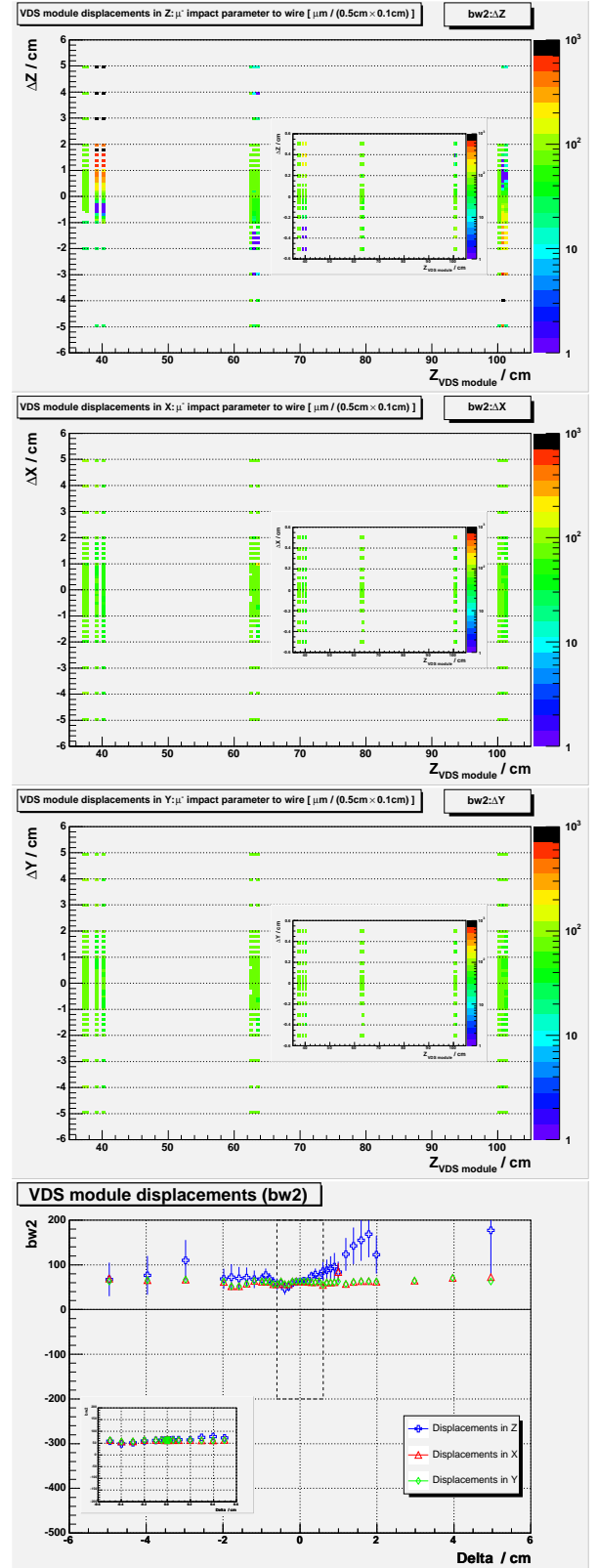


Figure A.14. Impact parameter (in micrometers) of μ^- to target wire. Computed with PI.

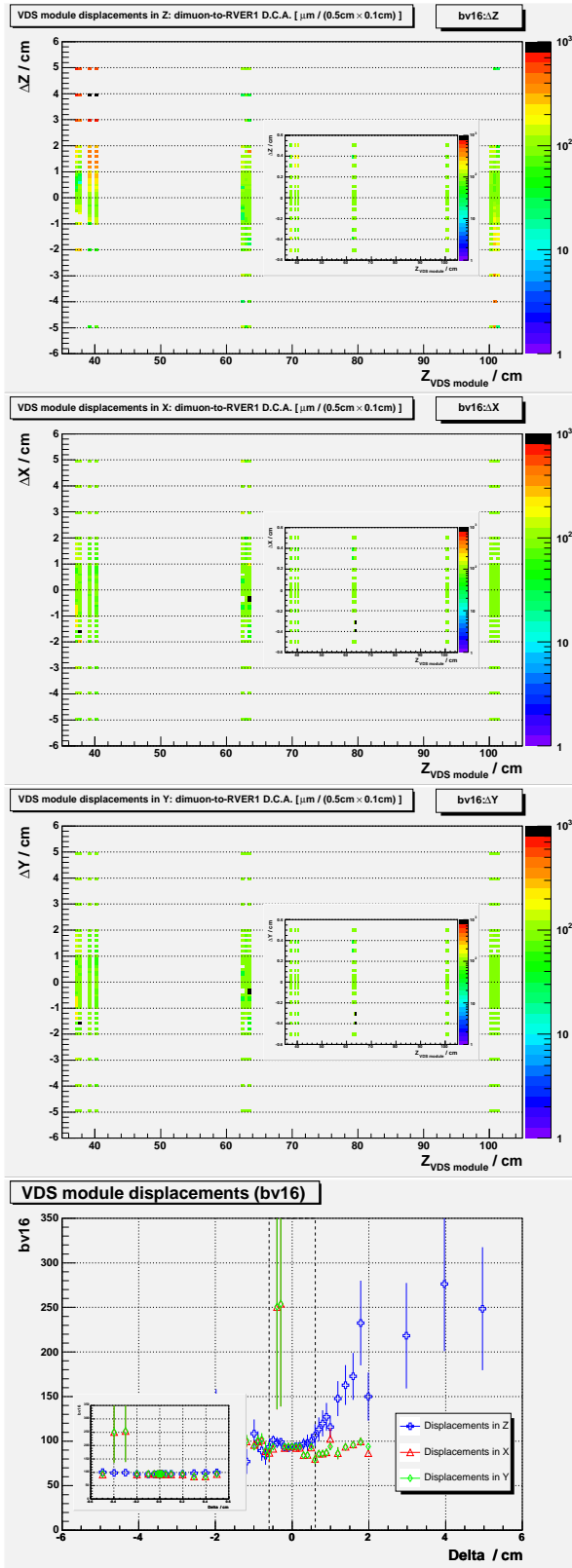


Figure A.15. D.C.A. (in micrometers) of dimuon to RVER 1. Computed with PI.

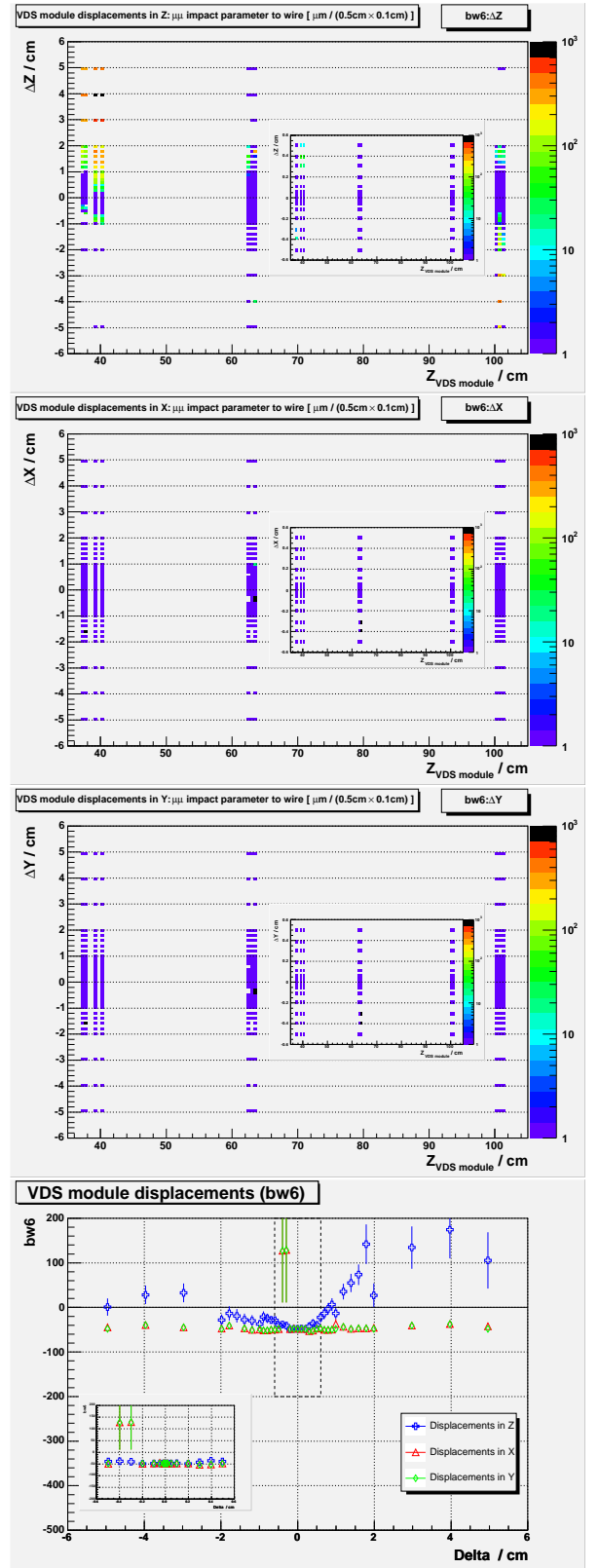


Figure A.16. Impact parameter (in micrometers) of dimuon to target wire. Computed with PI.

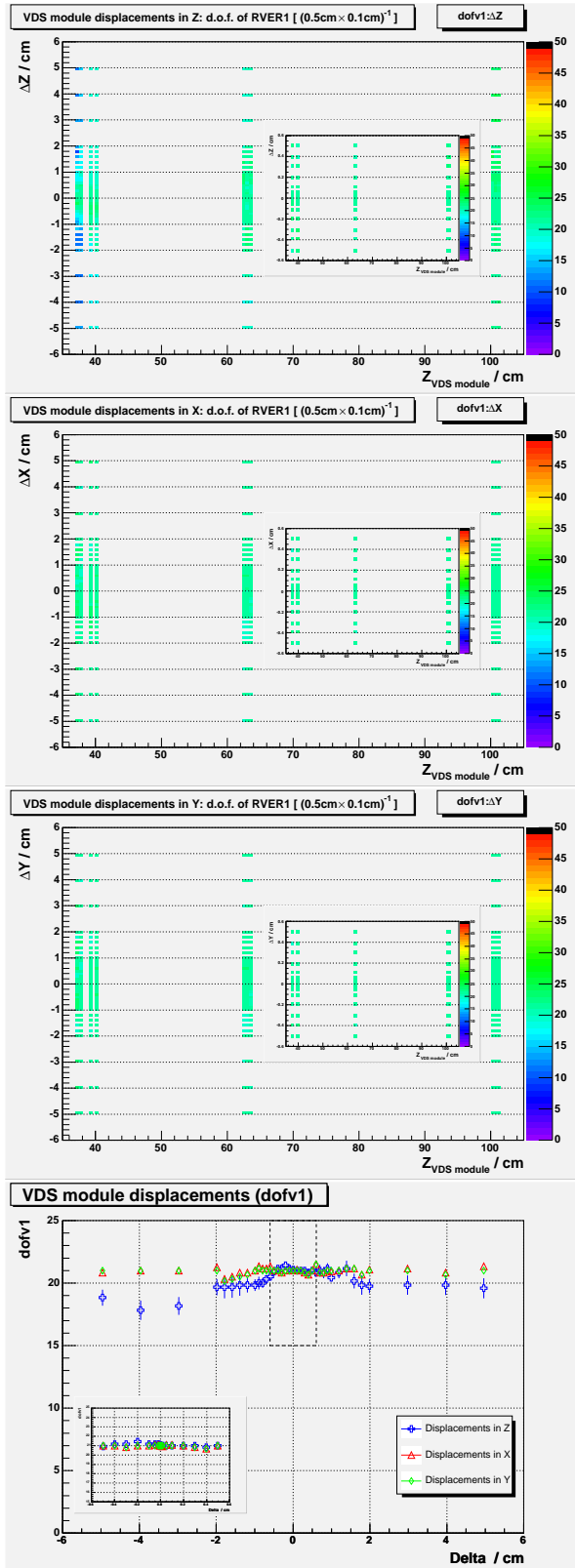


Figure A.17. Number of degrees of freedom for RVER 1 (ARTE).

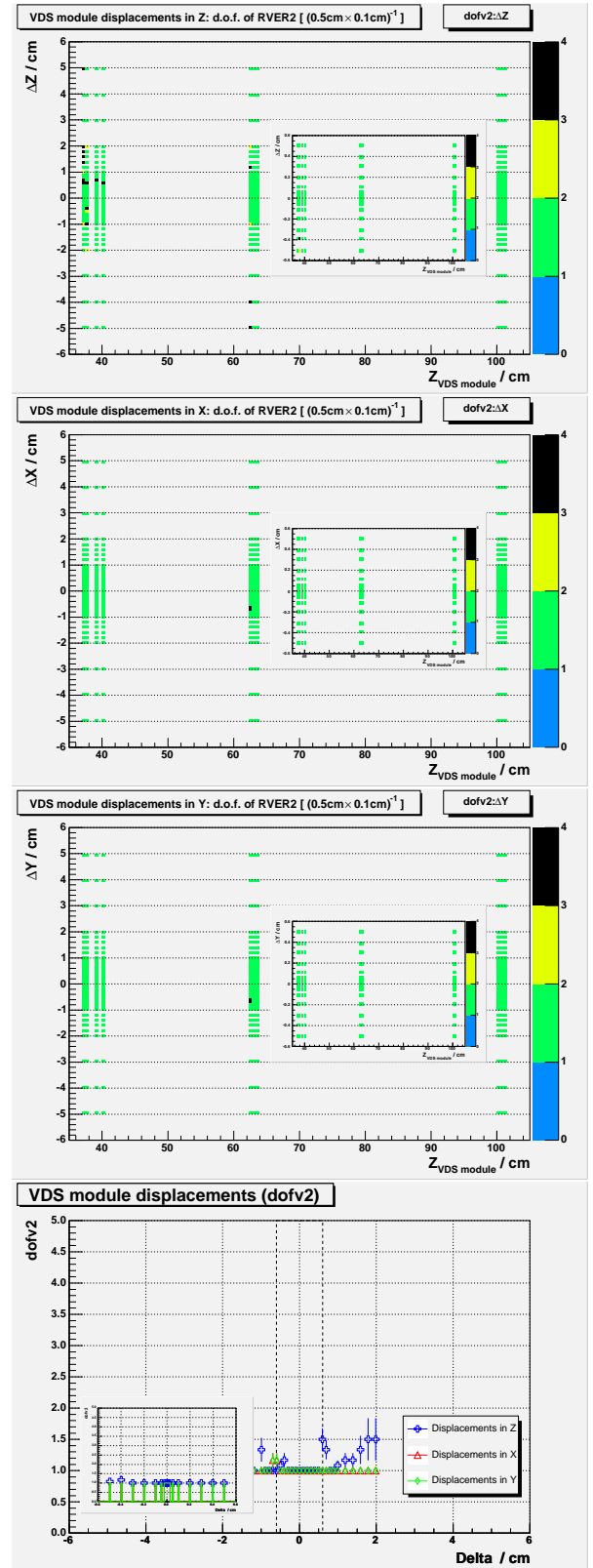


Figure A.18. Number of degrees of freedom for RVER 2 (ARTE).

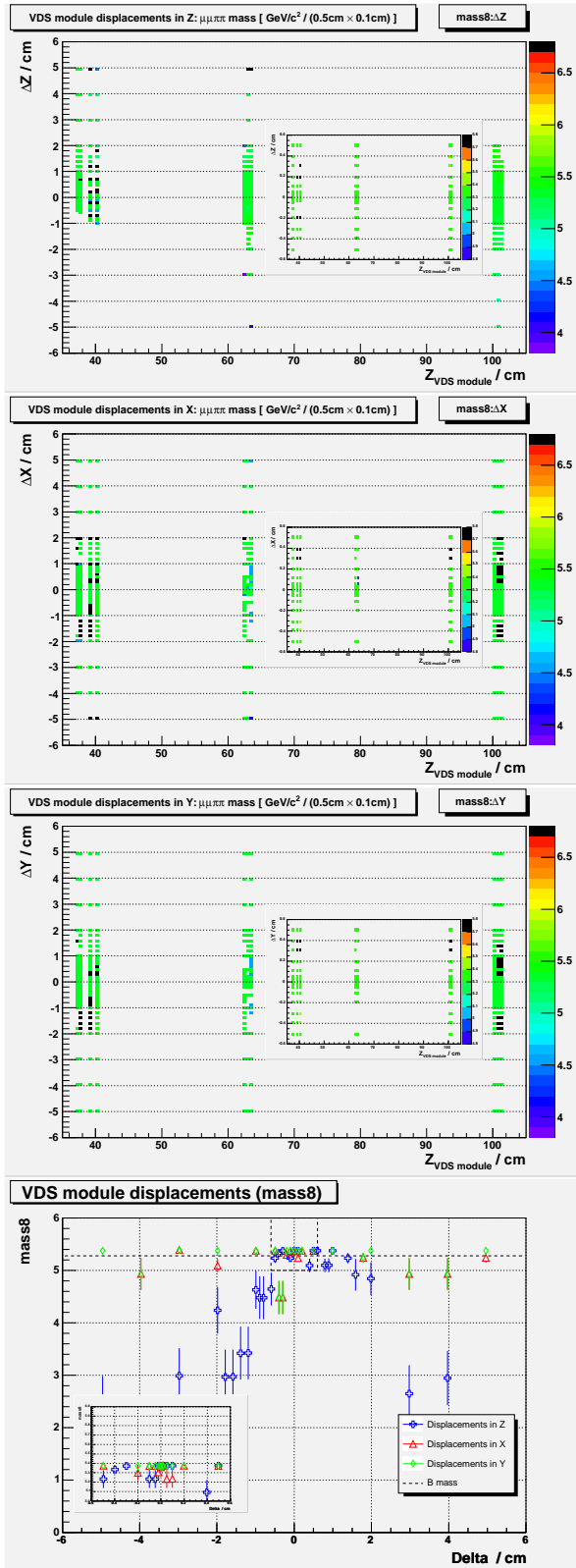


Figure A.19. $\mu\mu\pi\pi$ mass (computed with PI) for VDS module displacements in Z (top), X (middle) and Y (bottom).

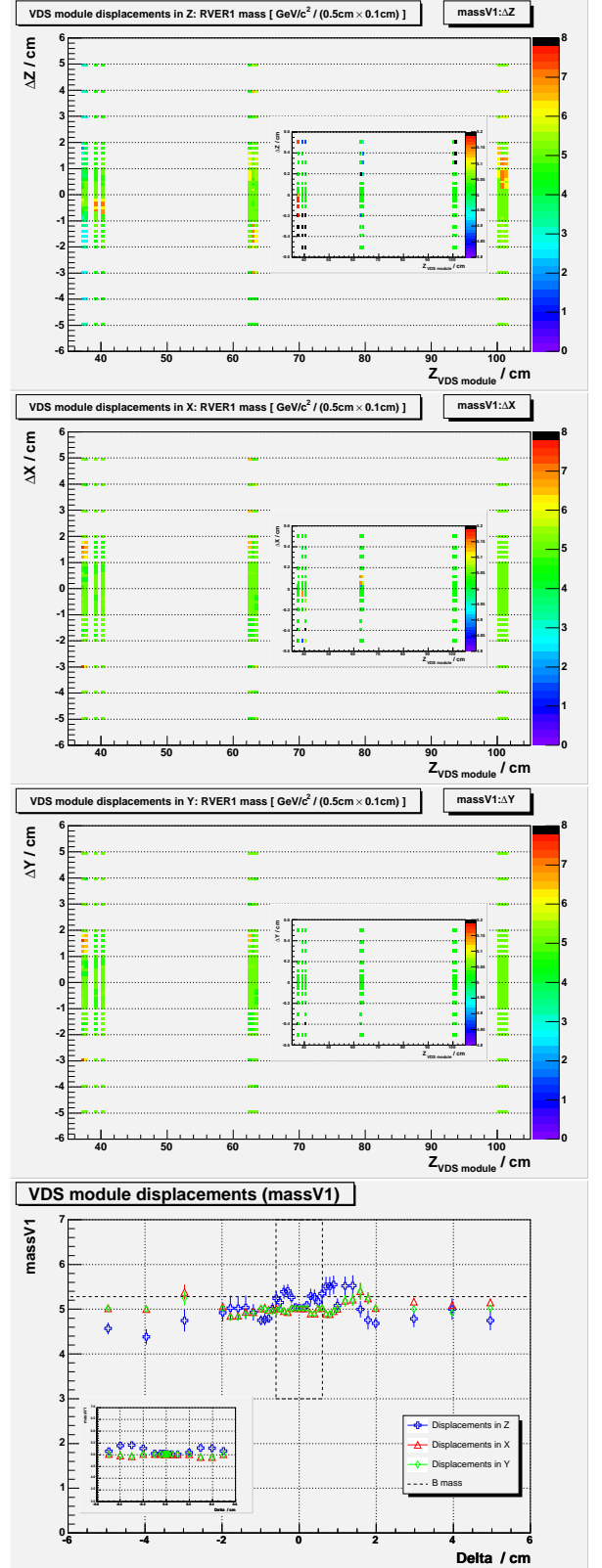


Figure A.20. RVER 1 mass (from ARTE) for VDS module displacements in Z (top), X (middle) and Y (bottom).

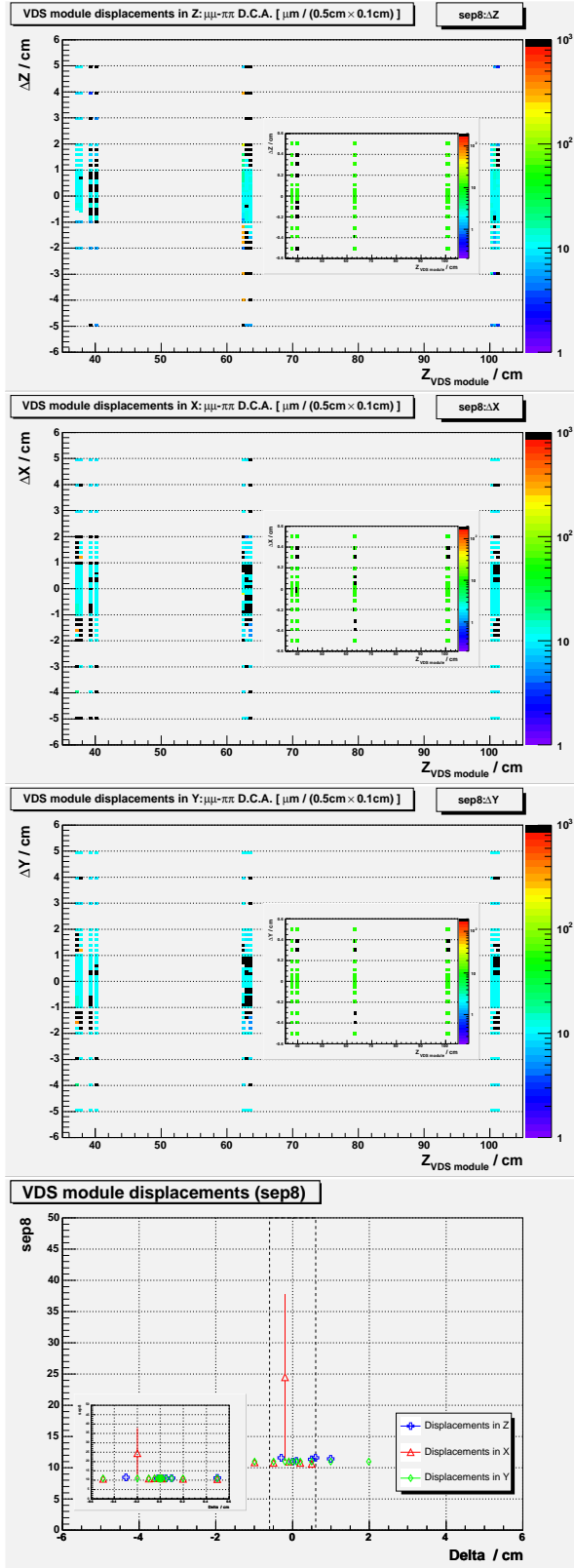


Figure A.21. Minimum separation (in micrometers) between the dimuon and the dipion. Computed with PI.

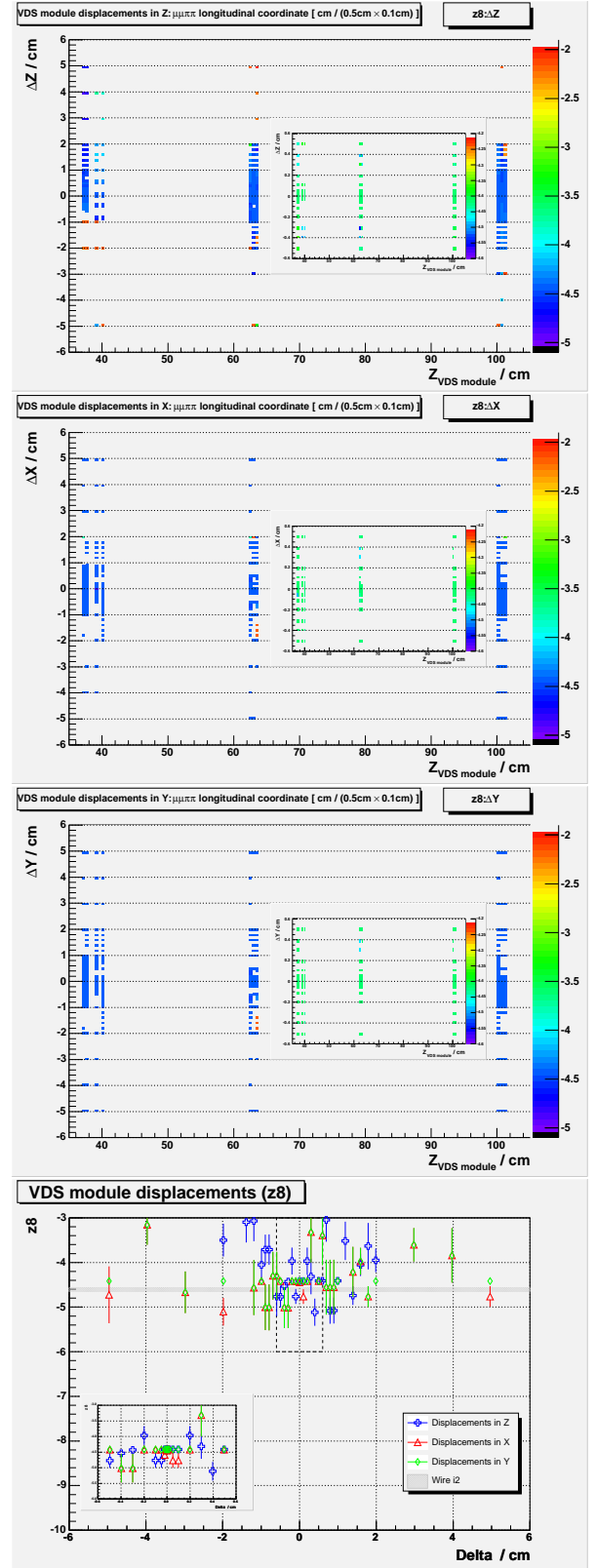


Figure A.22. Vertex longitudinal coordinate (in centimeters) of the $\mu\mu\pi\pi$. Computed with PI.

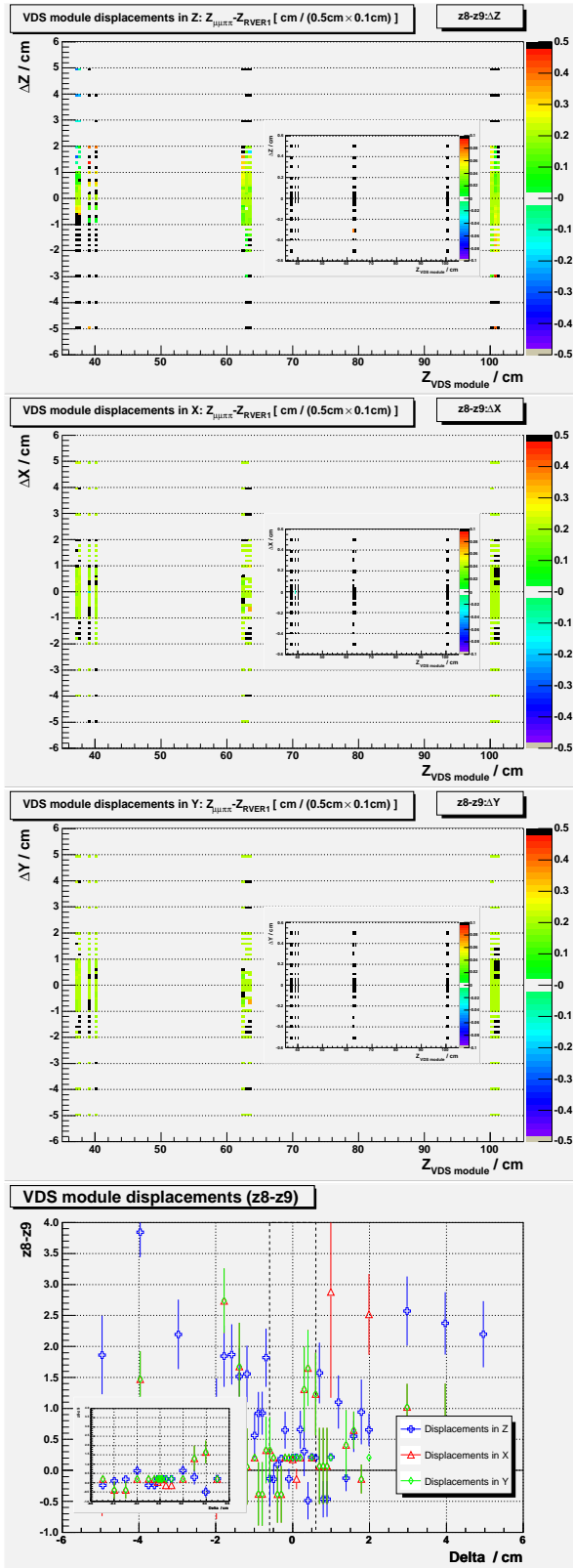


Figure A.23. Longitudinal separation (in centimeters) of the $\mu\pi\pi$ (PI) and the RVER 1 (ARTE).

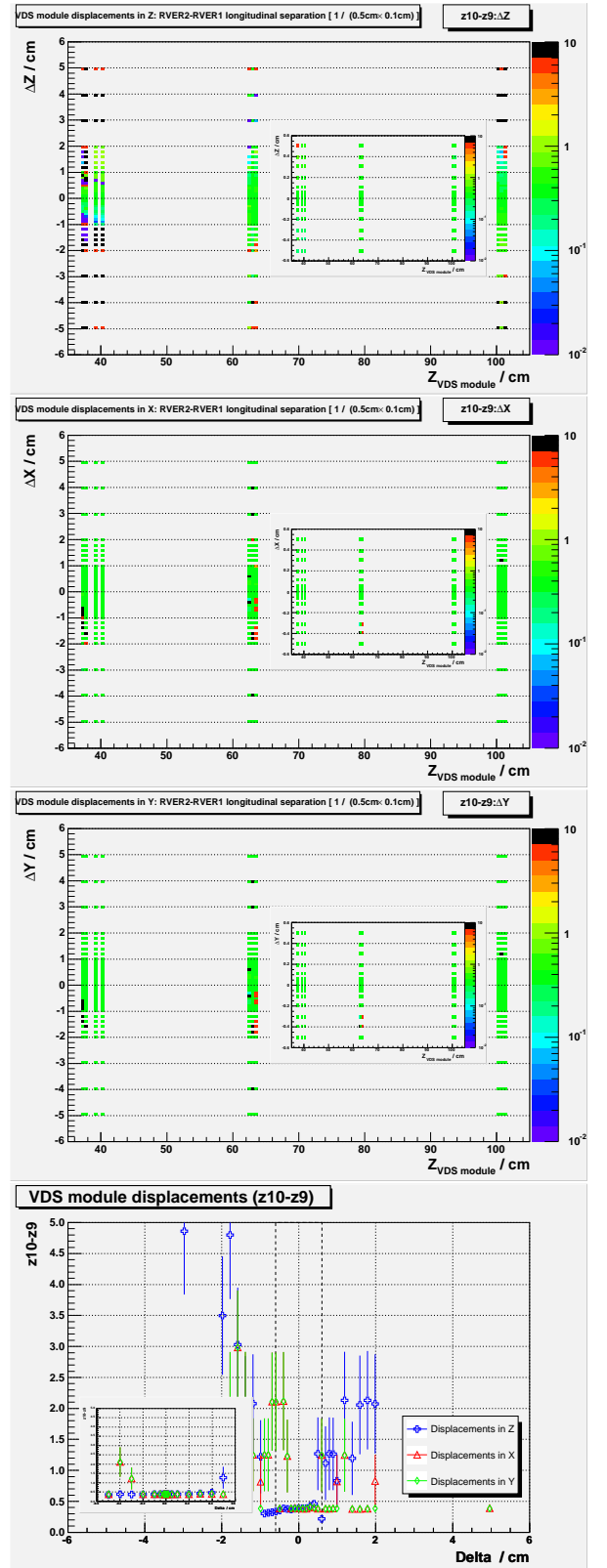


Figure A.24. Longitudinal separation (in centimeters) of the RVER 2 to the RVER 1 (ARTE).

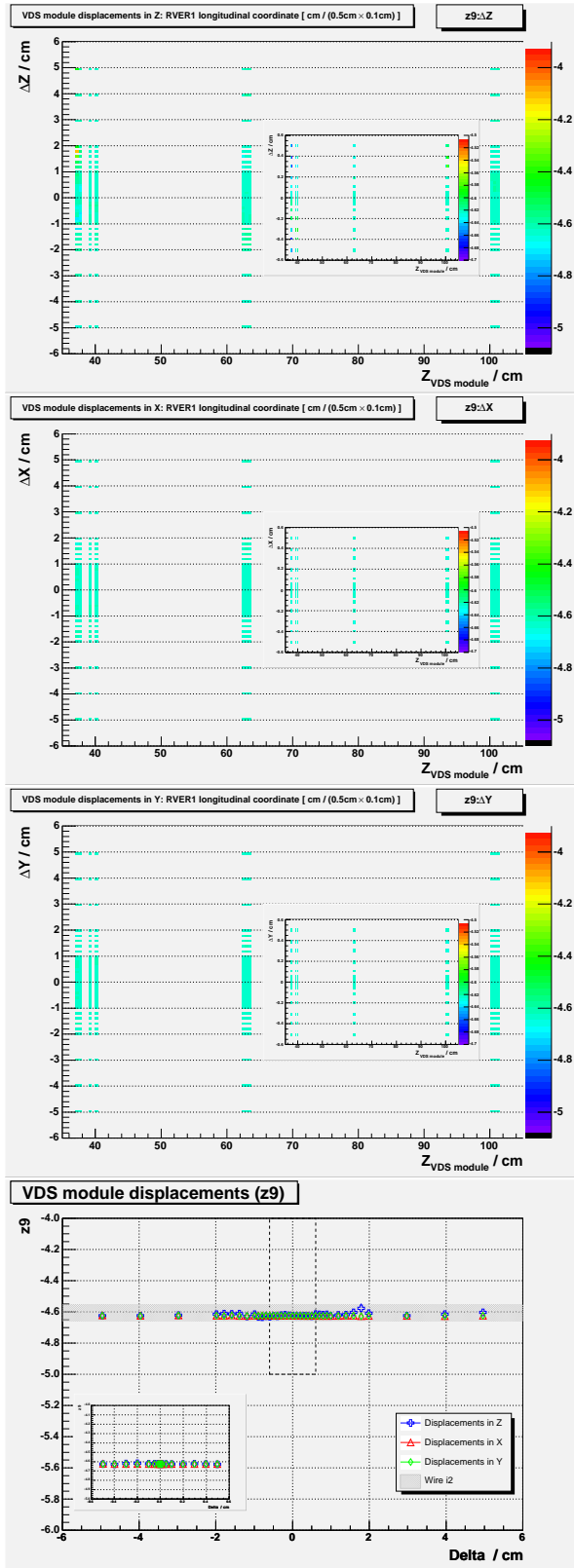


Figure A.25. RVER 1 longitudinal coordinate (ARTE).

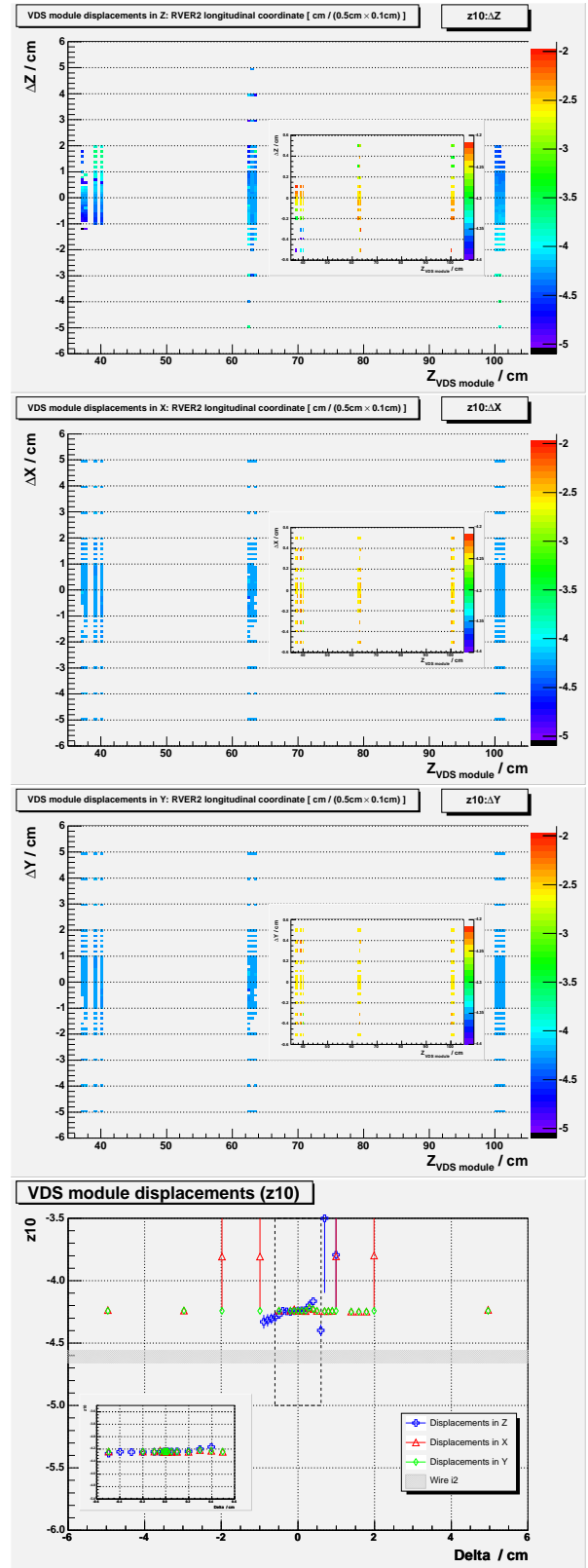


Figure A.26. RVER 2 longitudinal coordinate (ARTE).

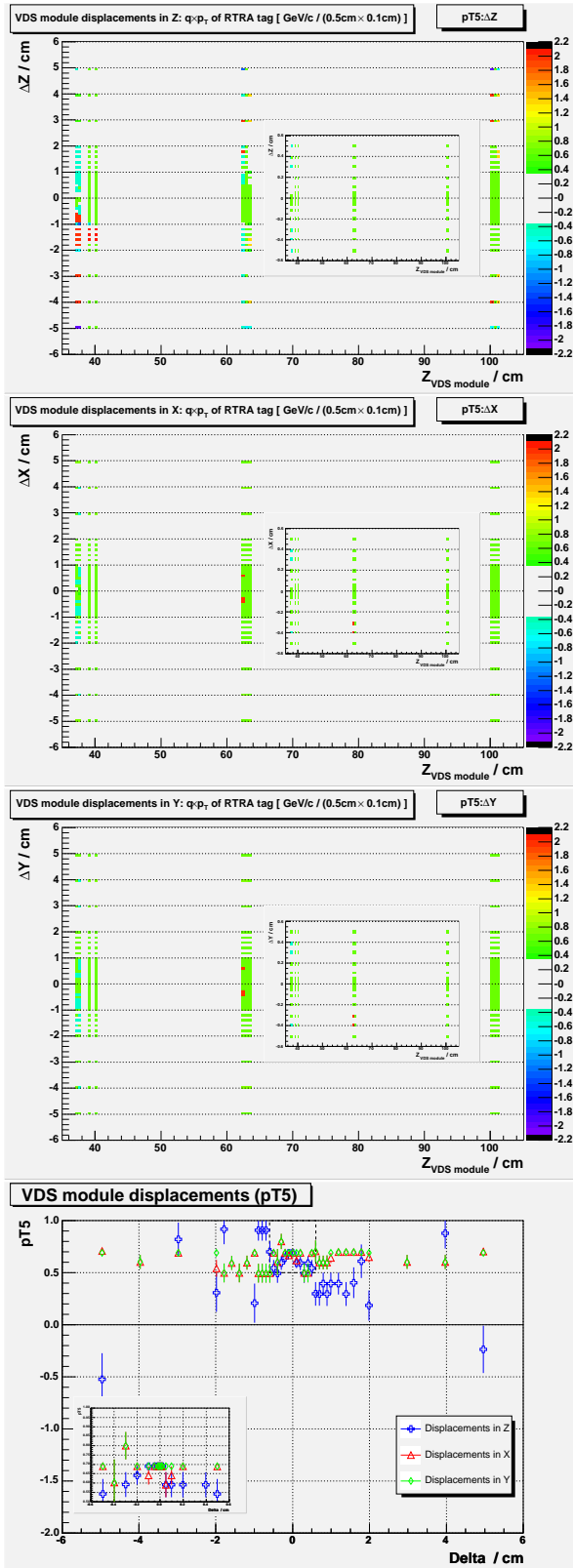


Figure A.27. $q \times p_T$ (in GeV/c) of RTRA selected (PI) for B flavour tag. The charge $q = \pm 1$ is the sign of deflection (in the zx projection) of RTRA inside the Magnet. The gap in the color scale corresponds to the cut $p_T > 0.3\text{GeV}/c$ applied.

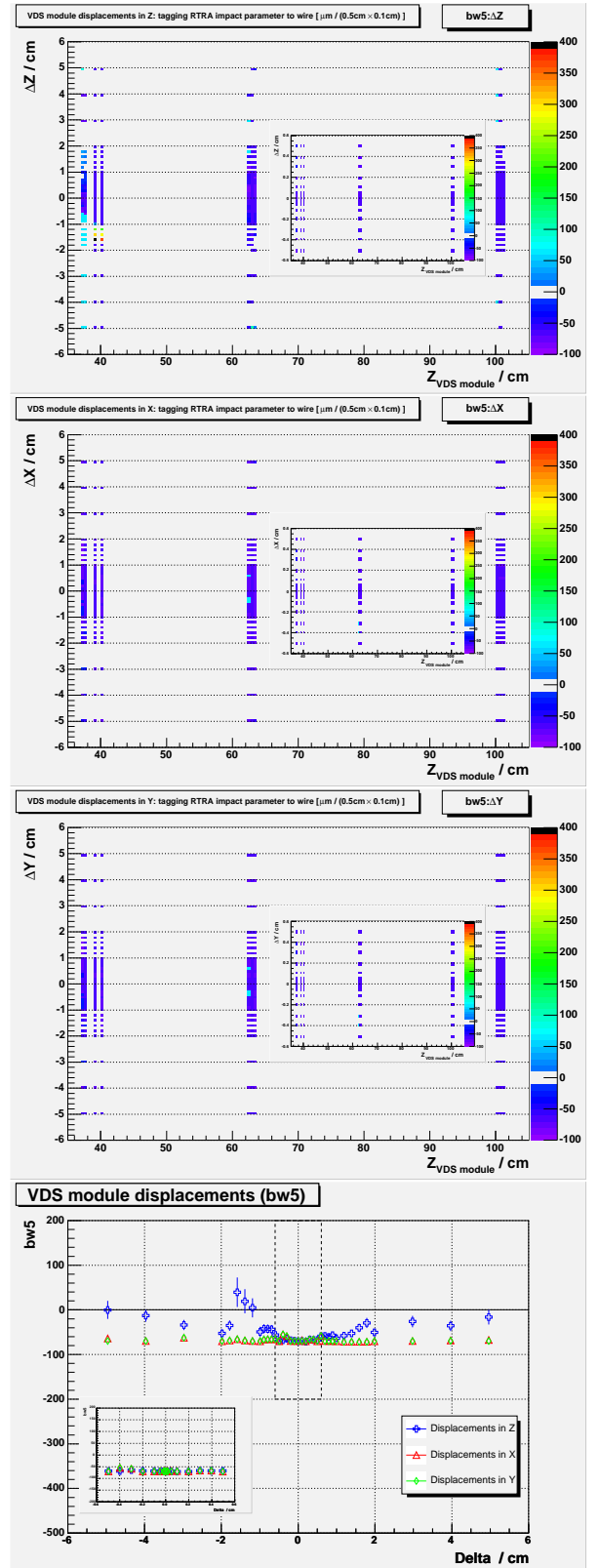


Figure A.28. Impact parameter (in micrometers) of the tagging RTRA. Computed with PI.

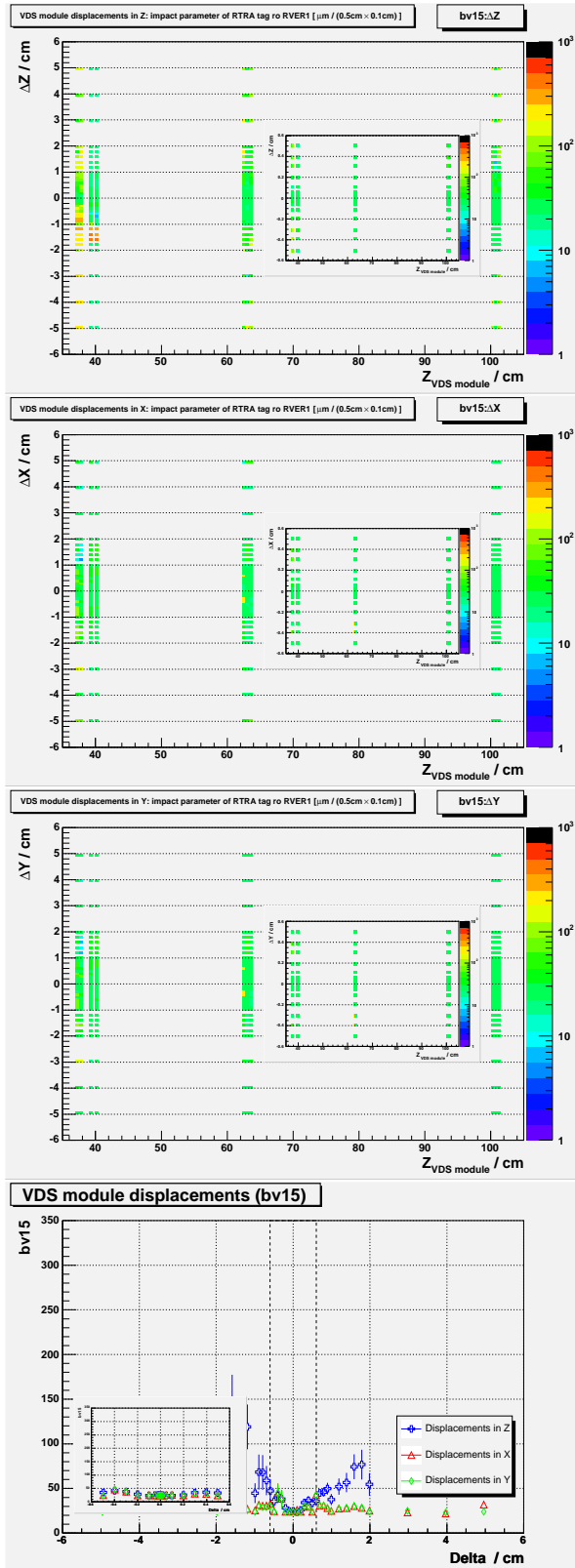


Figure A.29. D.C.A. of tagging RTRA to RVER 1. Computed with PI.

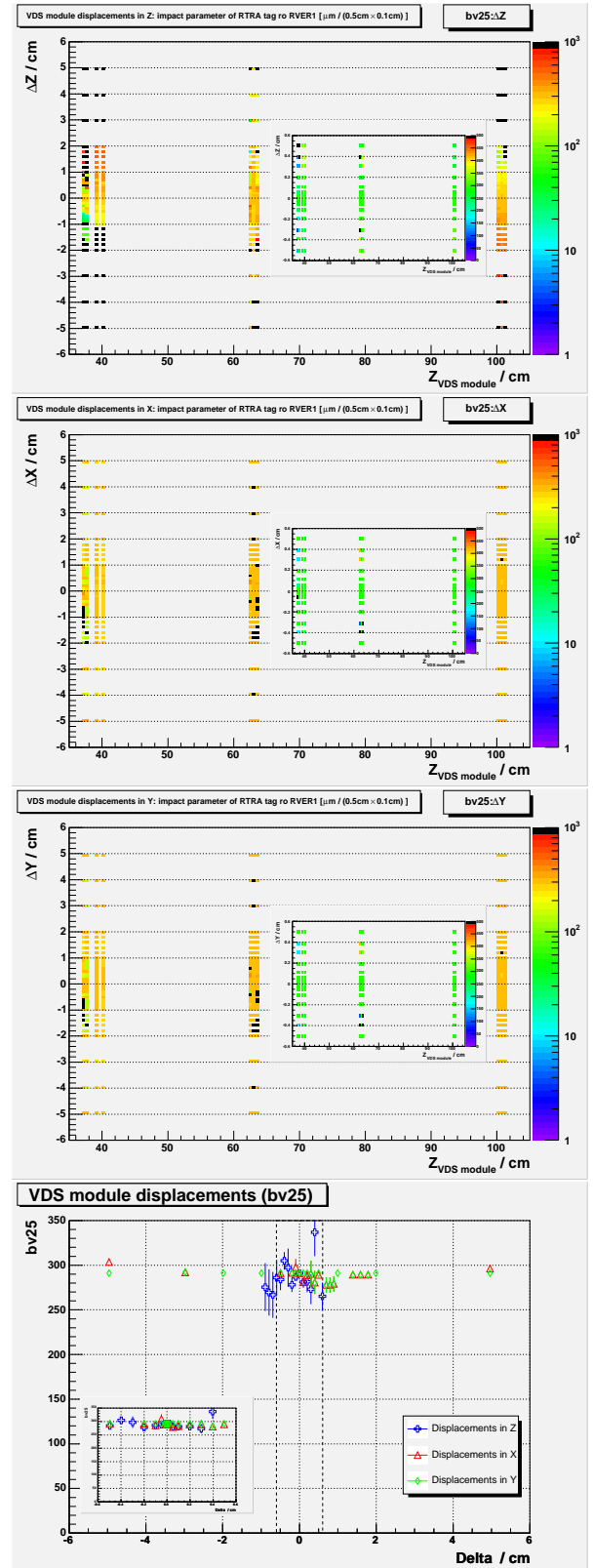


Figure A.30. D.C.A. of tagging RTRA to RVER 2. Computed with PI.

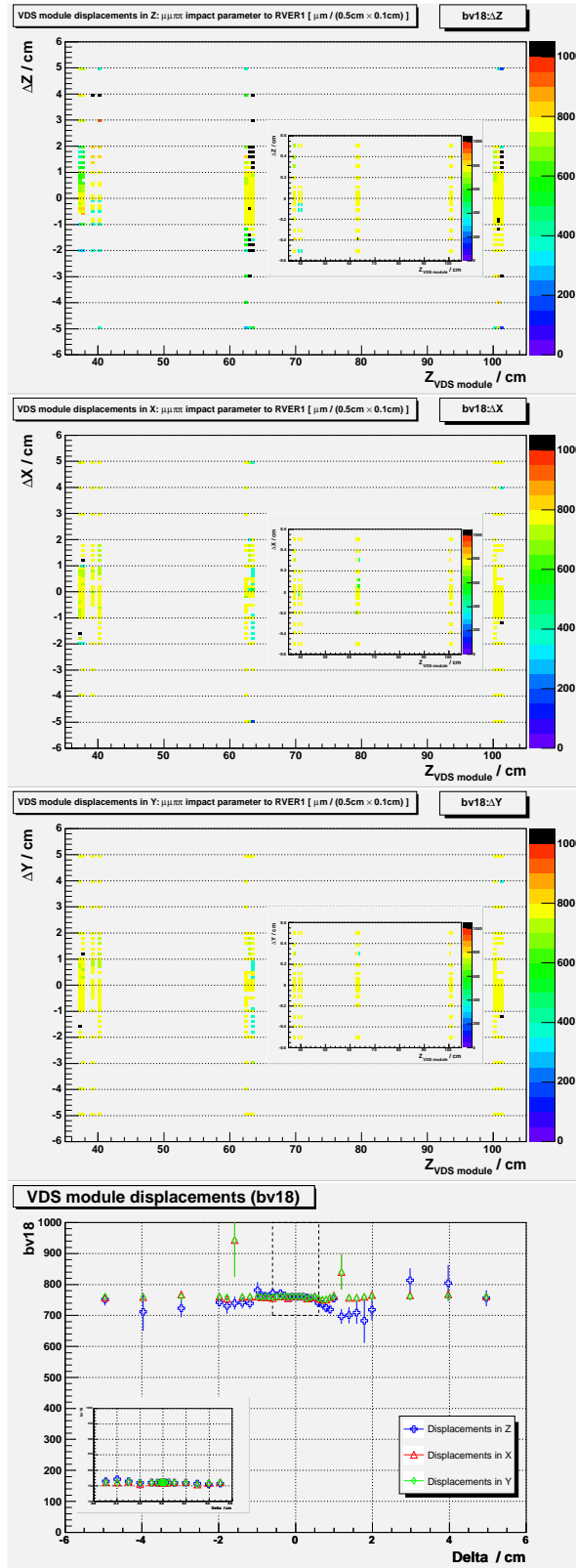


Figure A.31. Impact parameter (in micrometers) of $\mu\mu\pi\pi$ to RVER 1. Computed with PI.

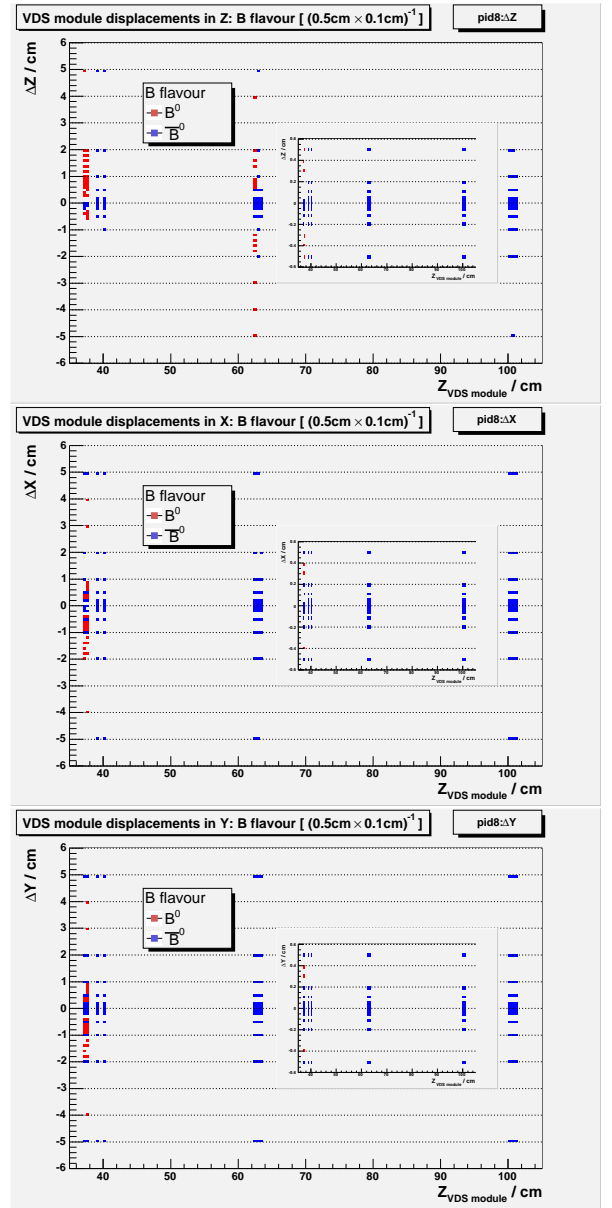


Figure A.32. Golden decay B meson flavour, obtained with charge tag from highest- p_T RTRA (ARTE).

A.2 Displacements of VDS, Main Tracker, RICH and Muon detector

The figures in this section are placed in columns, with ascending order of distance from the Target — VDS (topmost), Main Tracker (ITR and OTR), RICH and Muon detector (bottommost). Each column refers to one quantity — see the beginning of chapter 5.

Some graphics may overlap others (e.g. X and Y); for these, the results are the same for the corresponding “hidden” graphs. The markers used for displacements in z , x and y are, respectively: $+$ (blue), \triangle (red) and \diamond (green). All graphics (except for those in figures A.64–A.71) show a smaller graphic as inset, corresponding to a $10\times$ “zoom” of the axis for Δi (i.e., $|\Delta i| < 0.6\text{cm}$) centered at $\Delta i = 0$ ($i = z, x, y$). The inset’s bounds are marked by a dashed rectangle in each figure. The nominal masses for the J/ψ and B are plotted in the mass histograms for dimuon, $\mu\mu\pi\pi$, and RVERs 1 and 2. For histograms involving the coordinates of those four vertices, the longitudinal placement of the target wire is depicted by a gray horizontal band.

In the RICH and MUON detector histograms, there are less available points; for these, it was felt that the histogram granularity requirements could be relaxed. The sequence of sampled displacements follow a logarithmic scale with three values per decade n (i.e. 1×10^n , 2×10^n , 5×10^n).

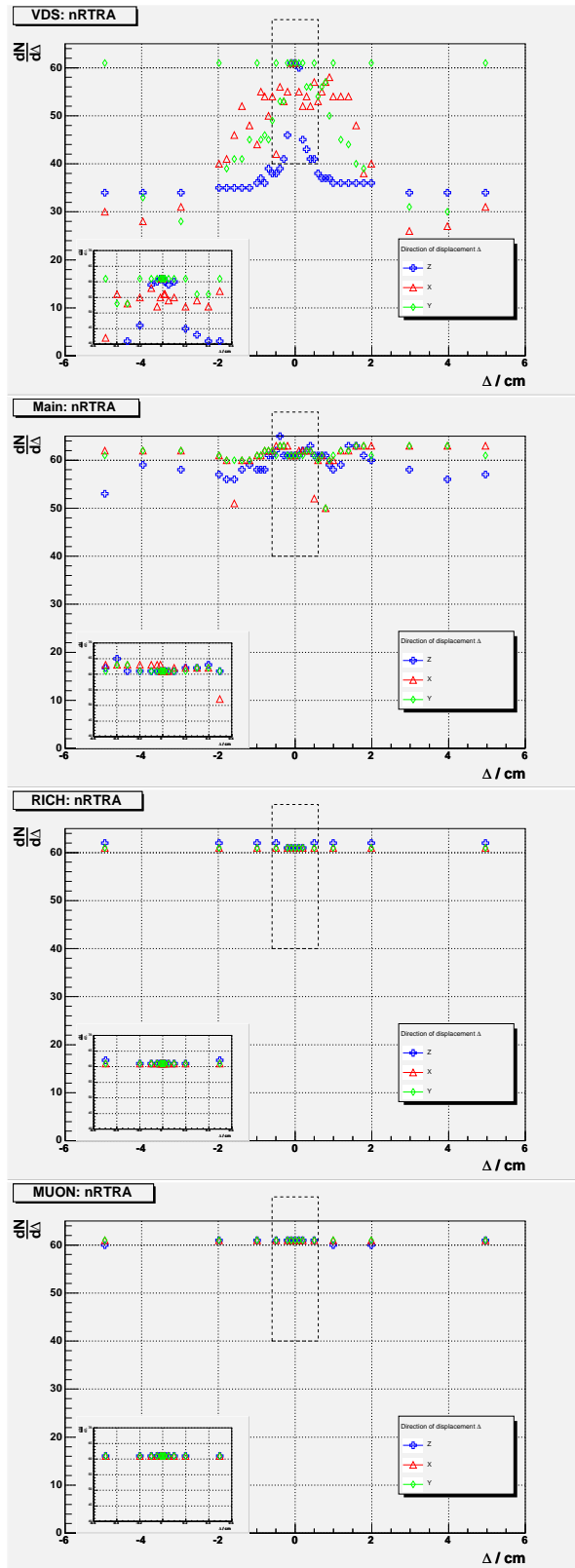


Figure A.33. Number of RTRAs in event for displacements of detectors along three orthogonal axes. From top to bottom: VDS, Main Tracker (ITR+OTR), RICH and Muon detector.

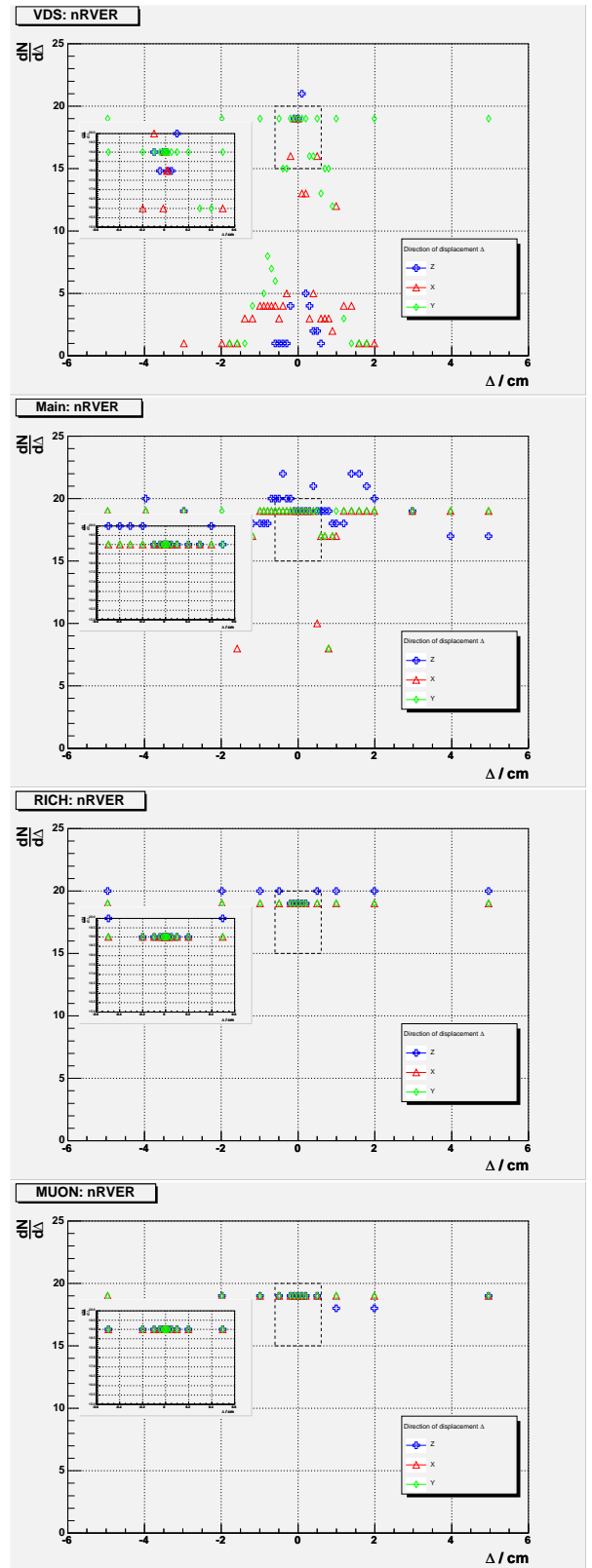


Figure A.34. Number of RVERs in event for displacements of detectors along three orthogonal axes. From top to bottom: VDS, Main Tracker (ITR+OTR), RICH and Muon detector.

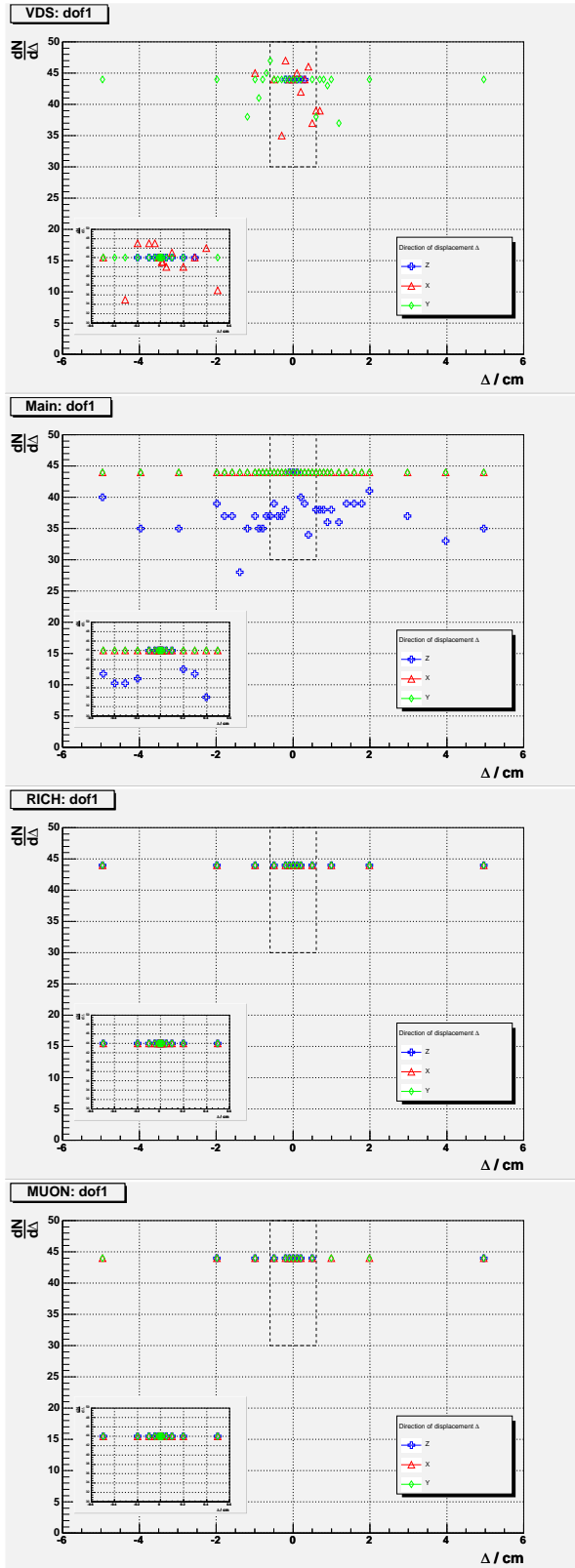


Figure A.35. Number of degrees of freedom for μ^+ RTRA (ARTE).

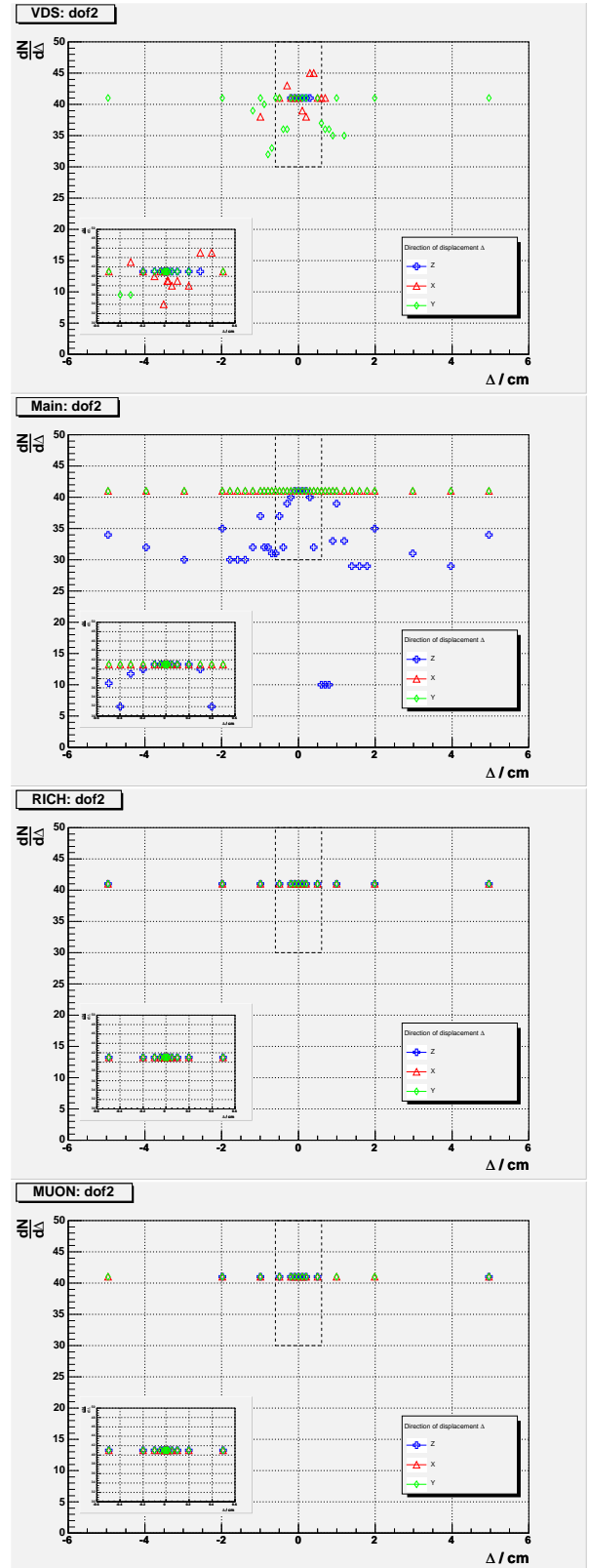


Figure A.36. Number of degrees of freedom for μ^- RTRA (ARTE).

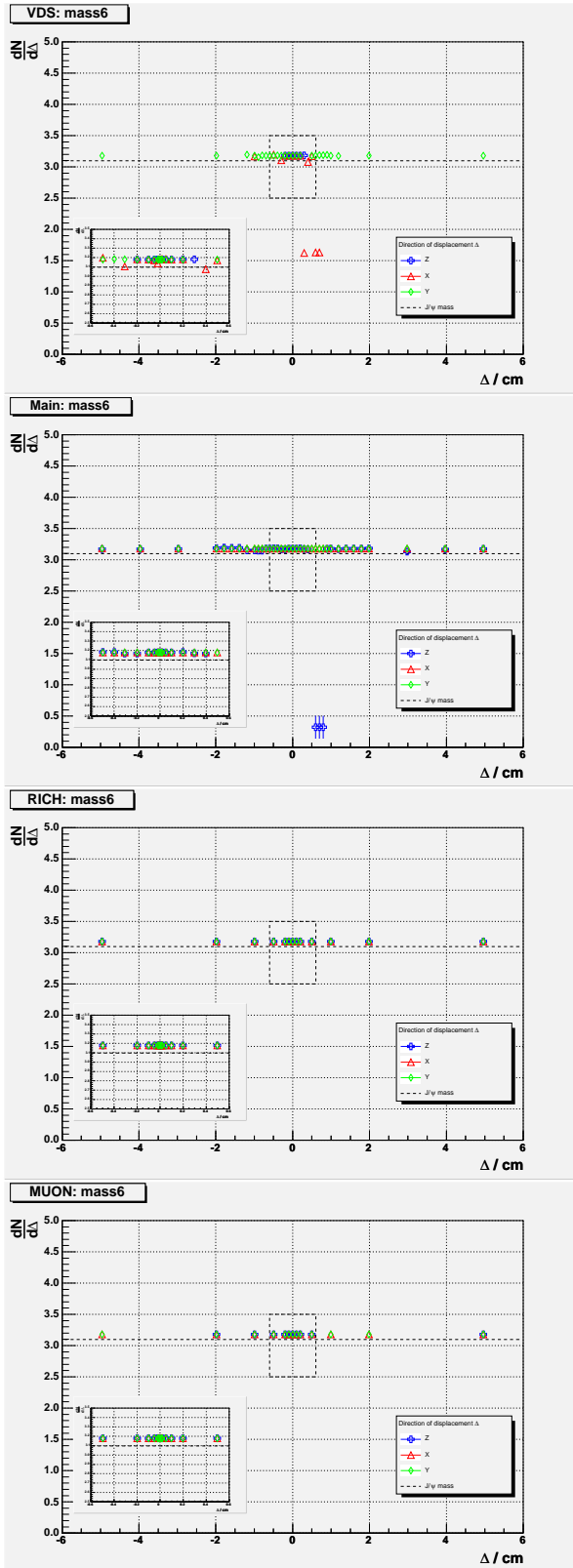


Figure A.37. Dimuon mass for Z, X, Y displacements (horizontal axes). From top to bottom: VDS; Main Tracker; RICH; and Muon detector displacements. The insets are for $|\Delta_i| < 200\mu\text{m}$. The masses were computed with PI.

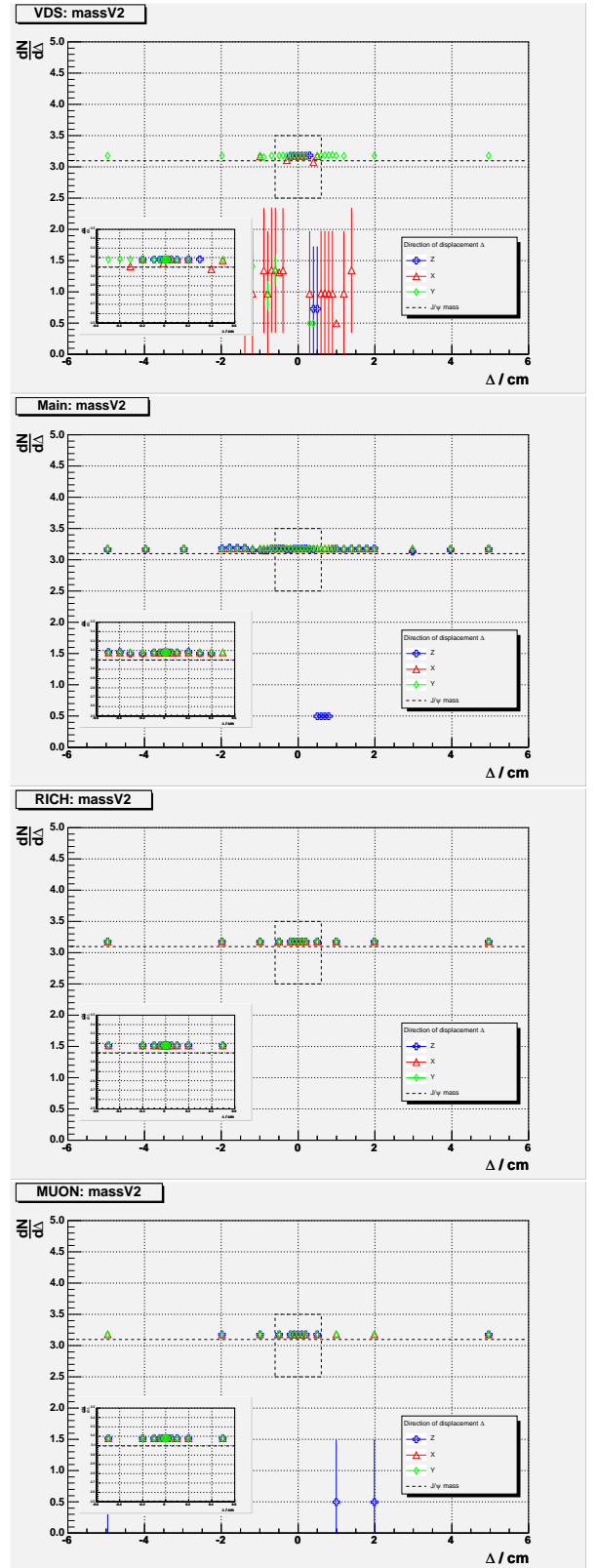


Figure A.38. RVER 2 mass for Z, X, Y displacements (horizontal axes). From top to bottom: VDS, Main Tracker, RICH, and Muon detector displacements. The insets are for $|\Delta_i| < 200\mu\text{m}$. The masses were obtained from ARTE table RVER.

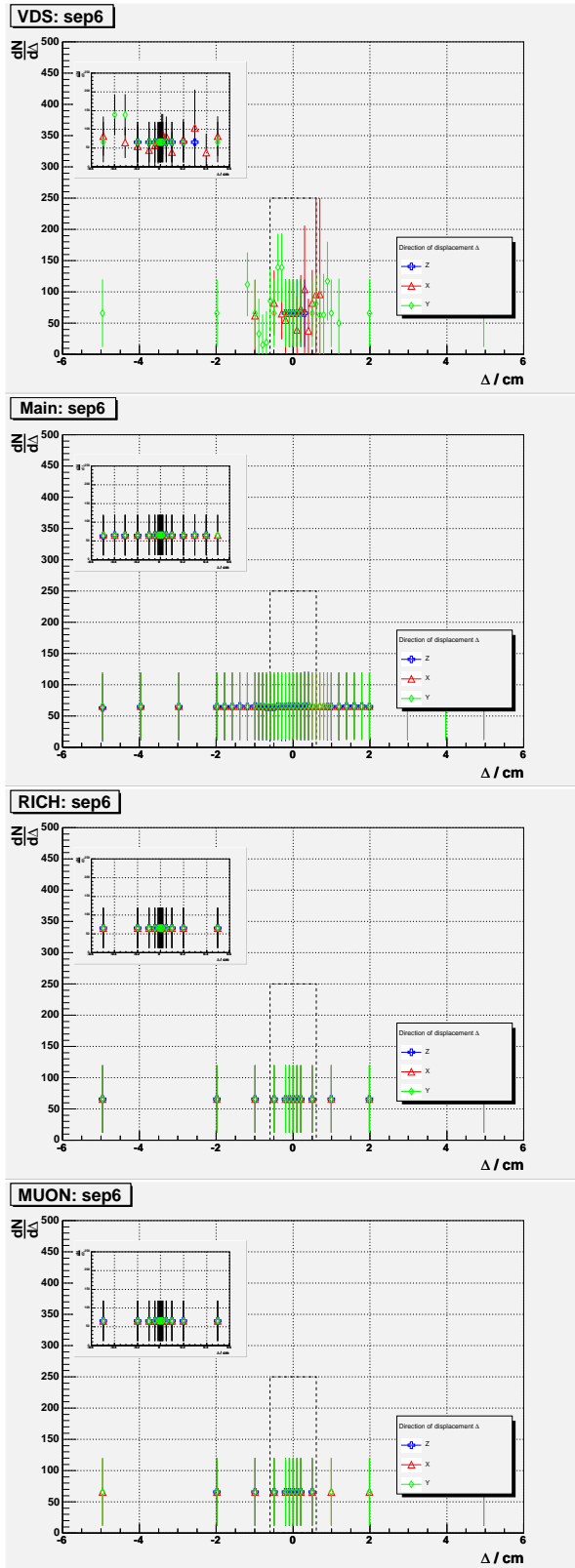


Figure A.39. Minimum separation (in micrometers) between the μ^\pm RTRAs.

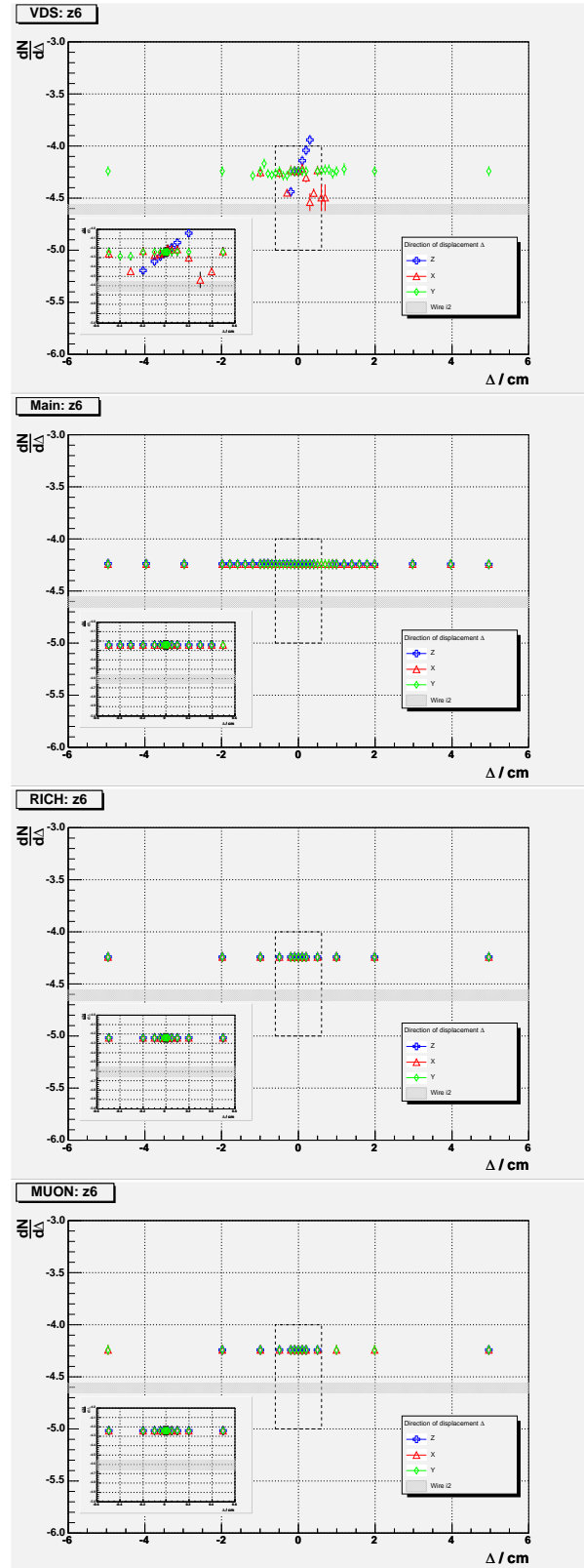


Figure A.40. Vertex longitudinal coordinate (in centimeters) of the dimuon, $z_{\mu\mu}$. The horizontal band represents the longitudinal bounds of the target wire.

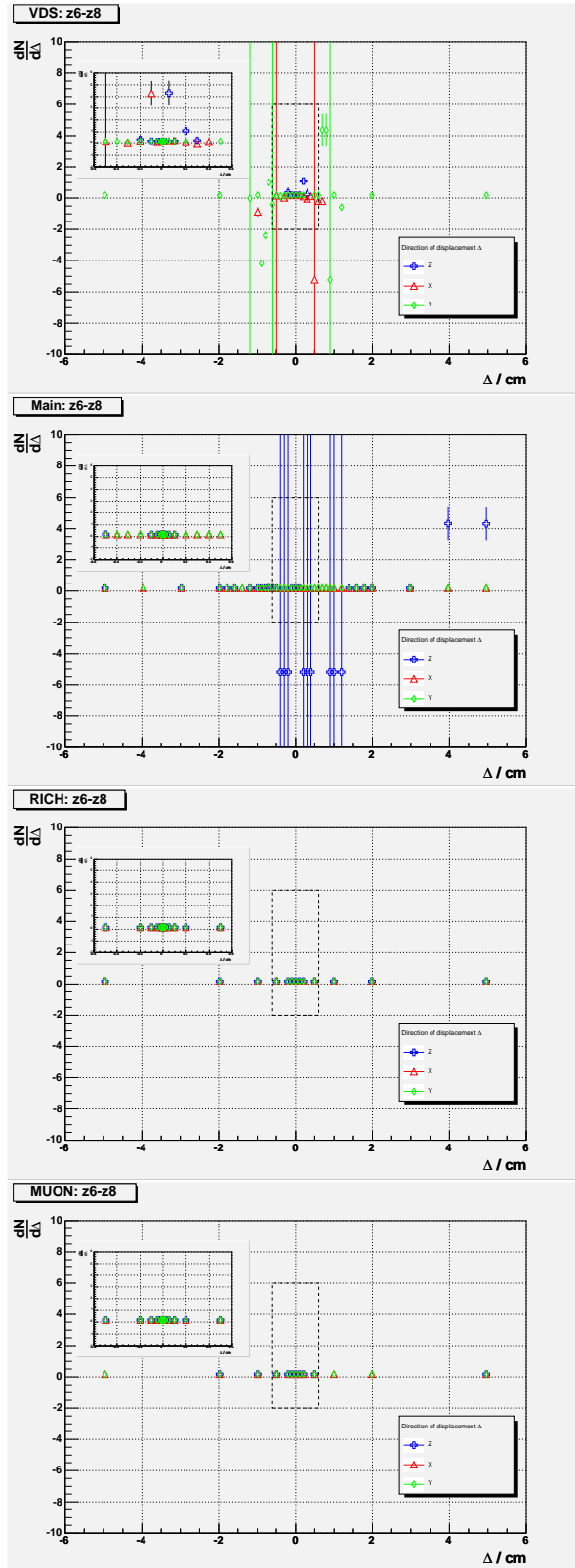


Figure A.41. Longitudinal separation (in centimeters) between the dimuon and the $\mu\mu\pi\pi$ (PI).

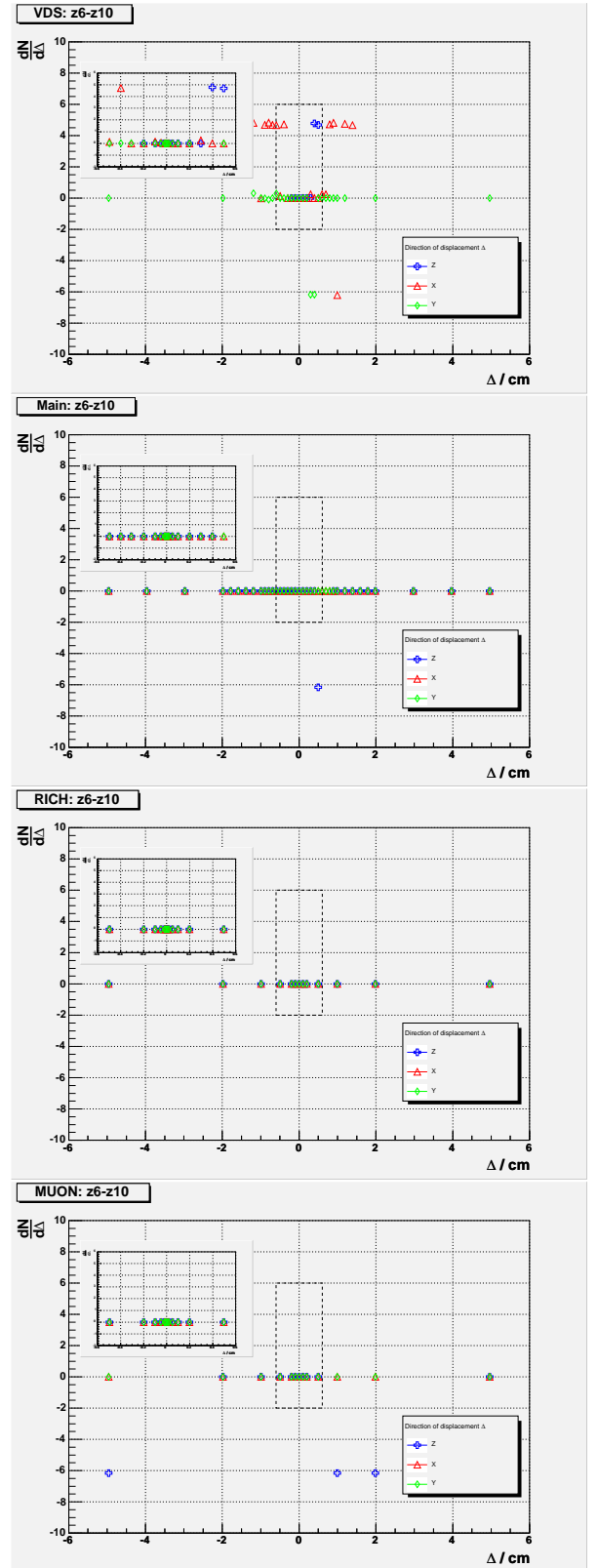


Figure A.42. Longitudinal separation (in centimeters) between the dimuon (PI) and the RVER 2 (ARTE).

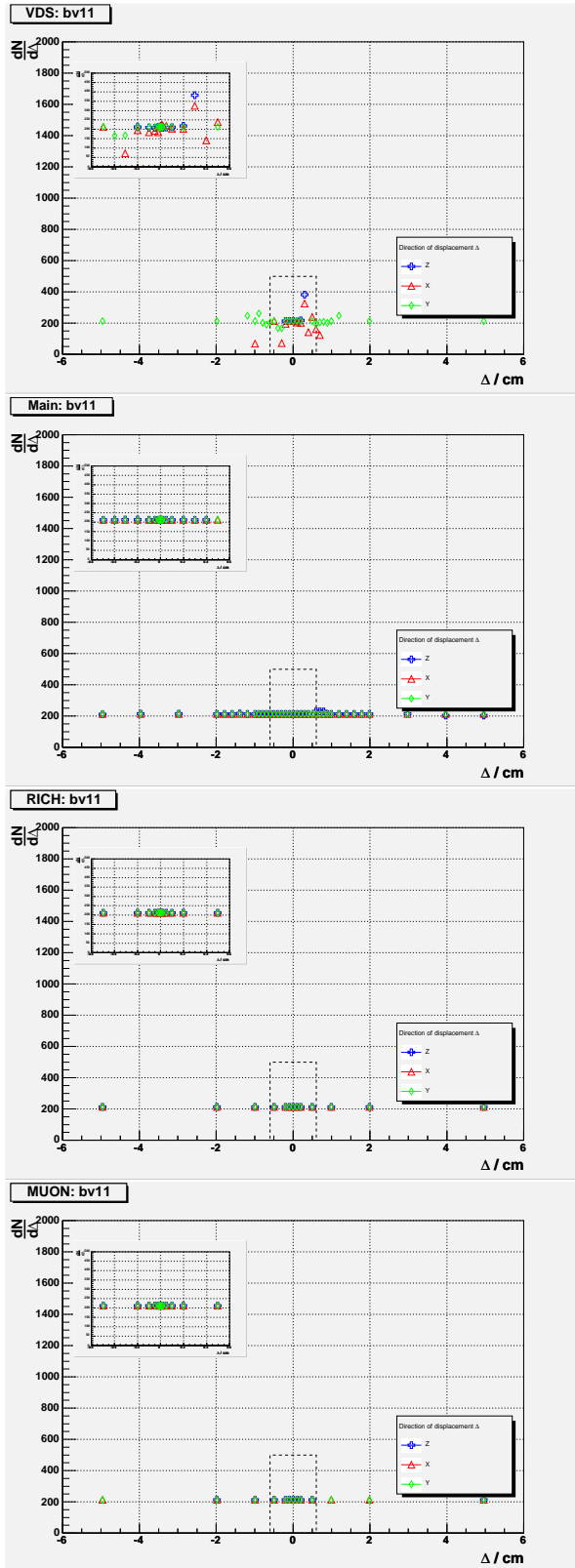


Figure A.43. D.C.A. (in micrometers) of μ^+ to RVER 1. Computed with PI.

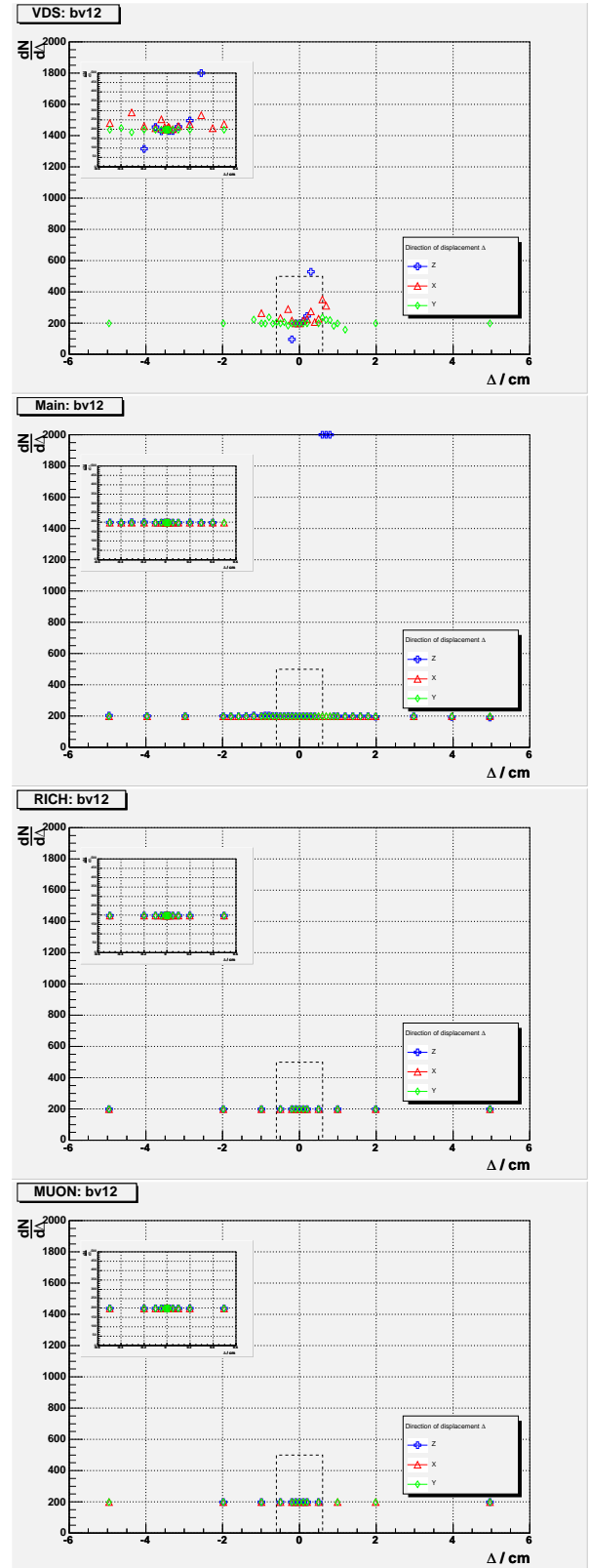


Figure A.44. D.C.A. (in micrometers) of μ^- to RVER 1. Computed with PI.

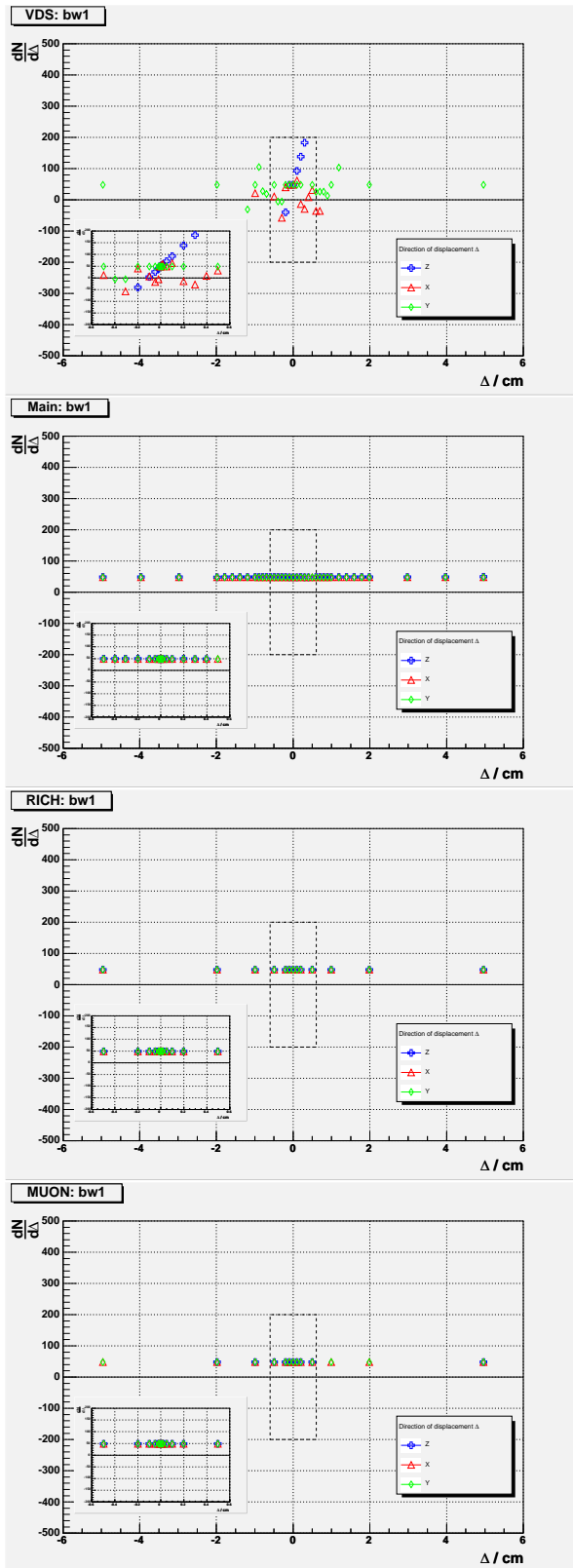


Figure A.45. Impact parameter (in micrometers) of μ^+ to target wire. Computed with PI.

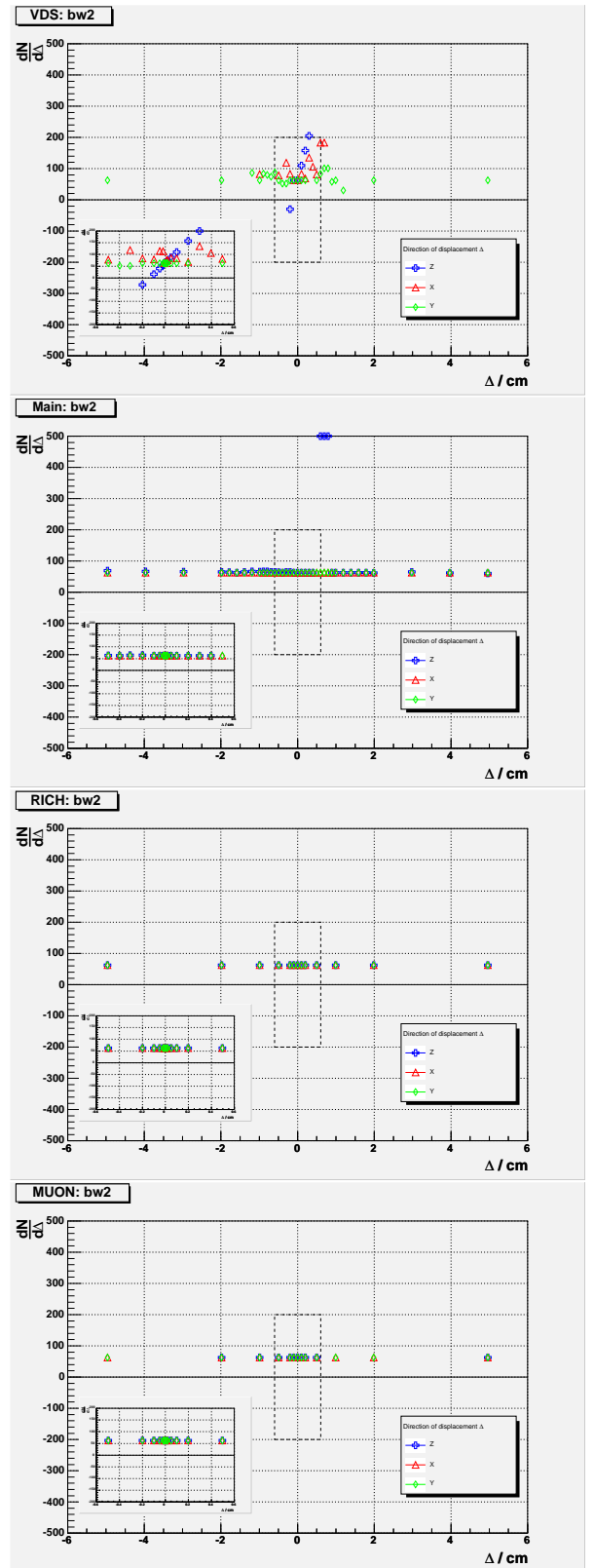


Figure A.46. Impact parameter (in micrometers) of μ^- to target wire. Computed with PI.

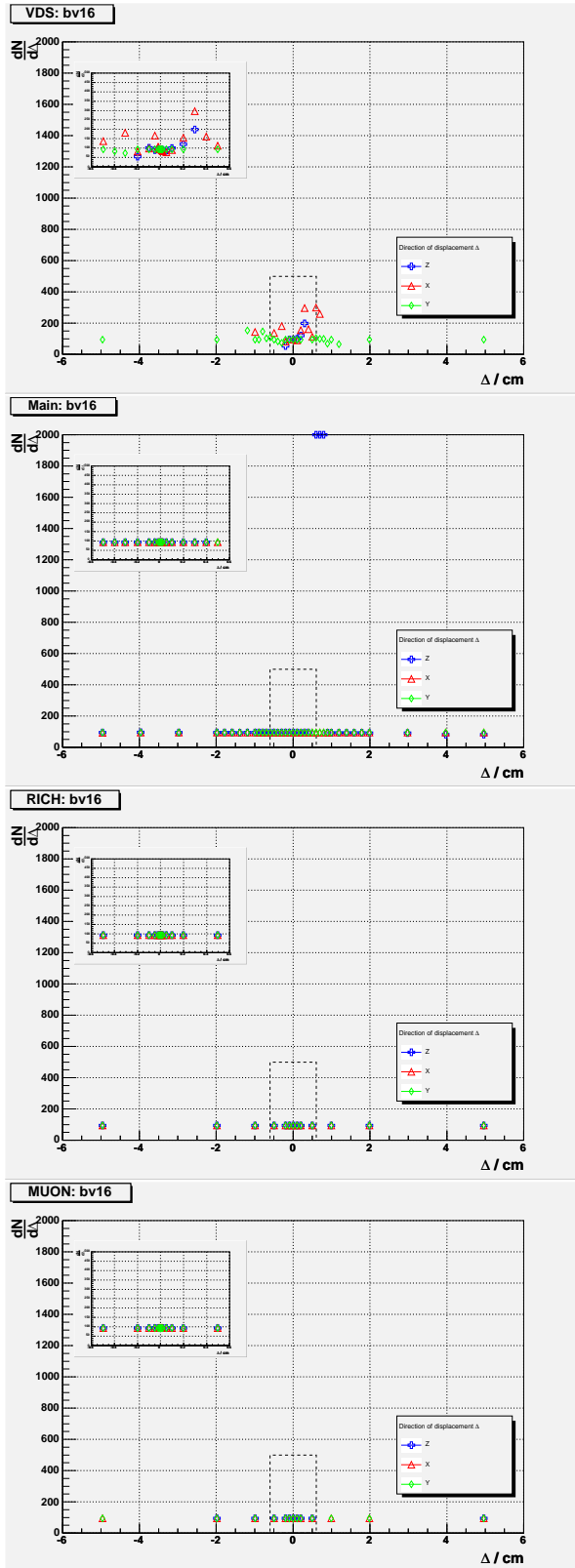


Figure A.47. D.C.A. (in micrometers) of dimuon to RVER 1. Computed with PI.

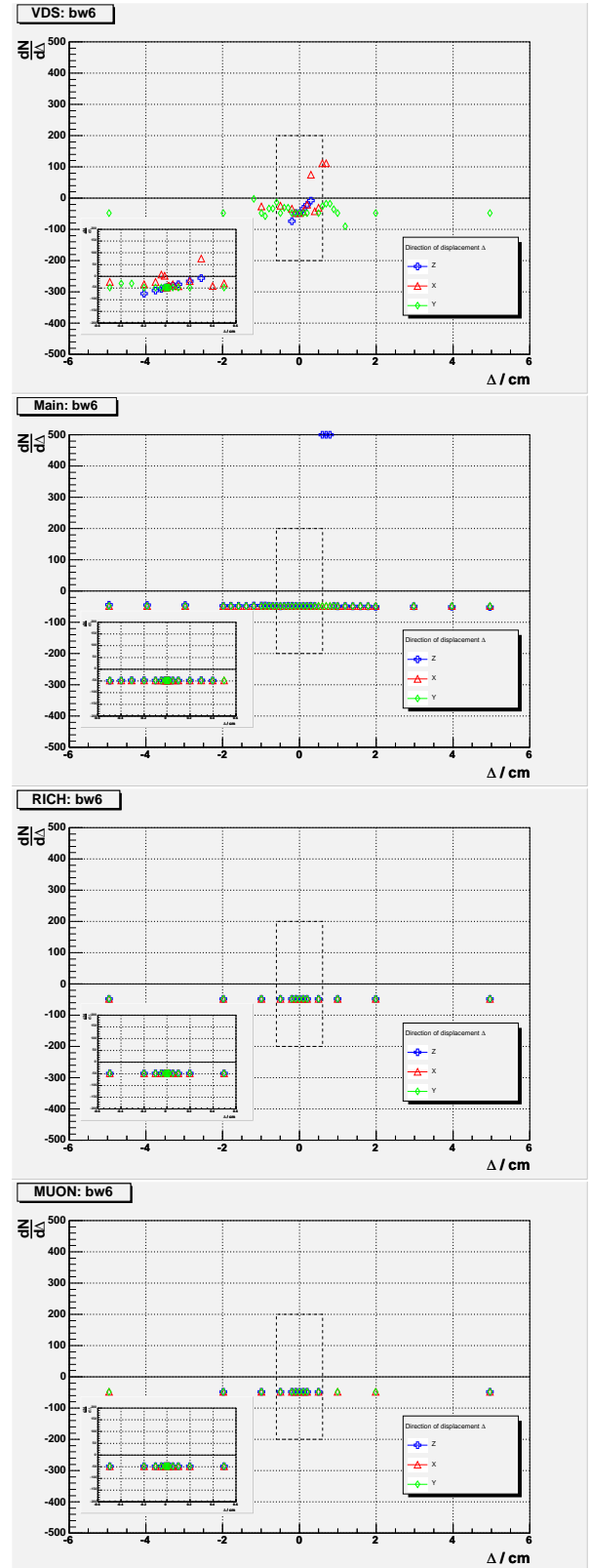


Figure A.48. Impact parameter (in micrometers) of dimuon to target wire. Computed with PI.

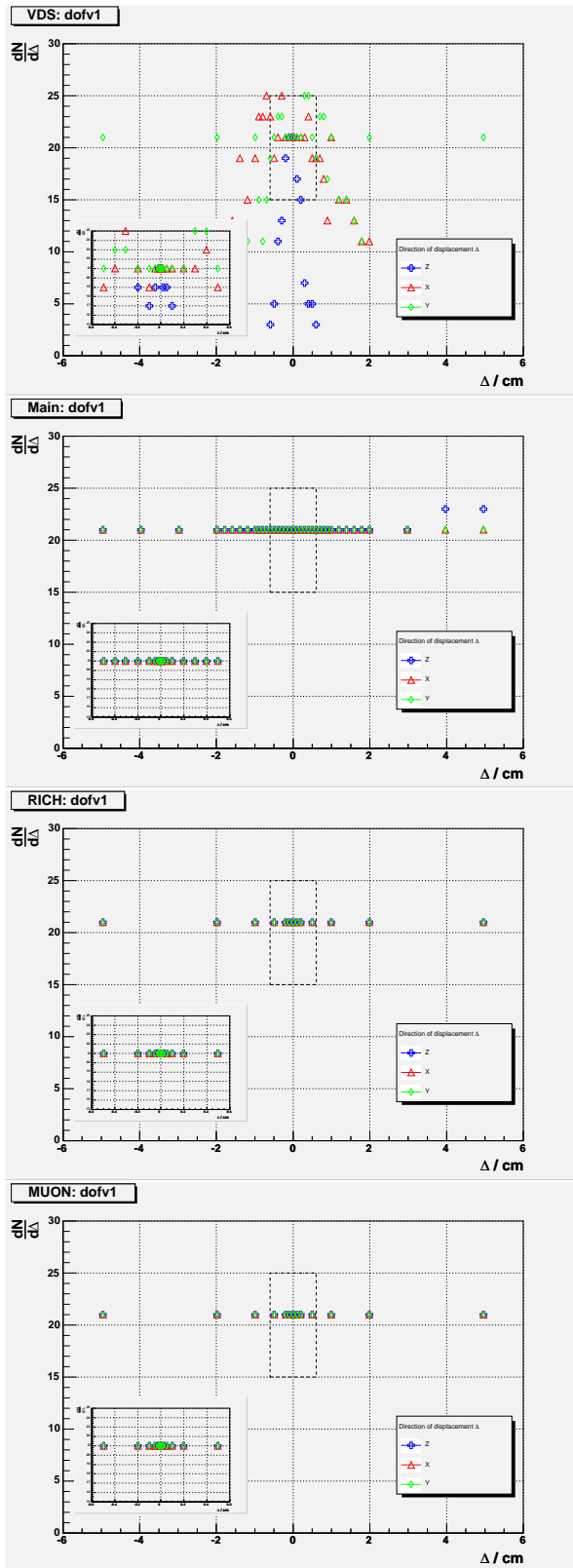


Figure A.49. Number of degrees of freedom for RVER 1 (ARTE).

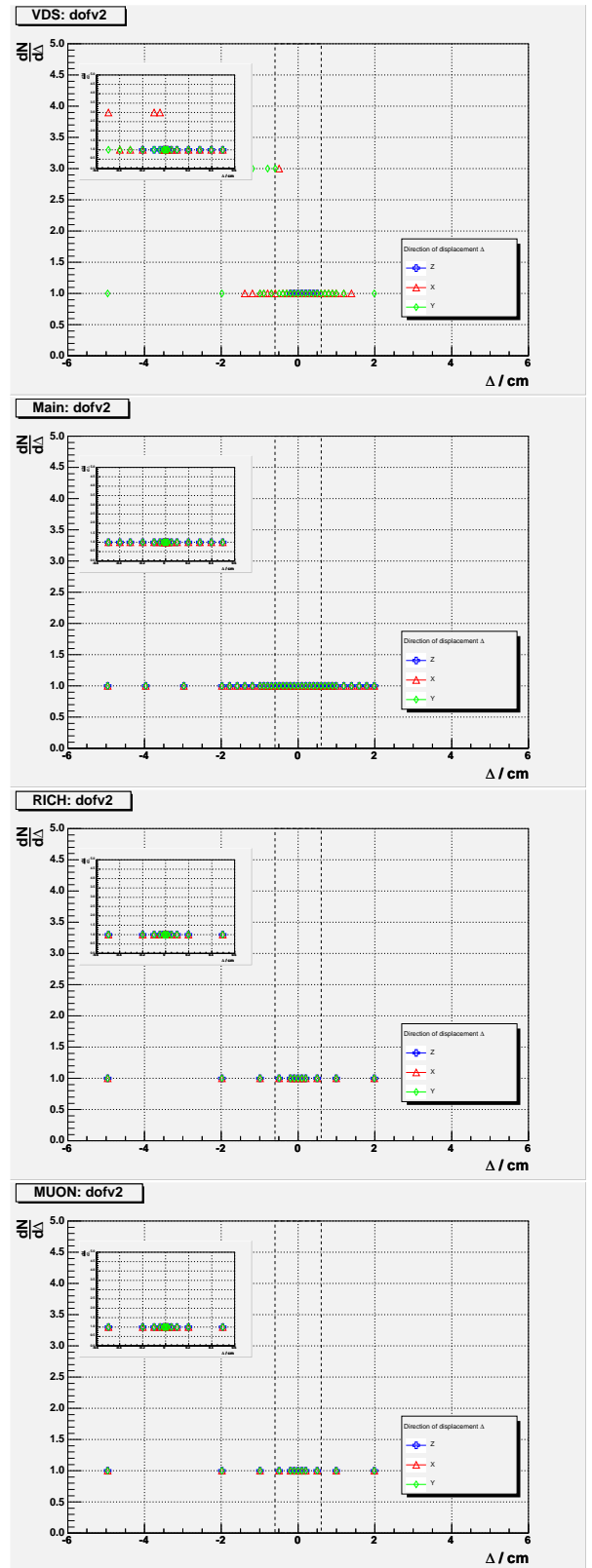


Figure A.50. Number of degrees of freedom for RVER 2 (ARTE).

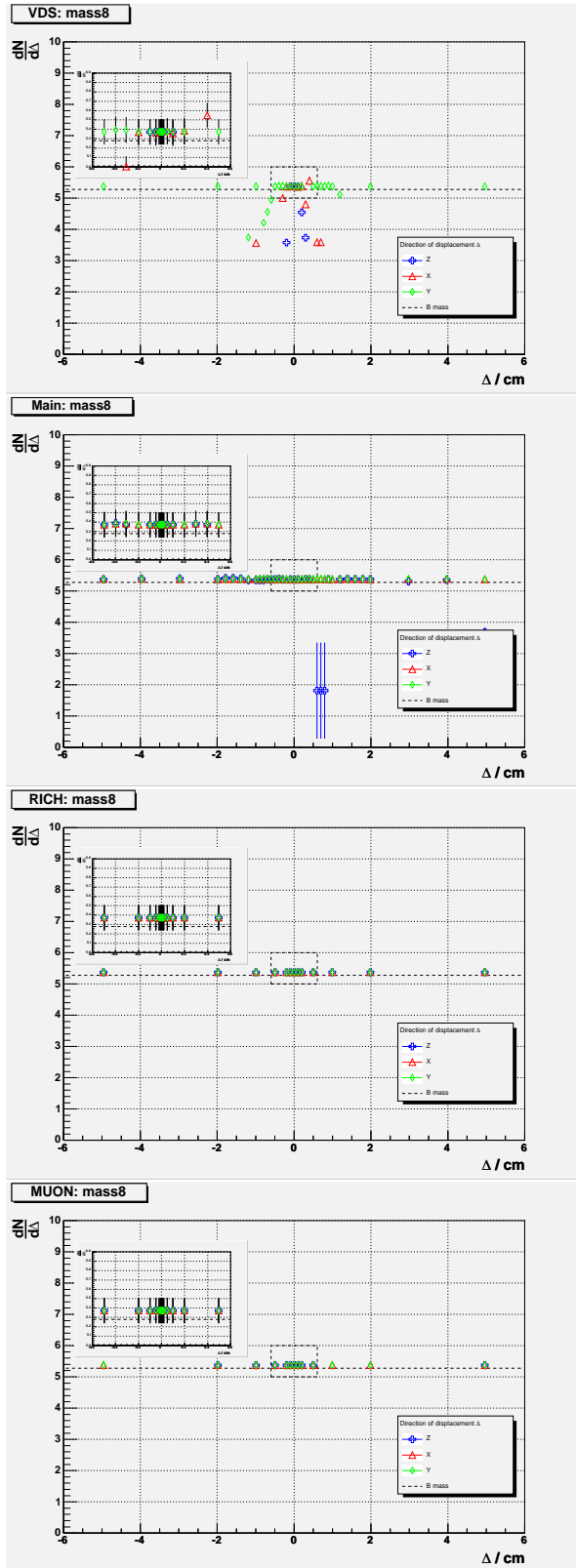


Figure A.51. $\mu\pi\pi$ mass (computed with PI) for VDS module displacements in Z (top), X (middle) and Y (bottom).

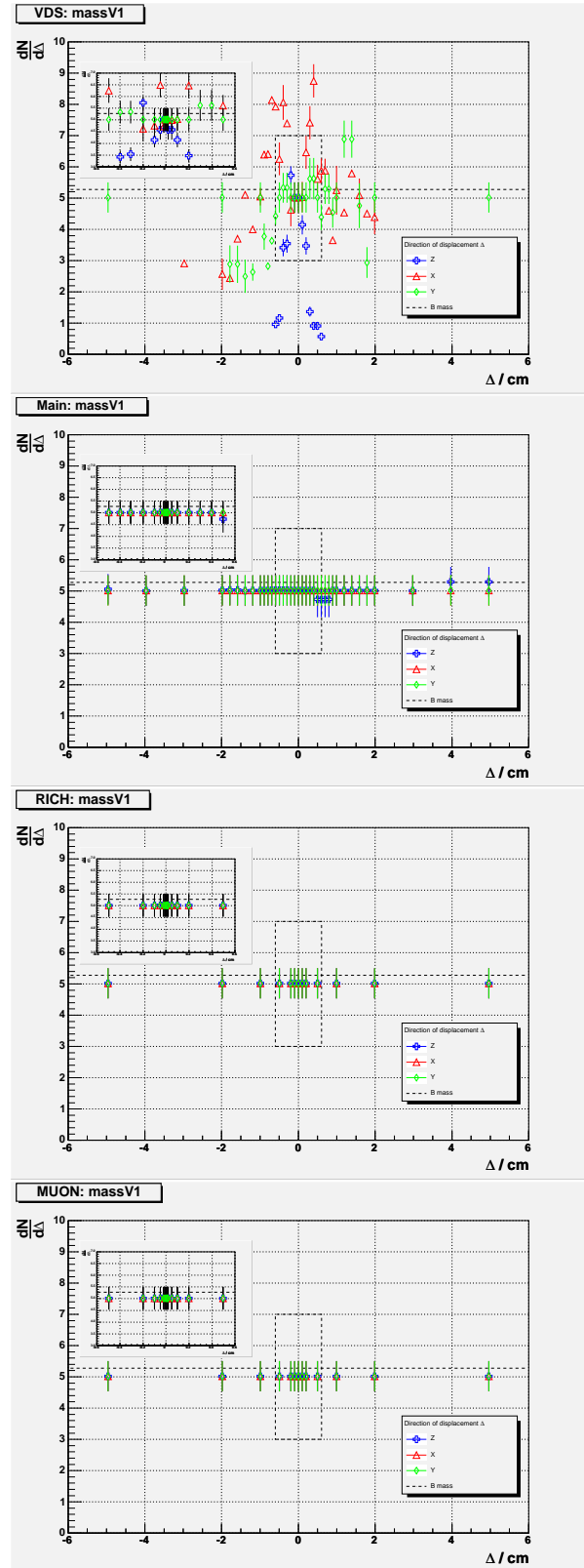


Figure A.52. RVER 1 mass (from ARTE) for VDS module displacements in Z (top), X (middle) and Y (bottom).

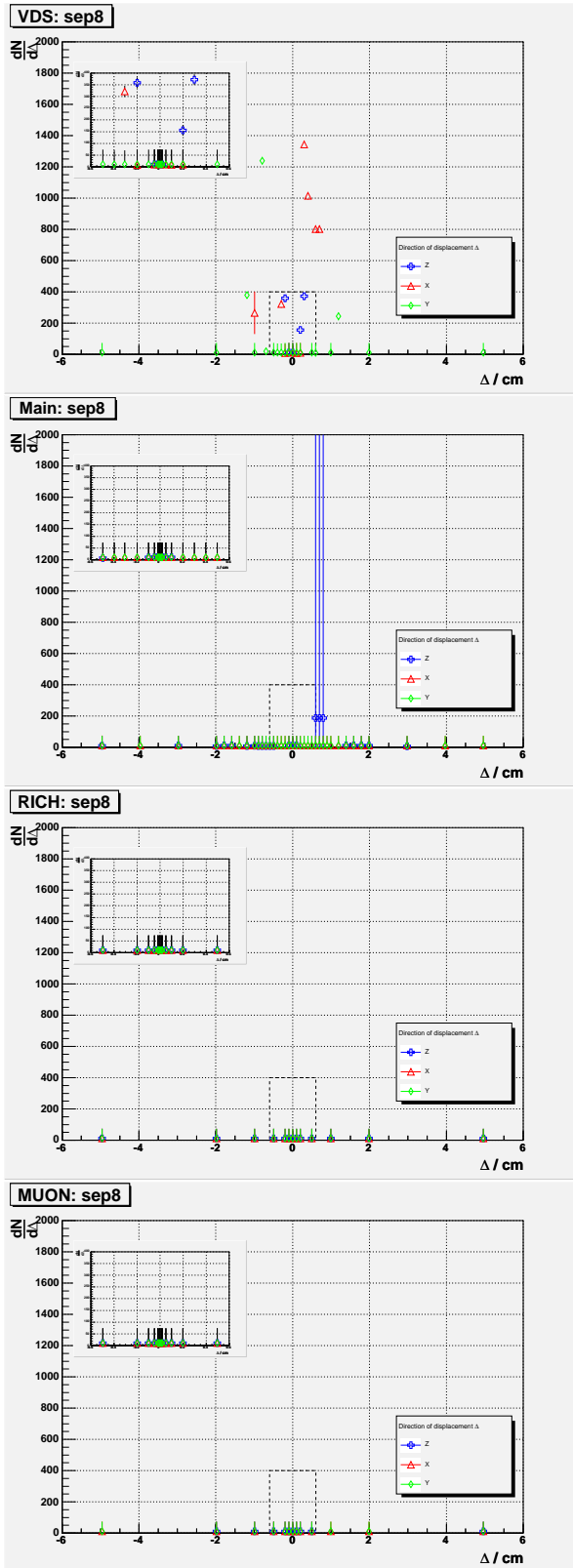


Figure A.53. Minimum separation (in micrometers) between the dimuon and the dipion. Computed with PI.

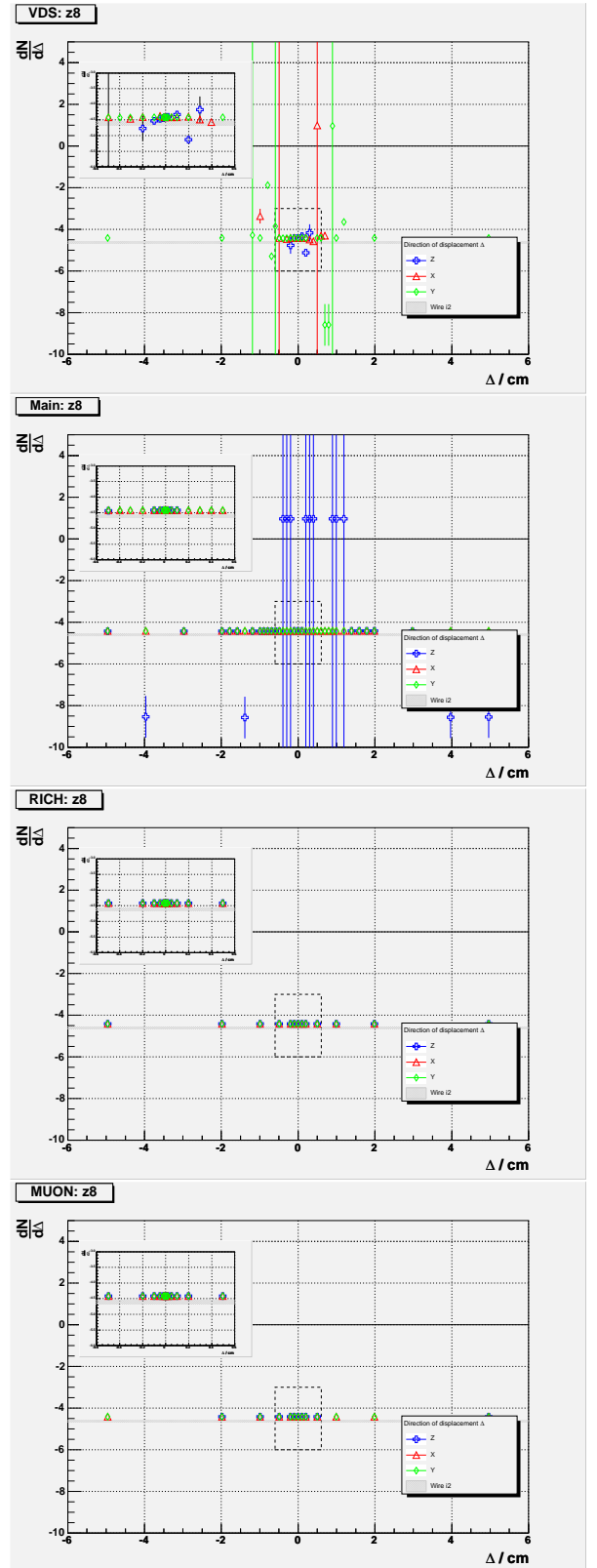


Figure A.54. Vertex longitudinal coordinate (in centimeters) of the $\mu\mu\pi\pi$. Computed with PI.

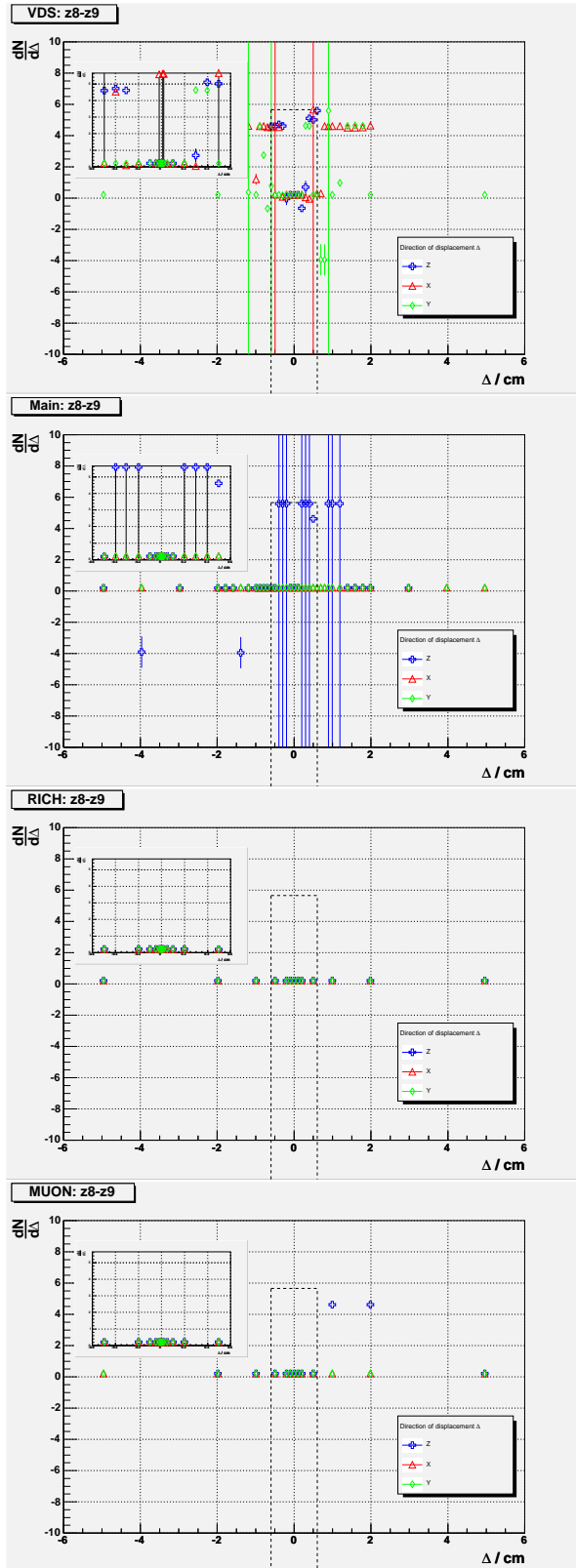


Figure A.55. Longitudinal separation (in centimeters) of the $\mu\pi\pi$ (PI) and the RVER 1 (ARTE).

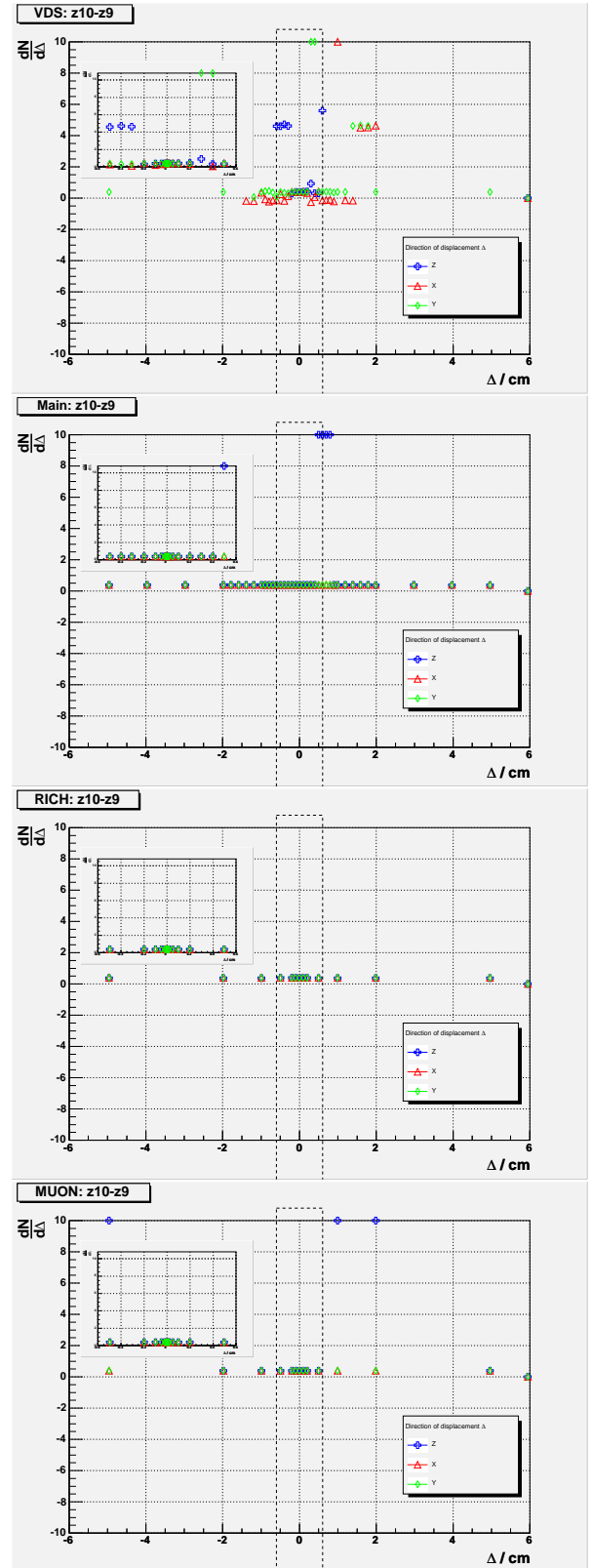


Figure A.56. Longitudinal separation (in centimeters) of the RVER 2 to the RVER 1 (ARTE).

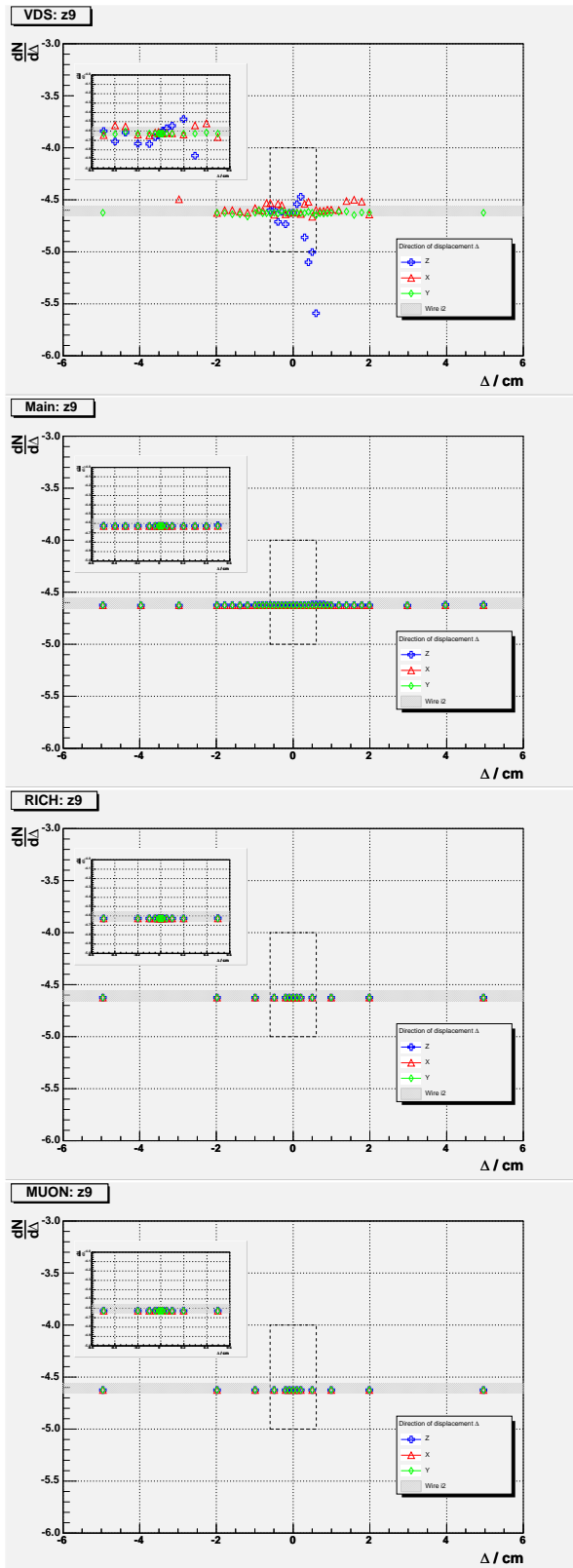


Figure A.57. RVER 1 longitudinal coordinate (ARTE).

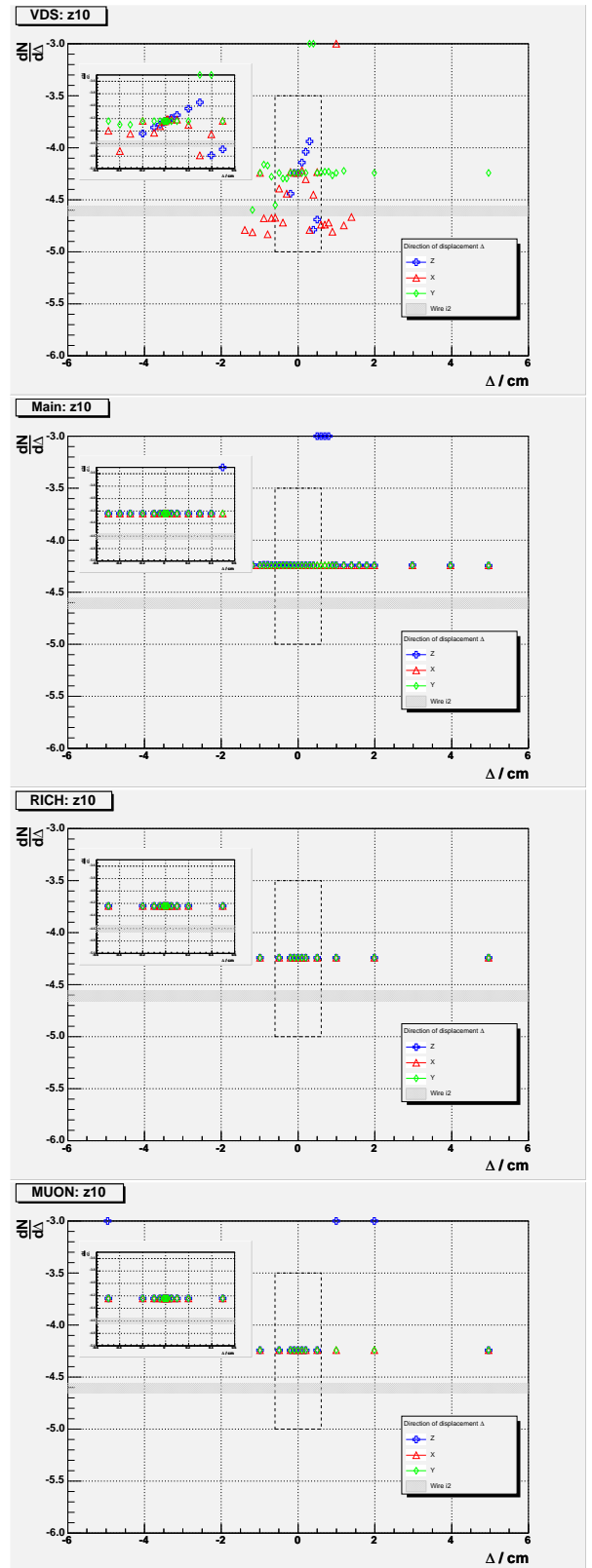


Figure A.58. RVER 2 longitudinal coordinate (ARTE).

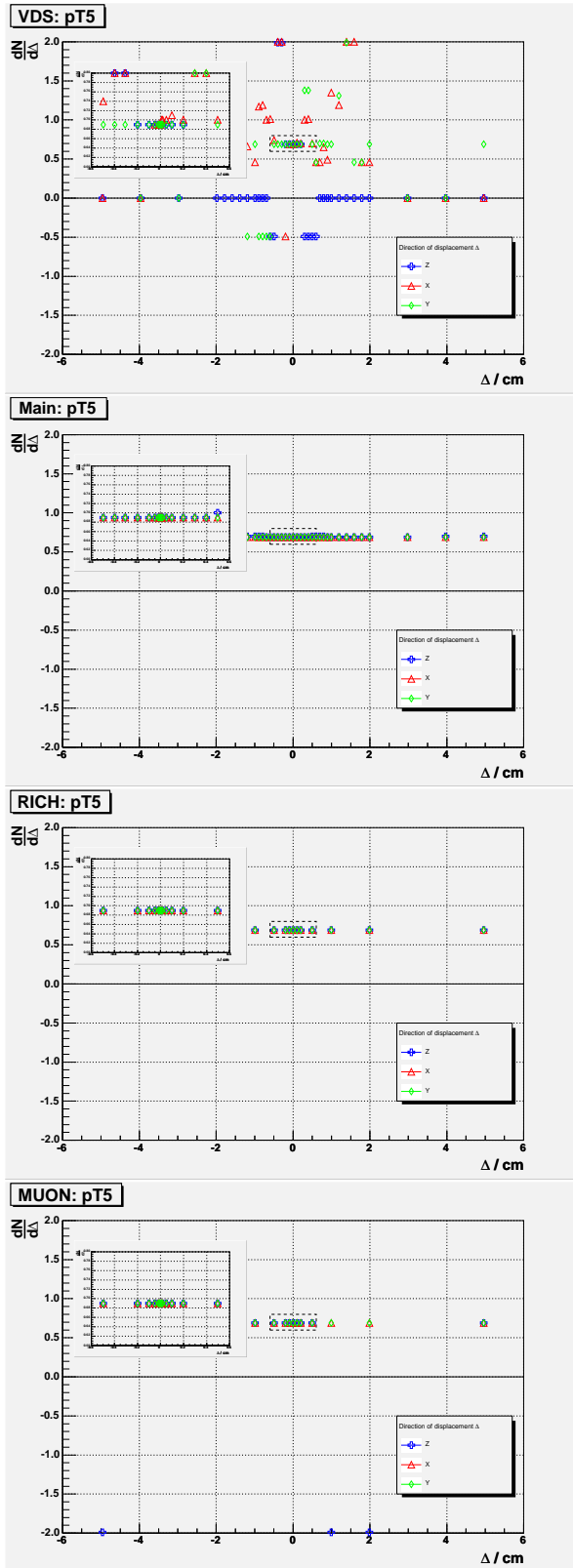


Figure A.59. $q \times p_T$ (in GeV/c) of RTRA selected (PI) for B flavour tag. The charge $q = \pm 1$ is the sign of deflection (in the zx projection) of RTRA inside the Magnet. The gap in the color scale corresponds to the cut $p_T > 0.3 \text{ GeV}/c$ applied.

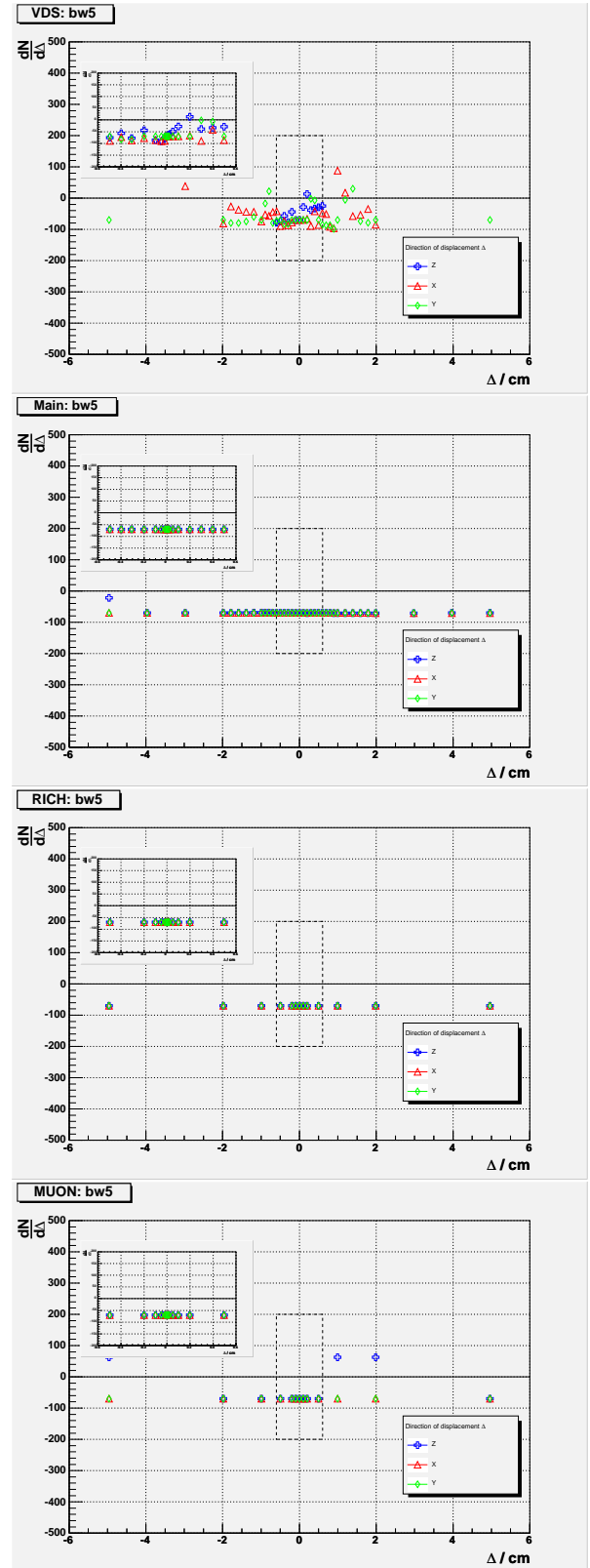


Figure A.60. Impact parameter (in micrometers) of the tagging RTRA. Computed with PI.

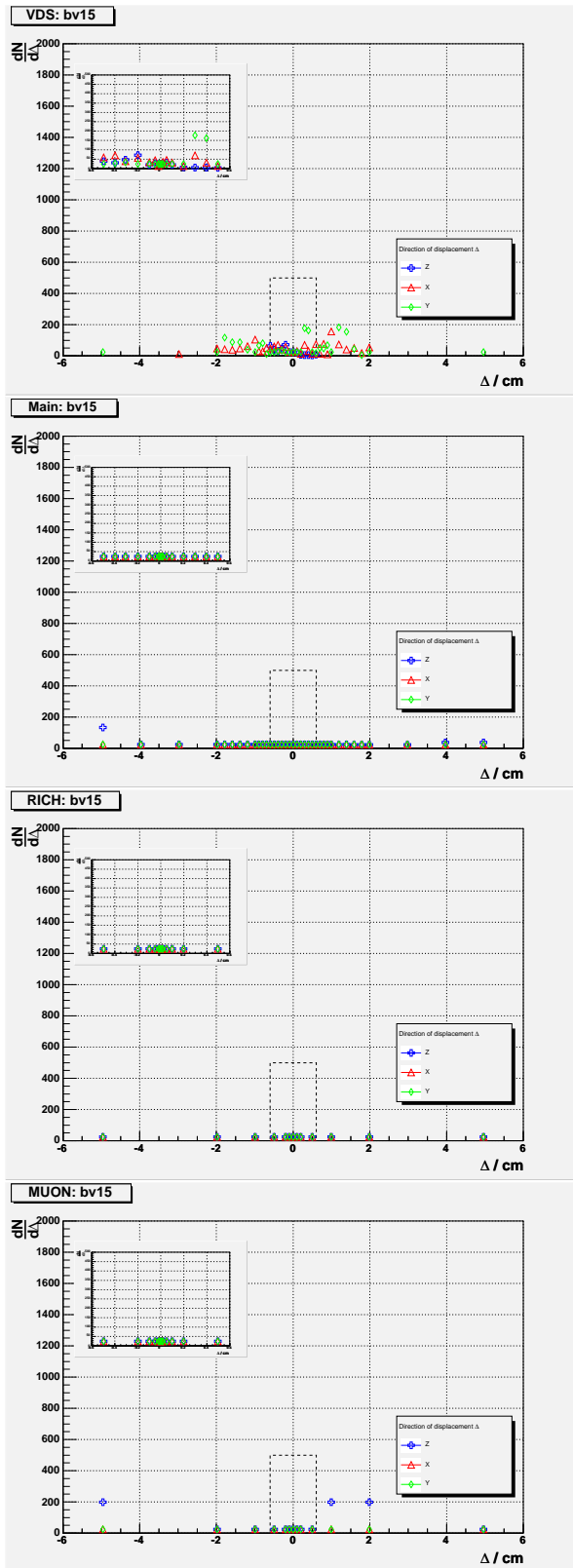


Figure A.61. D.C.A. of tagging RTRA to RVER 1. Computed with PI.

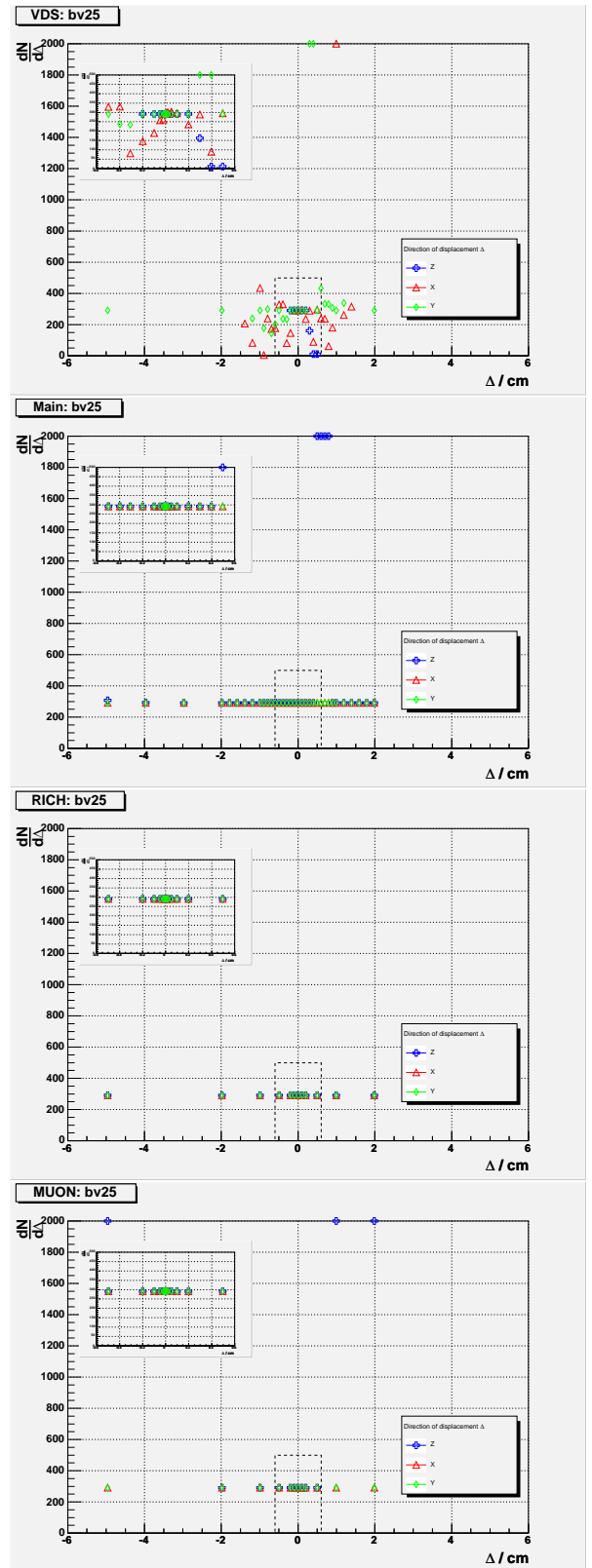


Figure A.62. D.C.A. of tagging RTRA to RVER 2. Computed with PI.

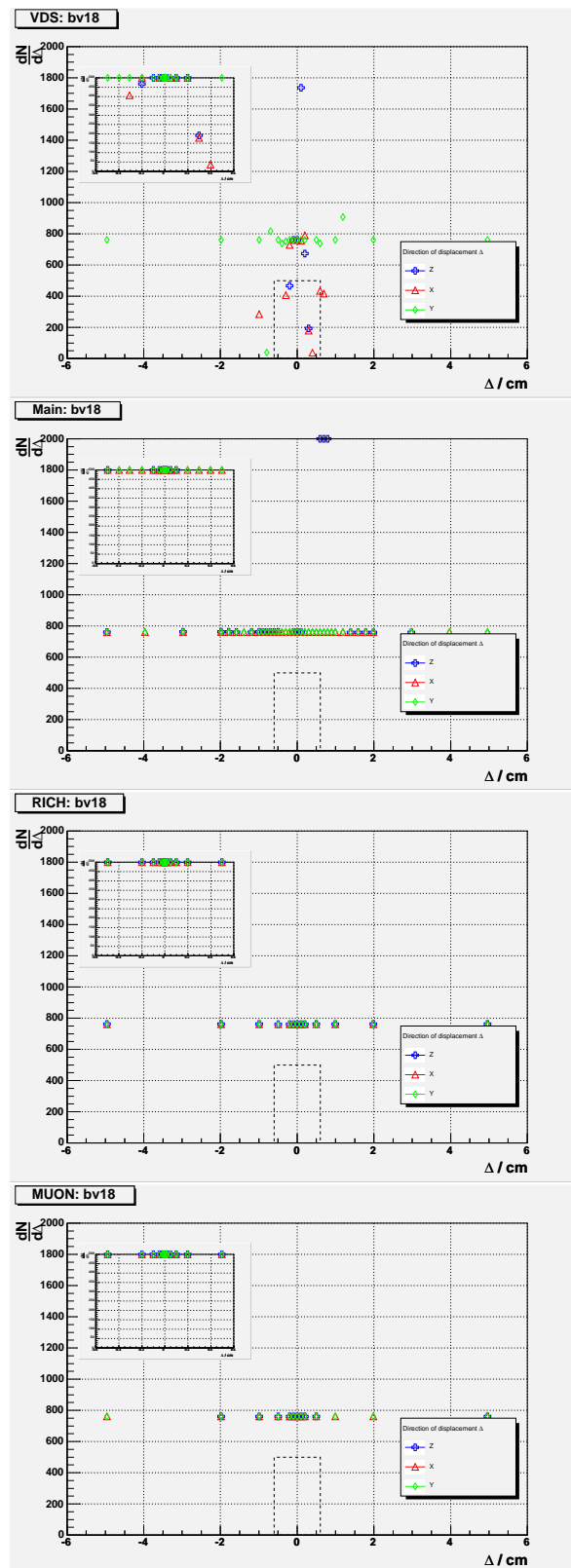
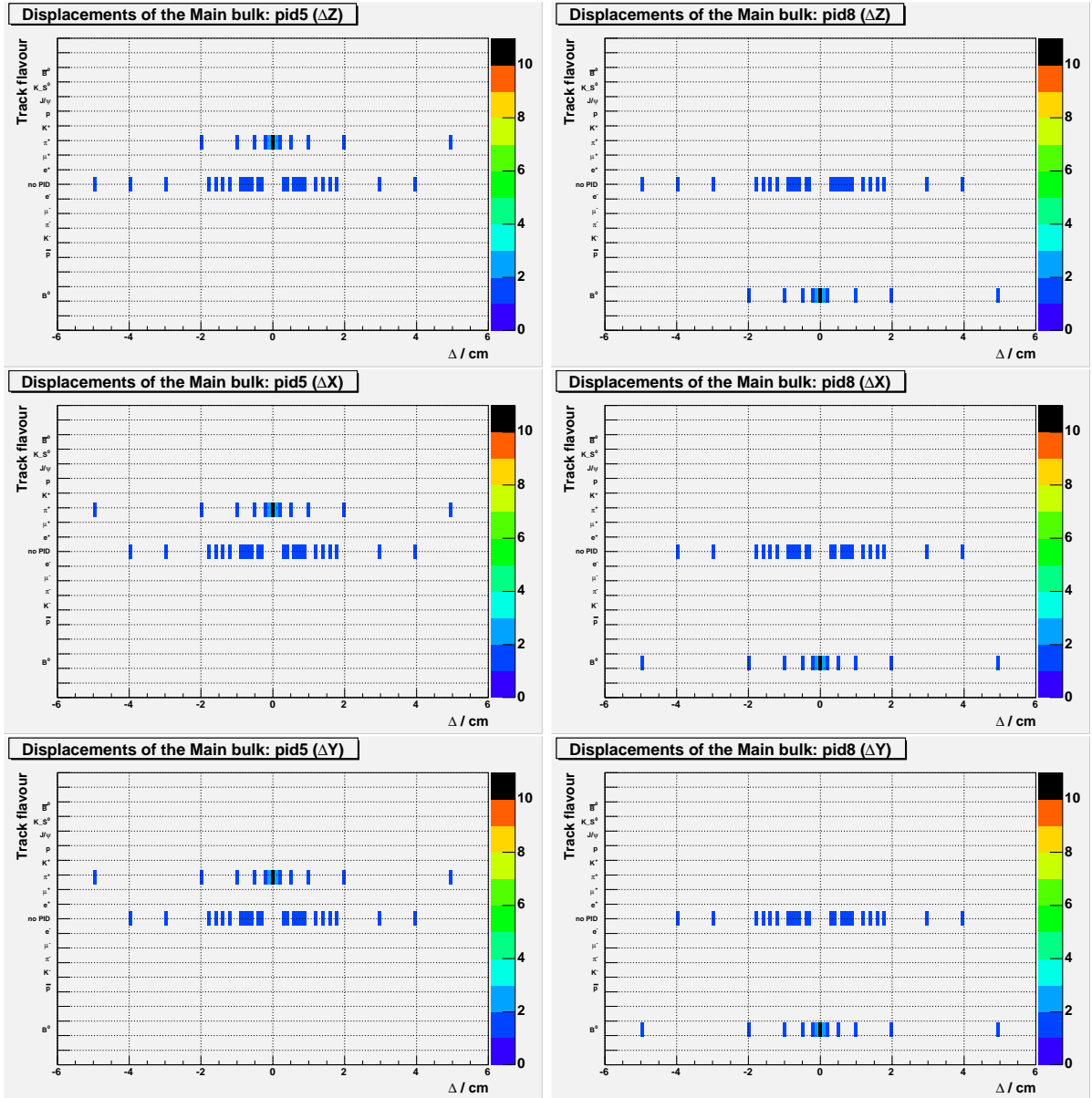


Figure A.63. Impact parameter (in micrometers) of $\mu\pi\pi$ to RVER 1. Computed with PI.



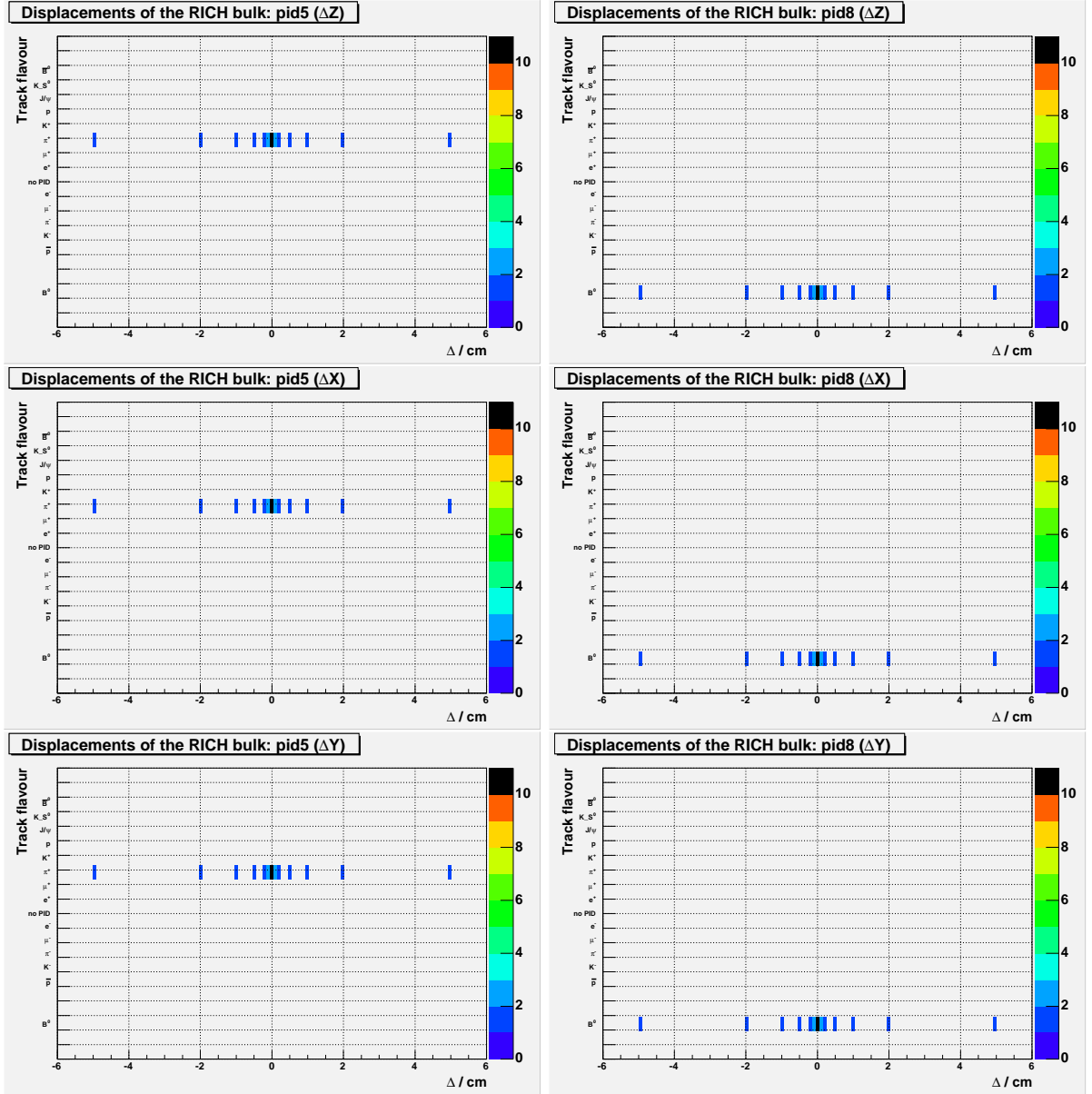


Figure A.68. Flavour of highest- p_T RTRA (ARTE) used for B flavour tagging, for RICH displacements.

Figure A.69. Golden decay B meson flavour, obtained with charge tag from highest- p_T RTRA (ARTE), for RICH displacements.

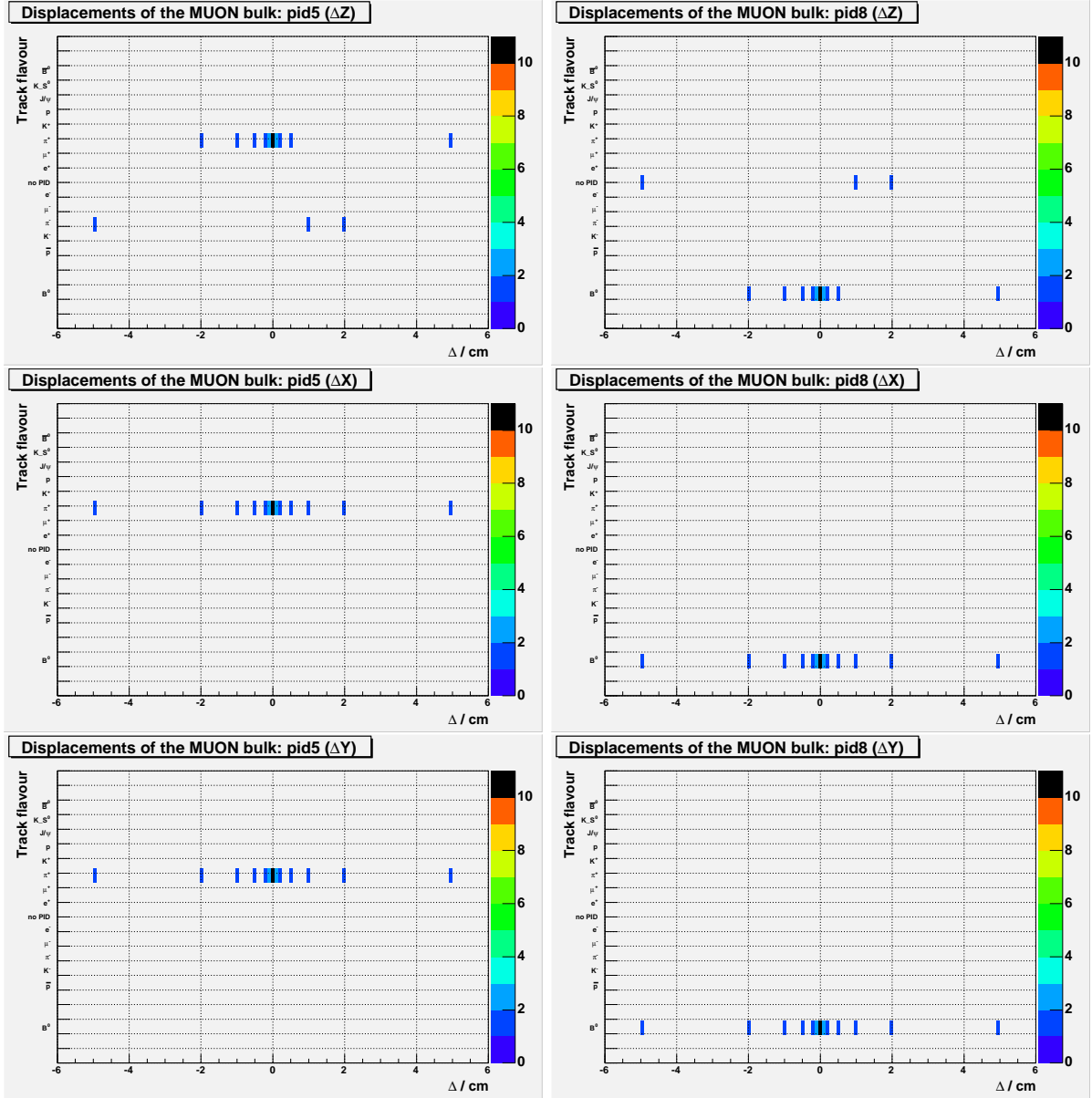


Figure A.70. Flavour of highest- p_T RTRA (ARTE) used for B flavour tagging, for Muon detector displacements.

Figure A.71. Golden decay B meson flavour, obtained with charge tag from highest- p_T RTRA (ARTE), for Muon detector displacements.

Useful algebraic expressions

B.1 Minimum distance between two skewed lines

Let \vec{r}_1 and \vec{r}_2 be two skewed lines of a euclidean space \mathbb{R}^3 , i.e. they are not parallel and do not touch:

$$\vec{r}_1 = \vec{d}_1 + \lambda_1 \vec{n}_1 , \quad (\text{B.1a})$$

$$\vec{r}_2 = \vec{d}_2 + \lambda_2 \vec{n}_2 . \quad (\text{B.1b})$$

Let A and B — two points of \vec{r}_1 and \vec{r}_2 , respectively — lie in the transversal lever that joins the two lines. Let this transversal have the direction of the unit vector \vec{n}_3 , and let ρ be the length of the transversal joining points A and B . Therefore, obtaining the minimum separation (and its direction) between the lines \vec{r}_1 and \vec{r}_2 is equivalent to finding λ_1 and λ_2 ,

$$\vec{r}_1 + \rho \vec{n}_3 = \vec{r}_2 \quad \Leftrightarrow \quad \rho \vec{n}_3 = \vec{d}_2 - \vec{d}_1 + \lambda_2 \vec{n}_2 - \lambda_1 \vec{n}_1 . \quad (\text{B.2})$$

By construction \vec{n}_3 is orthogonal to both \vec{n}_1 and \vec{n}_2 , therefore multiplying both members of the last equation by \vec{n}_3 yields

$$\rho = \left(\vec{d}_2 - \vec{d}_1 \right) \cdot \vec{n}_3 , \quad (\text{B.3})$$

since $\vec{n}_i \cdot \vec{n}_3 = \delta_{i3}$ for $i = 1, 2, 3$.

The vector product of two non-collinear \mathbb{R}^3 vectors yields a vector orthogonal to the other two; therefore, it is adequate to make $\vec{n}_3 \propto \vec{n}_1 \times \vec{n}_2$. To ensure \vec{n}_3 has unit module, we define

$$\vec{n}_3 = \frac{\vec{n}_1 \times \vec{n}_2}{|\vec{n}_1 \times \vec{n}_2|} . \quad (\text{B.4})$$

Finally, the minimum distance between the two skewed lines is given by

$$\rho = \left(\vec{d}_2 - \vec{d}_1 \right) \cdot \frac{\vec{n}_1 \times \vec{n}_2}{|\vec{n}_1 \times \vec{n}_2|} . \quad (\text{B.5})$$

After some simple vector algebra, we may also get from (B.3) the solutions for λ_1 and λ_2 . Let $\vec{d} \equiv \vec{d}_2 - \vec{d}_1$. We get:

$$0 = \vec{d} \times \vec{n}_1 + \lambda_2 \vec{n}_2 \times \vec{n}_1, \quad (\text{B.6})$$

$$0 = \vec{d} \times \vec{n}_2 - \lambda_1 \vec{n}_1 \times \vec{n}_2. \quad (\text{B.7})$$

since $\vec{n} \times \vec{n} = 0$ for an arbitrary $\vec{n} \in \mathbb{R}^3$. Therefore, and using the identity $(\vec{a} \times \vec{c}) \cdot (\vec{b} \times \vec{c}) = (\vec{a} \cdot \vec{b})(\vec{c} \cdot \vec{c}) - (\vec{a} \cdot \vec{c})(\vec{b} \cdot \vec{c})$, we get

$$\lambda_1 = \frac{\vec{d} \times \vec{n}_2}{|\vec{n}_1 \times \vec{n}_2|} \cdot \vec{n}_3 = \frac{(\vec{d} \cdot \vec{n}_1)\vec{n}_2^2 - (\vec{d} \cdot \vec{n}_2)(\vec{n}_1 \cdot \vec{n}_2)}{|\vec{n}_1 \times \vec{n}_2|^2}, \quad (\text{B.8a})$$

$$\lambda_2 = \frac{\vec{d} \times \vec{n}_1}{|\vec{n}_1 \times \vec{n}_2|} \cdot \vec{n}_3 = -\frac{(\vec{d} \cdot \vec{n}_2)\vec{n}_1^2 - (\vec{d} \cdot \vec{n}_1)(\vec{n}_1 \cdot \vec{n}_2)}{|\vec{n}_1 \times \vec{n}_2|^2}. \quad (\text{B.8b})$$

N.B. (a) In the equations (B.8) above, the \vec{n}_i^2 were retained; however, they are simplified by choosing $\vec{n}_i^2 = 1$. (b) $\lambda_i \neq \vec{d} \cdot \vec{n}_i$, $i = 1, 2$, since \vec{d} and \vec{n}_i in general do not lie in the plane defined by \vec{n}_i and \vec{n}_3 !

B.2 Distance of a point to a line

Let \vec{d}_2 be the position of a space point and $\vec{r} = \vec{d}_1 + \lambda_1 \vec{n}_1$ be the vector equation of a line. The vectors \vec{n}_1 and $\vec{d} \equiv \vec{d}_2 - \vec{d}_1$ define the plane where the unit vector \vec{n}_3 , orthogonal to \vec{n}_1 (but coplanar with \vec{d} and \vec{n}_1), gives the direction of the minimum distance segment, of length ρ , that joins the point and the line, giving the distance between the two. If \vec{n}_1 and \vec{d} are collinear, then obviously the distance of \vec{d}_2 to the line vanishes, otherwise

$$\vec{r} + \rho \vec{n}_3 = \vec{d}_2 \quad \Leftrightarrow \quad \rho \vec{n}_3 = \vec{d} - \lambda_1 \vec{n}_1. \quad (\text{B.9})$$

By construction, $\lambda_1 = \vec{d} \cdot \vec{n}_1$ (compare with the note on the previous section). The vectors \vec{d} , $\lambda_1 \vec{n}_1$ and $\rho \vec{n}_3$ form a right-angle triangle. Therefore,

$$\rho = \sqrt{\vec{d}^2 - (\vec{d} \cdot \vec{n}_1)^2}. \quad (\text{B.10})$$

By construction, the vectors \vec{d} , \vec{n}_1 and \vec{n}_3 satisfy $(\vec{d} \cdot \vec{n}_1)^2 + (\vec{d} \cdot \vec{n}_3)^2 = 1$.

B.3 Momentum estimation in the HERA-B Main Tracker

Event rejection at the FLT/SLT level involves measuring the invariant mass of selected track candidates in the Main Tracker. In turn, this requires that those track candidates' momenta be measured. The track momentum can be estimated as described next; for further detail, see reference [124].

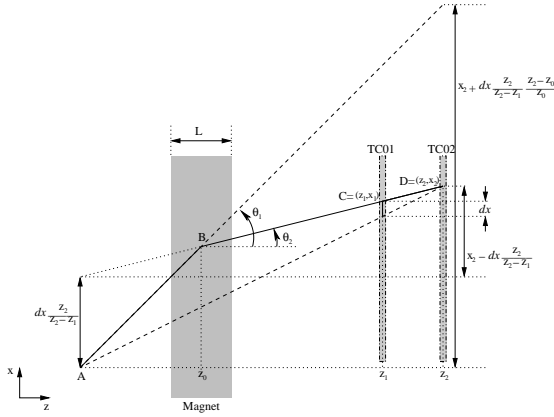


Figure B.1. Geometrical estimate of the momentum of a charged track found in the TC chambers. This track candidate is defined by a segment $[CD]$ between the TC01 and TC02 chambers. The segment's extremities' coordinates are (z_1, x_1) and (z_2, x_2) , measured in the bending plane. The angles θ_1 and θ_2 are defined relative to the beam direction, $\vec{z}_{12} = (z_2 - z_1, 0)$.

Let $C = (z_1, x_1)$ and $D = (z_2, x_2)$ be the extremities of a track candidate, measured in the bending plane of the Magnet between the TC01 and TC02 layers of the Tracker chambers in front of HERA-B's Electromagnetic Calorimeter. We define $dx = x_1 - x_2 z_1 / z_2$ as the difference between the x coordinates of the measured track and one of infinite momentum which goes through the target at $(0, 0)$ and through (z_2, x_2) . Extending the track $[CD]$ into the Magnet (which generates a magnetic field density $\vec{B} = B\vec{u}_z$), let $B = (z_0, x_0)$ be the track's locus at the Magnet's median.¹ From this point to the origin $A = (0, 0)$, a second segment of slope x_0/z_0 is then used to estimate the momentum of a track with charge qe , by using the angle $\Delta\theta$ defined by the two slopes [117],

$$p \simeq \frac{3}{10} \frac{qBL}{\Delta\theta} \left[\text{GeV}/c \cdot (\text{Tesla m/rad})^{-1} \right]. \quad (\text{B.11})$$

In figure B.1, the angle $\Delta\theta$ defined by the two segments $[AB]$ and $[CD]$, respectively upstream and downstream of the Magnet, can be obtained from

$$\tan \theta_1 - \tan \theta_2 = dx \frac{z_2}{z_0(z_1 - z_2)}. \quad (\text{B.12})$$

Assuming the two segments are well within geometric acceptance, the two angles $|\theta_{1,2}| \lesssim 200\text{mrad}$. Therefore, we may approximate $\Delta\theta = \theta_1 - \theta_2 \simeq \tan \theta_1 - \tan \theta_2$, and the momentum is calculated using (B.11). The factor $(BLz_0(z_1 - z_2)/z_2)^{-1}$ is calculated beforehand and distributed to the FLT hardware through the Calibration and Alignment scheme (see figure 3.33). The momentum is estimated in the FLT hardware by using Look-Up Tables (LUTs), which are a fast replacement for floating-point operations.

¹The tracks within VDS acceptance enter the Magnet close enough to the beamline that one may approximate the Magnet's circular section in the zx plane, as depicted in figure 3.9, by a rectangular section in figure B.1.

B.4 Momentum determination of a charged track in a uniform magnetic field

It is possible to measure the momentum of a track defined by two segments, one upstream and one downstream from the HERA- B Magnet. However, the equation presented at the end of this section is rather elaborate and a cheaper, faster alternative like (B.11) might be preferable.

A particle with electric charge q and velocity \vec{v} is sensible to the Lorentz force $\vec{F} = q\vec{v} \times \vec{B}$. Since \vec{F} is perpendicular to \vec{v} , the particle describes a circular motion projected in the plane defined by \vec{v} and \vec{F} at any given moment. By construction, \vec{F} turns out to be orthogonal to \vec{v} . If $\vec{B} \equiv \mathcal{B}\vec{e}_B$ is static (i.e. $\partial\mathcal{B}/\partial t = 0$) and uniform (has the same value and direction in every space point), the motion in the plane of \vec{F} and \vec{v} is circular and uniform. (If \vec{v} and \vec{B} are not orthogonal, there would be a velocity component in the direction of \vec{B} , and the trajectory would be a helicoidal curve.)

Such a static and uniform magnetic field \vec{B} is useful as a strategy for measuring the linear momentum of charged particles in High Energy Physics experiments. The formula for the Lorentz force can be written as

$$\vec{F} \equiv \frac{d\vec{p}}{dt} = q \frac{d\vec{r}}{dt} \times \vec{B} , \quad (\text{B.13})$$

or looking merely at the vectors' magnitudes,

$$\frac{dp}{dt} = q \frac{dr}{dt} \mathcal{B} . \quad (\text{B.14})$$

In particular, if $\partial\mathcal{B}/\partial t = 0$ we further get:

$$\frac{dp}{dt} = q \frac{dr\mathcal{B}}{dt} \implies \Delta p = q \int \mathcal{B} dr . \quad (\text{B.15})$$

This value of the momentum Δp is in fact the modulus of the momentum “kick” given to the particle by the magnetic field; the direction of such kick is found from (B.13), it is orthogonal to \vec{B} (the velocity component collinear with \vec{B} does not contribute). For a particle of given electric charge q , transversing a uniform magnetostatic field \vec{B} , the momentum “kick” orthogonal to \vec{B} is then related to the radius r of the circular track (or a segment of it) described in such field. Knowing the track direction when entering, and exiting, the magnetic field, and determining the momentum kick, lets us find the particle's total linear momentum when entering the field. If r is measured in meters, \mathcal{B} comes in Tesla and the electric charge $q = \pm e$ (with $e = \frac{3}{10} \text{GeV}/c \cdot \text{T}^{-1} \cdot \text{m}^{-1}$ as the elementary charge unit), the result for Δp comes out in units of GeV/c , i.e.

$$\Delta p = \frac{3}{10} \int \mathcal{B} dr \quad [\text{GeV}/c \cdot \text{T}^{-1} \cdot \text{m}^{-1}] . \quad (\text{B.16})$$

The momentum “kick” Δp can be found from tracking information, namely the entry and exit points at the magnetic field, and the track direction at those points. In the remaining of this section, the HERA-*B* reference frame is used, i.e. (z, x, y) , where the first coordinate is measured downstream in the beam direction. The uniform magnetostatic field is $\vec{B} = \mathcal{B}\vec{e}_y$, where $\vec{e}_y \equiv (0, 0, 1)$. The magnetic field region is assumed to be an (infinite height) rectangular box instead of cylindrical.

Let (z_1, x_1) and (z_2, x_2) , with $z_2 > z_1$, be the entry and exit points to the magnetic field, respectively, in the magnetic bending plane. These points are not necessarily measured coordinates (“hits”), but rather are estimated from the directions $\Delta_1 \equiv (\partial x/\partial z)|_1$ and $\Delta_2 \equiv (\partial x/\partial z)|_2$ and the positions of the track segments upstream and downstream of the magnetic field, respectively. Those two points belong in a circle of radius r , and Δ_1 and Δ_2 osculate the circle at those loci. Let (z_0, x_0) be the coordinates for the center of such circle. The equation for the circle is $(z - z_0)^2 + (x - x_0)^2 = r^2$, which after differentiation yields

$$(z_i - z_0) + (x_i - x_0)\Delta_i = 0 \quad (\text{B.17})$$

for $i = 1, 2$. Equaling the left hand side of the equations for $i = 1$ and $i = 2$, and eliminating the dependence on z_0 , gives:

$$x_0 = \frac{(z_2 - z_1) + x_2\Delta_2 - x_1\Delta_1}{\Delta_2 - \Delta_1} . \quad (\text{B.18})$$

For the point (z_1, x_1) results that

$$z_0 = z_1 + \frac{x_1 - x_0}{\Delta_1} . \quad (\text{B.19})$$

After some algebra we finally get that

$$r = |x_1 - x_0| \sqrt{1 + \Delta_1^2} . \quad (\text{B.20})$$

Let the trajectory in the magnetic field be a segment of circle of radius r and angular aperture α . Then, the length travelled in the magnetic field is $r\alpha$, where α is now the angle between the two slopes Δ_2 and Δ_1 ,

$$\alpha = \arctan \Delta_2 - \arctan \Delta_1 . \quad (\text{B.21})$$

The kick to the particle is the change in the linear momentum due to the passage through the magnetic field, $\Delta\vec{p} = \vec{p}_2 - \vec{p}_1$. The lengths of these vectors make a isosceles triangle. The linear momentum modulus is constant, $p_1 = p_2 = P$, because the magnetic field is uniform. Therefore,

$$P|\sin(\alpha/2)| = \frac{1}{2}\Delta p \quad (\text{B.22})$$

(the use of the absolute value in the sine eliminates the ambiguity in the definition of the aperture α). Finally, we obtain

$$P = \frac{\Delta p}{|\sin(\alpha/2)|} = qBr \frac{\alpha/2}{|\sin(\alpha/2)|} = Br \frac{\alpha/2}{\sin(\alpha/2)}, \quad (\text{B.23a})$$

with

$$r = \sqrt{1 + \Delta_1^2} \left| \frac{(z_2 - z_1) + \Delta_2(x_2 - x_1)}{\Delta_2 - \Delta_1} \right|. \quad (\text{B.23b})$$

The charge's sign is given by the direction of the track curvature, or yet by $\text{sign}(q) = \text{sign}(\Delta_2 - \Delta_1)$ if we restrict it to tracks of long-lived charged particles and hydrogen nuclei (and, possibly, single-charged ions A^\pm). Using Laurent expansions on some terms in (B.23a) yields (ignoring $o(x^3)$ terms and knowing that $\alpha^2 \ll 1$)

$$P \simeq |q|B \left(1 + \frac{\Delta_1^2}{2} \right) \frac{z_2 - z_1}{|\Delta_2 - \Delta_1|} \left| 1 + \Delta_2 \frac{x_2 - x_1}{z_2 - z_1} \right|.$$

Given HERA- B 's detector geometric acceptance (with 15% of the particles emitted from the target region at angles greater than 0.2 radians, see figure 3.8), we may set $\Delta_1^2 \ll 1$ and the large module approximately equal to one; we then get an equation similar to (B.11),

$$P \approx |q|B \frac{z_2 - z_1}{|\Delta_2 - \Delta_1|}, \quad (\text{B.23c})$$

making $L = z_2 - z_1$ and $\Delta\theta = \Delta_2 - \Delta_1$.

B.5 Useful relations of relativistic kinematics

The next subsections briefly describe some quantities associated with the relativistic and ultra-relativistic domains of particle kinematics. The variables described appear in e.g. differential cross section plots and formulas and geometric acceptance domain definitions.

B.5.1 Lorentz transforms and center-of-mass energy

We now recall the Lorentz transformation, in particular for energy and linear momentum. We shall then apply them to the case of collision of a beam particle with a target, laboratory-bound, particle. The coordinate set is the same as HERA- B 's, i.e. (z, x, y) .

Let E and $\vec{p} \equiv (p_z, p_x, p_y)$ be the energy and linear momentum of a particle measured in the laboratory, and let E' and $\vec{p}' \equiv (p'_z, p'_x, p'_y)$ be the same quantities measured in another inertial frame with velocity $\vec{\beta} \equiv (\beta, 0, 0)$ relative to the laboratory frame. The Lorentz transformation relates

the particle's dynamic quantities (energy and momentum, for example) as measured in the two inertial frames,

$$\begin{pmatrix} E' \\ p'_z \\ p'_x \\ p'_y \end{pmatrix} = \begin{pmatrix} \gamma & -\gamma\beta & 0 & 0 \\ -\gamma\beta & \gamma & 0 & 0 \\ 0 & 0 & 1 & 0 \\ 0 & 0 & 0 & 1 \end{pmatrix} \begin{pmatrix} E \\ p_z \\ p_x \\ p_y \end{pmatrix}, \quad (\text{B.24})$$

with $\gamma \equiv (1 - \beta^2)^{-1/2}$; see e.g. reference [81]. The Lorentz boost is along the z axis, i.e. the momentum components along the axes perpendicular to z remain unaltered by the transformation.

Let m_1 and m_2 be the masses of one beam particle and one target particle, respectively. Their energies and momenta, measured in the laboratory, are² E_1, \vec{p}_1 and $E_2 = m_2, \vec{p}_2 = 0$ respectively. The invariant mass of a single particle is³ $m_i = (E_i^2 - \vec{p}_i^2)^{1/2}$. The invariant mass M of a set of N particles is defined by

$$M^2 = \left(\sum_i^N E_i \right)^2 - \left(\sum_i^N \vec{p}_i \right)^2 = \sum_k^N m_k^2 + \sum_{i \neq j}^N 2E_i E_j (1 - \beta_i \beta_j \cos \theta_{ij}), \quad (\text{B.25})$$

where $\beta_i = v_i/c$ is the (modulus of) the i particle's velocity and θ_{ij} is the angle between i and j particles' velocities.

The center-of-mass energy is similarly defined, yielding $E_{\text{CM}} = M$. For the collision of particles 1 and 2, we get

$$E_{\text{CM}}^2 = m_1^2 + m_2^2 + 2E_1 E_2 (1 - \beta_1 \beta_2 \cos \theta), \quad (\text{B.26})$$

where β_1 and β_2 are (the modulus of) each particles' velocities and θ is the angle of the velocities. If particle 2 is static in the laboratory frame (i.e. a "target" particle, and then particle 1 is a "beam" particle), then $\beta_2 = 0$ and

$$E_{\text{CM}}^2 = s_{\text{CM}} \equiv m_1^2 + m_2^2 + 2E_1 m_2. \quad (\text{B.27})$$

If we further particularize to $m_1 = m_2$, the center-of-mass particles' energies $E'_1 = E'_2 = E_{\text{CM}}/2$ and the Lorentz factor γ for the beam particle is

$$\gamma = \frac{E'_1}{m_1} = \frac{E_{\text{CM}}}{2m_1}. \quad (\text{B.28})$$

In this situation, this factor can be then used to get a particle's energy and momentum in the center-of-mass frame, given these quantities in the laboratory frame.

²Until the end of this section, we use the convention $c = 1$, and therefore energies, masses and momenta have the same dimension.

³All quantities are expressed in the natural units system, thereby $c = 1$.

The angles θ_{lab} and θ_{CM} of the scattered particle relative to the boost direction, measured respectively in the laboratory and in the center-of-mass frames, are related by (see [117, p. 288]):

$$\tan \theta_{\text{lab}} \approx \sqrt{\frac{2m_2}{p_1}} \cdot \frac{\beta_{\text{CM}} \sin \theta_{\text{CM}}}{1 + \beta_{\text{CM}} \cos \theta_{\text{CM}}}, \quad (\text{B.29})$$

where $\beta_{\text{CM}} = v_{\text{CM}}/c$ is the (modulus of the) velocity of the particle in the center-of-mass frame; the approximation is valid as long as $E_1 \approx p_1$ (i.e. $m_1, m_2 \ll E_1, p_1$). Given (B.28) and $\gamma \equiv (1 - \beta_{\text{CM}}^2)^{-1/2}$, we get

$$\beta_{\text{CM}} = \frac{E_{\text{CM}} - 2m_1}{E_{\text{CM}}}. \quad (\text{B.30})$$

The solution $(E_{\text{CM}} + 2m_1)/E_{\text{CM}}$ is discarded, since it would give an unphysical velocity $\beta > 1$.

B.5.2 Rapidity and pseudo-rapidity

The rapidity y and pseudo-rapidity η are two significant dynamic quantities. An important reason for their use lies in the fact that they are additive quantities under Lorentz transformations; it becomes very easy to Lorentz-boost a particle's azimuthal angle, one simply adds (subtracts) the system's CM rapidity y_{CM} when boosting the particle's angle from (to) the CM frame to (from) the laboratory frame.

For a particle (emitted with an azimuthal angle θ (relative to the beam direction) and with E as its energy and p_z as the projection of its momentum in the beam direction), they are defined by, respectively,

$$y = \frac{1}{2} \log \frac{E + p_z}{E - p_z}, \quad (\text{B.31})$$

$$\eta = -\log \tan \frac{\theta}{2}. \quad (\text{B.32})$$

A particle moving orthogonally to the beam direction has $p_z = 0$, and its rapidity and pseudo-rapidity are therefore $y = 0$ and $\eta = 0$. The limits

$$\lim_{p_z \rightarrow E} y = \pm\infty \quad \text{and} \quad \lim_{-p_z \rightarrow E} y = 0$$

correspond, in terms of pseudo-rapidity, respectively to the angles⁴

$$\theta = 0 \quad \text{and} \quad \theta = \pi.$$

The pseudo-rapidity is the “cheaper” version of the rapidity, and is useful when the particle's energy and/or momentum are unknown.

⁴We may safely choose the arbitrary phase to vanish.

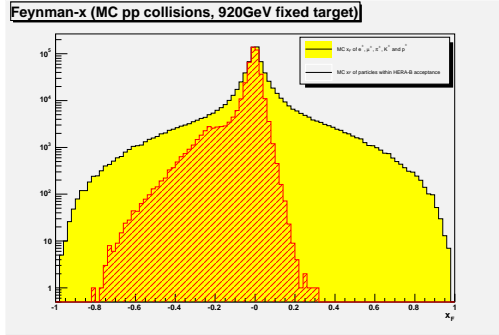


Figure B.2. Feynman- x of particles from a sample of 10^5 Monte Carlo pN events generated with PYTHIA. The values of x_F were Lorentz-boosted from the fixed-target frame into the pN CM frame. The solid histogram represents the final state particles, and the dashed histogram is for particles falling in HERA- B geometric acceptance, $10\text{mrad} < \theta_{\text{lab}} < 250\text{mrad}$. Compare with figure 3.8.

Particularizing for the case of a particle emitted orthogonally to the beam

$$\theta_{\text{lab}} \simeq \arctan \frac{\beta_{\text{CM}}}{\gamma_{\text{CM}}}, \quad (\text{B.33})$$

with $\gamma_{\text{CM}} \equiv E/\sqrt{s_{\text{CM}}}$ found from (B.28) and (B.27). Because $0 \leq \beta < 1$ and $\gamma \geq 1$, and since for large CM Lorentz boosts $\beta_{\text{CM}} \simeq 1$ and $\gamma_{\text{CM}} \gg 1$, we get $\arctan(\beta/\gamma) \simeq \beta/\gamma$ and the pseudo-rapidity reads

$$\eta = \log(\gamma_{\text{CM}} + \beta_{\text{CM}}\gamma_{\text{CM}}) \approx \log(2\gamma_{\text{CM}}). \quad (\text{B.34})$$

B.5.3 Feynman- x

The variable $x_F \equiv p_z/p_{z,\text{max}} = 2p_z/\sqrt{s}$ (with p_z measured in the system's CM frame and $\sqrt{s} = \sqrt{2p_{\text{beam}}m_{\text{target}}}$ as the system's center-of-mass energy) is named Feynman scaling variable, or simply Feynman x , and was introduced by Feynman [61] for the discussion of inclusive hadronic interactions at large energies. As its definition suggests, x_F measures the fraction of *forward* momentum carried by the particle, scaled to of half the CM's energy⁵ and it takes values in the interval $-1 \leq x_F \leq 1$.

For the HERA- B detector (figure B.2), the (horizontal) geometric acceptance of the full detector may be described in terms of the x_F variable. Its quoted bounds are $-0.35 < x_F < 0.15$ [142]; however, in figure B.2 it can be shown that the lower bound extends further from the central value $x_F = 0$, with $-0.75 \lesssim x_F \lesssim 0.20$. As seen in the figure, HERA- B has significant phase space sensitivity to backscattered particles.

B.5.4 Multiple scattering angle

For small angles, the multiple scattering angle [81] of a particle with momentum p , velocity β and charge number z , transversing a medium with a

⁵ *N.B.* Remember we are using natural units, $c = \hbar = k_B = 1$.

thickness of x/X_0 radiation lengths, is

$$\theta = \frac{13.6\text{MeV}/c}{\beta p} z \sqrt{x/X_0} (1 + 0.038 \ln(x/X_0)) ; \quad (\text{B.35})$$

the radiation length of a material layer, with different atomic species of atomic number Z_i and weight fractions w_i in the material, may be obtained from

$$\frac{1}{X_0} \simeq \sum_i w_i \frac{Z_i(Z_i + 1) \ln(287/\sqrt{Z_i})}{716.4\text{g cm}^{-2} A_i} . \quad (\text{B.36})$$

B.6 Cross section and decay width

The cross section σ and decay width⁶ Γ give significant information about the reactions which they characterize. The cross section can be used e.g. to find the number N of a given type of events, measured in some time interval, for a particle beam with time-integrated luminosity $\int L dt$ (a measure of integrated “flow intensity” of the particle beam), $N = \sigma \int L dt$.

Usually, σ and Γ are presented in differential form, $d\sigma$ and $d\Gamma$, which are ultimately useful in experimental HEP; the former are usually derived from the latter by integrating relative to the center of mass solid angle, in a region corresponding to the geometrical acceptance of the detector. Knowing the (time-integrated) beam luminosity (measured by other means, e.g. the number of events with well-known cross section), it is then possible to evaluate the cross section $\sigma(X)$ of a certain type of reaction X by measuring the particles transversing the sensitive parts of the detector, and then selecting the appropriate events after reconstruction. The definition of $d\sigma$ and $d\Gamma$ are found in many books, e.g. [82]. The definitions presented below are from [21].

Let us define $\lambda(x, y, z) = x^2 + y^2 + z^2 - 2xy - 2xz - 2yz$ as an auxiliary function, to simplify writing (B.37). The differential cross section for a reaction $a + b \rightarrow \mathcal{F}_n$, where \mathcal{F}_n represents the collection of n final state particles, can be written as

$$d\sigma = \frac{1}{2\sqrt{\lambda(s, m_a^2, m_b^2)}(2\pi)^{3n-4}} \sum_j |\mathcal{M}_j|^2 \delta^4 \left(p_a + p_b - \sum_i^n p_i \right) \prod_i^n \frac{d\vec{p}_i}{2E_i} , \quad (\text{B.37})$$

with p_i as the four-momentum of particle i , \vec{p}_i its three-momentum, E_i its energy, m_i its mass, and $s = (p_a + p_b)^2$. The definition of differential decay width of $a \rightarrow \mathcal{F}_n$ is similar to (B.37) and can be written as

$$d\Gamma = \frac{1}{2E_a(2\pi)^{3n-4}} \sum_j |\mathcal{M}_j|^2 \delta_j^4 \left(p_a - \sum_i^n p_i \right) \prod_i^n \frac{d\vec{p}_i}{2E_i} . \quad (\text{B.38})$$

⁶The term comes from the level widths of excited nuclei with different lifetimes $\tau = \hbar/\Gamma$.

In equations (B.37) and (B.38), the $\delta^4(x)$ symbol is equal to 1 when the four-momenta sum in its argument is $x = 0$, and is equal to 0 otherwise; the invariant amplitude \mathcal{M}_j is a function of the four-momenta of the initial- and final-state particles, in the form of products of propagators of those particles and any other gauge bosons in an interaction j (which can be represented in a Feynman diagram); the sum $\sum_j |\mathcal{M}_j|^2$ incorporates the core physics processes, and accounts for all combinations of initial- and final-state particles' allowed spin states. Expressions (B.37) and (B.38) are evaluated by integrating over the δ^4 functions to remove unconstrained degrees of freedom; for example, for a reaction $X \rightarrow a + b$,

$$\int \delta^4(p_X - p_a - p_b) \frac{d\vec{p}_a}{2E_a} \frac{d\vec{p}_b}{2E_b} = \frac{\sqrt{\lambda(p_X^2, p_a^2, p_b^2)}}{8p_X^2} d\Omega, \quad (\text{B.39})$$

with $d\Omega$ as the solid angle measured in X 's reference frame.

Using (B.39), the differential decay width for a reaction $X \rightarrow a + b$ can be written as

$$d\Gamma(X \rightarrow a + b) = \frac{1}{2E_X(2\pi)^2} \sum_j |\mathcal{M}_j|^2 \delta^4(p_X - (p_a + p_b)) \frac{d\vec{p}_a}{2E_a} \frac{d\vec{p}_b}{2E_b}. \quad (\text{B.40})$$

Once again, the sum $\sum_j |\mathcal{M}_j|^2$ involves all combinations of allowed spin states for the propagators of X , a and b and couplings for the Xab vertex. The decay width $\Gamma(X \rightarrow a + b)$ is calculated from (B.40) using (B.39).

B.7 Dynamics of the $B^0-\bar{B}^0$ meson system

The dynamics of the neutral B meson system's state [36]

$$|\Psi\rangle = a |B^0\rangle + b |\bar{B}^0\rangle \equiv \begin{pmatrix} a \\ b \end{pmatrix},$$

is governed by the time-dependent Schrödinger equation⁷

$$i \frac{d}{dt} |\Psi\rangle = \hat{H} |\Psi\rangle = \left(\hat{M} - \frac{i}{2} \hat{\Gamma} \right) |\Psi\rangle = \begin{pmatrix} M_{11} - \frac{i}{2} \Gamma_{11} & M_{12} - \frac{i}{2} \Gamma_{12} \\ M_{21} - \frac{i}{2} \Gamma_{21} & M_{22} - \frac{i}{2} \Gamma_{22} \end{pmatrix} |\Psi\rangle. \quad (\text{B.41})$$

In the hamiltonian operator \hat{H} , the terms

- M_{11} and M_{22} incorporate the B mesons quarks' masses and binding energy.

⁷Recall we are using the natural units $c = \hbar = k_B = 1$ system throughout.

- M_{12} and M_{21} reflect $B^0 \rightleftharpoons \bar{B}^0$ transitions involving virtual processes described by Feynman box diagrams.
- Γ_{11} and Γ_{22} are the inverse decay rates of $B^0 \rightarrow f$ and $\bar{B}^0 \rightarrow \bar{f}$, respectively.
- Γ_{12} and Γ_{21} reflect transitions $B^0 \rightleftharpoons f \rightleftharpoons \bar{B}^0$, where f is a real state common to both B^0 and \bar{B}^0 .

$\hat{C}\hat{P}\hat{T}$ conservation requires $M_{11} = M_{22} = M$ and $\Gamma_{11} = \Gamma_{22} = \Gamma$. Moreover, $M_{21} = M_{12}^*$ and $\Gamma_{21} = \Gamma_{12}^*$ because \hat{H} has to be hermitian. The diagonal matrix elements of \hat{H} describe the time evolution of the states $|B^0\rangle$ and $|\bar{B}^0\rangle$ of mass M and decay width Γ . In contrast, the weak transition of neutral mesons is described by the off-diagonal elements of the hamiltonian, which correspond to the elements of the CKM matrix given in the Feynman box diagrams. Diagonalization of the hamiltonian yields the eigenvalues

$$M_L - \frac{i}{2}\Gamma_L = \left(M - \frac{i}{2}\Gamma\right) + \frac{q}{p} \left(M_{12} - \frac{i}{2}\Gamma_{12}\right) \quad (\text{B.42a})$$

$$M_H - \frac{i}{2}\Gamma_H = \left(M - \frac{i}{2}\Gamma\right) - \frac{q}{p} \left(M_{12} - \frac{i}{2}\Gamma_{12}\right) \quad (\text{B.42b})$$

where

$$\frac{q}{p} = \sqrt{\frac{M_{12}^* - \frac{i}{2}\Gamma_{12}^*}{M_{12} - \frac{i}{2}\Gamma_{12}}} \quad (\text{B.43})$$

and the corresponding states can be described by the vectors

$$|\Psi_{\pm}\rangle = \begin{pmatrix} p \\ \pm q \end{pmatrix} \quad (\text{B.44})$$

which are the heavy and light mass eigenstates $|B_H^0\rangle$ and $|B_L^0\rangle$.

Using $|\Gamma_{12}| \ll |M_{12}|$ and the CKM matrix elements of the weak vertices in the Feynman box diagrams, we can further write

$$\frac{q}{p} = \sqrt{\frac{M_{12}^* - \frac{i}{2}\Gamma_{12}^*}{M_{12} - \frac{i}{2}\Gamma_{12}}} \approx \sqrt{\frac{M_{12}^*}{M_{12}}} = \frac{M_{12}^*}{|M_{12}|} = \frac{(V_{tb}^* V_{td})^2}{|V_{tb}^* V_{td}|^2} = \frac{V_{tb}^* V_{td}}{V_{tb} V_{td}^*} = e^{-2i\beta} . \quad (\text{B.45})$$

Error propagation formulas

Let $(x, y, tx, ty, Q/p)$ be the vector of five parameters describing one reconstructed track in ARTE; x and y are the coordinates, in the lab frame, of one point in the track for the longitudinal coordinate z of the detector element containing the hit with these coordinates, tx and ty are the track's slopes resp. in the zx and yx planes, and Q/p is related to the track's curvature radius in the Magnet. The sign of the track charge Q is related to the curvature of the track: for $Q > 0$ (resp. $Q < 0$) the track curves in the direction of increasing (resp. decreasing) x coordinate. In ARTE, $Q = +1$ for uncharged and positively charged particles, and $Q = -1$ for negatively charged particles.¹ The track momentum p is given in GeV/ c ; the slopes $tx \equiv p_x/p_z$ and $ty \equiv p_y/p_z$.

The track parameters result of the application of the Kalman filter technique to hits in successive detector layers. The standard deviation of these quantities are obtained from the covariance matrix calculated through the application of the Kalman filter. The covariance matrix $\mathbf{C} = [\sigma_{ij}^2]$ for the track parameters is a 5×5 (in this case) symmetric matrix and gives the tracks' parameter covariances, $\sigma_{i,j}^2 = \text{cov}(i, j) \equiv \langle (x_i - \mu_i)(x_j - \mu_j) \rangle$, with $\mu_i = \langle x_i \rangle$ and $\mu_j = \langle x_j \rangle$ [81]. When $i = j$, the corresponding element of \mathbf{C} is the variance σ_i^2 of parameter x_i ; the standard deviation is defined as $\sqrt{\sigma_i^2}$.

An arbitrary scalar $\alpha = \alpha(x_i)$ dependant on a set of parameters x_i (from tracks or vertices, for example) has its variance defined by

$$\sigma_\alpha^2 = \sum_{i,j} \left(\frac{\partial \alpha}{\partial x_i} \right) \left(\frac{\partial \alpha}{\partial x_j} \right) \sigma_{ij}^2. \quad (\text{C.1})$$

If the parameters x_i and x_j are uncorrelated, their respective covariance vanishes — this happens *a priori* for an arbitrary line segment (track) and space point (vertex).

In [121] and references therein, the variance of the impact parameter of

¹Cases such as ions and nuclei with charges $|Q| > 1$ are disregarded.

a track to a vertex is written as

$$\sigma_b^2 = \sum_{i,j} \left(\hat{b} \cdot \frac{\partial \vec{b}}{\partial x_i} \right) \left(\hat{b} \cdot \frac{\partial \vec{b}}{\partial x_j} \right) \sigma_{ij}^2, \quad (\text{C.2})$$

where \vec{b} is the vector with the magnitude of the impact parameter b and direction orthogonal to the track orientation, $\hat{b} = \vec{b}/b$ is the unit vector with the direction of \vec{b} , the i, j are indices to the vertex position and track parameters, and σ_{ij}^2 is the covariance of two given parameters i and j . The terms with the form $\hat{b} \cdot \partial b / \partial x_i$ ensure that the variance of the impact parameter scalar is measured along the orientation of the unit vector \hat{b} , i.e. the error for the impact parameter is $\delta b = \hat{b} \cdot \delta \vec{b}$. However, the expression (C.2) may be written in the form (C.1), since

$$\hat{b} \cdot \frac{\partial \vec{b}}{\partial x_i} = \frac{1}{b} \vec{b} \cdot \frac{\partial \vec{b}}{\partial x_i} = \frac{1}{2b} \frac{\partial (\vec{b} \cdot \vec{b})}{\partial x_i} = \frac{1}{2b} \frac{\partial b^2}{\partial x_i} = \frac{1}{2b} 2b \frac{\partial b}{\partial x_i} = \frac{\partial b}{\partial x_i}.$$

A priori, two reconstructed tracks (or one reconstructed track and one reconstructed vertex) are independent — when calculating the impact parameter of one track to either another track or a vertex, one might pick an uncorrelated pair. In other words, the covariances of two parameters x_1 and x_2 of the RTRA, and of either another one RTRA or RVER, are $\text{cov}(x_1, x_2) = 0$. Therefore, in the following sections the covariance matrix takes the form

$$\text{cov}(X_1, X_2) = \begin{bmatrix} \hat{\sigma}_1 & 0 \\ 0 & \hat{\sigma}_2 \end{bmatrix}, \quad (\text{C.3})$$

with $\hat{\sigma}_1$ and $\hat{\sigma}_2$ respectively as the covariance matrices of an RTRA and of either another RTRA or RVER. The covariance matrix of a RTRA under ARTE is written as (the diagonal elements $\sigma_\alpha^2 \equiv \sigma_{\alpha,\alpha}$ are variances of the α)

$$\hat{\sigma} = \begin{bmatrix} \sigma_x^2 & \sigma_{x,y} & \sigma_{x,t_x} & \sigma_{x,t_y} & \sigma_{x,1/p} \\ \sigma_{x,y} & \sigma_y^2 & \sigma_{y,t_x} & \sigma_{y,t_y} & \sigma_{y,1/p} \\ \sigma_{x,t_x} & \sigma_{y,t_x} & \sigma_{t_x}^2 & \sigma_{t_x,t_y} & \sigma_{t_x,1/p} \\ \sigma_{x,t_y} & \sigma_{y,t_y} & \sigma_{t_x,t_y} & \sigma_{t_y}^2 & \sigma_{t_y,1/p} \\ \sigma_{x,1/p} & \sigma_{y,1/p} & \sigma_{t_x,1/p} & \sigma_{t_y,1/p} & \sigma_{1/p}^2 \end{bmatrix}.$$

The derivatives' formulas presented in this chapter were calculated with the symbolic algebra program MAXIMA [43].

C.1 Error propagation of two-track invariant mass

Let $(z_1, x_1, y_1, tx_1, ty_1, Q_1/p_1)$ and $(z_2, x_2, y_2, tx_2, ty_2, Q_2/p_2)$ be the parameter vectors that describe two reconstructed tracks (RTRAs) or track segments (RSEGs) in ARTE. Notwithstanding the fact that these tracks may

not share a common vertex², the invariant mass of the pair is (equation (B.26) in its ultra-relativistic approximation $\beta_i = E_i/p_i \simeq 1$, $i = 1, 2$):

$$m = \sqrt{2(p_1 p_2 - \vec{p}_1 \cdot \vec{p}_2)} = \sqrt{2p_1 p_2 \left(1 - \frac{1 + tx_1 tx_2 + ty_1 ty_2}{N_1 N_2}\right)}, \quad (\text{C.4})$$

with $\vec{p}_i = p_i(1, tx_i, ty_i)/N_i$ and $N_i = \sqrt{1 + tx_i^2 + ty_i^2}$. The variance of m follows from (C.1):

$$\sigma_m^2 = \sum_i^{1,2} \sum_{f,g}^{tx,ty,1/p} \frac{2 - \delta_{f_i g_i}}{4} \left(\frac{\partial m}{\partial f_i}\right) \left(\frac{\partial m}{\partial g_i}\right) \sigma_{f_i g_i}^2. \quad (\text{C.5})$$

The factor $2 - \delta_{f_i g_i}$ accounts for the symmetry of the tracks' covariance matrices. The relevant derivatives of (C.4) are

$$\frac{\partial m}{\partial(1/p_i)} = -\frac{m}{2} p_i, \quad \forall i = 1, 2, \quad (\text{C.6a})$$

$$\frac{\partial m}{\partial f_i} = \frac{p_1 p_2}{N_i m} \left(\frac{f_i}{N_i} - \frac{f_j}{N_j}\right) - \frac{m}{2N_i} \frac{tx_i}{N_i}, \quad \forall f = tx, ty, \quad i \neq j = 1, 2. \quad (\text{C.6b})$$

The use of $1/p_i$ instead of p_i has to do with the track parametrization in ARTE, which uses the former.

The previous equations are a good approximation when the invariant mass to calculate is significantly higher than the masses of the decay products; such is the case of dileptonic J/ψ decays. For decays that do not verify this condition, the decay product's masses must be taken into account,³ i.e. following (B.25),

$$\begin{aligned} M^2 &= \sum_i m_i^2 + 2 \sum_{i \neq j} E_i E_j - \vec{p}_i \cdot \vec{p}_j = \\ &= \sum_i m_i^2 + \sum_{i,j} \sqrt{(m_i^2 + p_i^2)(m_j^2 + p_j^2)} - p_i p_j \frac{1 + tx_i tx_j + ty_i ty_j}{N_i N_j}. \end{aligned} \quad (\text{C.7})$$

For two particles,

$$M^2 = m_1^2 + m_2^2 + 2\sqrt{(m_1^2 + p_1^2)(m_2^2 + p_2^2)} - \frac{2p_1 p_2 (1 + tx_1 tx_2 + ty_1 ty_2)}{\sqrt{(1 + tx_1^2 + ty_1^2)(1 + tx_2^2 + ty_2^2)}}. \quad (\text{C.8})$$

²Experimentally, this is equivalent to requiring a cut of the two-track impact parameter at, say, 0.5mm.

³Naturally, a good estimation of the invariant mass requires that the tracks are correctly identified; this PID-related problem is beyond the scope of this section. For the $\mu^+ \mu^- \pi^+ \pi^-$ state of the B_d^0 golden decay, one might start with the approximation that all final state particles' masses are those of pions; this approximation is reasonable if one recalls that for massive particle decays — such as B mesons — the muons and pions have relatively similar masses, $m_{\mu^\pm} \simeq 0.106 \text{ GeV}/c^2$ and $m_{\pi^\pm} 0.140 \simeq \text{ GeV}/c^2$ [81].

Most final-state particles (pions, electrons, muons, protons) have experimentally well-defined masses and their resulting errors are very small; therefore the masses are hereby taken as well-defined constants. In this approximation, the relevant derivatives of the square root of equation (C.8) are

$$\frac{\partial M}{\partial(1/p_i)} = \frac{p_i}{M} \vec{p}_i \cdot \left(\vec{p}_j - \frac{E_j}{E_i} \vec{p}_i \right), \quad \forall i \neq j = 1, 2, \quad (\text{C.9a})$$

$$\frac{\partial M}{\partial f_i} = \frac{\vec{p}_1 \cdot \vec{p}_2}{M} \left(\frac{f_i}{N_i^2} - \frac{f_j}{1 + tx_1 tx_2 + ty_1 ty_2} \right), \quad \forall f = tx, ty, i \neq j = 1, 2. \quad (\text{C.9b})$$

C.2 Error propagation of minimum separation between two tracks

The impact parameter b of two reconstructed straight tracks (i.e., outside the bending magnetic field), given by unit vectors

$$\vec{n}_i = (n_{zi}, tx_i n_{zi}, ty_i n_{zi}), \quad n_{zi} = \frac{1}{\sqrt{1 + tx_i^2 + ty_i^2}}, \quad i = 1, 2, \quad (\text{C.10})$$

is given by the minimum separation between them (see equation (B.3)):

$$b = \left| \vec{D} \cdot \frac{\vec{n}_1 \times \vec{n}_2}{|\vec{n}_1 \times \vec{n}_2|} \right| = D |\cos \theta|, \quad (\text{C.11})$$

where $\vec{D} \equiv (D_z, D_x, D_y) = \vec{d}_2 - \vec{d}_1$ and D is its magnitude, $\vec{d}_i \equiv (z_i, x_i, y_i)$ are two fixed points in the RTRAs and $\theta = \arccos(\vec{D} \cdot \vec{n}_3 / D)$ is the angle between \vec{D} and the unit vector \vec{n}_3 defined by

$$\vec{n}_3 \equiv (n_{3z}, n_{3x}, n_{3y}) = \frac{\vec{n}_1 \times \vec{n}_2}{|\vec{n}_1 \times \vec{n}_2|} = \frac{1}{N} (tx_1 ty_2 - ty_1 tx_2, ty_1 - ty_2, tx_2 - tx_1), \quad (\text{C.12a})$$

with

$$N = \sqrt{(tx_1 ty_2 - ty_1 tx_2)^2 + (ty_1 - ty_2)^2 + (tx_2 - tx_1)^2} \quad (\text{C.12b})$$

as the normalizing factor of \vec{n}_3 .

The variance for the measure of b is written like (C.1):

$$\sigma_b^2 = \sum_{i=1}^2 \sum_{f \in \{x, y, tx, ty\}} \frac{2 - \delta_{f_i g_i}}{4} \left(\frac{\partial b}{\partial f_i} \right) \left(\frac{\partial b}{\partial g_i} \right) \sigma_{f_i g_i}^2. \quad (\text{C.13})$$

Assuming the tracks are uncorrelated, the covariances $\sigma_{f_1 g_2}^2$, $f, g = x, y, tx, ty$ of parameters of two different tracks vanish; see (C.3). The factor $2 - \delta_{f_i g_i}$

accounts for the symmetry of the covariance matrices of the tracks $i = 1, 2$. The relevant derivatives are given by:

$$\frac{\partial b}{\partial X_i} = (-1)^i n_{3X}, \quad \forall i = 1, 2, \quad X = z, x, y, \quad (\text{C.14a})$$

$$\frac{\partial b}{\partial tx_1} = \frac{D_z ty_2 - D_y}{N} - b(ty_2 n_{3z} - n_{3x}), \quad (\text{C.14b})$$

$$\frac{\partial b}{\partial tx_2} = -\frac{D_z ty_1 - D_y}{N} + b(ty_1 n_{3z} - n_{3x}), \quad (\text{C.14c})$$

$$\frac{\partial b}{\partial ty_1} = -\frac{D_z tx_2 - D_x}{N} + b(tx_2 n_{3z} - n_{3y}), \quad (\text{C.14d})$$

$$\frac{\partial b}{\partial ty_2} = \frac{D_z tx_1 - D_x}{N} - b(tx_1 n_{3z} - n_{3y}). \quad (\text{C.14e})$$

C.3 Error propagation of the track-to-vertex distance of closest approach

The impact parameter b of one track to one vertex is defined by the minimum distance between them, see equation (B.10):

$$b = \left[\left(\vec{d}_1 - \vec{d}_2 \right)^2 - \left(\left(\vec{d}_1 - \vec{d}_2 \right) \cdot \vec{n}_1 \right)^2 \right]^{1/2}, \quad (\text{C.15})$$

with the track described by a vector equation $\vec{r}_1 = \vec{d}_1 + \lambda_1 \vec{n}_1$, $\lambda_1 \in \mathbb{R}$, and the vertex has coordinates given by vector $\vec{d}_2 \equiv (z_2, x_2, y_2)$. This expression is in agreement with e.g. the C++ source code `$HBARTE/pro/cluearte/Dmain.C` of the ARTE source tree of HERA-B. The \vec{n}_1 can be written in terms of track parameters as $\vec{n}_1 = N^{-1}(1, tx, ty_1)$, with $N = \sqrt{1 + tx_1^2 + ty_1^2}$. Defining $\vec{D} = \vec{d}_1 - \vec{d}_2$, the unit vector

$$\hat{b} = \frac{\left(\vec{D} - \left(\vec{D} \cdot \vec{n}_1 \right) \vec{n}_1 \right)}{b} \quad (\text{C.16})$$

gives the orientation of the shortest lever joining the track to the vertex.

The variance of the impact parameter (C.15) is obtained once again from equation (C.1):

$$\sigma_b^2 = \sum_{f,g}^{z_2, x_2, y_2} \frac{2 - \delta_{fg}}{4} \left(\frac{\partial b}{\partial f} \right) \left(\frac{\partial b}{\partial g} \right) \sigma_{fg}^2 + \sum_{f,g}^{x_1, y_1, tx, ty} \frac{2 - \delta_{fg}}{4} \left(\frac{\partial b}{\partial f} \right) \left(\frac{\partial b}{\partial g} \right) \sigma_{fg}^2. \quad (\text{C.17})$$

The two sums relate to the vertex and track contributions, respectively; their parameters are assumed independent, in which case the covariance matrix takes the form (C.3). The factors $2 - \delta_{fg}$ account for the covariance matrices

$[\sigma_{fg}^2]$ being symmetric. When $f = g$, the matrix element is the variance σ_f^2 of parameter f . The relevant derivatives of the impact parameter are given by the following expressions:

$$\frac{\partial b}{\partial f_i} = -(-1)^i \frac{b_f}{b}, \quad \forall i = 1, 2, \quad f = z, x, y, \quad (\text{C.18a})$$

$$\frac{\partial b}{\partial t f} = \frac{b_f}{b} (b_z - (z_1 - z_2)), \quad \forall f = x, y, \quad (\text{C.18b})$$

with impact parameter vector $\vec{b} = \vec{D} - (\vec{D} \cdot \vec{n}_1) \vec{n}_1 = (b_z, b_x, b_y)$.

The equations presented here were used instead of those in reference [121, appendix A]. It was found that they produce slightly different results due to one sign error in the equations on that bibliographic source.

C.4 Error propagation of the coordinates of a two-track point of closest approach

The coordinates of the common vertex created by two (nearly) intersecting tracks, $\vec{r}_1(\lambda_1) = \vec{d}_1 + \lambda_1 \vec{n}_1$ and $\vec{r}_2(\lambda_2) = \vec{d}_2 + \lambda_2 \vec{n}_2$, are given by their average,

$$\vec{r}_{\text{C.A.}} = \frac{\vec{d}_1 + \lambda_1 \vec{n}_1 + \vec{d}_2 + \lambda_2 \vec{n}_2}{2}. \quad (\text{C.19a})$$

The λ_i parameters are such that minimize the distance $|\vec{r}_1(\lambda_1) - \vec{r}_2(\lambda_2)|$ between the tracks, and are given by equations (B.8),

$$\lambda_i = \vec{n}_i \cdot \frac{(\vec{d} \cdot \vec{n}_1) \vec{n}_1 - (\vec{d} \cdot \vec{n}_2) \vec{n}_2}{|\vec{n}_1 \times \vec{n}_2|^2}, \quad \forall i \neq j = 1, 2, \quad (\text{C.19b})$$

with $\vec{d} \equiv \vec{d}_2 - \vec{d}_1$ and $\vec{n}_i^2 = 1$. In the tracks' parametrization in ARTE, we have

$$\vec{n}_i = \frac{1}{N_i} (1, tx_i, ty_i), \quad N_i = \sqrt{1 + tx_i^2 + ty_i^2}, \quad \forall i = 1, 2. \quad (\text{C.20})$$

Therefore, it is possible to write the coordinates of $\vec{r}_{\text{C.A.}} \equiv (z, x, y)$ as

$$z = \frac{z_1 + z_2}{2} + \frac{\lambda_1}{2N_1} + \frac{\lambda_2}{2N_2}, \quad (\text{C.21a})$$

$$x = \frac{x_1 + x_2}{2} + \frac{\lambda_1 tx_1}{2N_1} + \frac{\lambda_2 tx_2}{2N_2}, \quad (\text{C.21b})$$

$$y = \frac{y_1 + y_2}{2} + \frac{\lambda_1 ty_1}{2N_1} + \frac{\lambda_2 ty_2}{2N_2}. \quad (\text{C.21c})$$

The tracks' parametrization in ARTE does not contain the measurement error of the z_i coordinates; however, one may take it as the width of the

VDS's silicon wafer's thickness, $\sigma_z = 280\mu\text{m}$ (see section 3.2.4). The tracks' covariances are obtained as explained in the introduction to this appendix.⁴ The relevant derivatives of the λ_i , $i = 1, 2$, can be condensately written as follows:

$$\frac{\partial \lambda_i}{\partial f_2} = -\frac{\partial \lambda_i}{\partial f_1} = (n_{1f}\vec{n}_2 - n_{2f}\vec{n}_1) \cdot \frac{\vec{n}_j}{|\vec{n}_1 \times \vec{n}_2|^2},$$

$$\forall f = z, x, y, \quad \forall i, j = 1, 2, \quad i \neq j, \quad (\text{C.22a})$$

$$\frac{\partial \lambda_i}{\partial t f_i} = (-1)^{i-1} \frac{(N_1 N_2)^{-1}}{|\vec{n}_1 \times \vec{n}_2|^2} \left(N_i d_f - t f_j (\vec{d} \cdot \vec{n}_j) \right) - \lambda_i \frac{t f_i}{N_i} \pm$$

$$\pm (-1)^i 2 \lambda_i \frac{t g_j n_{3z} - n_{3g}}{|\vec{n}_1 \times \vec{n}_2|}, \quad \forall f, g = x, y, \quad f \neq g, \quad \forall i, j = 1, 2, \quad i \neq j,$$

$$(\text{C.22b})$$

$$\frac{\partial \lambda_i}{\partial t f_j} = (-1)^i \frac{N_j^{-2} (\vec{n}_1 \cdot \vec{n}_2)}{|\vec{n}_1 \times \vec{n}_2|^2} \left(N_j d_f - 2 t f_j (\vec{d} \cdot \vec{n}_j) \right) + (-1)^i \frac{(\vec{d} \cdot \vec{n}_j)}{|\vec{n}_1 \times \vec{n}_2|^2} \frac{t f_i}{N_1 N_2} \pm$$

$$\pm (-1)^j 2 \lambda_i \frac{t g_j n_{3z} - n_{3g}}{|\vec{n}_1 \times \vec{n}_2|}, \quad \forall f, g = x, y, \quad f \neq g, \quad \forall i, j = 1, 2, \quad i \neq j.$$

$$(\text{C.22c})$$

with $\vec{n}_3 \equiv (n_{3z}, n_{3x}, n_{3y}) \equiv (\vec{n}_1 \times \vec{n}_2) / |\vec{n}_1 \times \vec{n}_2|$, and substituting \pm for $+$ when derivating by $t x_i$ and \pm for $-$ when derivating by $t y_i$. Other derivatives of use are:

$$\frac{\partial N_i}{\partial t f_i} = \frac{t f_i}{N_i}, \quad \forall f = x, y, \quad i = 1, 2, \quad (\text{C.23a})$$

$$\frac{\partial f}{\partial f_i} = \frac{1}{2}, \quad \forall f = z, x, y, \quad i = 1, 2; \quad (\text{C.23b})$$

and also:

$$\frac{\partial}{\partial f_i} \left(\frac{\lambda_j}{2 N_j} \right) = \frac{1}{2 N_j} \frac{\partial \lambda_j}{\partial f_i}, \quad \forall f = z, x, y, \quad i, j = 1, 2, \quad (\text{C.23c})$$

$$\frac{\partial}{\partial t f_i} \left(\frac{\lambda_j}{2 N_j} \right) = \frac{1}{2 N_j^2} \left(N_j \frac{\partial \lambda_j}{\partial t f_i} - \delta_{ij} \lambda_j \frac{t f_j}{N_j} \right), \quad \forall i, j = 1, 2, \quad \forall f = x, y,$$

$$(\text{C.23d})$$

$$\frac{\partial}{\partial t f_i} \left(\frac{t g_j \lambda_j}{2 N_j} \right) = \frac{1}{2 N_j^2} \left(\delta_{fg} \delta_{ij} \lambda_j N_j + t g_j N_j \frac{\partial \lambda_j}{\partial t f_i} - \delta_{ij} \lambda_j \frac{t f_i t g_j}{N_j} \right),$$

$$\forall i, j = 1, 2, \quad \forall f, g = x, y. \quad (\text{C.23e})$$

⁴The covariances of z are assumed to be much smaller than z 's variance, $|\sigma_{z\alpha}^2| \ll \sigma_z^2$, $\alpha = x, y, tx, ty$, and are therefore disregarded. This assumption is based on the sistematic observation that the covariances of the other tracks' parameters follow a similar rule, $|\sigma_{f\alpha}^2| \simeq o(10^{-4})\sigma_f^2$, $f \neq \alpha = x, y, tx, ty$.

The tracks' parameters are assumed to be uncorrelated, therefore there are no covariance terms involving the parameters of two different tracks, $\sigma_{\alpha_1\beta_2}^2 = 0, \forall \alpha, \beta = z, x, y, tx, ty$. Because (C.19a) contains no explicit dependence on the momenta of the tracks, the covariances relative to the tracks' momenta are cancelled too: $\sigma_{\alpha_i, 1/p_i}^2 = 0, \alpha = z, x, y, tx, ty, i = 1, 2$. The variances of the three vertex coordinates (C.21) are calculated as described in equation (C.1) and by making use of the derivatives (C.22) and (C.23); they take the form

$$\begin{aligned} \sigma_\alpha^2 = & \sum_{i=1}^2 \sum_f^{x,y,tx,ty} \left(\frac{\partial \alpha}{\partial f_i} \right)^2 \sigma_{f_i}^2 + 2 \sum_{i=1}^2 \sum_f^{x,y} \sum_g^{tx,ty} \left(\frac{\partial \alpha}{\partial f_i} \right) \left(\frac{\partial \alpha}{\partial g_i} \right) \sigma_{f_i g_i}^2 + \\ & + 2 \sum_{i=1}^2 \left(\frac{\partial \alpha}{\partial x_i} \right) \left(\frac{\partial \alpha}{\partial y_i} \right) \sigma_{x_i y_i}^2 + 2 \sum_{i=1}^2 \left(\frac{\partial \alpha}{\partial tx_i} \right) \left(\frac{\partial \alpha}{\partial ty_i} \right) \sigma_{tx_i ty_i}^2 + \\ & + \sum_{i=1}^2 \left(\frac{\partial \alpha}{\partial z_i} \right)^2 \Delta_{\text{VDS}}^2, \quad (\text{C.24}) \end{aligned}$$

with α as either z, x or y , and with $\Delta_{\text{VDS}} = 280\mu\text{m}$ as the thickness of the VDS silicon layer's thickness (it is assumed that these layers are placed rigorously perpendicular relative to the beam direction).

ARTE KUIP macros

This appendix presents the working KUIP macro (kumac) files used for event reconstruction analysis. The used settings are based on [71]. A full manual in L^AT_EX format can be produced by typing the command `manual / arteman.tex latex` in an interactive ARTE session.

D.1 Monte Carlo kumac

```

1  * =====
2  * p2mc.kumac: PRISM kumac for Monte-Carlo events
3  * João Batista <Joao.Batista@desy.de> November 2003
4  * =====
5
6  * ===== Settings for my analysis =====
7  mcnum=4
8     process=p30520
9     geov1='02'
10    geov2='1205'
11    wiremask='00001000'
12    genrec=gen
13    rundir=run05_00052
14    firstfile=15
15    lastfile=15
16    dstext = dst
17    runnumber = 0
18    eventnum = 61
19    keybrevision = 0
20    cnakey = -200211
21    inname=[rundir]_file0
22    indir=/acs/mc[mcnum]/[process]/d[geov1].[geov2]/w[wiremask]/[genrec]/[rundir]/
23
24 * ===== INPUT/OUTPUT (file) =====
25 trace off
26 do filename=[firstfile],[lastfile]
27   if ([filename]<10) then
28     filename1=[indir][inname]00[filename].[dstext]
29   elseif ([filename]<100) then
30     filename1=[indir][inname]0[filename].[dstext]
31   else
32     filename1=[indir][inname][filename].[dstext]
33   endif
34   iofile ev_in [filename1] -gi
35 enddo
36 trace on

```

```

37 * ===== GEOMETRY =====
38 DBOPEN GEODB -RO
39 DBREAD GEODB NGHD [geov1] [geov2] EQ
40 DBCLOSE GEODB
41
42 * ===== CnA =====
43 * http://www-hera-b.desy.de/subgroup/daq/cna/index.html
44 * http://www-hera-b.desy.de/subgroup/software/database
45 /CNA/KEYBOOK [keybrevision] /key_table keytable
46 /CNA/RUN2CNAKEY [cnakey]
47 /CNA/READ CNA ON
48
49 * ===== DIGITISATION =====
50 HBDIGI/DGSEL *
51 HBDIGI/DGSEL CMP -MXD
52 HBDIGI/DGSEL CMP -PTL
53
54 * ITR digitisation:
55 /HBDIGI/ITRDIGI/ITRPERF 1
56 /HBDIGI/ITRDIGI/ITRMCNOI 1
57 /HBDIGI/ITRDIGI/ITRALIGN 1
58 /ITR/ITRMASK 1
59
60 * OTR digitisation:
61 /HBDIGI/DGLEV OTR 3
62 /HBDIGI/OTRGAUSSMEARING 0.05
63 /HBDIGI/OTREFFICIENCY05MM 0.95
64 /HBDIGI/OTREFFICIENCY10MM 0.95
65
66 * ===== VDS =====
67
68 * ===== ITR =====
69 SETENV ITR_SETUPDB /ITR_Setup
70 SETENV ITR_ALIGNDB /ITR_Align
71 SETENV ITR_MONITORDB /ITR_MONITOR
72 /ITR/ITRHITR 0.02
73 /ITR/ITRH CUT 20
74
75 * ===== OTR =====
76 SETENV OtrHitPreparation 0
77 SETENV OtrEventSwitch 259
78
79 * ===== RICH =====
80 SETENV RICH_INSTALLDB /RICH_GEO
81 SETENV RICH_RECODB /RICH_RECO
82
83 * ===== ECAL =====
84 SETENV HBEALDB /ECAL_CALIB
85
86 * ===== MUON =====
87
88 * ===== RECO =====
89 /RECON/SUBD VDS ON CATS
90 /RECON/SUBD ITR ON
91 /RECON/SUBD OTR ON
92 /RECON/SUBD RICH ON
93 /RECON/SUBD ECAL ON
94 /RECON/SUBD MUON ON
95 /RECON/RTRA ON VDSOTR
96 /RECON/RTRA2001 1
97 /RECON/REFIT ON
98

```

```
99 * ===== RANGER =====
100 * www-hera-b.desy.de/subgroup/software/arte/ranger/ranger-steering/ranger-steering.html
101 /RANGER/FPAR rlevel=4 sltmode=3 sltmagn=y fitmagn=n
102 /RANGER/FPAR maxflt_x=4 maxflt_y=4
103 /RANGER/FPAR whmin_x=6 whmin_y=6
104 /RANGER/FPAR qmin_x=5 qmin_y=5
105 /RANGER/FPAR maxflt_tc=4 whmin_tc=5 qmin_tc=4.0
106 /RANGER/FPAR maxflt_mag=3 whmin_mag=6
107
108 * ===== MARPLE =====
109 * www-hera-b.desy.de/subgroup/software/arte/MARPLE/QuickstartKUIPcommands.html
110 /RECON/MATCH MARPLE VDS PC
111 /RECON/MATCH MARPLE VDS RICH
112 /RECON/MATCH MARPLE VDS ECAL
113
114 * ===== PID (MUON: seeded, MURECB) =====
115 /RECON/PID RICH ON RITER RISE
116 /RECON/PID ECAL ON
117 /RECON/PID MUON ON
118
119 * ===== RISE =====
120 /RISE/SEARCH rlevel=3 fit=1 choose=2
121 /RISE/SEARCH occup=0 soccup=5000
122 /RISE/SEEDHIT hsi=5 hio=15 hca=0 hmu=0
123 /RISE/BOOK rtra=1
124
125 * ===== RITER =====
126 /RITER/DWIN 1000
127
128 * ===== GROVER =====
129 /GROVER/STEERING/WIREFOLLOWING 0
130 /GROVER/STEERING/TSELECTION 1
131 /GROVER/STEERING/WRITE_RTAR 1
132 /GROVER/STEERING/FIND_PRIMARIES 1
133
134 * ===== CLASSIFICATION =====
135 * http://www-hera-b.desy.de/subgroup/software/arte/ECLASS.html
136 * (setting of bits, NO event selection!)
137 /RECON/CLASS ALL on
138 /RECON/CLASS JPSIEE on
139 /RECON/CLASS JPSIMM on
140 /RECON/CLASS CAL1HT on 4.0
141 /RECON/CLASS FCNC on
142 /RECON/CLASS VZERO on
143 /RECON/CLASS VZERO2 on
144 /RECON/CLASS DVTX on
145 /RECON/CLASS SLTYP on
146 /RECON/CLASS SLTCUT on
147 /RECON/CLASS SLTEEB on
148 /RECON/CLASS SLTEE on
149 /RECON/CLASS SLTMM on
150 /RECON/CLASS SLTDV on
151 /RECON/CLASS FLTRG on
152 /RECON/CLASS RNDTRG on
153 /RECON/CLASS RECYP on 6.0
154 /RECON/CLASS RECDV on 0.5
155 /RECON/CLASS DIMUON on
156 /RECON/CLASS ALIGN on
157
158 * ===== DQ =====
159
160
```

```

161 * ===== GLOBAL ALIGNMENT =====
162 SETENV DB_GLOBAL_ALIGNMENT /SETUP_ALIGN
163
164 * ===== AC =====
165 /AC/SUBD VDS      on
166 /AC/SUBD RICH     on
167 /AC/SUBD ECAL    on
168 /AC/SUBD GLOBAL  on
169 /AC/SUBD FLT     on
170
171 * ===== TRACKER ALIGNMENT =====
172 /AC/TAXX/MODE     FILL
173 /AC/TAXX/SUBD    ALL ON
174 /AC/TAXX/OTR/CUTS pcut=6 userefit=y
175 /AC/TAXX/OTR/OPT st=n ge=y
176 /AC/TAXX/ITR/CUTS nmc=4 npc=11 ntc=0 xcut=0.1 xexc=0.2 zcut=300.
177 /AC/TAXX/ITR/CUTS pcut=10. chi=0.
178
179 * ===== SLT & 4LT =====
180
181 * ===== Event selection =====
182 select 'event='//[eventnum]//''
183 skip
184 RUN 1
185
186 * ===== PRISM =====
187 * Display XZ geometry projection, MTRAs, RTRAs. Output to file p2mc.ps.
188 PRISM ./p2mc.ps
189 METAFILE on
190 SCOPE FULL ECAL MUON RICH PT
191 STYLE HEADER=n TARGET=y RTRA=y CHAIN=y HIT=y
192 PARAM CTOPP=B.
193 FRAME -50.0 2050.0 -400.0 400.0
194
195 * List Monte Carlo truth --- the whole event, and the B0 branch --- to stdout.
196 lmc
197 lmc B. ; lmc B-
198 lmc B~ ; lmc B+
199
200 lrow evhd
201 lrow rtar
202 lrow gtar
203 list/rver
204 list/rtra
205 list/rseg
206 lrow rver
207 lcol rrel 4
208 lrow rtra
209 lrow rseg
210 lrow rccl
211 lrow rpnt
212 lrow rhit
213 lrow hitb
214 lrow hitc
215
216 ENDKUMAC
217

```

D.2 Real data kumac

```

1  * =====
2  * p4rd.kumac: PRISM kumac for Real Data events
3  * João Batista <Joao.Batista@desy.de> November 2003
4  * Based on http://www-hera-b.desy.de/subgroup/software/arte/KUMAC.html
5  * =====
6
7
8  * ===== Settings for my analysis =====
9  * Run & event:
10     exp=4
11     year='02'
12     runnumber=20645
13     eventnum=1528001531
14  * Geometry:
15     geov1='02'
16     geov2='1205'
17  * Reprocessing version & Database information:
18     repro='rp0004'
19     keybreversion=28
20     SETENV HBNAME ROOT hb-dbsrv0
21  * Output files:
22     prismfile=run[runnumber]_evt[eventnum].ps
23
24  * ===== INPUT/OUTPUT (file) =====
25  io/dcache off
26  iofile dst_in_dir /acs/data/REAL/[year]/exp0[exp]/dst/run[runnumber]/[repro]_run[runnumber].idx -GI
27
28  * ===== GEOMETRY =====
29  DBOpen GEODB -RO
30  DBREAD GEODB NGHD [geov1] [geov2] EQ
31  DBCLOSE GEODB
32
33  * ===== CnA =====
34  * http://www-hera-b.desy.de/subgroup/daq/cna/index.html
35  * http://www-hera-b.desy.de/subgroup/software/database
36  * -----
37  /CNA/KEYBOOK [keybreversion] /key_table keytable
38  /CNA/READ CNA ON
39  /CNA/READ VDS ON
40  /CNA/READ HPT ON
41  /CNA/READ ITR ON
42  /CNA/READ OTR ON
43  /CNA/READ RICH ON
44  /CNA/READ ECAL ON
45  /CNA/READ MUON ON
46  /CNA/READ GLOBAL ON
47
48  * ===== DIGITISATION =====
49  HBDIGI/DGSEL *
50  HBDIGI/DGSEL CMP -MXD
51  HBDIGI/DGSEL CMP -PTL
52
53  * ITR digitisation:
54  /HBDIGI/ITRDIGI/ITRPERF 1
55  /HBDIGI/ITRDIGI/ITRMCNOI 1
56  /HBDIGI/ITRDIGI/ITRALIGN 1
57  /ITR/ITRMASK 1
58
59  * OTR digitisation:
60  /HBDIGI/DGLEV OTR 3

```

```

61 /HBDIGI/OTRGAUSSMEARING 0.05
62 /HBDIGI/OTREFFICIENCY05MM 0.95
63 /HBDIGI/OTREFFICIENCY10MM 0.95
64
65 * ===== VDS =====
66 SETENV VDS_MASKING DBS
67 setenv VDS_READ_ALIGNMENT_NO_RECO ON
68 setenv VDS_IGNORE_GEDE_GWAL_ERROR YES
69
70 * ===== HPT =====
71 setenv HPT_FEDS_PACK $HBROOT/HPT/dbase/99/feds_pack.0601
72 setenv HPT_HOT_CHANNELS $HBROOT/HPT/dbase/99/hot_channels.0899
73
74 * ===== ITR =====
75 SETENV ITR_SETUPDB /ITR_Setup
76 SETENV ITR_ALIGNDB /ITR_Align
77 SETENV ITR_MONITORDB /ITR_MONITOR
78 /ITR/ITRHITR 0.01
79 /ITR/ITRHCUT 50
80
81 * ===== OTR =====
82 SETENV OtrHitPreparation 0
83 SETENV OtrEventSwitch 259
84 SETENV OtrOccupancyCut 15000
85
86 * ===== RICH =====
87 SETENV RICH_INSTALLDB /RICH_GEO
88 SETENV RICH_RECODB /RICH_RECO
89
90 * ===== ECAL =====
91 SETENV HBEALDB /ECAL_CALIB
92
93 * ===== MUON =====
94 SETENV MUON_CONFIG $HBROOT/MUON/db/Mu.config
95 SETENV MUON_BADFILE $HBROOT/MUON/db/Mu.mupreslt.mask
96
97 * ===== RECO =====
98 /RECON/SUBD VDS ON CATS
99 /RECON/SUBD ITR ON
100 /RECON/SUBD OTR ON
101 /RECON/SUBD RICH ON
102 /RECON/SUBD ECAL ON
103 /RECON/SUBD MUON ON
104 /RECON/SUBD HPT ON
105 /RECON/RTRA ON VDSOTR
106 /RECON/RTRA2001 1
107 /RECON/REFIT ON
108
109 * ===== RANGER =====
110 * www-hera-b.desy.de/subgroup/software/arte/ranger/ranger-steering/ranger-steering.html
111 /RANGER/FPAR rlevel=5 sltmode=6
112 /RANGER/FPAR cats=Y
113 /RANGER/FPAR outlay=1 chmaxoutl=10.
114
115 * ===== MARPLE =====
116 * www-hera-b.desy.de/subgroup/software/arte/MARPLE/QuickstartKUIPcommands.html
117 /RECON/MATCH MARPLE VDS PC
118 /RECON/MATCH MARPLE VDS ECAL
119 /RECON/MATCH MARPLE RTRA RICH
120 MASVDECALNORTRA 1 1
121
122 * ===== PID (MUON: seeded, MURECB) =====

```

```
123 /RECON/PID RICH ON RITER
124 /RECON/PID ECAL ON
125 /RECON/PID MUON ON
126
127 * ===== RISE =====
128 rise/search occup=300 soccup=0 rlevel=0 fit=0
129 rise/ring drad=.007
130
131
132 * ===== RITER =====
133 /RITER/DWIN 1000
134 /RITER/NITER 0
135 /RITER/ETA 1.
136
137 * ===== GROVER =====
138 /GROVER/STEERING/WIREFOLLOWING 0
139 /GROVER/STEERING/TSELECTION 1
140 /GROVER/STEERING/WRITE_RTAR 1
141 /GROVER/STEERING/FIND_PRIMARIES 2
142
143 * ===== CLASSIFICATION =====
144 * www-hera-b.desy.de/subgroup/software/arte/ECLASS.html
145 * (setting of bits, NOT event selection!)
146 /RECON/CLASS ALL on
147 /RECON/CLASS SLTBYP off
148 /RECON/CLASS JPSIEE on
149 /RECON/CLASS JPSIMM on
150 /RECON/CLASS CAL1HT on 4.0
151 /RECON/CLASS FCNC on
152 /RECON/CLASS VZERO on
153 /RECON/CLASS VZERO2 on
154 /RECON/CLASS DVTX on
155 /RECON/CLASS SLTYP on
156 /RECON/CLASS SLTCUT on
157 /RECON/CLASS SLTEEB on
158 /RECON/CLASS SLTEE on
159 /RECON/CLASS SLTMM on
160 /RECON/CLASS SLTDV on
161 /RECON/CLASS TLT off
162 /RECON/CLASS FLTRG on
163 /RECON/CLASS RNDTRG on
164 /RECON/CLASS RECYP on 6.0
165 /RECON/CLASS RECDV on 0.5 5.0
166 /RECON/CLASS DIMUON on
167 /RECON/CLASS DIELEID on
168 /RECON/CLASS ALIGN on
169
170 * ===== DQ MONITORING =====
171
172 * ===== GLOBAL ALIGNMENT =====
173 SETENV DB_GLOBAL_ALIGNMENT /SETUP_ALIGN
174
175 * ===== AC =====
176 /AC/SUBD VDS on
177 /AC/SUBD RICH on
178 /AC/SUBD ECAL on
179 /AC/SUBD ITR off
180 /AC/SUBD OTR off
181 /AC/SUBD MUON off
182 /AC/SUBD GLOBAL off
183 /AC/SUBD LUMI off
184 /AC/SUBD FLT off
```

```

185
186 * ===== TRACKER ALIGNMENT =====
187
188 * ===== SLT =====
189 /SLT/FILL ON
190
191 * ===== TLT =====
192
193 * ===== 4LT =====
194
195 * ===== PRISM =====
196 PRISM [prismfile]
197 METAFILE on
198 SCOPE FULL ECAL MUON RICH PT
199 STYLE HEADER=y RTRA=y RVER=y CHAIN=y SLT=y TARGET=y
200 PARAM CTOPP=Jpsi
201 FRAME -50.0 2050.0 -400.0 400.0
202
203 * ===== Event selection =====
204 select 'run='//[runnumber]//' and event='//[eventnum]//'
205 run 1
206
207 * ===== List booked tables (output is stdout) =====
208
209 lrow evhd
210 lrow rtar
211 lrow gtar
212 list/rver
213 list/rtra
214 list/rseg
215 lrow rver
216 lcol rrel 4
217 lrow rtra
218 lrow rseg
219 lrow rccl
220 lrow rpnt
221 lrow rhit
222 lrow hitb
223 lrow hitc
224
225 * 3D view from the VDS:
226 scope sivid ; style target=y hit=y ; angle 10 150 ; view 3
227 * Shows RTRAs, hides MTRAs:
228 style rtra=y mtra=n ; draw
229
230 ENDKUMAC
231

```

Note. For the year 2000 runs, different settings should be used instead (check against lines 9–18 at the beginning of this listing, page 225):

```

exp=3
year='00'
geov1='99'
geov2='1015'
repro='rp0002'
keybrevision=14

```

C source code

This appendix presents the C language source codes used in the bulk (chapters 4 and 5 of this thesis’ work). The source code is also available in electronic format at <http://fisica.fc.ul.pt/~jbatista/HERA-B/>.

E.1 Impact parameters and invariant masses

The listing below shows the source code for a program designed to read and parse structured ASCII output from an ARTE session. This tool was named PI¹ and though it is far from being highly sophisticated, it is reasonably useful. As it is, it requires that the table list output (`lrow rver`, `lrow rtra`, etc.) has the same order as those from the kumac files in appendix D; it could be modified to cope with different table order and missing tables without hanging in an infinite loop.

The program is compiled and run outside the ARTE framework and performs the following actions:

1. Open the ASCII output from an ARTE session, parse the contents of the tables RVER, RTAR, RSEG and RCCL (in that order!) and fill an internal buffer with those elements’ data.
2. Output to standard output (`stdout`) an ASCII table, readable with e.g. a spreadsheet application (imported as a `.csv` file).

The program’s five output tables contain the results from the included routines, which calculate e.g. impact parameters, RTRA–RTRA and RTRA–RVER distances, invariant mass, 4-RTRA invariant mass, and respective standard deviation errors (see appendix C). A crude “Particle ID” is done by making basic assumptions from MUON and RICH information, singleing out protons, kaons, pions and muons; these distinctions are used to improve the invariant mass calculations of “good” RTRAs (i.e., those with hits on the VDS and the Main Tracker).

¹From the initials for “impact parameter” in Portuguese.

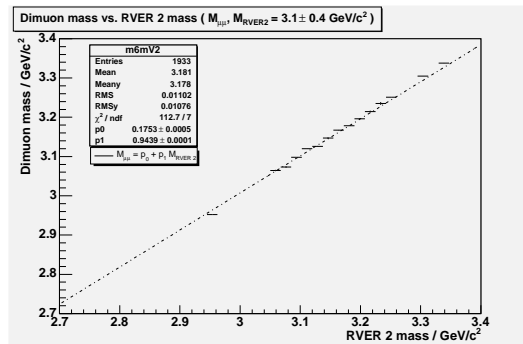


Figure E.1. Profile histogram of the dimuon invariant mass versus RVER 2 mass for Monte Carlo event 235 (see chapters 4 and 5). The function `InvMass_PID` in the `PI` tool (line 1096), to get the invariant mass of RTRA pairs, has a linear response in the range of the J/ψ mass for dimuon candidates.

The last output of the program gives an event summary, including the choice of dimuon and charged dipion which best fit the masses of the J/ψ and K_S^0 respectively, and of a B meson for all the four RTRAs. It is also required that the vertices for the four RTRAs, the dimuon and the dipion lie consecutively downstream of the target, i.e. $z_{\text{wire}} < z_B < z_{J/\psi} < z_{K_S}$. An RTRA is also presented as a candidate charge tag; it is required to not be one of the other four RTRAs, have the highest transverse momentum and above a chosen “cut” value, have hits on the VDS and Main Tracker and have a distance of closest approach to the primary vertex of less than a chosen cut value of e.g. $500\mu\text{m}$. A particle ID hypothesis on the tagging RTRA is not absolutely necessary — only its charge sign from tracking is required.²

The linearity of the routine `InvMass_PID`, used to obtain the invariant mass of RTRA pairs with PID hypothesis, was investigated. The dimuon invariant mass was compared with the secondary reconstructed vertex RVER 2 for different displacements of the detector described in chapter 5 — VDS layers, whole VDS, whole Main Tracker, whole RICH and whole MUON. The results are presented in figure E.1.

```

1  /*****/
2  /* PI.c -- calculate impact parameters, etc. from ASCII output from */
3  /* ARTE (http://www-hera-b.desy.de/subgroup/software/arte/). */
4  /* */
5  /* Author: Joao.Batista@desy.de */
6  /*****/
7  /* Invoke program with: PI.exe myArteOutput.txt [ --verbose ].
8  * NOTE: The myArteOutput.txt ASCII output assumes the following ARTE tables
9  * are presented in the following order:
10 * -> lrow evhd
11 * -> lrow rtar
12 * -> lrow gtar
13 * list/rver
14 * list/rtra
15 * list/rseg
16 * -> lrow rver
17 * lcol rrel 4

```

²To improve the tagging efficiency, transverse momentum cuts may be imposed on the RTRAs. These cuts depend on the PID hypothesis. See e.g. [108] [11].

```

18 * -> lrow rtra
19 *     lrow rseg
20 * -> lrow rccl
21 *     lrow rpnt
22 *     lrow rhit
23 *     lrow hitb
24 *     lrow hitc
25 * The arrowed ('->') entries **MUST** be present and in the indicated order.
26 * Anything else causes an endless loop! The remaining entries are optional.
27 */
28
29 #include <stdio.h>
30 #include <stdlib.h>
31 #include <math.h>
32
33 #define PI_VERSION "0.4.0"
34
35 #ifndef CUT_GOODP
36 #define CUT_GOODP 0
37 #endif
38 #ifndef CUT_NOPID
39 #define CUT_NOPID 0
40 #endif
41 #ifndef READ_TABLE_RCCL
42 #define READ_TABLE_RCCL 0
43 #endif
44
45 ////////////////////////////////// VECTOR/MATRIX INDICES //////////////////////////////////
46 // vertex indices
47 #define Vx 1
48 #define Vy 2
49 #define Vz 0
50 #define CVxx 0
51 #define CVxy 1
52 #define CVyx CVxy
53 #define CVyy 2
54 #define CVxz 3
55 #define CVzx CVxz
56 #define CVyz 4
57 #define CVzy CVyz
58 #define CVzz 5
59
60 // track indices
61 #define Z 0
62 #define X 1
63 #define Y 2
64 #define TX 1
65 #define TY 2
66 #define TZ 0
67 #define cZZ 0.50 // error of Z track coordinate, in cm
68 #define CXX 0
69 #define CXY 1
70 #define CYX CXY
71 #define CYY 2
72 #define CXTX 3
73 #define CTXX CXTX
74 #define CYTX 4
75 #define CTXY CXTY
76 #define CTXTX 5
77 #define CXTY 6
78 #define CTYX CXTY
79 #define CYTY 7

```

```

80 #define CTYY CYTY
81 #define CTXTY 8
82 #define CTYTX CTXTY
83 #define CTYTY 9
84 #define CXP 10
85 #define CPX CXP
86 #define CYP 11
87 #define CPY CYP
88 #define CXP 12
89 #define CPTX CXP
90 #define CTYP 13
91 #define CPTY CTYP
92 #define CPP 14
93
94 /* Number of elements in vectors/matrices. */
95 #define Vcoords 3
96 #define Vcovar 6
97 #define Rcoords 3
98 #define Rdirec 3
99 #define Rcovar 15
100
101 ////////////////////////////////////////////////// FUNCTIONS AND STRUCTURES //////////////////////////////////////
102 double const MAX_PI=2.5e9;
103 double const m_e=0.0005, m_mu=0.1057, m_pi=0.1396, m_K=0.4937, m_p=0.9383;
104 double const m_pi0=0.1350, m_K0=0.4977, m_Jpsi=3.097, m_B0=5.279, m_B=5.279;
105 double max(double x, double y) { if(x<y) return y; else return x; }
106 double min(double x, double y) { if(x<y) return x; else return y; }
107 int sign(double x) { if(x<0.0) return -1; else return 1; }
108 int Sign(double x) { if(x<0.0) return -1; else
109     if(x>0.0) return 1; else return 0; }
110 double Prob(double, int);
111 double ParamImpact(double*, double*, double*, double*);
112 double InvMass_PID(double, double, double*, double*, double, double);
113 double InvMass(double*, double*, double, double);
114 double Angle(double*, double*);
115 double pT(double*, double);
116 double stddev_p(double*, double);
117 double stddev_pT(double*, double*, double);
118 double stddev_Theta(double*, double*, double*, double*);
119 double stddev_Mass_PID(double, double, double*, double*,
120     double*, double*, double, double);
121 double stddev_Mass(double*, double*, double*, double*, double, double);
122 double stddev_ParamImp(double*, double*, double*, double*, double*, double*);
123 double stddev_PImp2(double*, double*, double*, double*, double*);
124 double PImp2(double*, double*, double*);
125 double PImp3(double*, double*, double*, double*, double*, double, double);
126 double stddev_PImp3(double*, double*, double*, double*, double*,
127     double*, double, double, double*, double*);
128
129 typedef struct s_RTRA { int rt; char PID[8]; int mtra;
130     double d[Rcoords]; double n[Rdirec]; double p; double c[Rcovar];
131     double mass; double lrich; double lecal; double lmuon; double ltrd;
132     double lre; double lrmu; double lrpi; double lrk; double lrp;
133     double lee; double lemi; double leh; double lmmu; double lmh;
134     double lte; double lth; double chi2; double prob;
135     int hsi; int hin; int hou; int hri; int hca; int htr; int hmu; } RTRA ;
136 typedef struct s_RVER { int rv; int wire; int type; int ndgf; double mass;
137     double merr; double d[Vcoords]; double c[Vcovar]; int nt; double chi2; } RVER ;
138 typedef struct s_RCCL { int rc; double d[Vcoords]; double n[Rdirec];
139     double Eclus; double c[Rcovar]; double wid; double asym;
140     double dcog[Vcoords]; double vcog[Vcoords]; double lemp; double lmp;
141     double lhad; } RCCL;

```

```

142 typedef struct s_RTAR { int itar; int wire; int Zmat; char Wire[4];
143     double d[Vcoords]; double s[Vcoords]; } RTAR;
144 typedef struct s_EVHD { int evt; int run; int exp; int date; int time; } EVHD;
145 EVHD evhd; RTAR rtar; RVER rver1;
146
147 double eval_Mass(RTRA, RTRA);
148 double eval_eMass(RTRA, RTRA);
149 double PI_rtar(RTRA, RTAR);
150 double PI_rtar_2RTRA(RTRA, RTRA, RTAR);
151 double PI_rtar_3RTRA(RTRA, RTRA, RTRA, RTAR);
152 double PI_rtar_4RTRA(RTRA, RTRA, RTRA, RTRA, RTAR);
153 double PImp_BO(RTRA, RTRA, RTRA, RTRA);
154 double stddev_PImp_BO(RTRA, RTRA, RTRA, RTRA);
155 double stddev_vtxcoord(char, RTRA, RTRA);
156 double posZ(char, RTRA, RTRA);
157 RTRA RTRAFusion(RTRA, RTRA, char*);
158 double jetCharge(RTRA*,int,RVER);
159 double stddev_jetCharge(RTRA*,int,RVER);
160
161 int goldenRTRA[5];          // dimuon and dipion, plus a charge tag
162
163 ///////////////////////////////////////////////////////////////////
164 /////////////////////////////////////////////////////////////////// MAIN ///////////////////////////////////////////////////////////////////
165 ///////////////////////////////////////////////////////////////////
166 int main(int argc, char *argv[]) {
167     int h, i, j, k, l, N=0, nt=0, nv=0, nc=0, event;
168     int kUseB0, quiet, really_quiet, assume_B0;
169     float ArteVersion; int isGoodRTRAs,carga;
170     double mass, rho, sep, emass, erho, esep, pt, ep, ept, theta, etheta, ZZZZ;
171     RTRA *list;      RVER *vtx;   RTAR *gtar;   RCCL *rccl;
172     RTRA Jpsi, KS, B0;
173     FILE *input, *lrver;
174     int hsi, hin, hou, hri, hca, htr, hmu, Rtar1, nGtar=0;
175     double lre, lrmu, lrpi, lrk, lrp;
176     double lee, lemi, leh, lmmu, lmh, lte, lth;
177     double lrich, ltrd, lecal, lmuon;
178     double masslist[4];
179     double z,x,y,tx,ty,pf,pz,px,py,cxx,cyy,ctx,cty,c1p,chi2,prob;
180
181     char dst[80], Arte[16], trash[80];
182     dst[79]='\0'; Arte[15]='\0'; trash[79]='\0';
183
184     if(argc<2) {
185         printf("%s %s: too few arguments\nUsage: %s <ARTE-session-output.txt> "
186             "[ --noB0-list | --quiet | --really-quiet | --verbose | "
187             "[--assume-B- ] ['<alternate summary label>']\n",
188             argv[0], PI_VERSION, argv[0]);
189         return -1;
190     }
191
192     kUseB0 = -1; assume_B0 = -1 ; quiet = 0; really_quiet = 1;
193     if(argc>2) {
194         if(!strcmp(argv[2],"--assume-B-")) { really_quiet = 1 ; assume_B0 = 0; }
195         else if(!strcmp(argv[2],"--really-quiet")) { really_quiet=1; }
196         else if(!strcmp(argv[2],"--verbose")) { really_quiet=0; }
197         else if(!strcmp(argv[2],"--noB0-list"))
198             { printf("No RTRA 4-sets will be print out.\n"); kUseB0=0; }
199         else if(!strcmp(argv[2],"--quiet"))
200             { printf("No GTARs/RTRAs, RCCLs and RTRA 4-sets "
201                 "will be print out\n"); quiet=1; }
202     } else if(!really_quiet) printf("All processed tables will be print out.\n");
203

```

```

204     input = fopen(argv[1],"r");
205     if(!input)
206     { printf("%s: could not open file %s\n", argv[0], argv[1]); return -1; }
207     else if(!really_quiet) printf("ARTE session filename is %s\n", argv[1]);
208
209     do {
210         do { fscanf(input, "%s", Arte); } while(strcmp(Arte,"ARTE"));
211         fscanf(input,"%s",Arte);
212         if(!strcmp(Arte,"version:")) {
213             fscanf(input,"%f",&ArteVersion);
214             if(!really_quiet) printf("ARTE version: %1.4f\n", ArteVersion);
215             break;
216         }
217     } while(!feof(input));
218
219     // read table EVHD
220     do {
221         do { fscanf(input, "%s", trash); } while(strcmp(trash,"lrow"));
222         fscanf(input,"%s",trash); if(!strcmp(trash,"evhd")) break;
223     } while(!feof(input));
224     if(!strcmp(trash,"evhd")) {
225         for(i=0; i<4; i++) fscanf(input,"%s",trash);
226         if(strcmp(trash,"empty")) { // check if table is not empty
227             do { fscanf(input,"%s",trash); } while(strcmp(trash,"|"));
228             fscanf(input,"%i %s",&evhd.evt,trash);
229             do { fscanf(input,"%s",trash); } while(strcmp(trash,"|"));
230             fscanf(input,"%i %s",&evhd.run,trash);
231             do { fscanf(input,"%s",trash); } while(strcmp(trash,"|"));
232             fscanf(input,"%i %s",&evhd.exp,trash);
233             do { fscanf(input,"%s",trash); } while(strcmp(trash,"|"));
234             fscanf(input,"%i %s",&evhd.date,trash);
235             do { fscanf(input,"%s",trash); } while(strcmp(trash,"|"));
236             fscanf(input,"%i %s",&evhd.time,trash);
237         }
238         do { fscanf(input,"%s",trash); } while(strcmp(trash,"flag"));
239         if(!really_quiet)
240             printf("RUN %i - EVT %i - EXP %i\n", evhd.run, evhd.evt, evhd.exp);
241     }
242
243     // read table RTAR/GTAR
244     /* read table GTAR */
245     if(evhd.exp>=0) { // evhd.exp>=0 means non-MonteCarlo events!!
246         do {
247             do { fscanf(input, "%s", trash); } while(strcmp(trash,"lrow"));
248             fscanf(input,"%s",trash);
249             if(!strcmp(trash,"rtar"))
250                 do { fscanf(input, "%s", trash); } while(strcmp(trash,"lrow"));
251             fscanf(input,"%s",trash); if(!strcmp(trash,"gtar")) break;
252         } while(!feof(input));
253         gtar = (RTAR*)malloc(0*sizeof(RTAR));
254         if(!strcmp(trash,"gtar")) {
255             for(i=0; i<6; i++) fscanf(input,"%s",trash);
256             if(strcmp(trash,"empty"))
257                 for(i=0; !strcmp(Arte,"GTAR") || i==0 ; i++) {
258                     gtar = (RTAR*)realloc(gtar, (i+1)*sizeof(RTAR));
259                     gtar[i].itar = i+1;
260                     do { fscanf(input,"%s",trash); } while(strcmp(trash,"|"));
261                     fscanf(input,"%i %s", &gtar[i].Zmat,trash);
262                     do { fscanf(input,"%s",trash); } while(strcmp(trash,"|"));
263                     fscanf(input,"%i %s", &gtar[i].wire,trash);
264                     switch((int)(gtar[i].wire)) {
265                         case 1: sprintf(gtar[i].Wire,"a1"); break;

```

```

266         case 2: sprintf(gtar[i].Wire,"b1"); break;
267         case 3: sprintf(gtar[i].Wire,"i1"); break;
268         case 4: sprintf(gtar[i].Wire,"o1"); break;
269         case 5: sprintf(gtar[i].Wire,"a2"); break;
270         case 6: sprintf(gtar[i].Wire,"b2"); break;
271         case 7: sprintf(gtar[i].Wire,"i2"); break;
272         case 8: sprintf(gtar[i].Wire,"o2"); break;
273         default: sprintf(gtar[i].Wire," "); break;
274     }
275     if(evhd.exp<0) switch((int)(gtar[i].Zmat)) {
276         case 6: sprintf(gtar[i].Wire,"C "); break;
277         case 13: sprintf(gtar[i].Wire,"Al"); break;
278         case 22: sprintf(gtar[i].Wire,"Ti"); break;
279         case 46: sprintf(gtar[i].Wire,"Pd"); break;
280         case 74: sprintf(gtar[i].Wire,"W "); break;
281         default: sprintf(gtar[i].Wire," "); break;
282     }
283     do { fscanf(input,"%s",trash); } while(strcmp(trash,"|"));
284     fscanf(input,"%lf %s",&gtar[i].s[Vx],trash);
285     do { fscanf(input,"%s",trash); } while(strcmp(trash,"|"));
286     fscanf(input,"%lf %s",&gtar[i].s[Vy],trash);
287     do { fscanf(input,"%s",trash); } while(strcmp(trash,"|"));
288     fscanf(input,"%lf %s",&gtar[i].s[Vz],trash);
289     do { fscanf(input,"%s",trash); } while(strcmp(trash,"|"));
290     fscanf(input,"%lf %s",&gtar[i].d[Vx],trash);
291     do { fscanf(input,"%s",trash); } while(strcmp(trash,"|"));
292     fscanf(input,"%lf %s",&gtar[i].d[Vy],trash);
293     do { fscanf(input,"%s",trash); } while(strcmp(trash,"|"));
294     fscanf(input,"%lf %s",&gtar[i].d[Vz],trash);
295     for(j=0; j<17; j++)
296     do { fscanf(input,"%s",trash); } while(strcmp(trash,"|"));
297     for(j=0; j<3; j++) fscanf(input,"%s",trash);
298     if(strcmp(trash,"Dend_out"))
299         printf("Error reading TARGET information -"
300              " unexpected GTAR table format!\n\n");
301     fscanf(input,"%s",Arte);
302     nGtar++;
303     if(!strcmp(Arte,"Table")) fscanf(input,"%s",Arte);
304 }
305 }
306 if(!really_quiet)
307     printf("Read %i GTAR %s.\n", nGtar, (nGtar!=1?"entries":"entry"));
308 } else {
309     gtar = (RTAR*)malloc(sizeof(RTAR)); nGtar=1;
310     sprintf(gtar[0].Wire,"i2"); gtar[0].itar=7;
311     rtar.Zmat = gtar[0].Zmat = 6;
312     rtar.wire = gtar[0].wire = 7;
313     rtar.d[Vz] = gtar[0].d[Vz] = -4.6061 ;
314     rtar.d[Vx] = gtar[0].d[Vx] = 0.366 ;
315     rtar.d[Vy] = gtar[0].d[Vy] = -0.057 ;
316     rtar.s[Vz] = gtar[0].s[Vz] = 0.05 ;
317     rtar.s[Vx] = gtar[0].s[Vx] = 0.01 ;
318     rtar.s[Vy] = gtar[0].s[Vy] = 4.2 ;
319     if(!really_quiet)
320         printf("NOTE: Using hard-coded target configuration (actual GTAR "
321              "readout is ignored!)\nWIRE %i (%s): \tz = %2.4f +/- %2.4f\t"
322              "x = %2.4f +/- %2.4f\ty = %2.4f +/- %2.4f\n\n",
323              rtar.wire, rtar.Wire, rtar.d[Vz],rtar.s[Vz],
324              rtar.d[Vx],rtar.s[Vx], rtar.d[Vy],rtar.s[Vy]);
325 }
326 // read table RVER
327

```

```

328 do {
329     do { fscanf(input, "%s", Arte); } while(strcmp(Arte,"lrow"));
330     fscanf(input, "%s", Arte); if(!strcmp(Arte,"rver")) break;
331 } while(!feof(input));
332 vtx = (RVER*)malloc(0*sizeof(RVER));
333 if(!strcmp(Arte,"rver")) { // found RVER table list?
334     for(i=0; i<6; i++) fscanf(input, "%s", Arte);
335     if(strcmp(Arte,"empty")) // check if table is not empty
336     for(nv=0 ; !strcmp(Arte,"Table") || nv==0 ; ) {
337         vtx = (RVER*)realloc(vtx, (nv+1)*sizeof(RVER));
338         vtx[nv].rv = nv+1;
339         vtx[nv].d[Vx]=vtx[nv].d[Vy]=vtx[nv].d[Vz]=0;
340         vtx[nv].wire=vtx[nv].type=vtx[nv].ndgf=vtx[nv].nt=0;
341         vtx[nv].mass=vtx[nv].merr=vtx[nv].chi2=0;
342         for(i=0; i<Vcovar; i++) vtx[nv].c[i]=0;
343         do { fscanf(input, "%s", Arte); } while(strcmp(Arte,"|"));
344         fscanf(input, "%lf", &(vtx[nv].d[Vx]));
345         do { fscanf(input, "%s", Arte); } while(strcmp(Arte,"|"));
346         fscanf(input, "%lf", &(vtx[nv].d[Vy]));
347         do { fscanf(input, "%s", Arte); } while(strcmp(Arte,"|"));
348         fscanf(input, "%lf", &(vtx[nv].d[Vz]));
349         for(i=0; i<Vcovar; i++) { // covariance matrix
350             do { fscanf(input, "%s", Arte); } while(strcmp(Arte,"|"));
351             fscanf(input, "%lf", &(vtx[nv].c[i]));
352         }
353         do { fscanf(input, "%s", Arte); } while(strcmp(Arte,"|"));
354         fscanf(input, "%lf", &(vtx[nv].mass));
355         do { fscanf(input, "%s", Arte); } while(strcmp(Arte,"|"));
356         fscanf(input, "%lf", &(vtx[nv].merr));
357         do { fscanf(input, "%s", Arte); } while(strcmp(Arte,"|"));
358         fscanf(input, "%i", &(vtx[nv].nt));
359         for(i=0; i<2; i++) do { fscanf(input, "%s", Arte); } while(strcmp(Arte,"|"));
360         fscanf(input, "%i", &(vtx[nv].wire));
361         do { fscanf(input, "%s", Arte); } while(strcmp(Arte,"|"));
362         fscanf(input, "%lf", &(vtx[nv].chi2));
363         do { fscanf(input, "%s", Arte); } while(strcmp(Arte,"|"));
364         fscanf(input, "%i", &(vtx[nv].type));
365         do { fscanf(input, "%s", Arte); } while(strcmp(Arte,"|"));
366         fscanf(input, "%i", &(vtx[nv].ndgf));
367         do { fscanf(input, "%s", Arte); } while(strcmp(Arte,"Dend_out"));
368         if(vtx[nv].nt<21) for(i=0; i<12+vtx[nv].nt; i++) fscanf(input, "%s", Arte);
369         else do { fscanf(input, "%s", Arte); } while(strcmp(Arte,"..."));
370         if(ArteVersion>4.0104) for(i=0; i<12; i++) fscanf(input, "%s", Arte);
371         fscanf(input, "%s", Arte);
372         nv++;
373     } else
374         if(!really_quiet) { printf("ARTE table RVER is empty.\n"); nv=0; }
375 }
376 if(!really_quiet) printf("Read %i RVER %s.\n", nv, (nv==1?"entry":"entries"));
377 rver1 = vtx[0];
378
379 // identify the wire from the primary RVER with the GTAR array
380 Rtar1=0; rtar.wire = -1;
381 for(i=0; i<nGtar; i++) if(gtar[i].wire == vtx[0].wire) Rtar1=i;
382 sprintf(rtar.Wire, "%s", gtar[Rtar1].Wire);
383 rtar.itar = gtar[Rtar1].itar;   rtar.Zmat = gtar[Rtar1].Zmat;
384 rtar.wire = gtar[Rtar1].wire;
385 rtar.d[Vz] = gtar[Rtar1].d[Vz];   rtar.d[Vx] = gtar[Rtar1].d[Vx];
386 rtar.d[Vy] = gtar[Rtar1].d[Vy];   rtar.s[Vz] = gtar[Rtar1].s[Vz];
387 rtar.s[Vx] = gtar[Rtar1].s[Vx];   rtar.s[Vy] = gtar[Rtar1].s[Vy];
388 if(!really_quiet) {
389     if(rtar.wire != -1)

```

```

390         printf("WIRE %i (%s):\tz = %2.3lf +/- %2.3lf"
391                "\tx = %2.3lf +/- %2.3lf\ty = %2.3lf +/- %2.3lf\n",
392                rtar.wire, rtar.Wire, rtar.d[Vz],rtar.s[Vz],
393                rtar.d[Vx],rtar.s[Vx], rtar.d[Vy],rtar.s[Vy]);
394     else printf("Error - could not relate RVER 1 with an GTAR entry!\n");
395     printf("RVER %i:\t\tz = %2.3lf +/- %2.3lf\tx = %2.3lf +/- %2.3lf\t"
396            "y = %2.3lf +/- %2.3lf\n\n", vtx[0].rv, vtx[0].d[Vz],
397            sqrt(vtx[0].c[CVzz]), vtx[0].d[Vx],sqrt(vtx[0].c[CVxx]),
398            vtx[0].d[Vy],sqrt(vtx[0].c[CVyy]));
399 }
400
401 // read table RTRA
402 do {
403     do { fscanf(input, "%s", Arte); } while(strcmp(Arte,"low"));
404     fscanf(input,"%s",Arte); if(!strcmp(Arte,"rtra")) break;
405 } while(!feof(input));
406 list = (RTRA*)malloc(0*sizeof(RTRA));
407 if(!strcmp(Arte,"rtra")) { // found RTRA table list?
408     for(i=0; i<6; i++) fscanf(input,"%s",Arte); k=0;
409     if(strcmp(Arte,"empty"))
410     for(N=0 ; !strcmp(Arte,"Table") || N==0 ; ) {
411         list = (RTRA*)realloc(list, (N+1)*sizeof(RTRA));
412         list[N].rt = N+1;
413         do { fscanf(input,"%s",Arte); } while(strcmp(Arte,"|"));
414         fscanf(input,"%lf",&(list[N].d[Z]));
415         do { fscanf(input,"%s",Arte); } while(strcmp(Arte,"|"));
416         fscanf(input,"%lf",&(list[N].d[X]));
417         do { fscanf(input,"%s",Arte); } while(strcmp(Arte,"|"));
418         fscanf(input,"%lf",&(list[N].d[Y]));
419         list[N].n[TZ]=1.0;
420         do { fscanf(input,"%s",Arte); } while(strcmp(Arte,"|"));
421         fscanf(input,"%lf",&(list[N].n[TX]));
422         do { fscanf(input,"%s",Arte); } while(strcmp(Arte,"|"));
423         fscanf(input,"%lf",&(list[N].n[TY]));
424         do { fscanf(input,"%s",Arte); } while(strcmp(Arte,"|"));
425         fscanf(input,"%lf",&pf); list[N].p=(pf?1.0/pf:0.0);
426         for(i=0; i<Rcovar; i++) { // covariance matrix
427             do { fscanf(input,"%s",Arte); } while(strcmp(Arte,"|"));
428             fscanf(input,"%lf",&(list[N].c[i]));
429         }
430         list[N].mass=0.0;
431         hsi = hin = hou = hri = hca = htr = hmu = 0;
432         lre=lrmu=lrpi=lrk=lrp = lte=lth = lee=lemi=leh = lmmu=lmh = 0.0;
433         do { fscanf(input,"%s",Arte); } while(strcmp(Arte,"|"));
434         fscanf(input,"%i",&hsi);
435         do { fscanf(input,"%s",Arte); } while(strcmp(Arte,"|"));
436         fscanf(input,"%i",&hin);
437         do { fscanf(input,"%s",Arte); } while(strcmp(Arte,"|"));
438         fscanf(input,"%i",&hou);
439         do { fscanf(input,"%s",Arte); } while(strcmp(Arte,"|"));
440         fscanf(input,"%i",&hri);
441         do { fscanf(input,"%s",Arte); } while(strcmp(Arte,"|"));
442         fscanf(input,"%i",&hca);
443         do { fscanf(input,"%s",Arte); } while(strcmp(Arte,"|"));
444         fscanf(input,"%i",&htr);
445         do { fscanf(input,"%s",Arte); } while(strcmp(Arte,"|"));
446         fscanf(input,"%i",&hmu);
447         do { fscanf(input,"%s",Arte); } while(strcmp(Arte,"|"));
448         do { fscanf(input,"%s",Arte); } while(strcmp(Arte,"|"));
449         fscanf(input,"%lf",&chi2);
450         do { fscanf(input,"%s",Arte); } while(strcmp(Arte,"|"));
451         fscanf(input,"%lf",&lre);

```

```

452     do { fscanf(input,"%s",Arte); } while(strcmp(Arte,"|"));
453     fscanf(input,"%lf",&lrmu);
454     do { fscanf(input,"%s",Arte); } while(strcmp(Arte,"|"));
455     fscanf(input,"%lf",&lrpi);
456     do { fscanf(input,"%s",Arte); } while(strcmp(Arte,"|"));
457     fscanf(input,"%lf",&lrk);
458     do { fscanf(input,"%s",Arte); } while(strcmp(Arte,"|"));
459     fscanf(input,"%lf",&lrp);
460     do { fscanf(input,"%s",Arte); } while(strcmp(Arte,"|"));
461     do { fscanf(input,"%s",Arte); } while(strcmp(Arte,"|"));
462     do { fscanf(input,"%s",Arte); } while(strcmp(Arte,"|"));
463     fscanf(input,"%lf",&lte);
464     do { fscanf(input,"%s",Arte); } while(strcmp(Arte,"|"));
465     fscanf(input,"%lf",&lth);
466     do { fscanf(input,"%s",Arte); } while(strcmp(Arte,"|"));
467     do { fscanf(input,"%s",Arte); } while(strcmp(Arte,"|"));
468     fscanf(input,"%lf",&lee);
469     do { fscanf(input,"%s",Arte); } while(strcmp(Arte,"|"));
470     fscanf(input,"%lf",&lemi);
471     do { fscanf(input,"%s",Arte); } while(strcmp(Arte,"|"));
472     fscanf(input,"%lf",&leh);
473     do { fscanf(input,"%s",Arte); } while(strcmp(Arte,"|"));
474     do { fscanf(input,"%s",Arte); } while(strcmp(Arte,"|"));
475     fscanf(input,"%lf",&lmmu);
476     do { fscanf(input,"%s",Arte); } while(strcmp(Arte,"|"));
477     fscanf(input,"%lf",&lmh);
478
479     list[N].hsi = hsi; list[N].hin = hin; list[N].hou = hou;
480     list[N].hri = hri; list[N].hca = hca; list[N].htr = htr;
481     list[N].hmu = hmu; list[N].lre = lre; list[N].lrmu = lrmu;
482     list[N].lrpi = lrpi; list[N].lrk = lrk; list[N].lrp = lrp;
483     list[N].lee = lee; list[N].lemi = lemi; list[N].leh = leh;
484     list[N].lmmu = lmmu; list[N].lmh = lmh;
485     list[N].lte = lte ; list[N].lth = lth;
486
487     lrich = max(lre,lrmu); lrich = max(lrpi,lrich);
488     lrich = max(lrk,lrich); lrich = max(lrp,lrich);
489     lecal = max(lee,lemi); lecal = max(leh,lecal);
490     ltrd = max(lte,lth); lmuon = max(lmmu,lmh);
491     list[N].lrich=lrich; list[N].lecal=lecal;
492     list[N].lmuon=lmuon; list[N].ltrd=ltrd;
493
494     list[N].chi2=chi2; list[N].prob = -1.0;
495
496     if(hmu>0 && (hsi>0 || hin>0 || hou>0)) list[N].mass = m_mu;
497     else if(hri>0) {
498         if(lrpi>lrk && lrpi>lrp) list[N].mass = m_pi;
499         else if(lrk>lrpi && lrk >lrp) list[N].mass = m_K;
500         else if(lrp>lrpi && lrp >lrk) list[N].mass = m_p;
501         else if(lre>lrpi && lre>lrk && lre>lrp) list[N].mass = m_e;
502     }
503     else if(hca>0) { if(lee>leh && lee>lemi) list[N].mass = m_e; }
504     else list[N].mass = 0.0; // don't know
505
506     sprintf(list[N].PID,""); // no PID
507     if(hmu>0 && (hsi>0 || hin>0 || hou>0))
508         sprintf(list[N].PID,"mu%c", (list[N].p<0?'-':'+')); // muons
509     else if(hri>0) {
510         if(lrpi>lrk && lrpi>lrp)
511             sprintf(list[N].PID,"pi%c", (list[N].p<0?'-':'+')); // pions
512         else if(lrk>lrpi && lrk >lrp)
513             sprintf(list[N].PID,"K%c", (list[N].p<0?'-':'+')); // kaons

```

```

514         else if(lrp>lrpi && lrp >lrk)
515             sprintf(list[N].PID,"p%c", (list[N].p<0?'-':'+')); // protons
516         else if(lre>lrpi && lre>lrk && lre>lrp)
517             if(hca>0 && lee>leh && lee>lemi)
518                 sprintf(list[N].PID,"e%c", (list[N].p<0?'-':'+')); // electrons
519     }
520     // If we still have no PID from RICH, try PID likelihoods from ECAL
521     if(!strlen(list[N].PID))
522         if(hca>0 && lee>leh && lee>lemi)
523             sprintf(list[N].PID,"e%c", (list[N].p<0?'-':'+')); // electrons
524         else sprintf(list[N].PID,""); // something
525     do { fscanf(input,"%s",Arte); } while(strncmp(Arte,"MTRA",4));
526     list[N].mtra=0;
527     if((char)Arte[4]==':') {
528         fscanf(input,"%i",&k); fscanf(input,"%i",&j);
529         if(j>8192) list[N].mtra=k;
530     }
531     do { fscanf(input,"%s",Arte); } while(strncmp(Arte,"RCCL",4));
532     if(!strncmp(Arte,"RCCL:",5))
533         do { fscanf(input,"%c",Arte); } while(Arte[0]!='\n');
534     if(ArteVersion>4.0104)
535         do { fscanf(input,"%s",Arte); } while(strncmp(Arte,"RTRD",4));
536     fscanf(input,"%s",Arte);
537     N++; k=j;
538     } else if(!really_quiet) { printf("Table RTRA is empty.\n"); N=0; }
539 }
540 if(!really_quiet) printf("Read %i RTRA %s.\n", N, (N==1?"entry":"entries"));
541 for(i=0; i<5; i++) goldenRTRA[i] = -1; // will be found later
542
543 #if READ_TABLE_RCCL
544 // read table RCCL (ECAL clusters)
545 do {
546     do { fscanf(input,"%s",Arte); } while(strcmp(Arte,"lrow"));
547     fscanf(input,"%s",Arte); if(!strcmp(Arte,"rccl")) break;
548 } while(!feof(input));
549 rccl = (RCCL*)malloc(0*sizeof(RCCL));
550 if(!strcmp(Arte,"rccl")) { // found RCCL table list?
551     for(i=0; i<6; i++) fscanf(input,"%s",Arte);
552     if(strcmp(Arte,"empty")) // check if table is not empty
553     for(nc=0 ; !strcmp(Arte,"Table") || nc==0 ; ) {
554         rccl = (RCCL*)realloc(rccl, (nc+1)*sizeof(RCCL));
555         rccl[nc].rc = nc+1;
556         do { fscanf(input,"%s",Arte); } while(strcmp(Arte,"|"));
557         fscanf(input,"%lf",&(rccl[nc].d[Vz]));
558         do { fscanf(input,"%s",Arte); } while(strcmp(Arte,"|"));
559         fscanf(input,"%lf",&(rccl[nc].d[Vx]));
560         do { fscanf(input,"%s",Arte); } while(strcmp(Arte,"|"));
561         fscanf(input,"%lf",&(rccl[nc].d[Vy]));
562         do { fscanf(input,"%s",Arte); } while(strcmp(Arte,"|"));
563         fscanf(input,"%lf",&(rccl[nc].n[TX]));
564         do { fscanf(input,"%s",Arte); } while(strcmp(Arte,"|"));
565         fscanf(input,"%lf",&(rccl[nc].n[TY]));
566         do { fscanf(input,"%s",Arte); } while(strcmp(Arte,"|"));
567         fscanf(input,"%lf",&(rccl[nc].Eclus));
568         for(i=0; i<Rcovar; i++) { // covariance matrix
569             do { fscanf(input,"%s",Arte); } while(strcmp(Arte,"|"));
570             fscanf(input,"%lf",&(rccl[nc].c[i]));
571         }
572         do { fscanf(input,"%s",Arte); } while(strcmp(Arte,"|"));
573         fscanf(input,"%lf",&(rccl[nc].wid));
574         do { fscanf(input,"%s",Arte); } while(strcmp(Arte,"|"));
575         fscanf(input,"%lf",&(rccl[nc].asym));

```

```

576         do { fscanf(input,"%s",Arte); } while(strcmp(Arte,"|"));
577         do { fscanf(input,"%s",Arte); } while(strcmp(Arte,"|"));
578         fscanf(input,"%lf",&(rccl[nc].lemp));
579         do { fscanf(input,"%s",Arte); } while(strcmp(Arte,"|"));
580         fscanf(input,"%lf",&(rccl[nc].lmip));
581         do { fscanf(input,"%s",Arte); } while(strcmp(Arte,"|"));
582         fscanf(input,"%lf",&(rccl[nc].lhadr));
583         rccl[nc].dcog[Vz]=rccl[nc].d[Vz];
584         do { fscanf(input,"%s",Arte); } while(strcmp(Arte,"|"));
585         fscanf(input,"%lf",&(rccl[nc].dcog[Vx]));
586         do { fscanf(input,"%s",Arte); } while(strcmp(Arte,"|"));
587         fscanf(input,"%lf",&(rccl[nc].dcog[Vy]));
588         for(i=0; i<3; i++) { // covariance matrix for the c.o.g.
589             do { fscanf(input,"%s",Arte); } while(strcmp(Arte,"|"));
590             fscanf(input,"%lf",&(rccl[nc].vcog[i])); // X^2, XY e Y^2
591         }
592         for(i=0; i<4; i++)
593             do { fscanf(input,"%s",Arte); } while(strcmp(Arte,"|"));
594         do { fscanf(input,"%s",Arte); } while(strcmp(Arte,"RSEG",4));
595         if(!strcmp(Arte,"RSEG:",5))
596             do { fscanf(input,"%c",Arte); } while(Arte[0]!='\n');
597         fscanf(input,"%s",Arte);
598         nc++;
599     }
600 } else { if(!really_quiet) printf("Table RCCL is empty.\n"); nc=0; }
601 if(!really_quiet) printf("Read %i RCCL %s.\n", nc, (nc==1?"entry":"entries"));
602 #endif
603
604 //////////////////////////////////////////////////////////////////// OUTPUT ////////////////////////////////////////////////////////////////////
605
606 if(!really_quiet) {
607     printf("\n\nRTRAs & RVERs:\t\t\t\t\tWire=%s",rtar.Wire);
608     for(i=0; i<nv; i++) printf("\tRVER %i\t", vtx[i].rv);
609     printf("\nRTRA\tPID\tp/GeV\te_p/GeV\tpT/GeV\tepT/GeV\tb/um");
610     for(i=0; i<nv; i++) printf("\tb/um\te_b/um");
611 }
612 for(i=0; i<N; i++) if(list[i].hsi>0 && (list[i].hin>0 || list[i].hou>0))
613     list[i].rt = -list[i].rt;
614 if(!really_quiet) for(i=0; i<N; i++) {
615     ep = stddev_p(list[i].c, list[i].p);
616     pt = pT(list[i].n,list[i].p);
617     ept = stddev_pT(list[i].n, list[i].c, list[i].p);
618     sep = PI_rtar(list[i],rtar);
619 #if CUT_GOODP
620     if(list[i].rt>0) continue;
621 #endif
622 #if CUT_NOPID
623     if(list[i].mass<=0.0) continue;
624 #endif
625     printf("\n%i\t%s\t%3.31f\t%3.31f\t%3.31f\t%3.31f\t%4.11f\t",
626           -list[i].rt, list[i].PID, list[i].p,ep, pt,ept, sep);
627     for(j=0; j<nv; j++) {
628         rho = PImp2(list[i].n, list[i].d, vtx[j].d);
629         erho = stddev_PImp2(list[i].n, list[i].d, vtx[j].d, list[i].c, vtx[j].c);
630         if(rho < MAX_PI) printf("%4.11f\t%4.11f\t", rho, erho);
631         else printf(" \t \t");
632     }
633 }
634
635 #if READ_TABLE_RCCL
636     if(!really_quiet) {
637         printf("\n\nList of RCCLs:\nRCCL\tx\tty\twidth\tEclus\tEclus\tE_T\tE_T\n");

```

```

638     for(i=0; i<nc; i++) {
639         pf = rccl[i].Eclus; ep = sqrt(rccl[i].c[CPP]);
640         pt = rccl[i].d[Vx]*rccl[i].d[Vx]+rccl[i].d[Vy]*rccl[i].d[Vy];
641         pt = pf*sqrt(pt)/rccl[i].d[Vz]; ept = -999.99;
642         printf("%i\t%3.0f\t%3.0f\t%i\t%3.2f\t%3.2f\t%3.2f\t%3.2f\n",
643             rccl[i].rc, rccl[i].d[Vx], rccl[i].d[Vy],
644             (int)(rccl[i].wid), pf, ep, pt, ept);
645     }
646     for(i=0,pf=0.0; i<nc; i++) pf+=rccl[i].Eclus;
647     printf(" Total energy:\t%3.2fGeV\n", pf);
648     printf(" \n\nPairs of RCCLs:\nRCCL1\tRCCL2\tsep\tE_T\tm\tm_T\n");
649     for(i=0; i<nc; i++) for(j=i+1; j<nc; j++) {
650         sep =(rccl[i].d[Vx]-rccl[j].d[Vx])*(rccl[i].d[Vx]-rccl[j].d[Vx]);
651         sep+=(rccl[i].d[Vy]-rccl[j].d[Vy])*(rccl[i].d[Vy]-rccl[j].d[Vy]);
652         sep =sqrt(sep);
653         mass = 1.0-cos(atan(2.0*sep/(rccl[i].d[Vz]+rccl[j].d[Vz])));
654         mass = sqrt(2.0*rccl[i].Eclus*rccl[j].Eclus*mass);
655         // pt = weighted transverse energy of pair
656         // emass = weighted transverse mass of RCCL pair
657         emass = (rccl[i].d[Vx]*rccl[i].Eclus+rccl[j].d[Vx]*rccl[i].Eclus)*
658             (rccl[i].d[Vx]*rccl[i].Eclus+rccl[j].d[Vx]*rccl[i].Eclus);
659         emass+= (rccl[i].d[Vy]*rccl[i].Eclus+rccl[j].d[Vy]*rccl[i].Eclus)*
660             (rccl[i].d[Vy]*rccl[i].Eclus+rccl[j].d[Vy]*rccl[i].Eclus);
661         emass = mass*sqrt(emass)/(rccl[i].Eclus+rccl[j].Eclus);
662         pt = rccl[i].Eclus*sqrt(rccl[i].d[Vx]*rccl[i].d[Vx]+
663             rccl[i].d[Vy]*rccl[i].d[Vy])/rccl[i].d[Vz];
664         pt += rccl[j].Eclus*sqrt(rccl[j].d[Vx]*rccl[j].d[Vx]+
665             rccl[j].d[Vy]*rccl[j].d[Vy])/rccl[j].d[Vz];
666         printf("%i\t%i\t%3.2f\t%3.2f\t%2.3f\t%2.3f\n",
667             rccl[i].rc, rccl[j].rc, sep, pt, mass, emass);
668     }
669 }
670 #endif
671
672 for(i=0; i<N; i++)
673     if(list[i].hsi>0 && (list[i].hin>0 || list[i].hou>0)) list[i].rt = -list[i].rt;
674 if(!really_quiet) {
675     printf("\n\nPairs of RTRAs:\t\t\t\t\t\t\tWire=%s\tSep./um\t",rtar.Wire);
676     for(i=0; i<nv; i++) printf("\tRVER %i\t", vtx[i].rv);
677     printf("\nRTRA1\tRTRA2\tz/cm\tx/cm\ty/cm\tdz/cm\t"
678         "m/GeV\te_m/GeV\tb/um\tb/um\te_b/um");
679     for(i=0; i<nv; i++) printf("\tb/um\te_b/um"); printf("\n");
680 }
681 for(i=0; i<N; i++)
682     if(list[i].hsi>0 && (list[i].hin>0 || list[i].hou>0)) list[i].rt = -list[i].rt;
683 if(!really_quiet) for(i=0; i<N; i++) for(j=i; j<N; j++) if(i!=j && i<j) {
684     z = posZ('Z', list[i], list[j]);
685     x = posZ('X', list[i], list[j]);
686     y = posZ('Y', list[i], list[j]);
687     pf = stddev_vtxcoord('Z', list[i], list[j]);
688
689     if(list[i].mass>0.0 && list[j].mass>0.0) {
690         mass = InvMass_PID(list[i].mass, list[j].mass, list[i].n,
691             list[j].n, list[i].p, list[j].p);
692         emass = stddev_Mass_PID(list[i].mass, list[j].mass, list[i].n, list[j].n,
693             list[i].c, list[j].c, list[i].p, list[j].p);
694     } else {
695         mass = InvMass(list[i].n, list[j].n, list[i].p, list[j].p);
696         emass = stddev_Mass(list[i].n, list[j].n, list[i].c,
697             list[j].c, list[i].p, list[j].p);
698     }
699     // Impact param. of di-RTRA to the target wire

```

```

700     sep = PI_rtar_2RTRA(list[i],list[j],rtar);
701     // Distance of closest approach for the two RTRAs, and respective error
702     rho = ParamImpact(list[i].n,list[j].n,list[i].d,list[j].d);
703     erho = stddev_ParamImp(list[i].n, list[j].n, list[i].c,
704                          list[j].c, list[i].d, list[j].d);
705 #if CUT_GOODP
706     if(list[i].rt>0 || list[j].rt>0) continue;
707 #endif
708 #if CUT_NOPID
709     if(list[i].mass<=0 || list[j].mass<=0) continue;
710 #endif
711     printf("%i %s\t%i %s\t%.2lf\t%.2lf\t%.2lf\t%.2lf\t%.2lf\t"
712           "%.2lf\t%.2lf\t%.2lf\t", -list[i].rt, list[i].PID,
713           -list[j].rt, list[j].PID, z,x,y,pf, mass,emass, sep, rho,erho );
714     if(rho < 1.0e3) {
715         for(k=0; k<nv; k++) { /* show for all events */
716             rho = PImp3(list[i].n, list[i].d, list[j].n, list[j].d,
717                       vtx[k].d, list[i].p, list[j].p);
718             erho = stddev_PImp3(list[i].n, list[i].d, list[j].n, list[j].d,
719                                list[i].c, list[j].c, list[i].p, list[j].p,
720                                vtx[k].d, vtx[k].c);
721             if(fabs(mass - m_Jpsi)/emass < 3.3) printf("%.2lf\t%.2lf\t", rho, erho);
722             else if(fabs(mass - m_K0)/emass < 5.0) printf("%.2lf\t%.2lf\t", rho, erho);
723             else printf(" \t \t");
724         }
725         rho = ParamImpact(list[i].n,list[j].n,list[i].d,list[j].d);
726         erho = stddev_ParamImp(list[i].n, list[j].n, list[i].c,
727                              list[j].c, list[i].d, list[j].d);
728         if(fabs(mass - m_Jpsi)/emass < 3.3) {
729             if(emass/mass<1.0e-2 && rho < 2.0e2 && fabs(sep) < MAX_PI
730                && list[i].hsi>0 && list[j].hsi>0) {
731                 mass = InvMass(list[i].n, list[j].n, list[i].p, list[j].p);
732                 emass = stddev_Mass(list[i].n, list[j].n, list[i].c,
733                                    list[j].c, list[i].p, list[j].p);
734                 printf("\tJ/psi!!\t(%.2lf +/- %.2lf)", mass,emass);
735             }
736             else printf("\tJ/psi?");
737         } else
738             if(fabs(mass - m_K0)/emass < 5.0) {
739                 if(emass/mass<1.0e-2 && rho < 2.0e2 && fabs(sep) < MAX_PI
740                    && list[i].hsi>0 && list[j].hsi>0) {
741                     mass = InvMass(list[i].n, list[j].n, list[i].p, list[j].p);
742                     emass = stddev_Mass(list[i].n, list[j].n, list[i].c,
743                                         list[j].c, list[i].p, list[j].p);
744                     printf("\tK_S0!!\t(%.2lf +/- %.2lf)", mass,emass);
745                 }
746                 else printf("\tK_S0?");
747             }
748         } if(!really_quiet) printf("\n");
749     }
750     for(i=0; i<N; i++)
751         if(list[i].hsi>0 && (list[i].hin>0 || list[i].hou>0)) list[i].rt = -list[i].rt;
752
753     mass=0.0; emass=0.0;
754     if(!really_quiet) {
755         printf("\n\nThe following RTRAs have good momentum:\t");
756         for(i=0; i<N; i++) for(j=i; j<N; j++)
757             if( (list[i].hsi>0 && (list[i].hin>0 || list[i].hou>0)) &&
758                (list[j].hsi>0 && (list[j].hin>0 || list[j].hou>0)) ) {
759                 if(i==j) { printf(" %i", i+1); continue; }
760                 mass += pow(eval_Mass(list[i],list[j]),2.0);
761                 emass += pow(eval_eMass(list[i],list[j]),2.0);

```

```

762     }
763     mass = sqrt(mass); emass=sqrt(emass);
764     printf("\n Their invariant mass is:  %3.31f +/- %3.31f GeV/c^2\n",
765           mass, emass);
766     mass=0.0; emass=0.0;
767     printf( "\nThe following RTRAs also have a PID tag and touch RVER 1 "
768           "downstream by less than %ium:\t", 500);
769     for(i=0; i<N; i++) for(j=i; j<N; j++)
770         if( (list[i].hsi>0 && (list[i].hin>0 || list[i].hou>0)) &&
771           (list[j].hsi>0 && (list[j].hin>0 || list[j].hou>0)) &&
772           list[i].mass>0.0 && list[j].mass>0.0) {
773         ZZZZ = posZ('Z', list[i], list[j]);
774         if(ZZZZ < vtx[0].d[Z]) continue;
775         if(PImp2(list[i].n, list[i].d, vtx[0].d)>500.0) continue;
776         if(PImp2(list[j].n, list[j].d, vtx[0].d)>500.0) continue;
777         if(i==j)
778             { printf(" %i(%ium)", i+1,
779                   (int)(PImp2(list[i].n, list[i].d, vtx[0].d)));
780               continue; }
781         mass += pow(eval_Mass(list[i],list[j]),2.0);
782         emass += pow(eval_eMass(list[i],list[j]),2.0);
783     }
784
785     mass = sqrt(mass); emass=sqrt(emass);
786     printf("\n Their invariant mass is:  %3.31f +/- %3.31f GeV/c^2\n",
787           mass, emass);
788 }
789
790 if(kUseB0!=0) {
791     if(!really_quiet) {
792         printf( "\n\nInvariant mass of 4-sets of RTRAs\n"
793               " (negative RTRA id signs represent 'bad' RTRA)\n");
794         printf("RTRA\tRTRA\tRTRA\tRTRA\tMass\teMass\tWire=%s\tJpsi-KS\t"
795               "(um)\tCandidate\n",rtar.Wire);
796     }
797     for(i=0; i<N; i++)
798         if(list[i].hsi>0 && (list[i].hin>0 || list[i].hou>0)) list[i].rt = -list[i].rt;
799     for(i=0; i<N; i++) for(j=i+1; j<N; j++)
800     for(k=j+1; k<N; k++) for(l=k+1; l<N; l++) {
801         isGoodRTRAs=0;
802         if(list[i].hsi>0 && (list[i].hin>0 || list[i].hou>0)) isGoodRTRAs++;
803         if(list[j].hsi>0 && (list[j].hin>0 || list[j].hou>0)) isGoodRTRAs++;
804         if(list[k].hsi>0 && (list[k].hin>0 || list[k].hou>0)) isGoodRTRAs++;
805         if(list[l].hsi>0 && (list[l].hin>0 || list[l].hou>0)) isGoodRTRAs++;
806         if(list[i].hsi || list[i].hin || list[i].hou)
807             if(list[j].hsi || list[j].hin || list[j].hou)
808                 if(list[k].hsi || list[k].hin || list[k].hou)
809                     if(list[l].hsi || list[l].hin || list[l].hou)
810                         if(isGoodRTRAs>2) {
811                             // total charge
812                             carga = list[i].p/fabs(list[i].p)+list[j].p/fabs(list[j].p);
813                             carga += list[k].p/fabs(list[k].p)+list[l].p/fabs(list[l].p);
814                             // invariant mass of the four RTRAs
815                             mass = 0.0; emass = 0.0;
816                             mass += pow(eval_Mass(list[i],list[j]), 2.0);
817                             mass += pow(eval_Mass(list[i],list[k]), 2.0);
818                             mass += pow(eval_Mass(list[i],list[l]), 2.0);
819                             mass += pow(eval_Mass(list[j],list[k]), 2.0);
820                             mass += pow(eval_Mass(list[j],list[l]), 2.0);
821                             mass += pow(eval_Mass(list[k],list[l]), 2.0);
822                             emass += pow(eval_eMass(list[i],list[j]),2.0);
823                             emass += pow(eval_eMass(list[i],list[k]),2.0);

```

```

824         emass += pow(eval_eMass(list[i],list[l]),2.0);
825         emass += pow(eval_eMass(list[j],list[k]),2.0);
826         emass += pow(eval_eMass(list[j],list[l]),2.0);
827         emass += pow(eval_eMass(list[k],list[l]),2.0);
828         mass = sqrt(mass); emass = sqrt(emass);
829         if(emass>mass) continue;
830     #if CUT_GOODP
831         if(list[i].rt>0 || list[j].rt>0 ||
832            list[k].rt>0 || list[l].rt>0) continue;
833     #endif
834     #if CUT_NOPID
835         if(list[i].mass<=0.0 || list[j].mass<=0.0 ||
836            list[k].mass<=0.0 || list[l].mass<=0.0) continue;
837     #endif
838     if(!really_quiet) {
839         printf("%i %s\t%i %s\t%i %s\t%i %s\t",
840              -list[i].rt, list[i].PID, -list[j].rt, list[j].PID,
841              -list[k].rt, list[k].PID, -list[l].rt, list[l].PID);
842         rho = PI_rtar_4RTRA(list[i],list[j],list[k],list[l],rtar);
843     }
844
845     /* sep = Separation between Jpsi and KS */
846     /* NOTE: PImp_B0 internally checks whether the four RTRAs
847      * are good Golden Decay candidates. Do not remove this
848      * call -- it's necessary at the Summary section!!
849      */
850     sep = PImp_B0(list[i],list[j],list[k],list[l]);
851     esep = stddev_PImp_B0(list[i],list[j],list[k],list[l]);
852
853     if(!really_quiet) {
854         if(sep>0.0)
855             printf("%2.4lf\t%2.4lf\t%4.2lf\t%4.2lf\t%4.2lf",
856                  mass, emass, rho, sep, esep);
857         else
858             printf("%2.4lf\t%2.4lf\t%4.2lf\t\t", mass, emass, rho);
859     }
860     if(!really_quiet)
861     if(fabs(mass-m_B0)/emass<5.0 && fabs(mass-m_B0)<0.3 &&
862        carga<2 && carga>-2) {
863         if(isGoodRTRAs==4 && carga==0 &&
864            list[i].mass>0 && list[j].mass>0 &&
865            list[k].mass>0 && list[l].mass>0) printf("\tB!!");
866         else printf("\tB?");
867         // Find 4-RTRA mass for massless tracks
868         masslist[0] = list[i].mass; list[i].mass = 0.0;
869         masslist[1] = list[j].mass; list[j].mass = 0.0;
870         masslist[2] = list[k].mass; list[k].mass = 0.0;
871         masslist[3] = list[l].mass; list[l].mass = 0.0;
872         mass = emass = 0.0;
873         mass += pow(eval_Mass(list[i],list[j]),2.0);
874         mass += pow(eval_Mass(list[i],list[k]),2.0);
875         mass += pow(eval_Mass(list[i],list[l]),2.0);
876         mass += pow(eval_Mass(list[j],list[k]),2.0);
877         mass += pow(eval_Mass(list[j],list[l]),2.0);
878         mass += pow(eval_Mass(list[k],list[l]),2.0);
879         emass += pow(eval_eMass(list[i],list[j]),2.0);
880         emass += pow(eval_eMass(list[i],list[k]),2.0);
881         emass += pow(eval_eMass(list[i],list[l]),2.0);
882         emass += pow(eval_eMass(list[j],list[k]),2.0);
883         emass += pow(eval_eMass(list[j],list[l]),2.0);
884         emass += pow(eval_eMass(list[k],list[l]),2.0);
885         mass = sqrt(mass); emass = sqrt(emass);

```

```

886             printf("\t(%.24lf +/- %.24lf)", mass, emass);
887             list[i].mass = masslist[0]; list[j].mass = masslist[1];
888             list[k].mass = masslist[2]; list[l].mass = masslist[3];
889         }
890         if(!really_quiet) printf("\n");
891     }
892 }
893 for(i=0; i<N; i++)
894     if(list[i].hsi>0 && (list[i].hin>0 || list[i].hou>0)) list[i].rt = -list[i].rt;
895 }
896
897 /* --- Print summary table for this event --- */
898
899 if(!really_quiet) printf("\n\n");
900 if(argc>3) { for(i=3; i<argc; i++) printf("%s ", argv[i]); printf("\n"); }
901 else printf("SUMMARY: Exp %i / Run %i / Event %i \n",
902            evhd.exp, evhd.run, evhd.evt);
903 printf("RVERs: %i RTRAs: %i RCCLs: %i\n", nv, N, nc);
904 printf("Target wire %i ('%s', Z=%02i):\n (z,x,y) = "
905        "( %.23f +/- %.23f , %.23f +/- %.23f , %.23f +/- %.23f )\n",
906        rtar.itar, rtar.Wire, rtar.Zmat, rtar.d[Vz], rtar.s[Vz],
907        rtar.d[Vx], rtar.s[Vx], rtar.d[Vy], rtar.s[Vy]);
908
909 printf("\nRVER\tz\tx\ty\tchi2\ttn_tr\tmass\t+/-\n");
910 for(i=0; i<3 && i<nv; i++)
911     printf("%i\t%.23f\t%.23f\t%.23f\t%.23f\t%i\t%.23lf\t%.23lf\n",
912            vtx[i].rv, vtx[i].d[Vz], vtx[i].d[Vx], vtx[i].d[Vy],
913            (vtx[i].chi2<1e4?vtx[i].chi2:-1), vtx[i].nt,
914            vtx[i].mass, (vtx[i].merr<1e4?vtx[i].merr:-1));
915 for(j=i; j<3; j++) printf("0\n");
916
917 // sep = separation in micrometers ; pt = transverse momentum in GeV
918 sep=500.0; pt=0.30; // lower cut on B flavor tag RTRA's transverse momentum
919 for(i=0; i<N; i++) { // choose goldenRTRA[4] as the B flavor tag
920     // skip RTRAs from golden decay
921     if(i==goldenRTRA[0] || i==goldenRTRA[1] ||
922        i==goldenRTRA[2] || i==goldenRTRA[3] ) continue;
923     if(list[i].hsi<5) continue; // must have VDS hits
924     if(list[i].hin<5 && list[i].hou<5) continue; // must have Main Tracker hits
925     ept=list[i].n[TX]*list[i].n[TX]+list[i].n[TY]*list[i].n[TY];
926     ept=fabs(list[i].p)*sqrt(ept); esep = PImp2(list[i].n, list[i].d, vtx[0].d);
927     /* next, select the RTRA with highest pT as the charge tag */
928     /* also cuts on RTRAs with impact parameters greater than "sep" micrometers */
929     if(ept>pt && esep<sep) { goldenRTRA[4]=i; pt=ept; sep=esep;}
930 }
931 // The surviving tagging RTRA should: have pT>0.3GeV/c, lie closer than
932 // 1000um to the primary RTRA, have VDS+MainTracker hits, and be neither
933 // of the RTRAs from the golden decay
934
935 printf("\nPID\tRTRA\tp\t+/-\tpT\t+/-\tz\tx\ty\ttx\t+/-\tty\t+/-\t"
936        "hsi\thin\thou\thri\thca\thmu\tchi^2\tWire7\t" );
937 for(j=0; j<nv && j<3; j++) printf("RVER%i\t\t", vtx[j].rv); printf("\n");
938 for(j=0; j<5; j++) { i = goldenRTRA[j];
939     if(i<0) printf("--\n"); else {
940         ep = stddev_p(list[i].c, list[i].p);
941         pt = pT(list[i].n, list[i].p);
942         ept = stddev_pT(list[i].n, list[i].c, list[i].p);
943         sep = PI_rtar(list[i], rtar);
944         if(nv>0) {
945             rho = PImp2(list[i].n, list[i].d, vtx[0].d);
946             erho= stddev_PImp2(list[i].n, list[i].d, vtx[0].d, list[i].c, vtx[0].c);
947         }

```

```

948         if(nv>1) {
949             tx = PImp2(list[i].n, list[i].d, vtx[1].d);
950             ty = stddev_PImp2(list[i].n, list[i].d, vtx[1].d, list[i].c, vtx[1].c);
951         }
952         if(nv>2) {
953             x = PImp2(list[i].n, list[i].d, vtx[2].d);
954             y = stddev_PImp2(list[i].n, list[i].d, vtx[2].d, list[i].c, vtx[2].c);
955         }
956         printf("%s\t%i\t%3.2f\t%3.2f\t%3.2f\t%3.2f\t%1.4g\t%1.4g\t%1.4g\t"
957             "%1.4g\t%1.4g\t%1.4g\t%1.4g\t%i\t%i\t%i\t%i\t%i\t%3.2f"
958             "\t%i",
959             (list[i].PID?(strlen(list[i].PID)?list[i].PID:"?"):"?"),
960             list[i].rt, fabs(list[i].p),ep, pt,ept, list[i].d[Z],
961             list[i].d[X], list[i].d[Y], list[i].n[TX],
962             sqrt(list[i].c[CTXTX]), list[i].n[TY],
963             sqrt(list[i].c[CTYTY]), list[i].hsi, list[i].hin,
964             list[i].hou, list[i].hri, list[i].hca, list[i].hmu,
965             list[i].chi2, (int)sep);
966         if(nv>0) printf("\t%i\t%i", (int)rho, (int)erho);
967         if(nv>1) printf("\t%i\t%i", (int)tx, (int)ty);
968         if(nv>2) printf("\t%i\t%i", (int)x, (int)y);
969         printf("\n");
970     }
971 }
972
973 printf( "\nPID\tz\t+/-\tx\ty\ttx\tty\tp\t"
974         "m\t+/-\tSep\t+/-\tWire7\tRVER1\t+/-\n");
975 Jpsi.mass=KS.mass=B0.mass=0.0;
976
977 i=goldenRTRA[0]; j=goldenRTRA[1];
978 if(i>=0 && j>=0) Jpsi=RTRAFusion(list[i],list[j],"J/psi");
979
980 k=goldenRTRA[2]; l=goldenRTRA[3];
981 if(k>=0 && l>=0) KS=RTRAFusion(list[k],list[l],"K_S0");
982
983 h=goldenRTRA[4];
984 if(assume_B0) {
985     if(i>=0 && j>=0 && k>=0 && l>=0) {
986         B0=RTRAFusion(Jpsi,KS,(list[h].p<0?"B0 ":"B~ "));
987     }
988 } else {
989     if(list[h].PID[0]=='K')
990         B0=RTRAFusion(Jpsi,list[h],(list[h].p<0?"B- ":"B+ "));
991     else
992         if(list[h].PID[0]=='p' && list[h].PID[1]=='i')
993             B0=RTRAFusion(Jpsi,list[h],(list[h].p<0?"B- ":"B+ "));
994 }
995
996 i=goldenRTRA[0]; j=goldenRTRA[1];
997 if(Jpsi.mass && i>=0 && j>=0) {
998     mass = emass = sep = rho = erho = etheta = tx = ty = 0.0;
999     if(list[i].mass>0.0 && list[j].mass>0.0)
1000         emass = stddev_Mass_PID(list[i].mass, list[j].mass, list[i].n, list[j].n,
1001             list[i].c, list[j].c, list[i].p, list[j].p);
1002     else
1003         emass = stddev_Mass(list[i].n,list[j].n, list[i].c,list[j].c, list[i].p,list[j].p);
1004     // sep = Impact param. to target wire
1005     sep = PI_rtar_2RTRA(list[i],list[j],rtar);
1006     rho = ParamImpact(list[i].n,list[j].n,list[i].d,list[j].d);
1007     erho = stddev_ParamImp(list[i].n, list[j].n, list[i].c, list[j].c, list[i].d, list[j].d);
1008     etheta = stddev_vtxcoord('Z',list[i],list[j]);
1009     tx = PImp3(list[i].n, list[i].d, list[j].n, list[j].d, vtx[0].d, list[i].p, list[j].p);

```

```

1010     ty = stddev_PImp3(list[i].n, list[i].d, list[j].n, list[j].d, list[i].c, list[j].c,
1011                       list[i].p, list[j].p, vtx[0].d, vtx[0].c);
1012     if(etheta>1.0e9) { etheta = erho = tx = ty = -1 ; }
1013     printf("%s\t%2.3f\t%2.3f\t%1.4f\t%1.4f\t%1.4g\t%1.4g\t%3.2f\t"
1014           "%2.3f\t%2.3f\t%i\t%i\t%i\t%i\t%i\n",
1015           (Jpsi.PID?(strlen(Jpsi.PID)?Jpsi.PID:"??"):"??"), Jpsi.d[Z],
1016           etheta, Jpsi.d[X], Jpsi.d[Y], Jpsi.n[TX], Jpsi.n[TY], Jpsi.p,
1017           Jpsi.mass,emass, (int)rho,(int)erho, (int)sep, (int)tx,(int)ty);
1018 } else printf("--\n");
1019
1020 i=goldenRTRA[2]; j=goldenRTRA[3];
1021 if(KS.mass && i>=0 && j>=0) {
1022     mass = emass = sep = rho = erho = etheta = tx = ty = 0.0 ;
1023     if(list[i].mass>0.0 && list[j].mass>0.0)
1024         emass = stddev_Mass_PID(list[i].mass, list[j].mass, list[i].n, list[j].n,
1025                                 list[i].c, list[j].c, list[i].p, list[j].p);
1026     else
1027         emass = stddev_Mass(list[i].n,list[j].n, list[i].c,list[j].c, list[i].p,list[j].p);
1028
1029     // Impact parameter of the tracks to the target itself.
1030     sep = PI_rtar_2RTRA(list[i],list[j],rtar);
1031     rho = ParamImpact(list[i].n,list[j].n,list[i].d,list[j].d);
1032     erho = stddev_ParamImp(list[i].n, list[j].n, list[i].c, list[j].c, list[i].d, list[j].d);
1033     etheta = stddev_vtxcoord('Z',list[i],list[j]);
1034     tx = PImp3(list[i].n, list[i].d, list[j].n, list[j].d, vtx[0].d, list[i].p, list[j].p);
1035     ty = stddev_PImp3(list[i].n, list[i].d, list[j].n, list[j].d, list[i].c, list[j].c,
1036                       list[i].p, list[j].p, vtx[0].d, vtx[0].c);
1037     if(etheta>1.0e9) { etheta = erho = tx = ty = -1 ; }
1038     printf("%s\t%2.3f\t%2.3f\t%1.4f\t%1.4f\t%1.4g\t%1.4g\t%3.2f\t"
1039           "%2.3f\t%2.3f\t%i\t%i\t%i\t%i\t%i\n",
1040           (KS.PID?(strlen(KS.PID)?KS.PID:"??"):"??"),
1041           KS.d[Z], etheta, KS.d[X], KS.d[Y], KS.n[TX], KS.n[TY], KS.p,
1042           KS.mass,emass, (int)rho,(int)erho, (int)sep, (int)tx,(int)ty);
1043 } else printf("--\n");
1044
1045 i=goldenRTRA[0]; j=goldenRTRA[1]; k=goldenRTRA[2]; l=goldenRTRA[3];
1046 h=goldenRTRA[4];
1047 if(assume_B0) {
1048     if(B0.mass && i>=0 && j>=0 && k>=0 && l>=0) {
1049         // Note: we use the 4-RTRA mass as the B meson's mass instead of
1050         // the Jpsi's and KS's, therefore avoiding this systematic error
1051         mass = emass = 0.0;
1052         mass += pow(eval_Mass(list[i],list[j]), 2.0);
1053         mass += pow(eval_Mass(list[i],list[k]), 2.0);
1054         mass += pow(eval_Mass(list[i],list[l]), 2.0);
1055         mass += pow(eval_Mass(list[j],list[k]), 2.0);
1056         mass += pow(eval_Mass(list[j],list[l]), 2.0);
1057         mass += pow(eval_Mass(list[k],list[l]), 2.0);
1058         emass += pow(eval_eMass(list[i],list[j]),2.0);
1059         emass += pow(eval_eMass(list[i],list[k]),2.0);
1060         emass += pow(eval_eMass(list[i],list[l]),2.0);
1061         emass += pow(eval_eMass(list[j],list[k]),2.0);
1062         emass += pow(eval_eMass(list[j],list[l]),2.0);
1063         emass += pow(eval_eMass(list[k],list[l]),2.0);
1064         B0.mass = mass = sqrt(mass); emass = sqrt(emass);
1065
1066         // sep = Impact parameter to target wire
1067         sep = PI_rtar_4RTRA(list[i],list[j],list[k],list[l],rtar);
1068         rho = ParamImpact(Jpsi.n,KS.n,Jpsi.d,KS.d);
1069         erho = stddev_ParamImp(Jpsi.n, KS.n, Jpsi.c, KS.c, Jpsi.d, KS.d);
1070         etheta = stddev_vtxcoord('Z',Jpsi,KS);
1071         tx = PImp3(Jpsi.n, Jpsi.d, KS.n, KS.d, vtx[0].d, Jpsi.p, KS.p);

```

```

1072         ty = stddev_PImp3(Jpsi.n, Jpsi.d, KS.n, KS.d, Jpsi.c, KS.c,
1073                          Jpsi.p, KS.p, vtx[0].d, vtx[0].c);
1074         if(etheta>1.0e9) { etheta = erho = tx = ty = -1; }
1075         printf("%s\t%2.3f\t%2.3f\t%1.4f\t%1.4f\t%1.4g\t%1.4g\t%3.2f\t"
1076              "%2.3f\t%2.3f\t%i\t%i\t%i\t%i\t%i\n\n",
1077              (strlen(B0.PID)?B0.PID:"???"),
1078              B0.d[Z], etheta, B0.d[X], B0.d[Y], B0.n[TX], B0.n[TY], B0.p,
1079              B0.mass,emass, (int)rho,(int)erho, (int)sep, (int)tx,(int)ty);
1080     } else printf("--\n\n");
1081 } else { // charged B meson ( mu+ mu- K_charged )
1082     if(i>=0 && j>=0 && h>=0) {
1083         mass = emass = 0.0;
1084         mass += pow(eval_Mass(list[i],list[j]),2.0);
1085         mass += pow(eval_Mass(list[i],list[h]),2.0);
1086         mass += pow(eval_Mass(list[j],list[h]),2.0);
1087         emass += pow(eval_eMass(list[i],list[j]),2.0);
1088         emass += pow(eval_eMass(list[i],list[h]),2.0);
1089         emass += pow(eval_eMass(list[j],list[h]),2.0);
1090         B0.mass = mass = sqrt(mass); emass = sqrt(emass);
1091         // sep = Impact parameter to target
1092         sep = PI_rtar_3RTRA(list[i],list[j],list[h],rtar);
1093         rho = ParamImpact(Jpsi.n,list[h].n, Jpsi.d,list[h].d);
1094         erho = stddev_ParamImp(Jpsi.n,list[h].n, Jpsi.c,list[h].c, Jpsi.d,list[h].d);
1095         etheta = stddev_vtxcoord('Z',Jpsi,list[h]);
1096         tx = PImp3(Jpsi.n, Jpsi.d, list[h].n, list[h].d, vtx[0].d, Jpsi.p, list[h].p);
1097         ty = stddev_PImp3(Jpsi.n, Jpsi.d, list[h].n, list[h].d, Jpsi.c, list[h].c,
1098                          Jpsi.p, list[h].p, vtx[0].d, vtx[0].c);
1099         if(etheta>1.0e9) { etheta = erho = tx = ty = -1; }
1100         printf("%s\t%2.3f\t%2.3f\t%1.4f\t%1.4f\t%1.4g\t%1.4g\t%3.2f\t"
1101              "%2.3f\t%2.3f\t%i\t%i\t%i\t%i\t%i\n\n",
1102              (strlen(B0.PID)?B0.PID:"???"),
1103              B0.d[Z], etheta, B0.d[X], B0.d[Y], B0.n[TX], B0.n[TY], B0.p,
1104              B0.mass,emass, (int)rho,(int)erho, (int)sep, (int)tx,(int)ty);
1105     } else printf("--\n\n");
1106 }
1107 printf("Charge from pT-weighted charge tag: %2.3f +/- %2.3f\n\n",
1108        jetCharge(list,N,vtx[0]), stddev_jetCharge(list,N,vtx[0]));
1109
1110     N=0;
1111     if(!really_quiet)
1112         printf("\nTerminating...\n Releasing list buffers.\n");
1113 #if READ_TABLE_RCCL
1114     if(rccl) free(rccl); // RCCLs
1115 #endif
1116     if(list) free(list); // RTRAs
1117     if(vtx) free(vtx); // RVERs
1118     if(gtar) free(gtar); // GTARs / RTARs
1119     if(!really_quiet) printf(" Closing files.\n");
1120     if(input) N+=1*fclose(input);
1121     if(!really_quiet) printf("Done.\n\n");
1122     exit(N); return N;
1123 }
1124
1125 ////////////////////////////////////////////////////////////////////////////////////////////////////////////////////////////////////
1126 //////////////////////////////////////////////////////////////////// QUANTITIES ////////////////////////////////////////////////////////////////////
1127 ////////////////////////////////////////////////////////////////////////////////////////////////////////////////////////////////////
1128
1129 double pT(double *n1, double p1) {
1130     double PT = 0.0, pf1 = 1.0/p1;
1131     PT = sqrt(n1[TX]*n1[TX]+n1[TY]*n1[TY])/fabs(pf1);
1132     return PT; // Units: GeV/c.
1133 }

```

```

1134
1135 double InvMass_PID(double m1, double m2, double *n1, double *n2,
1136                  double p1, double p2) {
1137     double mass, N1, N2, E1, E2, p1p2, cosAngle;
1138
1139     E1 = sqrt(m1*m1+p1*p1); E2 = sqrt(m2*m2+p2*p2);
1140     N1 = sqrt(1.0+n1[TX]*n1[TX]+n1[TY]*n1[TY]);
1141     N2 = sqrt(1.0+n2[TX]*n2[TX]+n2[TY]*n2[TY]);
1142     cosAngle = (1.0+n1[TX]*n2[TX]+n1[TY]*n2[TY])/(N1*N2);
1143     p1p2 = fabs(p1)*fabs(p2)*cosAngle;
1144     mass = sqrt( m1*m1 + m2*m2 + 2.0*E1*E2 - 2.0*p1p2);
1145     return mass;
1146 }
1147
1148 double InvMass(double *n1, double *n2, double p1, double p2) {
1149     double mass = 0.0, N1, N2;    double theta = Angle(n1,n2);
1150
1151     N1 = sqrt(1.0+n1[TX]*n1[TX]+n1[TY]*n1[TY]);
1152     N2 = sqrt(1.0+n2[TX]*n2[TX]+n2[TY]*n2[TY]);
1153     mass = 1.0 - (1.0+n1[TX]*n2[TX]+n1[TY]*n2[TY])/(N1*N2);
1154     mass *= 2.0*fabs(p1)*fabs(p2);
1155     mass = sqrt(mass);
1156     return mass;    // Units: GeV/c^2.
1157 }
1158
1159 // Use un-normalized track vectors.
1160 double Angle(double *n1, double *n2) {
1161     double theta = 0.0;
1162     theta += pow(atan(n2[TX])-atan(n1[TX]),2.0);
1163     theta += pow(atan(n2[TY])-atan(n1[TY]),2.0);
1164     theta = sqrt(theta);
1165     return theta;    // Units: radians.
1166 }
1167
1168 /* Distance of closest approach for two RTRAs. */
1169 double ParamImpact(double *N1, double *N2, double *D1, double *D2) {
1170     int i;
1171     double n1[Rdirec], n2[Rdirec], d1[Rcoords], d2[Rcoords];
1172     double n3[Rdirec], D[Rcoords];
1173     double rho = 0.0, n1n2=0.0, mn1 = 0.0, mn2 = 0.0;
1174
1175     /* Normalize the unit vectors n1 and n2. */
1176     for(i=0; i<Rcoords; i++) { d1[i]=D1[i]; d2[i]=D2[i]; }
1177     for(i=0; i<Rdirec; i++) { n1[i]=N1[i]; n2[i]=N2[i]; }
1178     for(i=0; i<Rdirec; i++) mn1 += n1[i]*n1[i]; mn1 = sqrt(mn1);
1179     for(i=0; i<Rdirec; i++) mn2 += n2[i]*n2[i]; mn2 = sqrt(mn2);
1180     for(i=0; i<Rdirec; i++) { n1[i] = n1[i]/mn1; n2[i] =n2[i]/mn2; }
1181
1182     // n3: unit vector orthogonal to the plane defined by n1 and n2. */
1183     n3[TZ] = n1[TX]*n2[TY] - n1[TY]*n2[TX];
1184     n3[TX] = n1[TY]*n2[TZ] - n1[TZ]*n2[TY];
1185     n3[TY] = n1[TZ]*n2[TX] - n1[TX]*n2[TZ];
1186     for(i=0; i<Rdirec; i++) n1n2 += n3[i]*n3[i]; n1n2 = sqrt(n1n2);
1187     if(n1n2 != 0.0) for(i=0; i<Rdirec; i++) n3[i] /= n1n2;
1188
1189     for(i=0; i<Rcoords; i++) D[i] = d2[i]-d1[i];
1190     if(n1n2 != 0.0) for(i=0; i<Rcoords; i++) rho += D[i]*n3[i];
1191     else { for(i=0; i<Rcoords; i++) rho += D[i]*D[i]; rho = sqrt(rho); }
1192
1193     return (fabs(rho)*1.0E4);    // Units: micrometers.
1194 }
1195

```

```

1196  /* Distance of closest approach of an RTRA to an RVER */
1197  double PImp2(double *N1, double *D1, double *D2) {
1198      int i; double PImpacto = 0.0;
1199      double D[Rcoords], n1[Rdirec], mn1 = 0.0, d = 0.0;
1200
1201      for(i=0; i<Rdirec; i++) mn1 += N1[i]*N1[i]; mn1 = sqrt(mn1);
1202      for(i=0; i<Rdirec; i++) n1[i] = N1[i]/mn1;
1203      for(i=0; i<Rcoords; i++) D[i] = D2[i]-D1[i];
1204      for(i=0; i<Rcoords; i++) { PImpacto += D[i]*n1[i]; d += D[i]*D[i]; }
1205      PImpacto = sqrt(d - PImpacto*PImpacto);
1206
1207      return PImpacto*1.0E4;    // Units: micrometers.
1208  }
1209
1210  /* Distance of closest approach of an RTRA pair, (D1,N1,P1) and (D2,N2,P2),
1211     to an RVER (D0). */
1212  double PImp3(double *N1, double *D1, double *N2, double *D2, double *D0,
1213              double P1, double P2) {
1214      int i;
1215      double n1[Rdirec], n2[Rdirec], d1[Rcoords], d2[Rcoords];
1216      double n3[Rdirec], D[Rcoords], N12[Rdirec];
1217      double rho = 0.0, n1n2=0.0, mn1 = 0.0, mn2 = 0.0, mN12 = 0.0;
1218      double dn1 = 0.0, dn2 = 0.0, n12 = 0.0, Vertex[Rcoords];
1219
1220      /* Normalize the unit vectors n1 and n2. */
1221      for(i=0; i<Rcoords; i++) { d1[i]=D1[i]; d2[i]=D2[i]; }
1222      for(i=0; i<Rdirec; i++) { n1[i]=N1[i]; n2[i]=N2[i]; }
1223      for(i=0; i<Rdirec; i++) { mn1 += n1[i]*n1[i]; mn2 += n2[i]*n2[i]; }
1224      mn1 = sqrt(mn1); mn2 = sqrt(mn2);
1225      for(i=0; i<Rdirec; i++) { n1[i] /= mn1; n2[i] /= mn2; }
1226
1227      /* n3: unit vector orthogonal to the plane defined by n1 and n2. */
1228      n3[TZ] = n1[TX]*n2[TY] - n1[TY]*n2[TX];
1229      n3[TX] = n1[TY]*n2[TZ] - n1[TZ]*n2[TY];
1230      n3[TY] = n1[TZ]*n2[TX] - n1[TX]*n2[TZ];
1231      for(i=0; i<Rdirec; i++) n1n2 += n3[i]*n3[i]; n1n2 = sqrt(n1n2);
1232      if(n1n2 != 0.0) for(i=0; i<Rdirec; i++) n3[i] /= n1n2;
1233      for(i=0; i<Rcoords; i++) D[i] = d2[i]-d1[i];
1234      if(n1n2 != 0.0) for(i=0; i<Rcoords; i++) rho += D[i]*n3[i];
1235      else { for(i=0; i<Rcoords; i++) rho += D[i]*D[i]; rho = sqrt(rho); }
1236      rho = fabs(rho)*1.0E4; // Impact parameter between RTRAs. Units: micrometers
1237
1238      /* Vertex: coordinates of the vertex given by RTRA1 and RTRA2. */
1239      for(i=0; i<Rdirec; i++) { N12[i] = fabs(P1)*n1[i] + fabs(P2)*n2[i]; }
1240      mN12 = sqrt(N12[0]*N12[0]+N12[1]*N12[1]+N12[2]*N12[2]);
1241      for(i=0; i<Rdirec; i++) { N12[i]/= mN12; }
1242      for(i=0; i<Rdirec; i++) { n12 += n1[i]*n2[i]; }
1243      for(i=0; i<Rdirec; i++) { dn1 += (D2[i]-D1[i])*n1[i]; dn2 += (D2[i]-D1[i])*n2[i]; }
1244      for(i=0; i<Rcoords; i++)
1245          Vertex[i] = 0.50*(D1[i]+D2[i]) + 0.50*(n1[i]*(dn1-n12*dn2)
1246              - n2[i]*(dn2-n12*dn1))/(n1n2*n1n2);
1247
1248      rho = PImp2(N12,Vertex,D0);
1249      return rho;
1250  }
1251
1252  double posZ(char coord, RTRA rtra1, RTRA rtra2) {
1253      int i;
1254      double lambda1=0.0, lambda2=0.0, zS,xS,yS;
1255      double D[Rcoords], n1[Rdirec], n2[Rdirec], n3[Rdirec];
1256      double n1n2=0.0, mn1=0.0, mn2=0.0;
1257

```

```

1258     for(i=0; i<Rcoords; i++) D[i] = rtra2.d[i] - rtra1.d[i];
1259     for(i=0; i<Rdirec; i++)
1260     { mn1 += rtra1.n[i]*rtra1.n[i]; mn2 += rtra2.n[i]*rtra2.n[i]; }
1261     mn1 = sqrt(mn1); mn2 = sqrt(mn2);
1262     for(i=0; i<Rdirec; i++)
1263     { n1[i] = rtra1.n[i]/mn1; n2[i] = rtra2.n[i]/mn2; }
1264     n3[TZ] = n1[TX]*n2[TY] - n1[TY]*n2[TX];
1265     n3[TX] = n1[TY]*n2[TZ] - n1[TZ]*n2[TY];
1266     n3[TY] = n1[TZ]*n2[TX] - n1[TX]*n2[TZ];
1267     for(i=0; i<Rdirec; i++) n1n2 += n3[i]*n3[i]; n1n2 = sqrt(n1n2);
1268     if(n1n2 != 0.0) {
1269         for(i=0; i<Rdirec; i++) n3[i] /= n1n2;
1270         lambda1 += (D[X]*n2[TY] - D[Y]*n2[TX]) * n3[TZ]/(n1n2);
1271         lambda1 += (D[Y]*n2[TZ] - D[Z]*n2[TY]) * n3[TX]/(n1n2);
1272         lambda1 += (D[Z]*n2[TX] - D[X]*n2[TZ]) * n3[TY]/(n1n2);
1273         lambda2 += (D[X]*n1[TY] - D[Y]*n1[TX]) * n3[TZ]/(n1n2);
1274         lambda2 += (D[Y]*n1[TZ] - D[Z]*n1[TY]) * n3[TX]/(n1n2);
1275         lambda2 += (D[Z]*n1[TX] - D[X]*n1[TZ]) * n3[TY]/(n1n2);
1276     }
1277     zS = rtra1.d[Z]+lambda1*n1[TZ] + rtra2.d[Z]+lambda2*n2[TZ];
1278     xS = rtra1.d[X]+lambda1*n1[TX] + rtra2.d[X]+lambda2*n2[TX];
1279     yS = rtra1.d[Y]+lambda1*n1[TY] + rtra2.d[Y]+lambda2*n2[TY];
1280     zS*=0.5; xS*=0.5; yS*=0.5;
1281
1282     switch((int)coord) {
1283         case 'Z': return zS; break;
1284         case 'X': return xS; break;
1285         case 'Y': return yS; break;
1286         default : return 0.0; break;
1287     }
1288     return 0.0; // Units: centimeters.
1289 }
1290
1291 double PImp_B0(RTRA r1, RTRA r2, RTRA r3, RTRA r4) {
1292     RTRA mup, mum, pip, pim, Jpsi, KS;
1293     int hasmup, hasmum, haspip, haspim;
1294     double PImp, mJpsi, mKS, dmJpsi, dmKS, z,p,tx,ty, P[3], D[3];
1295     static double mj=999,mk=999,smj=999,smk=999;
1296     static double zJpsi = -100, zKS = -100;
1297
1298     if(zJpsi<-50) zJpsi=rtar.d[Vz]; if(zKS<-50) zKS=rtar.d[Vz];
1299
1300     hasmup=hasmum=haspip=haspim=0;
1301     if(r1.mass==m_mu && !hasmup && r1.p>0) { mup=r1; hasmup++; }
1302     if(r1.mass==m_mu && !hasmum && r1.p<0) { mum=r1; hasmum++; }
1303     if(r1.mass==m_pi && !haspip && r1.p>0) { pip=r1; haspip++; }
1304     if(r1.mass==m_pi && !haspim && r1.p<0) { pim=r1; haspim++; }
1305     if(r2.mass==m_mu && !hasmup && r2.p>0) { mup=r2; hasmup++; }
1306     if(r2.mass==m_mu && !hasmum && r2.p<0) { mum=r2; hasmum++; }
1307     if(r2.mass==m_pi && !haspip && r2.p>0) { pip=r2; haspip++; }
1308     if(r2.mass==m_pi && !haspim && r2.p<0) { pim=r2; haspim++; }
1309     if(r3.mass==m_mu && !hasmup && r3.p>0) { mup=r3; hasmup++; }
1310     if(r3.mass==m_mu && !hasmum && r3.p<0) { mum=r3; hasmum++; }
1311     if(r3.mass==m_pi && !haspip && r3.p>0) { pip=r3; haspip++; }
1312     if(r3.mass==m_pi && !haspim && r3.p<0) { pim=r3; haspim++; }
1313     if(r4.mass==m_mu && !hasmup && r4.p>0) { mup=r4; hasmup++; }
1314     if(r4.mass==m_mu && !hasmum && r4.p<0) { mum=r4; hasmum++; }
1315     if(r4.mass==m_pi && !haspip && r4.p>0) { pip=r4; haspip++; }
1316     if(r4.mass==m_pi && !haspim && r4.p<0) { pim=r4; haspim++; }
1317
1318     mJpsi = InvMass_PID(mup.mass, mum.mass, mup.n, mum.n, mup.p, mum.p);
1319     mKS = InvMass_PID(pip.mass, pim.mass, pip.n, pim.n, pip.p, pim.p);

```

```

1320     dmJpsi = stddev_Mass_PID(mup.mass, mum.mass, mup.n, mum.n,
1321                             mup.c, mum.c, mup.p, mum.p);
1322     dmKS   = stddev_Mass_PID(pip.mass, pim.mass, pip.n, pim.n,
1323                             pip.c, pim.c, pip.p, pim.p);
1324
1325     z=posZ('Z',mup,mum);
1326     if(hasmup==1 && hasmum==1 && z>zJpsi &&
1327         fabs(mJpsi-m_Jpsi)<mj && fabs(mJpsi-m_Jpsi)/dmJpsi<smj) { // best J/psi
1328         goldenRTRA[0] = abs(mup.rt)-1; // muon+
1329         goldenRTRA[1] = abs(mum.rt)-1; // muon-
1330         mj = fabs(mJpsi-m_Jpsi); smj = mj/dmJpsi; zJpsi=z;
1331     }
1332     z=posZ('Z',pip,pim);
1333     if(haspip==1 && haspim==1 && z>zKS &&
1334         fabs(mKS-m_K0)<mk && fabs(mKS-m_K0)/dmKS<smk) { // best KS
1335         goldenRTRA[2] = abs(pip.rt)-1; // pion+
1336         goldenRTRA[3] = abs(pim.rt)-1; // pion-
1337         mk = fabs(mKS-m_K0); smk = mk/dmKS; zKS=z;
1338     }
1339
1340     /* bail out if we haven't the dimuon and dipion */
1341     if( hasmup!=1 || hasmum!=1 || haspip!=1 || haspim!=1 ) return -1;
1342
1343     /* cortes nas massas invariantes */
1344     if(fabs(mJpsi-m_Jpsi)>0.2 || fabs(mJpsi-m_Jpsi)/dmJpsi>3.0) return -2;
1345     if(fabs(mKS-m_K0)>0.1 || fabs(mKS-m_K0)/dmKS>5.0) return -3;
1346     if(posZ('Z',mup,mum)<(rtar.d[Vz]-rtar.s[Vz]) ||
1347         posZ('Z',pip,pim)<(rtar.d[Vz]-rtar.s[Vz]) ||
1348         posZ('Z',pip,pim)<posZ('Z',mup,mum) ) return -4;
1349
1350     P[Vz] = fabs(mup.p)/sqrt(1.0+mup.n[TX]*mup.n[TX]+mup.n[TY]*mup.n[TY]);
1351     P[Vz] += fabs(mum.p)/sqrt(1.0+mum.n[TX]*mum.n[TX]+mum.n[TY]*mum.n[TY]);
1352     P[Vx] = fabs(mup.p)*mup.n[TX]/sqrt(1.0+mup.n[TX]*mup.n[TX]+mup.n[TY]*mup.n[TY]);
1353     P[Vx] += fabs(mum.p)*mum.n[TX]/sqrt(1.0+mum.n[TX]*mum.n[TX]+mum.n[TY]*mum.n[TY]);
1354     P[Vy] = fabs(mup.p)*mup.n[TY]/sqrt(1.0+mup.n[TX]*mup.n[TX]+mup.n[TY]*mup.n[TY]);
1355     P[Vy] += fabs(mum.p)*mum.n[TY]/sqrt(1.0+mum.n[TX]*mum.n[TX]+mum.n[TY]*mum.n[TY]);
1356     tx = P[Vx]/P[Vz]; ty = P[Vy]/P[Vz];
1357     Jpsi.p = p = sqrt(P[Vz]*P[Vz]+P[Vx]*P[Vx]+P[Vy]*P[Vy]);
1358     D[Vz] = posZ('Z',mup,mum); D[Vx] = posZ('X',mup,mum); D[Vy] = posZ('Y',mup,mum);
1359     Jpsi.d[Z]=D[Vz]; Jpsi.d[X]=D[Vx]; Jpsi.d[Y]=D[Vy];
1360     Jpsi.n[TZ]=1.0; Jpsi.n[TX]=tx; Jpsi.d[TY]=ty;
1361
1362     P[Vz] = fabs(pip.p)/sqrt(1.0+pip.n[TX]*pip.n[TX]+pip.n[TY]*pip.n[TY]);
1363     P[Vz] += fabs(pim.p)/sqrt(1.0+pim.n[TX]*pim.n[TX]+pim.n[TY]*pim.n[TY]);
1364     P[Vx] = fabs(pip.p)*pip.n[TX]/sqrt(1.0+pip.n[TX]*pip.n[TX]+pip.n[TY]*pip.n[TY]);
1365     P[Vx] += fabs(pim.p)*pim.n[TX]/sqrt(1.0+pim.n[TX]*pim.n[TX]+pim.n[TY]*pim.n[TY]);
1366     P[Vy] = fabs(pip.p)*pip.n[TY]/sqrt(1.0+pip.n[TX]*pip.n[TX]+pip.n[TY]*pip.n[TY]);
1367     P[Vy] += fabs(pim.p)*pim.n[TY]/sqrt(1.0+pim.n[TX]*pim.n[TX]+pim.n[TY]*pim.n[TY]);
1368     tx = P[Vx]/P[Vz]; ty = P[Vy]/P[Vz];
1369     KS.p = p = sqrt(P[Vz]*P[Vz]+P[Vx]*P[Vx]+P[Vy]*P[Vy]);
1370     D[Vz] = posZ('Z', pip,pim);
1371     D[Vx] = posZ('X', pip,pim);
1372     D[Vy] = posZ('Y', pip,pim);
1373     KS.d[Z]=D[Vz]; KS.d[X]=D[Vx]; KS.d[Y]=D[Vy];
1374     KS.n[TZ]=1.0; KS.n[TX]=tx; KS.n[TY]=ty;
1375
1376     PImp = ParamImpact(Jpsi.n,KS.n, Jpsi.d, KS.d);
1377     return PImp; // Minimum separation between J/psi and KS.
1378                // Units: micrometers
1379 }
1380
1381

```

```

1382 RTRA RTRAFusion(RTRA rtra1, RTRA rtra2, char* PID) {
1383     RTRA rtra; int i;
1384     double mass, pf,tx,ty, pz,px,py, z,x,y;
1385
1386     mass = eval_Mass(rtra1,rtra2);
1387     pz = fabs(rtra1.p)/sqrt(1.0+rtra1.n[TX]*rtra1.n[TX]+rtra1.n[TY]*rtra1.n[TY]);
1388     pz+= fabs(rtra2.p)/sqrt(1.0+rtra2.n[TX]*rtra2.n[TX]+rtra2.n[TY]*rtra2.n[TY]);
1389     px = fabs(rtra1.p)*rtra1.n[TX]/sqrt(1.0+rtra1.n[TX]*rtra1.n[TX]+rtra1.n[TY]*rtra1.n[TY]);
1390     px+= fabs(rtra2.p)*rtra2.n[TX]/sqrt(1.0+rtra2.n[TX]*rtra2.n[TX]+rtra2.n[TY]*rtra2.n[TY]);
1391     py = fabs(rtra1.p)*rtra1.n[TY]/sqrt(1.0+rtra1.n[TX]*rtra1.n[TX]+rtra1.n[TY]*rtra1.n[TY]);
1392     py+= fabs(rtra2.p)*rtra2.n[TY]/sqrt(1.0+rtra2.n[TX]*rtra2.n[TX]+rtra2.n[TY]*rtra2.n[TY]);
1393     rtra.p = pf = sqrt(pz*pz+px*px+py*py); tx = px/pz; ty = py/pz;
1394     z = posZ('Z', rtra1,rtra2); x = posZ('X', rtra1,rtra2); y = posZ('Y', rtra1,rtra2);
1395     rtra.d[Z]=z; rtra.d[X]=x; rtra.d[Y]=y;
1396     rtra.n[TZ]=1.0; rtra.n[TX]=tx; rtra.d[TY]=ty;
1397     rtra.mass = mass; sprintf(rtra.PID,PID);
1398     for(i=0;i<Rcovar;i++) rtra.c[i]=0.0;
1399     rtra.c[CXX]=sqrt(rtra1.c[CXX])+sqrt(rtra2.c[CXX]); rtra.c[CXX]*=rtra.c[CXX];
1400     rtra.c[CYY]=sqrt(rtra1.c[CYY])+sqrt(rtra2.c[CYY]); rtra.c[CYY]*=rtra.c[CYY];
1401     rtra.c[CXY]=sqrt(fabs(rtra1.c[CXY]))*Sign(rtra1.c[CXY]) +
1402                 sqrt(fabs(rtra2.c[CXY]))*Sign(rtra2.c[CXY]); rtra.c[CXY]*=rtra.c[CXY];
1403     rtra.c[CTXTX]=sqrt(rtra1.c[CTXTX])+sqrt(rtra2.c[CTXTX]); rtra.c[CTXTX]*=rtra.c[CTXTX];
1404     rtra.c[CTYTY]=sqrt(rtra1.c[CTYTY])+sqrt(rtra2.c[CTYTY]); rtra.c[CTYTY]*=rtra.c[CTYTY];
1405     rtra.c[CPP]=sqrt(rtra1.c[CPP])+sqrt(rtra2.c[CPP]); rtra.c[CPP]*=rtra.c[CPP];
1406
1407     return rtra;
1408 }
1409
1410 /* Impact parameter an RTRA to the target rtar */
1411 double PI_rtar(RTRA rtra, RTAR target) {
1412     double PImp, z0,x0,y0;
1413     z0 = target.d[Z];
1414     x0 = rtra.d[X] + rtra.n[TX]*(z0-rtra.d[Z]);
1415     y0 = rtra.d[Y] + rtra.n[TY]*(z0-rtra.d[Z]);
1416     if(fabs(y0-target.d[Y]) < target.s[Y]) PImp = fabs(x0-target.d[X])-target.s[X];
1417     else {
1418         PImp = pow((fabs(x0-target.d[X])-target.s[X]),2.0);
1419         PImp+= pow((fabs(y0-target.d[Y])-target.s[Y]),2.0);
1420         PImp = sqrt(PImp);
1421     }
1422     return PImp*1.0e4;
1423 }
1424
1425 double PI_rtar_2RTRA(RTRA rtra1, RTRA rtra2, RTAR target) {
1426     double P[Vcoords], N[Vcoords], p, pT;
1427     double m1 = InvMass_PID(rtra1.mass,rtra2.mass,rtra1.n,rtra2.n,rtra1.p,rtra2.p);
1428     double z0,x0,y0, z,x,y, PImp;
1429
1430     z = target.d[Z];
1431     P[Vz]=P[Vx]=P[Vy]=0.0;
1432     P[Vz]+=fabs(rtra1.p)/sqrt(1.0+rtra1.n[TX]*rtra1.n[TX]+rtra1.n[TY]*rtra1.n[TY]);
1433     P[Vx]+=fabs(rtra1.p)*rtra1.n[TX]/sqrt(1.0+rtra1.n[TX]*rtra1.n[TX]+rtra1.n[TY]*rtra1.n[TY]);
1434     P[Vy]+=fabs(rtra1.p)*rtra1.n[TY]/sqrt(1.0+rtra1.n[TX]*rtra1.n[TX]+rtra1.n[TY]*rtra1.n[TY]);
1435     P[Vz]+=fabs(rtra2.p)/sqrt(1.0+rtra2.n[TX]*rtra2.n[TX]+rtra2.n[TY]*rtra2.n[TY]);
1436     P[Vx]+=fabs(rtra2.p)*rtra2.n[TX]/sqrt(1.0+rtra2.n[TX]*rtra2.n[TX]+rtra2.n[TY]*rtra2.n[TY]);
1437     P[Vy]+=fabs(rtra2.p)*rtra2.n[TY]/sqrt(1.0+rtra2.n[TX]*rtra2.n[TX]+rtra2.n[TY]*rtra2.n[TY]);
1438
1439     p = sqrt(P[Vz]*P[Vz]+P[Vx]*P[Vx]+P[Vy]*P[Vy]);
1440     pT = sqrt(P[Vx]*P[Vx]+P[Vy]*P[Vy]);
1441     z0 = posZ('Z',rtra1,rtra2);
1442     x0 = posZ('X',rtra1,rtra2);
1443     y0 = posZ('Y',rtra1,rtra2);

```

```

1444
1445     x = x0 + (P[Vx]/P[Vz])*(z-z0);
1446     y = y0 + (P[Vy]/P[Vz])*(z-z0);
1447
1448     if(fabs(y-target.d[Y]) < target.s[Y])
1449         PImp = fabs(x-target.d[X])-target.s[X];
1450     else {
1451         PImp = pow((fabs(x-target.d[X])-target.s[X]),2.0);
1452         PImp+= pow((fabs(y-target.d[Y])-target.s[Y]),2.0);
1453         PImp = sqrt(PImp);
1454     }
1455     return PImp*1.0e4;
1456 }
1457
1458 double PI_rtar_3RTRA(RTRA rtra1, RTRA rtra2, RTRA rtra3, RTAR target) {
1459     RTRA Rtra[3];
1460     double P[Vcoords], p, pT, tx, ty;
1461     double m1,m2, masses[3][3], dJpsi=0.2, dKS=0.1;
1462     double z0[3][3],x0[3][3],y0[3][3], z,x,y, PImp;
1463     int i,j, KS=0, Jpsi=0;
1464
1465     z = target.d[Z]; P[Vz]=P[Vx]=P[Vy]=0.0;
1466
1467     /* Total and transversal momenta, p and p_T for the B meson */
1468     P[Vz]+=fabs(rtra1.p)/sqrt(1.0+rtra1.n[TX]*rtra1.n[TX]+rtra1.n[TY]*rtra1.n[TY]);
1469     P[Vx]+=fabs(rtra1.p)*rtra1.n[TX]/sqrt(1.0+rtra1.n[TX]*rtra1.n[TX]+rtra1.n[TY]*rtra1.n[TY]);
1470     P[Vy]+=fabs(rtra1.p)*rtra1.n[TY]/sqrt(1.0+rtra1.n[TX]*rtra1.n[TX]+rtra1.n[TY]*rtra1.n[TY]);
1471     P[Vz]+=fabs(rtra2.p)/sqrt(1.0+rtra2.n[TX]*rtra2.n[TX]+rtra2.n[TY]*rtra2.n[TY]);
1472     P[Vx]+=fabs(rtra2.p)*rtra2.n[TX]/sqrt(1.0+rtra2.n[TX]*rtra2.n[TX]+rtra2.n[TY]*rtra2.n[TY]);
1473     P[Vy]+=fabs(rtra2.p)*rtra2.n[TY]/sqrt(1.0+rtra2.n[TX]*rtra2.n[TX]+rtra2.n[TY]*rtra2.n[TY]);
1474     P[Vz]+=fabs(rtra3.p)/sqrt(1.0+rtra3.n[TX]*rtra3.n[TX]+rtra3.n[TY]*rtra3.n[TY]);
1475     P[Vx]+=fabs(rtra3.p)*rtra3.n[TX]/sqrt(1.0+rtra3.n[TX]*rtra3.n[TX]+rtra3.n[TY]*rtra3.n[TY]);
1476     P[Vy]+=fabs(rtra3.p)*rtra3.n[TY]/sqrt(1.0+rtra3.n[TX]*rtra3.n[TX]+rtra3.n[TY]*rtra3.n[TY]);
1477     p = sqrt(P[Vz]*P[Vz]+P[Vx]*P[Vx]+P[Vy]*P[Vy]);
1478     pT = sqrt(P[Vx]*P[Vx]+P[Vy]*P[Vy]);
1479     tx = P[Vx]/P[Vz]; ty = P[Vy]/P[Vz];
1480
1481     Rtra[0]=rtra1; Rtra[1]=rtra2; Rtra[2]=rtra3;
1482     for(i=0; i<3; i++) for(j=0;j<3; j++) {
1483         if(i!=j && ((Rtra[i].p)*(Rtra[j].p)<0.0) {
1484             masses[i][j] = InvMass_PID(Rtra[i].mass, Rtra[j].mass, Rtra[i].n,
1485                                     Rtra[j].n, Rtra[i].p,Rtra[j].p);
1486             if(i<j) if(fabs(masses[i][j]-m_Jpsi) < dJpsi)
1487                 { dJpsi = fabs(masses[i][j]-m_Jpsi); Jpsi = i*4+j; }
1488             z0[i][j]=posZ('Z', Rtra[i],Rtra[j]);
1489             x0[i][j]=posZ('X', Rtra[i],Rtra[j]);
1490             y0[i][j]=posZ('Y', Rtra[i],Rtra[j]);
1491         }
1492         else z0[i][j]=x0[i][j]=y0[i][j]=masses[i][j]=0.0;
1493     }
1494     x = x0[Jpsi/4][Jpsi%4] + tx*(z-z0[Jpsi/4][Jpsi%4]);
1495     y = y0[Jpsi/4][Jpsi%4] + ty*(z-z0[Jpsi/4][Jpsi%4]);
1496
1497     if(fabs(y-target.d[Y]) < target.s[Y])
1498         PImp = fabs(x-target.d[X])-target.s[X];
1499     else {
1500         PImp = pow((fabs(x-target.d[X])-target.s[X]),2.0);
1501         PImp += pow((fabs(y-target.d[Y])-target.s[Y]),2.0);
1502         PImp = sqrt(PImp);
1503     }
1504     return PImp*1.0e4;
1505 }

```

```

1506
1507 double PI_rtar_4RTRA(RTRA rtra1, RTRA rtra2, RTRA rtra3, RTRA rtra4, RTAR target) {
1508     RTRA Rtra[4];
1509     double P[Vcoords], p, pT, tx, ty;
1510     double m1,m2, masses[4][4], dJpsi=0.2, dKS=0.1;
1511     double z0[4][4],x0[4][4],y0[4][4], z,x,y, PImp;
1512     int i,j, KS=0, Jpsi=0;
1513
1514     z = target.d[Z]; P[Vz]=P[Vx]=P[Vy]=0.0;
1515
1516     /* Total and transversal momenta, p and p_T for the B meson */
1517     P[Vz]+=fabs(rtra1.p)/sqrt(1.0+rtra1.n[TX]*rtra1.n[TX]+rtra1.n[TY]*rtra1.n[TY]);
1518     P[Vx]+=fabs(rtra1.p)*rtra1.n[TX]/sqrt(1.0+rtra1.n[TX]*rtra1.n[TX]+rtra1.n[TY]*rtra1.n[TY]);
1519     P[Vy]+=fabs(rtra1.p)*rtra1.n[TY]/sqrt(1.0+rtra1.n[TX]*rtra1.n[TX]+rtra1.n[TY]*rtra1.n[TY]);
1520     P[Vz]+=fabs(rtra2.p)/sqrt(1.0+rtra2.n[TX]*rtra2.n[TX]+rtra2.n[TY]*rtra2.n[TY]);
1521     P[Vx]+=fabs(rtra2.p)*rtra2.n[TX]/sqrt(1.0+rtra2.n[TX]*rtra2.n[TX]+rtra2.n[TY]*rtra2.n[TY]);
1522     P[Vy]+=fabs(rtra2.p)*rtra2.n[TY]/sqrt(1.0+rtra2.n[TX]*rtra2.n[TX]+rtra2.n[TY]*rtra2.n[TY]);
1523     P[Vz]+=fabs(rtra3.p)/sqrt(1.0+rtra3.n[TX]*rtra3.n[TX]+rtra3.n[TY]*rtra3.n[TY]);
1524     P[Vx]+=fabs(rtra3.p)*rtra3.n[TX]/sqrt(1.0+rtra3.n[TX]*rtra3.n[TX]+rtra3.n[TY]*rtra3.n[TY]);
1525     P[Vy]+=fabs(rtra3.p)*rtra3.n[TY]/sqrt(1.0+rtra3.n[TX]*rtra3.n[TX]+rtra3.n[TY]*rtra3.n[TY]);
1526     P[Vz]+=fabs(rtra4.p)/sqrt(1.0+rtra4.n[TX]*rtra4.n[TX]+rtra4.n[TY]*rtra4.n[TY]);
1527     P[Vx]+=fabs(rtra4.p)*rtra4.n[TX]/sqrt(1.0+rtra4.n[TX]*rtra4.n[TX]+rtra4.n[TY]*rtra4.n[TY]);
1528     P[Vy]+=fabs(rtra4.p)*rtra4.n[TY]/sqrt(1.0+rtra4.n[TX]*rtra4.n[TX]+rtra4.n[TY]*rtra4.n[TY]);
1529     p = sqrt(P[Vz]*P[Vz]+P[Vx]*P[Vx]+P[Vy]*P[Vy]);
1530     pT = sqrt(P[Vx]*P[Vx]+P[Vy]*P[Vy]);
1531     tx = P[Vx]/P[Vz];          ty = P[Vy]/P[Vz];
1532
1533     Rtra[0]=rtra1; Rtra[1]=rtra2; Rtra[2]=rtra3; Rtra[3]=rtra4;
1534     for(i=0; i<4; i++) for(j=0;j<i; j++) {
1535         if((Rtra[i].p)*(Rtra[j].p)<0.0) {
1536             masses[i][j] = masses[j][i] =
1537                 InvMass_PID(Rtra[i].mass, Rtra[j].mass, Rtra[i].n, Rtra[j].n,
1538                     Rtra[i].p,Rtra[j].p);
1539             if(fabs(masses[i][j]-m_Jpsi) < dJpsi)
1540                 { dJpsi = fabs(masses[i][j]-m_Jpsi); Jpsi = i*4+j; }
1541             if(fabs(masses[i][j]-m_K0) < dKS)
1542                 { dKS = fabs(masses[i][j]-m_K0); KS = i*4+j; }
1543             if(fabs(masses[i][j]-m_Jpsi) < dJpsi)
1544                 if(fabs(masses[i][j]-m_K0) < dKS) {
1545                     z0[i][j]=z0[j][i]=posZ('Z', Rtra[i],Rtra[j]);
1546                     x0[i][j]=x0[j][i]=posZ('X', Rtra[i],Rtra[j]);
1547                     y0[i][j]=y0[j][i]=posZ('Y', Rtra[i],Rtra[j]);
1548                 }
1549             } else {
1550                 z0[i][j]=x0[i][j]=y0[i][j]=masses[i][j]=0.0;
1551                 z0[j][i]=x0[j][i]=y0[j][i]=masses[j][i]=0.0;
1552             }
1553         }
1554     }
1555     x = x0[Jpsi/4][Jpsi%4] + tx*(z-z0[Jpsi/4][Jpsi%4]);
1556     y = y0[Jpsi/4][Jpsi%4] + ty*(z-z0[Jpsi/4][Jpsi%4]);
1557
1558     if(fabs(y-target.d[Y]) < target.s[Y])
1559         PImp = fabs(x-target.d[X])-target.s[X];
1560     else {
1561         PImp = (fabs(x-target.d[X])-target.s[X])*(fabs(x-target.d[X])-target.s[X]);
1562         PImp += (fabs(y-target.d[Y])-target.s[Y])*(fabs(y-target.d[Y])-target.s[Y]);
1563         PImp = sqrt(PImp);
1564     }
1565     return PImp*1.0e4;
1566 }
1567

```

```

1568 double eval_Mass(RTRA rtra1, RTRA rtra2) {
1569     double mass=0.0;
1570     if(rtra1.mass>0.0 && rtra2.mass>0.0)
1571         mass = pow(InvMass_PID(rtra1.mass,rtra2.mass,
1572                               rtra1.n, rtra2.n, rtra1.p, rtra2.p), 2.0);
1573     else
1574         mass = pow(InvMass(rtra1.n, rtra2.n, rtra1.p, rtra2.p), 2.0);
1575
1576     return sqrt(mass);
1577 }
1578
1579 /* Charge of a pT-weighted jet, see D.Sambtleben (HERA-B note 98-080) */
1580 double jetCharge(RTRA *list, int nRTRAs, RVER vtx0) {
1581     int i,j; double charge=0.0, Pimp=0.0;
1582     double wi=0.0, qi=0.0, sumw=0.0, sumwiqi=0.0;
1583     const double PimpCut = 200.0;
1584
1585     for(i=0; i<nRTRAs; i++) {
1586         if(list[i].hsi<=0 || (list[i].hin<=0 && list[i].hou<=0)) continue;
1587         if(i==goldenRTRA[0] || i==goldenRTRA[1]) continue;
1588         if(i==goldenRTRA[2] || i==goldenRTRA[3]) continue;
1589         Pimp = PImp2(list[i].n, list[i].d, vtx0.d);
1590         wi = list[i].n[TX]*list[i].n[TX]+list[i].n[TY]*list[i].n[TY];
1591         wi *= list[i].p*list[i].p;
1592         wi *= (Pimp>0? PimpCut/Pimp : 1.0);
1593         qi = list[i].p/fabs(list[i].p);
1594         sumw += wi;
1595         sumwiqi += wi*qi;
1596     }
1597     charge = (sumw>0 ? sumwiqi/sumw : -999);
1598     return charge;
1599 }
1600
1601 ///////////////////////////////////////////////////////////////////
1602 /////////////////////////////////////////////////////////////////// ERRORS ///////////////////////////////////////////////////////////////////
1603 ///////////////////////////////////////////////////////////////////
1604
1605 /* For the charge of a pT-weighted jet, see D.Sambtleben (HERA-B note 98-080) */
1606 double stddev_jetCharge(RTRA *list, int nRTRAs, RVER vtx0) {
1607     int i; double stddev_charge=0.0, Pimp=0.0;
1608     double wi=0.0, ewi=0.0, qi=0.0, sumew=0.0, sumqiewi=0.0;
1609     const double PimpCut = 200.0;
1610
1611     for(i=0; i<nRTRAs; i++) {
1612         if(list[i].hsi<=0 || (list[i].hin<=0 && list[i].hou<=0)) continue;
1613         if(i==goldenRTRA[0] || i==goldenRTRA[1]) continue;
1614         if(i==goldenRTRA[2] || i==goldenRTRA[3]) continue;
1615         Pimp = PImp2(list[i].n, list[i].d, vtx0.d);
1616         qi = list[i].p/fabs(list[i].p);         ewi = 0.0;
1617         wi = list[i].n[TX]*list[i].n[TX]+list[i].n[TY]*list[i].n[TY];
1618         wi *= list[i].p*list[i].p;
1619         wi *= (Pimp>0? PimpCut/Pimp : 1.0);
1620         ewi = list[i].n[TX]*list[i].c[CPTX]+list[i].n[TY]*list[i].c[CPTY];
1621         ewi *= (-1.0*list[i].p*wi);
1622         ewi += (list[i].p*list[i].p)*list[i].n[TX]*list[i].n[TY]*list[i].c[CTXTY];
1623         ewi *= 2.0; ewi += wi*wi*list[i].c[CPP];
1624         ewi += list[i].n[TX]*list[i].n[TX]*list[i].c[CTXTX];
1625         ewi += list[i].n[TY]*list[i].n[TY]*list[i].c[CTYTY];
1626         ewi *= 4.0*list[i].p*list[i].p;
1627         sumew += ewi; sumqiewi += qi*ewi;
1628     }
1629     stddev_charge = (sumew>0 ? sumqiewi/sumew : -1.0);

```

```

1630     stddev_charge = (stddev_charge>=0.0 ? sqrt(stddev_charge) : -1.0);
1631     return stddev_charge;
1632 }
1633
1634 double stddev_Mass_PID(double m1, double m2, double *n1, double *n2,
1635                       double *c1, double *c2, double p1, double p2) {
1636     double m, sm, N1, N2, dmdp1, dmdp2, dmdtx1, dmdtx2, dmdty1, dmdty2;
1637     double t1t2, p1p2, E1, E2;
1638
1639     m = InvMass_PID(m1,m2,n1,n2,p1,p2); sm = 0.0;
1640     N1 = sqrt(1.0+n1[TX]*n1[TX]+n1[TY]*n1[TY]);
1641     N2 = sqrt(1.0+n2[TX]*n2[TX]+n2[TY]*n2[TY]);
1642     t1t2 = 1.0+n1[TX]*n2[TX]+n1[TY]*n2[TY];
1643     p1p2 = fabs(p1)*fabs(p2)*t1t2/(N1*N2);
1644     E1 = sqrt(m1*m1+p1*p1); E2 = sqrt(m2*m2+p2*p2);
1645     dmdp1 = (p1/m)*(p1p2 - (E2/E1)*p1*p1);
1646     dmdp2 = (p2/m)*(p1p2 - (E1/E2)*p2*p2);
1647     dmdtx1 = (p1p2/m)*(n1[TX]/(N1*N1) - n2[TX]/t1t2);
1648     dmdty1 = (p1p2/m)*(n1[TY]/(N1*N1) - n2[TY]/t1t2);
1649     dmdtx2 = (p1p2/m)*(n2[TX]/(N2*N2) - n1[TX]/t1t2);
1650     dmdty2 = (p1p2/m)*(n2[TY]/(N2*N2) - n1[TY]/t1t2);
1651
1652     // Contribution from RTRA1
1653     sm += dmdp1*(dmdp1*c1[CPP]+2.0*dmdtx1*c1[CPTX]+2.0*dmdty1*c1[CPTY]);
1654     sm += dmdtx1*dmdtx1*c1[CTXTX] + dmdty1*dmdty1*c1[CTYTY];
1655     sm += 2.0*dmdtx1*dmdty1*c1[CTXTY];
1656
1657     // Contribution from RTRA2
1658     sm += dmdp2*(dmdp2*c2[CPP]+2.0*dmdtx2*c2[CPTX]+2.0*dmdty2*c2[CPTY]);
1659     sm += dmdtx2*dmdtx2*c2[CTXTX] + dmdty2*dmdty2*c2[CTYTY];
1660     sm += 2.0*dmdtx2*dmdty2*c2[CTXTY];
1661     sm = sqrt(sm);
1662     return (sm); // Unidades: GeV/c^2
1663 }
1664
1665 double stddev_Mass(double *n1, double *n2, double *c1, double *c2,
1666                  double p1, double p2) {
1667     double m,sm,N1,N2, dmdp1, dmdp2, dmdtx1, dmdtx2, dmdty1, dmdty2;
1668
1669     m = InvMass(n1,n2,p1,p2); sm = 0.0;
1670     N1 = sqrt(1.0+n1[TX]*n1[TX]+n1[TY]*n1[TY]);
1671     N2 = sqrt(1.0+n2[TX]*n2[TX]+n2[TY]*n2[TY]);
1672     dmdp1 = -m*p1/2.0; dmdp2 = -m*p2/2.0;
1673     dmdtx1 = p1*p2*(n1[TX]/N1-n2[TX]/N2)/(m*N1) - m*n1[TX]/(2*N1*N1);
1674     dmdty1 = p1*p2*(n1[TY]/N1-n2[TY]/N2)/(m*N1) - m*n1[TY]/(2*N1*N1);
1675     dmdtx2 = p1*p2*(n2[TX]/N2-n1[TX]/N1)/(m*N2) - m*n2[TX]/(2*N2*N2);
1676     dmdty2 = p1*p2*(n2[TY]/N2-n1[TY]/N1)/(m*N2) - m*n2[TY]/(2*N2*N2);
1677
1678     // Contribution from RTRA1
1679     sm += dmdp1*(dmdp1*c1[CPP]+2.0*dmdtx1*c1[CPTX]+2.0*dmdty1*c1[CPTY]);
1680     sm += dmdtx1*dmdtx1*c1[CTXTX] + dmdty1*dmdty1*c1[CTYTY];
1681     sm += 2.0*dmdtx1*dmdty1*c1[CTXTY];
1682
1683     // Contribution from RTRA2
1684     sm += dmdp2*(dmdp2*c2[CPP]+2.0*dmdtx2*c2[CPTX]+2.0*dmdty2*c2[CPTY]);
1685     sm += dmdtx2*dmdtx2*c2[CTXTX] + dmdty2*dmdty2*c2[CTYTY];
1686     sm += 2.0*dmdtx2*dmdty2*c2[CTXTY];
1687
1688     sm = sqrt(sm);
1689     return (sm); // Units: GeV/c^2
1690 }
1691

```

```

1692 /* Square root of variance for the minimum separation between two RTRAs */
1693 double stddev_ParamImp(double *n1, double *n2, double *c1, double *c2,
1694                       double *d1, double *d2) {
1695
1696     double sParImp=0.0, z,x,y, n,nz,nx,ny, b,bz,bx,by;
1697     double dbdz,dbdx,dbdy, dbdtx1,dbdtx2, dbdty1,dbdty2;
1698
1699     z=d2[Z]-d1[Z]; x=d2[X]-d1[X]; y=d2[X]-d1[X];
1700     nz=n1[TX]*n2[TY]-n1[TY]*n2[TX]; nx=n1[TY]-n2[TY]; ny=n2[TX]-n1[TX];
1701     n=sqrt(nz*nz+nx*nx+ny*ny);
1702     bz=z*nz/n; bx=x*nx/n; by=y*ny/n; b=sqrt(bz*bz+bx*bx+by*by);
1703
1704     dbdz=nz/n; dbdx=nx/n; dbdy=ny/n;
1705     dbdtx1 = ((z*n2[TY]-y)-b*(n2[TY]*nz-ny))/n;
1706     dbdtx2 = -((z*n1[TY]-y)-b*(n1[TY]*nz-ny))/n;
1707     dbdty1 = -((z*n2[TX]-x)-b*(n2[TX]*nz-nx))/n;
1708     dbdty2 = ((z*n1[TX]-x)-b*(n1[TX]*nz-nx))/n;
1709
1710     // contribuição do RTRA 2
1711     sParImp += dbdx * dbdx * c2[CXX] + dbdy * dbdy * c2[CYY];
1712     sParImp += dbdtx2*dbdtx2*c2[CTXTX] + dbdty2*dbdty2*c2[CTYTY];
1713     sParImp += 2.0*dbdx*dbdy*c2[CXY] + 2.0*dbdtx2*dbdty2*c2[CTXTY];
1714     sParImp += 2.0*dbdtx2*(dbdx*c2[CXTX]+dbdy*c2[CYTX]);
1715     sParImp += 2.0*dbdty2*(dbdx*c2[CXTY]+dbdy*c2[CYTY]);
1716
1717     // contribuição do RTRA 1
1718     dbdz = -dbdz; dbdx = -dbdx; dbdy = -dbdy;
1719     sParImp += dbdx * dbdx * c1[CXX] + dbdy * dbdy * c1[CYY];
1720     sParImp += dbdtx2*dbdtx2*c1[CTXTX] + dbdty1*dbdty1*c1[CTYTY];
1721     sParImp += 2.0*dbdx*dbdy*c1[CXY] + 2.0*dbdtx1*dbdty1*c1[CTXTY];
1722     sParImp += 2.0*dbdtx1*(dbdx*c1[CXTX]+dbdy*c1[CYTX]);
1723     sParImp += 2.0*dbdty1*(dbdx*c1[CXTY]+dbdy*c1[CYTY]);
1724
1725     sParImp = sqrt(sParImp);
1726     return sParImp*1.0E4; // Units: micrometers.
1727 }
1728
1729 /* Error in the impact parameter of two RTRAs, (D1,N1,P1,c1) and
1730 * (D2,N2,P2,c2), to an RVER (D0,c0). */
1731 double stddev_PImp3(double *N1, double *D1, double *N2, double *D2, double *c1,
1732                   double *c2, double P1, double P2, double *D0, double *c0) {
1733     int i;
1734     double sParImp=0.0, c12[Rcovar], d12[Rcoords], n12=0.0, mN12=0.0;
1735     double N12[Rdirec], mn1=0.0, mn2=0.0, n3[Rdirec], n1n2=0.0;
1736     double n1[Rdirec], n2[Rdirec], dn1=0.0, dn2=0.0, Vertex[Rcoords];
1737
1738     for(i=0; i<Rcovar; i++) c12[i] = (c1[i]+c2[i]);
1739     for(i=0; i<Rdirec; i++) { n1[i] = N1[i]; n2[i] = N2[i]; }
1740     for(i=0; i<Rdirec; i++) { mn1 += n1[i]*n1[i]; mn2 += n2[i]*n2[i]; }
1741     mn1 = sqrt(mn1); mn2 = sqrt(mn2);
1742     for(i=0; i<Rdirec; i++) { n1[i]/= mn1; n2[i]/= mn2; }
1743     n3[TZ] = n1[TX]*n2[TY] - n1[TY]*n2[TX];
1744     n3[TX] = n1[TY]*n2[TZ] - n1[TZ]*n2[TY];
1745     n3[TY] = n1[TZ]*n2[TX] - n1[TX]*n2[TZ];
1746     for(i=0; i<Rdirec; i++) n1n2 += n3[i]*n3[i]; n1n2 = sqrt(n1n2);
1747
1748     for(i=0; i<Rdirec; i++) { N12[i] = fabs(P1)*n1[i] + fabs(P2)*n2[i]; }
1749     mN12 = sqrt(N12[0]*N12[0]+N12[1]*N12[1]+N12[2]*N12[2]);
1750     for(i=0; i<Rdirec; i++) { N12[i]/= mN12; }
1751     for(i=0; i<Rdirec; i++) { n12 += n1[i]*n2[i]; }
1752     for(i=0; i<Rdirec; i++)
1753     { dn1 += (D2[i]-D1[i])*n1[i]; dn2 += (D2[i]-D1[i])*n2[i]; }

```

```

1754     for(i=0; i<Rcoords; i++)
1755         Vertex[i] = 0.50*(D1[i]+D2[i]) + 0.50*(n1[i]*(dn1-n12*dn2)
1756             - n2[i]*(dn2-n12*dn1))/(n1n2*n1n2);
1757
1758     sParImp = stddev_PImp2(N12, d12, D0, c12, c0);
1759     return sParImp;
1760 }
1761
1762 /* Impact parameter of an RTRA (D1,N1,c1) to an RVER (D2,c2). */
1763 double stddev_PImp2(double *N1, double *D1,double *D2, double *c1,double *c2) {
1764     double sParImp=0.0, d[3], n1[3], dn1=0.0, b=0.0, B[3];
1765     double dbdz,dbdx,dbdy, dbdtx,dbdty;     int i,j;
1766
1767     for(i=0; i<3; i++) d[i]=D1[i]-D2[i];
1768     n1[0]=1.0/sqrt(1.0+N1[TX]*N1[TX]+N1[TY]*N1[TY]);
1769     n1[1]=N1[TX]*n1[0]; n1[2]=N1[TY]*n1[0];
1770     for(i=0; i<3; i++) dn1+=d[i]*n1[i];
1771     for(i=0; i<3; i++) { B[i]=d[i]-dn1*n1[i]; b+=B[i]*B[i]; }
1772     b = sqrt(b);
1773
1774     dbdz = B[0]/b; dbdx = B[1]/b; dbdy = B[2]/b;
1775     dbdtx = -B[1]*n1[0]*dn1/b; dbdty = -B[2]*n1[0]*dn1/b;
1776
1777     sParImp = 0.0;
1778     // Contribution from vertex.
1779     sParImp += dbdz*dbdz*c2[CVzz]+dbdx*dbdx*c2[CVxx]+dbdy*dbdy*c2[CVyy];
1780     sParImp += 2.0*(dbdz*(dbdx*c2[CVzx]+dbdy*c2[CVzy])+dbdx*dbdy*c2[CVxy]);
1781
1782     // Contribution from track.
1783     dbdz = -dbdz; dbdx = -dbdx; dbdy = -dbdy;
1784     sParImp += dbdx*dbdx*c1[CXX] + dbdy*dbdy*c1[CYY];
1785     sParImp += dbdtx*dbdtx*c1[CTXTX] + dbdty*dbdty*c1[CTYTY];
1786     sParImp += 2.0*dbdx*dbdy*c1[CXY] + 2.0*dbdtx*dbdty*c1[CTXTY];
1787     sParImp += 2.0*dbdtx*(dbdx*c1[CXTX] + dbdy*c1[CYTX]);
1788     sParImp += 2.0*dbdty*(dbdx*c1[CXTY] + dbdy*c1[CYTY]);
1789
1790     sParImp = sqrt(sParImp);
1791     return sParImp*1.0E4; // Units: micrometers
1792 }
1793
1794 double stddev_p(double *c, double p) { return sqrt(p*p*p*c[CPP]); }
1795
1796 double stddev_pT(double *n, double *c, double p) {
1797     double pT = sign(p)*p*sqrt(n[TX]*n[TX]+n[TY]*n[TY]);
1798     double dptd1p, dptdtx, dptdty, stddev;
1799
1800     dptdtx = p*p*n[TX]/pT; dptdty = p*p*n[TY]/pT; dptd1p = -pT/p;
1801     stddev = dptd1p*dptd1p*c[CPP] + 2.0*dptdtx*dptdty*c[CTXTY];
1802     stddev+= dptdtx*dptdtx*c[CTXTX] + dptdty*dptdty*c[CTYTY];
1803     stddev+= 2.0*dptd1p*(dptdtx*c[CPTX]+dptdty*c[CPTY]);
1804     stddev = sqrt(stddev);
1805     return stddev;
1806 }
1807
1808 double stddev_Theta(double *n1, double *n2, double *c1, double *c2) {
1809     double stddev=0.0, theta, dtmtx,dtmty, atanx,atany;
1810
1811     atanx = atan(n2[TX])-atan(n1[TX]);
1812     atany = atan(n2[TY])-atan(n1[TY]);
1813     theta = atanx*atanx+atany*atany; theta = sqrt(theta);
1814     dtmtx = atanx/theta; dtmty = atany/theta;
1815

```

```

1816     stddev = dtdtx*dtdtx*(c1[CTXTX]+c2[CTXTX]);
1817     stddev += dtdty*dtdty*(c1[CTYTY]+c2[CTYTY]);
1818     stddev += 2.0*dtdtx*dtdty*(c1[CTXTY]+c2[CTXTY]);
1819
1820     stddev = sqrt(stddev);
1821     return stddev;
1822 }
1823
1824 double eval_eMass(RTRA rtra1, RTRA rtra2) {
1825     double emass=0.0;
1826     if(rtra1.mass>0.0 && rtra2.mass>0.0)
1827         emass = pow(InvMass_PID(rtra1.mass,rtra2.mass,
1828                                 rtra1.n, rtra2.n, rtra1.p, rtra2.p), 2.0) *
1829             pow(stddev_Mass_PID(rtra1.mass,rtra2.mass, rtra1.n, rtra2.n,
1830                                 rtra1.c, rtra2.c, rtra1.p, rtra2.p), 2.0);
1831     else
1832         emass = pow(InvMass(rtra1.n, rtra2.n, rtra1.p, rtra2.p), 2.0) *
1833             pow(stddev_Mass(rtra1.n, rtra2.n, rtra1.c, rtra2.c,
1834                                 rtra1.p, rtra2.p), 2.0);
1835     return sqrt(emass);
1836 }
1837
1838 double stddev_PImp_B0(RTRA r1, RTRA r2, RTRA r3, RTRA r4) {
1839     RTRA mup, mum, pip, pim, Jpsi, KS;
1840     int i, hasmup, hasmum, haspip, haspim;
1841     double ePImp, zB0, zJpsi, zKS, mJpsi, mKS, dmJpsi, dmKS, p,tx,ty;
1842     double P[3], D[3];
1843
1844     hasmup=hasmum=haspip=haspim=0;
1845     if(r1.mass==m_mu && !hasmup && r1.p>0) { mup=r1; hasmup++; }
1846     if(r1.mass==m_mu && !hasmum && r1.p<0) { mum=r1; hasmum++; }
1847     if(r1.mass==m_pi && !haspip && r1.p>0) { pip=r1; haspip++; }
1848     if(r1.mass==m_pi && !haspim && r1.p<0) { pim=r1; haspim++; }
1849     if(r2.mass==m_mu && !hasmup && r2.p>0) { mup=r2; hasmup++; }
1850     if(r2.mass==m_mu && !hasmum && r2.p<0) { mum=r2; hasmum++; }
1851     if(r2.mass==m_pi && !haspip && r2.p>0) { pip=r2; haspip++; }
1852     if(r2.mass==m_pi && !haspim && r2.p<0) { pim=r2; haspim++; }
1853     if(r3.mass==m_mu && !hasmup && r3.p>0) { mup=r3; hasmup++; }
1854     if(r3.mass==m_mu && !hasmum && r3.p<0) { mum=r3; hasmum++; }
1855     if(r3.mass==m_pi && !haspip && r3.p>0) { pip=r3; haspip++; }
1856     if(r3.mass==m_pi && !haspim && r3.p<0) { pim=r3; haspim++; }
1857     if(r4.mass==m_mu && !hasmup && r4.p>0) { mup=r4; hasmup++; }
1858     if(r4.mass==m_mu && !hasmum && r4.p<0) { mum=r4; hasmum++; }
1859     if(r4.mass==m_pi && !haspip && r4.p>0) { pip=r4; haspip++; }
1860     if(r4.mass==m_pi && !haspim && r4.p<0) { pim=r4; haspim++; }
1861
1862     /* bail out if we haven't the dimuon and dipion */
1863     if( hasmup!=1 || hasmum!=1 || haspip!=1 || haspim!=1 ) return -1;
1864
1865     mJpsi = InvMass_PID(mup.mass, mum.mass, mup.n, mum.n, mup.p, mum.p);
1866     mKS   = InvMass_PID(pip.mass, pim.mass, pip.n, pim.n, pip.p, pim.p);
1867     dmJpsi = stddev_Mass_PID(mup.mass, mum.mass, mup.n, mum.n,
1868                             mup.c, mum.c, mup.p, mum.p);
1869     dmKS   = stddev_Mass_PID(pip.mass, pim.mass, pip.n, pim.n,
1870                             pip.c, pim.c, pip.p, pim.p);
1871
1872     /* cut on invariant masses */
1873     if(fabs(mJpsi-m_Jpsi)>0.2 || fabs(mJpsi-m_Jpsi)/dmJpsi>3.0) return -2;
1874     if(fabs(mKS-m_K0)>0.1 || fabs(mKS-m_K0)/dmKS>5.0 ) return -3;
1875     if(posZ('Z',mup,mum)<(rtar.d[Vz]-rtar.s[Vz]) ||
1876         posZ('Z',pip,pim)<(rtar.d[Vz]-rtar.s[Vz]) ||
1877         posZ('Z',pip,pim)<posZ('Z',mup,mum) ) return -4;

```

```

1878
1879 P[Vz] = fabs(mup.p)/sqrt(1.0+mup.n[TX]*mup.n[TX]+mup.n[TY]*mup.n[TY]);
1880 P[Vz] += fabs(mum.p)/sqrt(1.0+mum.n[TX]*mum.n[TX]+mum.n[TY]*mum.n[TY]);
1881 P[Vx] = fabs(mup.p)*mup.n[TX]/sqrt(1.0+mup.n[TX]*mup.n[TX]+mup.n[TY]*mup.n[TY]);
1882 P[Vx] += fabs(mum.p)*mum.n[TX]/sqrt(1.0+mum.n[TX]*mum.n[TX]+mum.n[TY]*mum.n[TY]);
1883 P[Vy] = fabs(mup.p)*mup.n[TY]/sqrt(1.0+mup.n[TX]*mup.n[TX]+mup.n[TY]*mup.n[TY]);
1884 P[Vy] += fabs(mum.p)*mum.n[TY]/sqrt(1.0+mum.n[TX]*mum.n[TX]+mum.n[TY]*mum.n[TY]);
1885 tx = P[Vx]/P[Vz]; ty = P[Vy]/P[Vz];
1886 Jpsi.p = p = sqrt(P[Vz]*P[Vz]+P[Vx]*P[Vx]+P[Vy]*P[Vy]);
1887 D[Vz] = posZ('Z', mup,mum); zJpsi = D[Vz];
1888 D[Vx] = posZ('X', mup,mum);
1889 D[Vy] = posZ('Y', mup,mum);
1890 Jpsi.d[Z]=D[Vz]; Jpsi.d[X]=D[Vx]; Jpsi.d[Y]=D[Vy];
1891 Jpsi.n[TZ]=1.0; Jpsi.n[TX]=tx; Jpsi.d[TY]=ty;
1892 Jpsi.mass = mJpsi; sprintf(Jpsi.PID,"J/psi");
1893 for(i=0;i<Rcovar;i++) Jpsi.c[i]=0.0;
1894 Jpsi.c[CXX]=sqrt(mup.c[CXX])+sqrt(mum.c[CXX]); Jpsi.c[CXX]*=Jpsi.c[CXX];
1895 Jpsi.c[CYY]=sqrt(mup.c[CYY])+sqrt(mum.c[CYY]); Jpsi.c[CYY]*=Jpsi.c[CYY];
1896 Jpsi.c[CXY]=sqrt(fabs(mup.c[CXY]))*Sign(mup.c[CXY]) +
1897 sqrt(fabs(mum.c[CXY]))*Sign(mum.c[CXY]); Jpsi.c[CXY]*=Jpsi.c[CXY];
1898 Jpsi.c[CTXTX]=sqrt(mup.c[CTXTX])+sqrt(mum.c[CTXTX]); Jpsi.c[CTXTX]*=Jpsi.c[CTXTX];
1899 Jpsi.c[CTYTY]=sqrt(mup.c[CTYTY])+sqrt(mum.c[CTYTY]); Jpsi.c[CTYTY]*=Jpsi.c[CTYTY];
1900 Jpsi.c[CPP]=sqrt(mup.c[CPP])+sqrt(mum.c[CPP]); Jpsi.c[CPP]*=Jpsi.c[CPP];
1901
1902 P[Vz] = fabs(pip.p)/sqrt(1.0+pip.n[TX]*pip.n[TX]+pip.n[TY]*pip.n[TY]);
1903 P[Vz] += fabs(pim.p)/sqrt(1.0+pim.n[TX]*pim.n[TX]+pim.n[TY]*pim.n[TY]);
1904 P[Vx] = fabs(pip.p)*pip.n[TX]/sqrt(1.0+pip.n[TX]*pip.n[TX]+pip.n[TY]*pip.n[TY]);
1905 P[Vx] += fabs(pim.p)*pim.n[TX]/sqrt(1.0+pim.n[TX]*pim.n[TX]+pim.n[TY]*pim.n[TY]);
1906 P[Vy] = fabs(pip.p)*pip.n[TY]/sqrt(1.0+pip.n[TX]*pip.n[TX]+pip.n[TY]*pip.n[TY]);
1907 P[Vy] += fabs(pim.p)*pim.n[TY]/sqrt(1.0+pim.n[TX]*pim.n[TX]+pim.n[TY]*pim.n[TY]);
1908 tx = P[Vx]/P[Vz]; ty = P[Vy]/P[Vz];
1909 KS.p = p = sqrt(P[Vz]*P[Vz]+P[Vx]*P[Vx]+P[Vy]*P[Vy]);
1910 D[Vz] = posZ('Z', pip,pim); zKS = D[Vz];
1911 D[Vx] = posZ('X', pip,pim);
1912 D[Vy] = posZ('Y', pip,pim);
1913 KS.d[Z]=D[Vz]; KS.d[X]=D[Vx]; KS.d[Y]=D[Vy];
1914 KS.n[TZ]=1.0; KS.n[TX]=tx; KS.n[TY]=ty;
1915 KS.mass = mKS; sprintf(KS.PID,"K_S0");
1916 for(i=0;i<Rcovar;i++) KS.c[i]=0.0;
1917 KS.c[CXX]=sqrt(mup.c[CXX])+sqrt(mum.c[CXX]); KS.c[CXX]*=KS.c[CXX];
1918 KS.c[CYY]=sqrt(mup.c[CYY])+sqrt(mum.c[CYY]); KS.c[CYY]*=KS.c[CYY];
1919 KS.c[CXY]=sqrt(fabs(mup.c[CXY]))*Sign(mup.c[CXY]) +
1920 sqrt(fabs(mum.c[CXY]))*Sign(mum.c[CXY]); KS.c[CXY]*=KS.c[CXY];
1921 KS.c[CTXTX]=sqrt(mup.c[CTXTX])+sqrt(mum.c[CTXTX]); KS.c[CTXTX]*=KS.c[CTXTX];
1922 KS.c[CTYTY]=sqrt(mup.c[CTYTY])+sqrt(mum.c[CTYTY]); KS.c[CTYTY]*=KS.c[CTYTY];
1923 KS.c[CPP]=sqrt(mup.c[CPP])+sqrt(mum.c[CPP]); KS.c[CPP]*=KS.c[CPP];
1924
1925 /* quick hack: get B0 parameters from J/psi and KS */
1926 zB0 = posZ('Z', Jpsi, KS);
1927 mJpsi = ParamImpact(Jpsi.n,KS.n, Jpsi.d,KS.d);
1928 mKS = stddev_vtxcoord('Z', Jpsi, KS);
1929 tx = PImp3(Jpsi.n,Jpsi.d, KS.n,KS.d, rver1.d, Jpsi.p,KS.p);
1930 ty = stddev_PImp3(Jpsi.n,Jpsi.d, KS.n,KS.d, Jpsi.c,KS.c,
1931 Jpsi.p,KS.p, rver1.d,rver1.c);
1932 ePImp = stddev_ParamImp(Jpsi.n,KS.n, Jpsi.c,KS.c, Jpsi.d,KS.d);
1933 return ePImp; // Units: micrometers.
1934 }
1935
1936 double stddev_vtxcoord(char VTXcoord, RTRA rtra1, RTRA rtra2) {
1937 int i;
1938 const double stdDevZCoord = 0.0280; // VDS plane thickness, in centimeters;
1939 double lambda1=0.0,lambda2=0.0, zS,xS,yS, dzS, dxS, dyS;

```

```

1940 double D[Rcoords], n1[Rdirec], n2[Rdirec], n3[Rdirec];
1941 double N3=0.0, n1n2=0.0, mn1=0.0, mn2=0.0, Dn1=0.0, Dn2=0.0;
1942 double dl1dz1, dl1dx1, dl1dy1, dl1dz2, dl1dx2, dl1dy2;
1943 double dl1dtx1, dl1dty1, dl1dtx2, dl1dty2;
1944 double dl2dz1, dl2dx1, dl2dy1, dl2dz2, dl2dx2, dl2dy2;
1945 double dl2dtx1, dl2dty1, dl2dtx2, dl2dty2;
1946 double dzdz1, dzdz2, dzdx1, dzdx2, dzdy1, dzdy2;
1947 double dzdtx1, dzdty1, dzdtx2, dzdty2;
1948 double dxdz1, dxdz2, dxdx1, dxdx2, dxdy1, dxdy2;
1949 double dxdtx1, dxdtty1, dxdtx2, dxdtty2;
1950 double dydz1, dydz2, dydx1, dydx2, dydy1, dydy2;
1951 double dydtx1, dydty1, dydtx2, dydty2;
1952
1953 for(i=0; i<Rcoords; i++) D[i] = rtra2.d[i] - rtra1.d[i];
1954 for(i=0; i<Rdirec; i++)
1955 { mn1 += rtra1.n[i]*rtra1.n[i]; mn2 += rtra2.n[i]*rtra2.n[i]; }
1956 mn1 = sqrt(mn1); mn2 = sqrt(mn2);
1957 for(i=0; i<Rdirec; i++) { n1[i] = rtra1.n[i]/mn1; n2[i] = rtra2.n[i]/mn2; }
1958 n1n2 = n1[TZ]*n2[TZ] + n1[TX]*n2[TX] + n1[TY]*n2[TY];
1959 Dn1 = D[Z]*n1[TZ] + D[X]*n1[TX] + D[Y]*n1[TY];
1960 Dn2 = D[Z]*n2[TZ] + D[X]*n2[TX] + D[Y]*n2[TY];
1961 n3[TZ] = n1[TX]*n2[TY] - n1[TY]*n2[TX];
1962 n3[TX] = n1[TY]*n2[TZ] - n1[TZ]*n2[TY];
1963 n3[TY] = n1[TZ]*n2[TX] - n1[TX]*n2[TZ];
1964 for(i=0; i<Rdirec; i++) N3 += n3[i]*n3[i]; N3 = sqrt(N3);
1965 if(N3 != 0.0) {
1966     for(i=0; i<Rdirec; i++) n3[i]/=N3;
1967     lambda1 += (D[X]*n2[TY]-D[Y]*n2[TX]) * n3[TZ]/N3;
1968     lambda1 += (D[Y]*n2[TZ]-D[Z]*n2[TY]) * n3[TX]/N3;
1969     lambda1 += (D[Z]*n2[TX]-D[X]*n2[TZ]) * n3[TY]/N3;
1970     lambda2 += (D[X]*n1[TY]-D[Y]*n1[TX]) * n3[TZ]/N3;
1971     lambda2 += (D[Y]*n1[TZ]-D[Z]*n1[TY]) * n3[TX]/N3;
1972     lambda2 += (D[Z]*n1[TX]-D[X]*n1[TZ]) * n3[TY]/N3;
1973 }
1974
1975 /* derivadas de lambda1 */
1976 dl1dz2 = (n1[TZ]-n1n2*n2[TZ])/(N3*N3);
1977 dl1dx2 = (n1[TX]-n1n2*n2[TX])/(N3*N3);
1978 dl1dy2 = (n1[TY]-n1n2*n2[TY])/(N3*N3);
1979 dl1dz1 = -dl1dz2; dl1dx1 = -dl1dx2; dl1dy1 = -dl1dy2;
1980 dl1dtx1 = (mn2*D[X]-n2[TX]*Dn2)/(mn1*mn2*N3*N3) - lambda1*n1[TX]/(mn1*mn1)
1981           - 2.0*lambda1*(n2[TY]*n3[TZ]-n3[TY])/N3;
1982 dl1dty1 = (mn2*D[Y]-n2[TY]*Dn2)/(mn1*mn2*N3*N3) - lambda1*n1[TY]/(mn1*mn1)
1983           + 2.0*lambda1*(n2[TX]*n3[TZ]-n3[TX])/N3;
1984 dl1dtx2 = -n1n2*(mn2*D[X]-2.0*n2[TX]*Dn2)/(mn2*mn2*N3*N3)
1985           - (Dn2/(N3*N3))*n1[TX]/(mn1*mn2) + 2.0*lambda1*(n1[TY]*n3[TZ]-n3[TY])/N3;
1986 dl1dty2 = -n1n2*(mn2*D[Y]-2.0*n2[TY]*Dn2)/(mn2*mn2*N3*N3)
1987           - (Dn2/(N3*N3))*n1[TY]/(mn1*mn2) - 2.0*lambda1*(n1[TX]*n3[TZ]-n3[TX])/N3;
1988
1989 /* derivadas de lambda2 */
1990 dl2dz2 = (n2[TZ]-n1n2*n1[TZ])/(N3*N3);
1991 dl2dx2 = (n2[TX]-n1n2*n1[TX])/(N3*N3);
1992 dl2dy2 = (n2[TY]-n1n2*n1[TY])/(N3*N3);
1993 dl2dz1 = -dl2dz2; dl2dx1 = -dl2dx2; dl2dy1 = -dl2dy2;
1994 dl2dtx1 = n1n2*(mn1*D[X]-2.0*n1[TX]*Dn1)/(mn1*mn1*N3*N3)
1995           + (Dn1/(N3*N3))*n2[TX]/(mn1*mn2) - 2.0*lambda2*(n2[TY]*n3[TZ]-n3[TY])/N3;
1996 dl2dty1 = n1n2*(mn1*D[Y]-2.0*n1[TY]*Dn1)/(mn1*mn1*N3*N3)
1997           + (Dn1/(N3*N3))*n2[TY]/(mn1*mn2) + 2.0*lambda2*(n2[TX]*n3[TZ]-n3[TX])/N3;
1998 dl2dtx2 = -(mn1*D[X]-n1[TX]*Dn1)/(mn1*mn2*N3*N3) - lambda2*n2[TX]/(mn2*mn2)
1999           + 2.0*lambda2*(n1[TY]*n3[TZ]-n3[TY])/N3;
2000 dl2dty2 = -(mn1*D[Y]-n1[TY]*Dn1)/(mn1*mn2*N3*N3) - lambda2*n2[TY]/(mn2*mn2)
2001           - 2.0*lambda2*(n1[TX]*n3[TZ]-n3[TX])/N3;

```

```

2002
2003 /* derivadas da coordenada z do vertice */
2004 dzdz1 = dl1dz1/mn1 + dl2dz1/mn2; dzdz1 += 1.0;
2005 dzdz2 = dl1dz2/mn1 + dl2dz2/mn2; dzdz2 += 1.0;
2006 dzdx1 = dl1dx1/mn1 + dl2dx1/mn2;
2007 dzdy1 = dl1dy1/mn1 + dl2dy1/mn2;
2008 dzdx2 = dl1dx2/mn1 + dl2dx2/mn2;
2009 dzdy2 = dl1dy2/mn1 + dl2dy2/mn2;
2010 dzdtx1 = (mn1*dl1dtx1 - lambda1*n1[TX]/mn1)/(mn1*mn1) + dl2dtx1/mn2;
2011 dzdty1 = (mn1*dl1dty1 - lambda1*n1[TY]/mn1)/(mn1*mn1) + dl2dty1/mn2;
2012 dzdtx2 = dl1dtx2/mn1 + (mn2*dl2dtx2 - lambda2*n2[TX]/mn2)/(mn2*mn2);
2013 dzdty2 = dl1dty2/mn1 + (mn2*dl2dty2 - lambda2*n2[TY]/mn2)/(mn2*mn2);
2014 dzdz1*=0.5; dzdz2*=0.5; dzdx1*=0.5; dzdx2*=0.5; dzdy1*=0.5; dzdy2*=0.5;
2015 dzdtx1*=0.5; dzdty1*=0.5; dzdtx2*=0.5; dzdty2*=0.5;
2016
2017 /* derivadas da coordenada x do vertice */
2018 dxdz1 = n1[TX]*dl1dz1/mn1 + n2[TX]*dl2dz1/mn2;
2019 dxdz2 = n1[TX]*dl1dz2/mn1 + n2[TX]*dl2dz2/mn2;
2020 dxdx1 = n1[TX]*dl1dx1/mn1 + n2[TX]*dl2dx1/mn2; dxdx1 += 1.0;
2021 dxdy1 = n1[TX]*dl1dy1/mn1 + n2[TX]*dl2dy1/mn2; dxdx2 += 1.0;
2022 dxdx2 = n1[TX]*dl1dx2/mn1 + n2[TX]*dl2dx2/mn2;
2023 dxdy2 = n1[TX]*dl1dy2/mn1 + n2[TX]*dl2dy2/mn2;
2024 dxdtx1 = (n1[TX]*mn1*dl1dtx1 - lambda1*n1[TX]*n1[TX]/mn1)/(mn1*mn1) + n2[TX]*dl2dtx1/mn2;
2025 dxdty1 = (n1[TX]*mn1*dl1dty1 - lambda1*n1[TX]*n1[TY]/mn1)/(mn1*mn1) + n2[TX]*dl2dty1/mn2;
2026 dxdtx2 = (n2[TX]*mn2*dl2dtx2 - lambda2*n2[TX]*n2[TX]/mn2)/(mn2*mn2) + n1[TX]*dl1dtx2/mn1;
2027 dxdty2 = (n2[TX]*mn2*dl2dty2 - lambda2*n2[TX]*n2[TY]/mn2)/(mn2*mn2) + n1[TX]*dl1dty2/mn1;
2028 dxdtx1+= lambda1/mn1;
2029 dxdz1*=0.5; dxdz2*=0.5; dxdx1*=0.5; dxdx2*=0.5; dxdy1*=0.5; dxdy2*=0.5;
2030 dxdtx1*=0.5; dxdty1*=0.5; dxdtx2*=0.5; dxdty2*=0.5;
2031
2032 /* derivadas da coordenada y do vertice */
2033 dydz1 = n1[TY]*dl1dz1/mn1 + n2[TY]*dl2dz1/mn2;
2034 dydz2 = n1[TY]*dl1dz2/mn1 + n2[TY]*dl2dz2/mn2;
2035 dydx1 = n1[TY]*dl1dx1/mn1 + n2[TY]*dl2dx1/mn2;
2036 dydy1 = n1[TY]*dl1dy1/mn1 + n2[TY]*dl2dy1/mn2;
2037 dydx2 = n1[TY]*dl1dx2/mn1 + n2[TY]*dl2dx2/mn2; dydx1 += 1.0;
2038 dydy2 = n1[TY]*dl1dy2/mn1 + n2[TY]*dl2dy2/mn2; dydx2 += 1.0;
2039 dydtx1 = (n1[TY]*mn1*dl1dtx1 - lambda1*n1[TY]*n1[TX]/mn1)/(mn1*mn1) + n2[TY]*dl2dtx1/mn2;
2040 dydty1 = (n1[TY]*mn1*dl1dty1 - lambda1*n1[TY]*n1[TY]/mn1)/(mn1*mn1) + n2[TY]*dl2dty1/mn2;
2041 dydtx2 = (n2[TY]*mn2*dl2dtx2 - lambda2*n2[TY]*n2[TX]/mn2)/(mn2*mn2) + n1[TY]*dl1dtx2/mn1;
2042 dydty2 = (n2[TY]*mn2*dl2dty2 - lambda2*n2[TY]*n2[TY]/mn2)/(mn2*mn2) + n1[TY]*dl1dty2/mn1;
2043 dydty2+= lambda2/mn2;
2044 dydz1*=0.5; dydz2*=0.5; dydx1*=0.5; dydx2*=0.5; dydy1*=0.5; dydy2*=0.5;
2045 dydtx1*=0.5; dydty1*=0.5; dydtx2*=0.5; dydty2*=0.5;
2046
2047 dzS = dxS = dyS = 0.0;
2048
2049 /* dzS = variancia da coordenada Z do vertice */
2050 dzS += dzdx1*dzdy1*rtra1.c[CXY] + dzdx2*dzdy2*rtra2.c[CXY];
2051 dzS += dzdtx1*dzdty1*rtra1.c[CTXTY] + dzdtx2*dzdty2*rtra2.c[CTXTY];
2052 dzS += dzdx1*(dzdtx1*rtra1.c[CTX] + dzdty1*rtra1.c[CXTY]);
2053 dzS += dzdy1*(dzdtx1*rtra1.c[CYTX] + dzdty1*rtra1.c[CYTY]);
2054 dzS += dzdx2*(dzdtx2*rtra2.c[CTX] + dzdty2*rtra2.c[CXTY]);
2055 dzS += dzdy2*(dzdtx2*rtra2.c[CYTX] + dzdty2*rtra2.c[CYTY]);
2056 dzS ** 2.0;
2057 dzS += (dzdz1*dzdz1 + dzdz2*dzdz2)*stdDevZCoord*stdDevZCoord;
2058 dzS += dzdx1*dzdx1*rtra1.c[CXX] + dzdy1*dzdy1*rtra1.c[CYY];
2059 dzS += dzdtx1*dzdtx1*rtra1.c[CTXTX] + dzdty1*dzdty1*rtra1.c[CTYTY];
2060 dzS += dzdx2*dzdx2*rtra2.c[CXX] + dzdy2*dzdy2*rtra2.c[CYY];
2061 dzS += dzdtx2*dzdtx2*rtra2.c[CTXTX] + dzdty2*dzdty2*rtra2.c[CTYTY];
2062
2063 /* dxS = variancia da coordenada X do vertice */

```

```

2064     dxS += dxdx1*dxdy1*rtra1.c[CXY] + dxdx2*dxdy2*rtra2.c[CXY];
2065     dxS += dxdtx1*dxdtx1*rtra1.c[CTXTY] + dxdtx2*dxdtx2*rtra2.c[CTXTY];
2066     dxS += dxdx1*(dxdtx1*rtra1.c[CXTX] + dxdtx1*rtra1.c[CXTY]);
2067     dxS += dxdy1*(dxdtx1*rtra1.c[CYTX] + dxdtx1*rtra1.c[CYTY]);
2068     dxS += dxdx2*(dxdtx2*rtra2.c[CXTX] + dxdtx2*rtra2.c[CXTY]);
2069     dxS += dxdy2*(dxdtx2*rtra2.c[CYTX] + dxdtx2*rtra2.c[CYTY]);
2070     dxS *= 2.0;
2071     dxS += (dxdz1*dxdz1 + dxdz2*dxdz2)*stdDevZCoord*stdDevZCoord;
2072     dxS += dxdx1*dxdx1*rtra1.c[CXX] + dxdy1*dxdy1*rtra1.c[CYY];
2073     dxS += dxdtx1*dxdtx1*rtra1.c[CTXTX] + dxdtx1*dxdtx1*rtra1.c[CTYTY];
2074     dxS += dxdx2*dxdx2*rtra2.c[CXX] + dxdy2*dxdy2*rtra2.c[CYY];
2075     dxS += dxdtx2*dxdtx2*rtra2.c[CTXTX] + dxdtx2*dxdtx2*rtra2.c[CTYTY];
2076
2077     /* dyS = variancia da coordenada Y do vertice */
2078     dyS += dydx1*dydy1*rtra1.c[CXY] + dydx2*dydy2*rtra2.c[CXY];
2079     dyS += dydtx1*dydtx1*rtra1.c[CTXTY] + dydtx2*dydtx2*rtra2.c[CTXTY];
2080     dyS += dydx1*(dydtx1*rtra1.c[CXTX] + dydtx1*rtra1.c[CXTY]);
2081     dyS += dydy1*(dydtx1*rtra1.c[CYTX] + dydtx1*rtra1.c[CYTY]);
2082     dyS += dydx2*(dydtx2*rtra2.c[CXTX] + dydtx2*rtra2.c[CXTY]);
2083     dyS += dydy2*(dydtx2*rtra2.c[CYTX] + dydtx2*rtra2.c[CYTY]);
2084     dyS *= 2.0;
2085     dyS += (dydz1*dydz1 + dydz2*dydz2)*stdDevZCoord*stdDevZCoord;
2086     dyS += dydx1*dydx1*rtra1.c[CXX] + dydy1*dydy1*rtra1.c[CYY];
2087     dyS += dydtx1*dydtx1*rtra1.c[CTXTX] + dydtx1*dydtx1*rtra1.c[CTYTY];
2088     dyS += dydx2*dydx2*rtra2.c[CXX] + dydy2*dydy2*rtra2.c[CYY];
2089     dyS += dydtx2*dydtx2*rtra2.c[CTXTX] + dydtx2*dydtx2*rtra2.c[CTYTY];
2090
2091     /* retorna o "standard deviation" da coordenada VTXcoord */
2092     switch((int)VTXcoord) {
2093         case 'Z': return sqrt(dzS); break;
2094         case 'X': return sqrt(dxS); break;
2095         case 'Y': return sqrt(dyS); break;
2096         default: return 0.0; break;
2097     }
2098     return 0.0;
2099 }
2100
2101 /* ////////////////////////////////////// THE-END ////////////////////////////////////// */

```

E.2 Geometry misalignment

The list below is the source code used in ARTE to simulate detector misalignment. It is based on an original inception by Dmitri Goloubkov (HERA-*B*), and it is supposed to compile with ARTE and run at its initiation, i.e. inside the routine `usinit()`. The user should then call the necessary event reconstruction routines to fill the ARTE tables with the reconstruction elements (segments, tracks, vertices) from the digitized hits (which themselves are dragged with the displaced detector elements) — see figure 3.40.

```

1  #include <unistd.h>
2  #include <iostream.h>
3  #include <iomanip.h>
4  #include <vector.h>
5  #include "arte/arte.hh"

```

```

6
7 int remaskNEDEgeom(int option) {
8 // static int AlreadyRan = 0;
9   const char *NEDEfname = "NEDEfile.txt";
10  const float LEN = 1.00;
11  FILE *NEDEfile;
12  int iidx, idx = 0, numcomp = 0, found = 0, cmp, lay, sec, shp;
13  float xmin, xmax, ymin, ymax, zmin, zmax;
14  float sxmn, sxmx, symn, symx, cos, sin;
15  ArteTableIterator<HITB> hitb;
16  ArteTableIterator<HITC> hitc;
17  ArteTableIterator<NEDE> nede;
18  ArteTableIterator<GEDE> gede;
19  ArtePointer<GESL> gesl;
20  ArtePointer<NESL> nesl;
21  int isGESLchanged[128], isNESLchanged[128];
22
23  for(idx=0; idx<128; idx++) isGESLchanged[idx] = isNESLchanged[idx] = 0;
24
25  cout << "remaskGEDEgeom: Started, input file mask is '" << NEDEfname << "'";
26  cout << endl;
27
28  NEDEfile = fopen(NEDEfname,"r");
29  if(!NEDEfile)
30  { cout << "Could not open '" << NEDEfname << "'!" << endl; return -1; }
31
32  nede = ArteTable<NEDE>::begin();
33  if(!(nede->cmp)) {
34    cout << "Seems NEDE table is empty (method 1), nothing changed." << endl;
35    return -2;
36  }
37  nede = ArteTable<NEDE>::end();
38  cout << "Table NEDE has " << nede.index() << " entries." << endl;
39
40  while(!feof(NEDEfile)) {
41    fscanf(NEDEfile, "%i%i%i%f%f%f%f%f%f%f%f%f%i",
42           &cmp, &lay, &sec, &shp,
43           &xmin, &xmax, &ymin, &ymax, &zmin, &zmax,
44           &sxmn, &sxmx, &symn, &symx, &cos, &sin, &idx);
45    found = 0;
46    iidx=idx;
47    for(gede = ArteTable<GEDE>::begin();
48       gede != ArteTable<GEDE>::end(); ++gede) {
49      if(gede.index() != idx) continue;
50      if(gede->cmp != cmp || gede->lay != lay ||
51         gede->sec != sec || gede->shp != shp) continue;
52      gesl = gede->gesl;
53      if(option==0) { /* -- OPTION 0: only geometry is changed -- */
54         gede->xmin += xmin;      gede->xmax += xmax;
55         gede->ymin += ymin;      gede->ymax += ymax;
56         gede->zmin += zmin;      gede->zmax += zmax;
57         gede->sxmn += sxmn;     gede->sxmx += sxmx;
58         gede->symn += symn;     gede->symx += symx;
59         gede->sin += sin;       gede->cos += cos;
60         idx = (int)gesl.index();
61         if(isGESLchanged[idx]>0) continue;
62         else isGESLchanged[idx]++;
63         gesl->x1 += xmin;        gesl->x2 += xmax;
64         gesl->y1 += ymin;        gesl->y2 += ymax;
65         gesl->z1 += zmin;        gesl->z2 += zmax;
66         for(ArteTableIterator<GWAL> gwal = ArteTable<GWAL>::begin();
67            gwal != ArteTable<GWAL>::end(); ++gwal) {

```

```

68         if(gwal->gesl != gesl) continue;
69         gwal->xmin += xmin;         gwal->xmax += xmax;
70         gwal->ymin += ymin;         gwal->ymax += ymax;
71         gwal->zmin += zmin;         gwal->zmax += zmax;
72     }
73     } else if(option==1) { /* OPTION 1: only hits are changed */
74         for(hitb = ArteTable<HITB>::begin();
75             hitb != ArteTable<HITB>::end() ; ++hitb) {
76             if(hitb->gede == idx) {
77                 hitb->z += ((zmin+zmax)/2.0);
78                 // hitb->x += ((xmin+xmax)/2.0);
79                 // hitb->y += ((ymin+ymax)/2.0);
80             }
81         }
82     }
83 }
84 numcomp++;
85
86 /* --- NEDE table */
87 found = 0;
88 for(nede = ArteTable<NEDE>::begin();
89     nede != ArteTable<NEDE>::end(); ++nede) {
90     if(nede.index() != iidx) continue;
91     if(nede->cmp != cmp || nede->lay != lay ||
92         nede->sec != sec || nede->shp != shp) continue;
93     if(option==0) {
94         nede->xmin += xmin;         nede->xmax += xmax;
95         nede->ymin += ymin;         nede->ymax += ymax;
96         nede->zmin += zmin;         nede->zmax += zmax;
97         nede->sxmn += sxmn;         nede->sxmx += sxmx;
98         nede->symn += symn;         nede->symx += symx;
99         nede->sin += sin ;         nede->cos += cos ;
100     nesl = nede->nesl;
101     idx = (int)nesl.index();
102     if(isNESLchanged[idx]>0) continue;
103     else isNESLchanged[idx]++;
104     nesl->x1 += xmin;         nesl->x2 += xmax;
105     nesl->y1 += ymin;         nesl->y2 += ymax;
106     nesl->z1 += zmin;         nesl->z2 += zmax;
107     for(ArteTableIterator<NWAL> nwal = ArteTable<NWAL>::begin();
108         nwal != ArteTable<NWAL>::end(); ++nwal) {
109         if(nwal->nesl != nesl) continue;
110         nwal->xmin += xmin;         nwal->xmax += xmax;
111         nwal->ymin += ymin;         nwal->ymax += ymax;
112         nwal->zmin += zmin;         nwal->zmax += zmax;
113     }
114 }
115 }
116 /* --- NEDE table */
117
118 }
119
120 fclose(NEDEfile);
121 cout << "Finished reading '" << NEDEfname << "', " ;
122 cout << numcomp << " entries in table NEDE/GEDE were changed" << endl;
123 return numcomp;
124 }
125 /* -- end of routine remaskNEDEgeom() -- */
126

```

Bibliography

- [1] ABT, I. and OTHERS (HERA-*B* COLLABORATION), “HERA-*B*: Report on status and prospects,” *DESY Physics Research Committee report*, no. DESY-PRC 00-04, 2000.
- [2] ABT, I. and OTHERS (HERA-*B* COLLABORATION), “Measurement of the $b\bar{b}$ production cross section at HERA-*B* with the 2000 data sample,” *HERA-*B* internal note*, no. HERA-B 02-005, 2002.
- [3] ABT, I. and OTHERS (HERA-*B* COLLABORATION), “Inclusive V^0 production cross sections from 920GeV fixed target proton-nucleus collisions,” *European Physics Journal*, vol. C29, pp. 181–190, 2003. Preprint: hep-ex/0212040. Detailed report in DESY 02-213.
- [4] ABT, I. and OTHERS (HERA-*B* COLLABORATION), “ J/ψ production via χ_c decays in 920GeV pA interactions,” *Physics Letters*, vol. B561, pp. 61–72, 2003. Preprint: hep-ex/0211033. Detailed report in DESY 02-187.
- [5] ABT, I. and OTHERS (HERA-*B* COLLABORATION), “Measurement of the $b\bar{b}$ production cross-section in 920GeV fixed target proton-nucleus collisions,” *European Physics Journal*, vol. C26, pp. 345–355, 2003. Preprint: hep-ex/0205106. Detailed report in DESY 02-076.
- [6] ABT, I. and OTHERS (HERA-*B* COLLABORATION), “Limits for the central production of Θ^+ and Ξ^{--} pentaquarks in 920GeV pA collisions,” *Physical Review Letters*, vol. 93, no. 21, pp. 212003–1, 2004. Preprint: hep-ex/0408048.
- [7] ABT, I. and OTHERS (HERA-*B* COLLABORATION), “Search for the flavour-changing neutral current decay $D^0 \rightarrow \mu^+\mu^-$ with the HERA-*B* detector,” *Physics Letters B*, vol. 596, pp. 173–183, 2004. Preprint: hep-ex/0405059.
- [8] ABT, I., EMELIYANOV, D., KISEL, I., and MASCIOCCHI, S., “CATS: a cellular automaton for tracking in silicon for the HERA-*B* vertex detector,” *Nuclear Instruments and Methods in Physics Research*, vol. A489, pp. 389–405, 2002.
- [9] ACOSTA, D. E. A. C., “Search for the flavour-changing neutral current decay $D^0 \rightarrow \mu^+\mu^-$ in $p\bar{p}$ collisions at $\sqrt{s} = 1.96\text{TeV}$,” *Physical Review D*, vol. 68, p. 091101, 2003.
- [10] ADLER, S. *Physical Review*, vol. 177, pp. 2426–2438, 1969.

- [11] ALBRECHT, H. and OTHERS, *An Experiment to study CP Violation in the B System Using an Internal Target at the HERA Proton Ring – Letter of Intent*, 1992.
- [12] ALBRECHT, H. and OTHERS, “ARTE – the event reconstruction and analysis tool for HERA-B,” *HERA-B internal note*, no. HERA-B 95-065, 1995.
http://www-hera-b.desy.de/subgroup/software/arte/arte_manual.ps.
- [13] AMARAL, V., “The role of databases in high energy physics – the HERA-B case study,” *HERA-B internal note*, no. HERA-B 03-023, 2003.
- [14] AMARAL, V., SILVA, L., AMORIM, A., and BATISTA, J., “Standard multi-tier software technologies for HEP solutions,” *HERA-B internal note*, no. HERA-B 02-045, 2002. Also:
<http://kdataserv.fis.fc.ul.pt/~lsilva/nota/>.
- [15] AMARAL, V., SILVA, L., and BATISTA, J., “Mizzi database servers size in the on-line machines,” 2002.
<http://www-hera-b.desy.de/subgroup/software/database/statistics/ServersSize.html>.
- [16] AMORIM, A., AMARAL, V., and OTHERS, “The HERA-B database services for detector configuration, calibration, alignment, slow control and data classification,” in *Computing in High Energy and Nuclear Physics (CHEP 2000): Proceedings* (MAZZUCATO, M. and MICHELOTTO, M., eds.), vol. 140, pp. 469–472, 2000. Prepared for the International Conference for Computing in High Energy Physics and Nuclear Physics (CHEP 2000), Padova, Italy, 7-11 Feb 2000. http://chep2000.pd.infn.it/abst/abs_c252.htm.
- [17] AMORIM, A., AMARAL, V., and OTHERS, “The HERA-B database services for detector configuration, calibration, alignment, slow control and data classification,” *Computer Physics Communications*, vol. 140, pp. 172–178, 2001.
- [18] ANDERSON, C. D., “The positive electron,” *Physical Review*, vol. 43, pp. 491–494, 1933.
- [19] ARIÑO, I. and OTHERS, “The HERA-B ring imaging Čerenkov counter,” *Nuclear Instruments and Methods in Physics Research*, vol. A516, pp. 445–461, 2004. Preprint: hep-ex/0303012.
- [20] BABAR COLLABORATION (AUBERT, B. and OTHERS), “Direct $\hat{C}\hat{P}$ violating asymmetry in $B^0 \rightarrow K^+\pi^-$ decays,” *Physical Review Letters*, vol. 93, p. 131801, 2004. Preprint: hep-ex/0407057.
- [21] BARGER, V. D. and PHILLIPS, R. J. N., *Collider Physics*. Addison–Wesley, updated ed., 1996.
- [22] BARGIOTTI, M. and OTHERS, “Present knowledge of the Cabibbo–Kobayashi–Maskawa matrix,” *Rivista del Nuovo Cimento*, vol. 23, no. 3, pp. 1–72, 2000. Preprints: hep-ph/0001293, HERA-B 00-012.
- [23] BASTOS, J., *Medida da luminosidade e da fracção de decaimentos muónicos do mesão $\omega(782)$ em colisões protão-núcleo de alvo fixo*. PhD thesis, University of Coimbra, 2002. In Portuguese.

- [24] BATISTA, J., “Comportamento de programas que usam MIZZI perante a saturação do espaço no disco,” 2001. In Portuguese.
<http://kdataserv.fis.fc.ul.pt/~jbatista/rpmdbserver/nofree.ps.gz>.
- [25] BATISTA, J., “Monitoring pedestals and noise of the HERA-*B* vertex detector system,” 2001. DESY Summer Student Program.
<http://kdataserv.fis.fc.ul.pt/~jbatista/desysummer2001/VDSreport.ps.gz>.
- [26] BATISTA, J., “Performance do servidor rpmdbserver nos modos single-threaded e multi-threaded,” 2001. In Portuguese.
<http://kdataserv.fis.fc.ul.pt/~jbatista/rpmdbserver/dbmulti.ps.gz>.
- [27] BATISTA, J., “Keyreleases, keytables and all that stuff,” 2002.
<http://www.desy.de/~jbatista/keythings.ps.gz>.
- [28] BELL, J. S. and JACKIW, R. *Il Nuovo Cimento A*, vol. 60, pp. 47–60, 1969.
- [29] BENECKE, W., “Ergebnis der einmessung nach justierung im strahl vom 12.06.2001,” 2001. In HERA-*B* internal note (Excel spreadsheet) by J. Spengler.
- [30] “Sleepycat software homepage.” <http://www.sleepycat.com/>.
- [31] BIGI, I., “CP violation – an essential mystery in nature’s grand design,” in Kaidalov and Vysotsky [94]. Preprint: hep-ph/9712475.
- [32] BIGI, I. and SANDA, A., *CP Violation*. Cambridge University Press, 1999.
- [33] BOCK, R. and OTHERS, “HIGZ users guide,” *CERN Program Library*, no. Q120, 1991. CERN.
- [34] BOCK, R. K. and VASILESCU, A., *The Particle Detector BriefBook*. Springer, 1998.
- [35] BRANCO, C. C., *Amor de perdição*. 1861. In Portuguese. Title translation: “Doomed love”. Available online at
<http://www.biblio.com.br/templates/camilocastelobranco/mamorperdicaox.htm>.
- [36] BRANCO, G. C., LAVOURA, L., and SILVA, J. P., *CP Violation*. Clarendon Press, Oxford, 1999.
- [37] BRUN, R. and RADEMAKERS, F., “ROOT – an object oriented data analysis framework,” *Nuclear Instruments and Methods in Physics Research*, vol. A389, pp. 81–86, 1997. See also <http://root.cern.ch/>.
- [38] BRÄUER, M., *Die Alignierung des HERA-*B* Vertexdetektors*. PhD thesis, Ruprecht-Karls University of Heidelberg, 2001.
- [39] BULTEN, H. J., “Lecture notes in particle astrophysics,” 2001.
<http://www.nikhef.nl/~henkjan/>.
- [40] BURCHAM, W. E. and JOBES, M., *Nuclear and Particle Physics*. Longman Scientific & Technical, 1995.

- [41] CABIBBO, N., “Unitarity symmetry and leptonic decays,” *Physical Review Letters*, vol. 10, pp. 531–532, 1963.
- [42] CHRISTENSON, J. H., CRONIN, J. W., VITCH, V. L., and TURLAY, R., “Evidence for the 2π decay of the K_2^0 meson,” *Physical Review Letters*, vol. 13, pp. 138–140, 1964.
- [43] CLARKSON, M., “DOE-Maxima reference manual.” <http://starship.python.net/crew/mike/>. Program homepage: <http://maxima.sourceforge.net/>.
- [44] HERA-B COLLABORATION, “Status and plans for 2001/2,” *HERA-B internal note*, no. HERA-B 01-064, 2001.
- [45] HERA-B COLLABORATION (BAUER, T., DANILOV, M., MEDINNIS, M., ZOCCOLI, A., and OTHERS), “Plans for HERA-B after the shutdown 2003,” *HERA-B internal note*, 2002.
- [46] DEYANOVA, G.
<http://www-hera-b.desy.de/subgroup/software/database/newsite/analysis.html>.
- [47] DIRAC, P. A. M., “The quantum theory of the electron,” *Proceedings of the Royal Society (London) A*, vol. 117, pp. 610–612, 1928.
- [48] DOLGOV, A. D., “Non-GUT baryogenesis,” *Physics Reports*, vol. 222, pp. 309–386, 1992.
- [49] DOLGOV, A. D., “Baryogenesis, 30 years after,” in Kaidalov and Vysotsky [94]. Preprint: hep-ph/9707419.
- [50] DUJMIĆ, D., *Open charm production at HERA-B*. PhD thesis, University of Texas at Austin, 2001.
- [51] EHRET, K., “Time structure of HERA-B target IA and coasting beam,” *HERA-B internal note*, no. HERA-B 00-092, 2000.
- [52] EIDELMAN, S. and OTHERS, “Review of particle physics,” *Physics Letters B*, vol. 592, pp. 1+, 2004.
- [53] EISELE, F. and HAUSMANN, S., “The MSGC,” 1997.
http://www1.physi.uni-heidelberg.de/~eisele/MSGC_Introduction.html.
- [54] ELLIS, R. K., STIRLING, W. J., and WEBBER, B. R., *QCD and Collider Physics*. Cambridge University Press, 1996.
- [55] EMELIYANOV, D. and OTHERS, “Grover,” 2001.
<http://www-hera-b.desy.de/subgroup/software/arte/grover/grover.ps.gz>.
- [56] EMELIYANOV, D. and KISEL, I., “CATS track fitting algorithm based on the discrete Kalman filter,” *HERA-B internal note*, no. HERA-B 00-032, 2000.
- [57] FARRAR, G. R. and SHAPOSHNIKOV, M. E., “Baryon asymmetry of the universe in the minimal standard model,” *Physical Review Letters*, vol. 70, p. 2833, 1993.

- [58] FARRAR, G. R. and SHAPOSHNIKOV, M. E., “Baryon asymmetry of the universe in the standard model,” *Physical Review D*, vol. 50, p. 774, 1994.
- [59] FARRAR, G. R., “CP violation and the baryonic asymmetry of the universe,” *Nuclear Physics B - Proceedings Supplements*, vol. 43, pp. 312–332, 1995. Preprint: hep-ph/9502327.
- [60] FEYNMAN, R. P., “The theory of positrons,” *Physical Review*, vol. 76, pp. 749–759, 1948.
- [61] FEYNMAN, R. P., “Very high energy collisions of hadrons,” *Physical Review Letters*, vol. 23, p. 1415, 1969.
- [62] FIELDS, B. D. and SARKAR, S., “Big-Bang nucleosynthesis,” in Hagiwara *et al.* [81], ch. 19, pp. 1–11.
- [63] FOMINYKH, B. and NOWAK, S., “HERA-*B* muon detector in HBGEAN,” *HERA-*B* internal note*, no. HERA-B 97-075, 1997.
- [64] FRIXIONE, S., MANGANO, M. L., NASON, P., and RIDOLFI, G., “Charm and bottom production: theoretical results versus experimental data,” *Nuclear Physics*, vol. B431, pp. 453–483, 1994. Preprint: CERN-TH 7292/94.
- [65] FRÜHWIRTH, R., “Application of Kalman filtering to track and vertex fitting,” *Nuclear Instruments and Methods in Physics Research*, vol. A262, pp. 444–450, 1987.
- [66] GARDNER, M., “The fantastic combinations of John Conway’s new solitaire Game of ‘Life’,” *Scientific American*, vol. 223, no. 4, pp. 120–123, 1970.
- [67] GAVELA, M. B., HÉRNANDEZ, P., ORLOFF, J., and PÈNE, O., “Standard model CP-violation and baryon asymmetry,” *Modern Physics Letters A*, vol. 9, p. 795, 1994.
- [68] GAVELA, M. B., HÉRNANDEZ, P., ORLOFF, J., PÈNE, O., and QUIMBAY, C., “Standard model CP-violation and baryon asymmetry. Part II: Finite temperature,” *Nuclear Physics B*, vol. 430, pp. 382–426, 1994.
- [69] GAVELA, M. B., LOZANO, M., ORLOFF, J., and PÈNE, O., “Standard model CP-violation and baryon asymmetry. Part I: Zero temperature,” *Nuclear Physics B*, vol. 430, pp. 345–381, 1994.
- [70] “GEANT – detector description and simulation tool.” CERN, Geneva. Software homepage at <http://wwwasd.web.cern.ch/wwwasd/geant/>.
- [71] GELLRICH, A., “Kumac,” 2001. <http://www-hera-b.desy.de/subgroup/software/arte/KUMAC.html>.
- [72] GIACOBBE, B., “The HERA-*B* electromagnetic calorimeter,” 2004. Proceedings of the “9th Topical Seminar on Innovative Particle and Radiation Detectors”, 23–26 May 2004, Siena, Italy, to be published in Nucl.Phys.B (Proc.Suppl.). Text available at <http://www.bo.infn.it/sminiato/sm04/paper/bg/giacobbe.proc02.ps.gz>.

- [73] GIACOBBE, B., GIOVANNINI, P., MASCIOCCHI, S., MEVIUS, M., ZUR NEDDEN, M., VASSILIEV, I., VILLA, M., and WAHLBERG, H. P., “A new measurement of the $b\bar{b}$ production cross section at HERA-B,” *HERA-B internal note*, no. HERA-B 04-036, 2004.
- [74] GLASHOW, S. L., ILIOPOULOS, J., and MAIANI, L., “Weak interactions with lepton-hadron symmetry,” *Physical Review D*, vol. 2, p. 1285, 1970.
- [75] GOLDHABER, M., GRODZINS, L., and SUNYAR, A. W., “Helicity of neutrinos,” *Physics Review*, vol. 109, pp. 1015–1017, 1958.
- [76] GORIŠEK, A., *Cross section measurement of D^0 and D^{*+} meson production in inelastic collisions of 920 GeV protons with nuclei*. PhD thesis, University of Ljubljana, 2002.
- [77] GRADL, W. and OTHERS, “The HERA-B analysis software BEE,” 2003. <http://www-hera-b.desy.de/subgroup/software/clue/>.
- [78] GREINER, W., *Quantum Mechanics – An introduction*. Springer, third ed., 1994.
- [79] GREINER, W. and MÜLLER, B., *Gauge theory of weak interactions*. Springer, third ed., 2000.
- [80] GREINER, W. and REINHARDT, J., *Field Quantization*. Springer, 1996.
- [81] HAGIWARA, H. and OTHERS, “Review of particle physics,” *Physical Review D*, vol. 66, no. 1-I, pp. 010001+, 2002.
- [82] HALZEN, F. and MARTIN, A. D., *Quarks and leptons: an introductory course in modern particle physics*. John Wiley & Sons, 1984.
- [83] HARTOUNI, E. and OTHERS, *HERA-B: An Experiment to Study CP Violation in the B System Using an Internal Target at the HERA Proton Ring – Design Report*, 1995.
- [84] HERNÁNDEZ, J. M., “The TCP-based rpm_tflood/rpm_tfloodme protocol,” 2001.
- [85] HERNÁNDEZ, J. M., “HERA-B online computing infrastructure,” 2003. http://www-hera-b.desy.de/subgroup/online_cluster/online-computing-infrastructure.ps.
- [86] HERNÁNDEZ, J. M., RESSING, D., RYBNIKOV, V., SÁNCHEZ, F., AMORIM, A., and MEDINNIS, M., “HERA-B online calibration and alignment system,” Preprint: hep-ex/0409042. Submitted to Elsevier Science.
- [87] HOWE, D., “FOLDDOC: Free online dictionary of computing.” <http://foldoc.doc.ic.ac.uk/foldoc/>. Website supported by the Imperial College Department of Computing, Imperial College London.
- [88] HUET, P. and SATHER, E., “Electroweak baryogenesis and standard model $\hat{C}\hat{P}$ violation,” *Physical Review D*, vol. 51, p. 379, 1995.

- [89] HULSBERGEN, W. D., *A study of track reconstruction and massive dielectron production in HERA-B*. PhD thesis, University of Amsterdam, 2002.
- [90] HUSEMANN, U., “The Monte Carlo simulation chain from a user’s point of view,” *HERA-B mini-week*, 2003.
http://www.hep.physik.uni-siegen.de/herab/docs/husemann_20030318.pdf.
- [91] IGONKINA, O., “MARPLE version 1.03,” *HERA-B internal note*, no. HERA-B 98-129, 1998.
- [92] IGONKINA, O., “A manual on MARPLE package for HERA-B reconstruction program,” 2001.
<http://www-hera-b.desy.de/subgroup/software/arte/MARPLE/index.html>.
- [93] IVARSSON, J., “Reconstruction efficiencies for the golden decay,” *HERA-B internal note*, no. HERA-B 99-105, 1999.
- [94] KADALOV, A. B. and VYSOTSKY, M. I., eds., *Proceedings of the XXVth ITEP Winterschoold of Physics, Moscow, Feb. 18–27*, vol. 3, 1998.
<http://itepws.itep.ru/school97/School.html>.
- [95] KALMAN, R. E., “A new approach to linear filtering and prediction problems,” *Transactions of the American Society of Mechanical Engineers’ (ASME) Journal of Basic Engineering*, vol. 82, pp. 35–45, 1960.
- [96] KIHM, T., “MIZZI computer software,” 1995. Mannheim, Germany.
<http://www-hera-b.desy.de/subgroup/software/database/newsite/mizzi.html>.
- [97] KISEL, I. and MASCIOCCHI, S., “CATS: A cellular automaton for tracking in silicon for the HERA-B vertex detector,” *HERA-B internal note*, no. HERA-B 99-242, 1999.
- [98] KLINKBY, E. B., *$\Lambda/\bar{\Lambda}$ polarisation studies in proton nucleus collisions at 920 GeV proton beam energy*. PhD thesis, University of Copenhagen, 2004.
- [99] KNÖPFLE, K. T. and OTHERS, “Performance of the HERA-B Vertex Detector System,” *Nuclear Instruments and Methods in Physics Research*, vol. A501, pp. 39–48, 2003.
- [100] KOBAYASHI, M. and MASKAWA, T., “CP violation in the renormalizable theory of weak interaction,” *Progress of Theoretical Physics*, vol. 49, pp. 652–657, 1973.
- [101] KOLB, E. K. and TURNER, M. S., *The Early Universe*. Westview Press, 1994.
- [102] LABUDDA, A., *The proton LINAC control as part of the DESY accelerator chains control system*, 1999.
http://desyntwww.desy.de/mst/mst_home/Mst_content/LINAC3_control_system_1999.pdf.
- [103] LANYOV, A., “Introduction to ARTE tables,” 2000. Talk held at the HERA-B Dubna group meeting. Transparencies available at <http://mars.fis.uc.pt/hera-b/doc/arte.ps>.

-
- [104] LEE, T. D. and YANG, C.-N., “Question of parity conservation in weak interactions,” *Physical Review*, vol. 104, pp. 254–258, 1956.
- [105] LOEHR, B., WEISSENRIEDER, S., BARREIRO, F., and ROS, E., “An electromagnetic calorimeter with wavelength shifting fiber readout,” *Nuclear Instruments and Methods in Physics Research*, vol. A254, pp. 26–34, 1987.
- [106] LOHSE, T., “Vertex reconstruction and fitting,” *HERA-B internal note*, no. HERA-B 95-013, 1995.
- [107] LOHSE, T., “Wire target geometry and tagging performance,” *HERA-B internal note*, no. HERA-B 97-085, 1997.
- [108] LOHSE, T. and OTHERS, *HERA-B: An Experiment to Study CP Violation in the B System Using an Internal Target at the HERA Proton Ring – Proposal*, 1994.
- [109] LÜDERS, G. *Ann. Phys. (NY)*, vol. 2, p. 1, 1957. See also *Kgl. Danske Videnskab. Selskab Mat.-Fys. Medd.*, vol. 28, no. 5, 1954.
- [110] MANKEL, R., “Application of the Kalman filter technique in the HERA-B track reconstruction,” *HERA-B internal note*, no. HERA-B 95-239, 1995.
- [111] MANKEL, R., “PRISM – the HERA-B event display and its Tcl/Tk user interface (version 4.9),” 1997.
<http://www-hera-b.desy.de/subgroup/software/arte/prism/prism.html>.
- [112] MANKEL, R., “RANGER – a pattern recognition algorithm for the HERA-B main tracking system. Part I: the HERA-B pattern tracker,” *HERA-B internal note*, no. HERA-B 97-082, 1997.
- [113] MANKEL, R., “RANGER – a pattern recognition algorithm for the HERA-B main tracking system. Part IV: the object-oriented track fit,” *HERA-B internal note*, no. HERA-B 98-079, 1998.
- [114] MANKEL, R. and SPIRIDINOV, A., “RANGER – a pattern recognition algorithm for the HERA-B main tracking system. Part II: the HERA-B magnet tracker,” *HERA-B internal note*, no. HERA-B 98-154, 1998.
- [115] MANKEL, R. and SPIRIDINOV, A., “RANGER – a pattern recognition algorithm for the HERA-B main tracking system. Part III: tracking in the trigger chambers,” *HERA-B internal note*, no. HERA-B 98-206, 1998.
- [116] MANKEL, R. and SPIRIDINOV, A., “RANGER – a pattern recognition algorithm for the HERA-B main tracking system. Part V: compatibility analysis,” *HERA-B internal note*, no. HERA-B 99-111, 1999.
- [117] MARTIN, B. R. and SHAW, G., *Particle Physics*. John Wiley & Sons, second ed., 1999.
- [118] MARUYAMA, R., ROMALIS, M., ANDALKAR, A., and FORTSON, N., “Trapping ytterbium atoms for an EDM experiment,” 1999.
<http://www.phys.washington.edu/~reinam/GX/GX.html>.

- [119] MASCIOCCHI, S. Presented at HERA-B meeting of May 14th, 2003.
- [120] MATHER, J. C., FIXSEN, D. J., SHAFER, R. A., MOSIER, C., and WILKINSON, D., “Calibrator design for the *COBE* far-infrared absolute spectrophotometer (FIRAS),” *Astrophysical Journal*, vol. 512, pp. 511–520, 1999.
- [121] MUÍÑO, P. C., *Measurement of the ratio between the D^+ and the D^0 production cross section using an impact parameter method*. PhD thesis, University of Santiago de Compostela, 2002.
- [122] MUÍÑO, P. C., 2003. Private communication.
- [123] “The MySQL home page.” <http://www.mysql.com/>.
- [124] NÖRENBERG, M., *Tracking efficiency of the HERA-B First Level Trigger in the Single Lepton mode*. PhD thesis, University of Hamburg, 2002.
- [125] OUSTERHOUT, J. K., *Tcl and the Tk toolkit*. Addison–Wesley, 1994.
- [126] PAULI, W. and WEISSKOPF, V. F. *Helvetica Physica Acta*, vol. 7, p. 709, 1934.
- [127] “Physics analysis workstation PAW.” <http://wwasd.web.cern.ch/wwasd/paw/>.
- [128] PERKINS, D. H., *Introduction to high energy physics*. Cambridge University Press, 2000.
- [129] PESTOTNIK, R., *Identification of pions, kaons and protons in the HERA-B spectrometer*. PhD thesis, University of Ljubljana, 2001.
- [130] PESTOTNIK, R., “RITER: Iterative algorithm for PID in the HERA-B RICH,” 2001.
<http://www-hera-b.desy.de/subgroup/detector/rich/riter/>.
- [131] PETERSEN, B. A., *Beauty production at HERA-B: performance of the Second Level Trigger and the $b\bar{b}$ cross section in 920GeV pN collisions*. PhD thesis, University of Copenhagen, 2002.
- [132] PI, H., “An event generator for interactions between hadrons and nuclei – FRITIOF version 7.0,” 1992. Source code available at <http://www.thep.lu.se/ftp/pub/LundPrograms/Fritiof/>.
- [133] “PYTHIA and JETSET webpage.”
<http://www.thep.lu.se/~torbjorn/Pythia.html>.
- [134] RIOTTO, A., “Theories of baryogenesis,” 1998. Preprint: hep-ph/9807454.
- [135] RYBNIKOV, V., “The HERA-B message handler interface with POSIX threads,” 2001.
- [136] SAKHAROV, A., “Violation of CP invariance, C asymmetry, and baryon asymmetry of the universe,” *Soviet Physics Uspekhi*, vol. 34, pp. 392–393, 1991. Reprint of *JETP* 5 (1967) 24–27.

- [137] SAMTLEBEN, D., “Studies for a charge tag at HERA-B,” *HERA-B internal note*, no. HERA-B 98-080, 1998.
- [138] SAVELIEV, V., “The HERA-B transition radiation detector,” *Nuclear Instruments and Methods in Physics Research*, vol. A408, pp. 289–295, 1998.
- [139] SCHMIDT, B., “The HERA-B run statistics,” 2003.
<http://www-hera-b.desy.de/subgroup/shiftinfo/runstats/stats-man.html>.
- [140] SCHWANKE, U., *Trigger and reconstruction farms in the HERA-B experiment and algorithms for a Third Level Trigger*. PhD thesis, Humboldt University of Berlin, 2000.
- [141] SHAPOSHNIKOV, M. *JETP Letters*, vol. 44, p. 445, 1986.
- [142] SILVA, L., “Medida da secção eficaz de produção de pares $b\bar{b}$ em decaimentos semileptónicos de hádrões B em colisões de prótons em alvo fixo,” Master’s thesis, Universidade Técnica de Lisboa, 2004. In Portuguese.
- [143] SJÖSTRAND, T., “PYTHIA 5.7 and JETSET 7.4 physics and manual,” *Computer Physics Communications*, vol. 82, pp. 74–89, 1994. Preprint: hep-ph/9508391.
- [144] SPERGEL, D. N. and OTHERS, “First-year Wilkinson Microwave Anisotropy Probe (WMAP) observations: Determination of cosmological parameters,” *Astrophysical Journal Supplement*, no. 148, p. 175, 2003.
- [145] SPIRIDONOV, A., “Momentum and angular resolution in the HERA-B detector,” *HERA-B internal note*, no. HERA-B 02-069, 2002.
- [146] STEINBECK, S., “HERA-B muon detector software,” 1997.
<http://www-hera-b.desy.de/subgroup/software/muon/welcome.html>.
- [147] STÜCKELBERG, E. C. G., “Un nouveau modele de l’electron ponctuel en theorie classique,” *Helvetica Physica Acta*, vol. 14, p. 322, 1941.
- [148] ’T HOOFT, G. *Physical Review Letters*, vol. 37, pp. 8–12, 1976.
- [149] TOFFOLI, T. and MARGOLUS, N., *Cellular Automata Machines: A New Environment for Modelling*. MIT Press, 1987.
- [150] VAGNONI, V., “LEDA,” 1998.
<http://www-hera-b.desy.de/subgroup/software/database/newsite/leda.html>.
- [151] VILLA, M., “Progress report of the ECAL reconstruction software,” *HERA-B internal note*, no. HERA-B 97-135, 1997.
- [152] VILLA, M., “ECAL analysis status update,” *HERA-B internal note*, no. HERA-B 99-138, 1999.
- [153] VILLA, M., “Physics highlights from HERA-B,” 2004. Presented on the 57th PRC open session, DESY Hamburg.

-
- [154] WAGNER, G., *Aufbau und Test der mit Digitalen-Signal-Prozessoren realisierten Komponenten des Datennahmesystems von HERA-B*. PhD thesis, University of Hamburg, 2000.
- [155] WAGNER, W., “The HERA-B vertex detector: first results from detector commissioning,” *HERA-B internal note*, no. HERA-B 99-232, 1999.
- [156] WIGNER, E., “Über die Erhaltungssätze in der Quantenmechanik (On the Conservation Laws of Quantum Mechanics),” *Nachrichten von der Gesellschaft der Wissenschaften zu Göttingen*, p. 375, 1927.
- [157] WIKIPEDIA, “Positron — Wikipedia, the free encyclopedia,” 2005. [Online; accessed 22-Feb-2005].
- [158] WOLFENSTEIN, L., “Parametrization of the Kobayashi-Maskawa matrix,” *Physical Review Letters*, vol. 51, p. 1945, 1983.
- [159] WU, C.-S., AMBLER, E., HAYWARD, R. W., and OTHERS, “Experimental test of parity conservation in beta decay,” *Physical Review*, vol. 105, pp. 1413–1415, 1958.
- [160] ZANARINI, P., “KUIP: the user interface of PAW,” in *8th European Summer School on Computing Techniques: Man-Machine Interface in Scientific Environment (Proceedings)* (NADRCHAL, J., ed.), vol. 61, pp. 103–114, 1989. Skalsky Dvur, Czechoslovakia.
- [161] ZIMMERMANN, R., *Zeitmeßelektronik für den HERA-B-detektor*. PhD thesis, University of Rostock, 1999.
- [162] ŽIVKO, T., “B meson tagging and identification with the HERA-B RICH,” *Journal of High Energy Physics*, 1999. Prepared for the 8th International Symposium on Heavy Flavour Physics, Southampton, UK, July 1999.
- [163] ZUMINO, B. and LÜDERS, G. *Physical Review*, vol. 106, pp. 385–386, 1957.